

The Influence Of Cooling Rate On The Microstructure Of Stainless Steel Alloys

by

John Walter Elmer

B.Sc. METALLURGY, COLORADO SCHOOL OF MINES (1979)
M.Sc. METALLURGY, COLORADO SCHOOL OF MINES (1981)

SUBMITTED TO THE DEPARTMENT OF
MATERIALS SCIENCE AND ENGINEERING IN PARTIAL
FULFILLMENT OF THE REQUIREMENTS FOR THE DEGREE OF

DOCTOR OF SCIENCE in METALLURGY
at the
MASSACHUSETTS INSTITUTE OF TECHNOLOGY

September 1988

© John Walter Elmer, 1988

The author hereby grants to MIT permission to reproduce
and to distribute copies of this thesis document in whole or in part.

Signature of Author.....
Department of Materials Science and Engineering
August 5, 1988

Certified by.....
Thomas W. Eagar
Thesis Supervisor

Certified and Accepted by.....
Vol. 1
MASSACHUSETTS INSTITUTE OF TECHNOLOGY
Samuel M. Allen, Thesis Co-supervisor and Chairman
Departmental Committee on Graduate Students

OCT 03 1988

The Influence Of Cooling Rate On The Microstructure Of Stainless Steel Alloys

by

JOHN W. ELMER

Submitted to the Department of Materials Science and Engineering
on August 5, 1988 in partial fulfillment of the requirements
for the Degree of Doctor of Science in Metallurgy

ABSTRACT

The emergence of high energy density welding, laser surface modification and rapid solidification as commonly used metallurgical processing techniques has greatly increased the range of cooling rates that can be accessed during the solidification of metals and alloys. The microstructures which develop during these rapid cooling conditions may be significantly different from those which develop during low cooling rate conditions as the result of access to new metastable phases with the additional kinetic limitations that accompany rapid solidification.

This investigation explores the influence of cooling rate on a series of seven ternary alloys which span the line of two-fold saturation in the Fe-Ni-Cr system. High speed electron beam surface melting was used to resolidify these alloys at scan speeds up to 5 m/s. The resulting cooling rates were estimated from dendrite arm spacing measurements and were confirmed by heat flow modeling to vary from 7×10^0 °C/s to 8×10^6 °C/s. The microstructures that developed from each solidification condition were examined using optical metallography, electron microprobe analysis, scanning electron microscopy and a vibrating sample magnetometer. These results were used to create diagrams to predict the primary mode of solidification, the ferrite content and the complex microstructural morphologies which develop as a function of interface velocity and composition.

Changes in the primary mode of solidification with increasing cooling rate were observed in alloys that lie close to the line of two-fold saturation. The thermodynamics and kinetics of solidification were used to explain these changes by showing how epitaxially grown metastable phases can dominate solidification at high cooling rates, without the necessity of postulating the nucleation of metastable phases within the melt. The influence of cooling rate on interface stability and solidification segregation was evaluated by calculating the solutal diffusional characteristics at the tip of columnar dendrites growing under steady state conditions. These calculations were used to predict the dendrite tip undercooling for each solidification condition and the results were used to evaluate the influence of cooling rate on the amount of second phase formation, the ferrite content, and the absence of second phases at high cooling rates.

The solid state transformation of ferrite during the cooling of the resolidified Fe-Ni-Cr alloys was shown to be analogous to the decomposition of austenite in Fe-C alloys. Parallels were drawn between these two systems which allowed a wealth of analysis performed on the Fe-C system to be applied to the Fe-Ni-Cr system. The influence of cooling rate on the nucleation and growth kinetics of austenite was then used to explain the conditions which are responsible for the formation of grain boundary allotriomorphs, Widmanstätten platelets, Widmanstätten needles and massive austenite grains in the resolidified electron beam melts.

Thesis Supervisor : Dr. Thomas W. Eagar, Professor of Materials Engineering

Thesis Co-Supervisor : Dr. Samuel M. Allen , Assoc. Professor of Physical Metallurgy

Table Of Contents

Title Page	1
Abstract	2
List of Figure Captions	7
List of Table Captions	14
Acknowledgments	16
Chapter 1	
<i>Introduction And Background</i>	19
1.1 Previous Investigations	20
1.1.1 Constitution and Microstructure of Stainless Steel Alloys	20
1.1.2 The Effect of Rapid Solidification on the Microstructure	28
1.2 Present Investigation	31
1.2.1 Objectives	31
1.2.2 Approach	33
Chapter 2	
<i>Materials And Experimental Procedures</i>	37
2.1 Materials	37
2.1.1 Fabrication of the High Purity Alloys	37
2.1.2 Arc Cast Buttons	40
2.1.3 Melt Spun Ribbons	41
2.2 Surface Melting and Resolidification	42
2.2.1 Weld Coupon Preparation	42
2.2.2 Electron Beam Surface Melting	43
2.3 Microstructural Characterization	46
2.3.1 Optical Metallography	46
2.3.2 Dendrite Arm Spacing Measurements	47
2.3.3 Ferrite Measurements	48
2.3.4 Electron Probe Microanalysis	49
2.3.5 X-ray Diffraction	51
2.4 Density Measurements	54
2.5 Isothermal Studies of the Ferrite to Austenite Transformation	55
Chapter 3	
<i>Measuring the Ferrite Content of Rapidly Solidified Stainless Steel Alloys</i>	56
3.1 Review of Conventional Ferrite Measurement Techniques	56
3.2 The Vibrating Sample Magnetometer Method	57

3.3 The Saturation Magnetization of Ferrite	60
3.3.1 Background	60
3.3.2 Fully Ferritic Specimens	63
3.3.3 Saturation Magnetization Results	66
3.4 Predicting the Composition of Residual Ferrite	68
3.5 Verification and Application of the VSM Method	73
3.5.1 Ferrite Content of the Arc Cast Alloys	73
3.5.2 Commercial Stainless Steel Alloys	80
3.6 Conclusions	81
Chapter 4	
<i>The Cooling Rate of Electron Beam Surface Melts</i>	82
4.1 The Shape of Electron Beam Melts	83
4.2 Dendrite Arm Spacing Calculations	83
4.3 Analytic Solution to the Heat Flow Equation	89
4.3.1 The Temperature Distribution Surrounding a Melt	89
4.3.2 Derivation of an Analytic Expression for the Cooling Rate	92
4.3.3 Estimating the Cooling Rate in the Liquid Pool	93
4.4 Finite Element Model	97
4.4.1 Assumptions and Boundary Conditions	97
4.4.2 Temperature Gradient and Cooling Rate Calculations	99
4.5 Comparison of the Models and Summary	104
4.6 Conclusions	107
Chapter 5	
<i>The Influence Of Cooling Rate On The Primary Mode Of Solidification And Microstructural Morphology</i>	108
5.1 The Primary Mode of Solidification	109
5.1.1 Results of the Solidification Experiments	109
5.1.2 Epitaxial Growth and Plane Front Solidification	121
5.2 Cellular/Dendritic Solidification and Competitive Growth	129
5.2.1 Primary Austenite Solidified Alloys	131
5.2.2 Primary Ferrite Solidified Alloys	132
5.2.3 Alloys That Change Solidification Mode With Cooling Rate	134
5.3 Microstructural Features of Resolidified Stainless Steel Alloys	136
5.3.1 Characterizing the Ferrite and Austenite Morphologies	136
5.3.2 The Combined Effects of Cooling Rate and Composition	144
5.4 Conclusions	147

Chapter 6

<i>The Influence Of Cooling Rate On The Residual Ferrite Content Of Stainless Steel Alloys</i>	149
6.1 The Ferrite Content at Slow Cooling Rates	150
6.1.1 Full Diffusional Equilibrium	150
6.1.2 The Arc Cast Buttons	153
6.2 The Ferrite Content of Electron Beam Surface Melts	159
6.2.1 Primary Austenite Solidified Alloys 1,2 and 3	160
6.2.2 Alloy 4	162
6.2.3 Alloy 5	164
6.2.4 Fully Ferritic Solidified Alloys 6 and 7	167
6.3 Summary and Conclusions	170

Chapter 7

<i>The Influence Of Cooling Rate On Solute Redistribution And Second Phase Formation</i>	173
7.1 Solidification Paths and Parameters in the Fe-Ni-Cr System	174
7.1.1 Solidification Paths	175
7.1.2 Pseudobinary Diagrams to Represent Solidification Behavior	178
7.2 Interface Stability	184
7.2.1 Growth Rate and Temperature Gradient	185
7.2.2 Dendrite Tip Characteristics	191
7.2.3 Cellular to Dendrite Transition	199
7.3 Solute Redistribution Models	201
7.3.1 The Scheil Approximation	202
7.3.2 Back-diffusion and Undercooling	204
7.3.3 Ternary Alloy Systems	206
7.3.4 The Influence of Solidification Velocity on the Partition Ratio	207
7.4 Calculations of Solute Redistribution in the Electron Beam Melts	208
7.4.1 Solute Redistribution and Second Phase Formation	208
7.4.2 Back-diffusion Effects	212
7.4.3 Dendrite Tip Undercooling and Second Phase Formation	214
7.5 Summary and Conclusions	222

Chapter 8

<i>The Influence Of Cooling Rate On The Solid State Transformation Of Ferrite</i>	224
8.1 Diffusion Controlled Growth	225
8.1.1 A First Order Approximation	225
8.1.2 Finite Difference Approach	230

8.2 The Massive Transformation	232
8.2.1 Microstructural Characteristics	232
8.2.2 Thermodynamics	234
8.2.3 Nucleation Kinetics	239
8.2.4 Growth Kinetics	242
8.2.5 Massive Austenite Summary	243
8.3 The Decomposition of Single Phase Ferrite	243
8.3.1 Morphological Classification	245
8.3.2 The Effect of Cooling Rate on Austenite Morphology	251
8.3.3 Nucleation and Growth Kinetics	252
8.4 Isothermal Transformation Experiments	255
8.5 Summary and Conclusions	261
Chapter 9	
<i>Summary, Conclusions and Future Work</i>	263
9.1 Summary	264
9.1.1 Experimental Results	264
9.1.2 Analysis and Modelling	265
9.2 Conclusions	267
9.3 Future Work	274
References	276
Appendices	287
Appendix A Derivation of the Cooling Rate Equation	287
Appendix B FEM Temperature Gradient and Cooling Rate Calculations	289
Appendix C Thermodynamically Calculated Isothermal Sections	328
Ferrite-Austenite-Liquid equilibrium	331
Ferrite-Liquid metastable equilibrium	346
Austenite-Liquid metastable equilibrium	350
Appendix D Finite Difference Model for Diffusional Growth	356
Appendix E Dendrite Tip Calculations	362
Appendix F The Composition Of Delta Ferrite	371
Appendix G The Geometry of Electron Beam Surface Melts	376
Appendix H Computer Programs	383
Dendrite Tip Characteristics	383
Characteristic Diffusion Distance	386
Biographical Sketch	388

List Of Figure Captions

Figure 1.1	Liquidus projection showing the Fe-Ni peritectic, Cr-Ni eutectic and melting point minimum along the line of two-fold saturation, after Rivilin et al, [1.32].	22
Figure 1.2	Thermodynamically calculated isothermal section at 1400°C. Tie lines are indicated in the two-phase fields. F-ferrite, A-austenite, L-liquid.	23
Figure 1.3	Isopleth through the Fe-Ni-Cr system at 59% Fe, after Rivilin et al, [1.32].	24
Figure 1.4	The Fe-Ni-Cr line of two-fold saturation and Cr/Ni ratio of 1.5 superimposed on the Schaeffler diagram.	27
Figure 1.5	Shifting of the 0% and 100% ferrite boundaries of the Schaeffler diagram at high cooling rates. Pulsed laser welds at 10 ⁵ °C, after Katayama et al, [1.43].	30
Figure 2.1	Compositions of the seven Fe-Ni-Cr alloys plotted on the 59% Fe isoplethal section.	38
Figure 2.2	Melt pool width, length and depth as a function of electron beam scan speed. All melts made at 100kV, 20mA, sharp focus.	45
Figure 2.3	X-Ray diffraction results for a) single phase ferrite, b) single phase austenite and c) duplex stainless steel alloys.	53
Figure 3.1	a) Schematic drawing of the vibrating sample magnetometer, after Cullity [3.21] and b) a typical M-H curve from a duplex stainless steel alloy.	59
Figure 3.2	Slater-Pauling curves showing the saturation magnetization for various binary alloy combinations, after Cullity [3.21].	61
Figure 3.3	Comparison between the ferrite solvus and the composition of residual delta ferrite for alloys with different nominal iron contents.	64
Figure 3.4	The ferrite+austenite two-phase field in the Fe-Ni-Cr system at 1300°C.	64
Figure 3.5	Saturation magnetization of the fully ferritic melt spun ribbons as a function of Cr + Ni content.	67
Figure 3.6	Thermodynamic calculations of the chromium content in ferrite as a function of temperature and iron content of the ferrite.	69
Figure 3.7	Thermodynamic calculations of the nickel content in ferrite as a function of temperature and iron content of the ferrite.	70
Figure 3.8	Thermodynamic calculations of the Cr/Ni ratio of ferrite as a function of temperature and iron content of the ferrite.	70

Figure 3.9	Thermodynamic calculations of the ratio between the Fe content of ferrite and the Fe content of austenite as a function of temperature and iron content of the ferrite.	72
Figure 3.10	Figures a through f show the microstructures of the arc-cast alloys 2 through 7 respectively. The ferrite content increases from Alloy 2 (5%) to Alloy 7 (35%).	74
Figure 3.11	M-H curves at room temperature for the seven arc-cast alloys are compared with M-H behavior of a fully ferritic melt-spun ribbon (F).	75
Figure 3.12	Comparison of the ferrite measurements made on the arc-cast alloys by the vibrating sample magnetometer, Magne-Gage and Quantitative Metallographic techniques.	79
Figure 4.1	Variations in the dendrite arm spacing. Figures a and b compare the variation for a given set of welding parameters (100mm/s) at the fusion boundary and at the center of the melt respectively. Figures c and d compare the largest dendrite spacings in the casting with the smallest spacings in the highest speed melt.	85
Figure 4.2	Primary and secondary dendrite arm spacing as a function of electron beam scan speed +/- one standard deviation error bars are indicated.	87
Figure 4.3	Cooling rate, based on dendrite arm spacing measurements, plotted versus the electron beam scan speed.	88
Figure 4.4	Coordinate system used to represent the electron beam surface melts.	90
Figure 4.5	a) Dimensions of the base plate and b) finite element mesh of an electron beam melt used to calculate cooling rates and temperature gradients at the melt pool boundary.	98
Figure 4.6	FEM calculations of a) the cooling rate and b) the temperature gradient in the 6.4 mm/s electron beam melt. X-axis and Y-axis dimensions are in inches.	102
Figure 4.7	FEM calculations of a) the cooling rate and b) the temperature gradient in the 25.4 mm/s electron beam melt. X-axis and Y-axis dimensions are in inches.	103
Figure 4.8	Schematic cross section of a resolidified zone indicating the locations where the analytic expression, FEM model and dendrite arm spacing measurements apply.	105
Figure 4.9	Comparison of the maximum cooling rate predicted by the analytic equation with the average cooling rate predicted by dendrite arm spacing measurements for the 6 E-B melts.	106

Figure 5.1	Primary austenite solidification mode microstructures. a) single phase austenite dendrites, b) single phase austenite cells, c) interdendritic ferrite and d) intercellular ferrite.	113
Figure 5.2	Single phase ferrite solidification microstructures. a) single phase ferrite no transformation, b) initial growth of Widmanstätten austenite platelets, c) grain boundary allotriomorphs and Widmanstätten platelets and d) planar surface of the platelets.	114
Figure 5.3	Primary ferrite solidification mode microstructures. a) ferrite located at the cell cores in intercellular austenite mode, b) vermicular structure of ferrite dendrites, c) lacy ferrite and d) blocky austenite.	115
Figure 5.4	Comparison of the microstructures formed by a) primary austenite with second-phase ferrite, and b) primary ferrite with second-phase austenite at equal levels of residual ferrite.	116
Figure 5.5	a) Transition from the AF mode of solidification in the center of micrograph to the FA mode of solidification on the rhs of the micrograph. Alloy 4, 6.3 mm/s. b) Fine spacing of ferrite platelets formed during the solid state transformation of ferrite. Alloy 5, 100 mm/s.	117
Figure 5.6	Scan speed (cooling rate) versus composition map of the four modes of solidification. Multiple data points refer to different modes observed within the same melt.	119
Figure 5.7	Schematic representation of the temperature distribution surrounding a melt-pool. Section B shows that the temperature gradient in the travel speed direction is zero at the point of maximum melt width.	122
Figure 5.8	Schematic representation of the three principal views of the melt pool. Locations of the various microstructural features are illustrated on the cross sectional view and the origin of the different solidification growth morphologies are indicated on the top and longitudinal views.	123
Figure 5.9	Epitaxial growth at the fusion line of melt 2 (25.4 mm/s) in a) Alloy 1, b) Alloy 4 and c) Alloy 7.	125
Figure 5.10	Protrusion of the higher melting point ferrite into the molten zone of a two-phase substrate when subjected to a linear temperature gradient at temperatures close to the melting point.	127
Figure 5.11	The single phase nature of high speed resolidified melts. 'a' and 'b' show single phase austenite growing from Alloys 1 and 7 while 'c' shows single phase ferrite growing from Alloy 7 at 2000 mm/s.	130

Figure 5.12	Epitaxial growth of austenite from the base metal substrate quickly modulates to AF the FA and F modes of solidification in the high Cr/Ni ratio alloys. a) shows Alloy 5 where the ferrite undergoes substantial transformation and b) shows Alloy 7 where transformation is prevented by its high Cr/Ni ratio.	133
Figure 5.13	The transformation from FA to AF modes of solidification in Alloy 4 as the scan speed is increased a) 6.3 mm/s, showing primary ferrite dendrites, b) 25 mm/s, showing a large region (~50 microns) of AF solidification at the melt boundary and c) 100 mm/s, the entire resolidified region solidifies in the AF mode.	135
Figure 5.14	Microstructural features of lacy ferrite along its three principal directions. The primary dendrite core and the secondary dendrite arms can clearly be distinguished.	142
Figure 5.15	Scan speed (cooling rate) versus composition map of the microstructural morphologies that result from solidification and solid state transformation of stainless steel alloys.	145
Figure 6.1	Location of the seven Fe-Ni-Cr alloys with respect to the ferrite solvus, austenite solvus and the line of two-fold saturation, after Rivilin et al, [1.32].	151
Figure 6.2	Location of the seven Fe-Ni-Cr alloys on the Schaeffler diagram.	154
Figure 6.3	Percent residual ferrite as a function of Cr/Ni ratio in arc-welds of typical 304 type stainless steel alloys.	156
Figure 6.4	Residual ferrite on the seven arc-cast alloys compared to the residual ferrite predicted by the Schaeffler diagram for 59 wt% Fe alloys. The solidification modes, as determined from the cast alloys, are indicated.	157
Figure 6.5	The measured ferrite content of A and AF solidified alloys 1, 2 and 3 as a function of electron beam scan speed.	161
Figure 6.6	The estimated trend of ferrite content in A and AF solidified alloys as a function of solidification rate. The amount of ferrite that solidifies and the residual ferrite, after solid state transformation, are indicated.	161
Figure 6.7	The measured ferrite content of Alloy 4 which changes its mode of solidification from FA to AF to A as the scan speed is increased.	163
Figure 6.8	The estimated trend of ferrite content for the FA solidification mode as a function of solidification rate. The amount of ferrite that solidifies and the residual ferrite, after solid state transformation, are indicated.	163

Figure 6.9	The measured ferrite content of Alloy 5 as a function of electron beam speed. Scan speeds where massive and Widmanstätten austenite form in the fully ferritic solidified regions are indicated.	166
Figure 6.10	The estimated trend of ferrite content in Alloy 5 as a function of scan speed. The amounts of ferrite that solidify and the residual ferrite, after solid state transformation, are indicated.	166
Figure 6.11	The measured ferrite contents of the fully ferritic solidified Alloys 6 and 7 as a function of electron beam scan speed.	168
Figure 6.12	The estimated trend of ferrite content in fully ferritic solidified alloys as a function of solidification rate. The amount of ferrite that solidifies and the residual ferrite, after solid state transformation, is indicated.	168
Figure 6.13	Summary of the estimated trends of the amount of ferrite that solidifies for each of the seven alloys, as a function of cooling rate.	170
Figure 6.14	Summary of the measured residual ferrite contents in the seven alloys as a function of electron beam scan speed.	171
Figure 7.1	Thermodynamically calculated isothermal section through the Fe-Ni-Cr ternary system at 1413°C showing the orientation of tie-lines in the two-phase regions at temperatures close to the solidification range of the seven alloys.	176
Figure 7.2	Solidification paths for Alloys 1 and 7 estimated from the linear extrapolation of the tie lines shown in Figure 7.1.	177
Figure 7.3	Solidification paths for Alloys 1 and 7 calculated by solidification segregation modeling.	178
Figure 7.4	Pseudobinary diagram along the solidification path of Alloy 1, based on thermodynamic calculations. The solidification behavior of primary austenite solidified alloys is represented for chromium contents up to 31.5 wt%.	180
Figure 7.5	Pseudobinary diagram along the solidification path of Alloy 7, based on Thermodynamic calculations. The solidification behavior of primary ferrite solidified alloys is represented for Ni contents up to 16.3 wt%.	181
Figure 7.6	The estimated solidification paths and the intersection of these paths with the line of two-fold saturation, for the seven Fe-Ni-Cr alloys.	183
Figure 7.7	Schematic representation of a surface melt showing the relationship between the travel speed, S, melt geometry and the interfacial velocity, R.	187

Figure 7.8	Average temperature gradient on the melt pool surface, $\bar{\tau}$, and the estimated temperature gradients in the liquid, τ_l , and solid, τ_s , at the L/S interface. FEM temperature gradient calculations are plotted for comparison.	190
Figure 7.9	Peclet number versus interface velocity calculations for a) Alloy 1 and b) Alloy 7.	196
Figure 7.10	Dendrite radius versus interface velocity calculations for a) Alloy 1 and b) Alloy 7.	197
Figure 7.11	Dendrite tip temperature versus interface velocity for a) Alloy 1 and b) Alloy 7.	198
Figure 7.12	Temperature gradient versus interface velocity comparing the calculated and measured transitions for planar, cellular and dendritic growth conditions.	200
Figure 7.13	Schematic drawing showing the solute redistribution predicted by the Scheil equation.	209
Figure 7.14	The fraction ferrite that solidifies from the eutectic liquid as a function of temperature along the line of two-fold saturation, based on thermodynamic calculations.	212
Figure 7.15	Results of the Scheil calculations showing the relative amounts of primary and second phase ferrite and primary and second phase austenite that solidifies from each of the seven alloys.	213
Figure 7.16	Schematic binary alloy phase diagram showing the shift in eutectic composition with undercooling below the eutectic temperature.	217
Figure 7.17	Results of the solidification segregation model showing the relative amounts of ferrite and austenite that solidify for the slow cooling rate cast condition. The solidification mode changes from primary austenite to primary ferrite between Alloys 3 and 4.	218
Figure 7.18	Results of the solidification segregation model showing the relative amounts of ferrite and austenite that solidify at intermediate cooling rates in E-beam melt No. 4. The calculations were made for both primary phases in Alloy 4.	219
Figure 7.19	Results of the solidification segregation model showing the relative amounts of ferrite and austenite that solidify at high cooling rates in electron beam melt No. 6. The primary mode of solidification changes from primary austenite to primary ferrite between Alloys 4 and 5	219
Figure 8.1	Illustration of a model to predict the percentage of ferrite in the microstructure that transforms for a given characteristic diffusion distance, L.	229

Figure 8.2	Color metallographic technique used to distinguish between the austenite which forms during solidification and the austenite which forms during transformation of ferrite. a) shows ferrite dendrites and b) shows ferrite cells, both from Alloy 4.	231
Figure 8.3	Comparison of a) single phase ferrite microstructure and b) massive austenite which transformed from single phase ferrite in Alloy 5.	235
Figure 8.4	Electron microprobe scan across an untransformed ferrite region, surrounded by massive austenite in Alloy 5. The results indicate the composition invariance of the massive transformation.	236
Figure 8.5	Thermodynamically calculated vertical section through the Fe-Ni-Cr diagram along a path that represents partitioning in the F+A two-phase field. Equivalent compositions of the seven alloys are indicated and the T_0 line in the F+A region was calculated at 1575 and 1650 K.	237
Figure 8.6	Gibbs free energy versus composition plots along the 58 wt% Fe isopleth. a) at 1300°C, b) at 1375°C.	238
Figure 8.7	Gibbs free energy versus composition plot along the 58 wt% Fe isopleth showing the volume free energy change for ferrite transforming to austenite in Alloy 5.	241
Figure 8.8	The influence of scan speed on the percentage of the melt which undergoes the massive transformation in Alloy 5. Massively transformed areas appear as white regions, the remainder of the melt transforms by Widmanstatten austenite formation. a) 6.3 mm/s, b) 25 mm/s, c) 100 mm/s and d) 500 mm/s.	244
Figure 8.9	a) Widmanstatten austenite sideplates growing from grain boundary allotriomorphs at intermediate cooling rates, b) Widmanstatten sideplates at low cooling rates and c) intragranular Widmanstatten plates in Alloy 7.	248
Figure 8.10	a) Primary Widmanstatten sideneedles growing from grain boundary allotriomorphs and b) intragranular Widmanstatten needles in the heat affected zone of Alloy 7.	249
Figure 8.11	Degenerate forms of Widmanstatten sideplates. a) faceting, b) and c) sympathetically nucleated sideplates and d) branching.	250
Figure 8.12	Comparison of the isothermal transformation kinetics of Alloys 6 and Alloy 7.	256
Figure 8.13	Johnson-Mehl-Avrami analysis of the transformation kinetics of a) Alloy 6 and b) Alloy 7.	258

List Of Table Captions

Table 1.1	Estimated cooling-rate ranges for various solidification processing techniques.	28
Table 2.1	Compositions of the seven alloys (wt. percent)	39
Table 2.2	Chemical composition at different processing stages (wt. %)	41
Table 2.3	Electron beam melt summary. All melts at 100 kV and 20 mA.	46
Table 2.4	Average width, depth and length of the six single-pass surface melts in mm.	46
Table 2.5	Average compositions (wt. percent) of the ferrite and austenite phases in the arc cast buttons.	51
Table 2.6	Summary of X-ray diffraction results	52
Table 2.7	Density measurements made on the base metal alloys 1-7 and on fully ferritic specimens of alloy 6 and 7.	55
Table 3.1	Nomenclature used to describe the magnetic measurements	58
Table 3.2	Compositions of the fully ferritic, melt spun, alloys	65
Table 3.3	Spontaneous magnetization of fully ferritic specimens.	66
Table 3.4	QTM ferrite measurements	73
Table 3.5	VSM measurements of σ_s and ferrite.	76
Table 3.6	Magne-Gage measurements and calculated ferrite contents.	78
Table 4.1	Cooling rates calculated from primary and secondary dendrite arm spacing measurements.	86
Table 4.2	Nomenclature used in chapter 4	91
Table 4.3	P_t , δ and k'_t for the six electron beam melts.	94
Table 4.4	Physical properties for stainless steel	95
Table 4.5	Maximum cooling rate in the liquid at the L/S interface.	95
Table 4.6	Welding parameters, physical dimensions and mesh properties for the two welds to be studied by FEM analysis.	100
Table 4.7	Comparison of the FEM and DAS estimations of the cooling	104
Table 5.1	Summary of the primary modes of solidification for the seven alloys at low, intermediate and high cooling rates	120
Table 5.2	Liquidus and solidus temperatures for ferrite and austenite	126
Table 5.3	The ferrite content in the 1 mm deep electron-beam surface treated zone and in the base metal substrate.	131

Table 5.4	Comparison of the terminology used to describe the different microstructural morphologies in stainless steel alloys.	137
Table 5.5	Description of the ferrite and austenite phases.	139
Table 5.6	The solidification mode, solidification sequence and solid-state transformation events responsible for the different microstructures.	146
Table 6.1	Equilibrium ferrite contents at the solidus and at 1000°C.	153
Table 6.2	Predicted and measured ferrite contents of the arc cast buttons	154
Table 7.1	Partition coefficients and the slope of the liquidus lines for primary ferrite and primary austenite solidified alloys.	182
Table 7.2	Nominal, eutectic and maximum solid compositions (wt.%).	183
Table 7.3	Weld pool dimensions and average interface velocity for each of the six electron beam surface melting conditions.	187
Table 7.4	Average temperature gradients during solidification of the 6 electron beam melts.	189
Table 7.5	Properties used to calculate the dendrite tip characteristics.	194
Table 7.6	Nomenclature used to describe solute redistribution	204
Table 7.7	The Scheil approximation of the primary, secondary, and total amount of ferrite and austenite in the seven alloys	211
Table 7.8	The Brody and Flemings back-diffusion parameter calculated for alloys 1 and 7 at each of the solidification conditions	214
Table 7.9	Comparison of the solutal undercooling calculated for the casting and two electron beam melts with the undercooling necessary for single phase solidification.	221
Table 8.1	Volume diffusion in BCC Ferrite	226
Table 8.2	Volume diffusion in FCC Austenite	226
Table 8.3	Characteristic diffusion distance and dendrite arm spacings.	228
Table 8.4	The amount of ferrite that transforms as a function of cooling rate.	230
Table 8.5	Percentage of massive and Widmanstätten austenite that forms in the fully ferritic solidified portions of the E-beam melts in Alloy 5.	243
Table 8.6	Results of the isothermal transformation experiments listing wt. fraction ferrite as a function of time.	259
Table 8.7	Coefficients for the Johnson-Mehl-Avrami equation.	260

Acknowledgments

Over the course of four years at MIT and through my affiliations with Lawrence Livermore National Laboratory, I have been introduced to many new ideas and have met many people that have helped to shape this work into its final form. I would like to express my gratitude to all of those who have contributed their time, encouragement and support of my efforts.

I would like to first acknowledge the guidance and direction given to me by Professor T. W. Eagar, thesis supervisor and friend. He gave me the opportunity to pursue my own ideas and allowed me the freedom to be creative, while at the same time maintaining my research on a productive path.

The invaluable contributions of my thesis committee members have not only helped to direct my research but also to guide my professional advancement. I am grateful to Professor S. M. Allen, who, as co-supervisor, guided me through the rigors of academic life at MIT and added valuable phase transformation expertise to my work. I consider myself fortunate to have had the opportunity to work with Professor M. Cohen and Professor M. C. Flemings. As members of my thesis committee, they gave me insight into the theories of solid-state phase transformations and solidification and provided many helpful suggestions to this thesis. It is through their acceptance of this work that gives me the greatest sense of accomplishment. I would like to also express my thanks to Dr. Y. Shiohara who taught me solidification theory and offered friendly assistance to my project, as if it were his own.

The congenial atmosphere provided by the Joining group in room 4-047 at MIT has helped to make these years a rewarding and memorable experience. We have been through many good times and have seen many changes together. I am thankful to Dr. C. Sorensen for assisting with computer-related tasks in the laboratory and to Dr. M. L. Lin for writing the FEM code that added so much to this work. Special recognition goes to Dr. M. A. Khan and the other members of the 4 W's for our "non-technical" discussions.

I am grateful for the assistance offered by the knowledgeable and skilled people at MIT and Lawrence Livermore National Laboratory. Firstly, I would like to express

my thanks to the welding and joining group at LLNL, especially to D. M. Hoffman and B. L. Olsen for assisting with the electron beam surface melting. I would also like to thank Professor W. H. Giedt for discussions about high energy density welding and heat flow, Dr. K. Mahin for initial discussions concerning a suitable thesis topic, H. Weiss for his encouragement and for his belief in my abilities and C. E. Witherell for his assistance with the alloy castings. In addition, I would like to acknowledge the skilled metallographic assistance offered by P. K. Ambalal, W. L. Bell and S. S. Digallonardo. Special thanks go to M. K. Kong for his generous contributions in generating the 3-Dimensional FEM meshes and to S. Cowan for her friendly and timely help in typing many of the chapters of this thesis.

Secondly, I would like to thank the people at MIT who have kindly provided their time to this project. Dr. R. C. O'Handley for reviewing the portions of this thesis that deal with the magnetic behavior of materials, Dr. Y. Hara for introducing me to the VSM, H. M. Lee for showing me how to use the Thermocalc programs, and the UROP students: Michele Sequeira and Andre McFayden for help with laboratory experiments.

I would like to sincerely thank Glenn, Karen and Sarah Campbell, and Teiichi and Sumiko Ando who have offered their house and home to me upon many occasions in the Boston area. I would also like to express my deepest gratitude to my parents and brother who have always supported my work with their love, encouragement and their faith in my abilities.

Finally, the author, grateful for her affection, understanding and help with many aspects of the preparation of this document, would like to dedicate this thesis to S. L. Curry.

To Sandra Lee Curry

CHAPTER 1

Introduction And Background

The integrity of stainless steel castings and welds is known to depend on the presence of delta ferrite in the microstructure. Traditional studies [1.1-1.12] have shown that ferrite contents on the order of 5 volume % will reduce susceptibility to solidification cracking, improve hot workability, and lower the amount of non-metallic inclusions in the alloy. Masumoto [1.3] has shown that these effects predominate when ferrite is the first solid to form from the liquid, and Brooks [1.12] has summarized the reasons for this behavior. Two beneficial properties of ferrite in stainless steels are the higher solubility of sulfur and phosphorus in ferrite than in austenite, and the irregular, crack-resistant, grain boundaries that form during multi-phase solidification. Therefore, primary ferrite solidification reduces the amount of low melting-point liquids, by dispersing S and P, and increases the crack propagation resistance of the microstructure.

Despite such desirable properties, ferrite is not always beneficial to the microstructure of stainless steel alloys. For example, in austenitic stainless steels, during prolonged exposure to high temperatures, ferrite can transform to sigma phase which is brittle [1.13]. The severity of the embrittlement depends on the degree of transformation and the amount of ferrite in the microstructure. For this reason alone, ferrite contents are often minimized, but there are even further disadvantages. Ferrite can reduce the corrosion resistance, [1.14,1.15] and it can reduce the low-temperature fracture toughness of austenitic stainless steels [1.16-1.18].

The beneficial effects of ferrite in some applications and the deleterious effects in others requires a good understanding of the conditions which lead to the formation of ferrite in the microstructure. Numerous investigations of the relationship between chemical composition and ferrite content have been made and are summarized by Olson [1.19]. These studies have led to the development of methods and diagrams to predict ferrite content [1.20-1.24], ferrite morphology [1.25,1.26], and the primary solidification mode [1.27,1.28]. However, these results are only valid for conventional castings and welds which solidify at low cooling rates.

Advances in rapid solidification processing and the use of high energy density welding for an increasing number of applications have emphasized the importance of cooling rate in the evolution of stainless steel microstructures. Recent investigations have concluded that the amount of ferrite and the primary mode of solidification can be significantly altered in pulsed laser beam welds, in electron beam welds, and in atomized droplets. These microstructural modifications cannot be predicted using the conventional methods and there have only been a few studies of the microstructure of stainless steels solidified at high cooling rates. This chapter begins with a review of the literature concerning the constitution of Fe-Ni-Cr alloys for low cooling rate and high cooling rate processes which revealed many areas that required further investigation and helped to direct the research efforts presented in this thesis.

1.1 Previous Investigations

1.1.1 Constitution and Microstructure of Stainless Steel Alloys

Austenitic stainless steels of the AISI 300 series designation have two primary constituent phases: austenite and ferrite. A third phase, martensite, can be induced to form in these alloys by low temperature mechanical deformation. However, the martensitic transformation will not be studied here, since this investigation is only concerned with the phases which develop during solidification. The austenite phase has a face-centered cubic structure and is paramagnetic. Austenite can form during solidification, or during the solid-state transformation of ferrite. Nickel, manganese, carbon, and nitrogen promote the formation of austenite during solidification, and the majority of the AISI 300 series stainless steels contain austenite in excess of 80 vol%.

The ferritic phase, delta ferrite, has a body-centered cubic structure and is ferromagnetic. Ferrite forms only during solidification and transforms to austenite at lower temperatures. Frequently the transformation is incomplete, leaving residual ferrite in the microstructure. This residual ferrite can be present in several different morphologies, depending on the chromium-to-nickel ratio of the alloy [1.25,1.26,1.29-1.31]. Chromium, silicon, molybdenum, and niobium promote the

formation of ferrite during solidification and provide it with stability at lower temperatures. The residual ferrite present in the microstructure is therefore a result of the ferrite which solidifies minus the amount that transforms as the alloy cools.

The single most important factor in the development of the microstructure of a given stainless steel alloy is the primary mode of solidification (PMS). The PMS can either be austenite or ferrite and is primarily a function of composition. The PMS defines the primary phase to solidify from the melt and it also defines the solidification morphology which determines the conditions for the subsequent solid state transformation. Chromium rich alloys tend to solidify as primary ferrite while nickel rich alloys tend to solidify as primary austenite. The compositional range for each mode can be predicted by the line of two-fold saturation in the Fe-Ni-Cr system.

Figure 1.1 shows that the line of two-fold saturation extends from the Fe-Ni peritectic at 4.7% Ni to the Cr-Ni eutectic at 49% Ni and has a melting point minimum at 49% Cr, 43% Ni [1.32]. Solidification of compositions that lie on the line of two-fold saturation occurs by a peritectic mechanism at high iron contents and by an eutectic mechanism at low iron contents. The ternary composition where the peritectic behavior changes to eutectic behavior has been reported by Schurmann [1.33] to be 9% Ni, 16% Cr, and 75% Fe. This transition from eutectic to peritectic behavior lies close to the composition of many of the 18-8 stainless steel alloys. Thermodynamic calculations of the Fe-Ni-Cr system have been performed (see Appendix C) to determine the location of the tie lines in the two-phase fields. Figure 1.2 shows an isothermal section at 1400°C and indicates that the segregation ratios for Ni and Cr in Fe vary considerably in the ferrite-liquid, austenite-liquid and ferrite-austenite phase fields. These results will be discussed in detail in the chapters to come.

Vertical sections through the Fe-Ni-Cr ternary system can be determined by experimental measurements or by thermodynamic calculations. These diagrams are useful in describing the solidification and solid state transformation behavior of stainless steels. The experimentally determined liquidus, solidus, and isothermal sections reported by Rivlin and Raynor [1.32] were used to construct a vertical section through the Fe-Ni-Cr system at a constant iron content of 60%. Figure 1.3 shows this constant iron diagram which has been reported by many investigators to represent the

solidification behavior of stainless steels. By comparing the tie-lines presented in Fig. 1.2 with a constant Fe isopleth, one sees that although the vertical section presented in Fig. 1.3 has an appearance similar to a binary phase diagram, the tie-lines in the two-phase fields do not necessarily lie in the plane of the vertical section. This is particularly true for the liquid-solid fields that determine the solidification segregation ratios. A more accurate representation of the solidification behavior can be determined by taking the vertical sections along a path that contains the tie-lines of interest. Chapter 7 presents the results of thermodynamic calculations which were used to determine the pseudobinary diagrams for primary ferrite and primary austenite solidification. These modified vertical sections are useful in determining the solidification parameters and the segregation of solute during solidification.

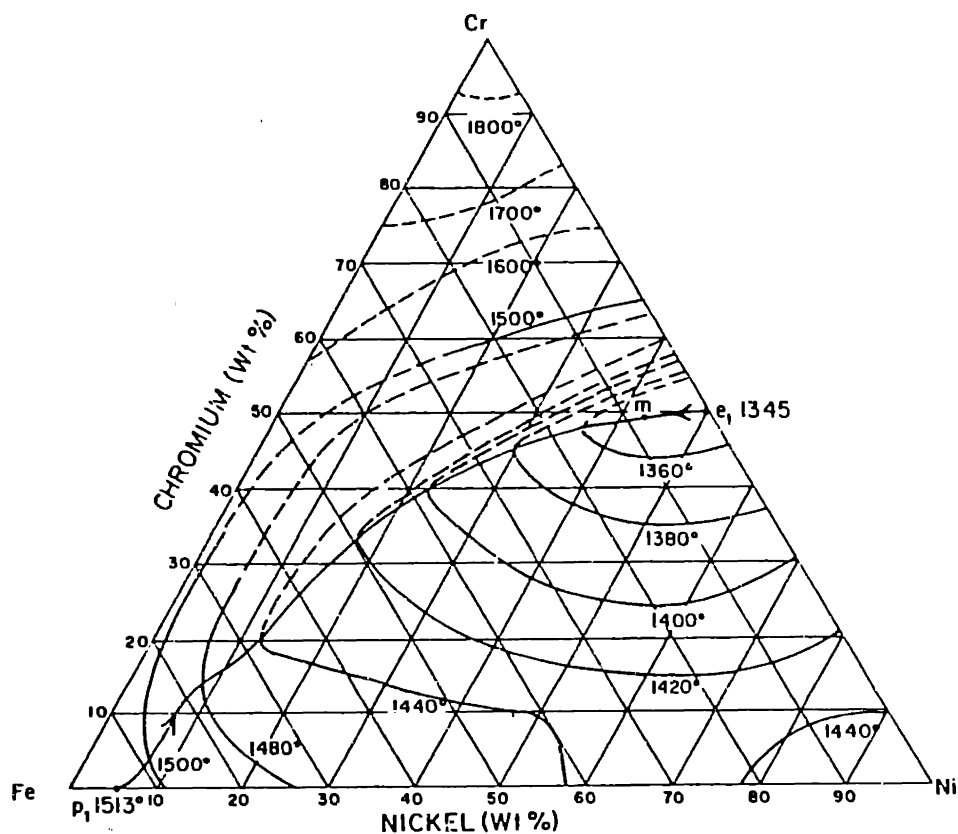


Figure 1.1 Liquidus projection showing the Fe-Ni peritectic, Cr-Ni eutectic and melting point minimum along the line of two-fold saturation, after Rivlin et al, [1.32].

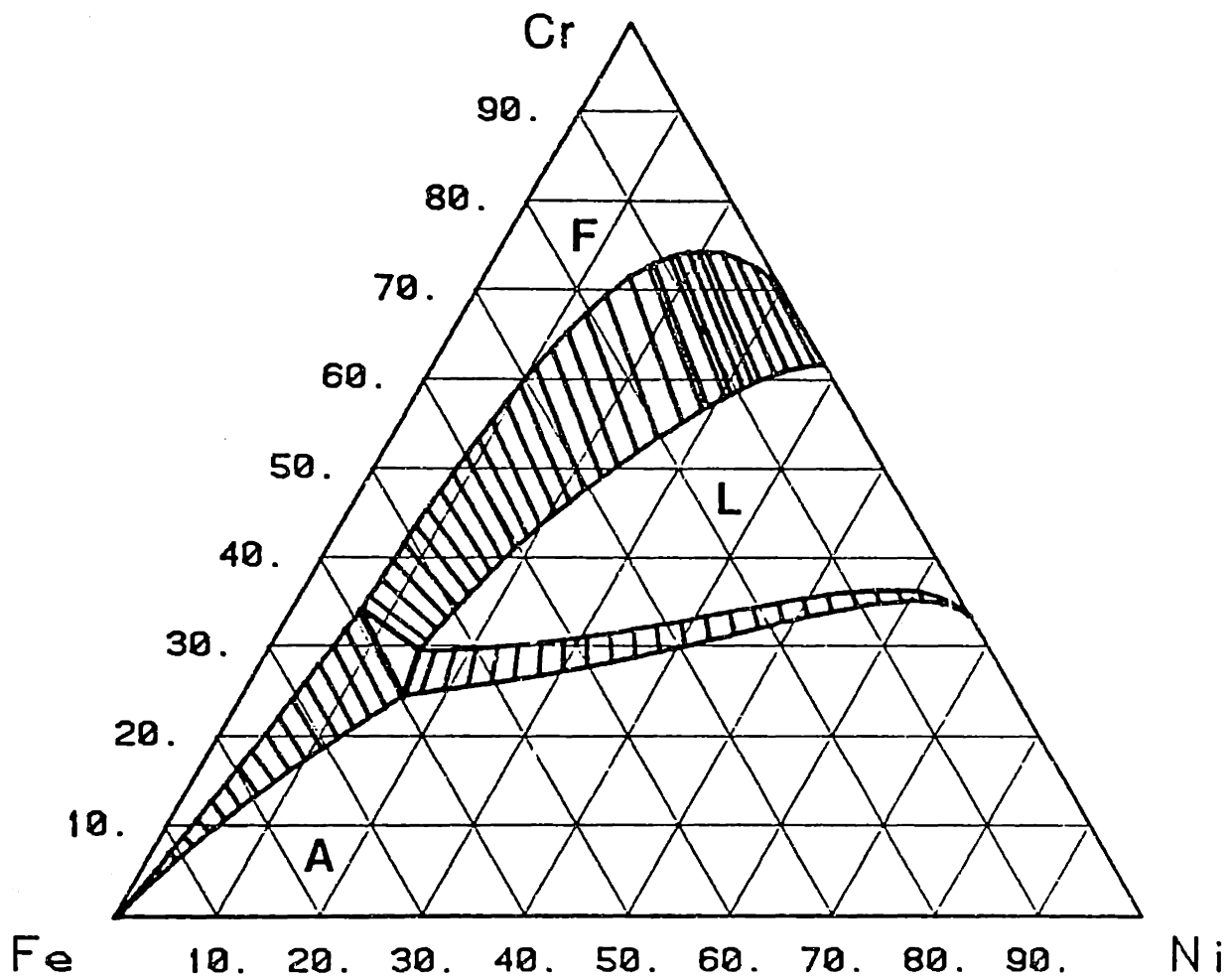


Figure 1.2 Thermodynamically calculated isothermal section at 1400°C. Tie lines are indicated in the two-phase fields.

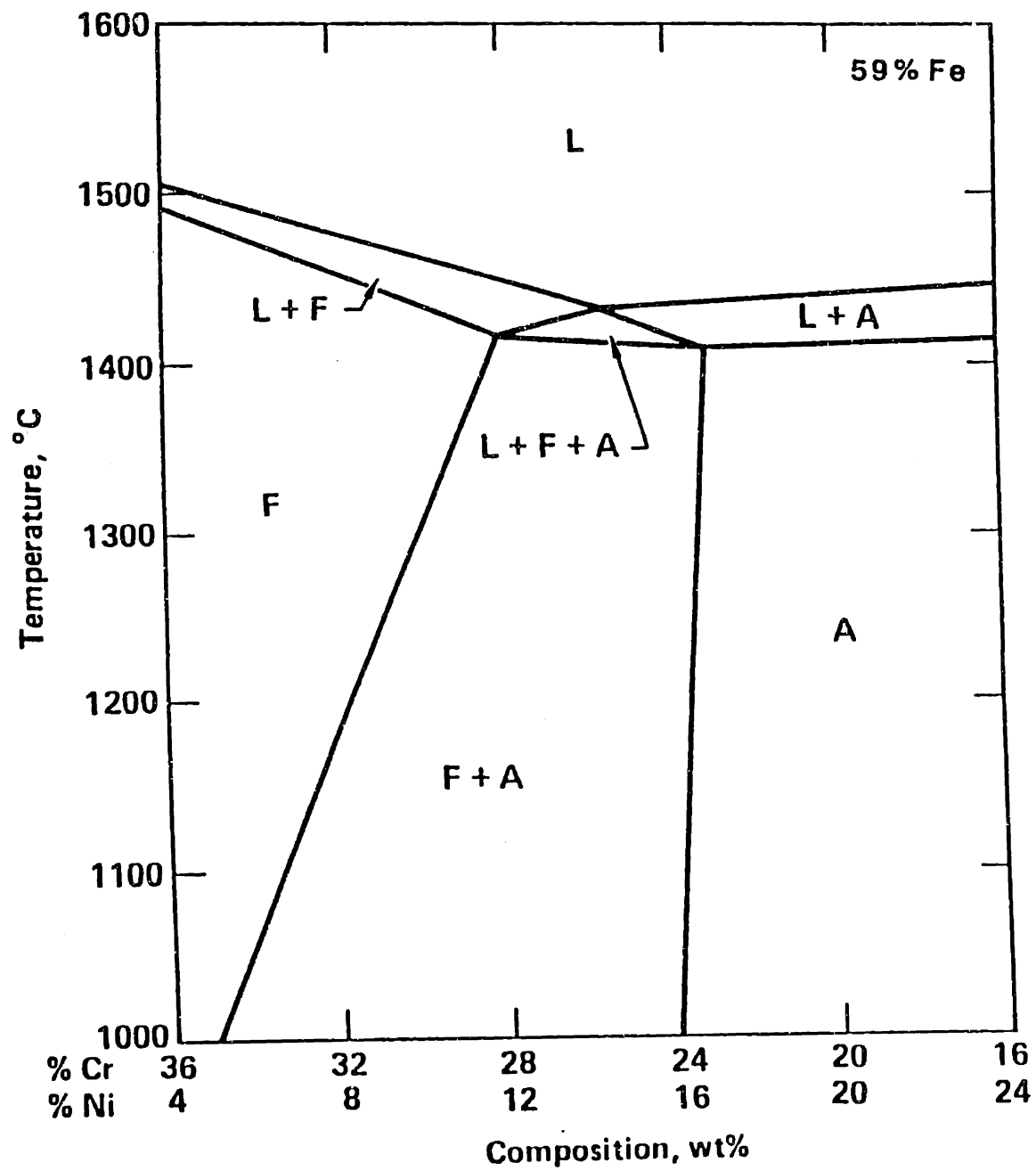


Figure 1.3 Isopleth through the Fe-Ni-Cr system at 59% Fe, after Rivilin et al, [1.32].

The line of two-fold saturation crosses the 60% Fe plane at a composition of 25.5% Cr and 14.5% Ni, which is a Cr/Ni ratio of 1.76. The maximum separation between the liquidus and solidus lines is about 50°C, and the slope of the liquidus is steeper for primary ferrite solidification than for the solidification of primary austenite. Under equilibrium conditions, five modes of solidification are possible depending on the composition of the alloy with respect to the line of two-fold saturation:

- F : Single-phase ferritic solidification. Ferrite solidifies as the primary and only solid phase. Austenite may nucleate and grow from grain boundaries or interdendritic boundaries at subsolidus temperatures.
- FA : Ferritic-austenitic solidification. Ferrite solidifies as the primary phase in a dendritic or cellular mode with second phase austenite forming at the cell walls. The second-phase austenite provides growth sites for the subsolidus austenite to ferrite transformation.
- E : Eutectic solidification. Ferrite and austenite both solidify from the eutectic liquid as conjugate solid phases. This reaction generally takes place after some primary solid phase has formed. The spacing of the eutectic microstructure is smaller than the primary phase spacing which makes the eutectic ferrite particularly susceptible to the solid state transformation.
- AF : Austenitic-ferritic solidification. Austenite solidifies as the primary phase in a dendritic or cellular mode with second-phase ferrite forming at the cell walls. The second-phase ferrite partially transforms to austenite at subsolidus temperatures.
- A : Single-phase austenite solidification. Austenite solidifies in a dendritic or cellular mode as the primary and only solid phase, segregation occurs to the cell walls but no ferrite is present in the microstructure.

Under the nonequilibrium conditions which occur during solidification, the same modes of solidification exist but some compositions may change mode with cooling

rate. Deviations from the equilibrium behavior become more pronounced as the cooling rate is increased and the cooling rate will be shown to have a significant effect on the solidification mode.

The amount of ferrite which solidifies from the melt is higher than the amount which is present at room temperature because ferrite transforms to austenite as the melt cools. Fig. 1.3 shows that the ferrite and austenite two-phase field shifts towards higher chromium contents at lower temperatures which reduces the stability of ferrite as the temperature decreases. The amount of ferrite which transforms depends on the composition and the cooling rate. Since isothermal sections through the Fe-Ni-Cr system are not available at room temperature and since welds cool under non-equilibrium conditions, other means have been developed for predicting the amount of ferrite in stainless steels.

Figure 1.4 shows the Schaeffler diagram which was published in 1949 [1.20,1.21] to predict the microstructure of conventional arc welds. This diagram is used to predict the amount of ferrite in stainless steel welds based on their nominal composition but does not incorporate cooling-rate effects. The chromium and nickel equivalents were developed by Schaeffler to account for the ferrite or austenite stabilizing effects of the alloying elements that are present in commercial stainless steels. These equivalents were revised in 1956 by DeLong [1.22] to incorporate the austenitizing effects of nitrogen, and are defined as follows:

$$\text{Ni equivalent} = \% \text{Ni} + 30 (\% \text{C} + \% \text{N}) + 0.5 \% \text{Mn} \quad (1.1)$$

$$\text{Cr equivalent} = \% \text{Cr} + \% \text{Mo} + 1.5 \% \text{Si} + 0.5 \% \text{Nb} \quad (1.2)$$

Modifications of the multiplication coefficients and the inclusion of other elements into the chromium and nickel-equivalent equations have been suggested by other authors [1.27,1.34-1.36], however, the DeLong equivalents are still the most frequently used equations.

Comparing the primary mode of solidification predicted by the phase diagram with the residual ferrite content predicted by the Schaeffler diagram is useful and can be done by superimposing the Fe-Ni-Cr line of two-fold saturation on the

Schaeffler diagram. This line separates primary ferrite solidification from primary austenite solidification for equilibrium conditions. Figure 1.4 shows that it varies around the 10% ferrite line, depending on the iron content of the alloy. Suutala [1.27,1.28] has proposed that the primary solidification phase can be predicted in welds by a Cr/Ni ratio of about 1.5; alloys with a higher Cr/Ni ratio than 1.5 will solidify as primary ferrite, while those lower than 1.5 will solidify as primary austenite. Suutala's Cr/Ni = 1.5 line is also shown on Fig. 1.4 and indicates that it is close to the line of two-fold saturation.

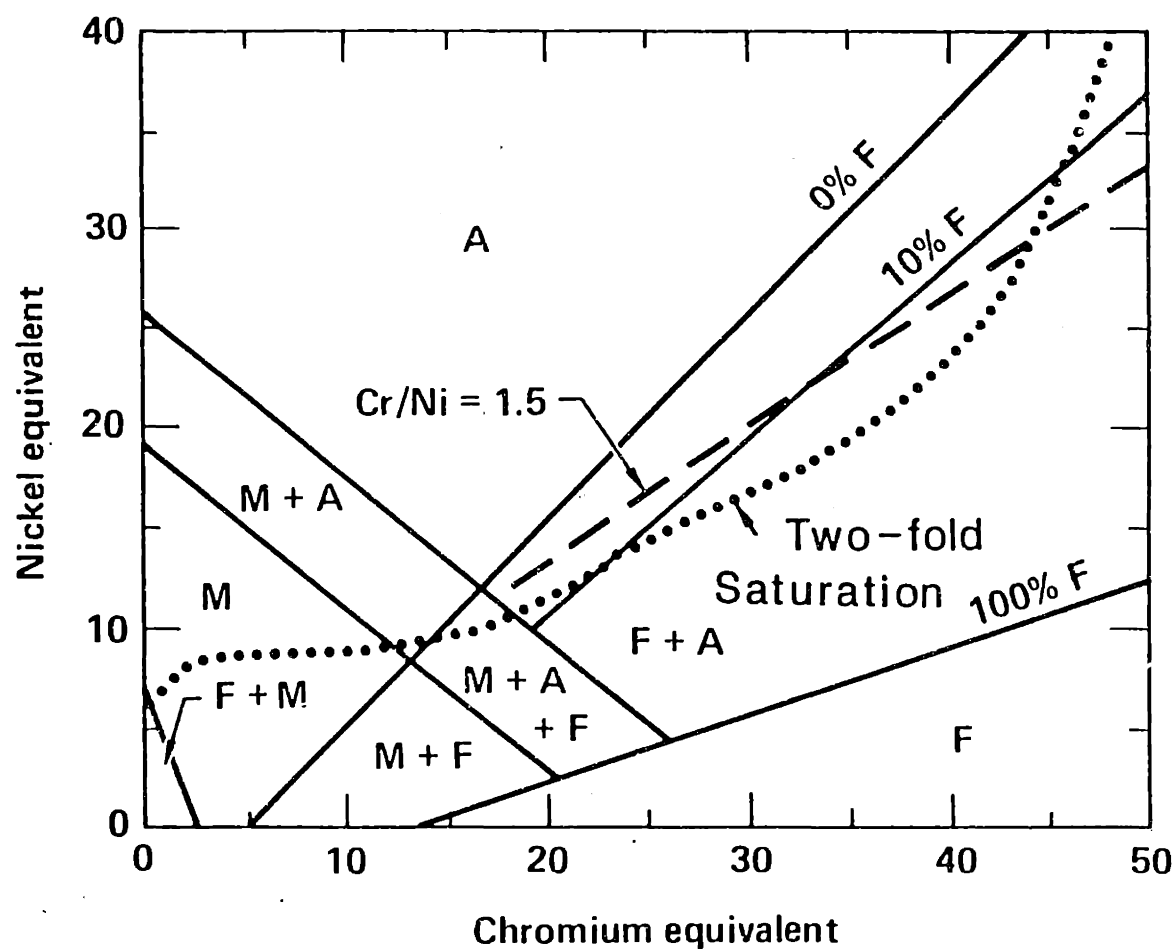


Figure 1.4 The Fe-Ni-Cr line of two-fold saturation and Cr/Ni ratio of 1.5 superimposed on the Schaeffler diagram.

Therefore, the primary mode of solidification and the amount of residual ferrite in stainless steel alloys can be predicted reasonably well at low cooling rates. However, at high cooling rates the empirically derived diagrams can not be used to predict ferrite contents, ferrite morphology or even the primary mode of solidification. The relatively recent emergence of rapid solidification processing and high energy density welding requires that a better understanding of the influence of cooling rate be developed in order to predict the effects of these processes on the microstructure of stainless steels.

1.1.2 The Effect of Rapid Solidification on the Microstructure

The influence of cooling rate on the microstructure of stainless steel alloys has been observed at low, medium and high cooling rates. However, the most dramatic effects occur at the high cooling rates produced by rapid solidification processing and high-energy density welding. The inherent variations in the cooling rate for different solidification processes are summarized in Table 1.1 and are shown to cover about 9 orders of magnitude.

Table 1.1: Estimated cooling-rate ranges for various solidification processing techniques.

Process	Cooling Rate (K/s)
Directional solidification	$10^{-1} - 10^1$
Casting	$10^0 - 10^2$
Arc welding	$10^1 - 10^3$
Electron beam welding	$10^2 - 10^4$
Laser beam welding	$10^2 - 10^6$
Rapid solidification processing	$10^3 - 10^7$
EB or LB surface modification	$10^5 - 10^7$
Single laser pulse	$10^7 - 10^8$

At the lowest cooling rates (10^{-1} to 10^1 °C/s) which occur in directional solidification or in large ingots, only small changes in the microstructure occur with variations in the cooling rate. Pereira [1.37] has shown that cooling-rate variations over the range of 2-40°/s will produce changes in the ferrite content: with increasing cooling rate, primary ferrite-solidified compositions will increase in ferrite content from 13 to 16%, while primary austenite-solidified compositions will decrease from 1.5 to 1.0%. Fredriksson [1.38] has also investigated the role of cooling rate on solidification mode and concludes that a cooling rate increase in the range of 10^0 to 10^{30} °/s favors the primary formation of ferrite.

Moderate cooling rates (10^1 to 10^{30} °/s), which are produced in arc welds, show only small changes in the microstructure as the cooling rate is increased. Suutala [1.28,1.39] has observed a gradual decrease in ferrite content as the weld travel speed is increased, and concludes that an increase in travel speed (which increases the cooling rate), favors the primary formation of austenite for dendritic solidification. DeLong [1.4] has also recognized the ability of the cooling rate to modify the microstructure of stainless steel welds and castings. He states that heat input has an effect on the ferrite number, but that this effect is only a minor consideration.

The high cooling rates which can occur in electron beam and laser beam welds significantly alter the microstructure. Vitek and David [1.40-1.42] have reported the changes in ferrite content associated with high cooling rates in a comparison of arc-welded and laser beam welded AISI 308 stainless steel. They reported a decrease in ferrite content from 10% to less than 1%, with a change from GTAW (low cooling rate) to LBW (high cooling rate) welding processes respectively. They believe that this behavior occurs because of a change in primary solidification mode from ferrite to austenite.

Katayama and Matsunawa [1.43] have also investigated the high cooling rate (10^5 to 10^{60} °/s) behavior of laser beam welded microstructures for about thirty different commercial AISI 300 series and high purity stainless steels. They conclude that the Schaeffler diagram requires modifications at high cooling rates, and they recommend a compression of the austenite-ferrite two-phase field as shown in Fig. 1.5. For high cooling rates their observations indicate that the ferrite content of low-ferrite welds is reduced while the ferrite content of high-ferrite welds is increased. Katayama and

Matsunawa attribute these two distinct behaviors to a change in primary solidification mode (from primary ferrite to primary austenite) in low ferrite content welds, and to a suppression of the solid-state transformation of ferrite in high ferrite content welds.

Changes in the solidification mode have also been observed at high cooling rates which can be induced in electron beam welds. Lippold [1.44] has examined the solidification conditions for a deep-penetration electron beam weld in 304L stainless steel and has shown that for certain conditions a change in the primary solidification mode occurs. Lippold concludes that welds which normally solidify as primary ferrite can solidify as primary austenite in the deep penetrating portion of the weld pool which has the highest cooling rate. These results support the observations of refs. 1.40-1.43 for laser beam welded stainless steel.

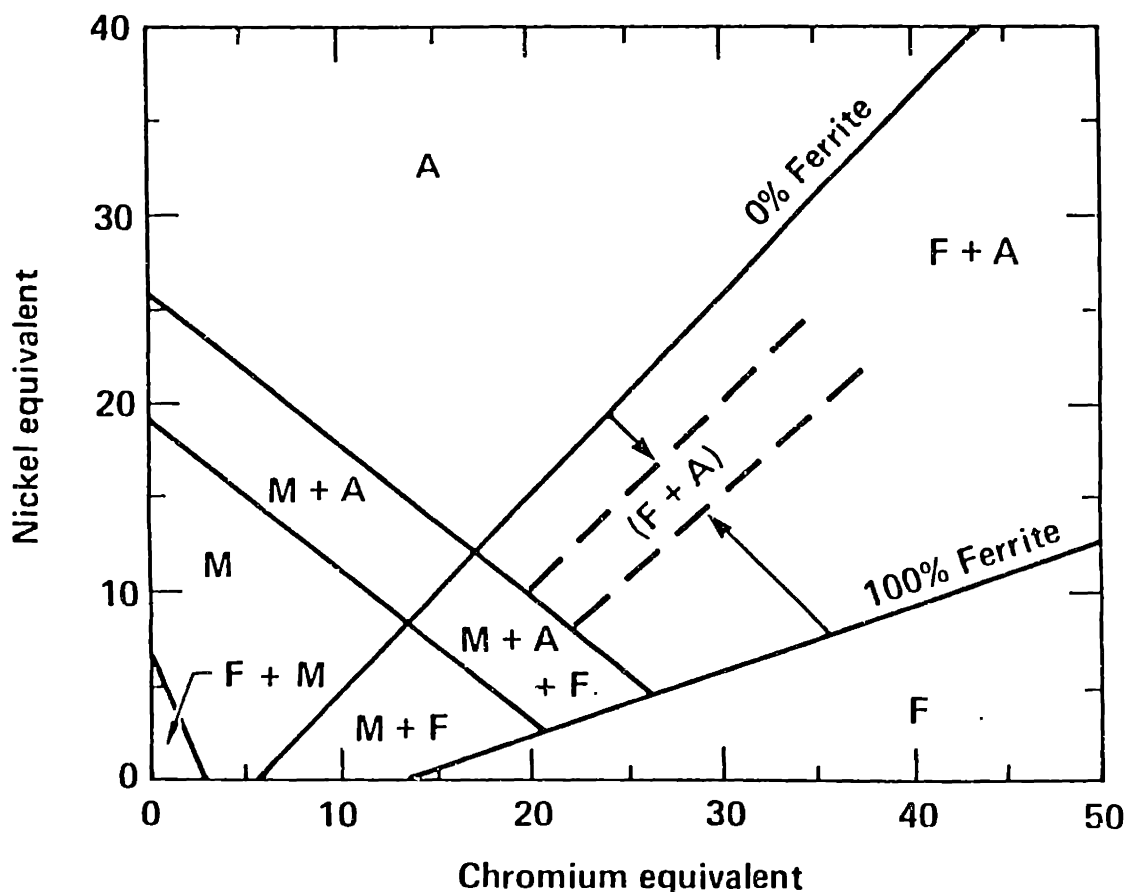


Figure 1.5 Shifting of the 0% and 100% ferrite boundaries of the Schaeffler diagram at high cooling rates. Pulsed laser welds at 10^{50}C , after Katayama et al, [1.43].

Changes in the primary solidification mode have been observed for rapidly solidified stainless steels. Kelly [1.45] has investigated microstructural and compositional variations that occur in atomized droplets of AISI 303 stainless steel, droplets which normally solidify with the formation of primary austenite. Such droplets achieve cooling rates on the order of 10^5C/s . Kelly's results show that, since the smallest droplets receive the largest thermal undercooling, ferrite preferentially nucleates in favor of austenite. He provides thermodynamic data and a kinetic model, which confirm the change in solidification mode for highly undercooled droplets. This work shows a preference for primary ferrite at high cooling rates while references 1.40-1.44 show a preference for primary austenite at high cooling rates. The apparent inconsistency is due to the difference in the nucleation behavior between homogeneously nucleated atomized droplets and heterogeneously nucleated welds.

In summary, the cooling rate plays a significant role in the evolution of stainless steel microstructure. Its influence can not be generalized and one must consider both the chemical composition and the solidification conditions of a given alloy. These two factors combine together in a complex way to influence 1) the primary solidification mode, 2) the amount of solidification segregation and 3) the nucleation and growth behavior of the ferrite to austenite solid-state transformation. These effects alter the ferrite content and ferrite morphology. However, a systematic investigation of the relative importance of these three effects in determining the microstructure has not been performed.

1.2 Present Investigation

1.2.1 Objectives

The purpose of this investigation was to study the microstructures which develop in Fe-Ni-Cr ternary alloys under rapid solidification conditions, with several objectives in mind. Firstly, the results of this study were to provide a basic understanding of the complex solidification and transformation behavior which occurs during the rapid resolidification of stainless steel alloys. Explaining this

behavior required solidification experiments to be performed on Fe-Ni-Cr ternary alloys and confirmation with rapid solidification theory. This type of analysis was used to predict the influence of cooling rate on the microstructure of stainless steel alloys and the basic concepts developed here can also be applied to other alloy systems that involve solidification and subsequent solid state transformation events.

Secondly, the experimental results will be used to create diagrams that can be used to predict the primary mode of solidification, the ferrite content and the ferrite morphology of stainless steels solidified over a large range of cooling rates. These diagrams can also be used to decouple the separate contributions of solidification mode, solidification segregation and the solid state transformation of ferrite on the resulting microstructure. These diagrams have practical significance in that they can predict the microstructures of stainless steel alloys which have been cast, welded or rapidly solidified at different cooling rates.

Thirdly, recent investigations [1.42,1.43] of high energy density welds and rapidly solidified melts have shown large differences between the microstructures which develop at high cooling rates and those which develop at low cooling rates. However, the theories that have been postulated to describe these differences have not yet been substantiated by a thorough scientific study. In particular, one author [1.40,1.42] believes that a change in the primary mode of solidification occurs by nucleation of metastable austenite in pulsed laser welds. A similar change in solidification mode is observed in electron beam surface melts, however, in the electron beam melts the amount of undercooling was shown to be 30°C or less. This undercooling is not large enough to explain the nucleation of metastable phases from within the melt and it was shown that the change in solidification mode can be explained by the preferential growth kinetics of the austenite phase at the melt periphery. Therefore, another objective of this study was to emphasize the importance of growth kinetics in rapidly solidified surface melts and to illustrate that the PMS may change at high cooling rates without necessity of postulating nucleation of metastable phases from the melt.

1.2.2 Approach

A series of Fe-Ni-Cr ternary alloys was made with systematic variations in composition. Seven alloys were cast from high purity elements, all having 0.59 % Fe but with different Cr/Ni ratios that ranged from 1.2 to 2.2. This variation in Cr/Ni ratio is representative of the general behavior of a wide range of stainless steel alloys. High purity alloys were selected in favor of commercial stainless steels so that the composition could be controlled in order to eliminate the effects of interstitial and other alloying element segregation.

Variations in the cooling rate were produced by an electron beam surface melting technique. The power level of the electron beam was held constant for all of the melts but the travel speed was varied from 6 mm/s to 5000 mm/s. This resulted in different cooling rates in the surface melted regions that varied from 4.7×10^2 °C/s for the slowest travel speed to 7.5×10^6 °C/s for the highest travel speed. All of the melts were compared to the arc-cast buttons which cooled at a rate of 7 °C/s. Electron beam surface melting was selected because the power input to the substrate can easily be characterized and because it can produce controlled speed surface melts at high velocities. A more detailed description of the materials, solidification experiments and other experimental procedures is presented in Chapter 2.

Chapter 3 describes a ferrite measurement technique that can be used to measure the ferrite content of rapidly solidified stainless steel alloys. This method is new and was developed as part of this investigation because the ferrite content of the rapidly cooled specimens could not be measured by conventional techniques. This method utilizes a Vibrating Sample Magnetometer to measure the saturation magnetization of an unknown specimen and by knowing the saturation magnetization of ferrite, the volume percent ferrite can be calculated. Since the ferrite content is related to the saturation magnetization of the specimen, this technique does not depend on the size, geometry or orientation of the specimen and can easily measure the ferrite content in the small volumes of material that are produced in rapid solidification processes. However, since the saturation magnetization of ferrite depends on the ferrite composition, a separate study was required to determine the composition of residual ferrite from the nominal alloy composition and to develop an empirical equation to

calculate the saturation magnetization of ferrite from its composition. The results of this study allow the Vibrating Sample Magnetometer to be calibrated so that the ferrite content of a wide range of stainless steel alloys can be measured.

Chapter 4 summarizes the methods used to estimate the cooling rate in the electron beam melts. Since the electron beam melts were small and were moving at high rates of speed, the temperature and cooling rates in these melts could not be measured by conventional techniques. Therefore, the cooling rates were estimated by 1) dendrite arm spacing measurements, 2) an analytic solution to the heat flow equation which was used to estimate the highest cooling rate in the surface melts and 3) a finite element model which was used to calculate thermal gradients and cooling rates at the liquid/solid interface for a few selected conditions. The three techniques agreed well with each other and showed that the cooling rates varied over 5 orders of magnitude. From the cooling rate measurements and the interface velocity, the average temperature gradient was also calculated in each melt. These temperature gradient calculations were confirmed using the FEM program and the results were used in later chapters to calculate interface stability and solute redistribution in the electron beam melts.

Chapter 5 summarizes the effects of cooling rate on the primary mode of solidification and the residual ferrite morphology for each of the seven alloys. The results of this chapter are based on the optical metallographic examination of the electron beam melts and are summarized in two diagrams. One diagram presents the primary mode of solidification as a function of cooling rate and composition while the second diagram presents the microstructural features which form from each mode of solidification. The first diagram describes the solidification behavior of stainless steel alloys while the second diagram describes the solid state transformation behavior as the melt cools to room temperature. From these diagrams, the mode of solidification and the ferrite morphology can be determined for a wide range of stainless steel alloys and for a wide range of solidification conditions. In addition to the predictive diagrams, the surface melts were studied to determine the method by which the primary solidification mode develops. These observations show that ferrite and austenite both grow epitaxially from the melt periphery. Microstructural examination of the high speed melts also showed that changes in solidification mode

which occur with increasing cooling rate are a result of the favorable growth kinetics of metastable austenite rather than the nucleation of metastable austenite from within the melt pool.

Chapter 6 investigates the influence of cooling rate on the ferrite content of the stainless steel alloys. The results of this chapter show that the ferrite content changes significantly with cooling rate and that the amount of residual ferrite in the microstructure depends on the primary mode of solidification, the Cr/Ni ratio of the alloy and the cooling rate. These observations confirm the earlier results [1.42-1.44] on laser beam and electron beam welded stainless steels at high cooling rates. In addition, these results show that the ferrite content decreases (or increases) in a continuous manner with cooling rate by studying intermediate cooling rates which had not been previously investigated.

Chapter 7 models solute redistribution and the amount of ferrite that forms during solidification as a function of interface velocity in the electron beam surface melts. This chapter is of central importance to this investigation in that it explains the results of the previous chapters, which are largely empirical in nature, based on a quantitative model of the solidification behavior. As part of this study, the solidification paths for each alloy were determined in the Fe-Ni-Cr system. These paths, along with thermodynamically calculated phase diagram information, were used to create pseudobinary diagrams to represent the solidification behavior for each of the alloys. From these diagrams, the solidification parameters were determined and were used in the interface stability and solute redistribution calculations. Dendrite tip calculations were performed for constrained columnar growth behavior for each alloy and for each solidification condition. These calculations were used to make predictions of the cellular to dendritic transition and were used to calculate the undercooling at the dendrite tip. A solute redistribution model that incorporates tip undercooling was then employed to calculate the amount of primary and secondary phases that solidify from the melt as a function of cooling rate and these results were used to explain the high cooling rate behavior observed in the actual electron beam melts.

Chapter 8 investigates the solid state transformation of ferrite that occurs as the melt cools to room temperature. Several transformation mechanisms were observed in the alloys depending on the primary mode of solidification and cooling rate. For alloys that solidify with both ferrite and austenite present in the microstructure, the transformation takes place by the growth of primary or second phase austenite. This transformation is controlled by the diffusion of alloying elements from the ferrite/austenite interface and can be modeled to predict the influence of cooling rate on the extent of the transformation. For alloys that solidify in the fully ferritic mode, nucleation of austenite is required before the transformation can proceed. The composition-dependent stability of the ferrite and the cooling rate each contribute to the nucleation and growth characteristics of the austenite to produce three different morphologies: Widmanstätten austenite platelets, Widmanstätten austenite needles and massive austenite grains. This chapter discusses the composition and cooling rate regimes where each morphology exists and explains the solid state transformation mechanisms by taking into account the thermodynamic and kinetic factors which are responsible for the nucleation and growth behavior. Furthermore, many parallels can be drawn between the phase transformation behavior of the Fe-C system and the Fe-Ni-Cr system. The austenite morphologies which develop during the decomposition of delta ferrite in the Fe-Ni-Cr system are identical to many of the ferrite morphologies which develop during the decomposition of austenite in the Fe-C system. The analogy between these two systems is presented as a useful starting point for understanding the solid state transformation of ferrite.

Chapter 9 integrates the empirical findings of Chapters 4, 5 and 6 with the theoretical results of Chapters 7 and 8 as a summary of the concepts which were developed during this investigation. These concepts represent the general framework of the influence that cooling rate has on the microstructure of stainless steel alloys from the initial stages of solidification through the final stages of the solid state transformation. Because of the many-faceted nature of the aspects involved during the solidification of stainless steel alloys, there were several areas that were identified where additional research needs to be performed. These areas are also summarized in Chapter 9 along with a summary of the major conclusions of this thesis.

CHAPTER 2

Materials And Experimental Procedures

2.1 Materials

2.1.1 Fabrication of the High Purity Alloys

The selection of the stainless steel alloys used in this study was based on two primary considerations. The alloys had to be of high purity to facilitate microchemical analysis so that solute redistribution could be modeled and the alloys had to span a large composition range so that the effects of both primary austenite and primary ferrite solidification could be investigated.

Seven high purity Fe-Ni-Cr ternary alloys were produced that contained 59% Fe but had different Cr/Ni ratios, which varied from 1.1 to 2.2. These compositions span the line of two-fold saturation as shown on the constant-iron vertical section in Fig. 2.1. Stainless steel alloys containing 59% iron were selected in favor of the more common 70% iron alloys (AISI 304, 316) for two reasons : 1) The lower iron content is clearly separated from the peritectic to eutectic transition, thus insuring eutectic solidification behavior for all of the alloys and 2) The lower iron content increased the probability that the selected chemical compositions would yield the desired solidification mode since the three-phase L+F+A region spans a larger composition range at lower iron contents.

The alloys were melted and hot worked at AMAX Materials Research Center in Ann Arbor, Michigan. All heats were vacuum/argon-induction melted from 99.93% pure electrolytic iron, 99.56% pure electrolytic chromium, and 99.94% pure carbonyl nickel powder. Two alloys were produced per 68 lb melt by a split heat technique. After melting of the initial charge and deoxidation with aluminum, the melt was cooled to the freezing point three times and then reheated, over a 15 minute time interval, in order to float off aluminum oxide inclusions derived from the high oxygen contents of electrolytic iron and chromium. After the first ingot had been poured and the alloying addition had been made for the second split, a 5 minute

floating-off period was used before pouring the second alloy. For each alloy, one ingot 90 mm in diameter and 250 mm high with an adequate hot top was cast in a seamless steel pipe mold. The cooling-rate of the ingot was estimated to be $0.33^{\circ}\text{C}/\text{s}$ by measuring the temperature on the outside of the steel mold at a location 75 mm below the hot-top.

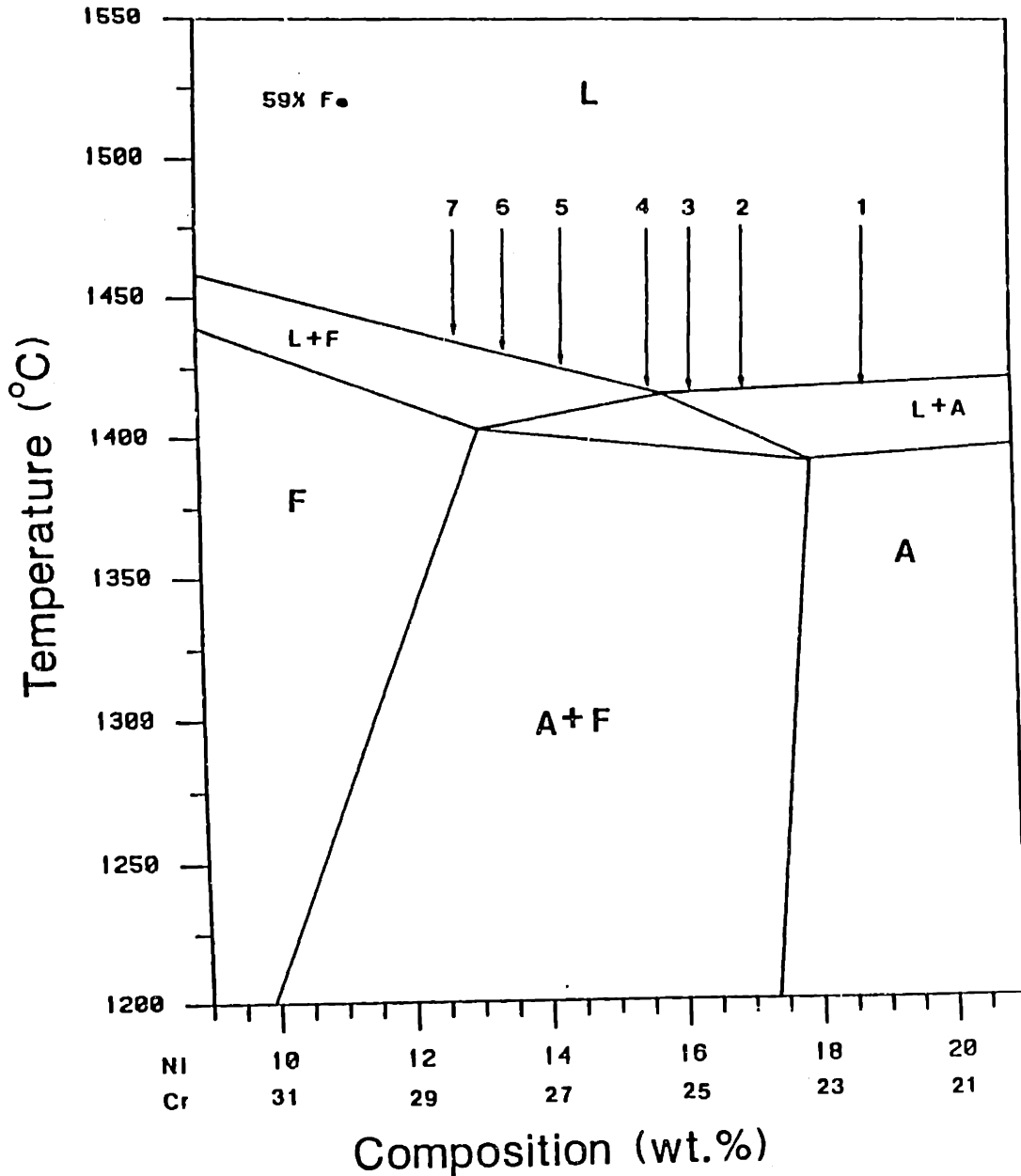


Figure 2.1 Compositions of the seven Fe-Ni-Cr alloys plotted on the 59% Fe isoplethal section.

Chemical analysis was performed by AMAX on a chill cast button which was removed from the bottom of the ingot. The concentrations of Mn, Si, Cr, Ni and P were determined by wet chemical methods; Al was analyzed by optical emission spectroscopy; C, N₂, O₂ and S were analyzed by gas/fusion techniques. The results of the chemical analysis are shown in Table 2.1 and indicate that the alloys are at least 99.9 wt. percent Fe + Ni + Cr. All of the alloys were intended to have identical iron contents and the chemical analysis shows that the iron content varies by no more than 0.5 percent from the mean value of 58.7 wt. percent.

Table 2.1 Compositions of the seven alloys (wt. percent)

Element	1	2	3	4	5	6	7
Cr	22.36	24.25	24.99	25.52	26.43	27.62	28.05
Si	0.051	0.056	0.042	0.032	0.048	0.042	0.044
Al	0.022	0.029	0.02	0.031	0.027	0.02	0.044
Ni	19.32	17.32	16.49	15.77	14.29	13.66	12.66
Mn	0.002	0.001	0.003	0.008	0.002	0.004	0.002
N	0.0028	0.0032	0.0026	0.0028	0.0038	0.0026	0.0035
C	0.0023	0.0022	0.0019	0.0026	0.011	0.0019	0.0039
O	0.0047	0.0053	0.0102	0.0034	0.0026	0.0075	0.0026
S	0.0018	0.0016	0.003	0.0022	0.0013	0.003	0.0012
P	0.001	0.001	0.001	0.002	0.001	0.001	0.001
(Fe)	58.23	58.33	58.44	58.63	59.2	58.64	59.19
Fe+Ni+Cr	99.91	99.9	99.92	99.92	99.9	99.92	99.9
Cr eq.	22.44	24.33	25.05	25.57	26.5	27.68	28.12
Ni eq.	19.48	17.48	16.63	15.94	14.44	13.8	12.88
(Cr/Ni) eq.	1.15	1.39	1.51	1.60	1.84	2.01	2.18

The main portion of each ingot was machined to a diameter of approximately 80 mm and hammer-forged at 1250 °C to develop a 70 mm round-cornered-square cross section. No cracks developed at this stage and the billets were broad-rolled to about 150 mm, measured perpendicular to the original ingot axis. The billets were then

long-rolled parallel to the original ingot axis. The reductions were 10% per pass, and typically from three to six passes were made per reheat, depending on the workability of the steel. Four of the alloys (1,2,3,4) were rolled to the desired 10 mm thickness without cracking. Slight-to-severe cracking, however, occurred in alloys 5,6 and 7. Whenever cracking was observed the plates were cooled and the cracked regions were cut away before resuming rolling. The final hot-rolled plates measured 150 mm wide, 10 mm thick and the lengths varied from approximately 100 mm to 400 mm.

2.1.2 Arc Cast Buttons

The slowest cooling rate condition was to be represented by the original cast ingot microstructure, however, the original ingot microstructure was altered during high-temperature homogenization and hot working of the ingots. Therefore, a new casting was made on each alloy to represent the slow cooling-rate microstructure.

Approximately 200 g of material was removed from each hot-rolled plate and descaled by machining off the surface layer. Part of this specimen was submitted for chemical analysis and the remainder was recast in an arc-melting furnace which was backfilled with argon gas to approximately 0.5 atm. Each alloy was melted in a water-cooled copper hearth which produced a button 80 mm long, 40 mm wide and 20 mm thick.

Chemical analysis was performed on each arc cast button and on the original hot rolled plate to verify the cleanliness of the arc casting process. These results which are shown in Table 2.2 indicate that the Ni and Cr contents vary by less than 0.5 percent from the starting composition. The chemical analysis also showed that the total wt. percent C + N was between 0.01 and 0.03 wt. percent which is slightly higher than the starting material. This slight contamination was not considered to be significant in this investigation.

Table 2.2: Chemical composition at different processing stages (wt. %)

Alloy	Element	Ingot	Plate	Button
1	Cr	22.36	22.35	22.53
	Ni	19.32	18.73	18.56
	Fe	58.23	58.7	58.7
2	Cr	24.25	24.45	24.48
	Ni	17.32	17.2	17.03
	Fe	58.33	58.1	58.1
3	Cr	24.99	24.99	25.05
	Ni	16.49	16.38	16.16
	Fe	58.44	58.4	57.3
4	Cr	25.52	25.56	25.5
	Ni	15.77	16.04	15.54
	Fe	58.63	57.9	58.7
5	Cr	26.43	26.54	26.66
	Ni	14.29	14.87	14.67
	Fe	59.2	58.4	58.4
6	Cr	27.62	27.78	27.46
	Ni	13.66	13.73	13.57
	Fe	58.64	58.3	58
7	Cr	28.05	28.28	28.31
	Ni	12.66	13.26	13.08
	Fe	59.19	57.70	58.4

2.1.3 Melt Spun Ribbons

Melt spun ribbons with cooling rates of about 10^6 °C/s were produced on a special series of Fe-Ni-Cr ternary alloys. The purpose was to rapidly solidify the alloys so that the microstructure consisted solely of single-phase metastable ferrite. The magnetic properties of the ferrite was then measured using a vibrating sample

magnetometer and the results were used as the magnetic calibration standards for calculating the ferrite content of austenitic/ferritic stainless steels. The composition of these alloys is summarized in Chapter 3.

The alloys were made by a two-step procedure. First, a 25 g ingot was induction melted and second, this ingot was remelted and melt spun into ribbon. The initial ingot was made from 99.9+ purity iron, nickel and chromium and melted in a 15 mm quartz crucible. The chamber was first evacuated to 30 μm Hg and backfilled with a partial pressure of argon gas. The charge was induction melted using a graphite susceptor and 20 kW of power. The total melting time was less than 180s prior to shutting off the power and allowing the ingot to cool.

The ingot was removed from the furnace and because of the high oxygen content of the electrolytic iron, an oxide scale had formed on its surface. The scale was removed by wire brushing and the ingot was cut into two equal parts. One half (12.5 g) was used for melt spinning, the other for characterization of the cast structure.

The 12.5 g charge was placed into a 16 mm diameter quartz crucible for melt spinning in a commercial unit, manufactured by Marko Materials. The crucible was manufactured with a 25 μm diameter hole at its base to allow the molten charge to flow onto the water cooled copper chill. The chamber was pumped down to 30 μm Hg, backfilled with argon, and the induction melting was performed using a graphite susceptor and 20 kW power. The charge was allowed to melt and was heated for 180s plus an additional 60s to superheat the liquid. The copper substrate was revolving at 1500 rpm and the superheated liquid was allowed to flow onto it from a distance of 3 mm above its surface. The ribbons measured 1 mm wide and about 38.1 μm thick and cooled at rates of about 10^5C/s [2.1]. The ribbons were verified to be single phase ferrite by X-ray diffraction.

2.2 Surface Melting and Resolidification

2.2.1 Weld Coupon Preparation

The hot rolled plate was cut into 38 mm wide strips across its width and these strips were machined into coupons which measured 140 mm long, 38 mm wide and 6.4

mm thick. The microstructure of these coupons revealed a very large primary dendrite arm spacing and a secondary dendrite arm spacing of about $35 \mu\text{m}$. This microstructure was considered to be too coarse for the high speed electron beam surface melts which penetrate less than $100 \mu\text{m}$.

The microstructure of the coupon was refined by melting the surface with overlapping electron-beam passes down the length of the coupon. This surface homogenization technique consisted of approximately 15 passes at 100 kV, 38 ma and 25.4 mm/s. A defocused beam was used and approximately 150s was allowed between passes for cool down. The surface of the plate was homogenized to a depth of about 1.5 mm with a primary dendrite arm spacing of less than $10 \mu\text{m}$. Each coupon was heated to 500°C for 1800s and hot pressed in a 300 ton forge to remove the distortion caused by the surface homogenization. The surface of the plates were lapped to an $8 \mu\text{m}$ rms finish in final preparation for the electron beam welds.

2.2.2 Electron Beam Surface Melting

It was desired to produce a series of melts on each alloy with increasing cooling rates from about 100°C/s to about 10^6°C/s . The technique chosen was similar to that used by Boettinger et al. [2.2] who kept the electron beam power level constant and varied the travel speed. Preliminary melts on stainless steel alloys showed that a 2 kW power level (100 kV, 20 mA) was sufficient to produce melting at travel speeds as high as 5 m/s, consequently, this power level was used throughout the study.

Single pass, and overlapping multiple pass melts were made across the 38 mm width of the coupon. All melts were made with a sharp focussed electron beam except for two melts made at the slowest travel speeds. These melts were made with an electron beam defocussed above the surface of the plate to prevent burn through. The complete set of melt parameters are listed in Table 2.3. Six single-pass melts were made at travel speeds which varied from 6.3 mm/s to 5,000 mm/s. Four sets of over-lapping multiple pass melts were also made on each coupon at travel speeds between 100 mm/s and 5,000 mm/s. The multiple passes were made with a 50 percent

overlap and approximately 120s was allowed between each pass for cooling down. The number of passes was selected to produce a 6 mm wide strip and required between 9 and 20 passes at each travel speed setting.

The cross sectional shape of the surface melts varied considerably as the travel speed was increased. Melts 1 and 2 had deep penetrations and were formed by a key-hole mode. Melt 3 was nearly semicircular in cross section and approximately 1 mm deep. Melt 4 had a double-humped appearance which was presumably caused by the non-uniform electron-beam force pushing the molten metal to the edge of the melt. Melts 5 and 6 had shallow and uniform penetrations of approximately 25 μm and 5 μm , respectively.

Table 2.4 summarizes the average width and depth of the surface melts as measured from the metallographic cross sections. The average length of each melt was optically measured on the surface of melts 1, 2, and 3 and metallographically measured on longitudinal sections for melts 4 and 5. Melt 6 was too shallow to examine and its length was assumed to be equal to the radius of the electron beam spot. Fig. 2.2 plots the melt dimensions versus travel speed and shows that the width approaches a limiting value at high speeds. This limiting value corresponds to the size of the electron-beam focal spot. At low speeds, the longer time for heat diffusion widens the fusion zone beyond the focal spot size. The length is approximately constant for melts 1, 2, and 3. However, the length of melts 4, 5, and 6 decrease and appear to approach the radius of the electron-beam spot. Melts 4, 5, and 6 are all characterized by depths which are shallow compared to their width and therefore solidification is controlled by heat flow through the depth rather than through the width of the fusion zone.

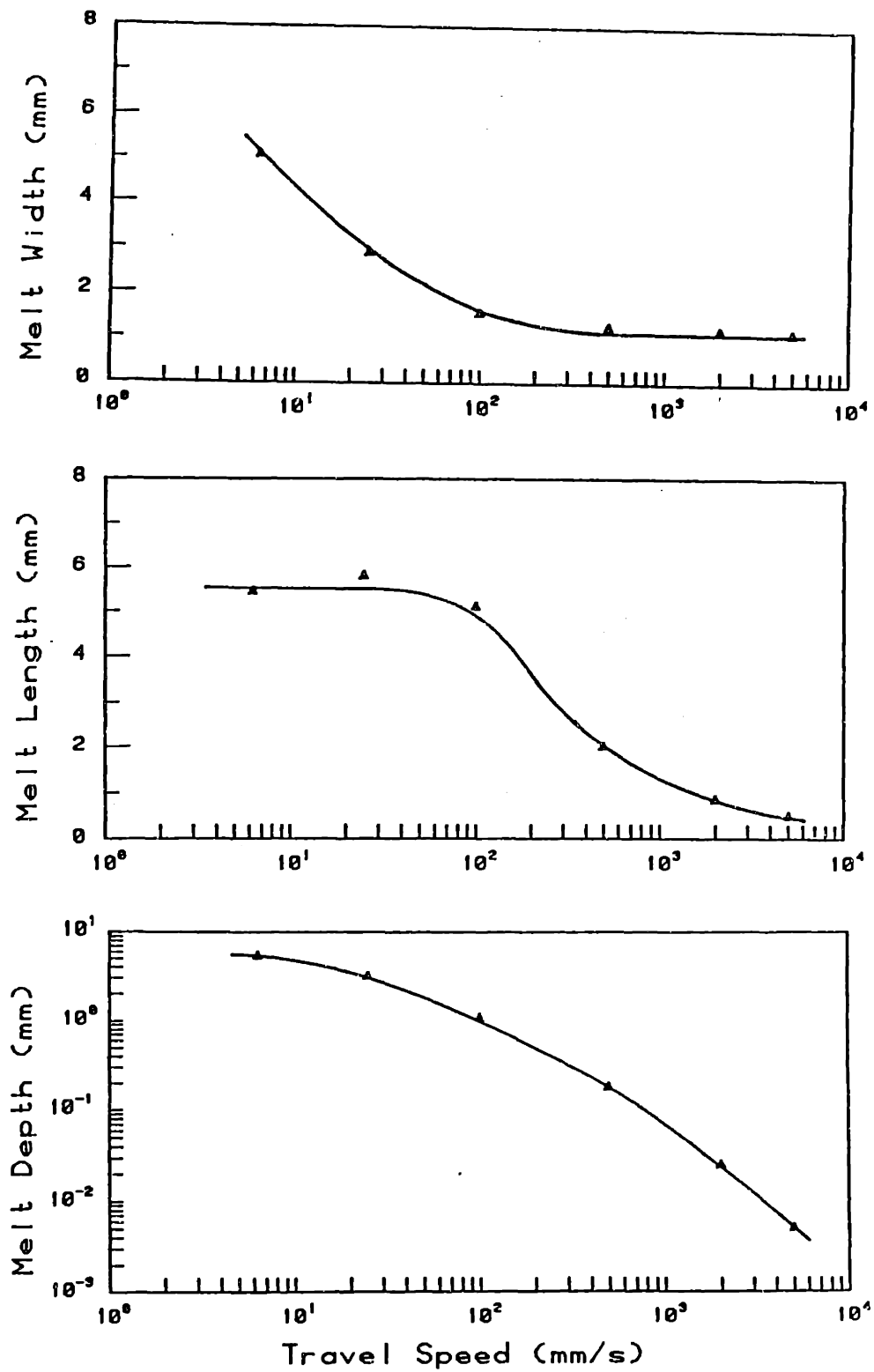


Figure 2.2 Melt pool width, length and depth as a function of electron beam scan speed. All melts made at 100kV, 20mA, sharp focus.

Table 2.3: Electron beam melt summary. All melts at 100 kV and 20 mA.

Scan No.	Travel Speed (mm/s)	No. of Passes	Overlap (%)
1	6.3	1	-
2	25	1	-
3	100	1	-
4	500	1	-
5	2,000	1	-
6	5,000	1	-
3'	100	9	50
4'	500	10	50
5'	2,000	12	50
6'	5,000	20	50

Table 2.4: Average width, depth and length of the six single-pass surface melts in mm.

melt	1	2	3	4	5	6
depth	5.33	3.10	1.07	0.178	0.025	0.005
width	5.08	2.89	1.55	1.24	1.17	1.11
length	5.44	5.80	5.10	2.00	0.86	(0.55)

2.3 Microstructural Characterization

2.3.1 Optical Metallography

Characterizing the primary mode of solidification and the ferrite morphology is an essential factor in determining the sequence at solidification and solid state

transformation effects which contribute to the final microstructure. The ferrite and austenite are dissimilar in crystal structure and in composition, therefore they are easily distinguished by optical metallographic techniques.

The metallographic specimens were polished by conventional methods and were etched by one of two techniques. The majority of the specimens were electrolytically etched in a saturated oxalic acid or 10 percent sodium hydroxide solution. An applied potential of approximately 1 volt was used at a current density of about 0.5 Amp/cm². These conditions preferentially dissolved the ferrite phase, giving the ferrite a dark appearance and leaving the austenite reflective and shiny in the bright field microscope.

For a few specimens, a second and more discriminating color etching technique was used. Beraha's color etch No. 14 [2.3] (20 g ammonium bifluoride, 0.5 g potassium metabisulfite and 100 ml distilled water) was prepared fresh and the specimen was immersed at room temperature for approximately 30s until the specimen had a heat-tinted appearance. The specimen was removed from the etchant and rinsed in water followed by acetone, reagent grade methanol and immediately blown dry with compressed air. When etched properly, the ferrite has a white appearance and the etch can distinguish between the two types of austenite. The austenite that solidified from the melt has a golden-brown color and the austenite that transformed from the ferrite phase has a dark brown color. This technique was valuable for determining the primary mode of solidification and was most successful on the slow cooling-rate melts of alloys 3, 4, and 5 which solidified as primary ferrite and contained between 10 and 25 percent ferrite.

The results of the microstructural characterization are summarized in Chapter 5 where both the primary mode of solidification and ferrite morphology were determined as a function of cooling rate.

2.3.2 Dendrite Arm Spacing Measurements

Dendrite arm spacing (DAS) measurements were made on the melts in order to estimate the cooling rates produced by the different travel speeds. The slow travel speed melts had a larger dendrite arm spacing and had correspondingly lower cooling

rates than the high speed melts. The castings and melts 1, 2, 3, and 4 solidified in a cellular or dendritic mode with a primary spacing larger than the $1 \mu\text{m}$. These cell sizes were able to be measured by optical metallographic methods. Melts 5 and 6 however, solidified at high cooling rates with a cell size smaller than $1 \mu\text{m}$ and required a scanning electron microscope to resolve the microstructure.

For the majority of the alloys, the low cooling rate microstructure consisted of primary dendrites with well defined secondary arms. However, as the cooling rate was increased, the microstructure refined in size and formed cells rather than dendrites. Since secondary arms were not always present in the higher cooling rate melts (3-6), secondary arm spacings could not be used to estimate the cooling rate. Therefore, primary DAS measurements were made on the alloys cooled at low rates and cell size measurements were made on the alloys cooled at high rates.

Microstructural characterization (Chapter 5) revealed that the cast alloys 1, 2, 3, 4, and 5 solidified in fully austenitic or austenitic/ferritic modes with well defined dendrites or cells. The DAS measurements were correspondingly direct and easily made. Alloys 6 and 7 however, solidified in a fully ferritic mode and the solidification substructure was 'erased' during the solid-state transformation of the ferrite. Therefore, DAS measurements were only able to be made on alloys 1 through 5.

The measurements were made by a line-intercept technique on the optical or SEM micrographs. All measurements were made in the upper portion of the melt, at a location half way between the fusion line and the melt centerline. The results are listed in Table 4.1 as the average value from the 5 alloys, \bar{x} , and standard deviations, s . These data will be used to calculate the cooling rate in chapter 4.

2.3.3 Ferrite Measurements

The ferrite content of the alloys, and particularly the influence that cooling rate has on the ferrite content of the alloys is of extreme importance to this investigation. Consequently, Chapter 3 is devoted to the calibration of the ferrite measuring devices and the ferrite measurement results. Measuring the ferrite content of the high speed

surface melts required the development of a new technique, using a vibrating sample magnetometer (VSM). This approach is discussed in detail in Chapter 3 and only the sample preparation techniques will be discussed here.

Conventional ferrite measuring techniques (Magne-Gage, ferrite meter, quantitative metallography) could not be used to measure the ferrite content of the high cooling rate melts because of the small physical dimensions of the rapidly cooled melts. However, the VSM technique could be used for small specimens which weighed as little as 10 mg. The specimens were increasingly difficult to extract as the cooling rate increased. The single-pass, slowest cooling rate melts 1 and 2 had deep enough penetrations and specimens were cut from the top center of the melt measuring approximately 6 mm x 3 mm x 1 mm. However, single pass melts 3, 4, 5 and 6 were too shallow for specimen removal. Therefore, multiple pass melts 3, 4, 5 and 6 were made (see section 2.2.2), which were wide enough to produce suitable specimens.

The specimens from shallow penetration melts were prepared by a hand lapping technique. A section of the plate was removed which contained a 6 mm wide by 10 mm long strip of the surface melted material and this specimen was mounted to a 15 mm thick brass block using organic resin. The base metal was then ground away from the surface melted region using 240 grit paper. By successively measuring the thickness of the block + resin + specimen between grinding steps, the thickness of the specimen (melt + base metal) could accurately be measured. Grinding was completed when the specimen thickness was smaller than the depth of penetration of the melt. Specimens were easily prepared with 10 μm thickness or larger but the 5 μm thick melts from the 5 m/s travel speeds were not successfully extracted without base metal contamination.

2.3.4 Electron Probe Microanalysis

The arc cast buttons had a coarse microstructure which allowed the composition of the ferrite and austenite phases to be measured by electron probe microanalysis (EPMA). The microprobe was focused in the center of the ferrite or austenite dendrites and a quantitative analysis was performed to determine the Fe, Cr and Ni

concentrations in each phase. The microprobe was calibrated using pure Fe, Cr and Ni standards. The voltage was held constant at 20 kV and a LiF crystal was used to analyze the X-rays.

Specimens were prepared for the microprobe by conventional metallographic techniques and polished with an alumina slurry to a final 0.3 μm finish. These specimens were very lightly electrolytically etched in saturated oxalic acid to outline the phase boundaries and then rinsed in water, followed by acetone, reagent grade methanol and finally blown dry with compressed air.

The microprobe was used to measure the atomic percent Fe, Ni and Cr in both the ferrite and austenite phase for each of the seven cast alloys. Five measurements were made in each phase and Table 2.5 gives the average composition in wt. percent. These values were converted from atomic percent using molecular weights of 55.9 (g/mole) for Fe, 58.7 (g/mole) for Ni and 52.0 (g/mole) for Cr. Statistics performed on each set of 5 data points showed that the typical standard deviation was small and varied between 1 to 2 percent of the mean value for Fe, and 1 to 8 percent of the mean value for Cr and Ni. Total atomic percents (Fe+Ni+Cr) varied between 99.0 and 101.0.

It is interesting to note that the composition of the ferrite and austenite phases in the castings does not vary significantly between the seven alloys. Only alloy 7 appeared to deviate from the invariant compositional trend. It is believed that this is a result of inaccurate EPMA measurements because of the very fine spacing between the ferrite and austenite 'plates' in alloy 7. This fine spacing (5 μm) is a result of the solid state transformation of ferrite and is unique to alloy 7.

Attempts were made to use the EPMA technique to measure the composition of the ferrite and austenite phase in the melts. However, the microstructure of the melts were, for the most part, too closely spaced to give accurate measurements. The few locations that were found to be suitable generally gave what appeared to be good results for the matrix phase but poor results for the second phase. These few measurements were valuable however, in characterizing the single-phase ferritic solidification behavior of the melts in alloys 6 and 7.

Table 2.5: Average compositions (wt. percent) of the ferrite and austenite phases in the arc cast buttons.

Casting	Ferrite				Austenite			
	Cr	Ni	Fe	Cr/Ni	Cr	Ni	Fe	Cr/Fe
1	-	-	-	-	-	-	-	-
2	35.4	10.1	54.5	3.50	25.3	16.1	58.6	1.57
3	35.8	9.2	54.9	3.89	24.9	16.0	59.1	1.56
4	36.2	8.7	55.1	4.16	25.7	16.6	57.7	1.55
5	35.0	9.3	55.7	3.76	25.9	16.7	57.4	1.55
6	35.1	8.3	56.6	4.23	26.4	14.8	58.7	1.78
7	39.9	6.3	53.8	6.33	27.1	15.1	57.8	1.79

2.3.5 X-ray Diffraction

X-ray diffraction experiments were performed to verify that the melt spun ribbons were fully ferritic. The single phase nature of the ribbons was of particular interest since the ribbons were to be used as ferrite standards to calibrate the vibrating sample magnetometer.

Two types of specimens were prepared for the X-ray experiments. Melt spun ribbons and powder specimens made from the cast alloys. The ribbons measured approximately 1 mm wide and were cut into 50 mm lengths. These samples were cleaned in acetone and then attached to a 75 mm long by 25 mm wide glass slide using double stick tape. The ribbon edges overlapped approximately 0.25 mm and the entire width of the glass slide was covered with the ribbons.

Powder specimens were prepared by filing the cast alloys with a fine-pitched file. The powder was then mixed with an organic binder and a portion, 25x25 mm, of the glass slide was covered with the mixture. The powder specimens consisted of a known fully-austenitic alloy and a known duplex alloy containing approximately 25 percent ferrite.

The X-ray diffractometer was equipped with a chromium tube and Cr $\kappa\alpha$ radiation was used, having a wavelength of 2.291 Å. The divergence slit and receiving slit angles were set at 3 deg. and 0.1 deg. respectively. The scan speed was set at 8 deg./min and the specimen was scanned between 2θ angles from 20 deg. to 160 deg.

For the above diffraction conditions, the following planes appear. BCC ferrite: (110), (200), (211) ; FCC austenite: (111), (200), (220). The lattice constant of ferrite was taken to be 2.871 Å [2.4] and the 2θ values for the ferrite peaks were calculated from this lattice parameter to be 68.7, 105.8, and 155.6 deg. for the (110), (200), and (211) planes respectively. Table 2.6 compares the 2θ values which were calculated with those which were experimentally determined. The calculated and experimentally determined values agree to within 0.3 deg. which indicates that the peaks are properly indexed. The austenite peaks were similarly indexed and from the experimentally determined peaks, the lattice parameter for austenite was determined to be 3.570 Å.

Fig. 2.3 illustrates the diffractometer chart records for a fully ferritic, a fully austenitic and a duplex alloy stainless steel specimen. With the peaks characterized, the melt spun ribbons were shown to be fully ferritic and all of the ribbons had X-ray charts characteristic of the type shown in Fig. 2.3 a.

Table 2.6: Summary of X-ray diffraction results

Phase	Plane	$h^2+k^2+l^2$	d (Å)	2θ calculated (deg)	2θ experimental (deg)
Ferrite	(110)	2	2.030	68.7	68.9
	(200)	4	1.436	105.8	106.1
	(211)	6	1.172	155.6	155.9
Austenite	(111)	3	2.061	67.5	67.4
	(200)	4	1.785	79.8	79.7
	(220)	8	1.262	130.4	129.8

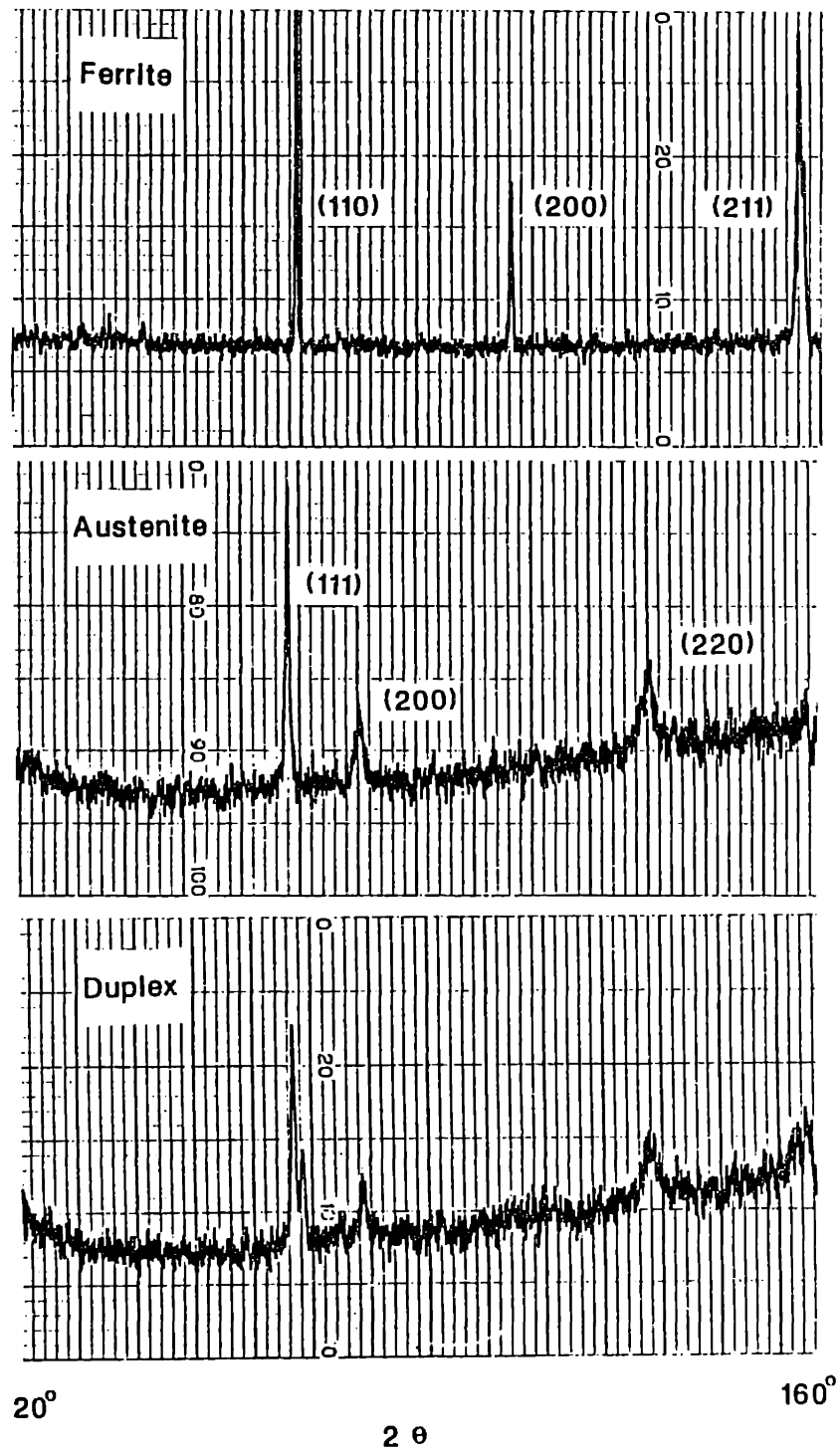


Figure 2.3 X-Ray diffraction results for a) single phase ferrite, b) single phase austenite and c) duplex stainless steel alloys.

2.4 Density Measurements

Density measurements were used to convert magnetic measurements from the units of emu/g to Gauss. These measurements were made on the seven base metal alloys which varied from 0 to about 35% ferrite and also on fully ferritic specimens. Base metal specimens weighing approximately 5g (20 mm x 5 mm x 5 mm) were removed from the hot-rolled plate. Fully ferritic specimens were produced on alloys 6 and 7 by electron beam melting at 20 mA, 100 kV and 12 mm/s, with a slightly defocused beam. The fusion zones measured approximately 4 mm deep and 1.5 mm wide at the half-depth position. A time-consuming, but effective, specimen removal technique was used to extract the all-weld-metal specimens. The technique consisted of cutting a 10 mm length of melt which was polished and macroetched on both cross sectional ends and on one longitudinal side of the melt. The longitudinal side was then successively ground down and macroetched several times to reveal the depth of the melt. At this point, the specimen was sliced, parallel to the longitudinal section, on a diamond wafering saw. This produced a thin wafer of all-weld-metal ferrite measuring about 3 mm x 0.75 mm x 10 mm. Confirmation of the fully ferritic structure was made by observing the six macroetched surfaces of the specimen.

The density measurements were made by a standard buoyancy test, ASTM C693-74 [2.5] with toluene as the immersion fluid. Density values of 0.867 g/cm³ and 0.001173 g/cm³ were used for toluene and air respectively. The density of the specimen was calculated from the equation:

$$\rho_s = (W_A \rho_T - W_T \rho_A) / (W_A - W_T) \quad (2.1)$$

where W is the weight in g and ρ is the density in g/cm³. The subscripts s, A and T correspond to the specimen, air and toluene respectively. Three density measurements were made on each specimen and, in accordance with the procedures, the measurements were repeated until all data fell within 0.01 g/cm³ of the mean value.

Table 2.7 summarizes the measurements and indicates that the density decreases from the fully austenitic alloy 1 (7.9622 g/cm³) to the fully ferritic specimens 6-F and 7-F (average value of 7.7661 g/cm³). These data reflect the lower density of the BCC ferrite phase and are consistent with the literature.

**Table 2.7: Density measurements made on the base metal alloys 1-7
and on fully ferritic specimens of alloy 6 and 7.**

ρ	1	2	3	4	5	6	7	6-F	7-F
(g/cm ³)	7.9662	7.9419	7.9198	7.9018	7.8671	7.8434	7.8102	7.7568	7.7754

2.5 Isothermal Studies of the Ferrite to Austenite Phase Transformation

The kinetics of the ferrite to austenite phase transformation were studied by measuring the fraction of ferrite that transformed as a function of time, under isothermal conditions. The data were analyzed using the Johnson-Mehl-Avrami approach and attempts were made to confirm diffusion coefficient data in the Fe-Ni-Cr system.

The isothermal heat treating was performed in a molten salt bath by immersing the specimen for the desired time, followed by a water quench. The specimens were placed in a wire basket made from chromel thermocouple wire and to protect the specimen from the corrosive molten salts, each specimen was wrapped in 0.051 mm thick type 304 stainless steel foil and double crimped shut on all edges.

The starting material was single phase ferrite of alloy 6 and alloy 7 compositions. The single phase ferrite specimens were prepared from the electron beam melted alloys using the same method of extraction that was presented in section 2.4. Each specimen weighed approximately 50 mg and was tested at 625°C and 720°C.

An initial magnetic measurement was made on the specimen using the VSM (see Chapter 3) to confirm that it was fully ferritic. After heat treating, the ferrite content was again measured to determine the amount of transformation. The heat-treating/magnetic measurement steps were repeated on each specimen by doubling the total transformation time with each additional heat treatment until the majority of the phase transformation had been completed.

CHAPTER 3

Measuring The Ferrite Content Of Rapidly Solidified Stainless Steel Alloys

3.1 Review of Conventional Ferrite Measurement Techniques

Many techniques have been used to measure the delta ferrite content of stainless steel welds. Constitution-diagrams, such as the Schaeffler diagram [3.1,3.2] and the Delong diagram [3.3], rely strictly on composition to predict the ferrite content of the resulting weld microstructure. These diagrams only provide accurate correlations between ferrite content and composition for 'typical' stainless steel alloy compositions [3.4,3.5], and for a narrow range of welding conditions that have cooling rates which are similar to those of gas tungsten arc welds [3.6,3.7]. Post-weld ferrite measurements are generally performed using magnetic instruments such as the Magne-Gage or ferrite meters [3.8, 3.9]. These instruments have been developed to measure the amount of the ferromagnetic ferrite in a duplex stainless steel alloy and are reasonably successful at measuring ferrite in arc-welds and castings for typical austenitic stainless steels containing about 70 percent iron. However, for alloys which deviate from this iron content, the composition-dependent magnetic properties of the ferrite must be taken into account [3.10,3.11] and these corrections are not well established.

The conventional magnetic instruments have an additional limitation which is caused by the uncertainty of the magnetic field generated by the measuring probe. These fields are non-uniform within the volume of the material tested and do not uniformly saturate the ferrite. Consequently, these instruments respond to the permeability which is not a material property. As a result, these instruments are sensitive to the orientation and shape of the ferrite as well as to the geometry and volume of the specimen being tested. In order to reliably measure ferrite with these instruments, the specimen must be large enough to obtain the maximum magnetic attraction between the probe and the specimen. For these cases, empirical relationships have been developed to convert the magnetic readings into an equivalent

ferrite content. However, these measurements are only valid if the specimen exceeds some minimum physical dimension, which is about 10 mm for a Magne-Gage and for other conventional magnetic instruments [3.9].

The limitation on the specimen size presents problems for high cooling-rate welds and rapidly solidified alloys. The size of electron beam welds may be less than 1 mm wide, pulsed laser welds may be only 0.25 mm deep and rapidly solidified alloys have even smaller physical dimensions. It is impossible to measure the ferrite content of these specimens with conventional magnetic instruments. Only quantitative metallography (QTM) can be used to inspect the rapidly solidified microstructures. However, QTM is not accurate for measuring ferrite in arc welds and rapidly solidified alloys because of the small size of the ferrite particles. AWS A4.2-86 [3.8] discusses the irreproducibility of quantitative metallography and concludes that QTM is only accurate for measuring the ferrite content of castings. Therefore, a new technique was investigated which is not limited by a small specimen size and which can be used to measure the ferrite content in rapidly solidified stainless steel alloys.

3.2 The Vibrating Sample Magnetometer Method

The vibrating sample magnetometer (VSM) measures the magnetic moment of a specimen when it is placed in a magnetic field. Figure 3.1a illustrates the VSM method which is based on the change in flux when the specimen is vibrated within a detection coil. The specimen is attached to the end of a rod which is fixed to a mechanical vibrator and the rod vibrates at about 80 hz in a direction which is at right angles to an applied magnetic field. Also attached to the rod is a small permanent magnet which acts as a reference specimen. Both the reference specimen and the unknown specimen induce an emf in their respective coils and the difference between the two signals is proportional to the magnetic moment of the unknown specimen. Since the reference specimen and unknown specimen vibrate at the same amplitude and frequency, the method is insensitive to vibration amplitude and frequency. The VSM is calibrated with a specimen of known saturation magnetization and when the VSM is properly aligned and calibrated, it can detect changes in the magnetization of less than 10^{-3} emu. The high sensitivity of the VSM is apparent

since a single gram of ferrite in stainless steel alloys has a saturation magnetization of about 100 emu. The nomenclature used to describe magnetic measurements is summarized in Table 3.1.

Table 3.1 : Nomenclature used to describe the magnetic measurements

Symbol	Description	Units	Value
$4\pi M_s$	saturation magnetization	Gauss	-
σ_F	specific (saturation) magnetization of ferrite	emu/g	-
σ_s	specific (saturation) magnetization of the specimen	emu/g	-
v_F	weight fraction ferrite	-	-
ρ_F	mass density of ferrite	g/cm ³	7.77
μ	saturation moment per atom	Bohr Magnetons	-
H	applied magnetic field	Oe	-
M (H)	field dependent magnetization	Gauss	-

The VSM measures the magnetization of a specimen, σ or M, in response to a known magnetic field, H. From these data, an M-H curve is constructed by performing a series of measurements with increasing magnetic fields which were varied from -10 kOe to +10 kOe in this investigation. At high H fields, the ferrite saturates and the saturation magnetization, M_s , of the specimen can be measured. The M_s value is a function of the weight fraction ferrite, v_F , in the specimen and the composition-dependent magnetic properties of the ferrite :

$$4\pi M_s = 4\pi\sigma_F v_F \rho_F \quad [Gauss] \quad (3.1)$$

where the specific saturation magnetization of the ferrite, σ_F , is measured in emu/g and ρ_F is the density of the ferrite in g/cm³. Therefore, if σ_F and the density of ferrite are known, then the volume fraction ferrite is easily calculated by a single, room-temperature, M-H measurement. The density of ferrite was measured to be 7.77 g/cm³ on a fully ferritic Fe-Ni-Cr specimen containing 59 wt.% Fe and since the density of ferrite does not change significantly with composition, this value was used

for all of the alloys in this study. However, σ_f is a strong function of composition and methods to predict the saturation magnetization of ferrite from its composition will be discussed in the following sections.

In austenitic-ferritic stainless steel alloys, the ferrite phase has no significant coercivity and the M-H curve passes through the origin with no hysteresis. Figure 3.1b shows a typical M-H curve to illustrate how M_s is determined. At high H fields, the ferrite saturates and the M-H behavior becomes linear. The spontaneous magnetization is graphically determined by extrapolating the high field susceptibility to zero applied field. The resulting value of M_s corresponds to the magnetization required to saturate the ferrite and is a material property. In this paper M_s will be used to represent the saturation magnetization of ferrite.

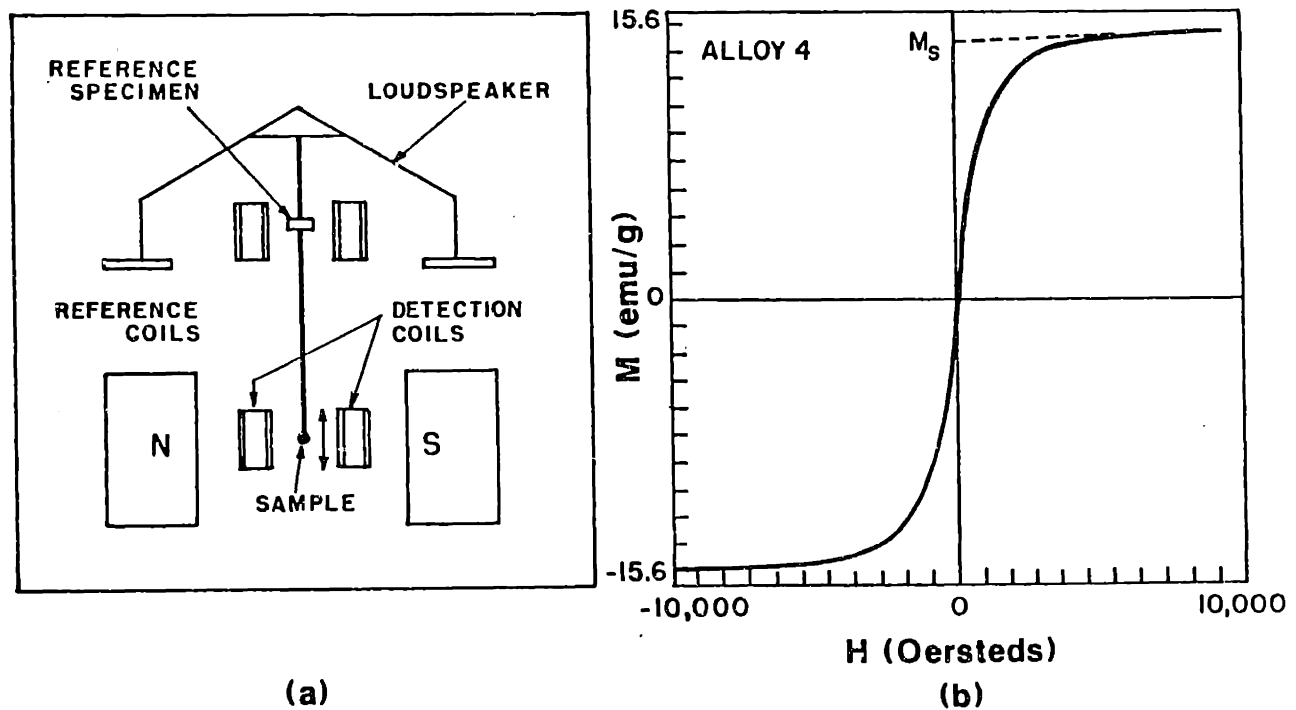


Figure 3.1 a) Schematic drawing of the vibrating sample magnetometer, after Cullity [3.21] and b) a typical M-H curve from a duplex stainless steel alloy.

The saturation magnetization tests were performed by calibrating the VSM with a pure nickel standard of known emu. Specimens from the welds were prepared as thin wafers (~ 0.5 x 3 x 3 mm) weighing between 10 and 50 mg. The samples were attached to a quartz holder using teflon tape and the M-H curves were generated in 200 Oe increments. M_s values were determined for each specimen and these measurements were converted into percent ferrite using equation 3.1.

3.3 The Saturation Magnetization of Ferrite

3.3.1 Background

The volume percent ferrite is easily calculated using equation 3.1 if the saturation magnetization of ferrite is known. However, σ_f is a function of composition and this presents two problems. First, in duplex alloy stainless steels, the ferrite phase has a different composition than the nominal alloy composition. Therefore, the composition of the ferrite phase is not known *a priori*. Measuring the composition by microchemical analysis techniques is only practical for careful laboratory experiments while estimating the composition of ferrite is not a standard calculation. One objective of this investigation was to develop a method to predict the ferrite composition as a function of nominal alloy composition, through the use of thermodynamically calculated phase diagrams.

A second problem occurs because magnetic theory can only predict σ_f from compositional data in certain single-phase binary-alloy solid-solutions. One method for estimating the saturation magnetization uses the Slater-Pauling curves which can predict the magnetic moment of an alloy as a function of composition [3.12]. This relationship assumes that the saturation magnetization of the alloy is related to the number, n , of (3d+4s) electrons per atom, according to the rigid band theory. For n values greater than about 8.3, there is good agreement with experiments and theory as long as the binary alloy consists of adjacent elements on the periodic table. For non-adjacent elements and for n values less than about 8.3, there is disagreement between simple rigid band theory and experiment.

Figure 3.2 shows the Slater-Pauling curves for a number of binary alloy systems. Additions of Cr, to Fe-Cr alloys lowers the saturation magnetization in proportion to

the amount of Cr added while additions of Ni to Fe-Ni alloys initially has little effect on the saturation magnetization. For nickel additions greater than approximately 15 atomic %, the saturation magnetization decreases in proportion to the amount of Ni in the alloy. For the addition of nontransition elements such as Si, Al, and Cu to iron rich alloys, the rate of decrease in magnetization is initially about the same for any element that is added. These elements correspond to typical alloying elements in commercial stainless steel alloys and tend to reduce the magnetization as if the Fe atoms were being replaced by atoms of zero magnetic moment. This behavior can not be explained by rigid band theory.

For ternary alloys or higher alloy systems, theory is even less capable of explaining the saturation magnetization as a function of composition. One attempt at deriving an equation to predict magnetization in the Fe-Ni-Cr ternary system was developed by Curtis and Sherwin [3.13]. Their model is based on a "rule of mixtures" approach, which predicts the saturation magnetization as follows:

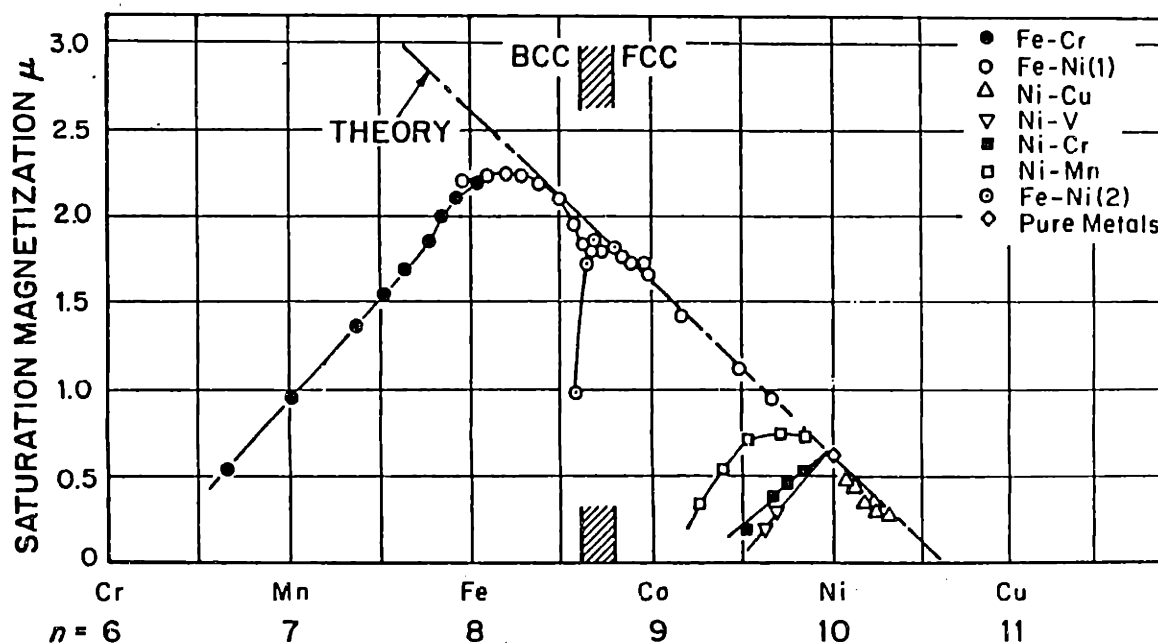


Figure 3.2 Slater-Pauling curves showing the saturation magnetization for various binary alloy combinations, after Cullity [3.21].

$$4\pi M_s = 4\pi \frac{N}{100} \left(0.22 \frac{\rho_{Cr}(\%Cr)}{A_{Cr}} + 0.6 \frac{\rho_{Ni}(\%Ni)}{A_{Ni}} + 2.2 \frac{\rho_{Fe}(\%Fe)}{A_{Fe}} \right) \times (0.927 \times 10^{-20}) \quad [Gauss] \quad (3.2)$$

where A_i refers to the atomic weight of element i , N is Avogadro's number and ρ is the density. This equation predicts a saturation magnetization for pure Fe of 21,910 Gauss and predicts a higher decrease in σ_f for Cr than for Ni additions. Unfortunately, there is not good agreement between this equation and experimental results. Therefore, empirical relationships have been derived to predict the saturation magnetization of ferrite as a function of composition.

The empirical relationships between composition and σ_f have been derived by measuring σ_s for a large number of alloys and measuring the ferrite content of these alloys by quantitative metallography. The saturation magnetization can then be calculated for each alloy by the ratio of σ_s to the volume fraction ferrite and these data can be fit by regression analysis. One such relationship was derived by Merinov et al. [3.10,3.11]:

$$4\pi M_s = 21,600 - 275(\%Cr) - 330(\%Ni) - 280(\%Mn) - 610(\%Si) - 260(\%Mo) - 670(\%Ti) - 630(\%Al) \quad [Gauss] \quad (3.3)$$

This relationship between composition and saturation magnetization confirms the general trend predicted by the Slater-Pauling curves and shows that σ_f is reduced by all of the typical alloying elements in stainless steel. The higher multiplication factors associated with the lower density elements suggest that this equation is written in terms of wt.% although the units are not specifically stated in Merinov's paper.

The major alloying elements in standard 300 series stainless steels are Cr and Ni. For these elements, Merinov's equation reduces to: $4\pi M_s = 21,000 - 275\%Cr - 330\%Ni$ and can be applied to Fe-Ni-Cr ternary alloys. The multiplying factors for chromium and nickel are similar and suggest that the iron content of the ferrite is the principal factor in determining σ_f in the ternary system, i.e., for a given Fe content, σ_f only changes a few percent for large differences in the Cr/Ni ratio.

A comparison of equation 3.2 with equation 3.3, for a chromium and nickel content representative of ferrite (35.5 %Cr, 9.1 %Ni, 55.4 %Fe), gives values of 13,600 and 8,300 Gauss respectively for σ_f . This large difference could not be reconciled from the data provided by the investigators and a separate study was initiated to determine σ_f as a function of chemical composition. The results of this study shows that the equation derived by Curtis and Sherwin is not accurate but that the equation derived by Merinov satisfactorily represents the saturation magnetization of ferrite in stainless steel alloys.

3.3.2 Fully Ferritic Specimens

A series of 100% ferrite specimens of different nominal iron contents were produced and the specific saturation magnetization of each alloy was measured by the VSM method. These alloys each have a Cr/Ni ratio which is similar to the Cr/Ni ratio found in second phase ferrite, therefore, by measuring the saturation magnetization of these alloys, the effect of iron content on σ_f could be determined.

The composition of residual ferrite in arc-welded stainless steels has been measured using EPMA and STEM techniques [3.14-3.18] and the results of these studies were used to plot the composition of ferrite on the Fe-Ni-Cr ternary diagram in Fig. 3.3. This figure shows that the experimentally determined composition of residual ferrite has a Cr/Ni ratio which varies between 3.5 and 10 for 55 and 70% Fe alloys respectively. This trend in the ferrite composition is related to the ferrite solvus at elevated temperatures.

Figure 3.4 shows an isothermal section through the Fe-Ni-Cr ternary system [3.22] which was used to determine the equilibrium between ferrite and austenite at 1300°C. The ferrite solvus is indicated and predicts the equilibrium composition of ferrite just below the solidification temperature. There is a correlation between the actual composition of the residual delta ferrite presented in Fig. 3.3 and the thermodynamically calculated (equilibrium) prediction. This relationship suggests that the composition of ferrite in the slow cooling rate welds is strongly influenced by the ferrite/austenite equilibrium and that the thermodynamic calculations can be used as a means to predict the composition of residual ferrite.

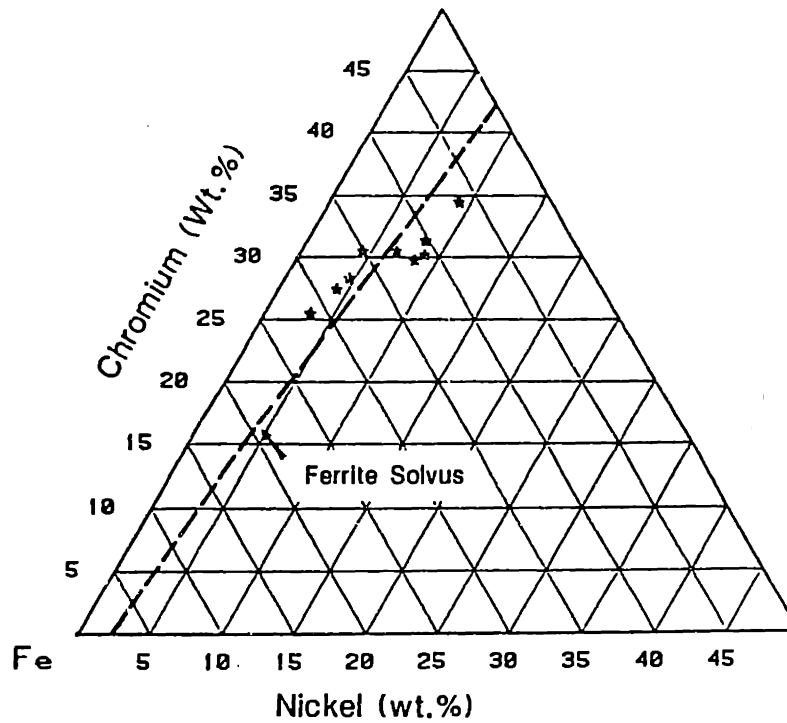


Figure 3.3 Comparison between the ferrite solvus and the composition of residual delta ferrite for alloys with different nominal iron contents.

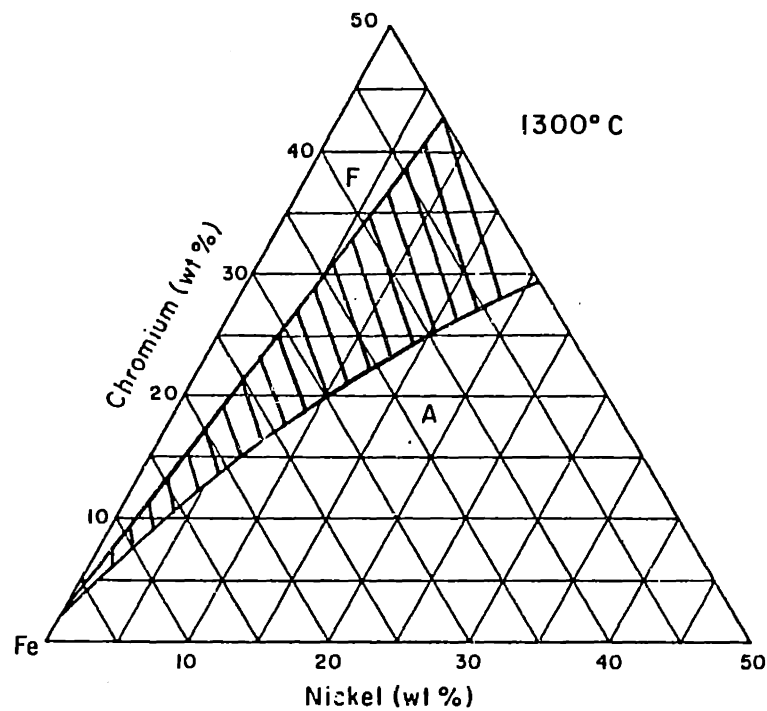


Figure 3.4 The ferrite+austenite two-phase field at 1300°C.

From these data, a series of alloys was prepared to meet the following criteria: 1) since these alloys were being selected to represent residual ferrite, their composition had to be close to that of residual ferrite in typical stainless steels and 2) the alloys had to be rich enough in chromium to allow them to solidify in the single phase ferrite mode. It was determined that alloys which meet the first criteria will also meet the second criteria, but only when the alloys are solidified at high rates. Therefore, to avoid the formation of austenite during the solidification, the alloys were solidified by a rapid solidification melt-spinning technique to suppress the solid state transformation of ferrite. The resulting ribbons were shown to be single phase ferrite by X-ray diffraction.

The composition of the alloys varied from 50 to 80 wt.% Fe and the Cr/Ni ratio of each alloy was maintained constant at 4.0. A 15g ingot of each alloy was induction melted from high purity elements for the compositions specified in Table 3.2 and then each ingot was melt spun into ribbons to solidify the alloys in the fully ferritic condition. Each ribbon measured about 2 mm wide and about 25 μm thick which resulted in cooling rates of about 10^4 to 10^5 $^\circ\text{C/s}$ [3.19].

Table 3.2 : Compositions of the fully ferritic, melt spun, alloys

Alloy	Fe	Ni	Cr	Cr/Ni
A	80.0	4.00	16.0	4
B	75.0	5.00	20.0	4
C	70.0	6.00	24.0	4
D	65.0	7.00	28.0	4
E	60.0	8.00	32.0	4
F	55.0	9.00	36.0	4
G	50.0	10.0	40.0	4

3.3.3 Saturation Magnetization Results

Three specimens, each weighing approximately 5 mg, were removed from each ribbon and the saturation magnetization was measured using the VSM. These measured values of the saturation magnetization are identical to the specific saturation magnetization of ferrite since the specimens are fully ferritic. Table 3.3 summarizes the data and indicates that the σ_F decreases from 169 emu/g to 77 emu/g as the iron content of the alloy decreases from 80 wt % to 50 wt % respectively.

Table 3.3 : Spontaneous magnetization of fully ferritic specimens.

Alloy	Specimen	M at 10 kOe (emu/g)	σ_F (emu/g)	$4\pi M_S^*$ (Gauss)
A	1	168	165	16,100
	2	171	168	16,400
	3	176	172	16,800
	Avg.	172	169	16,500
B	1	154	151	14,700
	2	158	155	15,100
	3	164	161	15,700
	Avg.	159	156	15,200
C	1	141	138	13,500
	2	145	142	13,900
	3	147	144	14,100
	Avg.	144	141	13,800
D	1	119	117	11,400
	2	119	117	11,400
	3	124	122	11,900
	Avg.	121	119	11,600
E	1	106	104	10,200
	2	107	104	10,200
	3	110	108	10,500
	Avg.	108	106	10,300
F	1	94	91	8,890
	2	98	95	9,280
	3	101	98	9,570
	Avg.	98	95	9,280
G	1	77	75	7,320
	2	80	78	7,620
	3	81	79	7,710
	Avg.	79	77	7,520

The composition of the melt spun alloys can be represented by the formula $\text{Fe}_{(1-x)}\text{Cr}_{(4x/5)}\text{Ni}_{(x/5)}$ where x represents the sum of the Ni and Cr. Using this notation, σ_f is plotted versus x in Fig. 3.5 and the results show a decrease in σ_f with x . Linear regression analysis of the 21 data points gives the following relationship between σ_f and the wt. fraction of Cr+Ni, x :

$$\sigma_f = -308(x) + 231 \quad [\text{emu/g}] \quad (3.4)$$

Extrapolating this data to pure iron, i.e. $x = 0$, shows that equation 3.4 would predict the specific saturation magnetization of pure iron to be 231 emu/g. This value is higher than that reported for pure iron of 218 emu/g [3.20] and suggests that a slight nonlinearity may exist between σ_f and composition.

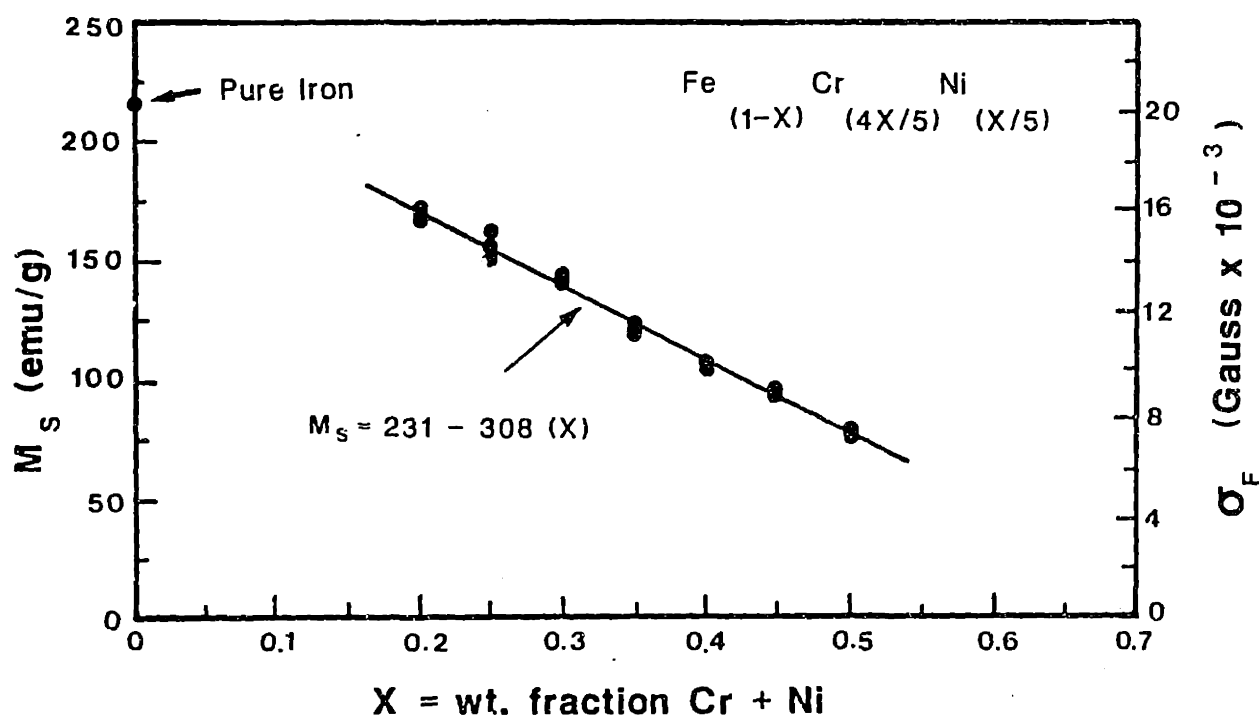


Figure 3.5 Saturation magnetization of the fully ferritic melt spun ribbons as a function of Cr + Ni content.

The specific saturation magnetization of ferrite, σ_f , was converted from the units of emu/g to Gauss using equation 3.1 and $v_f = 1.0$, $\rho_f = 7.77$ (g/cc). The saturation magnetization in the units of Gauss for the seven alloys are also reported in Table 3.3 and the average $4\pi M_s$ values for each alloy are plotted in Fig. 3.5 as an alternate y-axis. A regression analysis of the data shows the following relationship between $4\pi M_s$ and the weight fraction Cr+Ni, x :

$$4\pi M_s = -30,020(x) + 22,520 \quad [Gauss] \quad (3.5)$$

Extrapolating equation 3.5 to $x = 0$ shows the saturation magnetization of pure iron to be 22,520 Gauss which is 4% higher than the measured value of 21,580 Gauss [3.20].

The results of this study are summarized in eq. 3.5 and can be compared to Merinov's results which are summarized in eq. 3.3. For Fe-Ni-Cr alloys, with a Cr/Ni ratio of 4.0, eq. 3.5 predicts a decrease in σ_f of 300.2 Gauss for each percent Fe that is replaced by Cr and Ni. Merinov's equation predicts a decrease in σ_f of 275 Gauss for each percent Cr and 330 Gauss for each percent Ni. Therefore, for a Cr/Ni ratio of 4.0, Merinov's equation would predict a decrease in σ_f of 286 Gauss for each percent Fe that is replaced by Cr and Ni in this ratio. These two predictions are surprisingly similar when considering the differences in alloys studied and the differences in experimental techniques.

3.4 Predicting the Composition of Residual Ferrite

Using "Thermocalc" software [3.21], a series of isothermal sections were created through the Fe-Ni-Cr ternary system [3.22]. These diagrams were used to determine the equilibrium composition of ferrite as a function of temperature and the results of these calculations are summarized in Figures 3.6 through 3.8. These plots show the %Cr, %Ni and the Cr/Ni ratio of ferrite at temperatures between 1400°C and 950°C for 50, 60, 70 and 80 wt.% iron in the ferrite.

The chromium content of the ferrite increases and the nickel content of the ferrite decreases as the temperature decreases to 950°C. This results in higher Cr/Ni ratios at lower temperatures. Figure 3.8 shows that the Cr/Ni ratios of ferrite containing 50, 60 and 70 wt.% iron are similar at all temperatures, however, for ferrite containing more than 70% Fe, the Cr/Ni ratio increases significantly more with decrease in temperature.

Information beyond what was provided in the preceding figures is required in order to predict the composition of ferrite from the nominal alloy composition. Isothermal sections, such as the one presented in Fig. 3.4, can be used to determine the exact composition of ferrite at a given temperature. However, many such diagrams would be needed to represent a large range of temperatures. Since the most important parameter in determining σ_r is the iron content of the ferrite, a method was developed to estimate the iron content of ferrite by summarizing the results of many isothermal sections into a single diagram.

In stainless steel alloys, tie lines in the ferrite+austenite two-phase field show that the iron content of the ferrite is lower than the iron content of the nominal alloy. By taking the ratio of iron in the ferrite to iron in the austenite at the tie-line endpoints, one can place an upper limit on the difference in the Fe content of the ferrite and the Fe content of the nominal alloys because all of the alloys that lie on a given line have the same ferrite and austenite composition.

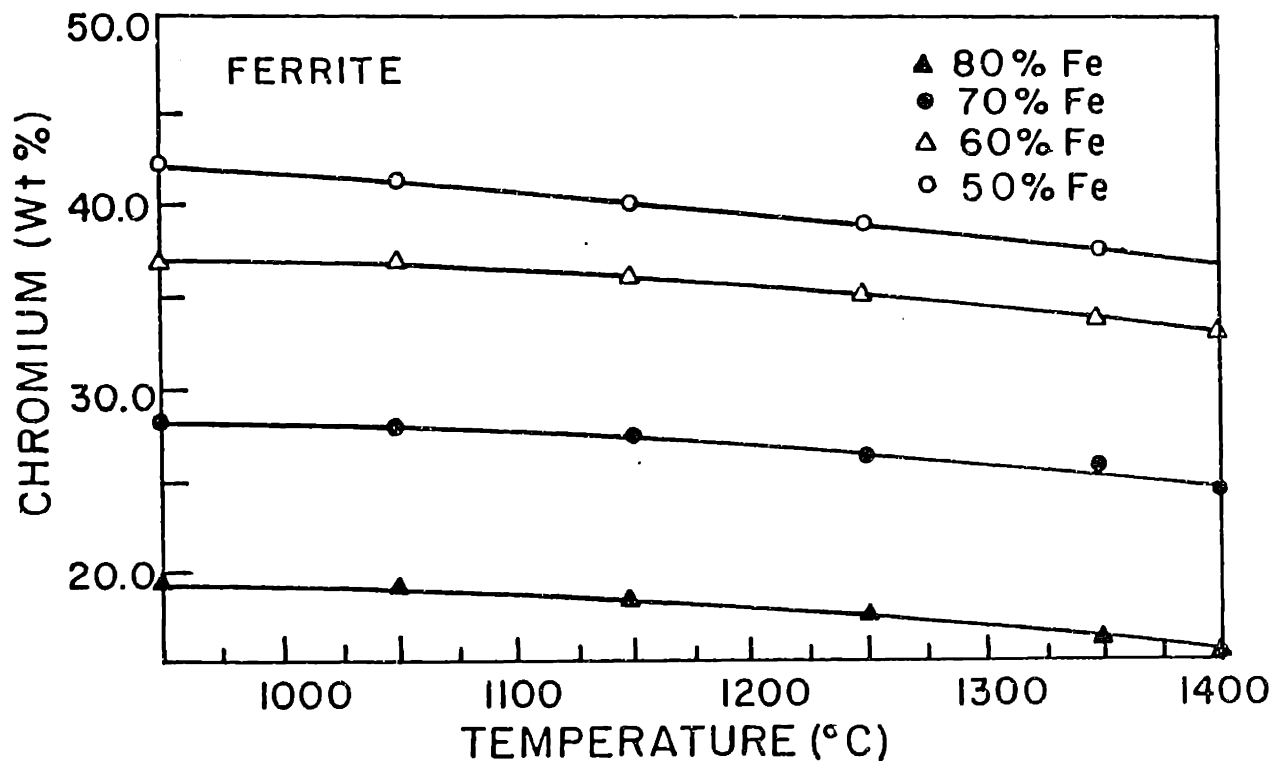


Figure 3.6 Thermodynamic calculations of the chromium content in ferrite as a function of temperature and iron content of the ferrite.

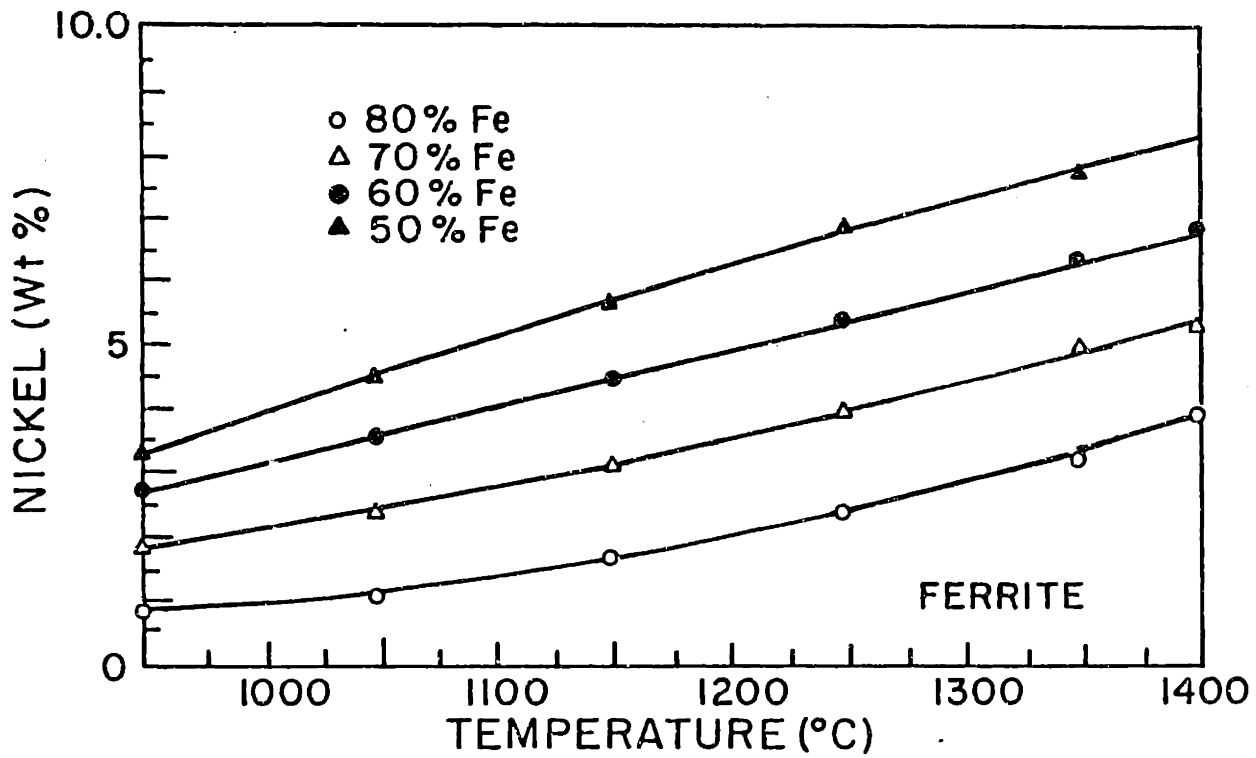


Figure 3.7 Thermodynamic calculations of the nickel content in ferrite as a function of temperature and iron content of the ferrite.

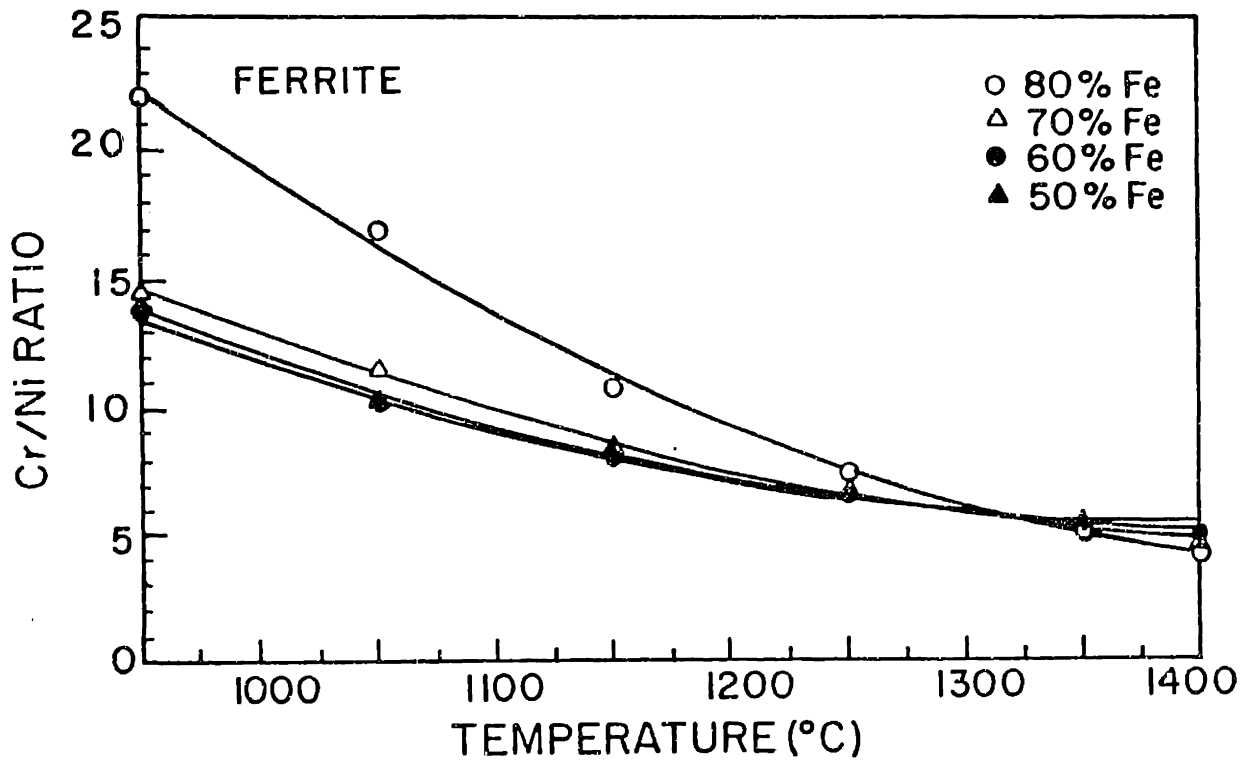


Figure 3.8 Thermodynamic calculations of the Cr/Ni ratio of ferrite as a function of temperature and iron content of the ferrite.

Figure 3.9 shows the ratio of the Fe in the ferrite to Fe in the austenite for ferrite containing 50, 60, 70 and 80 wt.% Fe. This figure was derived from the tie-lines generated by thermodynamic calculations and the results are plotted for temperatures between 1400°C and 950°C. To use this diagram, one must recall that: 1) a Fe ferrite/Fe austenite ratio of 1.0 corresponds to the nominal alloy composition being identical to the ferrite composition, i.e., 1.0 corresponds to a fully ferritic specimen with composition at the tie-line end point and 2) an alloy that has the same composition as the austenite tie-line end point will have an Fe ferrite/ Fe austenite ratio equal to that presented in Fig. 3.9. Therefore, to predict the iron composition of ferrite, select the desired temperature and select the % iron in ferrite line that is the same as the nominal Fe content of the alloy. This requires interpolation since only 50, 60, 70 and 80 % iron in ferrite trends are shown. The actual iron content of the ferrite lies between the Fe ferrite/ Fe austenite ratio of the nominal alloy and 1.0.

At high temperatures (>1300°C) and for low alloy stainless steels (>70% Fe), the iron content of the ferrite is within 2% of the nominal alloy composition. At lower temperatures (<1200°C), the range of possible Fe contents in the ferrite is larger. The temperatures at which the ferrite forms can be predicted by the effective quench temperature [3.23]. This temperature corresponds to the temperature where equilibrium can no longer be maintained during solidification and is a function of the cooling rate. The higher the cooling rate, the higher will be the effective quench temperature since less time is available for diffusion.

Comparing the equilibrium ferrite composition at 1300°C with the measured ferrite composition in the 59wt.% arc-cast buttons showed a good correlation, i.e., the 1300°C temperature appears to be close to the effective quench temperature for the arc-cast condition. Welds, which cool at higher rates, will have even higher effective quench temperatures and the ratio of the iron content of the ferrite to the iron content of the austenite that forms under these conditions will be even closer to unity.

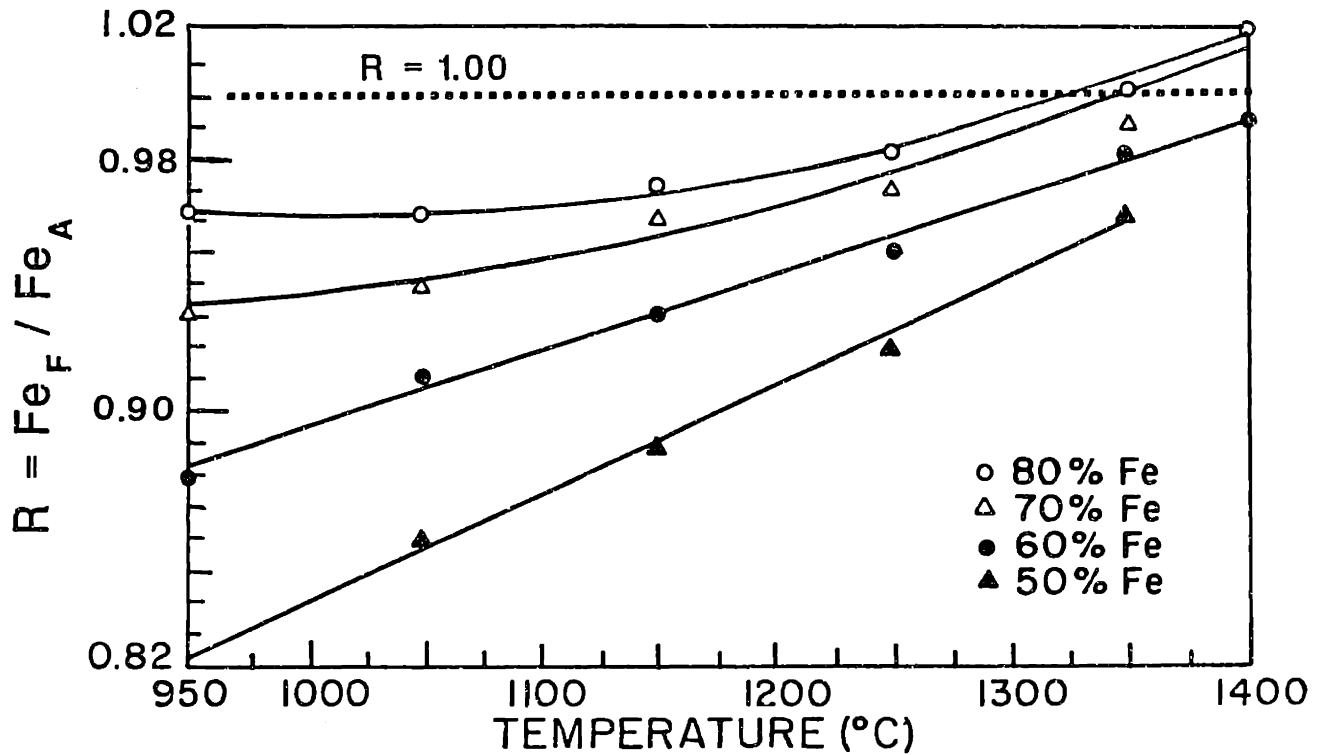


Figure 3.9 Thermodynamic calculations of the ratio between the Fe content of ferrite and the Fe content of austenite as a function of temperature and iron content of the ferrite.

For stainless steels containing 60% Fe or greater and having effective quench temperatures of 1300°C or greater, the Fe content of the ferrite can accurately be estimated from the nominal alloy composition. Figure 3.9 shows that the range of possible iron contents in the ferrite is small at high temperatures. For example, ferrite that forms from a typical 70wt.% Fe alloy at 1300°C has possible Fe contents that range from 68.8% ($0.983 \times 70\%$) to 70.0%. Therefore, by knowing the nominal alloy composition and the effective quench temperature (which can be taken to be 1300°C for castings and welds) the amount of iron in the ferrite can be predicted from Fig. 3.9. This information can then be used to calculate the saturation magnetization of the ferrite using the relationship between σ_s and atomic % iron in the ferrite which will be discussed in the following section.

3.5 Verification and Application of the VSM Method

3.5.1 Ferrite Content of the Arc Cast Alloys

To verify the accuracy of the vibrating sample magnetometer method, the VSM was compared with the Magne-Gage (MG) and quantitative television microscopy (QTM). Each technique was used to measure the ferrite content on a series of high-purity cast alloys and the results were compared. The composition of the cast alloys is shown in Table 2.2 and the microstructure of the alloys is shown in Fig. 3.10. Alloy 1 has no ferrite and the remaining alloys increase in ferrite content from Alloy 1 (0%) to Alloy 7 (32.1%). Results of this comparison are presented below and show that the VSM is as accurate as the other ferrite determination methods. The saturation magnetization of ferrite can also be used to convert the ferrite number, measured by the Magne-Gage, directly into percent ferrite for a wide range of stainless steel compositions.

Quantitative Metallography

The cast alloys were metallographically prepared for QTM analysis according to reference 3.19 using a KOH electrolytic etch. The ferrite which is present in the microstructure is the dark etching phase and because of the relatively coarse microstructure of the castings, the QTM measurements were easily performed. Six micrographs were analyzed from each alloy and the results are presented in Table 3.4. The number of micrographs analyzed, n , and the standard deviation, s , of the readings are indicated and the ferrite contents measured by this method are shown to vary from 0 to 37.2 %.

Table 3.4 : QTM ferrite measurements

Cast Alloy	n	s	Ferrite (%)
1	0	-	0
2	6	0.74	5.35
3	6	2.7	11.0
4	6	1.9	14.2
5	6	2.1	22.8
6	6	2.9	32.4
7	6	5.1	37.2

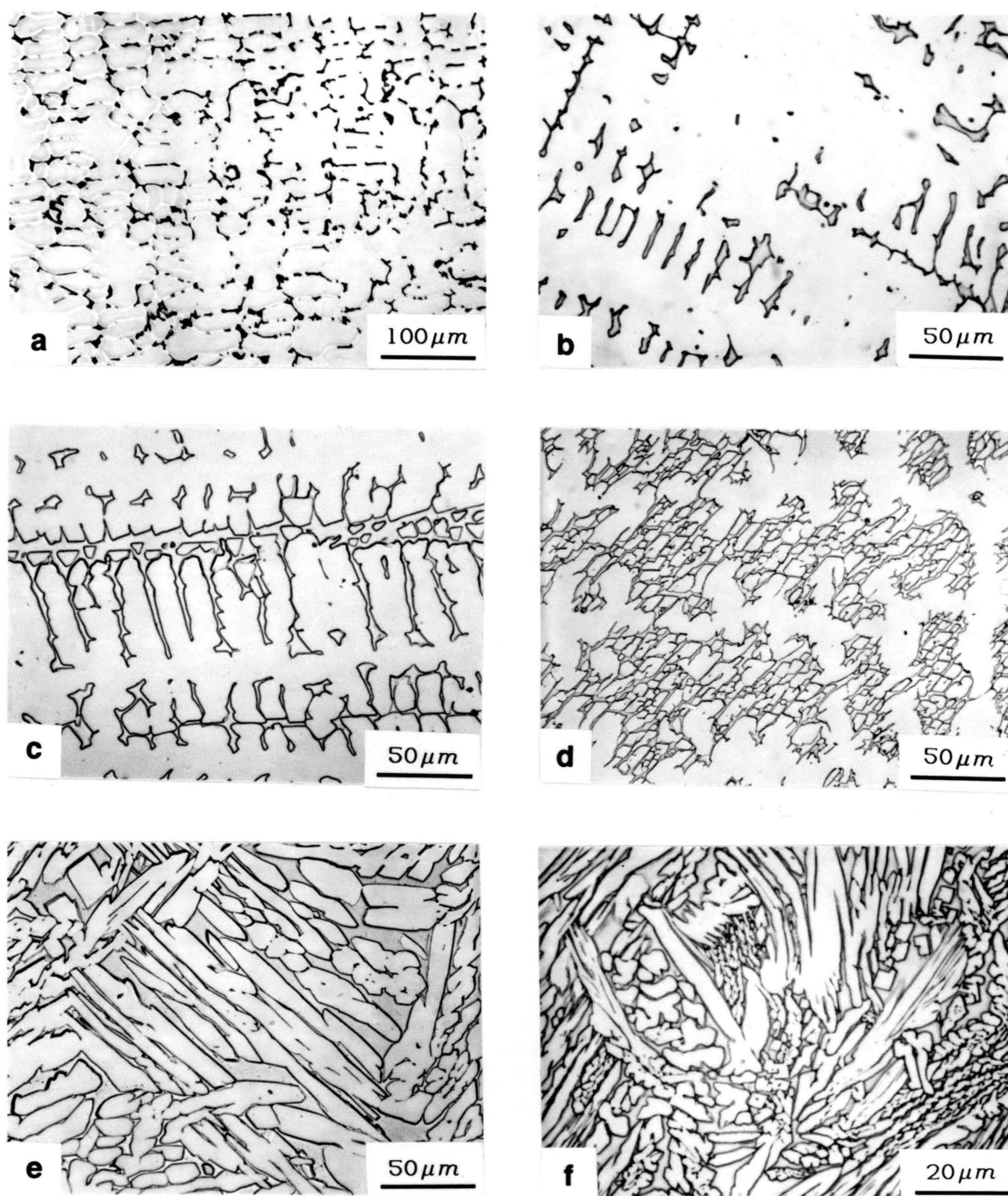


Figure 3.10 Figures a through f show the microstructures of the arc-cast alloys 2 through 7 respectively. The ferrite content increases from Alloy 2 (5%) to Alloy 7 (35%). The primary mode of solidification changes from primary austenite to primary ferrite between alloys 3 (b) and 4 (c) respectively.

Vibrating Sample Magnetometer

The VSM measurements were made on three samples from each cast alloy. Each specimen weighed approximately 50 mg and the room temperature magnetic properties were measured to determine the saturation magnetization. The M-H curves for the seven alloys are summarized in Fig.3.11. As the Cr/Ni ratio of the alloy is increased from alloy 1 to alloy 7, the spontaneous ferrite magnetization varies from 0 to 30 emu/g. The M-H behavior indicates that all of the alloys saturate at an applied magnetic field of about 4 kOe. The initial M-H behavior of a fully ferritic specimen, F, which has a saturation magnetization of 101 emu/g, is also shown on this figure for comparison.

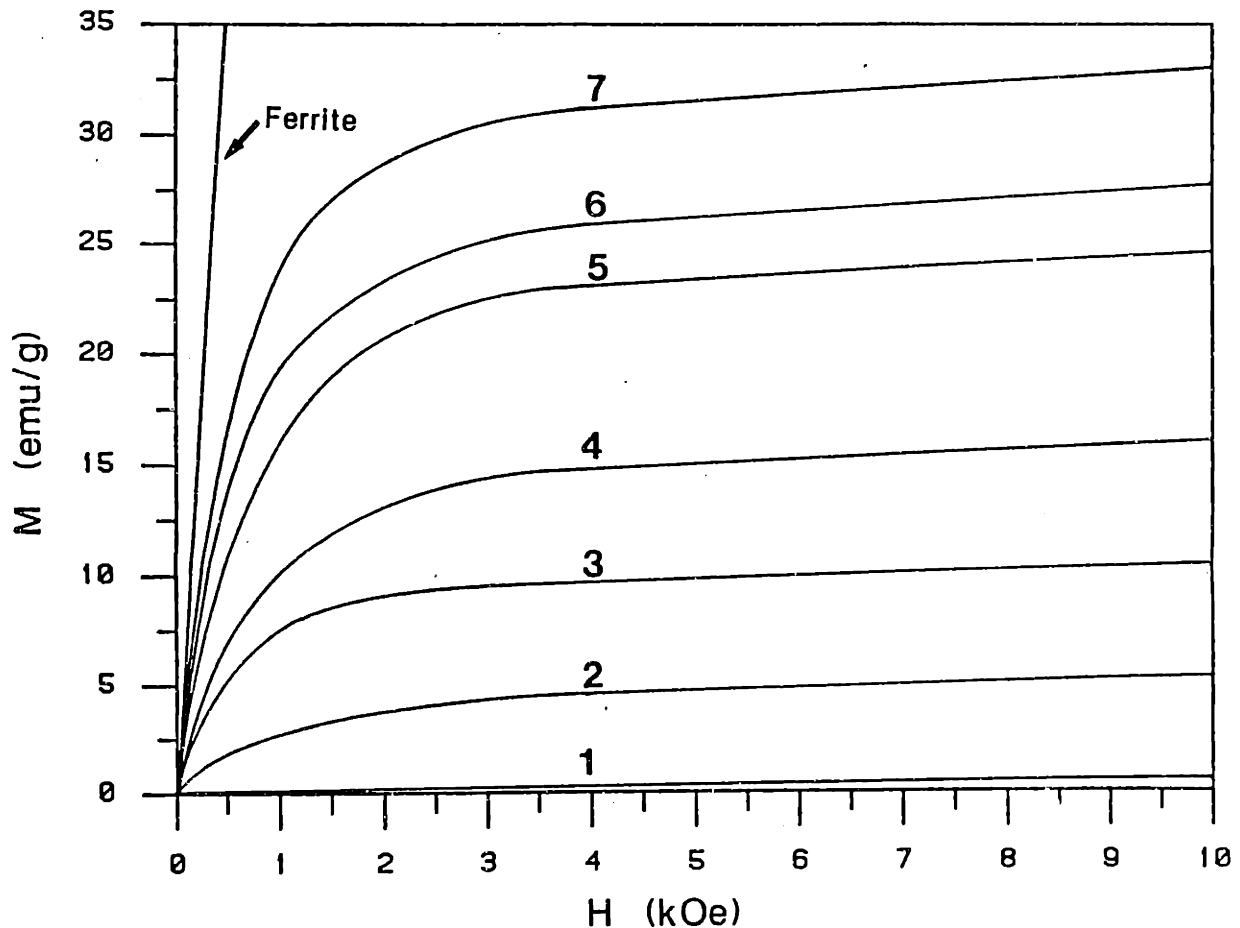


Figure 3.11 M-H curves at room temperature for the seven arc-cast alloys are compared with M-H behavior of a fully ferritic melt-spun ribbon

Table 3.5 summarizes the saturation magnetization results and reports the average of the three measurements for each alloy. The specific saturation magnetization of ferrite in the castings was estimated from its composition so that the M_s data could be converted into percent ferrite. To do this, the composition of the ferrite was measured in each alloy by electron microprobe analysis. These results are shown in Table 2.5 and indicate that the ferrite composition is similar for each of the alloys. The average ferrite composition is 35.5% Cr, 9.12% Ni and 55.4% Fe. Therefore, the Cr/Ni ratio of the ferrite is significantly higher than the nominal alloy composition but the Fe content of the ferrite is only slightly lower than the nominal alloy composition. Using the measured ferrite composition, the saturation magnetization was determined to be 93.6 emu/g (9,125 Gauss) as determined by equation 3.4.

Table 3.5 shows the percent ferrite in each of the alloys as calculated from the saturation magnetization of the castings and the above value for σ_s . The ferrite contents are shown to range from 0 to 32.1 percent and these values compare favorably to the quantitative metallographic measurements.

Table 3.5 : VSM measurements of σ_s and ferrite.

Cast Alloy	σ_s (emu/g)				Ferrite (%)
	1	2	3	Avg.	
1	0.01	0.00	0.00	0	0
2	4.77	4.02	4.13	4.31	4.6
3	9.08	9.01	9.45	9.18	9.8
4	15.0	14.6	14.7	14.8	15.8
5	20.8	21.0	21.4	21.8	23.2
6	24.9	24.4	24.9	24.7	26.4
7	30.2	28.7	31.2	30.0	32.1

Magne-Gage

Magne-Gage measurements were also made to determine the ferrite number, FN, of the cast alloys. The ferrite number is defined by the force of attraction [3.8] between the magnetic probe and the specimen. Higher ferrite numbers correspond to higher ferrite contents, however, since the saturation magnetization is a function of ferrite composition, the ferrite number does not uniquely define the amount of ferrite in the specimen. Therefore, correlations between FN and ferrite content can only be made for alloys of similar composition unless the ferrite composition can be taken into account.

The effect of ferrite composition on the FN is oftentimes neglected. However, the saturation magnetization of ferrite can easily be accounted for when converting from FN to % ferrite. To do this, a relationship will be derived to predict the % ferrite from the FN at a given ferrite composition. Then, for alloys that deviate from this composition, the saturation magnetization effects can be used to modify this equation.

Kotecki [3.25] measured the FN and the extended ferrite number, EFN, for a series of 15 cast alloys of CF8 and CF8M composition. The ferrite content of these alloys varied from 0.2 to 48.6% as determined from a point counting technique. A linear regression analysis on these data shows that the EFN can be related to the percent ferrite as follows:

$$\%F = 0.7(EFN) + 0.54 \quad (3.6)$$

The iron content of each alloy was reported and has an average value of 66.8% with a standard deviation of 2.1%. Therefore, since the composition of these alloys are similar, the composition of the residual ferrite in each alloy can be assumed to be the same. From Fig. 3.9, the iron content of the ferrite in the CF8M alloys will be 98 percent of the iron content in the alloy based on an effective quench temperature of 1300°C. Using this ratio, the saturation magnetization of the ferrite in these alloys was calculated using equation 3.5 to be 12,200 Gauss based on a Cr+Ni content of 100 %Fe.

In order to convert from EFN to % ferrite for alloys that have a different nominal composition, the EFN must be multiplied by the ratio of σ_f in the CF8 alloys to σ_f in the alloy being measured:

$$\%F = 0.7(EFN) \left(\frac{12,200}{\sigma_f} \right) + 0.54 \quad (3.7)$$

where σ_f can be determined from equation 3.5. For ferrite contents less than about 30% (alloys 1-5), the FN can be directly measured with a Magne-Gage and substituted for the EFN with no loss in accuracy. However, Alloys 6 and 7 contain more than 30% ferrite and the Magne-Gage was calibrated to directly measure the EFN.

The Fe content of the ferrite in the arc-cast buttons is lower than the iron content in the CF8 alloys. Therefore, the saturation magnetization of ferrite in the arc-cast buttons is lower than that in CF8 alloys and was shown to be 9,125 Gauss. Using this value of σ_f , the ferrite number was converted to % ferrite using equation 3.7 and the results are shown in Table 3.6. These results show that the ferrite content measured by this method compares favorably to the other two techniques.

Table 3.6 : Magne-Gage measurements and calculated ferrite contents.

Cast Alloy	WD Reading				FN	Ferrite (%)
	1	2	3	Avg.		
1	109	110	110	110	0	0
2	90	90	89	90	4.9	4.5
3	76	76	73	75	8.3	8.0
4	52	49	51	51	14.4	13.5
5	14	13	12	13	23.6	21.8
6*	63	67	69	66.3	29.7	27.4
7*	26	28	24	26	39.6	36.5

* EFN measurements

Comparison of the Three Methods

A summary of the results of the three measurement methods is plotted in Fig. 3.12 as % ferrite versus Cr/Ni ratio along the 59% Fe isopleth. The ferrite content appears to increase linearly with increasing chromium content and there is a good correlation between the average ferrite trend and each of the three measurement techniques. The deviation between the measurements is small at low ferrite contents but increases with increasing ferrite content. Each technique measures ferrite contents that lie above and below the average trend and it appears as though the three measurement techniques are showing the same trend. Therefore, the differences in ferrite contents between the techniques are most likely the result of the small population size used to calculate the statistics.

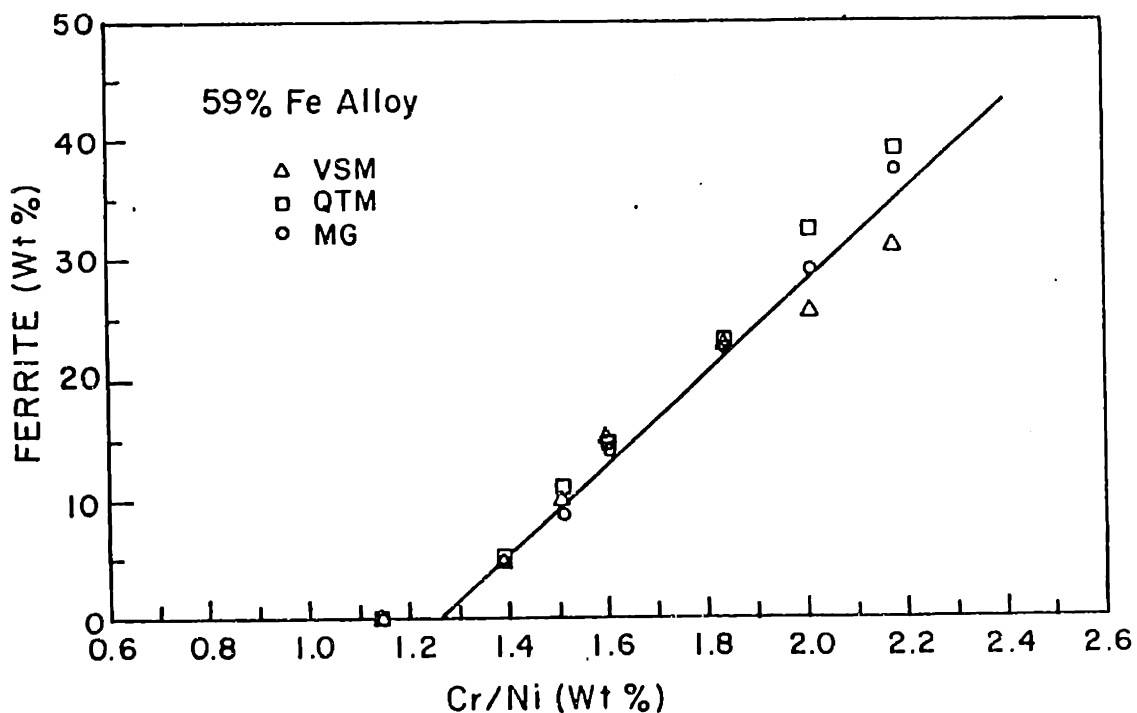


Figure 3.12 Comparison of the ferrite measurements made on the arc-cast alloys by the vibrating sample magnetometer, Magne-Gage and Quantitative Metallographic techniques.

3.5.2 Extending the VSM Method to Commercial SST Alloys

Commercial stainless steel alloys contain alloying elements other than Fe, Ni or Cr and the effect of the additional elements must be taken into account when calculating the saturation magnetization of ferrite. The most common additional elements are Mn, Si, Mo, Nb, N, C, S, and P. These elements are not ferromagnetic and do not contribute significant magnetic moment to the ferrite. Therefore, the iron content of the ferrite is still the most important factor in determining σ_f .

Equation 3.5 can be rewritten to predict σ_f in terms of atomic % Fe in the ferrite:

$$\sigma_F = 3.04(\text{at.\% Fe}) - 71.0 \quad [\text{emu/g}] \quad (3.8a)$$

or,

$$\sigma_F = 296(\text{at.\% Fe}) - 6,910 \quad [\text{Gauss}] \quad (3.8b)$$

Assuming that the alloying elements segregate to the ferrite and the austenite in equal amounts during solidification, then the atomic % Fe in the ferrite can be predicted from the atomic % Fe in the alloy using the methods in section 3.4.

Finally, the weight fraction ferrite can be calculated using equation 3.1. Only a small percentage correction is required to convert from weight fraction ferrite to volume fraction ferrite because the density of ferrite (7.77 g/cm³) is close to the density of austenite (7.96 g/cm³), .

3.6 Conclusions

1. The amount of ferrite in stainless steel alloys can be determined by measuring the saturation magnetization of a small stainless steel specimen with a vibrating sample magnetometer. This technique is not limited by sample size and can be used to measure the ferrite content of rapidly solidified stainless steel alloys.
2. The saturation magnetization of fully ferritic specimens was experimentally determined on a series of rapidly-solidified Fe-Ni-Cr alloys which had compositions similar to that of residual ferrite in stainless steel alloys. The results of these measurements can be used to predict the saturation magnetization of residual ferrite from its composition.
3. Methods were presented to show how the composition of ferrite can be predicted from the nominal alloy composition using thermodynamic calculations. In particular, a range of possible iron contents in the ferrite can be estimated from the nominal alloy composition and the concept of the effective quench temperature. By knowing the iron content of the ferrite, its saturation magnetization can be used to calibrate the VSM to measure the ferrite content of a wide range of stainless steel alloys.
4. The results of the saturation magnetization study can also be used as a basis to calibrate the Magne-Gage for non-standard stainless steel alloys. By considering the saturation magnetization of residual ferrite, the ferrite number can be converted directly into % ferrite for a wide range of nominal alloy compositions.

CHAPTER 4

The Cooling Rate Of Electron Beam Surface Melts

Variations in cooling rate were produced by controlling the travel speed of electron-beam surface melts. Each melt was made at a constant power level of 2 kW and the travel speed ranged from 6.3 to 5000 mm/s. The cooling rate could not be directly measured on the melts because they were too small to instrument with thermocouples or to monitor with optical temperature measurement devices. Therefore, the cooling rate was estimated, rather than measured, using the following techniques: 1) the dendrite arm spacing method, 2) an expression that was derived from Rosenthal's heat flow analysis for quasi-stationary conditions and 3) a numerical approach using the finite element method to calculate the cooling rate and temperature gradient at the melt interface. The heat flow calculations confirm the dendrite arm spacing estimations of the cooling rate and show that the alloys solidified at rates between 7°C/s and $8 \times 10^{6^{\circ}\text{C/s}}$.

The cooling rate is an easy concept to define in single phase materials as it is simply the change in temperature, ΔT , with respect to a change in time, Δt , at a given point. However, during the solidification of an alloy the physical meaning of the term cooling rate is not as easily defined. The presence of at least two phases at the liquid-solid interface having different physical properties, the fact that the interface is moving and releasing a latent heat of fusion, and the possibilities of a non-planar solidification front all contribute to the complexity of the temperature-time relationship for a fixed point in space being overtaken by a liquid-solid interface.

In this chapter, two types of cooling rates will be discussed and will be assumed to be equivalent measures of the solidification rate. The first method predicts the cooling rate by dendrite arm spacing measurements. This method represents an 'average' cooling rate from the inception to completion of solidification. Here, ΔT , is the change in temperature between the dendrite tip where solidification initiates and the dendrite 'base' where the last liquid solidifies. The change in time required to produce this change in temperature is the time necessary for the L/S interface to move the distance corresponding to the length of protrusion of the dendrite in front

of the interface and is consequently related to the interface velocity. The second method calculates the 'instantaneous' cooling rate at a given point. This method can be applied to the L/S interface to calculate the cooling rate at the solidification temperature but neglects the details of the interface by assuming plane-front rather than dendritic behavior. Here, the temperature gradient, G , and the interface velocity, R , are combined to represent the cooling rate during solidification. This method will be discussed in detail in the following sections.

In welds and surface melts, the travel speed, S , is held constant but the velocity of the L/S interface varies from zero to a maximum value of S on the melt interface. Variations in the temperature gradient are also present around the surface of the melt, therefore, neither the interface velocity nor the temperature gradient can be uniquely specified by the welding parameters. Consequently, the cooling rate, ϵ , and the dendrite arm spacing, λ , vary throughout the cross section of the weld. This chapter discusses methods that enable the cooling rate to be calculated and also presents results to show the variations of G , R , ϵ , and λ within a given weld.

4.1 The Geometric Shape of Electron Beam Melts

The geometric shape of the molten zone influences the depth of penetration, the width of the fusion zone and the cooling rate in the melt. These factors are of essential importance to welding and surface modification applications and a study was performed to determine the influence of electron beam parameters on the melt pool shape. The results of this separate study are presented in Appendix G and were used to select the electron beam melting parameters used throughout this study. In addition, by using dimensionless quantities to represent the weld pool shape, the results of this study can be used to predict the width, depth and length of the resolidified zone for a wide range of operating parameters.

4.2 Dendrite Arm Spacing Calculations

Two factors contribute to the dendrite arm spacing (DAS) [4.1]. Firstly, during solidification, the dendrites optimize their spacing to optimize both constitutional supercooling and interfacial surface energy effects. The free energy associated with constitutional supercooling is minimized by a small DAS while that of the surface

energy interface is minimized by a large DAS. Therefore, the actual spacing is a balance between these factors and each factor is influenced by the cooling rate. Secondly, after the solidification spacing has been established, coarsening of the dendrite arms can occur as the melt cools. The driving force for coarsening is a reduction in the total surface energy [4.2] and only the highest order arms are affected. For example, secondary arms, but not primary arms, will coarsen when secondary arms are present, while primary arms (or cells) will coarsen when no secondary arms are present.

Relationships between DAS and cooling rate (ϵ) have been developed and show that a linear relationship exists between \log DAS and $\log \epsilon$ [4.1, 4.2]. These relations have the following form :

$$\lambda = a(\epsilon)^{-n} \quad (4.1)$$

where a and n are material-dependent constants and λ represents the dendrite arm spacing. The cooling-rate exponent, n , is known to be close to 0.5 for primary dendrite arms and varies between 0.25 and 0.33 for secondary dendrite arms [4.1]. The lower value for secondary arms is a result of coarsening. If secondary arms are not present, the primary DAS may have an n value close to 0.3.

Microstructural examination of the electron-beam melts made in this investigation showed that the DAS was not uniform within the melt. Cross-sectional views of the deep penetrating, slow speed melts (1,2,3) showed that the spacing was typically small at the fusion line and increased towards the center line. Along the center line, there was a slight decrease in spacing at the top of the melt. Cross-sectional views of the shallow penetrating, higher speed melts (4,5,6) showed that the DAS was small at the fusion line and increased to a larger spacing within a few dendrite spacings of the boundary. The DAS then remained approximately constant to the top of the melt. Figure 4.1 a and b compare the microstructure at the fusion line with that at the center for melt 3, to illustrate the range of dendrite arm spacings observed within the same melt.

The DAS measurements show that the cooling rate is not constant throughout the melt. The variation in DAS is approximately a factor of three, which corresponds to a variation in cooling rate of approximately ten.

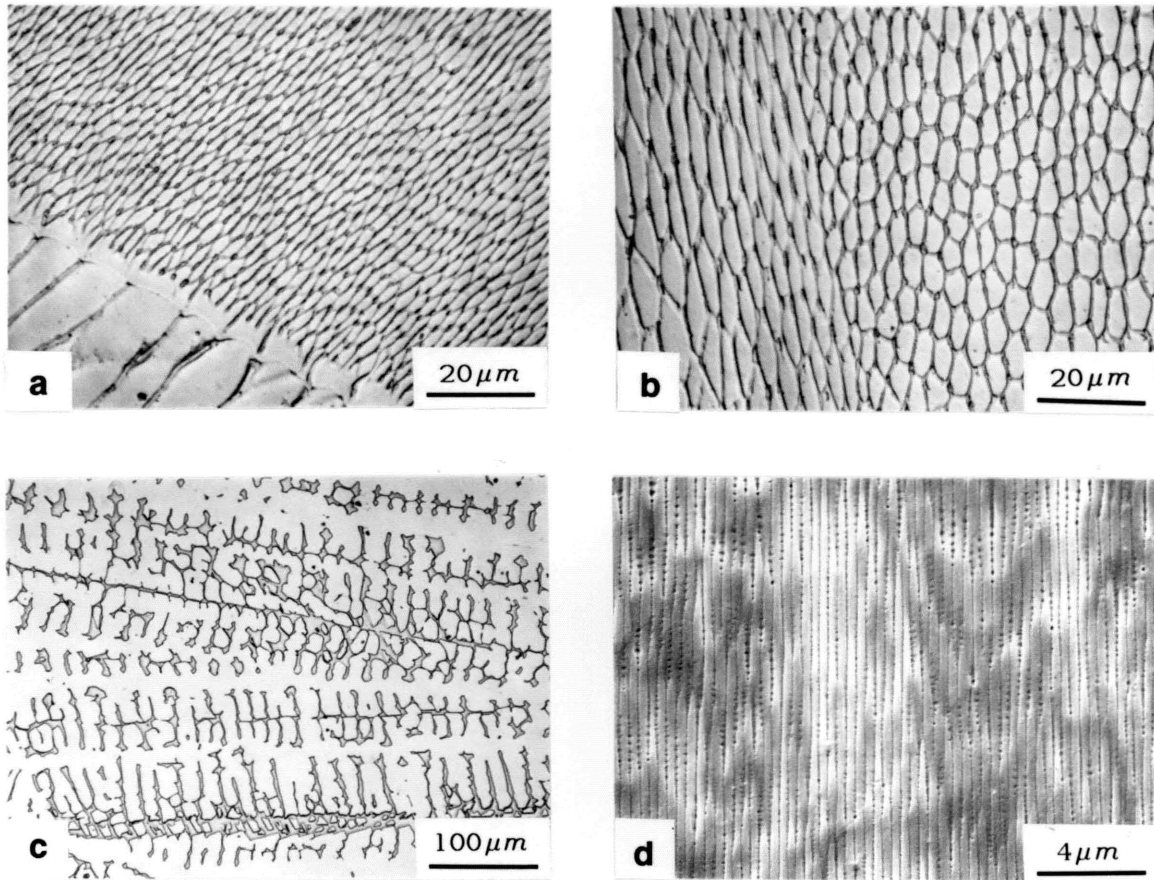


Figure 4.1 Variations in the dendrite arm spacing. Figures a and b compare the variation for a given set of surface melting parameters (100mm/s), at the fusion boundary and at the center of the melt respectively. Figures c and d compare the largest dendrite arm spacings in the casting with the smallest spacings in the highest speed melt.

However, a large percentage of the change in the DAS occurs close to the fusion line and the majority of the melt solidifies with a cooling rate variation of only a factor of five or less.

The DAS measurements were made in a location which is representative of the average behavior of the melt and where the specimens would later be extracted for ferrite content measurements (see section 2.3.2). The results of the dendrite arm spacing measurements are listed in Table 4.1 where λ_1 represent the primary dendrite arm spacing for melts 1, 2 and the arc cast button, and cell spacings for melts 3, 4, 5 and 6. The secondary dendrite arm spacing is represented by λ_2 , and was able to be measured on the low speed melts that solidified in a dendritic mode. These data show that the primary DAS decreases from a value of 42 μm for the casting to 0.43 μm for the highest travel speed. These two microstructures are compared in Fig. 4.1 c and d.

A plot of $\log \lambda$ versus $\log S$ is shown in Fig 4.2 for the six melts, where S refers to the travel speed. The best-fit linear relationship between λ and S has a slope of -0.49 and indicates the refinement in DAS with increasing travel speed.

Table 4.1 : Cooling rates calculated from primary and secondary dendrite arm spacing measurements.

Melt	Travel Speed (mm/s)	λ_1			λ_2		
		\bar{X} (μm)	s (μm)	ϵ (K/s)	\bar{X} (μm)	s (μm)	ϵ (K/s)
cast	-	42	3.9	-7.0	18.0	3.3	-3.2
1	6.3	10.5	1.5	-4.7×10^2	4.7	1.2	-3.9×10^2
2	25	6.6	1.8	-1.9×10^3	3.0	0.54	-1.9×10^3
3	100	3.2	0.9	-1.7×10^4	-	-	-
4	500	1.1	0.4	-4.4×10^5	-	-	-
5	2,000	0.73	0.05	-1.5×10^6	-	-	-
6	5,000	0.43	0.07	-7.5×10^6	-	-	-

Katayama et al. [4.5] experimentally determined values for the constant, a , and the cooling rate exponent, n , for type 310 stainless steel. They give the following relationship between dendrite arm spacing and cooling rate :

$$\lambda_1 = 80(\epsilon)^{-0.33} \quad (4.1a)$$

$$\lambda_2 = 25(\epsilon)^{-0.28} \quad (4.1b)$$

These values were used to calculate the cooling rate based on equation 4.1 and should apply to the alloys used in this investigation for two reasons. Firstly, type 310 stainless steel has a high alloy content and contains approximately 55 wt percent iron which is close to the 58 wt percent iron of the alloys used in this study. Secondly, the cooling rate exponent of 0.33 for the primary dendrite spacing suggests that the structure has possibly coarsened during solidification. Coarsening of the primary structure might also be expected in this study since the higher cooling rate melts solidified in a cellular manner with no secondary arms.

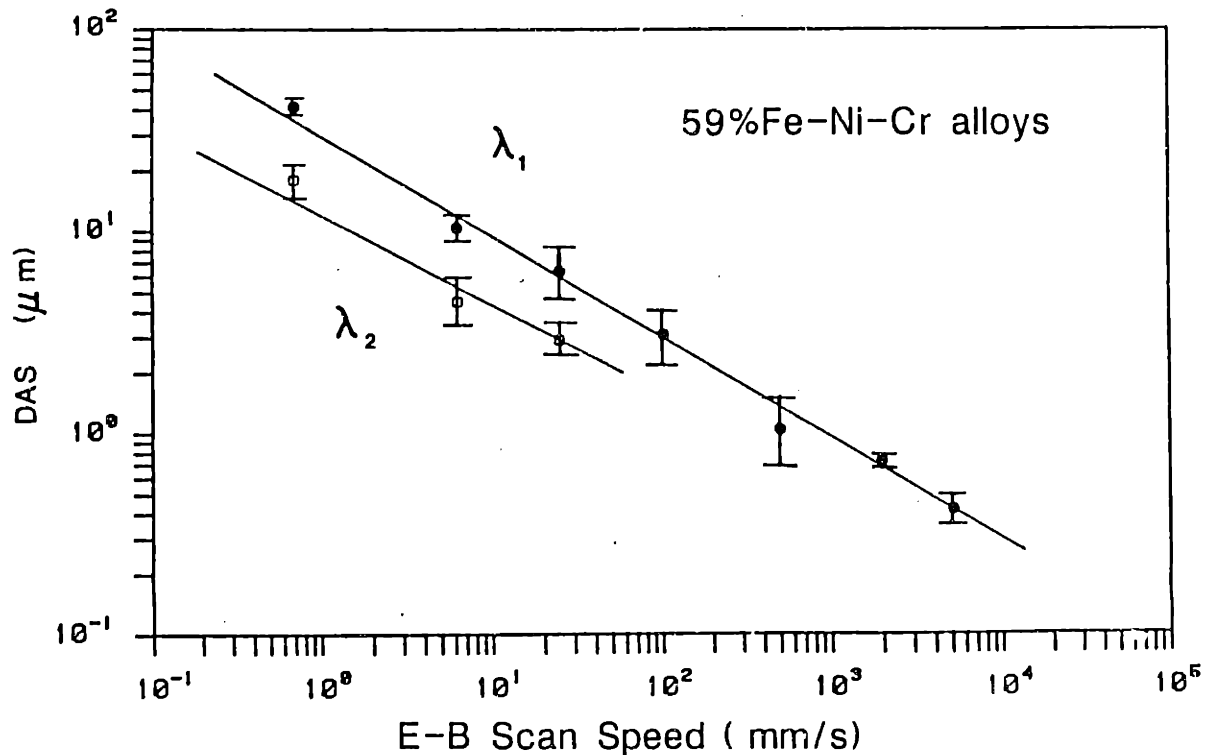


Figure 4.2 Primary and secondary dendrite arm spacing as a function of electron beam scan speed +/- one standard deviation error bars are indicated.

A plot of the cooling rate versus travel speed is shown in Fig 4.3 for the electron beam melts and the casting. Since the travel speed could not be controlled for the casting, an effective interface velocity of 0.7 mm/s was calculated using a DAS of 42 μm and an extrapolation of Fig 4.2. The primary DAS results predict a cooling rate variation of over 6 orders in magnitude, from 7°C/s for the casting to 7.5×10^6 °C/s for the highest speed melt. The secondary DAS prediction of the cooling rate confirms these values for the low cooling rate melts.

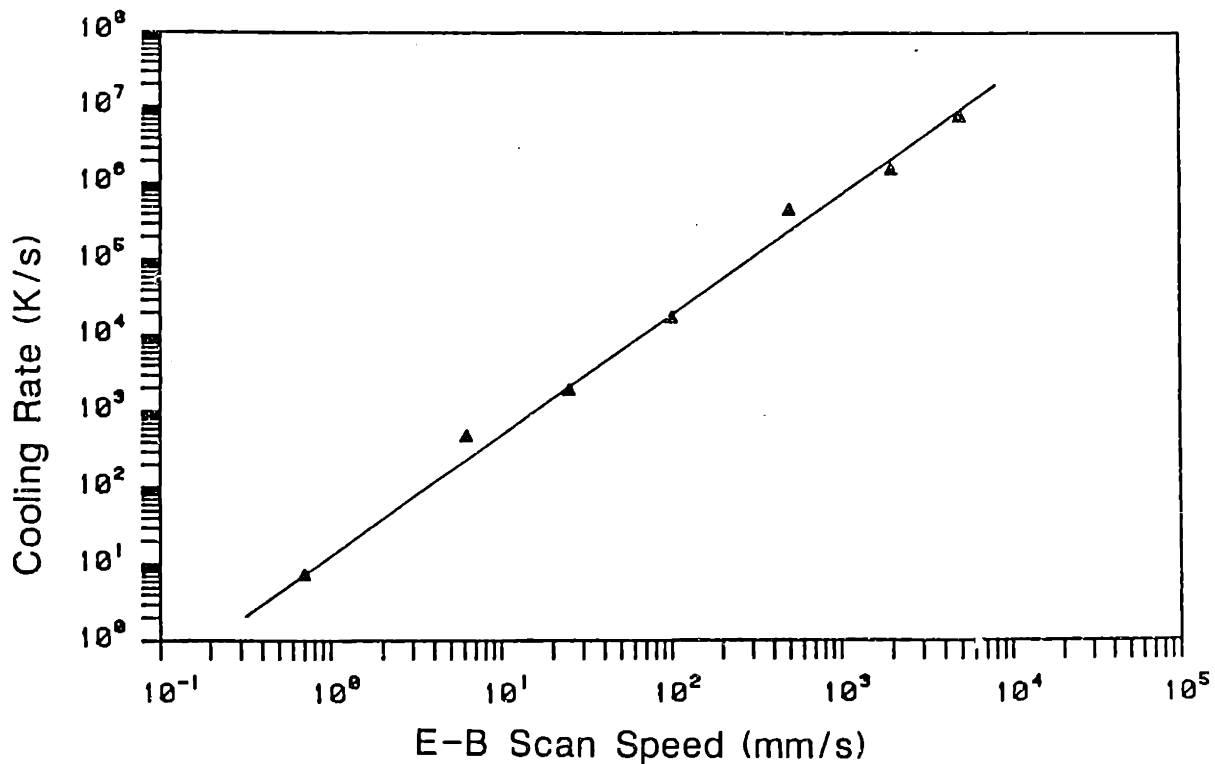


Figure 4.3 Cooling rate, based on dendrite arm spacing measurements, plotted versus the electron beam scan speed.

4.3 Analytic Solution to the Heat Flow Equation

4.3.1 The Temperature Distribution Surrounding a Melt

The theory of heat flow due to a moving point source was first examined and applied to welds by Rosenthal in 1946 [4.6]. Since then, other investigators have analyzed the moving-source heat-flow problem. In 1965, Christensen et al. [4.7] solved the problem using dimensionless variables which allowed a large spectrum of situations and materials to be compared. In 1983, Eagar and Tsai [4.8] replaced the point source assumption with a distributed heat source and solved the problem by a numerical procedure. In this section, Rosenthal's approach will be used to calculate the temperature distribution in the solid plate since it allows an analytic solution to be derived for the cooling rate. Experiments have shown that the isotherms in the base metal which surround the heat source soon become constant in the moving frame of reference. This condition is called quasi-stationary heat flow and the mathematical formulation used by Rosenthal incorporates this assumption. Several other assumptions are required in order to derive the analytic solution :

- 1 The material properties are independent of temperature and the material is considered homogeneous and isotropic.
- 2 The heat source strength is constant and is concentrated at a point.
- 3 The travel speed is constant and there is no heat loss at the boundaries.

The equations are formulated with the heat source moving at travel speed S in the positive x direction as indicated in Fig. 4.4. The heat flow equation is written for quasi-stationary conditions in three dimensions with the source at the origin and by replacing the x coordinate with $\xi = x - vt$ to account for the moving source :

$$\nabla^2 T = \frac{\partial^2 T}{\partial \xi^2} + \frac{\partial^2 T}{\partial y^2} + \frac{\partial^2 T}{\partial z^2} = -S \left(\frac{\rho c}{k} \right) \left(\frac{\partial T}{\partial \xi} \right) \quad (4.2)$$

The nomenclature used in this chapter is summarized in Table 4.2.

The solution to this differential equation assumes that the base plate is semi-infinite and that the heat flow is three dimensional. These conditions most accurately approximate the high travel speed surface-melts because of their shallow depth of penetration.

The boundary condition for this assumption becomes $(\partial T / \partial t)$ approaches 0 as i approaches $\pm \infty$, where $i = \xi, y$ and z and the heat flux approaches its maximum value at the source ($-4\pi r^2 k (\partial T / \partial r)$ approaches Q as r approaches 0). The solution for the temperature distribution in the solid then becomes [4.6]:

$$T - T_o = \theta = \frac{Q}{2\pi k r} \exp\left(-\frac{S}{2\alpha}(r+x)\right) \quad (4.3)$$

where ξ has been replaced by x in the exponential term and thus the temperature distribution is assumed to be made in the moving frame of reference for an observer situated at the origin. The form of equation 4.3 predicts a skewed temperature distribution which has an infinite temperature at the source origin. The isotherms are compressed ahead of the heat source and expanded behind the heat source and their distribution is related to the material properties as well as the heat source strength and travel speed. The size of the liquid melt pool is often estimated by solving equation 4.3 for the locus of points which represent the melting temperature

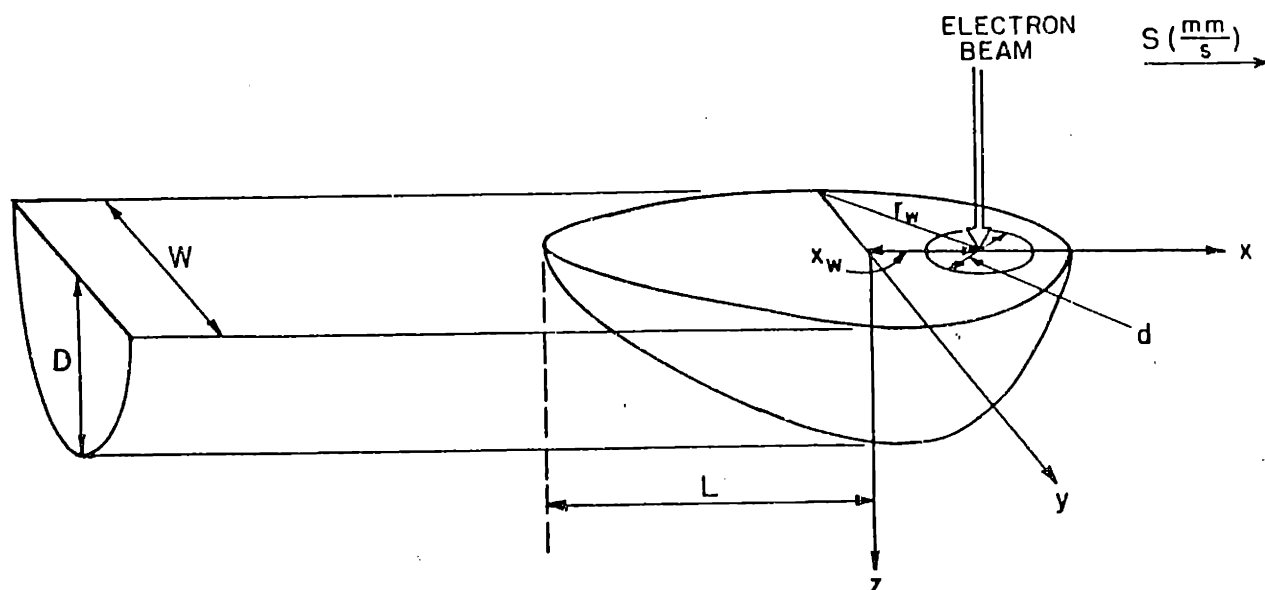


Figure 4.4 Coordinate system used to represent the electron beam surface melts.

of the alloy. This approach predicts a melt pool which is semi-circular in shape with the depth being equal to one half the width. In real melts, this "ideal" shape is altered by convection of the liquid in the melt pool.

Table 4.2 : Nomenclature used in chapter 4

Symbol	Description	MKS units
T, T_o, T_L	temperature, ambient, liquidus	K
$\theta = (T - T_o)$	temperature rise	K
$\theta_m = (T_L - T)$	temperature rise	K
\dot{c}	cooling rate	K/s
$t, \Delta t$	time, time increment	s
λ	dendrite arm spacing	μm
a, n	DAS constants	-
d	electron beam diameter	mm
v	velocity of the L/S interface	-
r	radial coordinate	mm
x, y, z	orthogonal coordinates	mm
x_m, r_m	coordinates on melt isotherm	mm
x_w	value of x at max. melt width	mm
r_w	value of r at max. melt width	mm
$\xi = x - vt$	x -coordinate transformation	mm
S	velocity of the heat source	mm/s
\bar{n}	unit vector normal to weld pool	-
\bar{i}	unit vector in the x direction	-
ρ	density	kg/m ³
c	heat capacity	J/kg-K
k	thermal conductivity	W/m-K
k'	effective thermal conductivity	W/m-K
α	thermal diffusivity	m ² /s
Q	rate of heat input	J/s

4.3.2 Derivation of an Analytic Expression for the Cooling Rate

Equation 4.3 represents the instantaneous temperature distribution in the plate with the source at the origin. At the next instant in time, the temperature at each point in the plate changes because the source has moved an amount $v\Delta t$. This change in temperature causes a cooling or a heating effect at each point in the plate. For a given material and heat source strength, the cooling rate is therefore dependent on how rapidly the source moves across the surface of the plate. In Appendix A, an analytic expression is derived which represents the cooling rate at any point in the plate. This expression is described in the following paragraphs and is used to calculate the cooling rate at the L/S interface.

The cooling rate at any point in the base metal is defined as the change in temperature with respect to time and is dimensionally equivalent to the product of a temperature gradient and a velocity. For the heat source moving in the positive x direction at a constant speed, S , the cooling rate at a given point becomes :

$$\frac{dT}{dt} = -\nabla T \cdot \vec{v} = -S \frac{dT}{dx} \quad (4.4)$$

Therefore, the cooling rate can be calculated as the product of the temperature gradient in the x direction and the travel speed.

Starting with the equation which represents the temperature distribution in the plate, eq. 4.3, an expression for the cooling rate can be derived which is valid at any point in the base plate :

$$\frac{\partial \theta}{\partial t} = \theta \left(\frac{v^2}{2\alpha} \right) \left(1 + \frac{x}{r} + \frac{2\alpha x}{vr^2} \right) \quad (4.5a)$$

where θ is defined as the local temperature rise and v represents the velocity of the L/S interface. However, to make correlations with the dendrite arm spacing measurements, only the cooling rate at the liquid/solid interface is of interest. The temperature at the interface is defined by the liquidus temperature of the alloy, T_L , and at this location, θ , r and x are replaced by θ_m , r_m and x_m respectively. The expression for the cooling rate in the solid at the liquid solid interface is therefore :

$$\frac{\partial \theta}{\partial t} \Big|_{T=T_L} = \theta_m \left(\frac{v^2}{2\alpha} \right) \left(1 + \frac{x_m}{r_m} + \frac{2\alpha x_m}{vr_m^2} \right) \quad (4.5b)$$

Application of equation 4.5b to a general weld requires knowledge about the physical properties of the alloy (T_L , α), the travel speed, and the weld pool shape (x_m , r_m).

Equation 4.5b can be simplified to represent the cooling rate at one specific location on the weld pool. This location corresponds to the top back center of the weld pool, i.e., $z = 0$, $y = 0$, and $x = x_m$. Since the radial coordinate is always positive and x is always negative on the trailing edge of the weld pool, $r_m = -x_m$ at this location and equation 4.5b reduces to the following expression :

$$\frac{\partial \theta}{\partial t} = \frac{-S \theta_m}{x_m} \quad (4.6)$$

where v has been replaced by S since the velocity of the L/S interface can be assumed to be equal to the travel speed at this location. Therefore, the cooling rate at the trailing tip of the weld pool can be calculated from the melting temperature of the alloy, the travel speed and the length of the weld pool. Equation 4.6 represents the maximum cooling rate on the liquid/solid surface and can be used as an easy method to calculate the upper bound for the cooling rate in a weld.

4.3.3 Estimating the Cooling Rate in the Liquid Pool

The cooling rate equations derived in the previous section are based on a heat conduction model which is strictly valid only in the solid metal. Convective effects within the molten melt pool can not be incorporated into a simple analytic heat flow model and therefore, the temperature distribution in the bulk of the melt pool can not be easily calculated. However, since the melt pool is assumed to be quasi-stationary, there is continuity of heat flow across the liquid/solid interface. Therefore, the temperature gradient in the liquid, at the liquid/solid interface, is related to the temperature gradient in the solid by their respective thermal conductivities :

$$\nabla \theta_L = \frac{k_s}{k'_L} \nabla \theta_s \quad (4.7)$$

where the subscripts L and s refer to liquid and solid respectively and k'_L refers to the effective thermal conductivity of the liquid.

Equation 4.7 is only valid at the liquid solid interface and close to this interface, a solute boundary layer develops which is only a few dendrite arm spacings in length. This boundary layer can be approximated by the ratio of the thermal diffusivity of the liquid to the travel speed [4.9] and Table 4.3 indicates that the boundary layer is a small percentage of size of the weld pool. Since the solidification characteristics are determined by this boundary layer, and since this boundary layer is close to the liquid/solid interface, equation 4.7 can be used to predict the temperature gradient in the liquid for the purpose of estimating the solidification related behavior that occurs on a microscopic scale at the dendrite tip. However, equation 4.7 can not be used to represent the cooling rate far from the interface because of the fluid flow within the weld.

Table 4.3 : P_t , δ and k'_L/k_s for the six electron beam melts.

Melt	Travel Speed (mm/s)	~Fluid Velocity (mm/s)	L (mm)	P_t	δ (A°)	k'_L/k_s
1 top	6.3	1,500	2.0	1,320	1,590	2.5
1 root	6.3	375	0.5	80	1,590	1.5
2 top	25	750	0.75	250	400	2.0
2 root	25	388	0.25	47	400	1.0
3	100	450	0.6	162	100	1.0
4	500	150	0.2	12	20	0.5
5	2,000	23	0.03	0.28	5	0.5
6	5,000	6	0.008	0.024	2	0.5

$$P_t = Lu/\alpha_L, \alpha_L = 2.2 \text{ (mm}^2/\text{s)}$$

$$\delta = D_L/V, D_L = 1 \times 10^{-3} \text{ (mm}^2/\text{s)}$$

The effective thermal conductivity of the liquid depends on the ratio of the ability of the fluid to transfer heat by convection to that by conduction. This ratio is defined by the dimensionless thermal Peclet number, P_t :

$$P_t = \frac{Lu}{\alpha} \quad (4.8)$$

where u is the fluid velocity, L is the distance from the solid interface, and α is the thermal diffusivity. For small Peclet numbers, conduction will be more important than convection and for these conditions, $k'_L = k_L$ and is approximately equal to $k_S/2$ [4.10]. For large Peclet numbers, convection will be more important than conduction and k'_L will increase with P_t . Measurements of k'_L for high Peclet numbers are difficult to make and are not available. Estimations of k'_L for liquid steels would suggest however that k'_L is 3 to 5 times higher than k_L [4.10]. The estimated Peclet number, liquid diffusion boundary layer thickness and effective thermal conductivity of the liquid are shown in Table 4.3 for the six travel speeds used in this investigation.

Estimations of the fluid velocity were made by assuming Marangoni driven flow to be a maximum in melt No.1 with a magnitude of about 1.5 m/s [4.10]. This value was assumed to decrease in proportion to L as the travel speed increased and P_t was calculated from the estimated fluid velocity. P_t was then used to estimate the effective thermal conductivity in the liquid.

Combining equations 4.5 and 4.7 gives an expression for the cooling rate in the liquid at the melt isotherm :

$$\left(\frac{\partial\theta}{\partial t}\right)_L |_{T=T_L} = \frac{k_s}{k'_L} \left(\frac{\theta_m S}{2\alpha}\right) \left(1 + \frac{x_m}{r_m} + 2\frac{\alpha x_m}{S r_m^2}\right) \quad (4.9)$$

For the highest cooling rate portion of the liquid, at the top back center of the melt pool $x = x_m$, $y = 0$, and $z = 0$, equation 4.9 simplifies to the following :

$$\left(\frac{\partial\theta}{\partial t}\right)_L |_{T=T_L} = \frac{k_s}{k'_L} \left(\frac{S\theta_m}{x_m}\right) \quad (4.10)$$

The physical properties for typical austenitic stainless steels are listed in Table 4.4 and indicate that the ratio of thermal conductivities between the solid and the liquid is a factor of 2. The average length of the melts (x_m) was measured (see

section 2.2.2) and is listed in Table 4.4. With the above values, and assuming the ambient temperature to be 25°C, the maximum cooling rate in the melts was calculated using equation 4.10. The results of these calculations are summarized in Table 4.5 and predict cooling rates between 6.6×10^2 and 2.6×10^7 °C/s. A comparison of these data with the DAS predictions is presented in section 4.4.

Table 4.4 : Physical properties for stainless steel

Material Property	Value
k_s	18 (W/m-k)
c_s	500 (J/kg-k)
ρ_s	7,900 (kg/m ³)
α_s	4.6×10^{-6} (m ² /s)
k_L	$\sim 1/2 k_s$
c_L	$\sim c_s$
ρ_L	$\sim \rho_s$
α_L	$1/2(\alpha_s)$
T_L	1440°C

Table 4.5 : Maximum cooling rate in the liquid at the L/S interface.

Melt	S (mm/s)	ϵ max. (K/s)
1	6.3	-6.6×10^2
2	25	-3.1×10^3
3	100	-2.8×10^4
4	500	-7.1×10^5
5	2,000	-7.1×10^6
6	5,000	-2.6×10^7

4.4 Finite Element Model

A three-dimensional, finite element method (FEM) model was developed to calculate the temperature distribution in the solid surrounding the molten zone. This data was then used to calculate the cooling rate in the melt at the liquid/solid interface. The FEM model utilizes the three-dimensional shape of the melt pool as a Dirichlet boundary condition to solve the heat equation. Therefore, it can only be applied to specific melts, once the melt pool shapes as been determined by post-melt metallographic analysis. Results from this model were used to confirm the cooling rates which were predicted by dendrite arm spacing measurements on several specific melts. The FEM program also gave information about the temperature gradient at the liquid/solid interface as well as showing the distribution of cooling rates and temperature gradients around the surface of the L/S interface.

4.4.1 Assumptions and Boundary Conditions

The model is formulated by assuming quasi-stationary welding conditions which imply that the weld pool shape does not vary with time. The base metal plate is assumed large compared to the weld, which is a realistic assumption for the high travel speed welds. This assumption allows the problem to be solved by treating the plate edges to be insulated and at a constant (ambient) temperature. Radiation heat loss from the top surface of the plate is assumed to be small and the material properties, Table 4.4, are assumed to be independent of temperature. The problem therefore becomes one of heat conduction, where the heat from the source is distributed into the solid base metal plate through the irregularly shaped liquid/solid interfacial surface of the weld pool. The program uses an ellipsoidal weld pool shape assumption which is reasonable for shallow penetrating welds but can not be used to represent deep penetrating welds because of their keyhole appearance.

The FEM program requires a three-dimensional mesh to represent the base metal plate and the weld pool. Symmetry allows the calculations to be made on one-half of the plate which simplifies the calculations. Figure 4.5a shows the dimensions of the base plate, the location of the weld pool and the coordinate system which was used

for the calculations. Figure 4.5b shows a typical mesh [4.11] which has 1,398 nodal points in the plate, 67 of which are on the liquid/solid boundary, and the entire plate contains 6840 tetrahedral elements.

The FEM code was developed at MIT [4.12] and the data which is input to the program consists of the three-dimensional mesh, the weld travel speed and the material properties. The FEM program solves an 'inverse' heat flow problem to calculate the temperature distribution which is required to maintain the weld pool

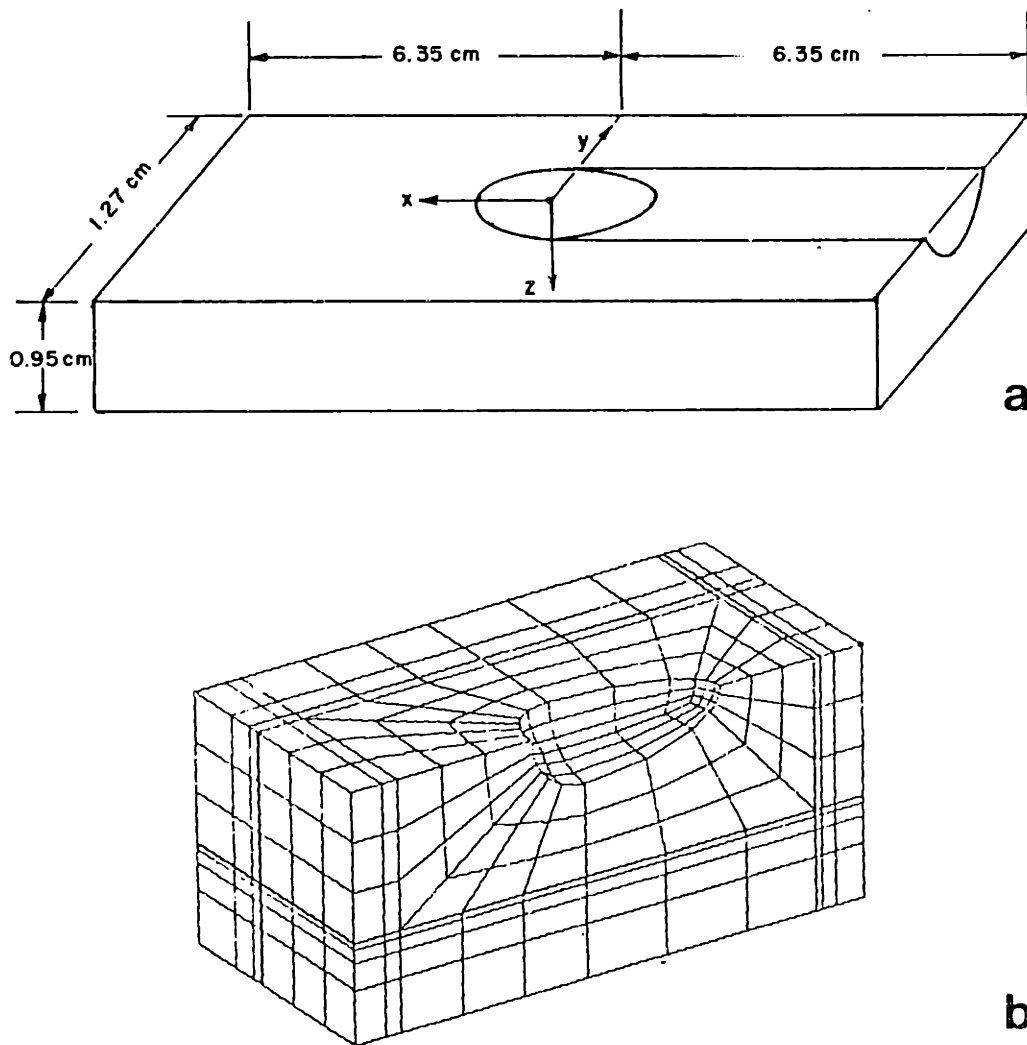


Figure 4.5 a) Dimensions of the base plate and b) finite element mesh of an electron beam melt used to calculate cooling rates and temperature gradients at the melt pool boundary.

boundary at its liquidus temperature. From this temperature distribution, the program calculates the temperature gradient in the solid, ∇T , in a direction which is normal to the liquid/solid interface for each nodal point on the weld boundary. The product of this temperature gradient and the velocity of the weld boundary gives the cooling rate at the boundary in the solid :

$$\epsilon_s = -\nabla T \cdot \bar{v} = -|\nabla T| v(i \cdot \bar{n}) \quad (4.11)$$

where the unit vector \bar{n} is normal to the liquid/solid interface and the unit vector i is in the positive x direction. The cooling rate in the liquid can be calculated by the ratio of the thermal conductivities as discussed in the preceding section :

$$\epsilon_L = -\frac{k_s}{k_L} |\nabla T| v(i \cdot \bar{n}) \quad (4.12)$$

The output from the program consists of the temperature gradient and the cooling rate at each of the nodal points on the weld isotherm. The typical mesh contained between 30 and 40 points on the solidifying portion of the weld pool.

4.4.2 Temperature Gradient and Cooling Rate Calculations

The intent of the FEM program was to calculate the cooling rate of the electron beam melts examined in this study. However, the non-uniform cross sectional shapes of the low speed melts and the highly elongated shapes of the high speed melts did not allow the six electron beam melts to be easily modeled. Therefore, two additional melts were made on 304 stainless steel to determine the distribution and magnitude of the cooling rates and temperature gradients for typical electron beam melts. Table 4.6 lists the electron beam parameters that were selected to produce ellipsoidal shaped melt-pools that could be modeled. The dimensions of the weld pools, as determined by metallographic analysis are also reported in this Table. These data and the physical property data from Table 4.3 were input to the FEM program to calculate the temperature gradient in the solid, T_s , the cosine between the normal to the melt pool and the travel speed direction, N , and the cooling rate in the liquid, ϵ_s , at each boundary nodal point on the solidifying half of the melt pool. The results of the calculations are listed in Tables B.1 and B.2 in Appendix B for the cooling rate and temperature gradient at the liquid/solid interface.

Table 4.6 : Welding parameters, physical dimensions and mesh properties for the two welds to be studied by FEM analysis.

Parameter	Melt A	Melt B
speed (mm/s)	6.4	25.4
current (mA)	3.0	3.0
voltage (kV)	100	100
length (mm)	1.29	1.52
depth (mm)	1.19	0.58
width (mm)	2.39	1.17

Cooling Rates

Figure 4.6a and 4.7a show 'topographical' projections of the cooling rate in the liquid at the liquid/solid interface on to the $x = 0$ cross-section of each melt. The cooling rate in the liquid was calculated from the cooling rate in the solid using equation 4.11 while the data outside the melt pool was ignored. Constant cooling rate contours are plotted through the data and it is clear that the cooling rate increases from 0 on the melt periphery to a maximum at the top center of the melt. The contours represent the general ellipsoidal shape of the melt and one can see that there are no sudden changes in the cooling rate throughout the cross section. An orthographic representation of the cooling rate in three dimensions is also shown in Appendix B and is an effective means of illustrating the distribution of cooling rates around the melt pool interface. The influence of travel speed on the cooling rate can be determined by comparing the melts made at 6.4 mm/s and 25.4 mm/s. This fourfold increase in the travel speed produces a tenfold increase in the cooling rate and reduces the size of the molten zone by a factor of about two.

To show that the cooling rate approaches zero on the melt periphery, the location of the melt periphery must be mathematically determined and then inserted into equation 4.8. Figure 4.4 illustrates the location where the pool achieves its maximum

width, x_w , on the melt pool surface. This point is located at a distance behind the center of the heat source. The melt pool periphery is defined by curve which maps x_w as a function of z and an expression for x_w is derived in Appendix A and shows:

$$x_w = \frac{-vr_w^2}{vr_w + 2\alpha} \quad (4.13)$$

where r_w is defined as the radius at the maximum width :

$$r_w = \frac{Q}{2\pi k\theta_m} \exp\left(\frac{-vr_w}{vr_w + 2\alpha}\right) \quad (4.14)$$

In order to determine x_w , equation 4.14 must be solved for r_w by a trial and error method and then this value can be used to calculate x_w from equation 4.13. By substituting the calculated values of x_w into equation 4.8, it can be shown that the cooling rate approaches zero on the melt periphery.

There is ample metallographic evidence to show that slow cooling rates occur in the region close to the melt periphery. Figure 4.1a shows the microstructure of a typical melt and at the melt boundary, a planar growth region of only a few dendrite arm spacings wide exists; cells or dendrites form throughout the remainder of the melt. Planar growth is the result of low interface velocities which stabilize the liquid/solid interface and consequently are associated with low cooling rates.

Temperature Gradients

Temperature gradient calculations are also listed in Tables B.1 and B.2 in the Appendix B. Figures 4.6b and 4.7b show the 'topographical' plots of the temperature gradient calculations for the 6.4 mm/s and 25.4 mm/s melts respectively. These data represent the cooling rate in the solid at the L/S interface and are projected on to the $x=0$ cross section of the melt. These results show that T_g does not vary as much as the cooling rate around the surface of the melt and also show that the temperature gradient is not influenced as much as the cooling rate with changes in the travel speed. For example, T_g varies by no more than 30% from its maximum value throughout the cross section of each melt and the four-fold increase in travel speed only produces a three-fold increase in T_g . Orthographic representations of T_g are shown in Appendix B. It is clear from these figures that at the lower travel speed, T_g

is nearly invariant across the L/S interface while at the higher travel speed, the locations of maximum melt depth, length and width become locations of local maximums in T_g .

The relatively constant nature of the temperature gradient was expected since the melt isotherm defines an isothermal boundary and the temperature gradients which develop in the substrate at the L/S interface depend primarily on the geometrical shape of the melt. Locations of small radius of curvature allow for more divergence of heat flow and are associated with higher temperature gradients but since the shape of the 6.4 mm/s and 25.4 mm/s melts are ellipsoids with L-D-W, this factor is not as pronounced as it might be in deep penetrating electron beam welds that have a keyhole shape in cross section. Divergence of heat at the points of small radius of curvature does explain why the highest values of T_g are found close to the maximum melt depth, width and length locations. At these points, the radius of curvature is smaller than at the other points on the surface of the melt pool. The variation in temperature gradient was shown to be more extreme for the higher speed melt which can be explained by the smaller shape of the higher speed melt, leading to smaller radii of curvature.

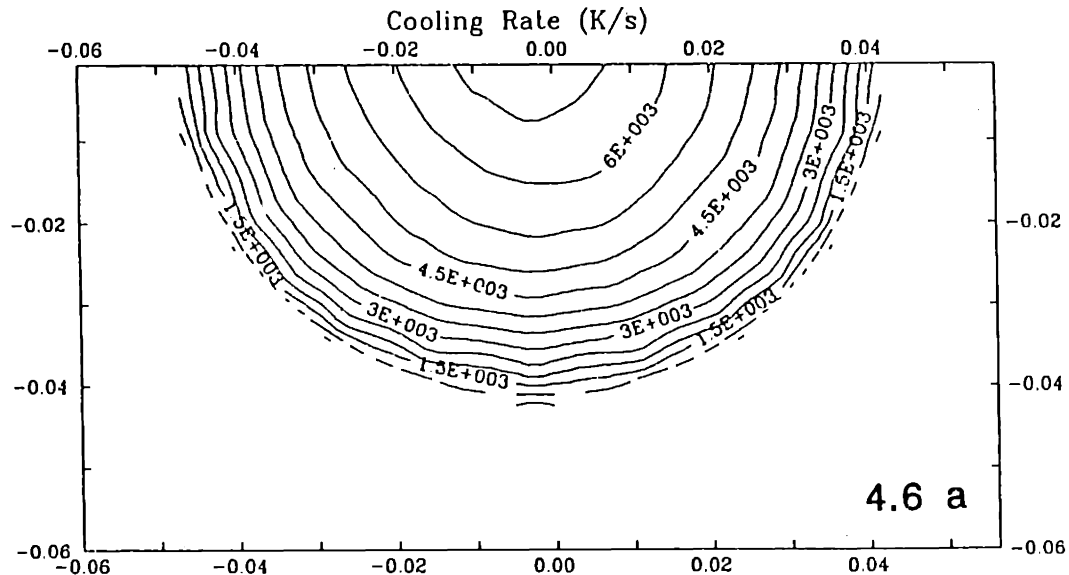


Figure 4.6 FEM calculations of a) the cooling rate and b) (see next page) the temperature gradient in the 6.4 mm/s electron beam melt. Spatial coordinates are in inches.

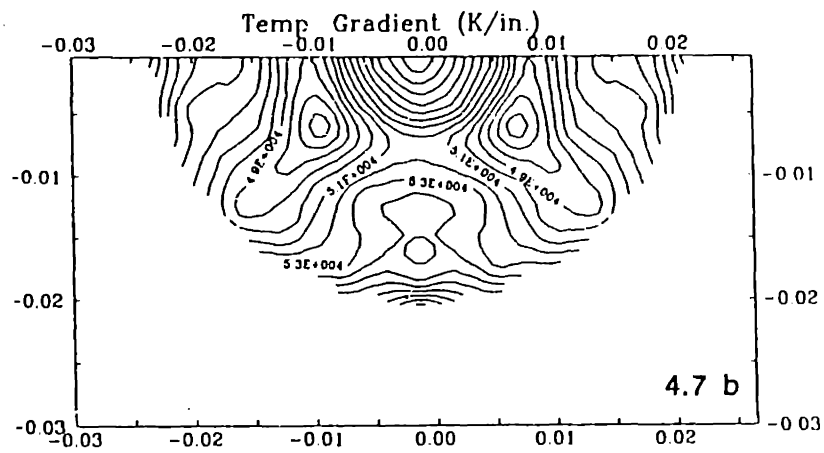
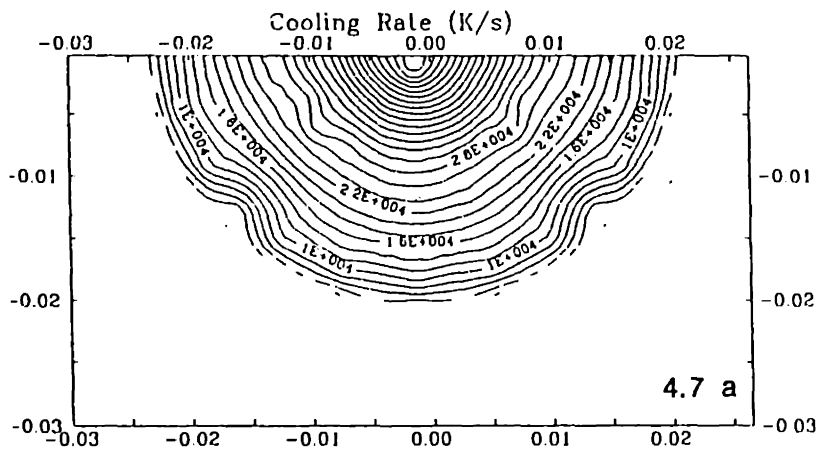
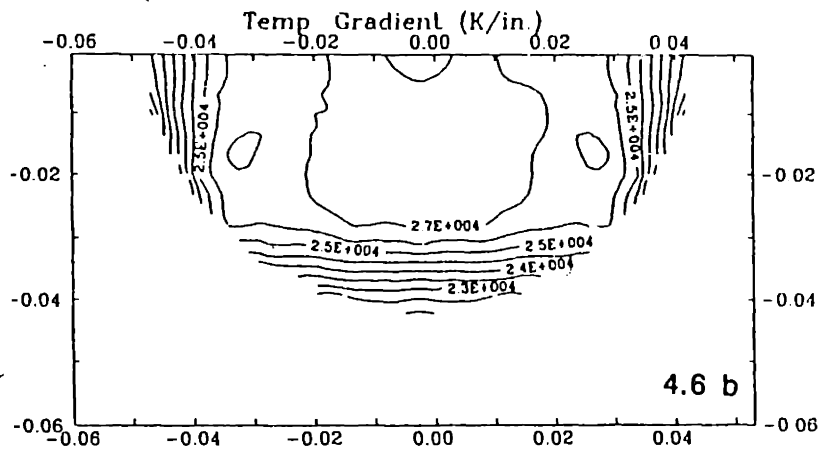


Figure 4.7 FEM calculations of a) the cooling rate and b) the temperature gradient in the 25.4 mm/s electron beam melt. Spatial coordinates are in inches.

4.5 Comparison of the Models and Summary

The major purpose of the heat flow modeling was to provide evidence to support the use of dendrite arm spacing measurements to estimate the cooling rate of the the electron beam melts. Comparisons of the different techniques showed that they agreed with each other to better than a factor of five throughout the cross section of the melt. This correlation was considered to be good considering the empirical nature of the DAS estimations and the various approximations that were made in the heat flow models.

Figure 4.8 indicates 5 nodal points along the center line of the 25.4 mm/s melt on 304 stainless steel where the cooling rate calculation techniques were applied to directly compare the three methods. The results listed in Table 4.7 show that the FEM model and DAS estimations of the cooling rate agree reasonably well with each other throughout the melt, however, the FEM program appears to give higher cooling rates in general.

Table 4.7 : Comparison of the FEM and DAS estimations of the cooling rate in the liquid at the five points indicated in Fig. 4.7.

Point	Z (mm)	T_s (K/mm)	ϵ (K/s)		
			FEM	DAS	Analytic
1	0	2.4×10^3	-6.1×10^4	-2.4×10^4	-4.0×10^4
2	-1.2	2.1×10^3	-4.1×10^4	-1.2×10^4	-
3	-3.5	1.9×10^3	-3.2×10^4	-2.5×10^4	-
4	-4.3	2.1×10^3	-2.4×10^4	-5.8×10^4	-
5	-5.8	2.4×10^3	0	0	0

This disparity is most likely a result of the melt pool being modeled by an "ellipsoidal" shape which typically overestimates the solidification front velocity, and consequently overestimates the cooling rate at the top central portion of the melt pool. The analytic expression presented in equation 4.9 was also applied to this melt. Since this approach predicts the maximum cooling rate in the melt, it should provide an upper bound for the other estimations. Table 4.7 shows that the analytic expression

predicts a cooling rate that is about twice as high as the dendrite arm spacings estimations and again, the FEM model gives high values of the cooling rate at the top center of the melt for the reasons stated above.

The cooling rate versus travel speed relationship for the six electron beam melts is shown in Fig. 4.9. In this plot, the results of the analytic expression are compared with the results from the dendrite arm spacing measurements. The analytic expression always predicts a higher cooling rate than the DAS measurements by about a factor of 2.5 and in general, there is good agreement between the two techniques.

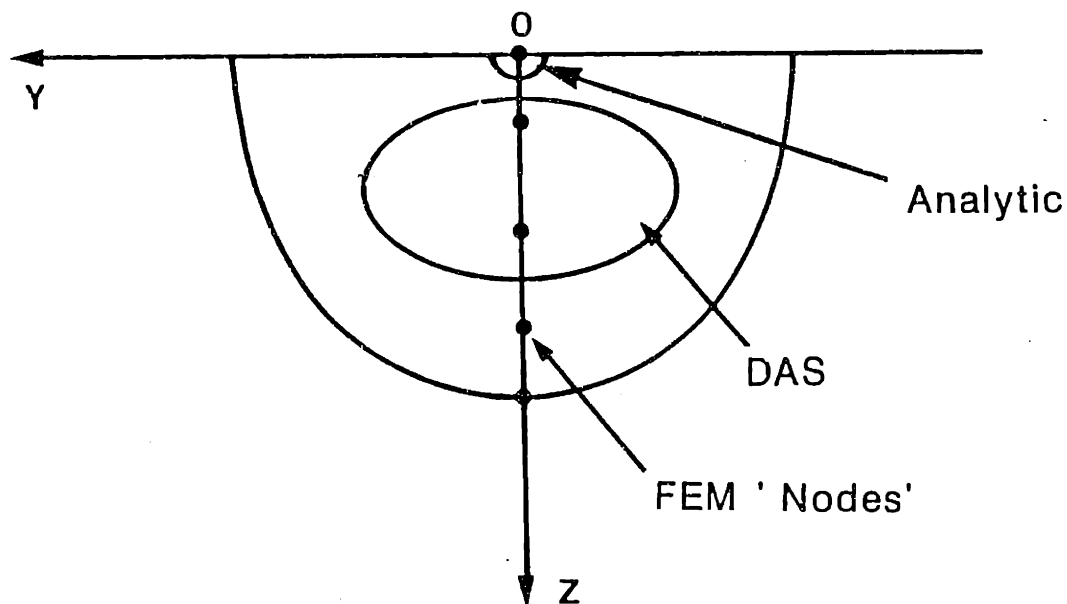


Figure 4.8 Schematic cross section of a resolidified zone indicating the locations where the analytic expression, FEM model and dendrite arm spacing measurements apply.

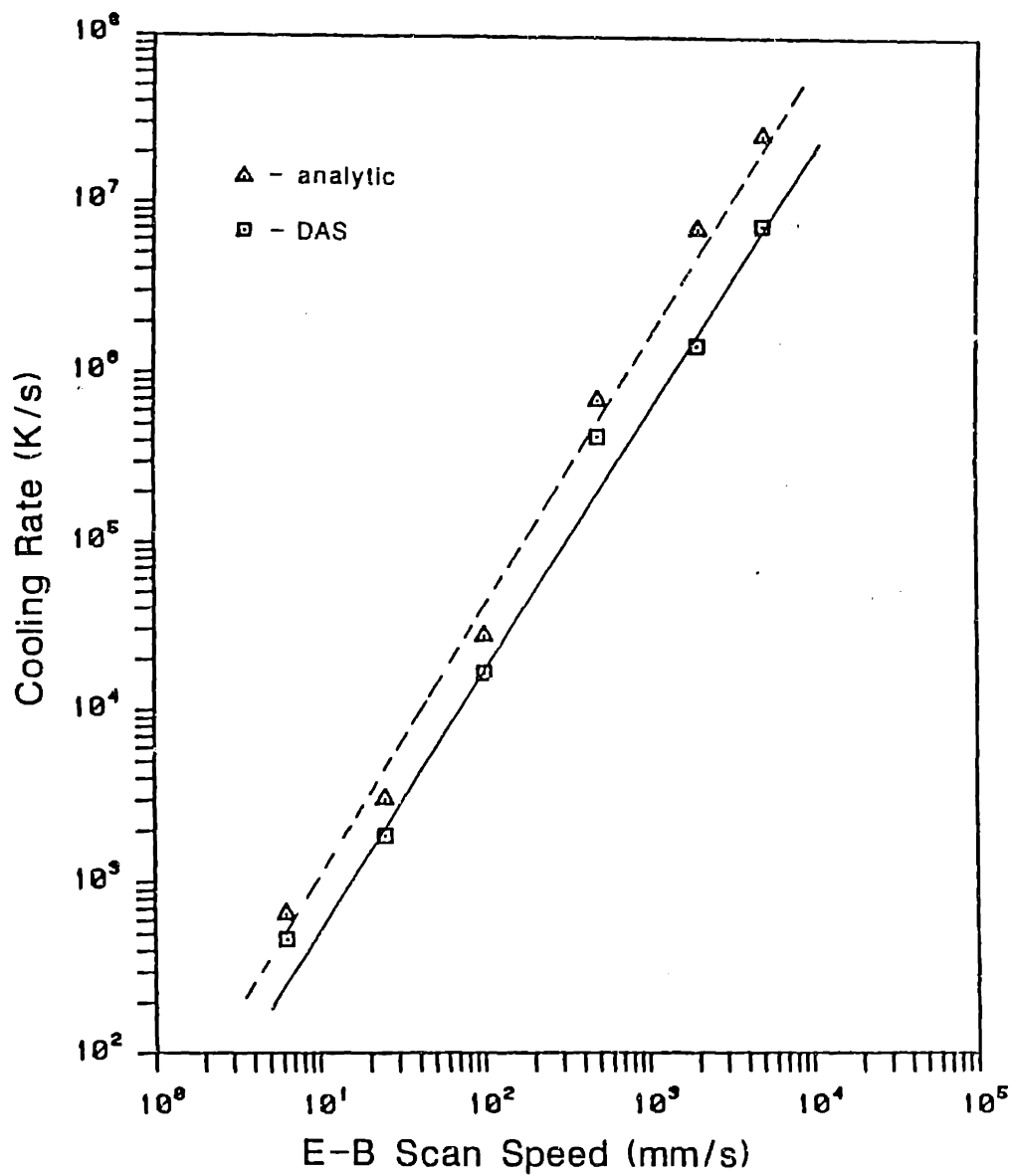


Figure 4.9 Comparison of the maximum cooling rate predicted by the analytic equation with the average cooling rate predicted by dendrite arm spacing measurements for the 6 E-B melts.

4.6 Conclusions

1. Dendrite arm spacing estimations of the cooling rate show that the arc cast button solidified at 7°C/s and that the six electron-beam melts solidified at rates which varied between 4.7×10^2 $^{\circ}\text{C/s}$ and 7.5×10^6 $^{\circ}\text{C/s}$. These measurements are supported by the cooling rate calculations.
2. An analytic expression, eq. 4.5b, was derived to represent the cooling rate in the solid at any location on the surface of the weld. This expression can be simplified to represent the maximum cooling rate in the weld (eq. 4.6) and requires only the length of the weld, the travel speed and the melting temperature of the alloy to be known. Similar expressions are derived (eq. 4.9 and eq. 4.10) to estimate the cooling rate in the liquid at the L/S interface.
3. The DAS measurements and the FEM calculations show that there is a variation in cooling rate within a given weld. The majority of the variation occurs close to the melt periphery and the remainder of the weld cools within a factor of about five.
4. Heat flow calculations showed that the highest cooling rate occurs at the top center of the weld pool while the lowest cooling rate occurs at the melt periphery. On the melt periphery, the cooling rate is zero but rapidly increases within a few dendrite arm spacings of the boundary. Metallographic observations of the microstructure confirm these calculations.
5. The FEM calculations showed that the temperature gradient varied only about 30% around the surface of the melt. These calculations also showed that the temperature gradient increases by a factor of 2 to 3 for a fourfold increase in travel speed.

CHAPTER 5

The Influence Of Cooling Rate On The Primary Mode Of Solidification And Microstructural Morphology

Surface melting allows resolidification to take place while the liquid is in contact with its solid substrate. The primary phase which solidifies is therefore limited to a phase that is initially present in the base metal since epitaxial growth, rather than nucleation of new phases, occurs under these conditions [5.1,5.2]. Exceptions to epitaxial growth during resolidification have been observed in alloys with high glass-forming tendencies that have been solidified at high rates [5.2,5.3], but this does not appear to be the case in the Fe-Ni-Cr ternary system.

The first section of this chapter investigates the influence of cooling rate and composition on the primary solidification mode (PSM) through microstructural observations of the electron beam melts. In duplex stainless steels, since both austenite and ferrite are present in the microstructure, either phase can grow epitaxially from the substrate. Therefore, the primary solidification mode is not governed by nucleation but instead, by the growth kinetics of the two phases. At the melt periphery, the two phases initially compete, however, one phase dominates to become the primary solid phase and its growth kinetics depend on the nominal alloy composition and the cooling rate.

The second section of this chapter investigates the microstructural morphologies that develop from each PSM. The morphology of the residual ferrite is largely a result of the ferrite to austenite solid-state transformation. However, the PSM establishes the microstructure prior to the transformation and plays an equally important role in developing the resulting microstructure. The principal factors responsible for the ferrite to austenite transformation are 1) the availability of sites for nucleation and growth of austenite which are determined by the solidification conditions, 2) the thermodynamic stability of the ferrite which is determined by its composition and 3) the time-temperature relationship for the ferrite to austenite phase transformation which is determined by the cooling rate of the melt. This chapter investigates each of these factors, qualitatively, through the microstructural examination of the E-B melts.

5.1 The Primary Mode of Solidification

Observations of the solidification behavior of stainless steels indicate that austenite forms as the primary phase at low Cr/Ni ratios and ferrite forms as the primary phase at high Cr/Ni ratios. At low cooling rates ($<10^3\text{°C/s}$), the transition in solidification behavior occurs at a Cr/Ni ratio of approximately 1.5 [5.4,5.5], and the morphology of the primary phase is typically dendritic with well defined secondary arms. However, at high cooling rates ($>10^4\text{°C/s}$), the transition in the primary solidification mode occurs at higher Cr/Ni ratios. Alloys with Cr/Ni ratios approaching 2.0 have been observed to solidify entirely as austenite in laser beam welds [5.6,5.7], and they solidify in a cellular rather than a dendritic mode. Other investigators have observed a change in the solidification mode from primary ferrite to primary austenite with increasing cooling rate in welds [5.6-5.9] as well. The inverse behavior, in which the solidification mode changes from primary austenite at low cooling rates to primary ferrite at high cooling rates has not been observed in welds but has been observed in rapidly solidified powders which achieve large thermal undercoolings [5.10].

In this study, the seven Fe-Ni-Cr ternary alloys were surface melted and resolidified at cooling rates between 7 and $7.5 \times 10^6\text{°C/s}$. The microstructures of these alloys were studied using optical and electron-optical techniques with specific attention being given to the growth of phases from the melt periphery and to competitive growth within the surface melt. These metallographic observations were used to develop a cooling rate versus composition map showing the different regions of solidification behavior and this diagram can be used to predict the PSM for a wide range of cooling rates and nominal alloy compositions.

5.1.1 Results of the Solidification Experiments

5.1.1.1 Characterizing the Primary Mode of Solidification

The primary mode of solidification was determined by optical examination of metallographic specimens. The polishing and etching techniques are presented in Chapter 2 and this section describes the microstructural features which are associated

with the primary modes of solidification: (A) single phase austenite, (AF) primary austenite with second phase ferrite, (E) eutectic ferrite and eutectic austenite, (FA) primary ferrite with second phase austenite and (F) single phase ferrite.

Single phase austenite and single phase ferrite solidification modes are easily characterized and distinguished from each other. Single phase austenite solidification is shown in Fig. 5.1 a and b. This mode is dendritic at low cooling rates and cellular at high cooling rates. At both low and high cooling rates, compositional variations caused by microsegregation at the cell boundaries outlines the usually six-sided austenite cells by etching darker than the interior of the cells. Figure 5.1b shows that the austenite cell boundaries typically etch as darkly as the grain boundaries and the overall appearance of the microstructure is a regular array of cells appearing as a mesh. Perpendicular to the axis of the cells, the boundaries appear as hexagonal shapes. When viewed at an angle to their axes, the hexagonal shapes become elongated and, in the limit, the cells appear as long parallel laths.

Single phase ferrite solidification is easily detected at high cooling rates when no solid state transformation to austenite has occurred. This microstructure is shown in Fig. 5.2a and illustrates that the ferrite grain boundaries outline the microstructure. The solidification substructure is difficult to etch and, in general, is cellular at high cooling rates and vaguely cellular-dendritic at low cooling rates. The cellular-dendritic microstructure is interrupted by what appears to be sub-grain boundaries throughout the grains. The origin of these non-regular shaped boundaries has not been investigated. At intermediate and low cooling rates, the ferrite undergoes a partial solid state transformation to austenite and is easily characterized by the presence of Widmanstätten austenite which nucleates and grows from the grain boundaries. Figures 5.2 b, c, and d show the microstructures formed by fully ferritic solidification, followed by differing amounts of solid state transformation

The primary austenite with second phase ferrite (AF) and primary ferrite with second phase austenite (FA) modes are easily characterized when the alloy solidifies with a large volume fraction of the primary phase. However, distinguishing between these modes can be difficult when the amount of the second phase is high. The difficulty arises because the primary ferrite dendrites can partially transform to austenite as the weld cools, leaving a vermicular microstructure. This microstructure

is easily confused with the second-phase ferrite that forms during primary austenite solidification and both microstructures have a similar appearance to the eutectic microstructure. These modes of solidification can often be discriminated by careful metallographic examination to determine if the ferrite is present at the cell walls or at the cell cores. Otherwise, the microchemical gradients across the ferrite dendrites must be determined by electron microprobe analysis or by scanning transmission electron microscopy [5.11].

A primary austenite solidified alloy with a small amount of second phase ferrite is shown in Fig. 5.1c at low cooling rates and 5.1d at high cooling rates. The microstructure is very much like that of single phase austenite except that ferrite particles are present at the cell boundary triple points and cell walls. Some solid state transformation has occurred, leaving isolated spheres of ferrite at the cell or dendrite walls.

Figure 5.3 shows the microstructure of alloys that have solidified with a large fraction of ferrite and only a small fraction of second phase austenite. The ferrite has gone through a significant amount of solid state transformation from growth of austenite at the dendrite walls. These microstructures will be discussed later and are easily characterized as being formed from the FA solidification mode.

Figure 5.4a and 5.4b compare AF and FA solidification modes when large amounts of the second phase are present. It is obvious that the ferrite is restricted to the cell walls in the AF mode, Fig. 5.4a, but it is more difficult to characterize the ferrite at the cell cores in the FA mode. The cell walls are more difficult to locate in the FA mode, Fig. 5.4b, which is often a sign of primary ferrite solidification because the ferrite preferentially etches and the cell walls, which are located in the austenite, do not etch. A consequence of the less prominent cell walls is that the FA microstructure has a more random appearance than the AF solidification mode, particularly at low magnifications.

Alloys that solidify with a volume fraction of the second phase close to 50% can exhibit AF, FA and E modes of solidification. Under these conditions, it is possible for the primary mode to change within a given melt. An example of this transition is shown in Fig. 5.5a. The alloy is solidifying in an AF mode on the left hand side of the micrograph and in an FA mode on the right hand side of the micrograph. The

transition takes place approximately at the center of the micrograph, where ferrite at the cell wall becomes ferrite at the cell cores. Similar transitions can be made to and from eutectic solidification and oftentimes it is difficult, if not impossible, to distinguish between these microstructures.

Figure 5.5b shows the appearance of the eutectic microstructure formed in Alloy 4 which is a result of simultaneous growth of ferrite and austenite from the liquid. This microstructure forms most readily in alloys with compositions near the line of two-fold saturation but may also be present in small amounts in primary phase austenite or ferrite solidified alloys. The relative amounts of ferrite and austenite that form during eutectic solidification will later be shown to be about 40% and 60% respectively. This condition should lead to a lamellar microstructure, however, a lamellar-type microstructure is not frequently observed. There are two possible reasons for this behavior. A first possibility is that the lamellar microstructure forms during solidification but due to the solid state transformation of ferrite, the final microstructure has been significantly altered. A second possibility is that solidification leads to a divorced eutectic or a rod-type eutectic microstructure. A divorced eutectic seems reasonable, particularly at moderately high cooling rates where the secondary dendritic arm spacing is small and prevents the formation of lamellar eutectic. This microstructure would be similar to the intercellular ferrite and intercellular austenite morphologies that solidify with a high volume fraction of the second phase.

The results of the microstructural examination of the alloys used in this investigation showed that the PSM can be determined through optical metallographic examination. For the most part, the PSM is easily characterized for alloy compositions that solidify with a large volume fraction of the primary phase. However, alloys that have compositions close to the line of two-fold saturation can be difficult to characterize and may be combinations of intercellular ferrite, intercellular austenite or the eutectic modes of solidification.

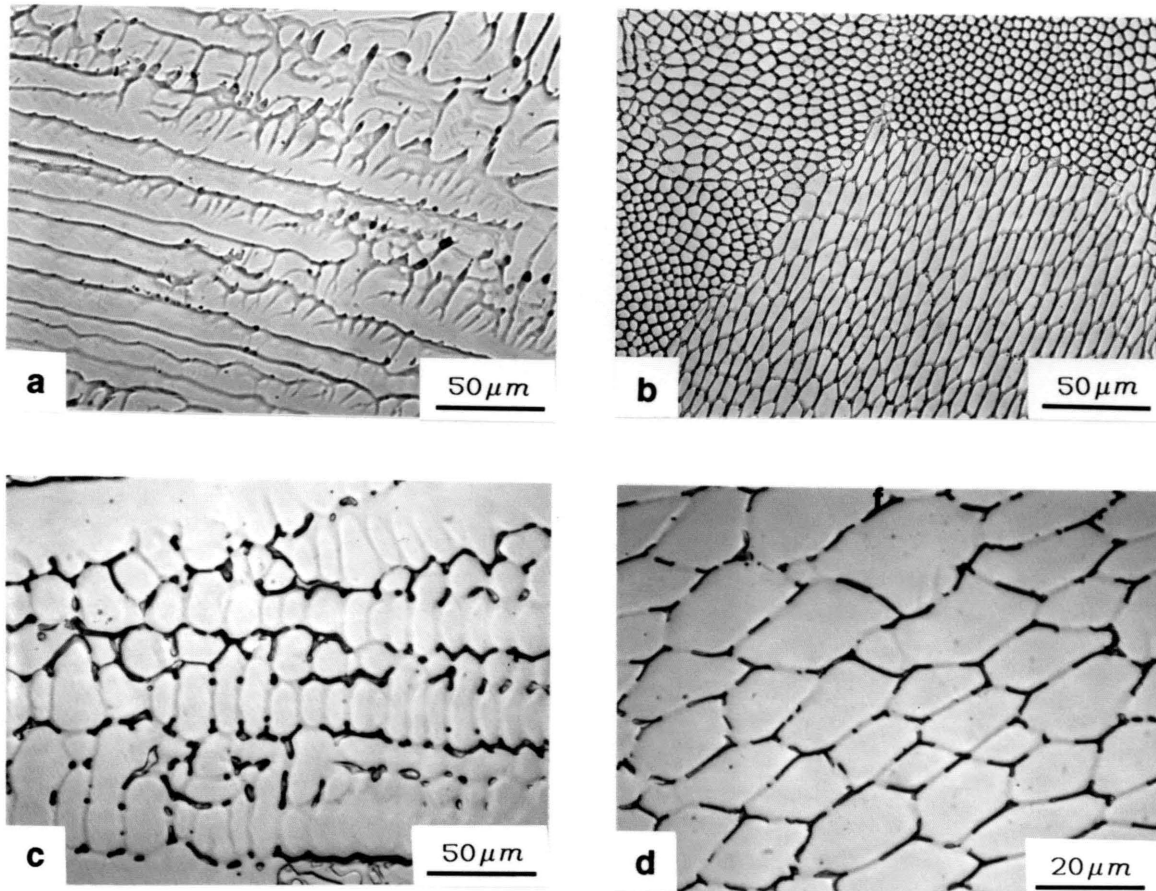


Figure 5.1 Primary austenite solidification mode microstructures. a) Single phase austenite dendrites, b) single phase austenite cells, c) interdendritic ferrite and d) intercellular ferrite.

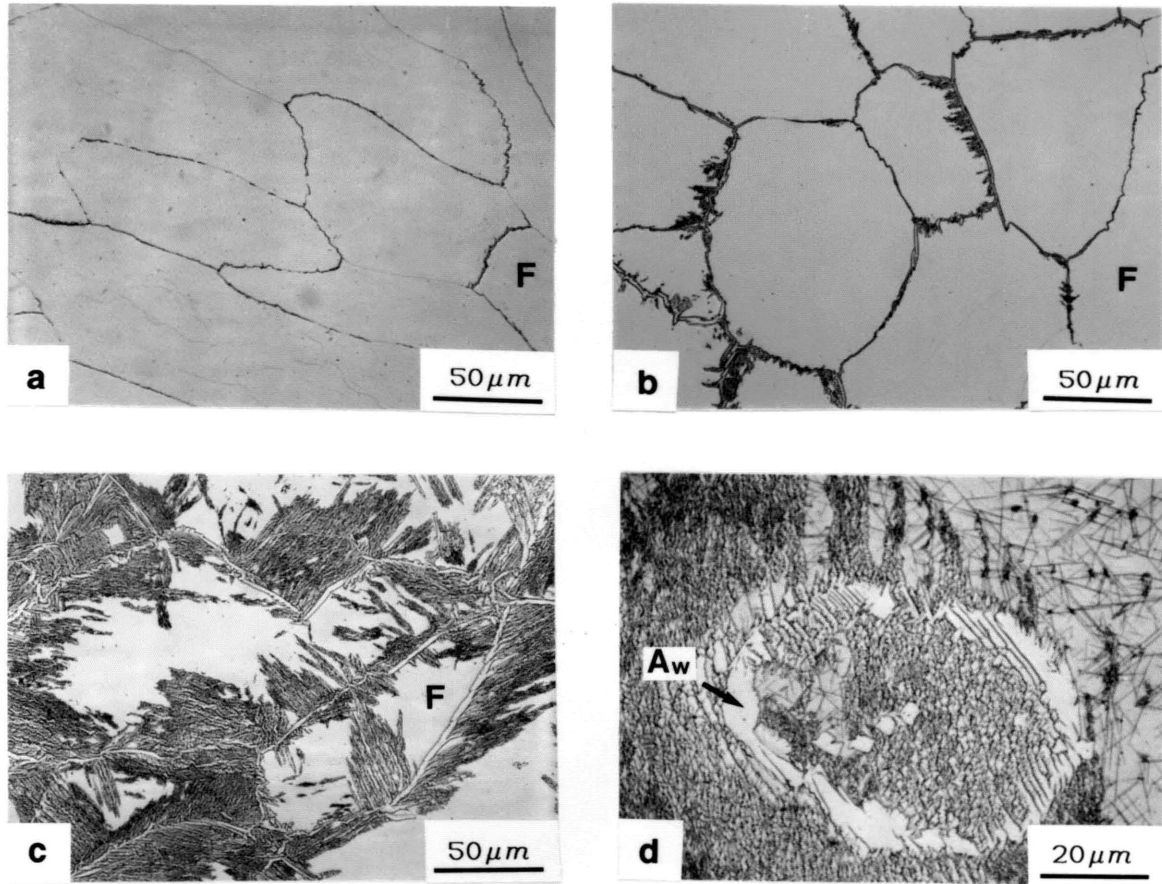


Figure 5.2 Single phase ferrite solidification microstructures. a) Single phase ferrite with no solid-state transformation, b) initial growth of Widmanstatten austenite platelets, c) grain boundary allotriomorphs and Widmanstatten platelets and d) the planar surface of the Widmanstatten platelets.

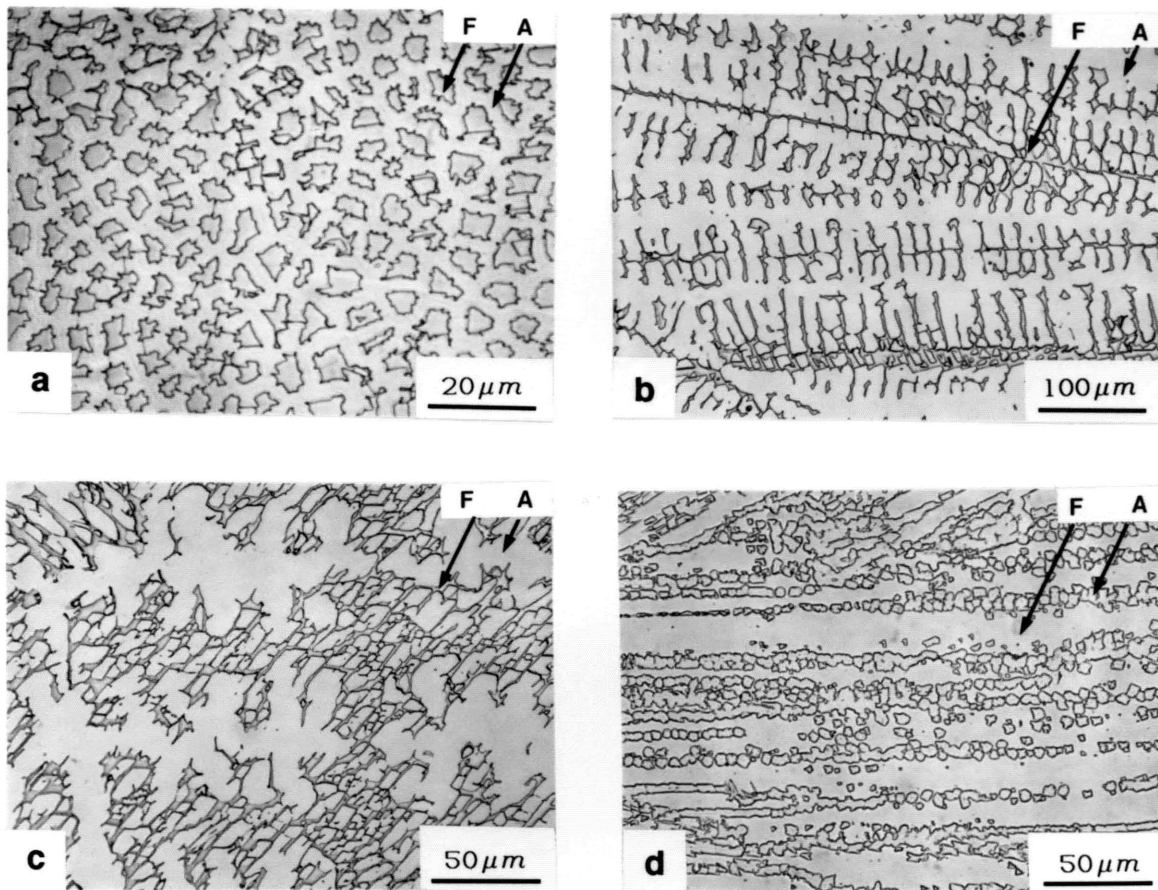


Figure 5.3 Primary ferrite solidification mode microstructures. a) Ferrite located at the cell cores in the intercellular austenite solidification mode, b) vermicular microstructure of ferrite dendrites, c) lacy ferrite and d) blocky austenite.

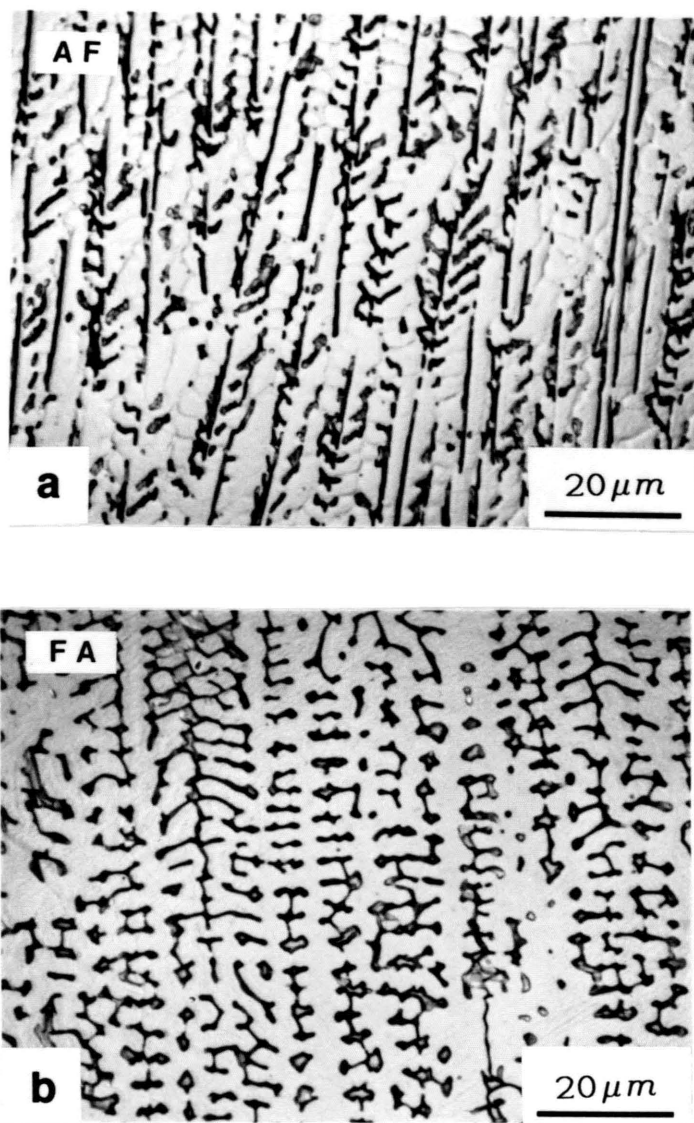


Figure 5.4 Comparison of the microstructures formed by a) primary austenite with second-phase ferrite and b) primary ferrite with second-phase austenite, at equal levels of residual ferrite.

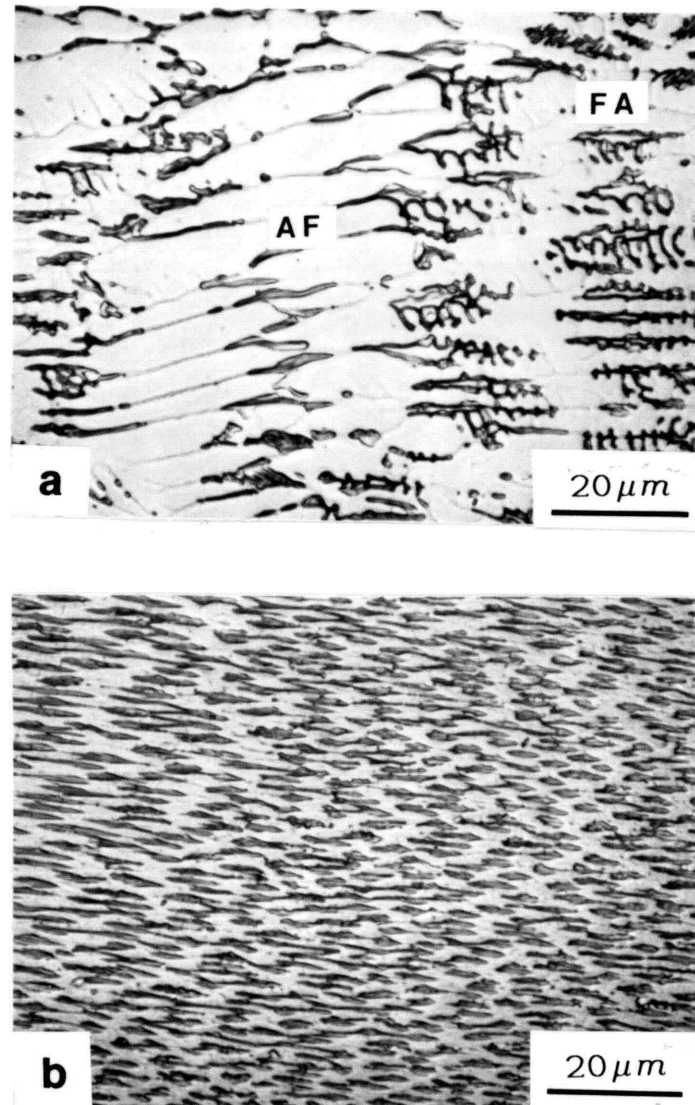


Figure 5.5 a) Transition from the AF mode of solidification in the center of micrograph to the FA mode of solidification on the rhs of the micrograph. Alloy 4, 6.3 mm/s. b) Fine spacing of ferrite platelets formed during the solid state transformation of ferrite. Alloy 5, 100 mm/s.

5.1.1.2 Mapping the PSM as a Function of Cooling Rate and Composition

The seven alloys, containing 59% Fe and varying Cr/Ni ratios (Table 2.1), were cast and surface melted at six different travel speeds (Table 4.1). These forty-nine specimens were analyzed by optical microscopy to determine the primary mode of solidification. Some of the surface melts showed more than one mode of solidification because of inherent variations in the cooling rate within a given melt. For these cases, the predominant mode was denoted by the one which was responsible for more than 50% of the microstructure.

Table 5.1 summarizes the general behavior of the seven alloys. Alloys 1, 2 and 3 solidify in primary austenitic modes for all cooling rates while Alloys 5, 6 and 7 solidify in primary ferrite modes for all cooling rates. Alloy 4 changes its mode of solidification from predominantly primary ferrite at low cooling rates to entirely primary austenite at high cooling rates.

Figure 5.6 plots four PSM regions as a function of cooling rate and composition. Since the eutectic mode was difficult to characterize and can be present with the FA and AF modes of solidification, it was not given a unique distinction on this diagram. The scan speed is plotted on the ordinate and the composition is plotted on the abscissa but both axes required minor corrections prior to plotting. Firstly, each of the alloys contained approximately 59% Fe but varied $\pm 0.5\%$ from the initial aim composition. Therefore, to plot the alloys on a common composition plane in the Fe-Ni-Cr system, a small adjustment was made to the Fe content to bring them to the 59% Fe isopleth while at the same time maintaining their measured Cr/Ni ratio. Secondly, the scan speeds were controlled for all the electron-beam surface melts but not for the casting. Therefore, an equivalent scan speed of 0.7 mm/s was estimated for the castings based on the primary dendrite arm spacing of the castings. The cooling rates for each solidification condition, as estimated by dendrite arm spacings, are presented as an alternate ordinate scale.

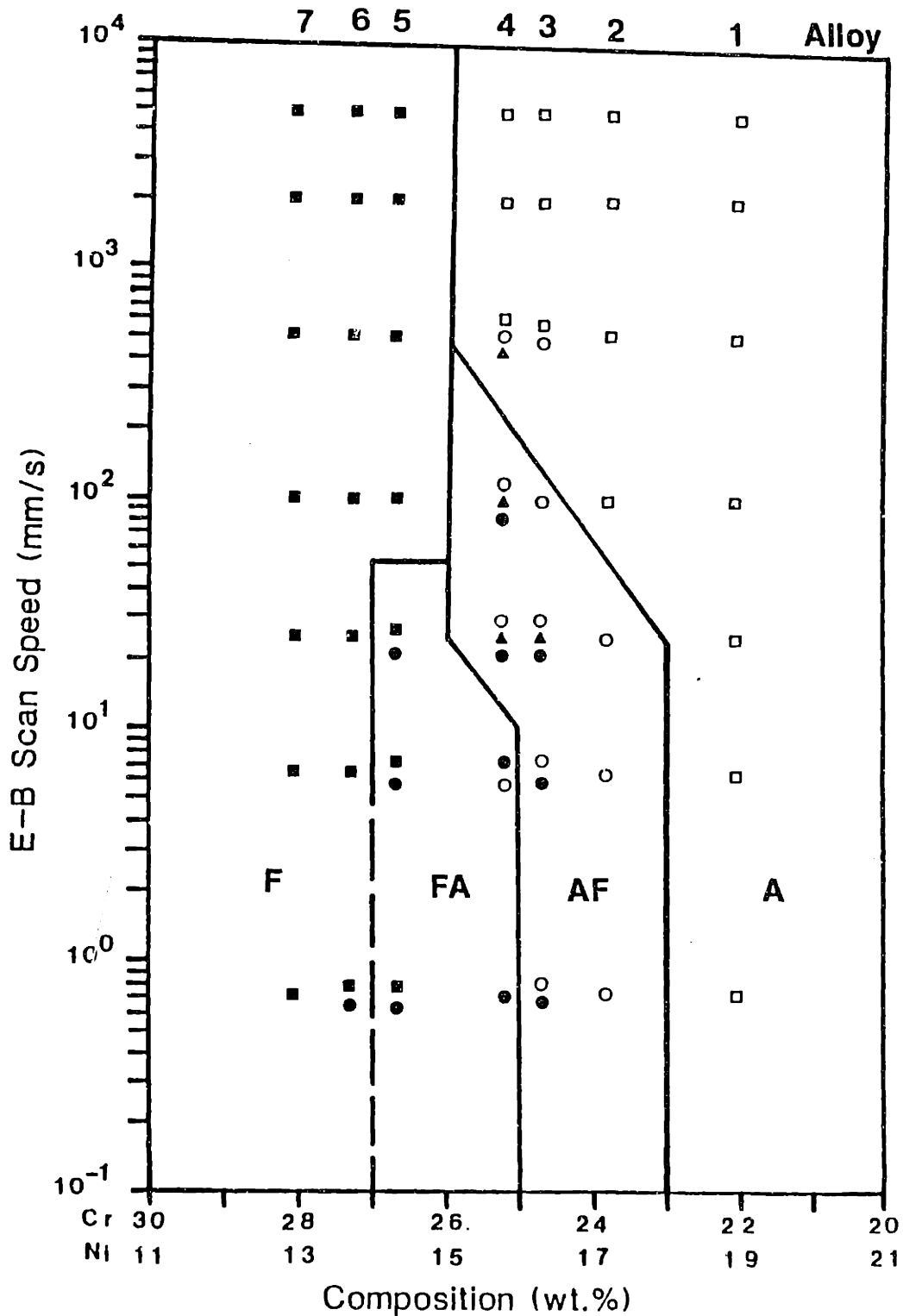


Figure 5.6 Scan speed (cooling rate) versus composition map of the four modes of solidification. Multiple data points refer to different modes observed within the same melt; the upper-most and lower-most symbols correspond to the highest and lowest cooling rate portions of the respective melts. The solid squares and circles represent the F and FA modes, the open squares and circles represent the A and AF modes and the triangles represent the eutectic.

Table 5.1: Summary of the primary modes of solidification for the seven alloys at low, intermediate and high cooling rates

Alloy	Cooling Rate		
	low	intermediate	high
1	A	A	A
2	AF	AF	A
3	AF/FA	AF/E	A
4	FA/AF	AF/E/FA	A
5	FA/F	F	F
6	FA/F	F	F
7	F	F	F

The points plotted on Fig. 5.6 are coded such that open squares and open circles correspond to single phase austenite (A) and austenitic-ferritic (AF) solidification respectively while solid squares and solid circles correspond to single phase ferrite (F) and ferritic-austenitic (FA) solidification respectively. The eutectic (E) is represented by a solid triangle. For the surface melts that showed more than one mode of solidification, two or more symbols are stacked on top of each other. The symbol on the top of the stack represents the mode which forms in the higher cooling rate portions of the melt, i.e., close to the melt periphery, while the symbol on the bottom represents the mode which forms at the lower cooling rate portions of the melt, i.e., towards the center of the resolidified zone.

The different regions of solidification behavior are indicated in Fig. 5.6 and the results show the effect that cooling rate has on the microstructure. There are two important points to be noted on this diagram. Firstly, at low scan speeds (<100 mm/s) four modes of solidification are present while at high scan speeds (>500 mm/s) only two modes of solidification are present, single phase austenite and single phase ferrite. Secondly, Alloy 4 changes its mode of solidification from primary ferrite to primary austenite as the scan speed is increased and it appears to do so in a gradual way. As the scan speed is increased, Alloy 4 changes from the FA mode to mixed

FA/AF/E modes with the amount of eutectic and primary ferrite solidified areas decreasing as the scan speed is increased. With further increases in speed, Alloy 4 solidifies in the single-phase austenitic mode.

Alloy 3 also shows signs of ambivalent solidification behavior in the low cooling rate portions of the low travel speed melts. In Alloy 3, at 6.3 and 25 mm/s, the AF mode forms at the melt boundary and the FA mode forms towards the center of the resolidified zone. It is not clear as to which side of the line of two-fold saturation Alloy 3 belongs but it is obvious that it is very near the line of two-fold saturation. Since a majority of the microstructure solidifies in the AF mode, Alloy 3 was denoted as a primary austenite solidifying alloy.

The change in primary solidification mode and the elimination of the FA and AF modes at high scan speeds can be explained by the influence that scan speed (cooling rate) has on solidification segregation. In order to describe how the PSM develops and is influenced by the scan speed, it is necessary to first examine how the solidification mode originates from the melt periphery and how this structure grows into the melt.

5.1.2 Epitaxial Growth and Plane Front Solidification

5.1.2.1 Epitaxial Growth from the Melt Interface

Surface melting and resolidification on a metal substrate with an electron-beam moving at a constant velocity establishes a liquid-solid interface which can be assumed to be quasi-stationary in the moving frame of reference. The shape of the liquid-solid interface depends on the processing variables and in three dimensions tends to be hemispherical at slow scan speeds and tear-drop shaped at high speeds. Figure 5.7 illustrates a simplified temperature distribution along the centerline of a surface melt. As the heat source approaches, the metal ahead of the L/S interface is being heated to its melting and the metal behind the L/S interface is being cooled. After incipient melting at the weld centerline, the liquid-solid region expands to its maximum width and then contracts back towards the centerline as the heat source passes and at the widest point of the liquid advancement, defined as the melt periphery, the heat flow is balanced. In front of this point the metal is being heated

and behind this point the metal is being cooled. At this point, the alloy is at its liquidus temperature and there is no driving force for solidification.

In three dimensions, the shape of the melt periphery is a two dimensional surface which can easily be identified in a metallographic cross section. Figure 5.8 illustrates the three principal views of the L/S region to illustrate how the grains develop from the melt periphery. A plane-front solidification zone extends for a short distance from the base metal grains. This zone quickly becomes unstable and breaks down into cells within a short distance from the interface. The instability of the planar front develops into perturbations that lead to cellular solidification as the interface advances. At high cooling rates, the cellular zone can extend through the entire melt, however, at lower cooling rates which are typical of castings and arc welds,

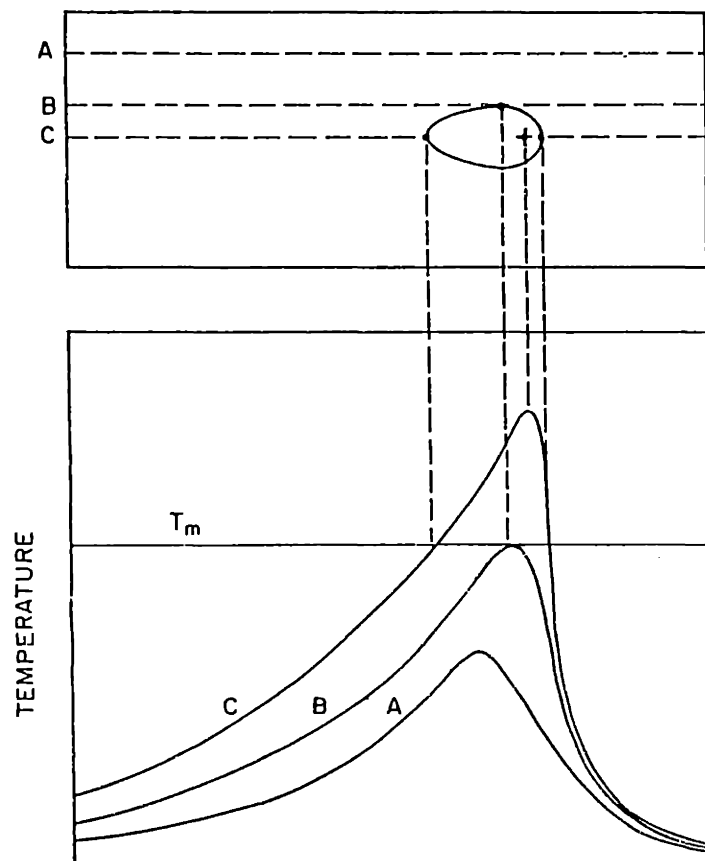


Figure 5.7 Schematic representation of the temperature distribution surrounding a melt-pool. Section B shows that the temperature gradient in the travel speed direction is zero at the point of maximum melt width.

the cells are replaced by dendrites. During the final stages of solidification, the dendrites are replaced by an equiaxed zone at the top center of the melt if the solidification conditions (G and R) permit.

The melt periphery is an important feature because from it grow all of the crystals that are present in the resolidified region. It is along this melt periphery that the primary solidification mode first develops and one of two possibilities for the inception of the PSM exist: 1) epitaxial growth from the substrate or 2) nucleation of phases not initially present in the substrate. Examination of the forty-two surface melts produced in this investigation showed that epitaxial growth appears to be present in all cases but failed to show the presence of an amorphous phase or nucleation of metastable phases, even at surface scan speeds as high as 5 m/s.

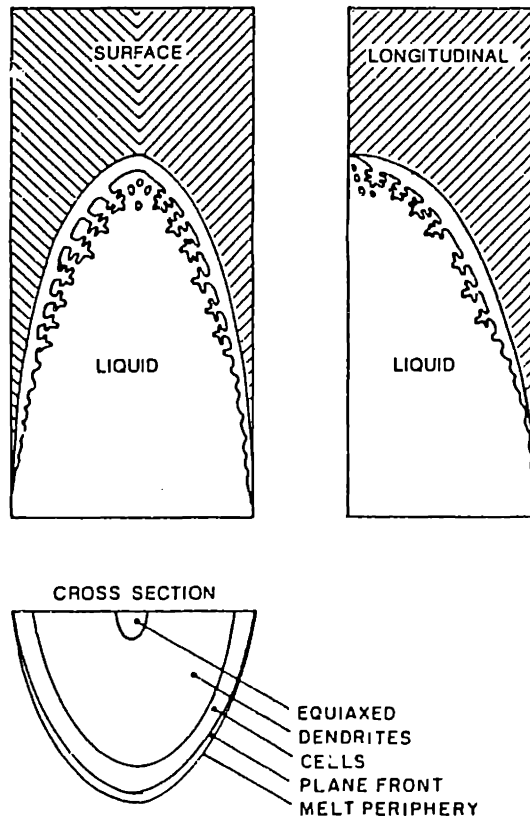


Figure 5.8 Schematic representation of the three principal views of the melt pool. Locations of the various microstructural features are illustrated on the cross sectional view and the origin of the different solidification growth morphologies are indicated on the top and longitudinal views.

In general, nucleation of new phases at the melt periphery is the exception rather than the rule. It requires a combination of both high solidification velocities, to achieve sufficient undercooling, and a composition which is susceptible to metastable phase formation [5.1-5.3]. Epitaxial growth from the substrate occurs in the majority of surface melting processes [5.1]. In the Fe-Ni-Cr ternary system only two solids crystallize from the melt, ferrite and austenite. To the author's knowledge, the conditions necessary to produce an amorphous phase in this alloy system have not been experimentally achieved during surface melting. Studies of atomized droplets of a commercial stainless steel alloy [5.10] also failed to show the presence of an amorphous phase in highly undercooled droplets. Nucleation of metastable phases at the melt periphery has also not been observed to the author's knowledge. Epitaxial growth is the leading candidate for the initiation of crystallization.

The seven base metal substrates varied in composition such that Alloy 1 was fully austenitic and Alloys 2 through 7 increased in ferrite content from approximately 5 to 35 volume percent respectively. Therefore, in all but one alloy, both phases were present in the substrate to allow for epitaxial growth. The plane-front solidification zone which surrounds each melt is visible in optical metallographic cross sections. This zone indicates that epitaxial growth has occurred and the thickness of this zone depends on the processing variables. Its width is only a few cell spacings before it becomes unstable and breaks down into cellular solidification. If crystals grow epitaxially from the melt periphery, then austenite will grow from austenite and ferrite will grow from ferrite. This appeared to be the behavior under all melt conditions, however, some cases were difficult to distinguish because of the solid state transformation of ferrite which made the growth of ferrite into the resolidified region difficult to characterize.

5.1.2.2 Epitaxial Growth at Low Cooling Rates

At low cooling rates the effects of epitaxial growth are easily observed. Figure 5.9 compares the behavior near the root of weld 2 (25 mm/s) for Alloys 1, 4 and 7. Single phase austenite in the melt zone is shown growing from an austenite base-metal grain in Fig. 5.9a.

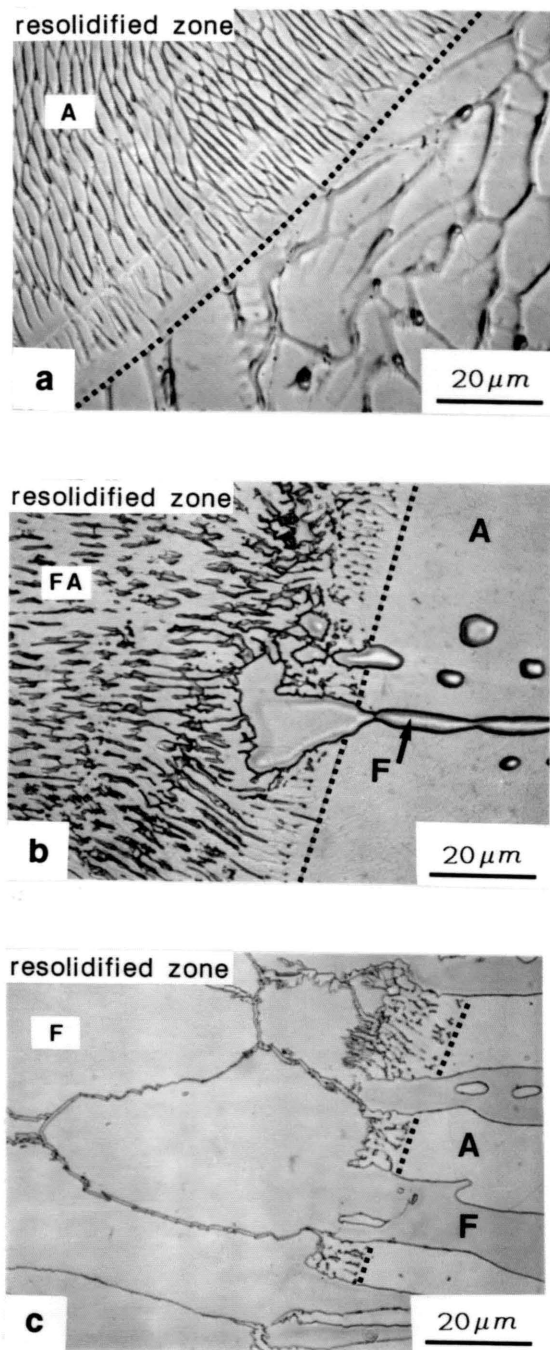


Figure 5.9 Epitaxial growth at the fusion line of melt 2 (25.4 mm/s) in a) Alloy 1, b) Alloy 4 and c) Alloy 7. F and A refer to the ferrite and austenite phases respectively while R and B refer to the resolidified and base metal regions respectively.

The growth is epitaxial and a plane-front solidification zone extends for about 2 microns prior to breaking down into cellular solidification with microsegregation to the cell boundaries. Figure 5.9b illustrates the typical behavior of an alloy which solidifies in an FA mode with a significant amount of second phase austenite. Examination of the interface region shows that the melt periphery extends farther into the austenite than the ferrite. This behavior was observed in all melts and can be explained by the higher melting point of the ferrite.

Table 5.2 compares the liquidus temperatures and solidus temperatures for ferrite and austenite. The average composition of ferrite (34.4 Cr, 9.2 Ni, 56.1 Fe) and austenite (24.5 Cr, 17.0 Ni, 58.9 Fe) was taken from microprobe measurements of the arc cast button, see Table 2.5 and these compositions were used to estimate the liquidus and solidus temperatures of ferrite and austenite [5.12]. The results show that $F_S < A_S < A_L < F_L$ where A and F refers to austenite and ferrite and the subscripts S and L refer to the solidus and liquidus temperatures respectively.

Table 5.2: Liquidus and solidus temperatures for ferrite and austenite

Phase	Liquidus (°C)	Solidus (°C)
Ferrite	1485	1398
Austenite	1418	1402

Figure 5.10 illustrates the behavior of a two-phase substrate at the melt periphery when subjected to a linear temperature gradient, G . The ferrite from the substrate protrudes into the melt for a distance greater than or equal to $(F_L - A_L)/G$. In the actual substrate, the ferrite and austenite phases have composition gradients caused by nonequilibrium solidification leaving less solute in the dendrite core. Taking this into account, and using the above relative values for the liquidus and solidus temperatures indicates that the ferrite should protrude into the melt and that the austenite/ferrite interfaces should melt back farther than the cores. This is exactly what is observed in the surface melts.

Returning to Fig. 5.9b, the epitaxial growth from austenite is apparent with its associated plane front zone. However, the plane front solidification zone extending from the ferrite does not show clearly in the micrographs. It is believed that growth from the ferrite is epitaxial with an associated plane front but that this region has been obscured by the subsequent solid state transformation of ferrite to austenite. Evidence for transformation is present in many of the ferrite particles which have a continuous ferrite network extending into the melt. Other evidence is present from the faceted surface of the ferrite/austenite interface which suggests that a significant amount of transformation has occurred. Figure 5.9b also shows large ferrite particle extending into the melt and has a network of ferrite fingers extending further into the melt. These fingers eventually lead to a primary ferrite solidified microstructure that has undergone a significant amount of solid state transformation.

At higher Cr/Ni ratios, the percentage of ferrite in the substrate and the percentage of ferrite which solidifies from the melt, increases. This larger volume

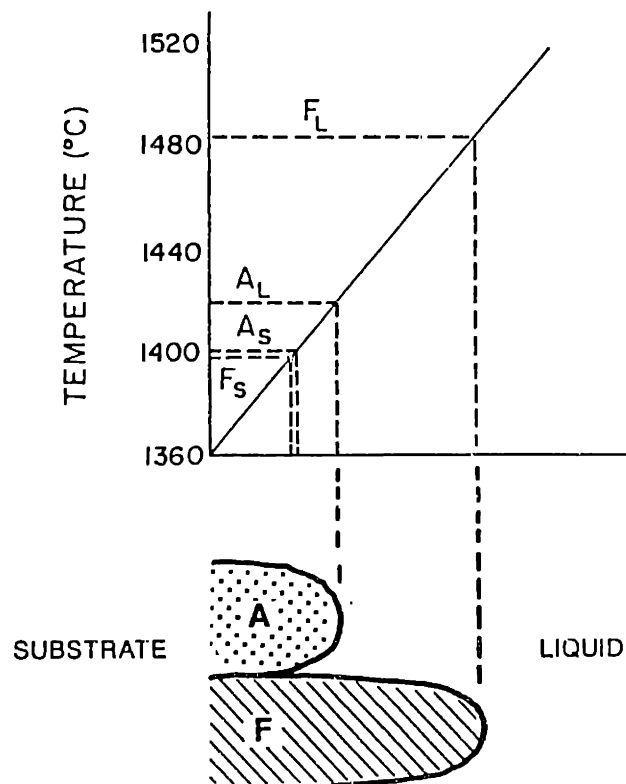


Figure 5.10 Protrusion of the higher melting point ferrite into the molten zone of a two-phase substrate when subjected to a linear temperature gradient at temperatures close to the melting point.

fraction of more stable ferrite makes epitaxial growth from the ferrite easier to observe. Figure 5.9c shows the interface region from Alloy 7 where the substrate contains approximately 30 percent ferrite. Epitaxial growth from both phases is apparent. The austenite plane front breaks down into a cellular mode which leads into single phase ferrite solidification. The ferrite phase is continuous from the substrate to the resolidified region but the melt periphery is difficult to observe.

5.1.2.3 Epitaxial Growth at High Cooling Rates

At high cooling rates the width of the plane front zone is reduced. This makes resolution of the microstructural features at the interface more difficult. A careful analysis of the interface region would require transmission electron microscopy, however, sample preparation on such small melts with the additional requirement of analyzing the interface region is difficult and precluded such analysis from this investigation. Instead, optical metallographic observations were used and were found to be sufficient to support the epitaxial growth theory. However, these observations were not able to definitively prove epitaxial growth at high cooling rates.

Figure 5.11 compares the behavior of Alloys 1, 4 and 7 solidified at 2000 mm/s. At the high cooling rates, the alloys solidify in a single phase austenitic mode (Alloys 1-4) or in a single phase ferritic mode (Alloys 5-7). Figure 5.11a shows the growth of single-phase austenite cells in the melt from single phase austenite cells in the substrate. Observation of the interface region shows a plane front zone extending from the austenite grains in the substrate. The plane front zone quickly reverts to cellular solidification with microsegregation to the cell boundaries.

Figure 5.11b illustrates the behavior of single phase austenite growing from the two-phase substrate in Alloy 4. A thin plane front surrounds the melt periphery and breaks down into a highly refined cellular network within the remelted zone. The cell axes are nearly perpendicular to the substrate and the microstructure of the remelted zone is similar to that which occurs in the fully austenitic Alloy 1. The ferrite in the substrate melts back close to the periphery and extending from the ferrite is a dark etching phase. This phase is also ferrite and typically finds its way to the cell walls in the resolidified zone. Close to the melt periphery are blocks of ferrite which only appear in Alloy 4 at the high cooling rates and look to be a continuation of the

ferrite dendrites from the substrate. The origin of these blocks is thought to be caused by incomplete mixing close to the melt periphery. Because the mixing is incomplete, regions of high Cr/Ni ratios extend from the ferrite dendrites in the substrate into the melt zone. These regions then have enough chemical driving force to change the PSM from single phase austenite to single phase ferrite. The ferritic solidification quickly vanishes because of convective mixing in the bulk of the melt zone.

Figure 5.11c illustrates the high cooling rate behavior of Alloys 5, 6 and 7. The resolidified region is single phase ferrite and the solidification substructure is apparent. Single phase ferrite grows epitaxially from ferrite in the substrate and careful examination of the austenite blocks in the substrate show that they have melted back and that austenite appears to have grown epitaxially from them. The plane front austenite zone is small and it directly changes to single phase ferritic solidification close to the melt periphery. The resulting microstructure is fully ferritic with no solid state transformation to austenite.

In summary, analysis of the melt periphery shows that epitaxial growth occurs from the substrate at low and at high cooling rates. Since the substrate is a two phase material, both ferrite and austenite grow from the interface. One of the two phases eventually dominates the PSM throughout the resolidified region and this dominant mode is a function of composition and cooling rate. The next section discusses how the primary mode develops from the two phase epitaxial growth at the melt periphery.

5.2 Cellular/Dendritic Solidification and Competitive Growth

The principal factor in determining the PSM is the composition. High Cr/Ni ratio alloys solidify as primary ferrite while low Cr/Ni ratio alloys solidify as primary austenite. However, for compositions which are close to the line of two fold saturation, the PSM was shown to change with increasing cooling rate. The reason for this behavior is related to the growth kinetics which allow epitaxial metastable austenite to grow throughout the resolidified melt at high cooling rates.

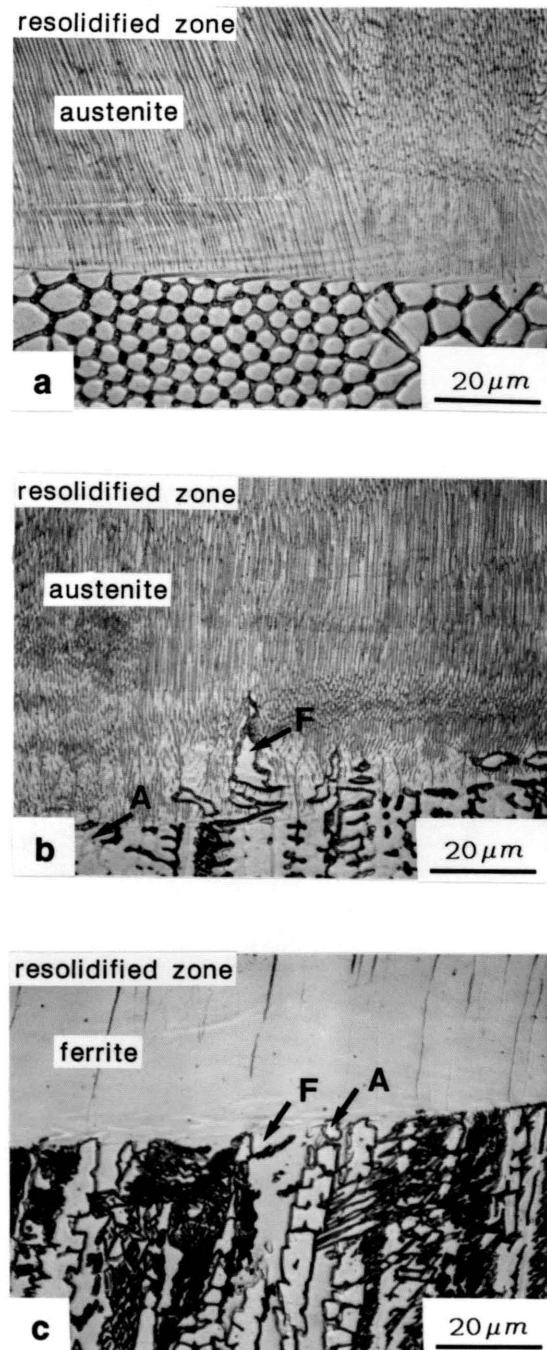


Figure 5.11 The single phase nature of high speed resolidified melts. Microstructures 'a' and 'b' show single phase austenite growing from Alloys 1 and 7 while 'c' shows single phase ferrite growing from Alloy 7 at 2000 mm/s.

5.2.1 Primary Austenite Solidified Alloys

Alloys 1, 2 and 3 solidify in a primary austenitic mode (A or AF) at low and at high cooling rates. Table 5.3 shows that the base metal substrate from Alloy 1 contains no ferrite and the base metal substrate from Alloys 2 and 3 contains less than 6 percent ferrite. This leads to a plane front austenite zone which surrounds the entire melt zone in Alloy 1 and the vast majority (>99%) of the melt in Alloys 2 and 3. Therefore, epitaxial growth of austenite dominates the microstructure at the melt periphery and where ferrite is present in the substrate at the periphery, it rapidly forms second phase ferrite at the cell boundaries.

Table 5.3: The ferrite content in the 1 mm deep electron-beam surface treated zone and in the base metal substrate.

	Condition	Alloy						
		1	2	3	4	5	6	7
Ferrite (%)	base metal	0	1.6	5.9	9.6	22.4	26.7	36.3
	surface treated	0	0.7	3.4	12.0	23.4	49.4	86.9

In the case of single phase austenite (Alloy 1) and AF solidification (Alloys 2 and 3), chromium segregates to the cell boundaries. However, because of the low initial Cr/Ni ratios of these Alloys, the amount of chromium which segregates to the boundaries is not sufficient to change the mode of solidification from primary austenite to primary ferrite. Therefore, even at low cooling rates, where segregation of ferrite stabilizing chromium to the cell boundaries is high, the mode of solidification is primary austenite throughout the entire resolidified zone.

5.2.2 Primary Ferrite Solidified Alloys

Alloys 5, 6 and 7 solidify in a primary ferrite mode (F or FA) at low and at high cooling rates. The Cr/Ni ratios of these alloys is much higher than that of Alloys 1 and 2 which leads to two significant differences. Firstly, Table 5.3 shows that the ferrite content of the substrate is much higher and this reduces the amount of epitaxial austenite that forms at the melt periphery. Secondly, the liquid metal is enriched in chromium to the point where a large percentage (>80%) of the microstructure solidifies as ferrite. Epitaxial growth of ferrite and austenite is evident in Alloys 5, 6 and 7 and becomes increasingly easier to observe as the amount of ferrite in the substrate increases.

Fig. 5.12a shows that the plane front austenite zone in Alloy 5 breaks down into primary austenite solidified cells within a few microns of the interface at slow scan speeds. The primary austenite cellular region extends for only an additional few microns before it transforms into primary ferrite (F or FA) solidified cells, however, the solidification mode is difficult to determine because of the substantial amount of solid state transformation. The ferrite cells then grow into columnar dendrites and finally equiaxed dendrites. At higher speeds, the plane front austenite and cellular austenite regions are compressed into a region of about 1 micron or less. The remainder of the weld solidifies in an FA or F cellular mode.

The Cr/Ni ratio of Alloys 6 and 7 is high enough so that both alloys solidify in the single phase ferritic mode. Furthermore, because of the high Cr/Ni ratio of the alloys, less of the ferrite transforms as the alloy cools. Figure 5.12b shows the development of the microstructure from the melt periphery in Alloy 7. The epitaxial growth of austenite breaks down into cells and then single phase ferrite within a few microns of the interface. The epitaxial growth of ferrite leads directly into the single phase ferrite solidified structure which continues to grow throughout the remainder of the resolidified region. Austenite appears to be present as occasional grain boundary allotriomorphs, but no intercellular austenite appears to solidify from the melt.

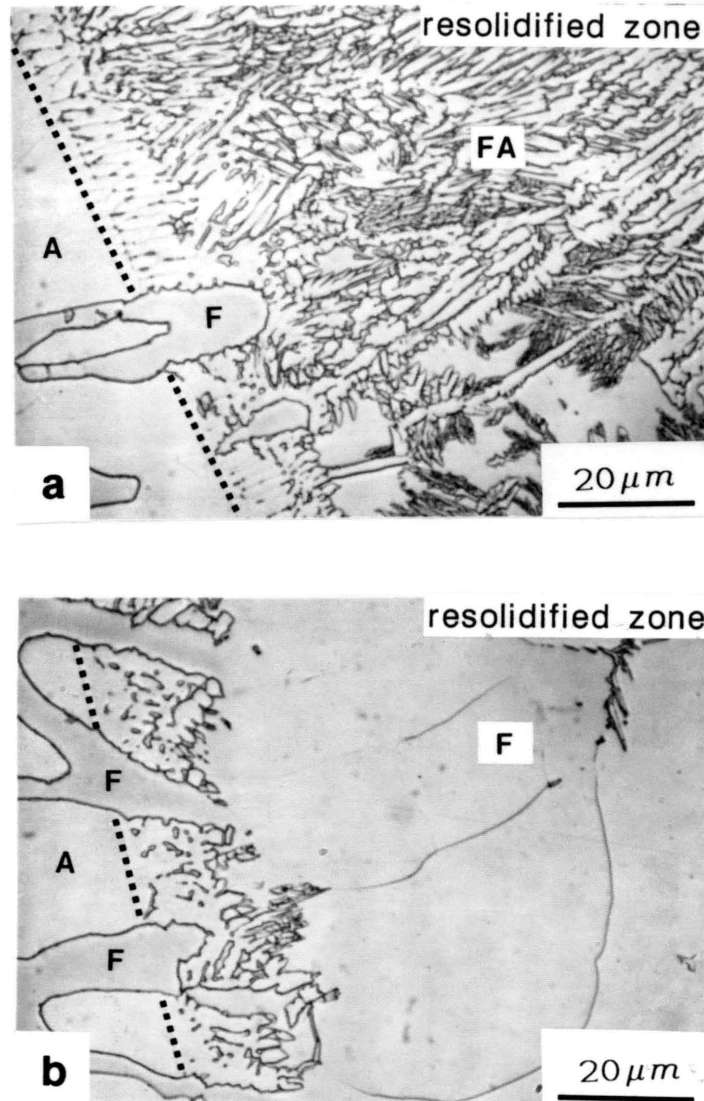


Figure 5.12 Epitaxial growth of austenite from the base metal substrate quickly modulates to the AF, FA and F modes of solidification in the high Cr/Ni ratio alloys. a) Shows Alloy 5 in which the ferrite undergoes substantial transformation and b) shows Alloy 7 where the transformation is prevented by the high Cr/Ni ratio of the alloy.

5.2.3 Alloys That Change Their Mode of Solidification With Cooling Rate

Alloys 1, 2 and 3 solidify as primary austenite while Alloys 5, 6 and 7 solidify as primary ferrite for all the cooling rate conditions. This behavior indicates that the line of two-fold saturation lies somewhere between Alloys 3 and 5 and as indicated in Fig. 5.6, Alloy 4 changes its mode of solidification. At low rates, Alloy 4 solidifies as primary ferrite (FA) and at high rates it solidifies as primary austenite (AF or A). Analysis of the microstructure shows that Alloy 4 lies on the primary ferrite side of the line of two fold saturation, and that primary austenite forms at high cooling rates in this alloy due to the favorable growth kinetics of the austenite from the melt periphery.

Figure 5.13a shows that the resolidified zone of Alloy 4 consists mostly of primary ferrite dendrites at low scan speeds although the majority of the melt periphery is austenite. This behavior is caused by a change in solidification modes from the epitaxially grown austenite to primary ferrite. AF cells grow from the epitaxial austenite and transform to FA cells within a few microns of the melt periphery at 6.3 mm/s. These FA cells then grow into columnar and finally equiaxed ferrite dendrites which coarsen in spacing towards the center of the cross section. Figure 5.13b indicates that the epitaxial growth of austenite leads to a much larger ($\sim 50\mu m$) zone of AF cells at 25 mm/s. These AF cells transform into the eutectic or intercellular ferrite phase which continues throughout the remainder of the resolidified zone. At 100 mm/s and faster the entire resolidified zone is composed of AF cells or eutectic as indicated in Fig 5.13c and the amount of intercellular ferrite decreases with increasing travel speed.

Therefore, as the speed is increased two transitions occur in Alloy 4. The dendritic mode is replaced by cells or the eutectic phase and the amount of primary austenite and eutectic solidified areas increase at the expense of the primary ferrite solidified regions. This transition is gradual and is related to the reduced amount of time available for segregation as the cooling rate is increased. Although these alloys solidify as a large volume fraction ferrite, only a small amount of ferrite (<10%) is present in the substrate because of the solid state transformation of ferrite. Since the substrate provides epitaxial growth sites at the melt periphery, the majority of the periphery (>90%) initiates growth as primary austenite. At low speeds, there is

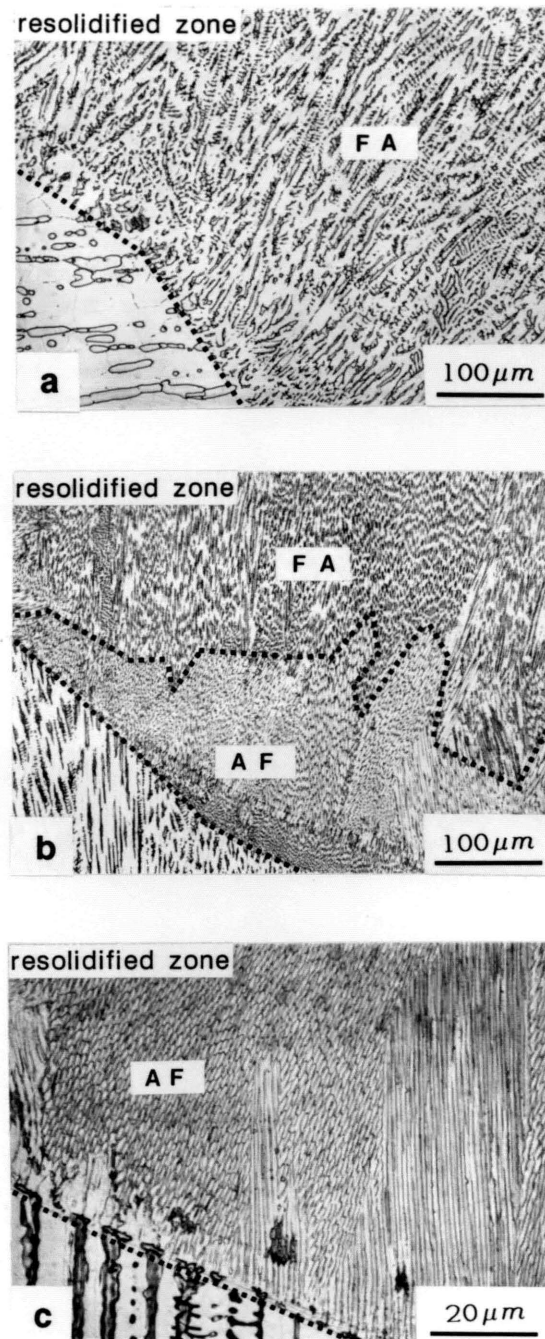


Figure 5.13 The transformation from the FA to AF modes of solidification in Alloy 4 as the scan speed is increased a) 6.3 mm/s, showing primary ferrite dendrites, b) 25 mm/s, showing a large AF solidification region (~50 microns) at the melt boundary and c) 100 mm/s, showing that the entire resolidified region solidifies in the AF mode.

enough time for solidification segregation to alter the epitaxially grown austenite to a primary ferrite mode. This fact is evidenced by the formation of ferrite dendrites which imply a large amount of segregation. However, at high speeds, there is less time for segregation, as evidenced by the lack of dendrites and the presence of austenite cells. Under these conditions, the epitaxial grown primary austenite zone does not change its solidification mode to the thermodynamically preferred primary ferrite phase.

5.3 Microstructural Features of Resolidified Stainless Steel Alloys

This section describes the origin of the complex microstructures which develop in solidified stainless steel alloys. These microstructures form as a result of five different solidification modes and are further modified by the solid state transformation of ferrite.

The mode of solidification has a large influence on the ferrite morphology by providing nucleation sites for austenite. Optical metallographic examination of the resolidified zones showed that eleven distinct morphologies exist and these morphologies can be thought of as subgroups of the primary modes of solidification. The microstructures which develop during the solidification of stainless steels have been investigated [5.11,5.13-5.18], however, the terminology used to describe the microstructures varies somewhat between authors. Table 5.4 summarizes the names given to the ferrite and austenite morphologies in this study and compares the terminology used by several other investigators.

5.3.1 Characterizing the Ferrite and Austenite Morphologies

5.3.1.1 Ferrite Morphologies in A and AF Solidified Alloys

Second phase ferrite forms in primary austenite solidified alloys and is present at the cell or dendrite walls. The amount of ferrite which forms during AF solidification is small and is surrounded by austenite. Therefore, during the ferrite to austenite phase transition, the amount of second phase ferrite is reduced even further as it transforms to austenite.

Table 5.4 : Comparison of the terminology used to describe the different microstructural morphologies in stainless steel alloys.

Mode	Reference					
	This Study	Katayama et al.	David	Lippold et al.	Brooks et al.	Suutala et al.
A	dendritic A cellular A	fully A	fully A	-	austenite	fully A
AF	inter-dendritic F	-	-	-	-	inter-dendritic F
	inter-cellular F	inter-cellular F	inter-cellular F	inter-cellular F	-	-
E	eutectic	eutectic F	-	-	eutectic	-
FA	inter-cellular A	-	-	-	-	-
	vermicular F	vermicular F	vermicular F	vermicular F	skeletal F	vermicular F
	lacy F	lacy F	lacy F	acicular A	-	lath F
	blocky A	-	-	-	-	-
F	Widman-statten A	Widman-statten A	acicular F	Widman-statten A	Widman-statten A	lath A
	massive A	-	-	-	-	-
	acicular A	acicular A	-	-	-	-
	dendritic F cellular F	fully F	fully F	-	-	-

Because of the high austenite/ferrite interfacial areas and small volumes of ferrite that form during AF solidification, nucleation of austenite from within the ferrite does not occur in these alloys.

The microstructures that form from the A or AF modes are easily characterized. In the single phase austenite solidification mode, there is no ferrite present. Under these conditions, primary austenite dendrites form at low cooling rates, Fig. 5.1a, and

primary austenite cells, Fig. 5.1b, form at high cooling rates. Microsegregation of chromium to the cell walls results in the observed etching differences but is not sufficiently high enough in concentration to form second phase ferrite.

In the AF solidification mode, segregation of chromium to the cell and dendrite walls is sufficient to form second phase ferrite. Interdendritic ferrite, Fig. 5.1c, forms at low cooling rates when the primary phase is austenite dendrites. Intercellular ferrite, Fig. 5.1d, forms at high cooling rates when the primary phase is austenite cells.

5.3.1.2 The Eutectic Microstructure

The eutectic microstructure forms from the simultaneous solidification of austenite and ferrite. Its microstructure was discussed in section 5.1.1.2 and is shown in Fig 5.8b. Since this microstructure is similar in appearance and tends to form with intercellular ferrite and intercellular austenite, its presence is often difficult to detect. In this study, the term eutectic will be given to those microstructures which are difficult to judge and might in fact be intercellular ferrite or intercellular austenite with a high volume fraction second phase.

5.3.1.3 Ferrite Morphologies Which Develop From FA Solidified Alloys

The ferrite morphologies which develop from the FA solidification mode are more complex than those which develop from the A or AF modes. The complexity arises from the substantial amount of solid state ferrite transformation that occurs as the melt cools. The ferrite which forms during solidification of duplex stainless steels is thermodynamically stable at elevated temperatures, however, as the temperature is lowered, the compositional range over which ferrite is stable decreases. Austenite becomes the more stable phase at lower temperatures and the decrease in temperature provides a driving force for the solid state transformation of ferrite.

This transformation can begin by the growth of existing primary or second phase austenite. If no austenite is present in the microstructure, as would be the case for

single phase ferrite solidification, then austenite can nucleate and grow from the ferrite. The preferred heterogeneous nucleation sites for austenite are areas of low Cr/Ni ratios such as grain boundaries or cell walls.

In order to describe the microstructures which develop, a distinction must be made between the austenite and ferrite which form during solidification and that which forms during the solid state transformation of ferrite. The terminology used to describe the various microstructural features is summarized in Table 5.5.

Table 5.5 : Description of the ferrite and austenite phases.

Symbol	Description
F_R	Residual ferrite in the microstructure at room temperature.
F_P	Primary ferrite which solidifies from the F or FA modes.
F_E	Second phase (eutectic) ferrite which solidifies from the AF mode.
A_P	Primary austenite which solidifies from the A or AF modes.
A_E	Second phase (eutectic) austenite which solidifies from the FA mode.
A_T	Austenite which forms during the solid state transformation of ferrite by diffusion controlled growth of austenite from F/A boundaries.
A_N	Austenite which nucleates within primary ferrite dendrites.
A_M	Austenite which forms during the solid state transformation of ferrite by a massive phase transformation within a ferrite matrix.
A_W	Widmanstatten austenite "platelets" which nucleate and grow from the grain boundaries in single phase ferrite solidified alloys.
A_A	Acicular austenite "needles" which nucleate intragranularly in the heat affected zone of single phase ferrite solidified alloys.
F_E, A_E	Eutectic ferrite, eutectic austenite.

There are four basic morphologies which develop from the FA mode of solidification. Intercellular austenite, vermicular ferrite, lacy ferrite and blocky austenite. The vermicular and lacy ferrite morphologies have been recognized by other authors while the intercellular ferrite and blocky austenite morphologies have not been given unique distinction in the past.

Figure 5.3a shows the appearance of intercellular austenite which can occur under two conditions. At moderately high cooling rates the microstructure consists of primary ferrite cells growing approximately parallel to the heat flow direction. The solidification mode is FA and each cell is surrounded by second phase austenite. This microstructure has an appearance of a semiregular array of ferrite cores with austenite at the cell walls. During the solid state transformation of ferrite, the ferrite which is located at the cell cores partially transforms to austenite. The final microstructure is an array of ferrite cores which have angular edges because of the solid state transformation. The orientation relationship between ferrite and austenite is known to be of a Kurdjumov-Sachs type [5.19] and leads to the angular edges at the transformation interface. The resulting microstructure shows ferrite cores surrounded by a layer of transformed austenite, A_T , and an outer layer of second phase austenite, A_E . A second set of conditions that produce this type of microstructure are those where equiaxed ferrite cells form in the center of melts which were cooled at low rates. Here the cellular mode is produced by nucleation of ferrite cells in the equiaxed zone but the microstructures are quite similar.

Figure 5.3b shows the typical appearance of vermicular ferrite. This morphology forms at low cooling rates and is the result of columnar dendritic ferrite solidification followed by a substantial amount of solid state transformation. The ferrite dendrites have well defined secondary arms with second phase austenite present at the secondary and primary dendrite arm walls. During the solid state transformation, the second phase austenite, A_E , grows into the ferrite dendrites leaving transformed austenite, A_T , behind. The transformation is seldom complete, and leaves the residual ferrite dendrite core in the microstructure.

Figure 5.3c shows the lacy ferrite morphology which was observed only in Alloy 5. This microstructure forms from primary ferrite dendrites which occur at low cooling rates and higher Cr/Ni ratios than vermicular ferrite. These alloys solidify

with a very high volume fraction ferrite and some of the morphological features are the same as dendritic ferrite. The second phase austenite, A_E , is present between the secondary arms and provides heterogeneous nucleation sites for the ferrite transformation. This austenite grows into the secondary ferrite arms and into the dendrite core leaving a roughened outline of the original ferrite dendrite. However, because of the large volume fraction ferrite, the transformation does not appear to be completed by the growth of secondary austenite into the ferrite dendrite alone. Austenite may possibly nucleate within the dendrite core which would help to explain its microstructural appearance shown in Fig. 5.14. Intradendritic austenite, A_N , appears to nucleate at many sites within the dendrite and its growth is controlled by the diffusion of ferrite stabilizing elements ahead of austenite/ferrite interface. When adjacent austenite regions approach each other, the transformation stops and leaves a wall of ferrite between the two advancing fronts. The microstructural appearance of lacy ferrite in its three principal directions is shown in Fig. 5.14. The top of the cube shows dendrites with their axes normal to the plane of the metallographic cross section while the sides of the cube show the dendrites with their axes parallel to the plane of the section. However, in order to definitely prove the existence of intradendritically nucleated austenite, additional experimental work would have to be performed.

Figure 5.3d shows the microstructural features of blocky austenite. Austenite blocks outline the columnar dendrite boundaries and were only observed in Alloy 6 at low cooling rates. This alloy solidified with a volume fraction ferrite which is close to 100% and the origin of the austenite blocks is most likely to be that of heterogeneously nucleated grain boundary allotriomorphs. Since the ferrite has a higher Cr/Ni ratio, it is more stable than the ferrite of the previous two cases. This stability prevents intradendritic nucleation of austenite and only growth of the allotriomorphs occurs and is restricted to the grain boundary vicinity for certain cooling rates. Therefore, the microstructure consists of a high volume fraction ferrite with blocks of austenite, A_T , oriented along the columnar grains. This austenite grows as the ferrite transforms, however, because of the higher stability of the ferrite, less transformation occurs.

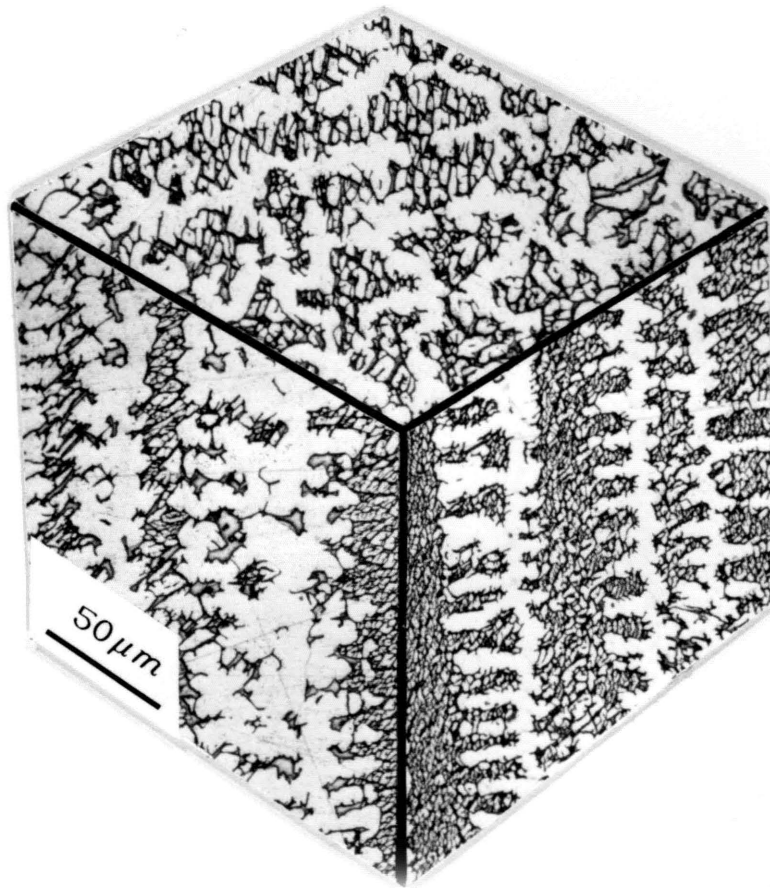


Figure 5.14 Microstructural features of lacy ferrite along its three principal directions. The primary dendrite core and the secondary dendrite arms can clearly be distinguished.

Occasionally, austenite blocks are located between the dendrites, indicating that possibly some second phase austenite may have been present at the secondary dendrite arm locations to provide a location for heterogeneous nucleation of austenite.

5.3.1.4 Single Phase Ferrite Solidified Alloys

Fig.5.2a shows the appearance of the single phase ferrite grains which form from the fully ferritic solidification mode in high Cr/Ni ratio alloys. Ferrite cells grow at high rates and ferrite dendrites grow at low rates. The cell boundaries do not etch as prominently as the grain boundaries which makes the ferrite grains the most prominent features in the microstructure. The microstructure remains fully ferritic as the alloy cools if the nucleation of austenite can be suppressed. This can be accomplished by rapidly cooling the alloy through the transformation temperature range. This occurred in the melts that solidified at 10^4C/s or faster.

At lower cooling rates, there is sufficient time to nucleate and grow austenite as the ferrite cools. The grain boundaries, which may have some second phase austenite, provide heterogeneous nucleation sites for Widmanstätten austenite. Figure 5.2b shows this microstructure before significant growth has occurred and indicates that thin adjacent platelets of austenite nucleate at the grain boundaries and grow into the ferrite matrix. Fig.5.2c shows the Widmanstätten microstructure at low cooling rates when the austenite platelets have grown entirely across the ferrite grain. This microstructure has been called acicular ferrite by other authors, however, since the mechanism is the same, both morphologies will be referred to as Widmanstätten austenite. Figure 5.2d shows that the plate-like appearance of the Widmanstätten austenite which can be observed when the plane of the platelet lies nearly parallel with the polished surface.

The formation of massive austenite was only observed in Alloy 5 and only at high cooling rates. This alloy solidifies in the fully ferritic mode prior to transformation and this microstructure undergoes a massive transformation to austenite at subsolidus temperatures. The morphology of massive austenite has been studied in stainless steel alloys [5.20] and is the result of undercooling the ferrite below the austenite/ferrite T_0 temperature and will be discussed in detail in Chapter 8.

Intragranular austenite needles were observed in the heat affected zone of the high Cr/Ni ratio alloys. Examples of this microstructure are shown in Chapter 8 and indicate that this microstructure presumably forms during the reheating of single phase ferrite which can occur in the heat affected zone of a weld. The nucleation characteristics of acicular needles are discussed in detail in Chapter 8.

5.3.2 The Combined Effects of Cooling Rate and Composition

The microstructures which develop during rapid resolidification were first shown to be related to the primary solidification mode and second, to compositional and cooling rate variations within a given PSM. Table 5.6 summarizes the solidification and solid state transformation sequences that lead to the different morphologies. These morphologies were described in the previous section and all were observed during surface melting and resolidification except for acicular austenite, which was observed only in the heat affected zone.

The relationship between the various morphologies can be plotted on a scan-speed versus composition diagram in the same way as the four PSM regions were plotted. Figure 5.15 shows the map of the morphologies and since the morphologies are "subsets" of the PSM, each PSM region is divided into several different areas which represent the predominant morphology.

Variations in the cooling rate exist within each resolidified zone. Therefore, a mixture of morphologies may be present for a given set of electron beam parameters. The higher cooled regions of the melt which have small dendrite arm spacings tend to be located close to the melt periphery and at the root of deep penetrating welds. These regions tend to have morphological characteristics which do not represent the bulk of the solidified metal but do have characteristics which are more like the alloys solidified at the next higher travel speed. These aspects were taken into account in drafting Fig. 5.15.

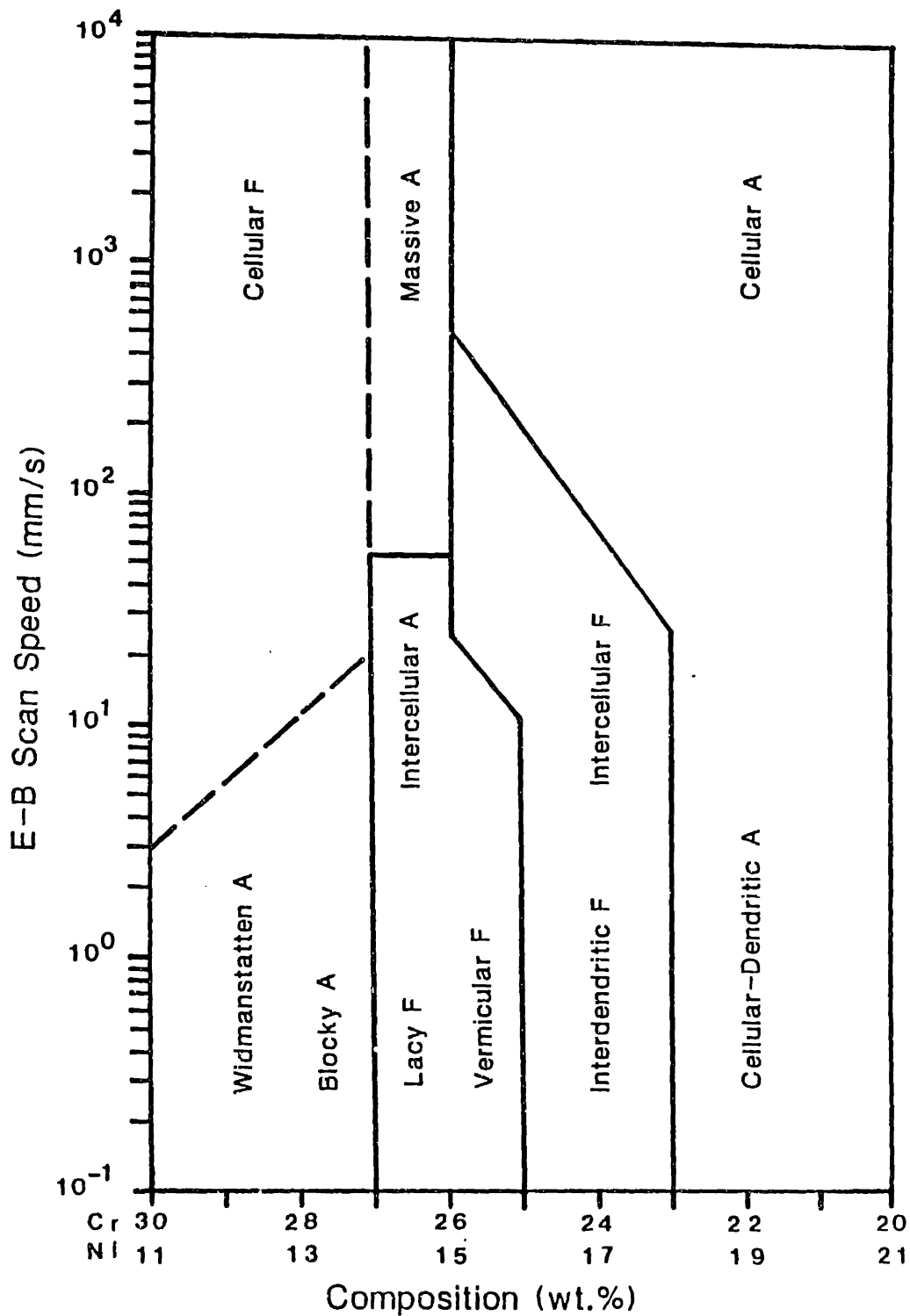


Figure 5.15 Scan speed (cooling rate) versus composition map of the microstructural morphologies that result from solidification and solid state transformation of stainless steel alloys.

Table 5.6 : The solidification mode, solidification sequence and solid-state transformation events responsible for the different microstructures.

Mode	Solidification Sequence	Solid State Transformation	Morphology
A	$L \rightarrow (L+A_P) \rightarrow A$	None	Dendritic A Cellular A
AF	$L \rightarrow (L+A_P) \rightarrow (L+A_P+F_E) \rightarrow (A_P+F_E)$	$F_E \rightarrow A_T$	Interdendritic F Intercellular F
E	$L \rightarrow (L+F_E+A_E) \rightarrow (F_E+A_E)$	$F_E \rightarrow A_T$	Eutectic
FA	$L \rightarrow (L+F_P) \rightarrow (L+F_P+A_E) \rightarrow (F_P+A_E)$	$F_P \rightarrow A_T$	Intercellular A Vermicular F Blocky A
		$F_P \rightarrow A_T, A_N$	Lacy F
F	$L \rightarrow (L+F_P) \rightarrow F_P$	$F_P \rightarrow A_W$	Widmanstätten A
		$F_P \rightarrow A_M$	Massive A
		$F_P \rightarrow A_A$	Acicular A
		None	Dendritic F Cellular F

The results presented in this diagram represent the combined effects of two factors. Firstly, the composition axis represents the thermodynamic stability of the ferrite phase. As the Cr/Ni ratio is increased, a higher volume fraction of ferrite solidifies from the melt and the ferrite that forms becomes more resistant to the solid state phase transformation. Secondly, the scan speed (cooling rate) axis represents the kinetic response of the system. As the speed is increased, there is an increased resistance to change. That is, the amount of solidification segregation decreases and the amount of ferrite that transforms to austenite decreases. In the limit, partitionless solidification would occur, however, these conditions were not observed in this study. A more thorough analysis of the microstructures which were observed in the resolidified electron beam melts is presented in Chapter 8 which includes discussions on the thermodynamic and kinetic factors responsible for the transformation mechanisms.

5.4 Conclusions

In summary, five modes of solidification and eleven morphologies were observed during the resolidification of the seven alloys. These microstructural characteristics are believed to be a complete 'set' of the possible solidification and solid state transformation events that occur in typical stainless steel alloys and can be related to the alloy composition, the cooling rate and the extent of the solid state transformation of ferrite.

The results of this study were used to create diagrams which can be used to predict the primary solidification mode and the austenite and ferrite morphologies, based on chemical composition and cooling rate. Figure 5.6 shows the relationship between the primary mode of solidification and the cooling rate for the seven alloys which cross the line of two-fold saturation while Fig. 5.15 shows the microstructural morphologies which develop from these solidification conditions.

Careful metallographic examination of the surface melts showed that ferrite and austenite grow epitaxially from the base metal substrate. Epitaxial growth from the resolidification of a two-phase substrate requires that the two phases compete to become the primary solid phase to solidify in the remelted zone. At low cooling rates, the thermodynamic factors take preference and the PSM is dictated by the more thermodynamically stable phase which can be predicted by the line of two-fold saturation. However, at high cooling rates, the growth kinetics of the metastable phase may supersede the formation of the equilibrium primary phase. This situation was observed in Alloy 4 which solidifies in the FA mode at low rates and in the AF mode at higher rates and in the fully austenitic mode at the highest rates.

One of the objectives of this investigation was to determine if the change in solidification modes with cooling rate was caused by the nucleation of metastable phases from within the melt. Although one cannot rule out the possibility of metastable phase nucleation from within the molten zone at high cooling rates, it does seem unlikely that this nucleation event would occur because of the lack of heterogeneous sites in the liquid. It is a much more likely possibility that the changes in stainless steel solidification mode observed by other investigators [5.6,5.7] is also

the result of the epitaxially grown metastable austenite developing into the primary solid phase due to the favorable growth kinetics of austenite under certain solidification conditions.

In the next chapter, the influence that cooling rate has on the ferrite content will be investigated with specific reference to the primary modes of solidification and the microstructural morphologies presented in figures 5.6 and 5.15.

CHAPTER 6

The Influence Of Cooling Rate On The Residual Ferrite Content Of Stainless Steel Alloys

Residual ferrite is present in the microstructure of duplex stainless steel alloys in volume fractions as high as 50 percent. Even at low volume fractions, ferrite can influence the integrity of stainless steel alloys and many investigators have tried to develop relationships between the alloy composition and the ferrite content of stainless steel castings and welds. At slow cooling rates, the principal factor which controls the amount of ferrite is the composition, however, rapid solidification processing has been shown to dramatically alter the amount of ferrite in the microstructure. Under these conditions, the cooling rate becomes as important as the composition in determining the resulting ferrite content. These effects are not well understood and an important aspect of this investigation was to develop a relationship between cooling rate and the residual ferrite content in stainless steels.

This chapter examines the results of the cooling rate experiments which were performed on the series of seven Fe-Ni-Cr ternary alloys that span the line of two-fold saturation along the 59% Fe isopleth. Cooling rate variations were produced by electron-beam surface melting the alloys at rates between 4.7×10^2 °C/s and 7.5×10^6 °C/s. The results show that the cooling rate has a significant effect on the ferrite content but that its influence is not easily generalized. The solidification mode, cooling rate and composition were shown to be equally important, and interrelated, factors in the determination of the ferrite content.

For primary austenite solidified alloys, the ferrite content was shown to decrease with increasing cooling rate, while for primary ferrite solidified alloys the ferrite content was shown to increase with increasing cooling rate. These effects are so dramatic that at high cooling rates ($>10^4$ °C/s) the alloys are either fully austenitic or fully ferritic depending on their primary mode of solidification. The reasons for this behavior can be explained by the influence of cooling rate on solidification segregation, Chapter 7, and solid state transformation, Chapter 8.

6.1 The Ferrite Content at Slow Cooling Rates

The amount of residual ferrite present in stainless steel alloys is equal to the amount of ferrite which forms during solidification minus the amount of ferrite which transforms as the melt cools to room temperature. Both the solidification and solid state transformation effects are influenced by cooling rate and are difficult to isolate from each other. At slow cooling rates, the largest amount of ferrite transforms as the melt cools and this section examines the ferrite content of slow cooling rate melts by first estimating the amount of ferrite which would be present if equilibrium conditions could be achieved. Then, these results are compared with the ferrite content of the slow-cooling-rate arc-cast buttons.

6.1.1 Full Diffusional Equilibrium

Full diffusional equilibrium means that there is enough time during the solidification process so that composition gradients are eliminated in both the liquid and solid phases. Under these conditions, the amount of ferrite which solidifies from the melt, the solidification path, and the composition of the liquid and solid phases can be determined from the equilibrium phase diagram.

The liquidus and solidus projections are shown on a portion of the Fe-Ni-Cr system in Fig.6.1a. These data are taken from experimental measurements [6.1] and the compositions of the seven alloys examined in this investigation are plotted on this figure. The location of these alloys with respect to the liquidus and solidus lines shows that Alloy 1 will solidify in the fully austenitic mode, Alloys 2 and 3 in the AF mode, Alloys 4, 5 and 6 in the FA mode and Alloy 7 in the fully ferritic mode. There is good agreement with the primary modes of solidification predicted by Fig. 6.1a and those examined in Chapter 5 for the slow cooling rate arc cast buttons, however, the line of two-fold saturation predicted by thermodynamic calculations deviates at higher chromium contents.

Fig. 6.1b shows the location of the line of two-fold saturation as determined by various investigators. The results of Kundrat [6.2], Chang [6.3] and Thermocalc [6.4] are predictions based on thermodynamic calculations while those of Rivlin et al. [6.1] were derived from experiments. The thermodynamic calculations all fall within 2 percent chromium of the experimentally determined value, however, this relatively

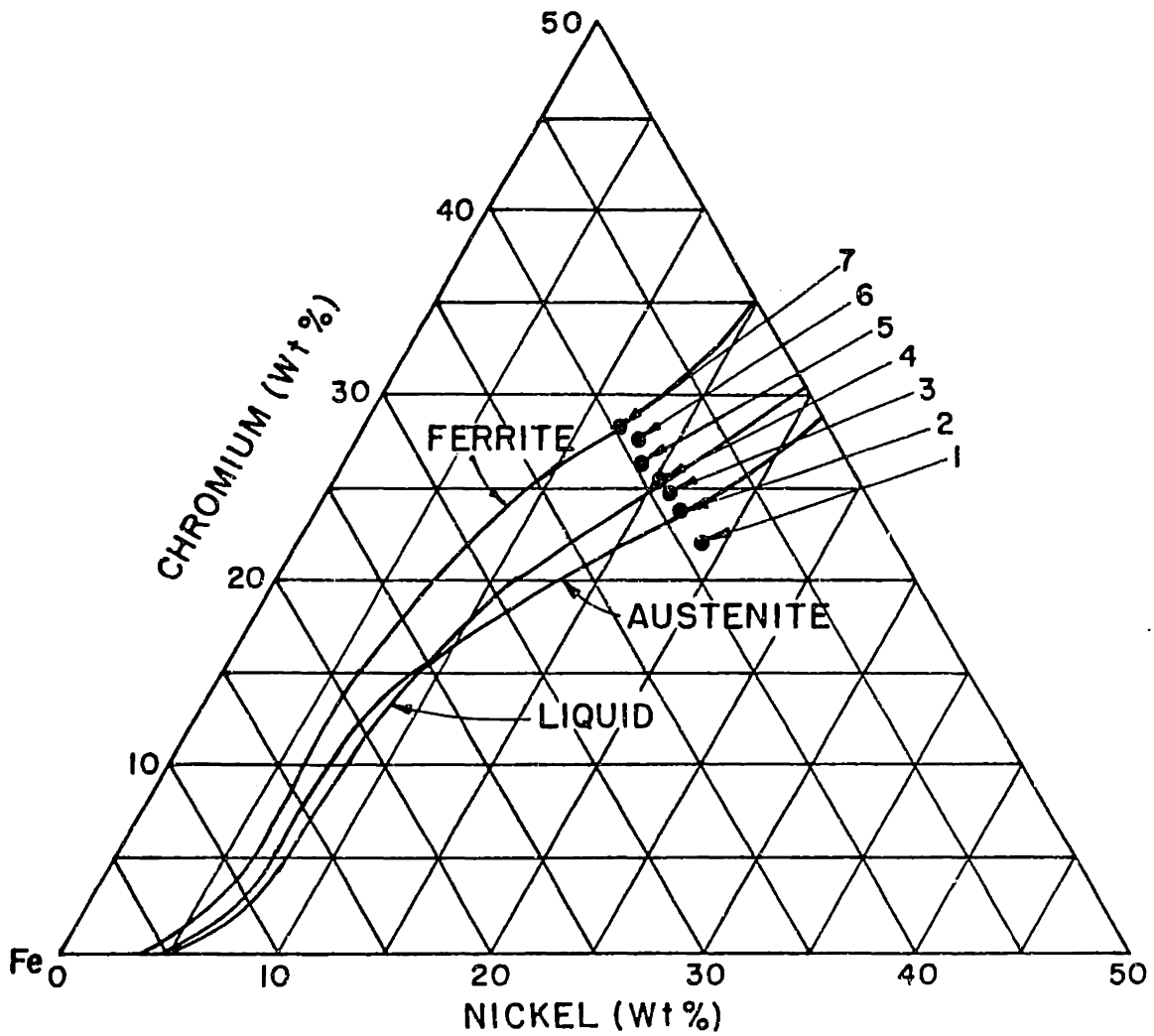


Figure 6.1 Location of the seven Fe-Ni-Cr alloys with respect to the ferrite solvus, austenite solvus and the line of two-fold saturation, after Rivilin et al, [1.32].

small difference in the location of the line of two-fold saturation can be misleading when trying to predict the PSM. Throughout this investigation, the experimentally determined liquidus and solidus lines by Rivlin and Raynor will be assumed to be the 'true' values since they match the experimental results of this investigation. However, when comparisons are made between thermodynamic predictions and experimental measurements, a shift in the alloy compositions needs to be made so that the two methods agree on the location of the line of two-fold saturation.

For equilibrium solidification conditions, Fig. 6.1 indicates that Alloy 1 cools through the L+A two-phase field and directly into the single phase austenite field with no ferrite in the microstructure. Alloys 2 and 3 cool through the L+A two-phase field and then into the L+A+F three phase field where second-phase ferrite forms in the microstructure. Alloys 4, 5 and 6 cool through the L+F two-phase field and then through the L+A+F three phase field where second-phase austenite forms. Finally, Alloy 7 cools through the L+F two-phase field and directly into the single-phase ferrite field with no austenite in the microstructure.

From this figure, the amount of ferrite that forms in the alloys can be estimated by applying the lever rule to the tie lines in the F+A two phase field which are nearly parallel to the constant Fe section at these temperatures. Table 6.1 shows the amount of ferrite which will solidify from each alloy under equilibrium conditions. These calculations were predicted from Fig. 6.1a and indicate that the ferrite content at the solidus temperature varies from 0% in Alloy 1 to 100% in Alloy 7.

The phase diagram can also be used to estimate the amount of ferrite which transforms to austenite under equilibrium conditions. At elevated temperatures, the tie-lines in the F+A region are nearly parallel to the 59% Fe isopleth and the isopleth can be used to estimate the ferrite content. Table 6.1 shows the equilibrium residual ferrite content of the alloys at 1000°C. At this temperature, all of the ferrite has transformed to austenite in Alloy 2 and 60% has transformed in Alloy 7. By extrapolating the ferrite and austenite solvus lines to lower temperatures one can see that the second phase ferrite in Alloys 2 and 3 should completely transform and that a majority of the primary ferrite contained in Alloys 4-7 should transform by the time the alloy cools to room temperature under equilibrium conditions. However, in actual melts, kinetic limitations prevent the transformation at low temperatures and some residual ferrite remains in the microstructure.

Table 6.1 Equilibrium ferrite contents at the solidus and at 1000°C.

Alloy	% Ferrite that solidifies	% Residual Ferrite at 1000°C
1	0	0
2	20	0
3	35	8
4	55	14
5	70	24
6	92	31
7	100	40

6.1.2 The Arc Cast Buttons

The arc cast buttons represent the slowest cooling rates examined and were used as a standard with which to compare the high cooling rate microstructures. In Chapter 4 it was shown that the primary and secondary dendrite arm spacings of the arc castings were 42 and 18 μm respectively and that this spacing corresponds to a cooling rate of about 7 °C/s. Arc welds typically solidify with cooling rates between 10 and 1000°C/s, therefore, the cooling rate in the arc cast buttons can be considered to be similar but on the slow cooling rate side of arc welding.

The Schaeffler diagram was used to predict the ferrite content of the arc cast buttons. The alloy compositions are plotted in Fig. 6.2. Alloy 1 is in the fully austenitic region and Alloys 2-7 are in the duplex, ferrite-austenite, region. The ferrite contents estimated from the Schaeffler diagram are shown in Table 6-2 and range from 0% for Alloy 1 to 32% for Alloy 7.

A second, and less conventional, method was used to estimate the amount of residual ferrite. Based on several investigations [6.5,6.6,6.7], where the ferrite content of a large number of commercial stainless steel (AISI 304, 308, 309, 316) arc-welds was measured, Fig. 6.3 can be used to predict the ferrite content for different Cr/Ni ratio alloys.

Table 6.2 Predicted and measured ferrite contents of the arc cast buttons

Alloy	Predictive Methods (%)		Measured (%)			Avg. (%)
	Schaeffler	Cr/Ni	MG	VSM	QTM	
1	0	0	0	0	0	0
2	5	7	5.4	4.6	5.4	5.5
3	7.5	11.5	8.7	9.8	11.0	9.7
4	12	14.8	14.6	15.8	14.2	14.3
5	16	23.5	23.6	23.2	22.8	21.8
6	27	29.7	27.4	26.4	32.4	28.6
7	32	35.9	36.5	32.1	39.2	35.1

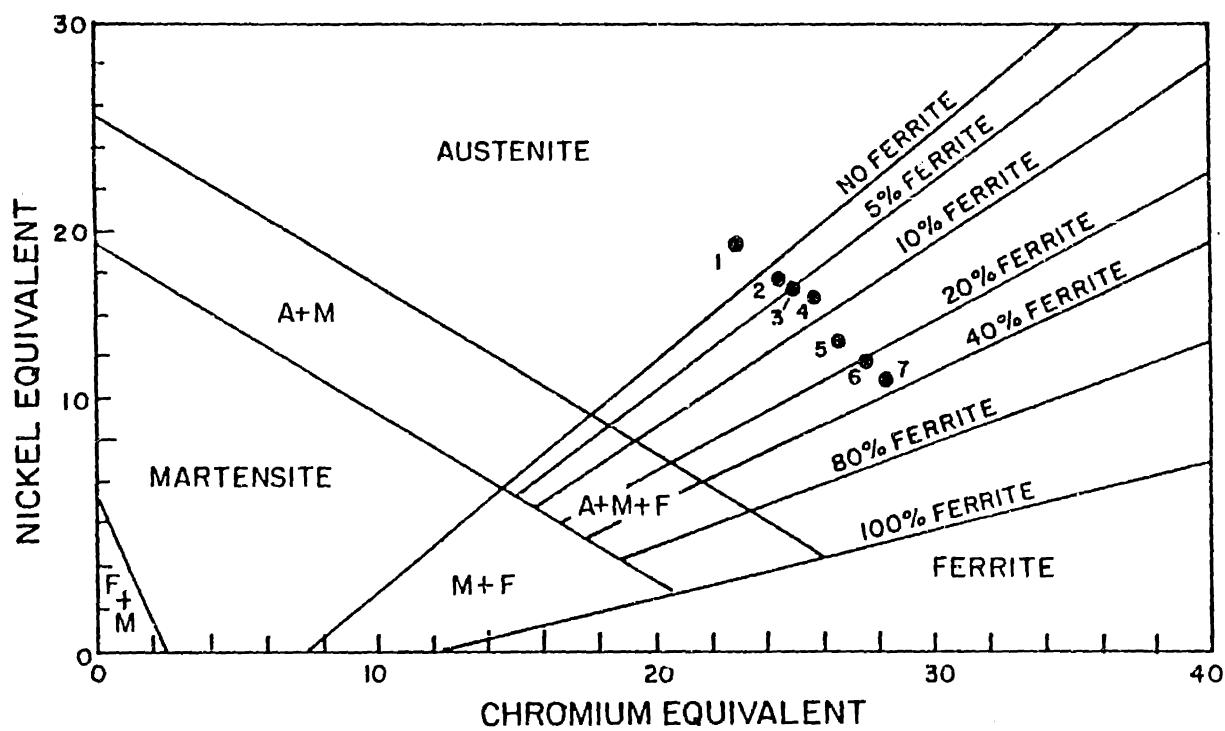


Figure 6.2 Location of the seven Fe-Ni-Cr alloys on the Schaeffler diagram.

For Cr/Ni ratios below 1.20 the ferrite content is zero while for Cr/Ni ratios between 1.20 and 2.0, a regression analysis shows the following relationship between Cr/Ni ratio and ferrite content:

$$\%F = 36.6 (\text{Cr/Ni}) - 43.8 \quad (6.1)$$

The ferrite is estimated in weight percent and the Cr and Ni equivalents suggested by DeLong (eq. 1.1 and 1.2) should be used. Table 6.2 shows that this approach also predicts ferrite contents of the cast alloys should vary from 0 to above 30 percent.

The ferrite content of the castings was measured using several techniques. Since the castings had a thickness greater than 10 mm, the ferrite number could be measured using the Magne-Gage. Since the castings had a coarse microstructure, the ferrite could be directly measured using quantitative metallography. These Magne-Gage readings were converted to percent ferrite using the procedure that was discussed in Chapter 3. Using the extended ferrite measurement method [3.4] the ferrite content was determined and the results are shown in Table 6.2. These measurements indicate that the ferrite content varies from 0 to 35%. The VSM technique was used as the second measurement method and is also described in Chapter 3. The results of these measurements are also presented in Table 6.2 and indicate that the ferrite contents vary from 0 to 32.1 percent. Finally, quantitative metallographic measurements were used to confirm the ferrite content of the seven alloys.

Figure 6.4 compares the measured ferrite content (VSM) with the predicted ferrite content (Schaeffler) along the 59 wt. % Fe composition axis of the Fe-Ni-Cr ternary system. The Schaeffler prediction shows that the ferrite content varies from 0% at 23.3 wt.% Cr to 100% at 34 wt.% Cr and predicts a linear increase in ferrite content for the compositions studied that varies from 23.3 to 26.5 wt.% Cr. The predicted amount of ferrite deviates sharply from this linear relationship to higher ferrite contents at chromium levels greater 26.5 wt. %. The measured ferrite contents are close to the predicted values and follow an interesting trend. For chromium contents above 26.5%, i.e. in the nonlinear Schaeffler region, the measured values are lower than the predicted values. For chromium contents below 26.5%, i.e. in the linear Schaeffler region, the measured values are higher than the predicted values.

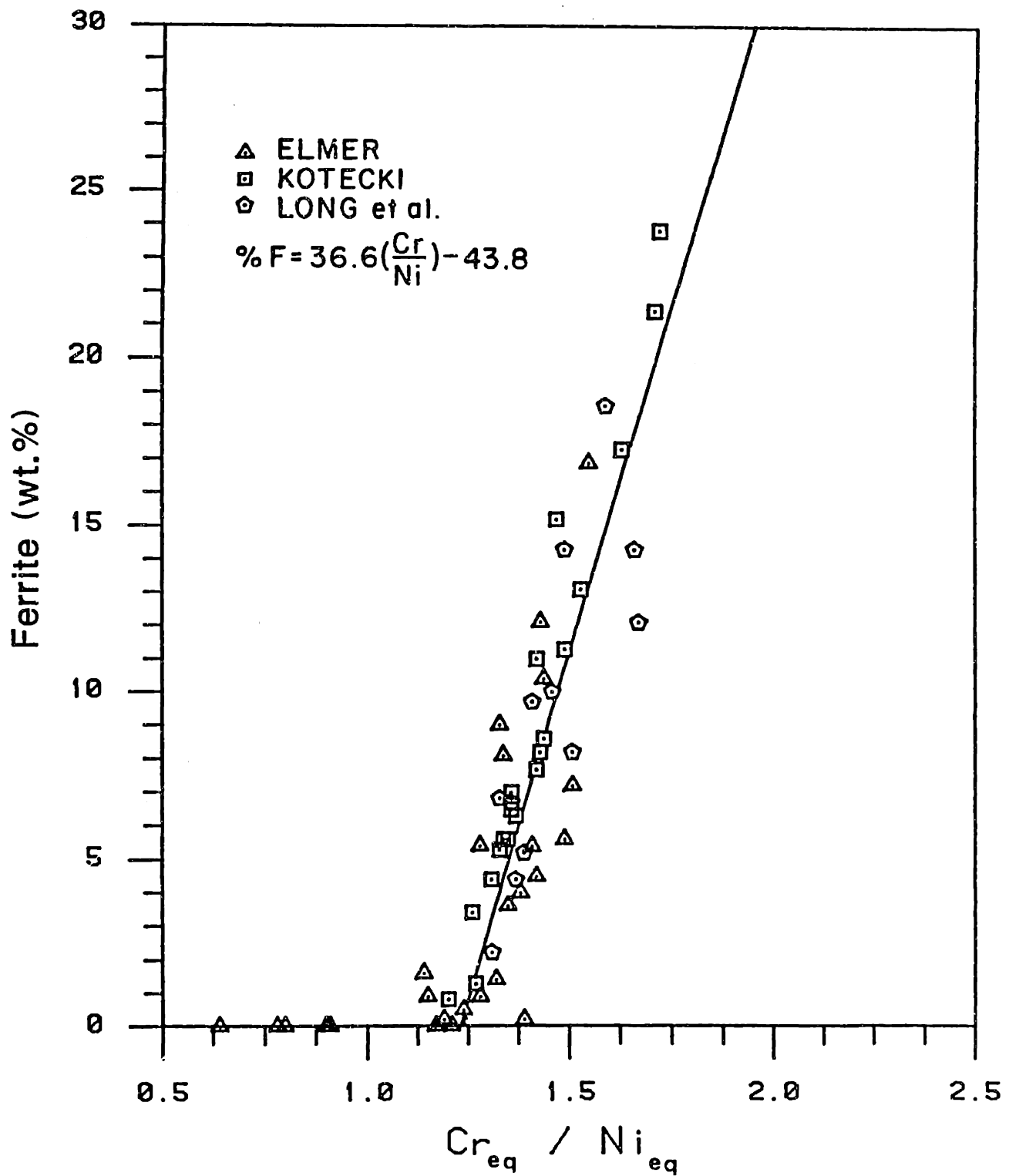


Figure 6.3 Percent residual ferrite as a function of Cr/Ni ratio in arc-welds of typical 304 type stainless steel alloys.

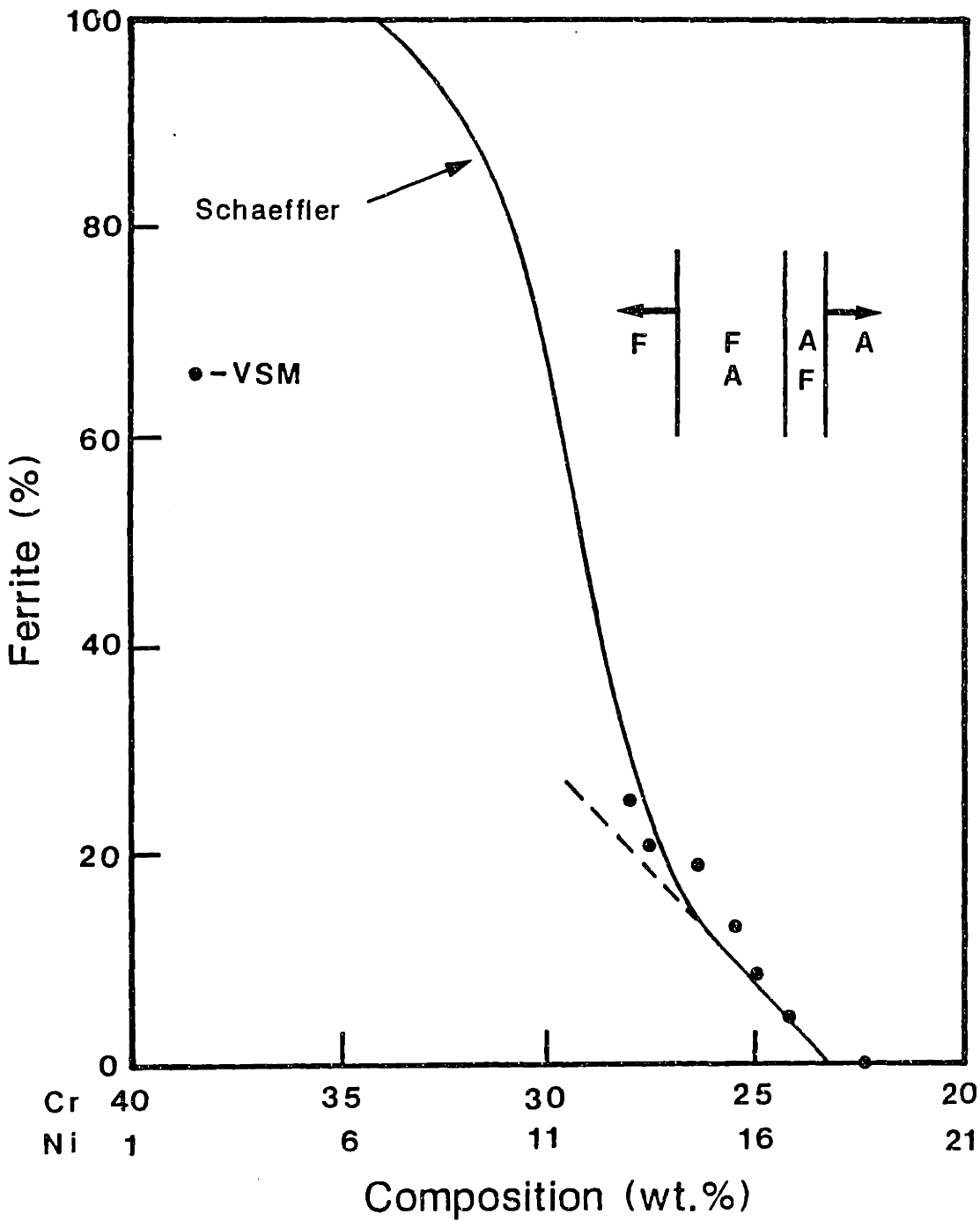


Figure 6.4 Residual ferrite on the seven arc-cast alloys compared to the residual ferrite predicted by the Schaeffler diagram for 59 wt% Fe alloys. The solidification modes, as determined from the cast alloys, are indicated.

The differences between the measured and predicted values can be explained by the fact that the cast alloys cool at a slower rate than what the Schaeffler predictions are based on. It was shown in Chapter 5 that below 27 wt. % chromium, the cast alloys containing 59% Fe solidify in a duplex ferrite-austenite modes while above 27 wt. % chromium, the alloys solidify in the fully ferritic mode. This change in solidification modes at 27% Cr can be used to explain the deviation in linearity of the Schaeffler prediction and also can be used to explain the difference in predicted and measured values above and below 27% Cr.

The deviation of the Schaeffler prediction from its initial, low Cr, linear behavior is associated with the change in solidification modes from the FA to the F mode. In the FA mode, increases in chromium content increase the amount of ferrite that solidifies from the melt. Therefore, there is a general increase in the ferrite content with increasing chromium. When the chromium level is increased to the point where the solidification becomes fully ferritic, there is no further increase in the amount of ferrite that forms during solidification with increasing chromium and the resulting ferrite content is solely dependent upon the amount of ferrite to austenite transformation that occurs. This transformation requires nucleation of Widmanstatten austenite at the ferrite grain boundaries. Since the grain boundary area is much less than the interdendritic area where austenite is present in the FA mode, less transformation occurs in the fully ferritic mode.

The difference between the measured ferrite content of the castings and the predicted values from the Schaeffler diagram can be explained by transformation kinetics. The ferrite content of alloys which solidify in the fully ferritic mode are very sensitive to cooling rates. A slower cooling rate allows more time for austenite to nucleate and grow from the fully ferritic microstructure. Therefore, slower cooling rates always result in lower residual ferrite contents. Since the castings cool at a slower rate than the Schaeffler predictions, a lower ferrite content is expected in the castings.

In the FA mode however, the situation is more complicated because two phases solidify from the melt. A slower cooling rate allows for more segregation, creates a large dendrite arm spacing and allows more time for the ferrite to austenite transformation. These factors have mixed effects on the residual ferrite content. In the FA mode, more segregation means less ferrite, however, the ferrite that forms will

have a higher Cr/Ni ratio and will be more resistant to transformation. A larger dendrite arm spacing has less austenite/ferrite interfacial area which provides less area for austenite growth during the transformation, however, the slower cooling rate allows for more transformation and helps to balance this factor. Therefore, the situation is complicated and the effect of a slower cooling rate is difficult to predict in the FA mode. The experimental results show that the castings have more ferrite than the Schaeffler diagram estimates and indicates that the larger dendrite arm spacing and higher stability of the ferrite outweigh the lower initial amount of ferrite and the greater time for the ferrite to transform at lower cooling rates.

6.2 The Ferrite Content of Electron Beam Surface Melts

Electron beam surface melts were performed on each of the alloys to produce cooling rates that varied from 4.7×10^2 °C/s to 7.5×10^6 °C/s. The ferrite content was shown to change significantly with cooling rate. These changes can be described by the influence of cooling rate on the mode of solidification, the amount of solidification segregation and the extent of the solid state transformation of ferrite.

The ferrite content of each alloy was measured by the vibrating sample magnetometer method which is described in Chapter 3 and the results of the ferrite measurements are presented in Table 6.3 for each of the seven alloys and each of the solidification conditions. Three readings were made on each cast alloy and one reading was made on each electron-beam melt. At the highest travel speed, 5 m/s, the samples were too small to be extracted without substrate contamination. Nevertheless, the results showed the ferrite content of these melts to be close to 100% ferrite for the primary ferrite solidified alloys and close to 0% ferrite for the primary austenite solidified alloys.

Two types of diagrams representing the ferrite content as a function of cooling rate are shown in this chapter. The actual measured ferrite content is plotted versus scan speed on figures 6.5, 6.7, 6.9, 6.11 and 6.14. The second type of diagram is schematic in nature and represent the estimated amount of ferrite for particular idealized solidification modes. Figures 6.6, 6.8, 6.10, 6.12 and 6.13 are plotted as approximate ferrite content versus approximate cooling rate where the cooling rate scale of these figures is similar to that of the actual ferrite content versus scan speed

figures. By selecting the scales of ferrite content and cooling rate to be the same for the actual and schematic drawings, figures 6.5 through 6.13 can be directly compared to observe changes in the ferrite content with cooling rate.

6.2.1 Primary Austenite Solidified Alloys 1, 2 and 3

The behavior of alloys which solidify in the A or AF modes will be described by examining the behavior of alloys 1, 2, and 3. Alloy 1 solidifies in a fully austenitic mode at all cooling rates and contains no ferrite. Alloys 2 and 3 both solidify in an austenitic-ferritic mode at low cooling rates and in a fully austenitic mode at high cooling rates. Therefore, the ferrite content of these alloys decreases as the cooling rate increases. The results presented here show that the amount of second phase ferrite decreases with increasing scan speed. This behavior can be explained by undercooling at the dendrite tip. Chapter 7 will present calculations which show that the dendrite tip undercooling increases with increasing scan speed and that the amount of second phase which forms decreases accordingly.

Figure 6.5 shows the measured ferrite content versus scan speed relationship for alloys 1, 2 and 3. Alloy 1 is fully austenitic at all speeds and its ferrite content is zero regardless of the cooling rate. Alloys 2 and 3 both have ferrite contents in the arc cast condition (0.7 mm/s equivalent speed) which are close to the Schaeffler prediction and both have a gradual decrease in ferrite content as the scan speed is increased. Alloy 2 reaches zero percent ferrite at a scan speed of about 100 mm/s while Alloy 3 reaches zero percent ferrite at slightly higher speeds. The fact that Alloy 3 has more ferrite and requires higher scan speeds to reach zero percent ferrite than Alloy 2 is a result of its higher Cr/Ni ratio.

The cooling rate influences the ferrite content in two ways. Firstly, it influences the amount of ferrite which solidifies from the melt. Sarreal and Abbaschian [6.9] have shown that the amount of second phase that forms reaches a maximum value at intermediate cooling rates. At high rates, dendrite tip undercooling increases the percentage of primary phase and reduces the amount of second phase that forms.

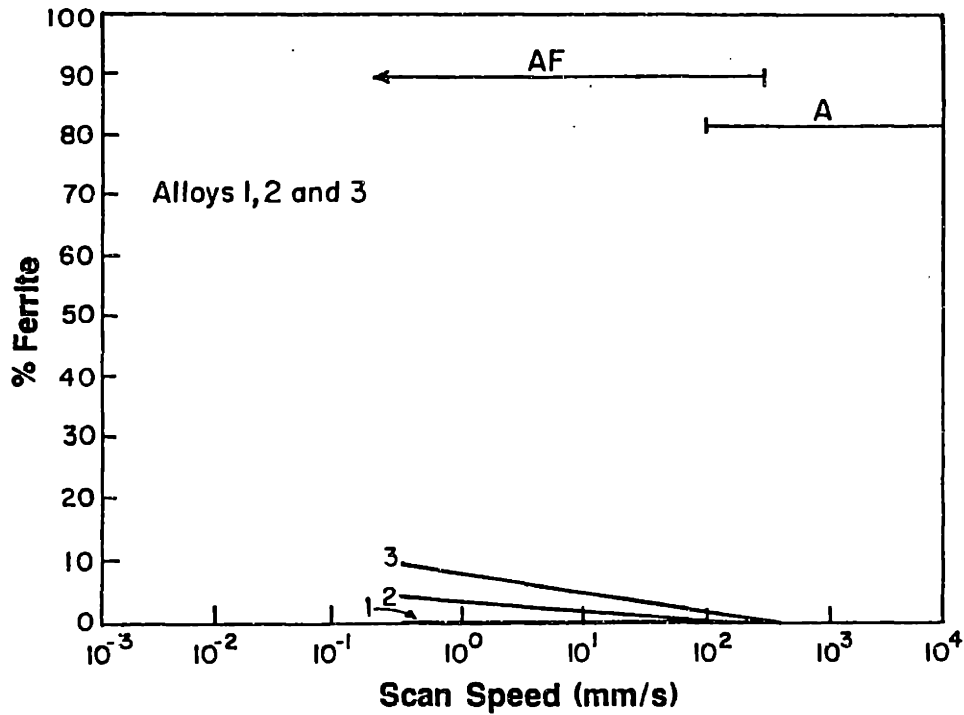


Figure 6.5 The measured ferrite content of A and AF solidified alloys 1, 2 and 3 as a function of electron beam scan speed.

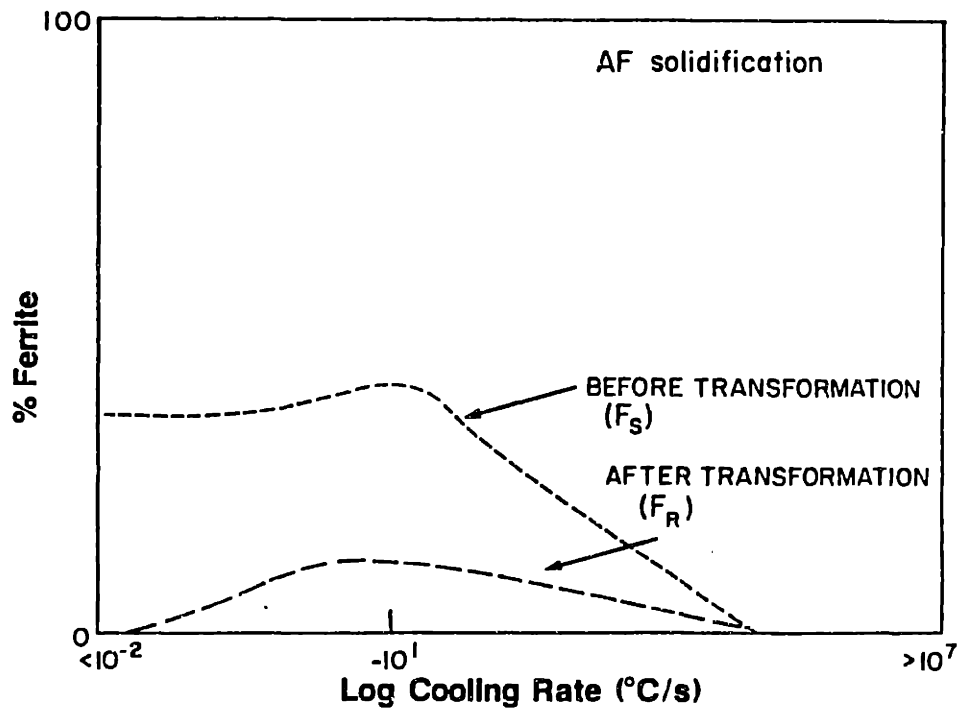


Figure 6.6 The estimated trend of ferrite content in A and AF solidified alloys as a function of solidification rate. The amount of ferrite that solidifies and the residual ferrite, after solid state transformation, are indicated.

At low cooling rates, back diffusion in the solid reduces the amount of second phase which forms. Between these extremes, the second phase reaches a maximum amount at a cooling rate of about 100°C/s in the Al-Cu system and this amount corresponds to the amount of second phase predicted by the Scheil equation. Secondly, the cooling rate influences the amount of ferrite which transforms to austenite. At high rates there is no time for transformation to occur while at low rates the maximum amount of ferrite transforms and the ferrite content approaches its equilibrium value.

These two factors are schematically shown in Fig. 6.6. At low cooling rates, a high percentage of ferrite transforms to austenite while at high cooling rates, the percentage that transforms approaches zero. Therefore, a maximum in the amount of residual ferrite also occurs at an intermediate cooling rate for primary austenite solidified alloys. Comparing the actual amount of residual ferrite in Alloys 2 and 3 (Fig. 6.5) with Fig. 6.6 shows that the tests performed in this study all occur at the high cooling rate side of Fig. 6.4 since a peak in the actual ferrite content was not observed. This fact is confirmed by a small value ($\alpha < 0.1$) of the Brody-Flemings back diffusion parameter in the arc cast buttons and even smaller values for the electron-beam melts.

6.2.2 Alloy 4

Alloy 4 behaves uniquely because it solidifies in a primary ferritic mode (FA) at low cooling rates and in a primary austenitic mode (AF or A) at high cooling rates. This change in solidification behavior has a significant effect on the ferrite content. Figure 6.7 shows the actual ferrite content of Alloy 4 as a function of the electron beam scan speed. The ferrite content was measured by the vibrating sample magnetometer and the results are compared to the amount predicted by the Schaeffler diagram.

As the scan speed increases from 0.7 to 100 mm/s, the ferrite level increases from 14 to 18 percent. In this region, the mode of solidification is FA and the increase in ferrite content is caused by the increase in the amount of primary ferrite that solidifies and the decrease in the amount of ferrite that transforms. At scan speeds above 100 mm/s, the ferrite content decreases because the FA mode of solidification is being replaced by the AF or E mode of solidification and finally

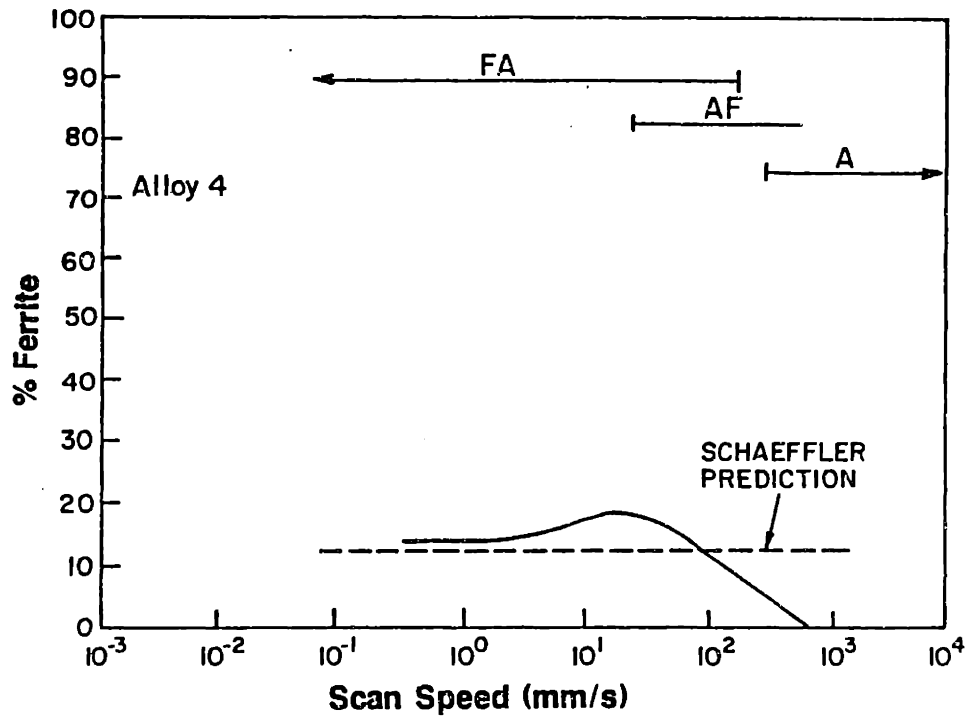


Figure 6.7 The measured ferrite content of Alloy 4 which changes its mode of solidification from FA to AF to A as the scan speed is increased.

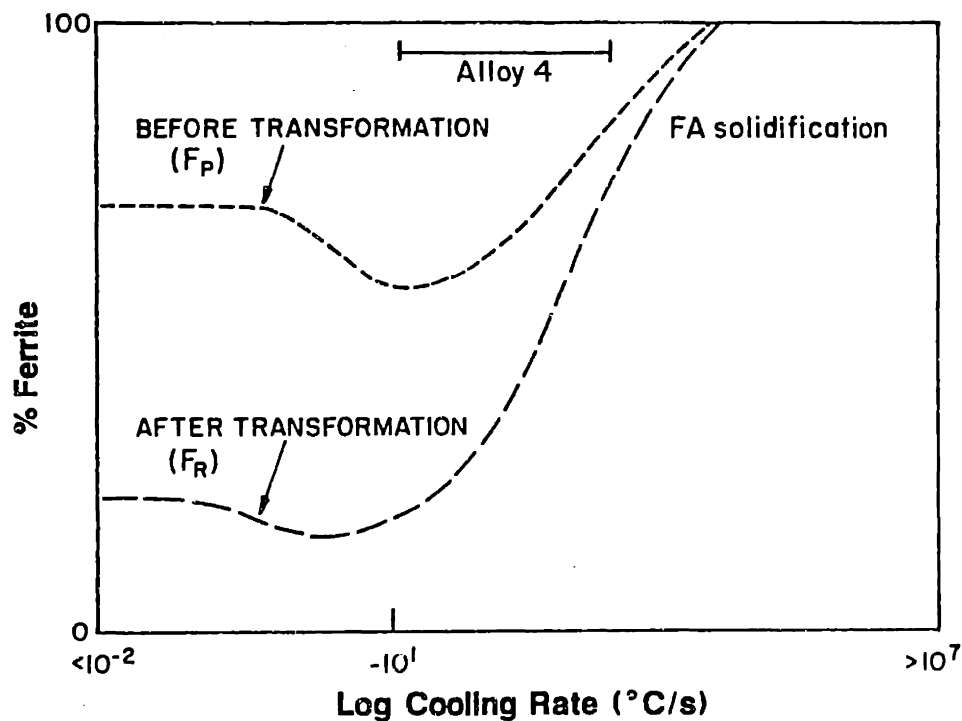


Figure 6.8 The estimated trend of ferrite content for the FA solidification mode as a function of solidification rate. The amount of ferrite that solidifies and the residual ferrite, after solid state transformation, are indicated.

the fully austenitic mode of solidification. The change in solidification modes with scan speed was discussed in Chapter 5 and is shown in Fig. 5.11.

The separate contributions of solidification and solid-state transformation are schematically shown in Fig. 6.8 for primary ferrite solidified alloys. This figure illustrates both the amount of ferrite that solidifies from the melt and the amount of ferrite that transforms as a function of cooling rate. The ferrite content versus cooling rate behavior passes through a minimum for primary ferrite solidified alloys rather than a maximum as it did for primary austenite solidified alloys and the minimum occurs at an intermediate cooling rate when the highest volume fraction of second phase austenite solidifies. The range of cooling rates over which alloy 4 solidifies in the FA mode is indicated on this diagram and occurs where the amount of ferrite is shown to increase with cooling rate.

At scan speeds greater than 100 mm/s, the residual ferrite content of Alloy 4 decreases and reaches zero percent at speeds above 500 mm/s. The decrease in ferrite content can not be explained by primary ferrite solidification. Examination of the microstructure showed primary austenite (AF and A) solidified regions in the high speed melts. At 100 mm/s, approximately 20% of the microstructure solidified in the AF mode but at 2000 mm/s, 90% of the microstructure solidified in the A or AF modes. This change in solidification mode explains the decrease in ferrite content after the initial increase in ferrite with increasing cooling rate. The microstructure of Alloy 4 at low and at high scan speeds was discussed in Chapter 5 and is shown in Fig. 5.12.

6.2.3 Alloy 5

Alloy 5 solidifies in a fully ferritic mode or in an FA mode at low cooling rates and follows a similar pattern as Alloy 4 up to 100 mm/s. However, at higher travel speeds, Alloy 5 solidifies only in the fully ferritic mode and the low cooling rate portions of the melt undergoes a transformation to Widmanstätten austenite while the high cooling rate portions of the melt undergo a transformation to massive austenite. Therefore, the amount of ferrite which solidifies from the melt in Alloy 5 is quite different from that in Alloy 4, but, because of the massive transformation of ferrite, the residual ferrite content in Alloy 5 also decreases at high cooling rates.

The measured ferrite content of Alloy 5 is plotted versus scan speed in Fig. 6.9. The solidification mode is primary ferrite, FA, at scan speeds below 100 mm/s. The ferrite content increases with cooling rate just as in the FA solidification mode region of Alloy 4. At scan speeds greater than 100 mm/s, the solidification mode begins to convert to the fully ferritic mode. At 100 mm/s, approximately 30% of the melt solidifies in the F mode and these regions are concentrated close to the melt periphery. At scan speeds of 500 mm/s and higher, 100% of the melt solidifies in the fully ferritic mode. This transition was discussed in Chapter 5 and the microstructures of the melts are shown in Fig. 5.10.

The massive transformation only occurs in alloys which solidify in the fully ferritic mode. If second phase austenite is present, FA mode, the austenite provides heterogeneous nucleation sites which begin to transform before the alloy has reached sufficient undercooling to nucleate the massive austenite grains. Alloy 5 becomes fully ferritic at cooling rates of 10^5 °C or greater but the actual ferrite content of Alloy 5 does not show a sharp drop in ferrite content with travel speed. This occurs because the surface melts do not cool at a uniform rate and allows a percentage of the melt to transform as massive austenite and the remainder of the melt to transform as Widmanstätten austenite. The percentage of the microstructure that transforms into massive austenite grains increases with cooling rate and creates a smooth transition between the FA and F modes. This behavior is responsible for the maximum in the ferrite versus cooling rate curve.

At scan rates greater than 2000 mm/s the ferrite content begins to increase. Examination of the microstructure shows that these melts also solidify in a fully ferritic mode and that this ferrite also undergoes a massive transformation, however, some of the original ferrite is left behind in the microstructure because only a portion of the ferrite transforms to austenite. This behavior will be discussed in more detail in Chapter 8 and is a result of incomplete mixing in the high speed surface melts which leave regions of high Cr/Ni ratio ferrite that are resistant to the massive transformation.

Figure 6.10 schematically shows the behavior of Alloy 5 which solidifies as primary ferrite and then undergoes a massive transformation of ferrite in the fully ferritic solidified regions. The amount of ferrite that solidifies from the melt is the same as that which is schematically indicated in Fig. 6.8 in the FA regions, however,

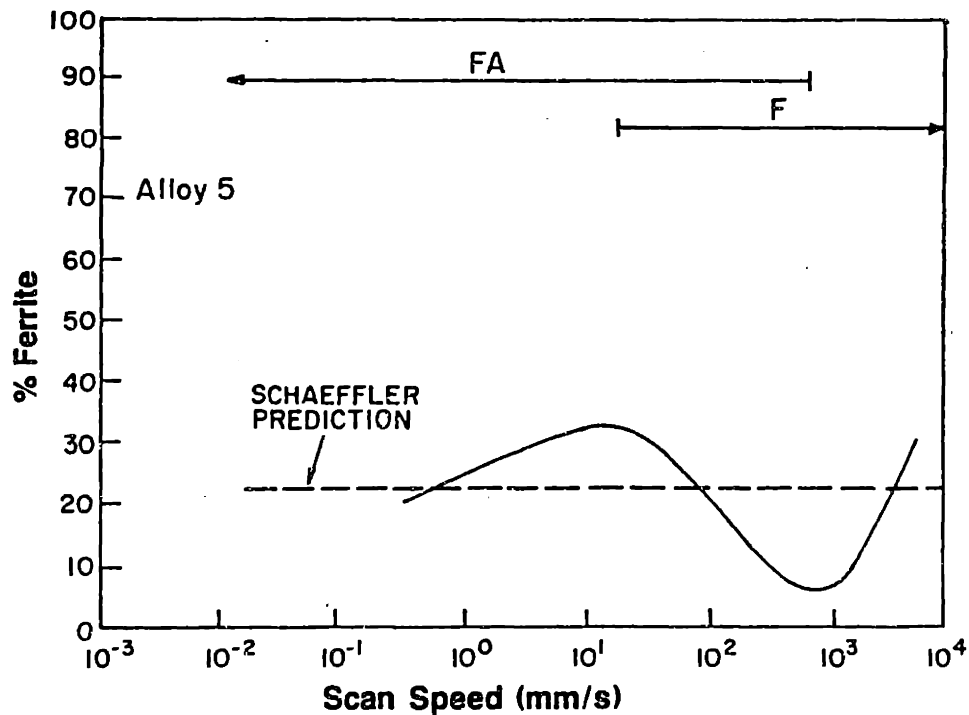


Figure 6.9 The measured ferrite content of Alloy 5 as a function of electron beam speed. Scan speeds where massive and Widmanstatten austenite form in the fully ferritic solidified regions are indicated.

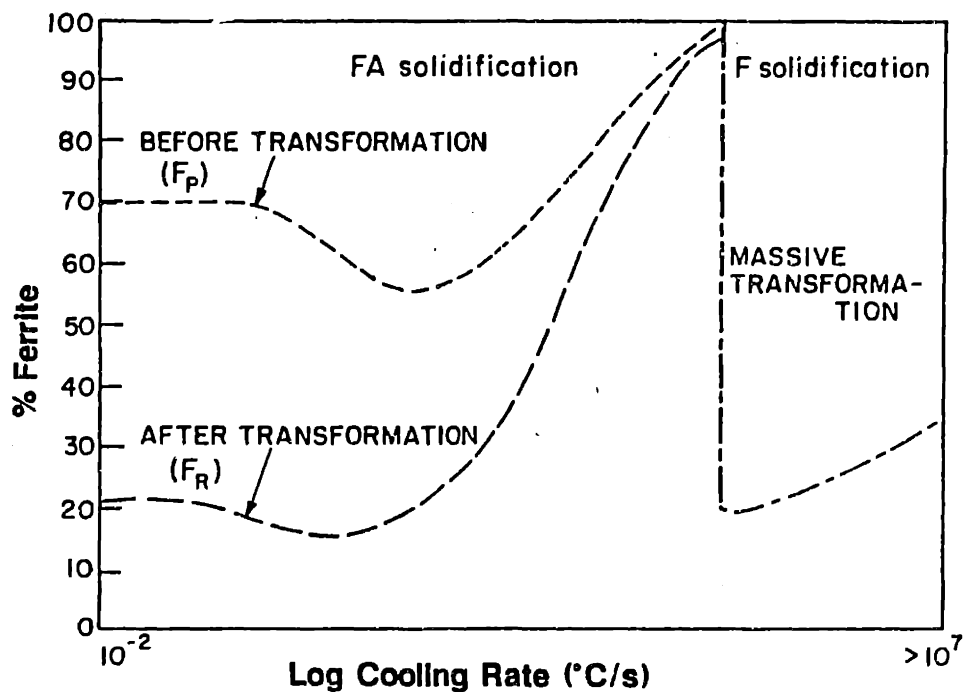


Figure 6.10 The estimated trend of ferrite content in Alloy 5 as a function of scan speed. The amounts of ferrite that solidify and the residual ferrite, after solid state transformation, are indicated.

because of the change in the solid state transformation mechanism at high cooling rates, the residual ferrite content is drastically reduced. The massive transformation occurs without long-range diffusion and requires undercooling below its T_0 temperature, therefore it is only observed at high cooling rates. Alloy 5 is the only alloy to show this behavior because the remaining alloys which solidify in a fully ferritic mode have higher Cr/Ni ratios and have ferrite compositions which are stable enough to prevent the massive transformation.

6.2.4 Fully Ferritic Solidified Alloys 6 and 7

Alloy 7 solidifies in the fully ferritic mode at all of the scan speeds investigated in this study and Alloy 6 solidifies in the fully ferritic mode at scan speeds greater than 25 mm/s. Under these conditions, changes in the ferrite content with cooling rate are directly related to the extent of the ferrite to austenite solid state phase transformation.

The ferrite content versus scan speed relationship is shown for Alloys 6 and 7 in Fig. 6.11. This diagram indicates that the residual ferrite content increases from its arc cast value of about 30% to 100% at a scan speed of 6 mm/s in Alloy 7 and 25 mm/s in Alloy 6. The ferrite contents are compared with the Schaeffler predicted values and show that in the cast condition (0.7 mm/s equivalent scan speed) the ferrite contents are slightly lower than predicted by the Schaeffler diagram. This fact has already been discussed and is caused by the difference in cooling rates between the castings and arc welds. The influence of cooling rate on the microstructure of fully ferritic solidified alloys is the best understood of the cases studied because the amount of ferrite that solidifies from the melt is known to be 100% and the average ferrite composition is the same as the nominal alloy composition.

The schematic solidification and solid-state transformation behavior of these alloys is shown in Fig. 6.12. The 100% ferrite line represents the amount of ferrite that solidifies from the melt and the residual ferrite is related to the amount of time for the solid state transformation to occur. At slow cooling rates, more time is allowed for the transformation and a lower ferrite content results.

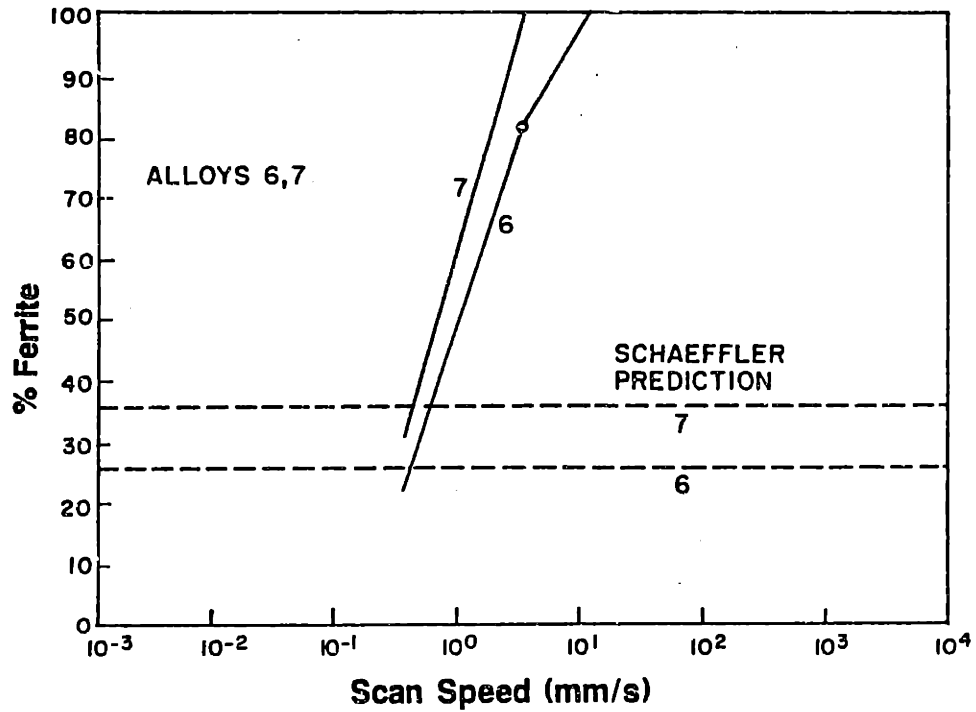


Figure 6.11 The measured ferrite contents of the fully ferritic solidified Alloys 6 and 7 as a function of electron beam scan speed.

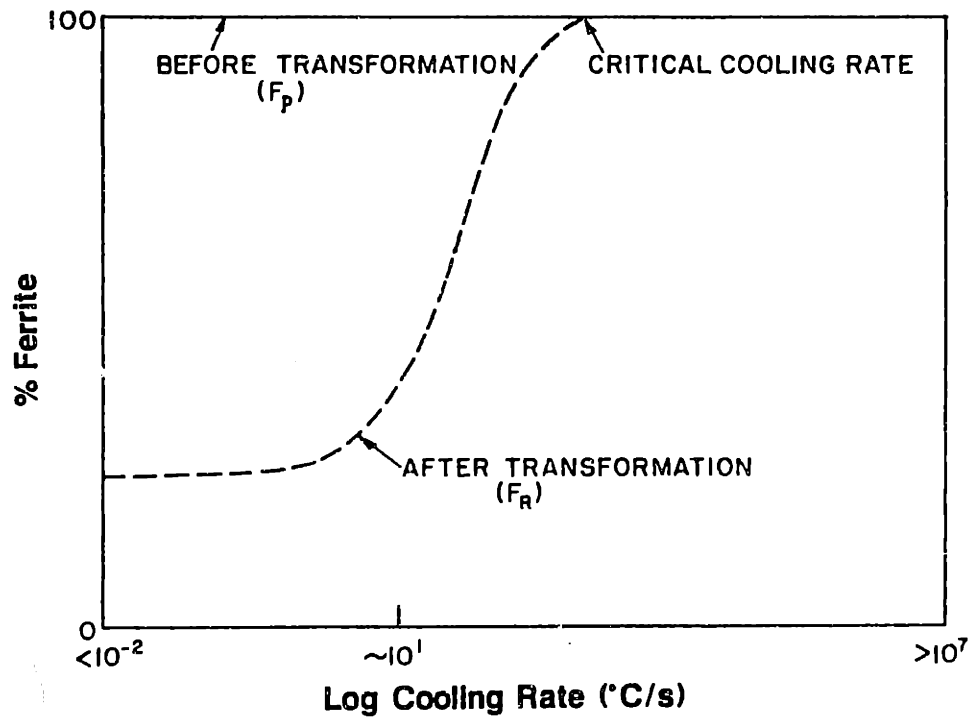


Figure 6.12 The estimated trend of ferrite content in fully ferritic solidified alloys as a function of solidification rate. The amount of ferrite that solidifies and the residual ferrite, after solid state transformation, is indicated.

Therefore, the ferrite content increases with cooling rate to the point where no transformation occurs and the microstructure remains fully ferritic. The critical cooling rate where transformation is suppressed is a function of composition and this critical cooling rate decreases with increasing Cr/Ni ratio of the alloy.

6.3 Summary and Conclusions

For alloys which solidify in the AF mode, the residual ferrite content was shown to decrease with increasing cooling rate. This behavior is easily explained by the decrease in the amount of ferrite that solidifies from the melt as the cooling rate is increased and a quantitative analysis of solidification segregation will be presented in Chapter 7 to describe this behavior. Figure 6.13 shows that the ferrite content of Alloys 1, 2, and 3, which solidify in the AF mode, approaches zero as the scan speed is increased. The measured residual ferrite content of Alloys 1, 2, and 3 is shown in figure 6.14 to confirm this behavior. The scan rate required to produce fully austenitic behavior increases with increasing Cr/Ni ratio of the alloy due to the higher amounts of chromium and nickel 'solute' that are associated with higher Cr/Ni ratio alloys. Alloy 4 solidifies in the AF mode at scan speeds greater than 100 mm/s, therefore, its ferrite content also approaches zero at the high speeds.

Alloy 4, at scan speeds less than about 100 mm/s, and Alloy 5, at scan speeds less than about 10 mm/s, solidify in the FA mode and the amount of ferrite that forms during solidification increases with increasing cooling rate. The approximate amount of ferrite that solidifies from the melt in these alloys is indicated in Figure 6.13. The equilibrium ferrite content is represented at low cooling rates and this figure shows that a smaller amount of second phase ferrite forms at intermediate cooling rates. However, this trend is reversed at higher cooling rates which leads to a minimum in the ferrite cooling-rate curve. Neither Alloy 4 nor Alloy 5 solidify in the FA modes at high cooling rates and their solidification behavior becomes fully austenitic or fully ferritic respectively.

The effect of cooling rate on the solid state transformation behavior in the FA solidified alloys is such that less of the ferrite transforms as the cooling rate increases. This fact is discussed in Chapter 8 by considering both the reduction in

dendrite arm spacing and the reduction in characteristic diffusion distance as the cooling rate is increased. Therefore, the residual ferrite of FA solidified alloys, shown in Figure 6.14, is reduced more at low cooling rates and this tends to remove the minimum in the residual ferrite versus cooling rate behavior of these alloys.

Although Alloy 4 and Alloy 5 solidify with different primary modes of solidification at high cooling rates, their ferrite versus cooling rate behavior is similar. This apparent anomaly was related to the formation of massive austenite in Alloy 5 at high cooling rates which rapidly transforms the ferrite to austenite because of its high interface velocity. These aspects will be discussed in more detail in Chapter 8 and since the massive transformation leaves some residual ferrite in the microstructure, Alloy 5 does not approach zero ferrite at high cooling rates.

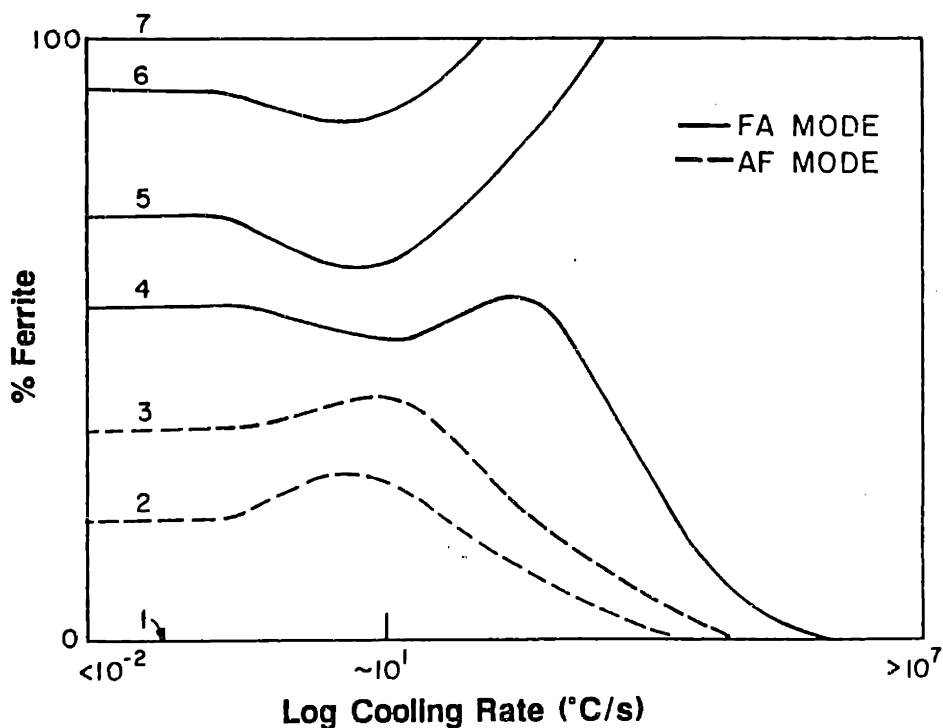


Figure 6.13 Summary of the estimated trends of the amount of ferrite that solidifies for each of the seven alloys, as a function of cooling rate.

Alloys 6 and 7 solidify in the fully ferritic mode for all of the conditions studied. During cooling, the ferrite transforms by the nucleation and growth of Widmanstatten platelets. Therefore, the residual ferrite content of these alloys increases with increasing cooling rate due to the reduced amount of time for growth of austenite. A critical cooling rate was observed, where no transformation occurs in these alloys. This cooling rate is higher for the lower Cr/Ni ratio alloys due to the reduced thermodynamic stability of ferrite of the lower Cr/Ni compositions.

Based on the measured ferrite contents of the electron beam melts and the metallographic observations of the microstructure, the following conclusions can be made relating the effects of cooling rate to the ferrite content of stainless steel alloys.

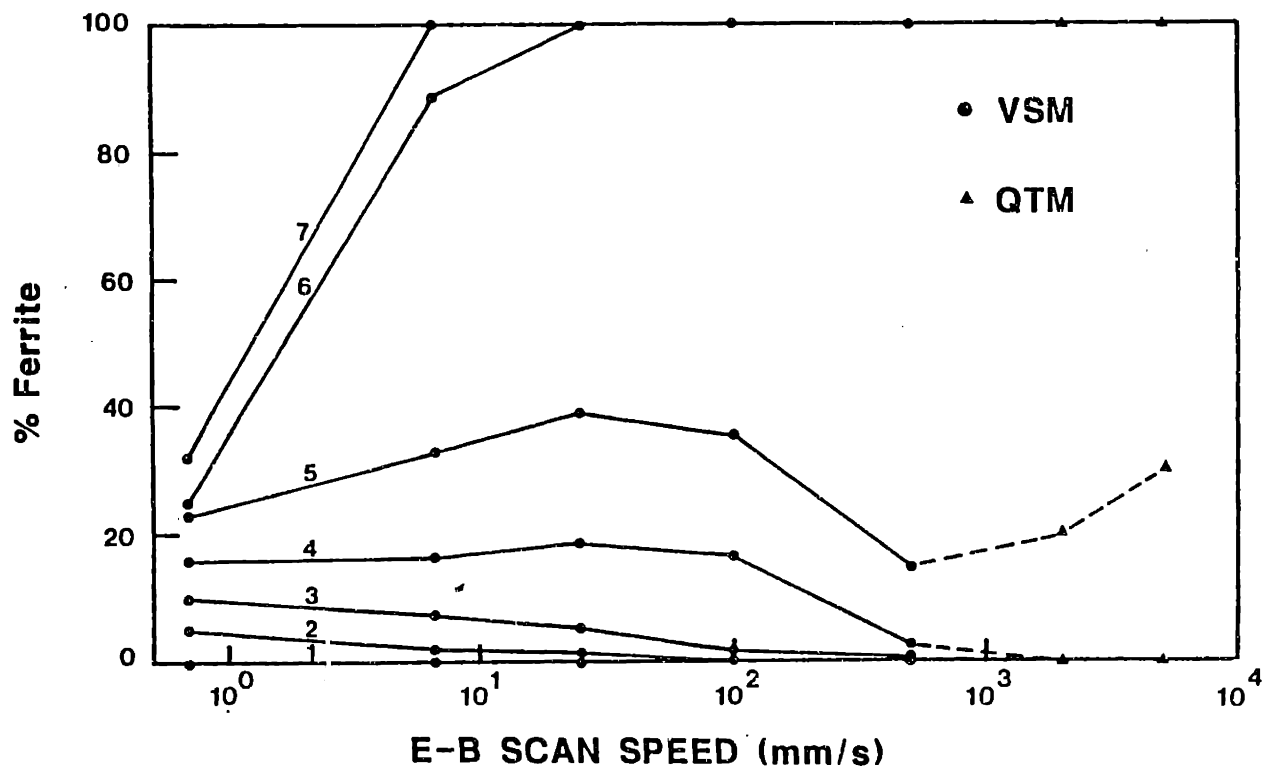


Figure 6.14 Summary of the measured residual ferrite contents in the seven alloys as a function of electron beam scan speed.

Conclusions

1. The composition and the primary mode of solidification determine how the cooling rate will influence the amount of ferrite that solidifies from the melt.
2. At high cooling rates the alloys solidify in either the fully ferritic or fully austenitic modes with no second phase in the microstructure.
3. At low cooling rates, the residual ferrite content increases for F and FA solidified alloys but decreases for AF solidified alloys. This behavior can be explained by the combined effects of the decreasing amount of solute segregation and the decreasing amount of ferrite transformation with increasing cooling rate.
4. Based on conclusions 2 and 3, one would expect the ferrite content in the alloys to either increase towards the fully ferritic condition or decrease towards the fully austenitic condition as the cooling rate increases. However, the residual ferrite content of Alloys 4 and 5 goes through a maximum at intermediate cooling rates. This behavior was explained by 1) the change in solidification mode of Alloy 4 from FA to AF with increasing cooling rate and 2) the formation of massive austenite in Alloy 5 at high cooling rates.

CHAPTER 7

The Influence Of Cooling Rate On Solute Redistribution And Second Phase Formation

The preceding chapters investigated the effects that cooling rate and composition have on the ferrite content and morphology of resolidified stainless steel alloys. For the most part, the results were empirical and were based on the observations of the electron beam surface melts. This chapter takes a more fundamental approach, by studying the effect of cooling rate on the factors which are responsible for solidification segregation.

Microsegregation can be modeled sufficiently well to predict the influence of cooling rate on solute redistribution in binary alloy systems [7.1]. The factors which influence microsegregation include the physical properties of the alloy, the solidification parameters and the kinetic response of the system, all of which are known or can be estimated in many binary alloy systems. In ternary alloy systems, such as the Fe-Ni-Cr, the redistribution of solute during solidification is much more difficult to model and to verify because of the lack of information about the behavior of ternary alloys.

The difficulties associated with predicting microsegregation in ternary alloy systems are related to the lack of information about the solidification parameters. For example, the ternary component gives the system an additional degree of freedom which leaves the solidification path unspecified, therefore, it must be determined experimentally or estimated by solidification modeling. Methods to predict the solidification paths in the Fe-Ni-Cr system will be presented in the first section of this chapter and once the solidification path has been established, the remaining parameters which influence solidification can be determined from the equilibrium phase diagram.

Predicting the amount of microsegregation involves other difficulties as well. Interface instabilities leading to cellular or dendrite growth need to be taken into account and the solute redistribution models are based on assumptions which have to

be carefully justified. These factors were studied in the Fe-Ni-Cr ternary system and the results were used to calculate solute redistribution as a function of interface velocity for the electron-beam surface-melted alloys. The solute redistribution calculations incorporate undercooling at the dendrite tip using a constrained dendritic growth model and the results were used to predict the amount of primary and second phase ferrite that solidifies in each alloy as a function of electron beam scan speed.

The solidification segregation model predicts the amount of ferrite that forms during solidification but does not incorporate the effects of the solid state transformation that occurs in the low cooling rate melts. Therefore, the calculated ferrite contents represent an upper bound for the residual ferrite content and this upper bound provides a useful starting point for understanding microstructures which develop in resolidified stainless steel alloys. In addition, the dendrite tip calculations can be used to predict the solidification conditions that lead to the undercooling necessary for the growth of metastable phases by comparing the undercooling at the dendrite tip with the thermodynamically calculated equilibrium and metastable phase diagrams.

7.1 Solidification Paths and Parameters in the Fe-Ni-Cr System

During the solidification of binary alloys, the composition of the solid and liquid phases are given by the solidus and liquidus lines respectively. Therefore, the solidification path and tie lines are known by virtue of the fact that the Gibbs phase rule allows zero degrees of freedom for two phases in equilibrium at constant temperature and pressure.

If a third component is added to the system, two phases will be in equilibrium at constant temperature and pressure but one degree of freedom still exists. This compositional degree of freedom extends the liquidus and solidus lines into surfaces. The tie lines which join the liquidus and solidus surfaces are not fixed in any given temperature-composition plane and are not known *a priori*. Therefore, without knowledge of the tie line locations, the path that the solid and liquid compositions follow during solidification is also not known.

Fortunately, thermodynamic calculation of phase equilibria in ternary alloy systems has been refined to the point where tie lines can be predicted in many systems. These types of calculations will be briefly summarized in this section and results will be presented which show the location of tie lines and solidification paths for the alloys studied in this investigation. From these solidification paths, pseudobinary diagrams will be determined to represent the solidification behavior of each alloy and the solidification parameters can be determined from these diagrams.

7.1.1 Solidification Paths

Isothermal sections were calculated in the Fe-Ni-Cr system using the Thermocalc software package. Details of the computations and plots of the isothermal sections are summarized in Appendix C. The results of the calculations give information regarding phase equilibria, including tie lines in all of the two-phase regions, for temperatures ranging from 1023K to the melting point of chromium.

From a solidification standpoint, the most important isothermal sections are those which are close to the liquidus temperature. Figure 7.1 shows the 1412^oC isotherm and illustrates the tie line locations for primary austenite and primary ferrite solidification. The Fe-Ni-Cr system has a small temperature difference between the liquidus and solidus and the orientation of the tie lines does not change significantly from the beginning to the end of solidification. Therefore, these tie lines can be used to approximate the solidification path because segregation will be in the general tie line "direction" until the remaining liquid reaches the line of two-fold saturation. At this temperature, the liquid composition follows the line of two-fold saturation while three phases (liquid, austenite and ferrite) coexist until solidification is completed at the minimum in the line of two-fold saturation (49%Cr, 43%Ni, 8%Fe). The solidification paths for alloy 1 (primary austenite) and alloy 7 (primary ferrite) are shown in Fig. 7.2, based on the extrapolated tie lines, the initial composition of the alloys and the line of two-fold saturation [1.32].

The solidification path can be determined more accurately by accounting for tie line movement with temperature. This requires a solidification model which incorporates thermodynamically calculated tie lines and adjusts the interfacial

compositions as a function of solidification temperature. One such model was developed by Kundrat [7.2, 7.3] and utilizes the Scheil approximation to represent solute redistribution. Kundrat's model was used to calculate solidification paths for alloys 1 and 7 in the Fe-Ni-Cr ternary system [7.4] and these paths are shown in Fig. 7.3. Also plotted in this figure are the tie lines predicted by Thermocalc to show that the two methods of predicting the solidification paths give similar results. The closeness of these estimations is related to the narrow separation between liquidus and solidus temperatures and the fact that the tie-lines generated by Kundrat's model are nearly identical to those generated by Thermocalc.

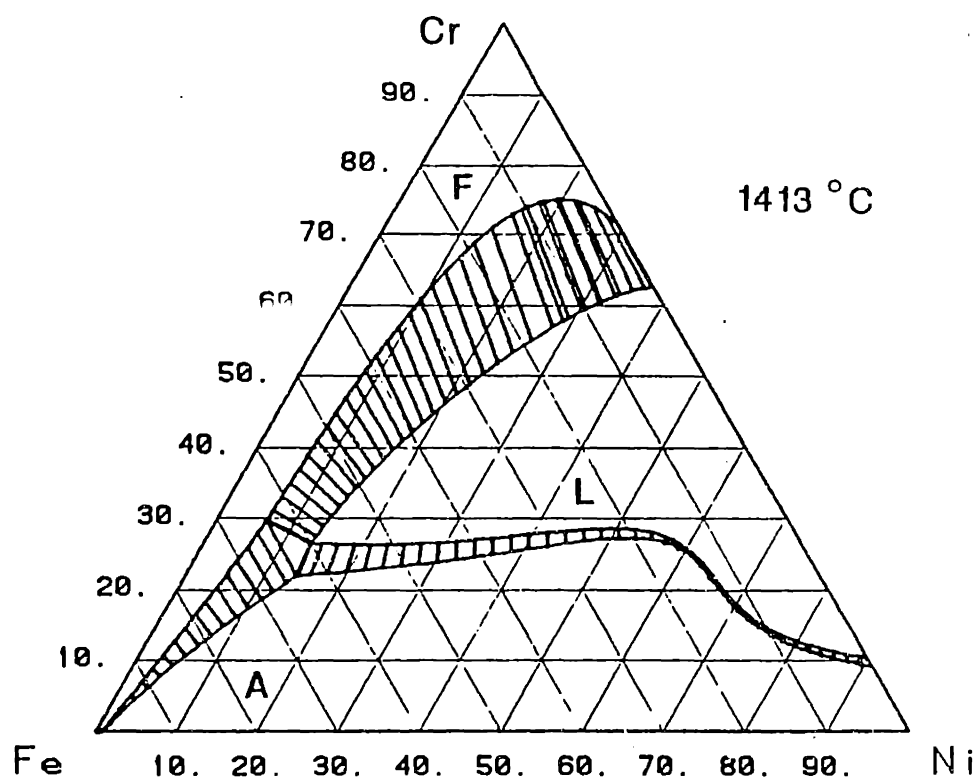


Figure 7.1 Thermodynamically calculated isothermal section through the Fe-Ni-Cr ternary system at 1413°C showing the orientation of tie-lines in the two-phase regions at temperatures close to the solidification range of the seven alloys.

Figure 7.2 shows that the solidification paths do not curve significantly from the initial solidification composition to the composition where the liquid reaches the line of two-fold saturation. Therefore, the solidification paths can be approximated by straight lines which is fortunate because it allows the ternary alloys to be treated in a manner similar to that of binary alloys. The pseudobinary diagram, which represents the solidification behavior along these paths, can be determined by plotting the temperature-composition vertical plane containing these paths.

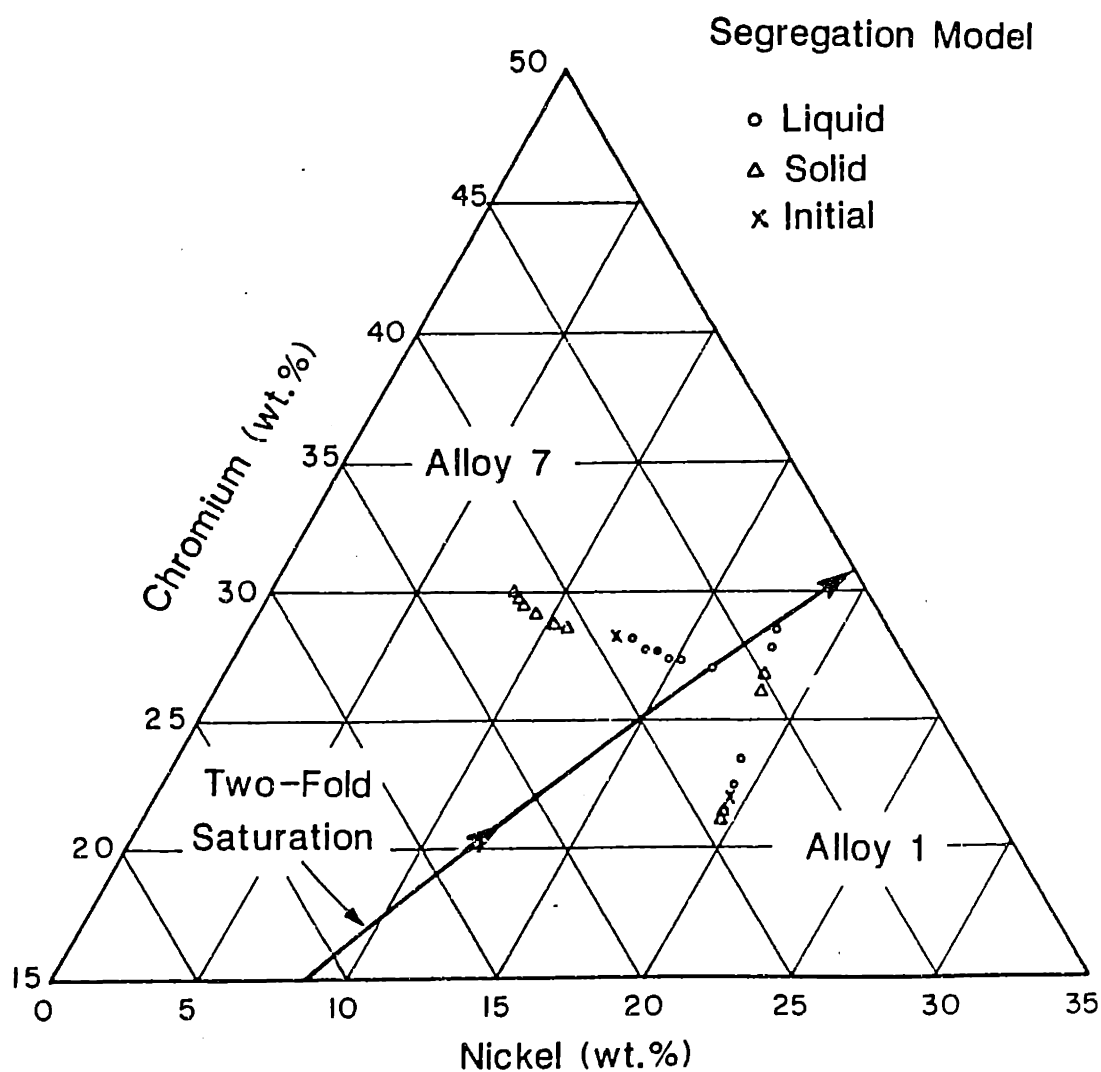


Figure 7.2 Solidification paths for Alloys 1 and 7 estimated from the linear extrapolation of the tie lines shown in Figure 7.1.

7.1.2 Pseudobinary Diagrams to Represent Solidification Behavior

Pseudobinary diagrams were determined for primary austenite and primary ferrite solidification behavior using the thermodynamically calculated isothermal phase diagrams and the solidification paths presented in Fig. 7.3. These diagrams are shown in Figures 7.4 and 7.5 and represent the solidification behavior for primary ferrite and primary austenite solidified alloys that contain 59 wt.% Fe. Constant Fe vertical sections have been used in the past to estimate the solidification behavior of stainless steel alloys by many investigators. However, these diagrams do not accurately

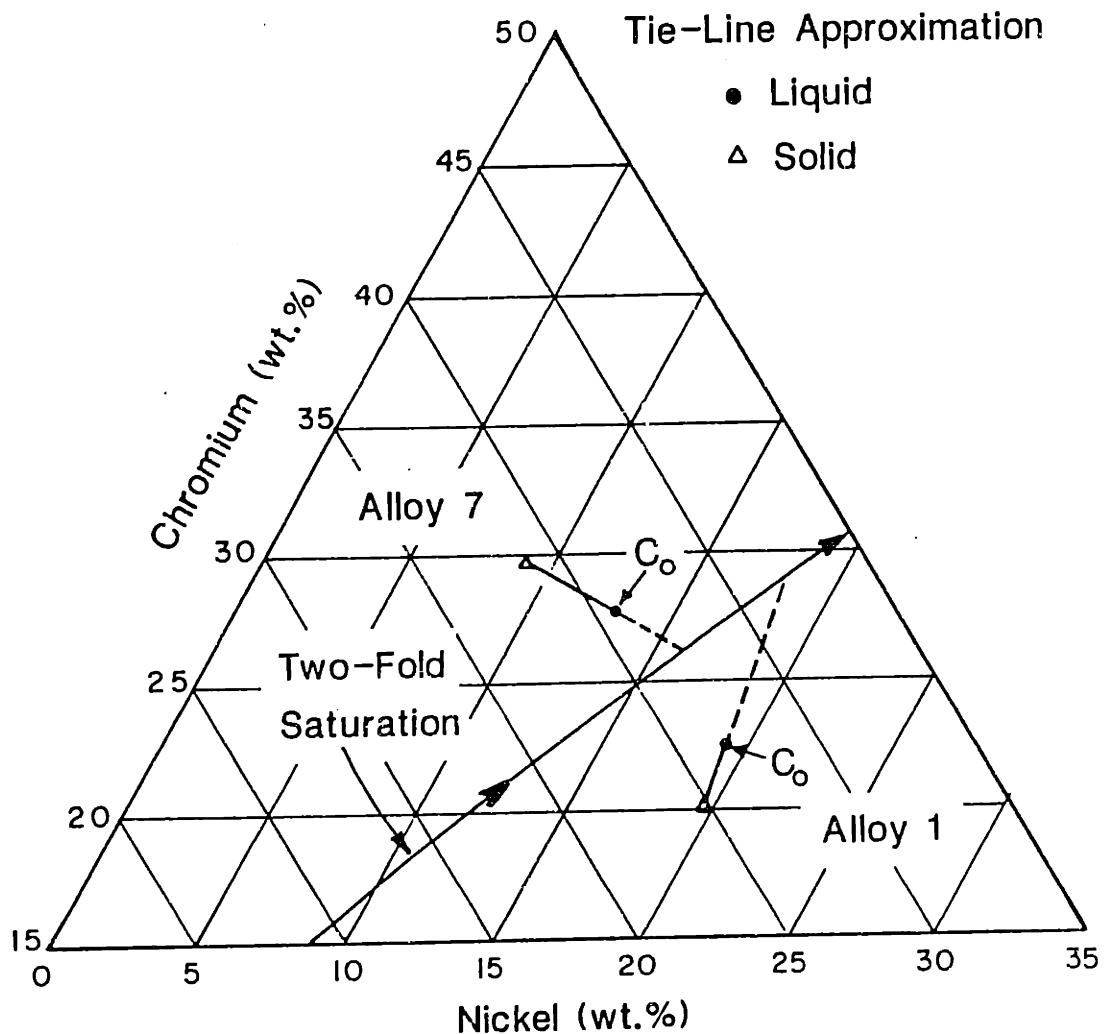


Figure 7.3 Solidification paths for Alloys 1 and 7 calculated by solidification segregation modeling.

represent the solidification segregation since the tie lines in the L+S phase fields do not lie in the constant Fe plane. By choosing the vertical sections presented in Figures 7.4 and 7.5 to lie along the solidification path, the tie-lines also lie in these planes. Therefore, the diagrams presented in Figures 7.4 and 7.5 accurately represent the solidification behavior of primary ferrite and primary austenite solidification conditions. These new diagrams are significant improvements over the constant Fe vertical sections used in the past.

Partition ratios, k , and the slope of the liquidus surface, m_L , can be determined for Cr and for Ni partitioning from the pseudobinary diagrams using the following equations [7.5]:

$$k_{ij} = \frac{C_{ij}}{C_{iL}} \quad (7.1)$$

$$m_{iL} = \frac{\partial T_L}{\partial C_{iL}} \quad (7.2)$$

where L refers to liquid, the subscript i denotes Cr or Ni and the subscript j denotes the austenite or ferrite phases. The other nomenclature which are used in this chapter are summarized in Table 7.6. Figure 7.4 can be used to calculate k and m_L for Alloy 1 (primary austenite) where the subscript j denotes the austenite phase while Figure 7.5 can be used to calculate k and m_L for alloy 7 (primary ferrite) where the subscript j now denotes the ferrite phase.

Since the liquidus and solidus lines along the solidification paths are nearly linear with composition, k and m_L can be treated as constant throughout the solidification process and their numerical values are summarized in Table 7.1. Since the initial compositions of the primary austenite solidified alloys (1,2,3) are similar it can be assumed that k and m_L will not be significantly different for alloys 1, 2 and 3. Likewise, the compositions of the primary ferrite solidified alloys (4,5,6,7) are similar and should have similar solidification segregation behavior. Therefore, the values of k and m_L calculated for alloy 1 can be used to represent the behavior of alloys 2 and 3 while k and m_L calculated for alloy 7 can be used to represent the behavior of alloys 4, 5 and 6.

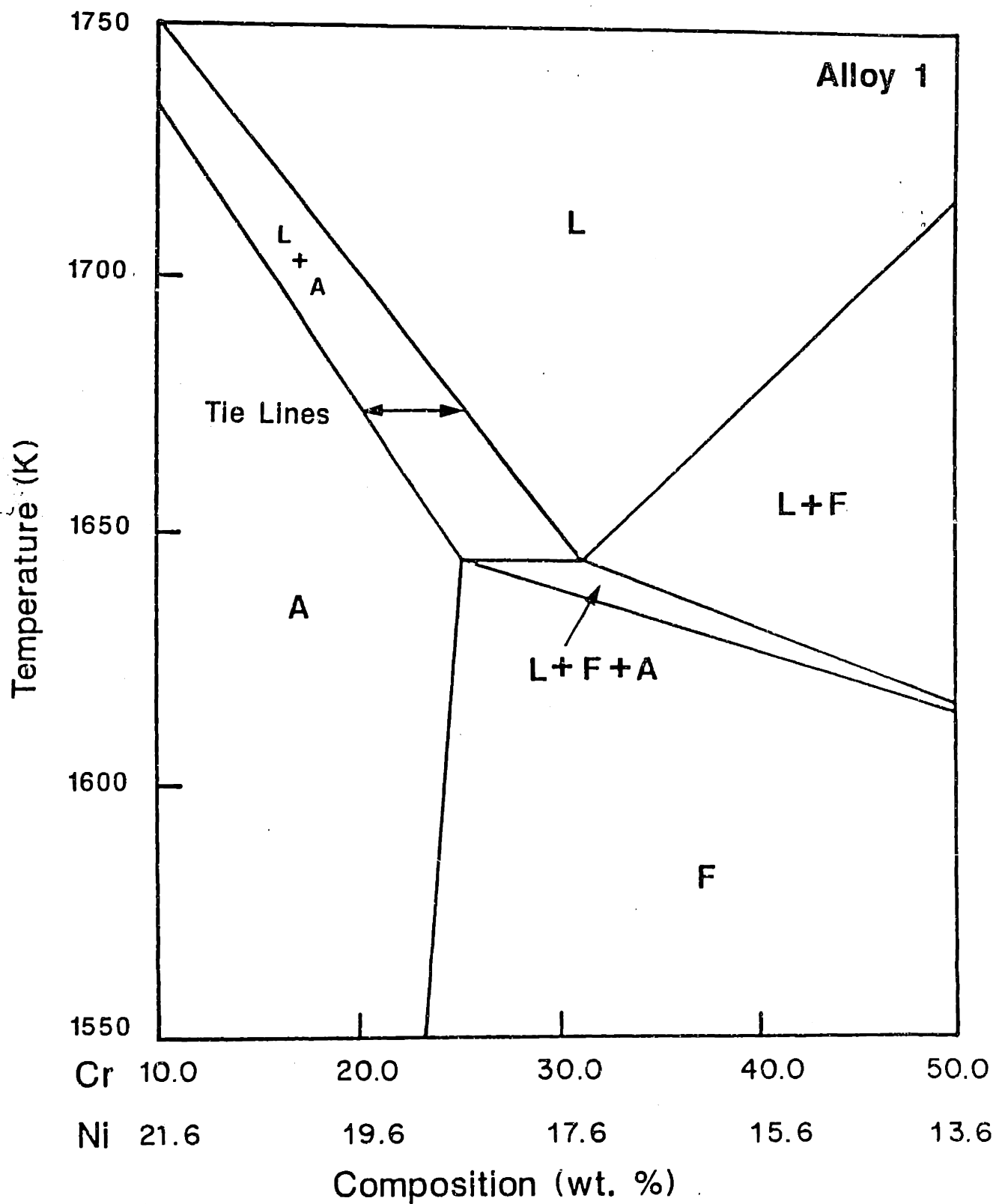


Figure 7.4 Pseudobinary diagram along the solidification path of Alloy 1, based on thermodynamic calculations. The solidification behavior of primary austenite solidified alloys is represented for chromium contents up to 31.5 wt%.

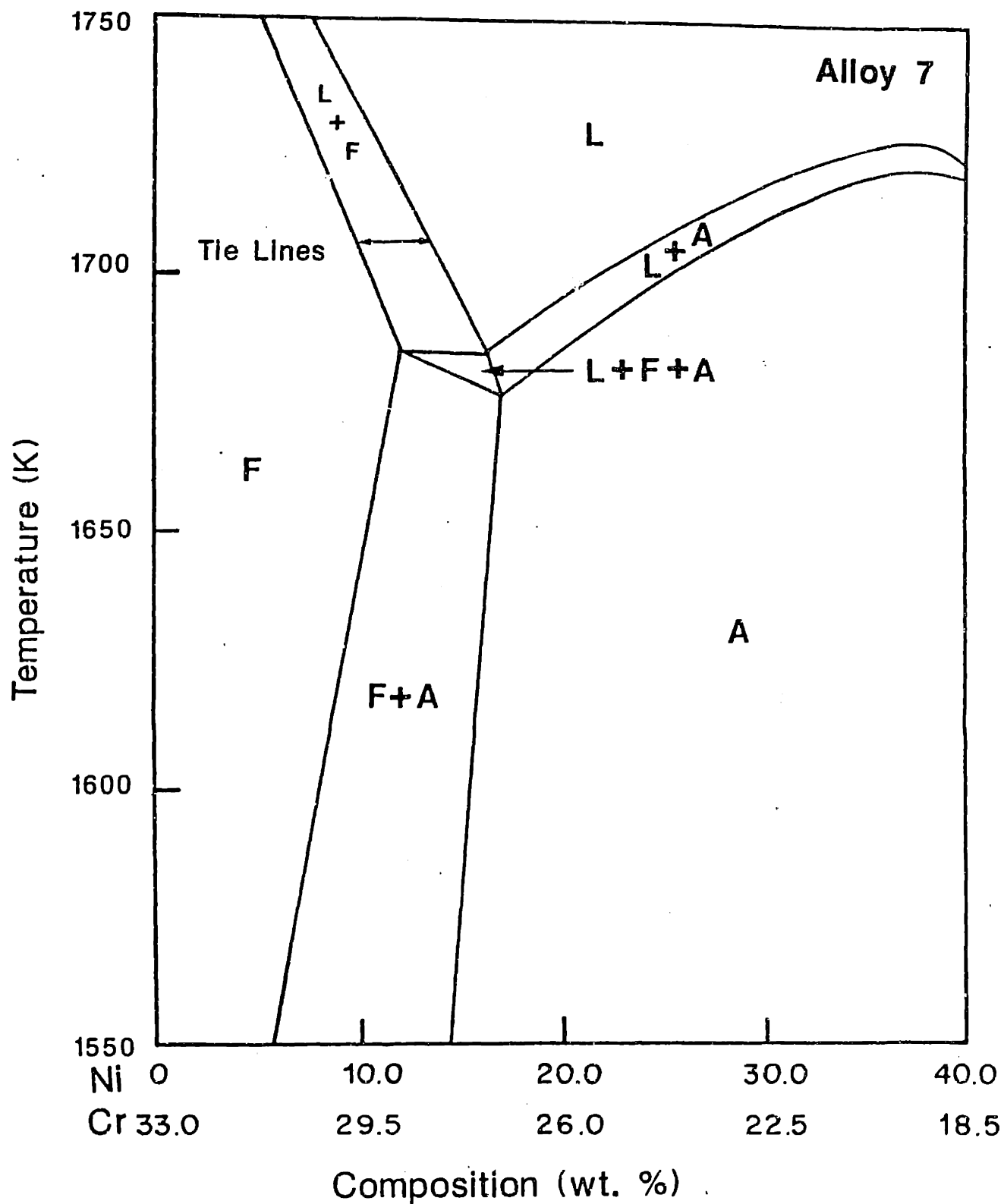


Figure 7.5 Pseudobinary diagram along the solidification path of Alloy 7, based on Thermodynamic calculations. The solidification behavior of primary ferrite solidified alloys is represented for Ni contents up to 16.3 wt.%.

Table 7.1: Partition coefficients and the slope of the liquidus lines for primary ferrite and primary austenite solidified alloys.

Primary Phase	Quantity	Value
Ferrite	$m_{L,Cr}^F$	13.1°C/%Cr
	$m_{L,Ni}^F$	-7.4°C/%Ni
	k_{Cr}^F	1.10
	k_{Ni}^F	0.74
Austenite	$m_{L,Cr}^A$	-5.6°C/%Cr
	$m_{L,Ni}^A$	12.4°C/%Cr
	k_{Cr}^A	0.80
	k_{Ni}^A	1.05

Another essential solidification parameter is the composition that corresponds to the line of two-fold saturation of the liquid with respect to ferrite and austenite, C_E . When the liquid composition reaches this point then a second solid phase begins to cosolidify with the primary phase. Since C_E is the intersection of the solidification path and the line of two-fold saturation, each alloy has a different C_E composition. Assuming the solidification path 'direction' for alloys 2 and 3 are parallel to alloy 1 and that the solidification path direction for alloys 4, 5 and 6 are parallel to alloy 7, C_E can be determined for each alloy. Figure 7.6 shows the solidification paths for the seven alloys and their intersection with the line of two-fold saturation. Compositions of C_E for each of the seven alloys are listed in Table 7.2.

In summary, the 'linear' solidification paths which were determined in section 7.1.1 allowed pseudobinary diagrams to be determined for primary austenite and primary ferrite solidification. These diagrams were used to predict values of k and m_L for Cr and Ni partitioning for primary austenite and primary ferrite solidification behavior. The composition of the liquid where the second phase first begins to develop during solidification was also determined for each alloy by the intersection of the solidification path with the line of two-fold saturation. These solidification parameters will be used in following sections to quantify solute redistribution during solidification.

Table 7.2: Nominal, eutectic and maximum solid compositions (wt.%).

Alloy	Primary Phase	C_o		C_E		$C_{S,M}$	
		Cr	Ni	Cr	Ni	Cr	Ni
1	Austenite	22.0	19.0	31.0	18.0	25.0	18.5
2		23.7	17.3	28.0	17.0	24.0	17.1
3		24.6	16.4	26.2	16.1	22.0	16.6
4	Ferrite	25.4	15.6	25.5	15.9	26.8	11.8
5		26.6	14.4	26.0	16.0	27.5	12.0
6		27.4	13.6	26.5	16.1	28.0	12.1
7		27.8	12.8	27.0	16.3	28.5	12.2

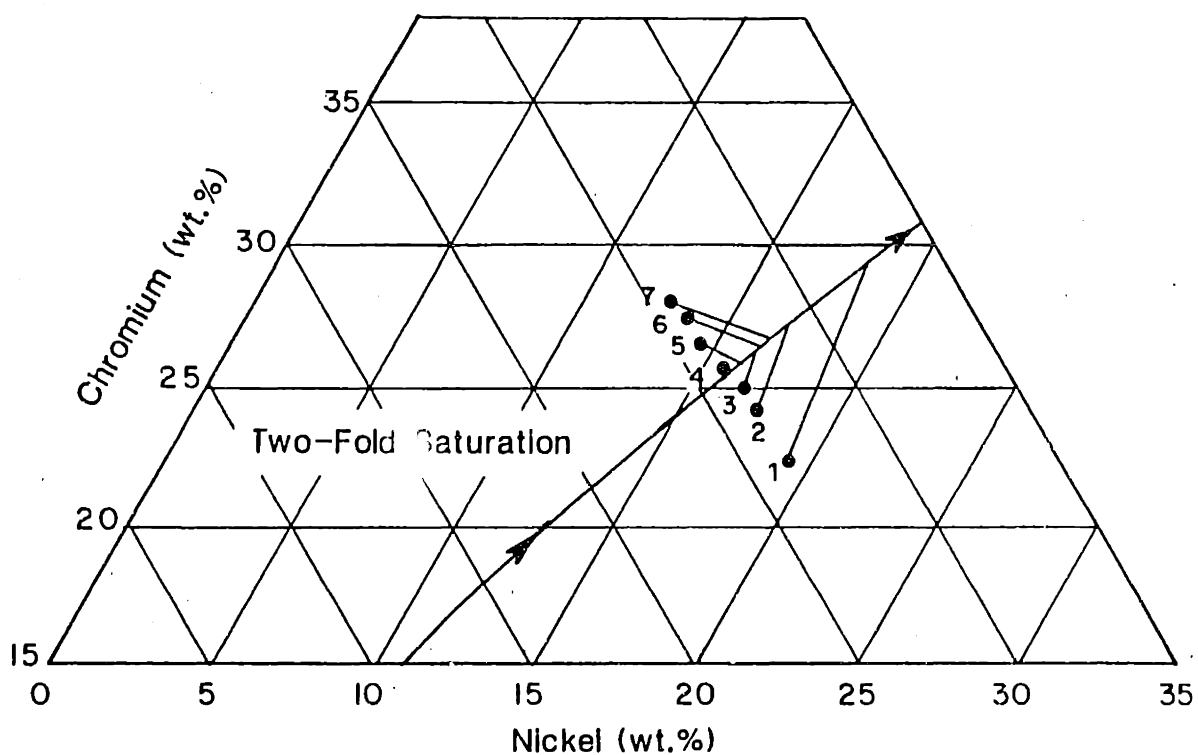


Figure 7.6 The estimated solidification paths and the intersection of these paths with the line of two-fold saturation, for the seven Fe-Ni-Cr alloys.

7.2 Interface Stability

During plane front solidification, the liquid/solid interface is assumed to be a smooth plane traveling in a direction normal to its surface. A solute-rich boundary layer builds up ahead of the interface and this configuration is stable at low growth rates, R , and high temperature gradients, G . However, typical castings, welds and surface melts solidify by a cellular or dendritic mode rather than by a plane front. Constitutional supercooling, caused by the solute-rich boundary layer, is responsible for instabilities in the plane-front that lead to cellular dendritic growth. Since this theory is well developed it will only be briefly discussed here.

The conditions necessary to cause instabilities in the plane front are related to G , R and the alloy properties k , C_o , m_L , and D by the following equation [7.5]:

$$G_L/R \geq \frac{-m_L C_o (1-k)}{k D_L} \quad (7.3)$$

Where D refers to the diffusivity and the subscript L refers to the liquid. If the above inequality is satisfied, solidification will take place via a plane-front. If the inequality is not satisfied, the interface is unstable but equation 7.3 only indicates that instability is present and does not relate any further information about the details of the L/S interface.

In 1963, Mullins and Sekerka [7.6] provided a rigorous solution to the dynamics of the L/S interface in a constitutionally supercooled liquid. They analyzed the conditions under which a small sinusoidal perturbation will grow or shrink by taking into account solute and thermal fields, L/S surface energy (σ), and kinetics of the interface. Their results incorporate the solidification parameters and alloy properties and refine the stability criteria presented in equation 7.3.

Mullins and Sekerka predict a transition from plane front to the cellular mode as the growth rate is increased. They also predict a reverse transition from cellular to plane front at high (>1.0 m/s) growth rates. This reversion to plane front solidification is termed absolute stability and is caused by the reduction in dendrite arm spacing at high rates. The small dendrite arm spacing, and associated small dendrite tip radius, give the interface a high surface area. This factor increases the surface energy of the interface which opposes the driving force produced by

constitutional supercooling. Therefore, a lower limit is placed on the dendrite arm (cell) spacing when these two effects are equal and below this limit, the interface becomes planar.

The above mentioned stability criteria have been introduced to illustrate the three interrelated solidification parameters which are important to the stability of the interface: the growth rate R , the temperature gradient G , and the dendrite tip radius r_t . The extent to which these factors are known depends on the solidification process. For example, during the surface resolidification experiments performed in this study, R can be estimated from the imposed scan velocity of the electron beam, however, G and r_t must be calculated from first principles.

In the following section, methods for estimating R and for calculating G will be applied to the different solidification conditions used in this study. From these data, r_t will be calculated and used to predict undercooling at the dendrite tip.

7.2.1 Growth Rate and Temperature Gradient

The growth rate is defined as the local rate of advance of the liquid/solid interface. For surface resolidified melts, the quasi-steady-state heat flow assumptions were discussed in Chapter 4. These assumptions allow the L/S interface shape to be treated as constant, therefore, the growth rate can be estimated from the travel speed, S , and the weld pool shape.

For a given quasistationary surface melt, growth rates vary from zero to a maximum value which can not exceed the travel speed of the source. Variations in growth rates around the melt pool surface were shown in Chapter 4 to be related to changes in the solidification direction with respect to the direction of the heat source. Although the growth rate varies from 0 to a maximum of S , the majority of the L/S interface moves at some intermediate growth rate. This "average" growth rate of a given weld can be approximated from the geometry of the molten zone and can be determined by metallographic examination of the resolidified zone.

At slow travel speeds, the width of the fusion zone is smaller than its depth and the growth direction is predominantly across the width of the weld. For these conditions, the surface topography of the resolidified melt can be used to estimate the

growth rate. The 2α angle which represents the trailing edge of the melt pool and is observed on the surface of resolidified melts is illustrated in Fig. 7.7. The angle of interest, θ , lies between R and S and can be calculated from 2α , or from the length, L, and the width, W, by the following geometric equation:

$$\theta = \left(90^\circ - \sin^{-1} \left(\frac{w/2}{L} \right) \right) \quad (7.4)$$

The solidification front velocity, R, can be calculated from θ by the following equation:

$$\bar{R} = S \cos \theta \quad (7.5)$$

where R represents the average solidification rate of the melt.

At high travel speeds, the depth becomes smaller than the width and the growth direction is predominantly from the bottom to the surface of the weld. For these conditions, θ should be estimated from the length and depth of the surface melt:

$$\theta = \left(90^\circ - \sin^{-1} \left(\frac{D}{L} \right) \right) \quad (7.6)$$

where D represents the depth of the melt. The average solidification front velocity can then be calculated for these conditions using eqn. 7.5.

The average length, width and depth of the surface melts performed in this investigation are shown in Table 7.3. From these data, α , θ and $\cos \theta$ were calculated and are also summarized in Table 7.3. Equation 7.4 was used to calculate θ for the low speed melts 1, 2 and 3 while equation 7.6 was used to calculate θ for the high speed melts 4, 5 and 6. The average growth rate for each travel speed was calculated from S and $\cos \theta$ using equation 7.5.

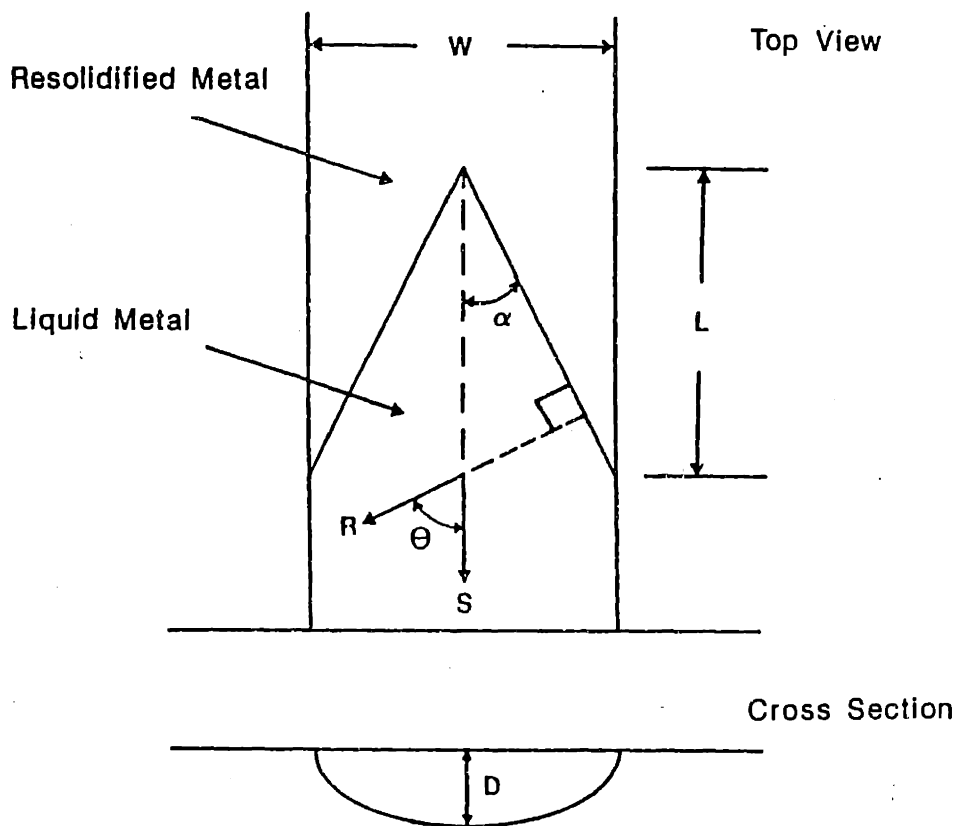


Figure 7.7 Schematic representation of a surface melt showing the relationship between the travel speed, S , melt geometry and the interfacial velocity, R .

Table 7.3 Weld pool dimensions and average interface velocity for each of the six electron beam surface melting conditions.

Melt	S (mm/s)	$W/2$ (mm)	L (mm)	D (mm)	θ (deg)	$\cos \theta$	\bar{R} (mm/s)
1	6.3	2.5	5.4	5.3	31	0.86	5.4
2	25	1.5	5.8	3.1	76	0.26	6.5
3	100	0.8	5.1	1.1	81	0.16	16
4	500	0.63	2.0	0.20	84.3	0.10	50
5	2,000	0.60	0.80	0.040	89.62	0.08	100
6	5,000	0.50	0.55	0.008	89.92	0.02	175

The average calculated growth rates were shown to vary from 5.4 to 175 mm/s for variations in travel speed from 6.3 to 5000 mm/s respectively. The 5000 mm/s melt was too shallow to metallographically examine for its melt pool length. Therefore, its length was initially assumed to be equal to the radius of the electron beam spot. Table 2.4 gives this radius as 0.55 mm and using this value, an average interface velocity of 100 mm/s was calculated. However, this value of R is questionable since there was no apparent increase in velocity as the travel speed was increased from 2000 to 5000 mm/s. Therefore, the average interface velocity for the 5000 mm/s speed melt was estimated by extrapolating the S versus R behavior of the first 5 melts. This gave the average interface velocity of 175 mm/s which is reported in Table 7.3.

It is apparent that at the high travel speeds, the shallow nature of the surface melt reduces the growth rate substantially. This fact has sometimes been ignored by other investigators who have used either the travel speed or the velocity estimated from the melt width to incorrectly represent the interface velocity of high-speed directed-energy resolidified melts. The maximum interface velocity observed in the high speed electron beam melts in this study was only 175 mm/s which is not high enough to produce the conditions necessary for partitionless solidification.

Equation 4.4 was used to determine the average temperature gradient surrounding the electron beam melts produced in this investigation. As discussed in Chapter 4, this equation relates R , G and the cooling rate, ϵ . Assuming the temperature gradient is in the direction of heat flow, G is normal to the L/S interface and R can be assumed to be in this same direction. Therefore, the average cooling rates which were estimated by the dendrite arm spacing measurements in Chapter 4 and R which was calculated above from the melt pool geometry were used to determine the average temperature gradient on the L/S interface:

$$\bar{G} = \frac{\epsilon}{R} \quad (7.7)$$

Using this relationship, \bar{G} was calculated for each surface melt and these values are summarized in Table 7.4.

Table 7.4 Average temperature gradients during solidification of the 6 electron beam melts.

Melt	ϵ (°C/s)	\bar{R} (mm/s)	\bar{G} (°C/s)	k_s/k'_L	\bar{G}_L	\bar{G}_s
1	4.7×10^2	5.4	8.7×10^1	0.4	6.1×10^1	1.5×10^2
2	1.9×10^3	6.0	3.3×10^2	0.5	2.5×10^2	4.9×10^2
3	1.7×10^4	16	1.3×10^3	0.5	9.8×10^2	2.0×10^3
4	4.4×10^5	50	8.0×10^3	1	8.0×10^3	8.0×10^3
5	1.5×10^6	100	2.0×10^4	2	3.0×10^4	1.5×10^4
6	7.5×10^6	175	4.6×10^4	2	6.9×10^5	3.5×10^4

The average temperature gradient varies from 8.7×10^1 to 4.6×10^4 °C/mm as the travel speed is increased from 6.3 to 5000 mm/s. These values are plotted in Fig. 7.8. \bar{G} can also be defined as the conductivity-weighted thermal gradient [7.7]:

$$\bar{G} = \frac{k_s G_s + k'_L G_L}{k_s k'_L} \quad (7.8)$$

and using the relationship between G_s and G_L ($G_s = (k_L/k_s)G_L$), the average temperature gradient in the solid, \bar{G}_s , and liquid, \bar{G}_L , can be calculated. Values for \bar{G}_L and \bar{G}_s are reported in Table 7.4 and are plotted in Fig. 7.8. At low travel speeds the Peclet number is large and \bar{G}_L is less than \bar{G}_s because convection in the melt is important. At high travel speeds, the Peclet number is small and convection becomes less important, reversing the relationship between \bar{G}_L and \bar{G}_s .

The average temperature gradient in the solid was also calculated by the finite element method for two travel speeds. These calculations are summarized in Chapter 4 and are plotted in Fig. 7.8. There is good correlation between the calculated temperature gradients and the estimated temperature gradients. The calculated values of \bar{G}_s are within a factor of two and have the same apparent slope as the estimated values of \bar{G}_s based on the weld pool geometry and DAS calculations.

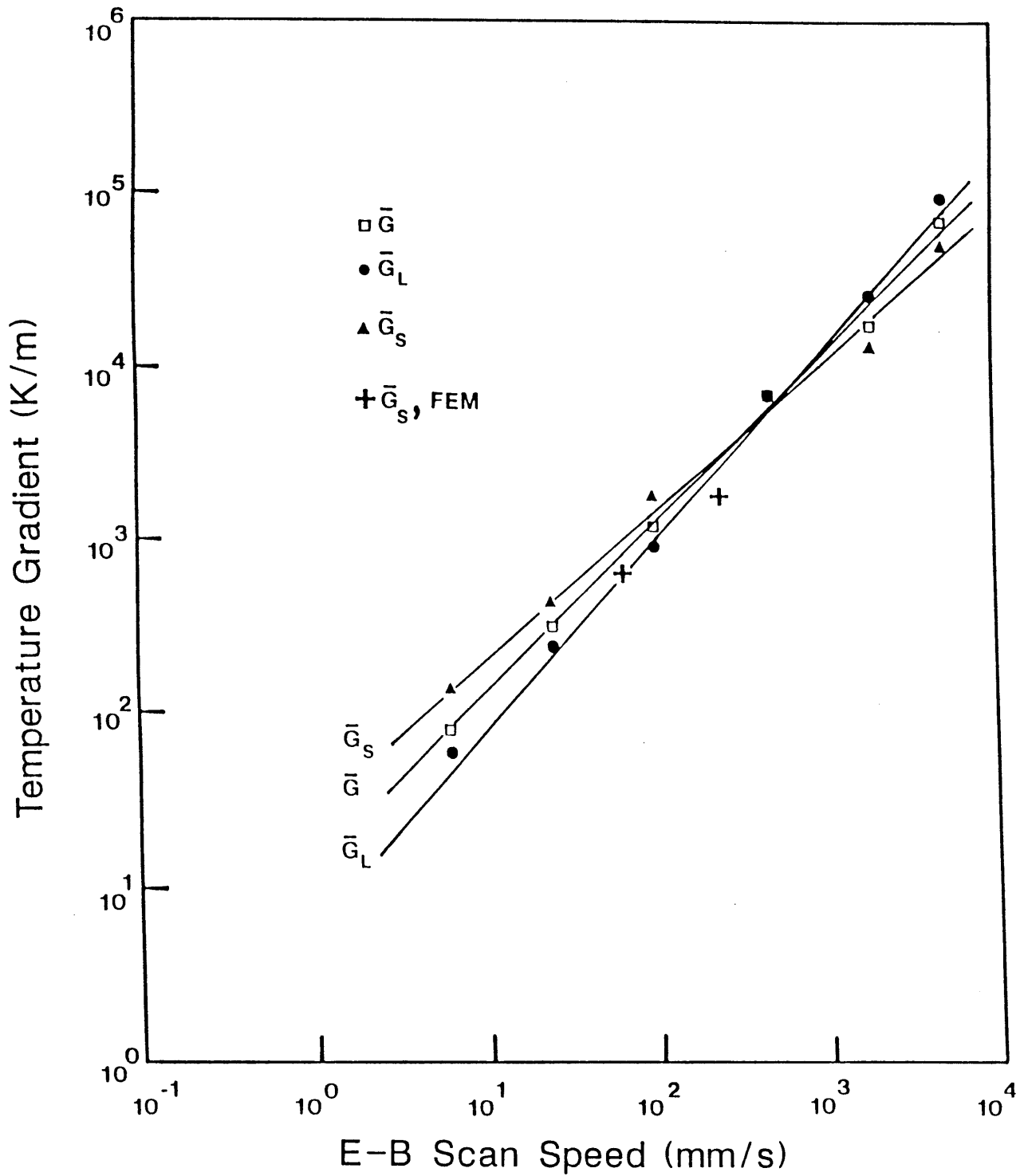


Figure 7.8 Average temperature gradient on the melt pool surface, $\bar{\tau}$, and the estimated temperature gradients in the liquid, $\bar{\tau}_L$, and solid, $\bar{\tau}_S$, at the L/S interface. FEM temperature gradient calculations are plotted for comparison.

7.2.2 Dendrite Tip Characteristics

The diffusion of solute away from the solid/liquid interface controls the growth rate of columnar dendrites growing parallel to the heat flux direction [7.8]. For solute diffusion-controlled growth, needle-like crystals can grow at higher rates than a planar interface because the redistribution of solute is more efficient around a tip with a small radius of curvature. The rejected solute creates a boundary layer, δ_c , around the tip and the diffusion of solute is controlled by the solute gradients created in the liquid. Therefore, the growth rate and morphological characteristics of the dendrites are dependent on the behavior at the dendrite tip.

The driving force for diffusion of solute at the dendrite tip is represented by the supersaturation, Ω :

$$\Omega = \frac{\Delta C}{\Delta C^*} = \frac{C_l^* - C_o}{C_l^*(1-k)} \quad (7.9)$$

Since a relationship exists between the temperature and the composition of the liquid, Ω also represents the related undercooling, ΔT_c , which drives the solidification process:

$$\Delta T_c = m(C_o - C_l^*) = mC_o \left(1 - \frac{1}{1 - \Omega(1-k)} \right) \quad (7.10)$$

The shape of the dendrite tip is closely represented by a paraboloid of revolution [7.8] and for this geometric shape, the mathematical solution to the diffusion problem was derived by Ivanstov [7.9]. This relationship equates Ω to r_t and R via the solutal Peclet number, P_c , and the Ivanstov function $I(P_c)$:

$$\Omega = I(P_c) \quad (7.11)$$

where

$$P_c = \frac{Rr_t}{2D} \quad (7.12)$$

and

$$I(P_c) = P_c \exp[P_c] E_1(P_c) \quad (7.13)$$

Here, E_1 is the exponential integral function and D is the interdiffusion coefficient in the liquid. For numerical calculations $E_1(P_c)$ and $I(P_c)$ can be approximated from the following equations [7.8]:

for $0 \leq P_c \leq 1$

$$E_1(P_c) = C_0 + C_1 P_c + C_2 P_c^2 + C_3 P_c^3 + C_4 P_c^4 + C_5 P_c^5 - \ln(P_c) \quad (7.14a)$$

where,

$$\begin{aligned} c_0 &= -0.577216 & c_1 &= 0.999992 \\ c_2 &= -0.249911 & c_3 &= 0.055200 \\ c_4 &= -0.009760 & c_5 &= 0.001079 \end{aligned}$$

for $1 \leq P_c \leq \infty$

$$I(P_c) = \frac{P_c^4 + a_1 P_c^3 + a_2 P_c^2 + a_3 P_c + a_4}{P_c^4 + b_1 P_c^3 + b_2 P_c^2 + b_3 P_c + b_4} \quad (7.14b)$$

where,

$$\begin{aligned} a_1 &= 8.573329 & b_1 &= 9.573322 \\ a_2 &= 18.059017 & b_2 &= 25.632956 \\ a_3 &= 8.634761 & b_3 &= 21.099653 \\ a_4 &= 0.267774 & b_4 &= 3.958497 \end{aligned}$$

Equation 7.11, $n = I(P_c)$, does not specify a unique functional dependence between the tip radius and the interface velocity, therefore, another equation is required. This additional equation comes from the stability criterion and relates the tip radius to the surface energy and the temperature gradient. According to Trivedi [7.10], a relationship can be derived to describe growth at the limit of morphological stability. The marginal stability theory is based on a dendrite tip having a small radius would increase its radius due to the growth of perturbations close to the tip. However, a dendrite tip with large radius would decrease its curvature due to instabilities. Consequently, growth occurs at an intermediate tip radius which is represented by the following equation:

$$r_t^2 = \frac{4\pi^2 \Gamma}{m G_c - G} \quad (7.15)$$

where Γ is the Gibbs-Thompson parameter (ratio of surface energy to melting entropy), G_c is the concentration gradient in the liquid and G is the temperature gradient in the liquid at the L/S interface. G_c is given by Lipton et al [7.7] to be:

$$G_c = \frac{-2P_c C_L^*(1-k)}{r_t} \quad (7.16)$$

Therefore, by combining equations 7.9, 7.11, 7.12, 7.15 and 7.16 the following relationship can be derived which relates R , r_t and G :

$$R^2 - \left(\frac{DP_c^2 m(1-k)C_o}{\pi^2 \Gamma (1(P_c)(1-k)-1)} \right) R + \left(\frac{D^2 P_c^2 G}{\pi^2 \Gamma} \right) = 0 \quad (7.17)$$

This equation is identical to that described by Esaka and Kurz [7.11] as the parabolic model II. Solving equation 7.17 explicitly for r_t is an impossible task since the product Rr_t is incorporated in P_c . Therefore, the equation is solved by choosing specific values for P_c and G and calculating R from equation 7.17. Knowing R and P_c , the tip radius can be calculated from the definition of the Peclet number, equation 7.12. For surface melting, R is considered the independent variable and yet it must be calculated from a selected value of P_c . Therefore to calculate r_t for a specific R and G combination requires an iterative scheme to guess the Peclet number which corresponds to the desired velocity. Alternately, a plot of r_t vs. R can be generated by selecting a range of Peclet numbers and calculating the relationship between these variables.

Once the dendrite tip radius is known, the undercooling created by the solutal boundary layer, ΔT_c , can be calculated from equation 7.10 and undercooling caused by the radius of curvature, ΔT_r , can be calculated from the Gibbs-Thompson relationship:

$$\Delta T_r = T_L - T_t = \frac{2\Gamma}{r_t} \quad (7.18)$$

ΔT_r describes the depression of the equilibrium melting point of solid with infinite radius of curvature, T_L , with the actual temperature at the tip, T_t .

Finally, the composition of the liquid at the dendrite tip can be calculated by combining equations 7.9 and 7.11:

$$C_L^* = \frac{C_o}{1 - (1 - k)I(P_c)} \quad (7.19)$$

A computer program was used to generate P_c vs. R , r_t vs. R and T_t vs R curves for all seven alloys. To simplify the calculations, the pseudobinary approximations described in section 7.1 were used and only partitioning of the dominant segregating element was considered, ie., Ni for primary ferrite alloys and Cr for primary austenite alloys. The physical property values for the alloys are listed in Table 7.5 and the calculations were performed for a series of temperature gradients that ranged from 10^5 (K/m) to 10^9 (K/m).

Table 7.5 Properties used to calculate the dendrite tip characteristics.

Property	Units	Alloy 1	Alloy 7
$m_{L,Ni}$	(K/%)	-	-7.4
$m_{L,Cr}$	(K/%)	-5.6	-
k_{Ni}	-	~1.0	0.74
k_{Cr}	-	0.8	~1.0
$\bar{D}_{L,Ni}$	(m ² /s)	-	4.67×10^{-9}
$\bar{D}_{L,Cr}$	(m ² /s)	3.0×10^{-9}	-
σ	(J/m ²)	0.403	0.269
ΔS_f	(J/m ³ K)	1.21×10^6	9.37×10^5
Γ	(mK)	3.33×10^{-7}	2.86×10^{-7}
ρ	(kg/m ³)	8,000	7,750
\bar{V}	(m ³ /mole)	6.98×10^{-6}	7.21×10^{-6}
T_L	(K)	1691.0	1709.4
$\Delta T_o = T_L - T_E$	(K)	46.0	24.4
$\bar{D}_{S,Ni}^F$	(m ² /s)	1.14×10^{-12}	-
$\bar{D}_{S,Cr}^A$	(m ² /s)	-	1.40×10^{-12}

Figure 7.9 shows the plots of Peclet number versus velocity for alloys 1 and 7. At large Peclet numbers ($P_c > 10^2$) a critical velocity is approached ($V_c = GD/\Delta T_c$) which corresponds to the limit of constitutional supercooling. As R is increased, P_c drops rapidly to a minimum value which is strongly dependent on the temperature gradient. As R is increased further, P_c continues to increase but becomes independent of the temperature gradient at high growth velocities. Alloys 1 and 7 behave in a similar manner and there is little difference between the P_c versus R curves for the two alloys. The behavior of the remaining alloys falls between these two extremes.

Figure 7.10 shows the plots of dendrite tip radius versus velocity for alloys 1 and 7. Large tip radii are found at low velocities. As the velocity is increased, the radius drops sharply and is strongly dependent on the temperature gradient. This regime corresponds to the planar ($r_t = \infty$) to cellular transition. At higher velocities the tip radius becomes independent of temperature gradient. Here, solidification takes place in a dendritic mode until the tip radius is reduced to the point where capillarity effects become dominant and the structure reverts to cellular and finally planar at the limit of absolute stability. The tip radius versus velocity behavior of all of the alloys are quite similar.

Figure 7.11 shows the plots of dendrite tip temperature, T_t , versus velocity for alloys 1 and 7. The amount of undercooling ($\Delta T = \Delta T_c + \Delta T_s$) can be determined from these plots by subtracting the equilibrium temperature, T_m , from the tip temperature. At high growth rates, the undercooling increases with increasing velocity and is independent of the temperature gradient. This behavior is associated with the capillarity contribution, ΔT_s , to the undercooling. As the velocity decreases, deviations from this general behavior occur and are dependent on the temperature gradient. These deviations are caused by solutal effects, ΔT_c , and are associated with the transition from dendritic to planar solidification as the growth rate approaches its critical velocity. The maximum amount of undercooling that can be achieved by solutal effects is equal to ΔT_c and the lower limit of the tip temperature at low velocities is the equilibrium solidus temperature. Alloys 1 through 7 again behave in a similar manner. The remaining alloys were shown to have similar characteristics and the results of the calculations are summarized in Appendix D.

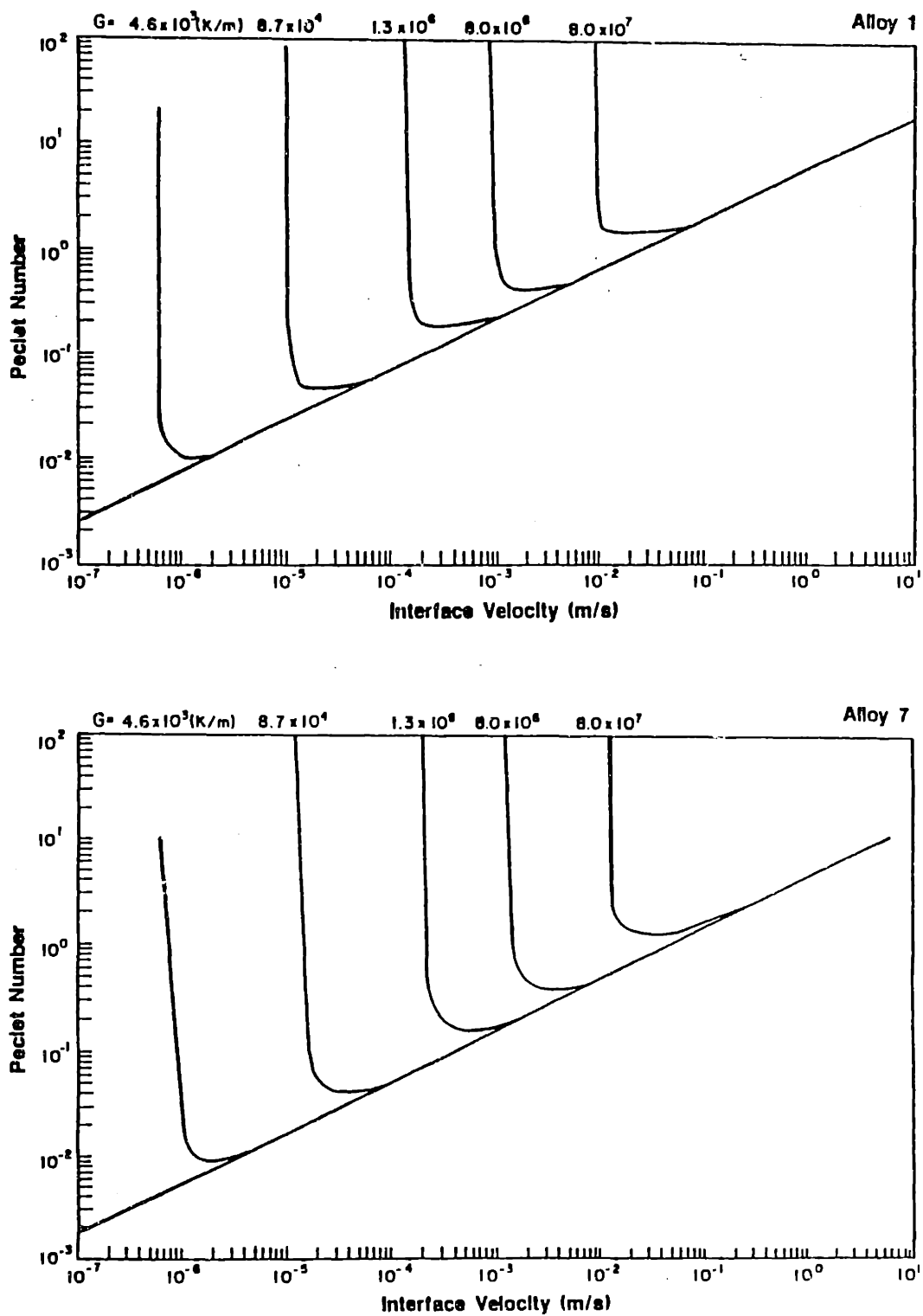


Figure 7.9 Peclet number versus interface velocity calculations for a) Alloy 1 and b) Alloy 7.

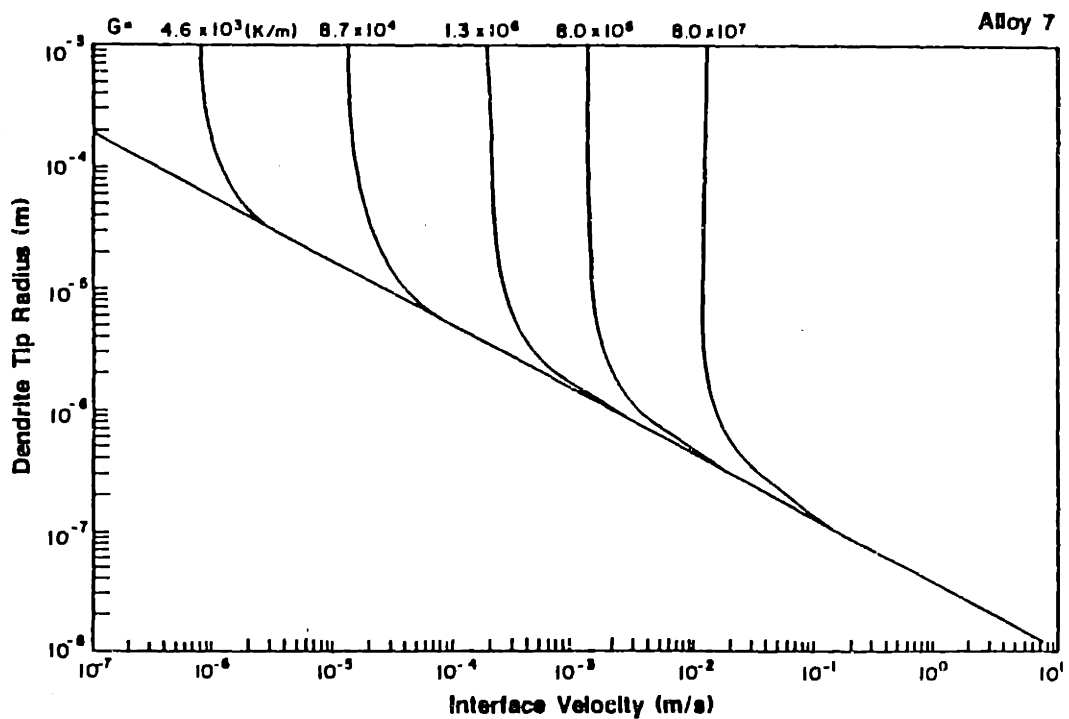
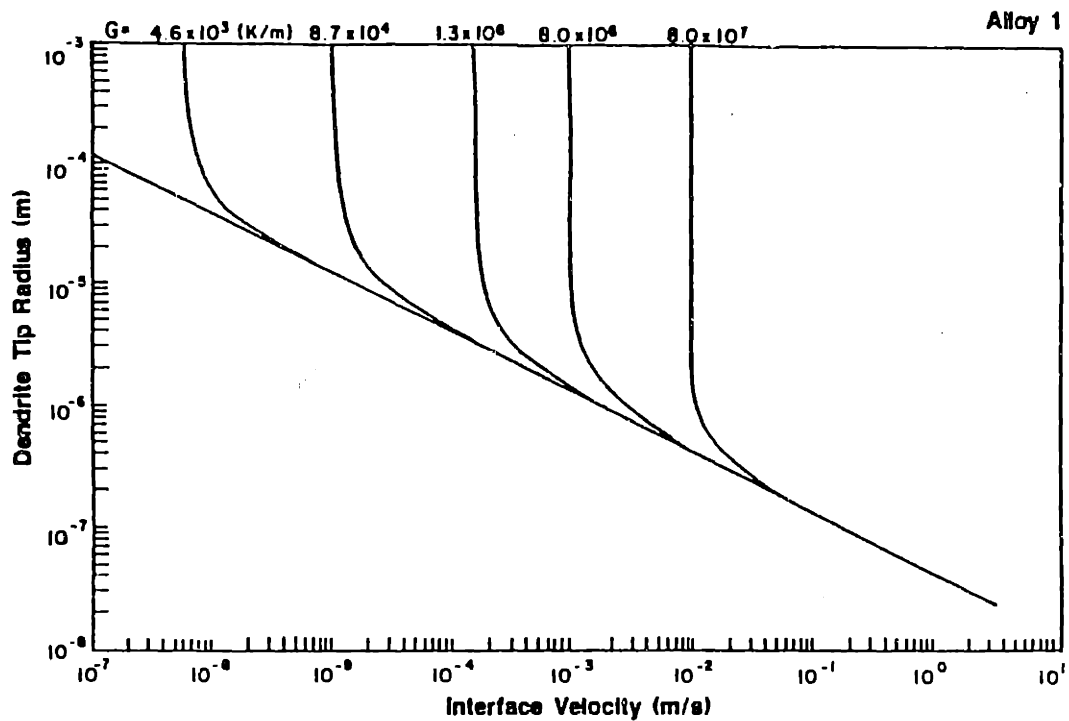


Figure 7.10 Dendrite radius versus interface velocity calculations for a) Alloy 1 and b) Alloy 7.

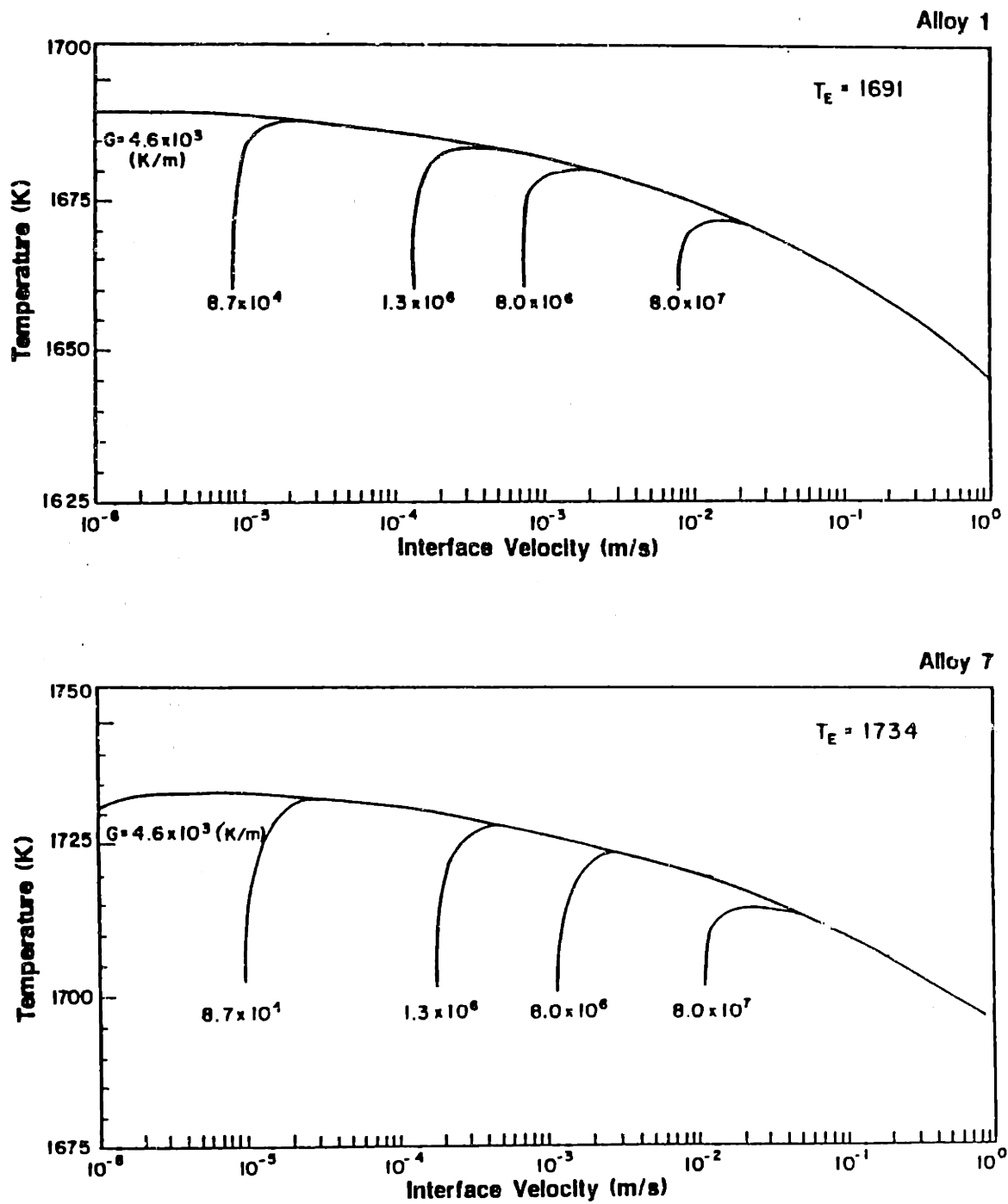


Figure 7.11 Dendrite tip temperature versus interface velocity for a) Alloy 1 and b) Alloy 7.

7.2.3 Cellular to Dendritic Transition

The stability of the liquid-solid interface was shown to be related to the amount of undercooling in the solute boundary layer and the growth kinetics of surface perturbations. These factors were in turn shown to be related to the solidification parameters G and R . Equation 7.3 can be used to describe the conditions under which a plane front will break down into cells based on constitutional supercooling theory and the alloy properties listed in Table 7.5 were used to show that the critical G/R value for the plane front to cellular (P/C) transition is 3.50×10^9 Ks/m² for Alloy 1 and 3.6×10^9 Ks/m² for Alloy 7. A plot of this relationship is shown in Fig. 7.12 where G/R values higher than this relationship will result in plane front solidification while G/R values lower than this relationship will be unstable.

G/R values which correspond to an unstable interface can solidify as cells or dendrites. However, the conditions under which the cellular to dendritic (C/D) transition takes place are not as easily defined as the planar to cellular transition. One theory for the cellular to dendritic transition is based on the P_c versus R curves which were calculated from the dendrite tip characteristics.

Somboonserk et al [7.12] proposed that the cellular to dendritic transition takes place close to the minimum in the P_c versus R relationship. Let P_c^* represent the Peclet number at the minimum in the curve, see Fig. 7.9, and let R^* represent the velocity at this point. P_c^* and thus R^* are functions of the temperature gradient, therefore, a plot of R^* versus G will separate the conditions for cellular and dendritic solidification. The Peclet number versus velocity plots presented in Fig. 7.9 for Alloy 1 and 7 were both shown to have similar critical values and are plotted as a single line in Fig. 7.12. For temperature gradients below this line, dendritic solidification behavior would be expected by this theory.

A comparison can be made between the cellular to dendritic transition predicted by the dendrite tip characteristics and the experimental results. The specific τ and R values for each of the six surface melting conditions are listed in Table 7.4 and are also plotted in Figure 7.12. The morphological characteristics of each melt was discussed in Chapter 5 and dendrites with well defined secondary arms were only observed in the two lowest growth-rate melts. The remaining four, higher growth-rate, melts were composed entirely of cells. Therefore, the two low speed

melts which solidified in a dendritic manner should lie below the C/D transition line while the remaining melts should lie above the C/D line but below the P/C transition line. The experimental results show that all of the melts lie below the P/C transition as they should, however, the C/D transition is not correctly predicted by the minimum in the Peclet number versus velocity curve theory.

The experimental data points which are plotted in Figure 7.12 are coded. The solid circles represent the melts that contained dendrites with well defined secondary arms and the open circles are entirely composed of finely spaced cells.

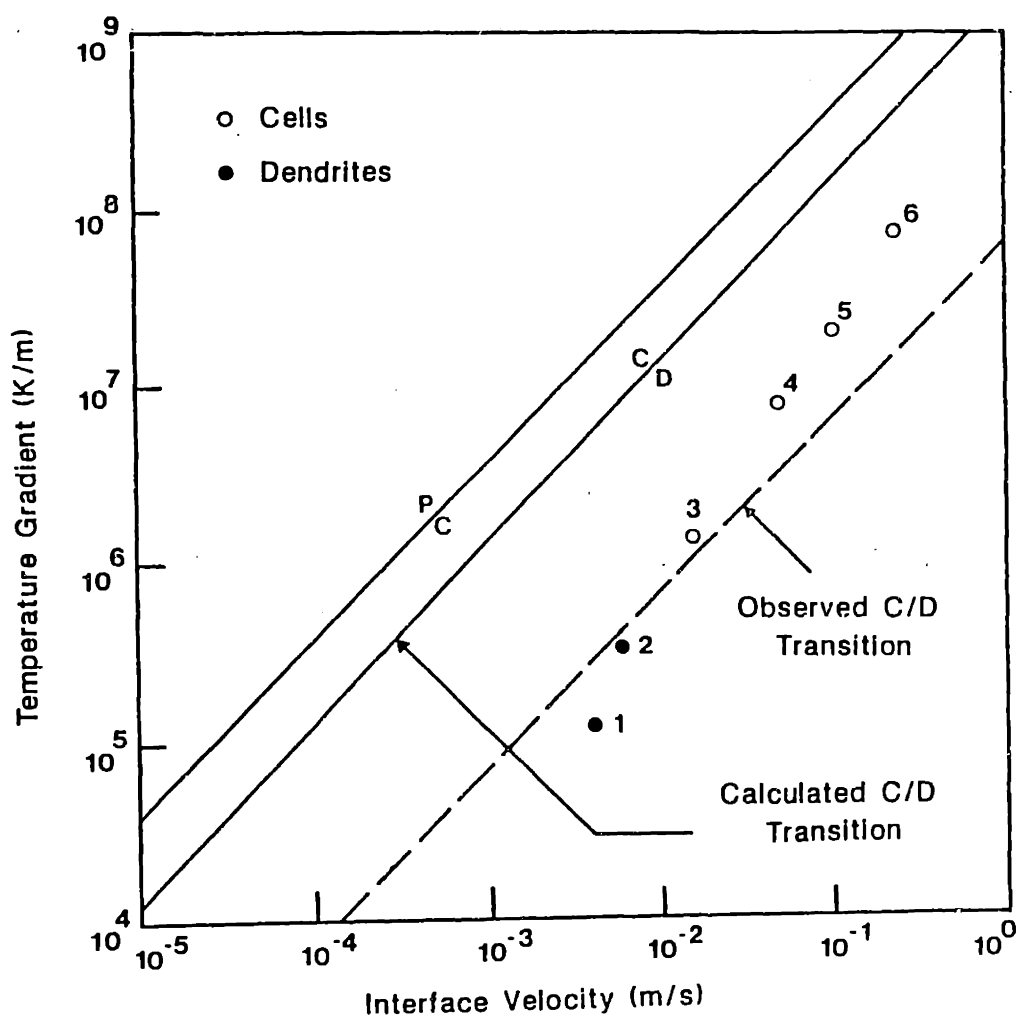


Figure 7.12 Temperature gradient versus interface velocity comparing the calculated and measured transitions for planar, cellular and dendritic growth conditions.

Therefore, the C/D transition should separate the solid from the open circles and this would require a lowering of the C/D line from 1.2×10^9 Ks/m² to 7.0×10^7 Ks/m² which is a factor of about 17. Several possible explanations for this discrepancy exist.

First, although the C/D transition is known to take place close to the minimum in the Peclet number versus growth rate curve, it most likely occurs at higher velocities. Miyata et al [7.13] have evidence for this but their data only appears to account for a factor of 5 or so and does not in itself explain the factor of 17. Second, the 59wt. percent iron alloys studied in this investigation contain a large percentage of solute. The dendrite tip characteristics were calculated based on assumptions that are more likely to be valid for less concentrated solutions. Third, concentration independent diffusivities were assumed and the effect of ternary alloy additions on diffusivity was not taken into account when calculating the dendrite tip characteristics. These effects might change the calculated Peclet number versus growth rate characteristics. Finally, the fine cells that appear in the microstructure may possibly have solidified as dendrites which have coarsened during solidification. It is not possible to determine which of these effects has contributed to the differences between observation and theory without further investigation.

In summary, the growth rate and velocities were calculated for each of the surface melting conditions. These measurements were used to calculate the dendrite tip characteristics and one of these characteristics, the minimum in the Peclet number versus velocity curve, was used to predict the cellular to dendritic transition. This transition was compared to the experimental data and was shown to be off by a constant multiplying factor of about 17. This difference can be rationalized by the assumptions used to calculate the dendrite tip characteristics and uncertainty in the C/D transition theory itself.

7.3 Solute Redistribution Models

Solute redistribution occurs during the cellular or dendrite solidification of all alloys. The amount of solute which segregates is related to the solidification parameters, G , R and r_t . Solute redistribution can influence the amount, composition

and structure of the primary and secondary solidification phases which, in turn, can influence mechanical properties. Many investigators have attempted to understand and model solute redistribution during solidification, however, because of the numerous factors involved, no analytical treatment has been developed which is capable of describing solidification redistribution without making assumptions.

In this section, the more prominent models for solute redistribution in binary alloy systems will be discussed. The classical nonequilibrium treatment by Scheil will be presented first, along with its ranges of applicability. Modifications to this treatment include the effects of undercooling at high cooling rates and back diffusion at low cooling rates. The behavior of the more complicated ternary alloys will be addressed and approximations will be made to allow the ternary alloy system to be treated as a binary alloy system. These approximations will be used to predict solute redistribution and the amount of ferrite which solidifies from the seven alloys for each of the solidification conditions studied in this investigation.

7.3.1 The Scheil Approximation

Chemical potential differences which exist between the solid and liquid phases provide the driving force for solute redistribution during solidification. In an attempt to minimize chemical potential gradients, the elements preferentially diffuse to their respective phases. This requires a redistribution of the atoms from their random solution in the liquid state. During the redistribution, concentration gradients are established in the liquid and solid phases because of kinetic limitations placed on the diffusing atoms. Therefore, the factors which control a steady-state redistribution of solute become those factors which attempt to remove concentration gradients from the system.

For the special case of equilibrium solidification, concentration gradients are eliminated and the solid and liquid phases have uniform composition. Under these conditions, the Lever rule can be applied to calculate the composition as a function of temperature or fraction solidified. For linear liquidus and solidus lines these equations are :

$$C_s^* = \frac{kC_o}{f_s(k-1)+1} \quad (7.20a)$$

$$f_s = \left(\frac{1}{1-k} \right) \left(\frac{T_L - T}{T_f - T} \right) \quad (7.20b)$$

Table 7.6 summarizes the nomenclature used to represent the solidification related variables.

During most solidification processes, the concentration gradients can not be eliminated and nonequilibrium conditions exist. For these cases, assumptions are made to simplify the problem. The classical nonequilibrium treatment assumes perfect diffusion in the liquid phase and no diffusion in the solid phase. These assumptions provide for a maximum amount of solute to be stored in the remaining liquid, which represents an upper limit on the amount of second phase which can form during solidification. This treatment is often referred to as the Scheil approach and represents the interfacial composition in terms of temperature or fraction solidified:

$$C_s^* = k C_o (1 - f_s)^{(k-1)} \quad (7.21a)$$

$$f_s = 1 - \left(\frac{T_s - T}{T_s - T_L} \right)^{(1/(k-1))} \quad (7.21b)$$

The differential form of equation 7.21 a can easily be derived by a mass balance and is often useful:

$$C_L(1-k)df_s = (1-f_s)dC_L \quad (7.22)$$

The Scheil equation can be used to predict the composition and relative amounts of the primary and secondary phases. However, this method can only be applied to systems in which the diffusivities of the alloying elements are similar and for intermediate cooling rates [7.1]. At slow cooling rates [7.1, 7.15] or for systems with fast diffusing elements such as interstitials [7.14], back diffusion into the solid phase limits the applicability of the Scheil equation. At high cooling rates, dendrite tip undercooling [7.1, 7.16, 7.17] and eutectic temperature depression [7.1, 7.18] also limit the applicability of the Scheil equation. Therefore, the Scheil equation represents solute redistribution reasonably well, but only for intermediate cooling rates. Modifications are required for the high and low cooling rate regimes.

Table 7.6 Nomenclature used to describe solute redistribution

Variables	Description
C,T	composition, temperature
k	equilibrium partition ratio
f_s	fraction solid
D	volume diffusion coefficient
θ_f	local solidification time
α, α'	coefficient for back-diffusion
Ω	solotal supersaturation
Γ	Gibbs-Thompson parameter

Subscripts	Description
s	solid, solidus
L	liquid, liquidus
o	nominal

Superscripts	Description
*	interface
E,M,C	eutectic, maximum, solotal
r,t	radius of curvature, dendrite tip

7.3.2 Back-diffusion and Undercooling

Brody and Flemings [7.15] modified the Scheil equation to account for the back-diffusion which occurs at low cooling rates. In their model, they assume perfect diffusion in the liquid and account for volume diffusion in the solid for two types of dendrite shapes: linear and parabolic plates. In practice, cells and dendrites tend to be shaped close to a paraboloid and this approximation is more accurate. For this case, the composition of the solid at the interface was shown to be [7.15]:

$$C_s^* = kC^o(1 - (1 - 2\alpha k)f_s)^{[(k-1)/(1-2\alpha k)]} \quad (7.23)$$

$$\alpha = \frac{4D_s\theta_f}{\lambda^2} \quad (7.24)$$

Clyne and Kurz [7.14] show that these equations remain approximately valid, providing the diffusion boundary layer in the solid is small (small α) compared to the cell spacing. Otherwise, for large α solute is not conserved and errors become apparent. Clyne and Kurz [7.14] modified equation 7.24 to ensure that the model approaches the Scheil equation as α approaches zero and that the model approaches the lever rule as α approaches infinity. Their modification to α for a parabolic dendrite shape is:

$$\alpha' = \alpha \left(1 - \exp\left[\frac{-1}{\alpha}\right] \right) - \frac{1}{2} \exp\left[\frac{-1}{2\alpha}\right] \quad (7.25)$$

Although this equation is not based on a physical model at intermediate values of α [7.1], it remains to be a useful relationship for describing solute diffusion at low to intermediate cooling rates.

At high cooling rates, back-diffusion is eliminated but other deviations from the Scheil equation occur. The lever law and Scheil models both assume that the temperature at the dendrite tip is the equilibrium liquidus temperature. However, because of incomplete diffusion of solute in the liquid and because of radius of curvature effects, the dendrite tip temperature is depressed. These conditions cause a reduction in the amount of second phase which forms and can be described by the overall undercooling which is present at the dendrite tip.

During surface melting, the heat is extracted by the substrate and no thermal undercooling exists ahead of the dendrite. Therefore, the only contributions to the overall undercooling are the constitutional effects caused by solute buildup at the tip, (ΔT_c), radius of curvature effects (ΔT_r) and the attachment kinetics of the atoms at the interface (ΔT_i). The interface kinetic term is known to be small for nonfaceted materials and can be ignored [7.8]. This leaves two terms to represent the overall undercooling ΔT :

$$\Delta T = \Delta T_c + \Delta T_r \quad (7.26)$$

Both ΔT_c and ΔT_s depend on the radius of the dendrite tip. These quantities were calculated and the results were used to calculate solidification segregation and will be discussed in following sections.

7.3.3 Ternary Alloy Systems

The principles for solute redistribution in ternary alloy systems are the same as those in binary alloy systems. However, the additional degree of freedom in ternary alloy systems not only complicates the computations but also results in additional problems caused by a lack of phase diagram information regarding tie lines and solidification paths. Unless simplifying assumptions are made, solutions to the solute redistribution equations require a numerical approach since the partition coefficient is a function of temperature. Although the tie-lines, which define the partition coefficient, are not generally known in ternary systems, computer-calculated phase-diagram information can be used to generate the necessary data. In this section, the basic solute redistribution equations for ternary alloy systems will be discussed and simplifications will be presented for the case where the solidification path allows the ternary system to be represented by a pseudobinary diagram.

Interface stability and solute redistribution can each be mathematically described by models of varying complexity in binary alloy systems. This ternary alloy representation of the basic models has been made. For example, the three-component analog to the Mullins and Sekerka interface-stability analysis and the three-component analog to the Scheil equation have been investigated but are not widely used because of a lack in phase diagram and physical property data. However, to the author's knowledge, the more descriptive dendrite-tip radius calculations have not been applied to ternary alloy systems.

The three component analog to the Scheil equation can be derived from a mass balance of the two segregating species. Initially, the primary phase begins to solidify from the melt and assuming no diffusion in the solid and perfect diffusion in the liquid, the differential form of the Scheil equation (7.22) can be written with respect to each component.

$$\frac{df_L}{dC_{LA}} = \frac{-f_L}{C_{LA}(1-k_{\alpha A})} \quad (7.27a)$$

$$\frac{df_L}{dC_{LB}} = \frac{-f_L}{C_{LB}(1-k_{\alpha B})} \quad (7.27b)$$

Where C_{LA} and C_{LB} refer to the liquid composition of elements A and B respectively while $k_{\alpha A}$ and $k_{\alpha B}$ refer to the partition ratios between the liquid and primary phase α for elements A and B respectively. Therefore, by knowing the tie line locations as a function of temperature C_{LA} , C_{LB} , k_A and k_B can be determined and equations 7.27 can be solved to predict the composition of the solid phase.

At some point during the solidification process, the liquid will be sufficiently enriched in solute to reach the line of two-fold saturation. At this temperature a second phase starts to form and an additional term must be added to the solute redistribution equations:

$$\frac{df_L}{dC_{LA}} = \frac{-f_L}{C_{LA}(1-k_{\alpha A})} - \left(\frac{k_{\beta A} - k_{\alpha A}}{1 - k_{\alpha A}} \right) \frac{df_{\beta}}{dC_{LA}} \quad (7.28a)$$

$$\frac{df_L}{dC_{LB}} = \frac{-f_L}{C_{LB}(1-k_{\alpha B})} - \left(\frac{k_{\beta B} - k_{\alpha B}}{1 - k_{\alpha B}} \right) \frac{df_{\beta}}{dC_{LB}} \quad (7.28b)$$

where f_{α} , f_{β} refer to the weight fraction of second phase α and β respectively while $k_{\alpha A}$ and $k_{\alpha B}$ refer to the partition ratio between the liquid and β phase for components A and B respectively. If dC_L is taken to be the independent variable and the segregation ratios are defined by the phase diagram then there are two unknown quantities : df_{β} and f_L . Therefore, equations 7.28a and 7.28b are both required to solve for the change in fraction liquid with a change in liquid composition along the line of two-fold saturation.

7.3.4 The Influence of Solidification Velocity on the Partition Ratio

The calculations presented so far have utilized the equilibrium phase diagram to determine the relationship between the solid and liquid composition. This relationship is defined by the tie-lines in the two-phase liquid and solid fields and is called the equilibrium partition ratio, k . At high interfacial velocities, the local equilibrium

assumption used to represent partitioning at the liquid/solid interface has been shown to be invalid [7.20, 7.21]. Models of the interface kinetics have been developed to represent the deviations from equilibrium and indicate that k increases with increasing R from its equilibrium value at low rates to unity at high rates.

One model for solute redistribution during rapid solidification was developed by Aziz [7.22] and predicts equilibrium partitioning from $R \ll D_L/a$ and complete solute trapping ($k=1$) for $R > D_L/a$ where a is the interatomic spacing. For the alloys studied in this investigation, D_L/a is approximately 7.5 m/s.

Table 7.3 lists the average interface velocity for each imposed travel speed. Although the travel speed, S , reaches velocities close to that of 7.5 m/s, the maximum interface velocity, R , is only 0.175 m/s at its highest value because of the geometry of the shallow surface melts. Therefore, assuming 0.175 m/s is significantly less than 7.5 m/s, the partition ratio can be assumed to be close to its equilibrium value for all of the travel speeds investigated in this study.

7.4 Calculations of Solute Redistribution in the Electron Beam Melts

7.4.1 Solute Redistribution and Second Phase Formation

The Scheil equation can be used to predict solute redistribution and the amount of second phase that forms during solidification. This model relies on some basic assumptions which limit its usefulness to a narrow cooling rate change. However, the results provided by the Scheil equation are an important point of reference because they predict the maximum amount of second phase which can form during any solidification process. The assumptions and details of the Scheil equation have already been discussed and in this section they will be used to provide first-order solution to the amount of ferrite which solidifies from the melt for each of the seven alloys.

Figure 7.13 shows the solute distribution predicted by the Scheil equation (7.20a) for a hypothetical binary alloy eutectic system with $k < 1$. The composition of the first solid to form is kC_0 and since solute is rejected in the liquid, the composition of the solid increases with fraction solidified. When $f_S = f_S^*$, the composition of the liquid is

enriched in solute to the eutectic composition and at this point the composition of the solid is C_{SM} and the composition of the liquid is C_E . The remaining liquid solidifies at this eutectic composition.

The amount of primary phase α that solidifies is represented by the fraction f_S^* while the amount of second phase, β , that solidifies is represented by $(1-f_S^*)x$, where $x = (C_E - C_0)/(C_E - C_{SM})$ is derived from the lever rule at the eutectic temperature. The total amount of α phase is therefore the amount of primary α plus the amount of α that solidifies as eutectic $(1-f_S^*)(1-x)$.

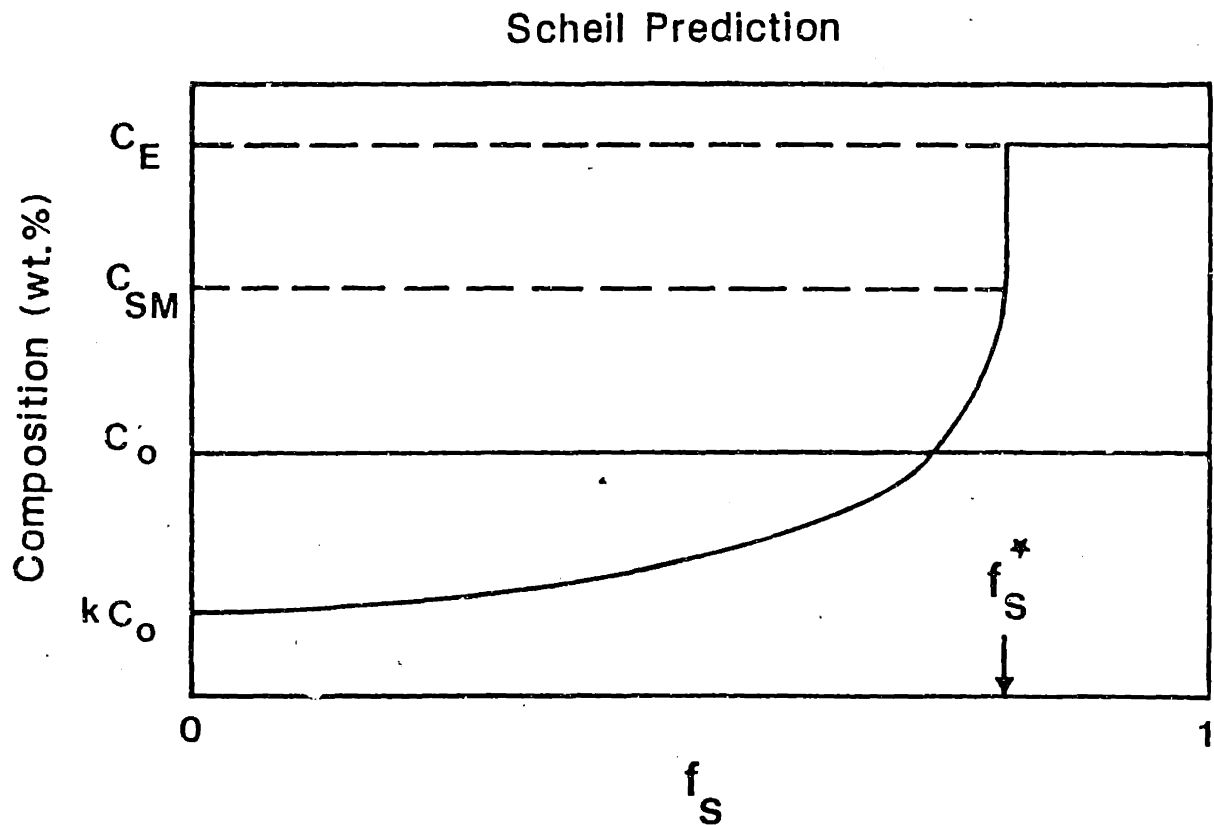


Figure 7.13 Schematic drawing showing the solute redistribution predicted by the Scheil equation.

A similar approach can be applied to the pseudobinary diagrams. Following the method described by equations 7.27, segregation of Cr and Ni can be independently predicted using figures 7.4 and 7.5. The amount of the primary phase can therefore be predicted by noting f_S when the eutectic composition is reached. The amount of second phase that forms can then be predicted using equations 7.28 and partition ratios from the thermodynamically calculated isothermal sections.

The Scheil equation can be used to predict f_S^* for either Cr or Ni partitioning and in theory, both elements would give the same numerical value for f_S^* . However, in practice, the approximations made in deriving the pseudobinary diagrams result in small differences in f_S^* when considering Cr or Ni segregation. The more accurate value of f_S^* is calculated by the element that partitions the greatest extent during solidification since this element averages out the uncertainties in the phase diagram. The solidification paths presented in Fig. 7.6 show that Ni segregates to a greater extent than Cr during primary ferrite solidification and Cr segregates to a greater extent than Ni during primary austenite solidification. Therefore, the Scheil equation was solved by considering nickel segregation during primary ferrite solidification ($k_{Ni}^f = 0.74$, $k_{Cr}^f = 1.0$) and chromium segregation during primary austenite solidification ($k_{Cr}^a = 0.80$, $k_{Ni}^a = 1.0$).

Using the above partition ratios and the C_0 and C_E compositions listed in Table 7.2, the Scheil equation was used to calculate the amount of primary (P), secondary (S) and total (T) amounts of phases that form during solidification of the seven alloys. These values are listed in Table 7.7 and show that the amount of primary phase decreases as the nominal composition nears the line of two-fold saturation, which is located between alloys 3 and 4. The amount of eutectic is similarly presented. From this eutectic, the second phase forms and additional amounts of the initial phase will also form, but of the eutectic and not the primary composition.

Table 7.7 The Scheil approximation of the primary, secondary, and total amount of ferrite and austenite in the seven alloys:

Alloy	F_P	F_S	F_T	A_P	A_S	A_T
1	0	7.2	7.2	82	10.8	92.8
2	0	18	18	55	27	82
3	0	30	30	26	44	70
4	7	37	44	0	56	56
5	33	27	60	0	40	40
6	47	21	68	0	32	32
7	60	16	76	0	24	24

The amount of second phase that forms is a fraction of the amount of eutectic liquid. This fraction can be estimated by the lever rule and the isothermal section at the eutectic temperature. Comparison of the line of two-fold saturation with the tie-triangles from the isothermal sections shows the percentage of the liquid that solidifies as ferrite and the percentage that solidifies as austenite. Figure 7.14 shows the amount of ferrite that forms from the eutectic liquid as a function of temperature, for liquid compositions ranging from 59%Fe (1450 °C) to the minimum in the line of two-fold saturation (1310°C). Using an average value of this ratio, 25% ferrite, the amount of second phase that forms during the solidification of eutectic-composition liquid was calculated and is listed in Table 7.7.

A histogram of these results is shown in Fig.7.15, indicating the relative amounts of primary and second phase austenite and primary and second phase ferrite that solidify from the seven alloys. The amount of primary ferrite and the total ferrite content increases from alloy 1 to alloy 7 as the amount of primary and secondary austenite decrease. The maximum ferrite content predicted in alloy 7 is 76 percent with a majority (60%) being the primary phase. In subsequent sections of this chapter, a model will be utilized to predict segregation during dendritic solidification and the results of this model will be compared with the results of the Scheil approximation which are summarized in Fig. 7.15.

7.4.2 Back-diffusion Effects

The Brody and Flemings model was presented in section 7.3.2 to describe the effects of back-diffusion on solute redistribution. This model was shown to be useful at low cooling rates where diffusion in the solid is significant but is an unnecessary modification at high cooling rates where the characteristic diffusion distance is small.

Therefore, there is a cooling rate that separates the low from the high rate behavior. This cooling rate can be estimated from the Brody and Flemings parameter α . For α values greater than unity, back-diffusion is important because the characteristic diffusion distance is on the order of the dendrite arm spacing. For α values much less than unity back-diffusion can be neglected.

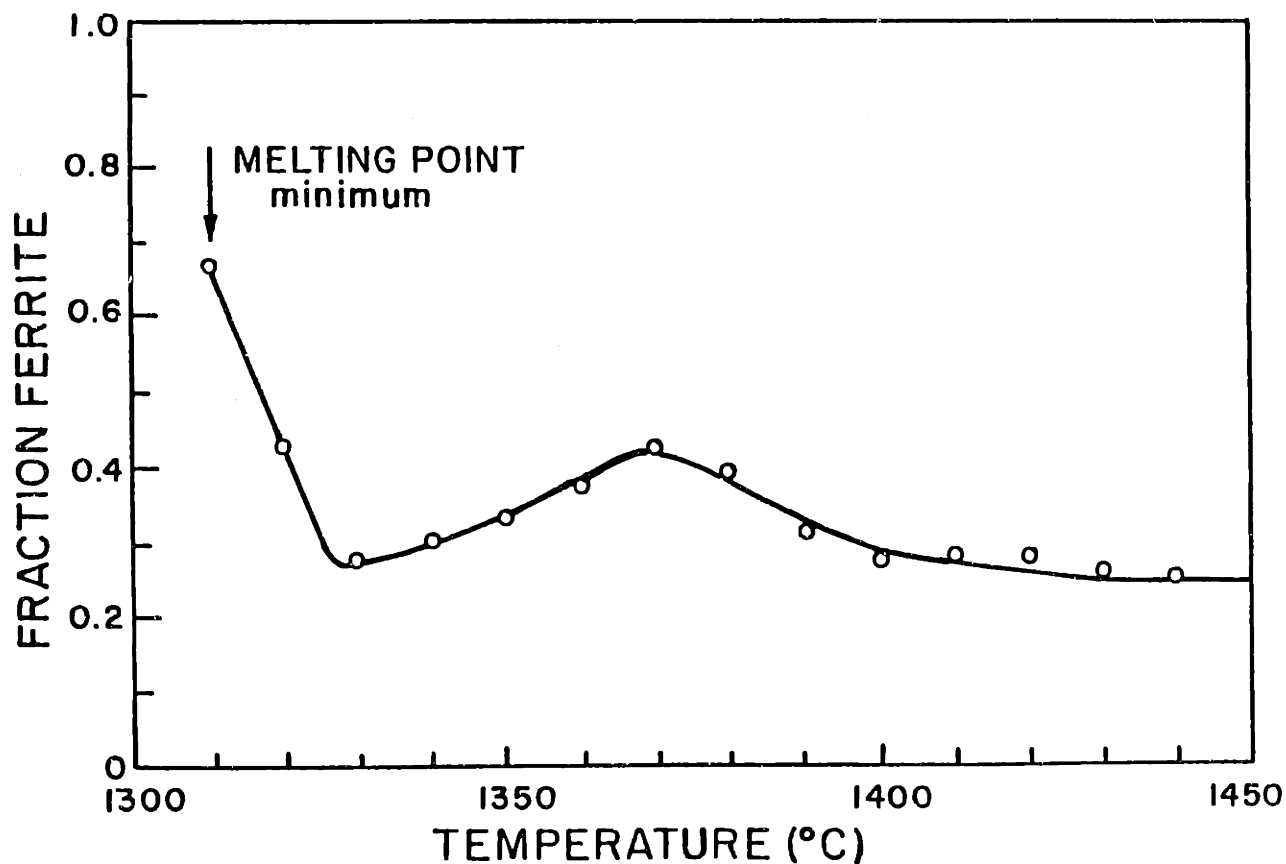


Figure 7.14 The fraction ferrite that solidifies from the eutectic liquid as a function of temperature along the line of two-fold saturation, based on thermodynamic calculations.

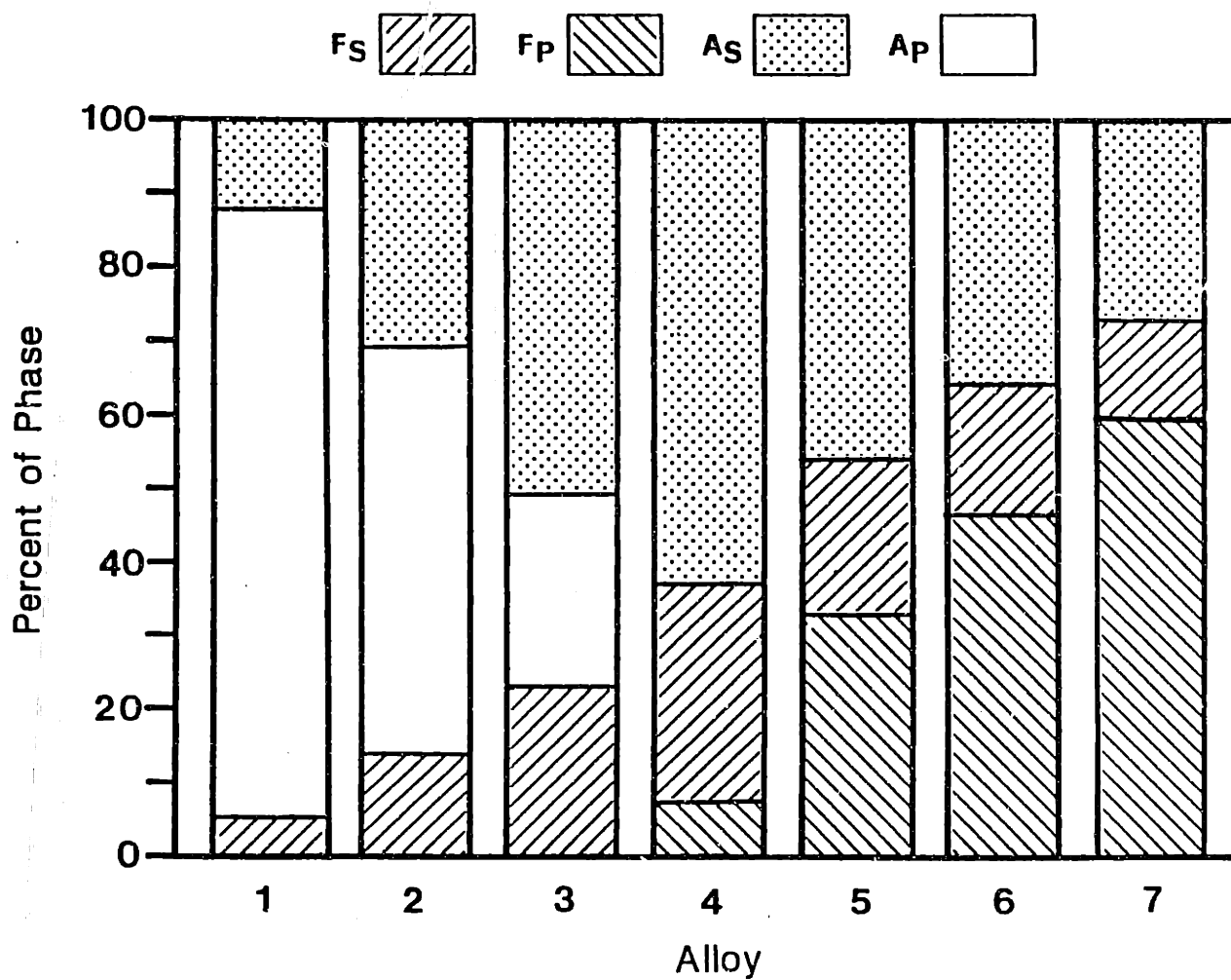


Figure 7.15 Results of the Scheil calculations showing the relative amounts of primary and second phase ferrite and primary and second phase austenite that solidifies from each of the seven alloys.

Values of α for the casting and each of the six electron beam melts are presented in Table 7.8 for primary austenite and primary ferrite solidification conditions. These calculations were made using the secondary dendrite arm spacings of the casting, melt 1 and melt 2 and cell spacing measurements for melts 4-6.

Table 7.8 The Brody and Flemings back-diffusion parameter calculated for alloys 1 and 7 at each of the solidification conditions:

Melt	ϵ (K/s)	θ_f (s)	λ_1 (μm)	λ_2 (μm)	α Alloy 7	α Alloy 1
Cast	7.0	5.7	-	18.0	7.4×10^{-2}	8.4×10^{-2}
1	4.7×10^2	4.7×10^{-2}	-	4.7	8.8×10^{-3}	1.2×10^{-2}
2	1.9×10^3	9.6×10^{-3}	-	3.0	4.4×10^{-3}	6.0×10^{-3}
3	1.7×10^4	1.3×10^{-3}	3.2	-	5.3×10^{-4}	1.9×10^{-3}
4	4.4×10^5	4.1×10^{-5}	1.1	-	1.4×10^{-4}	1.9×10^{-4}
5	1.5×10^6	1.2×10^{-5}	0.73	-	9.4×10^{-5}	1.2×10^{-4}
6	7.5×10^6	2.4×10^{-6}	0.43	-	5.3×10^{-5}	7.2×10^{-5}

The highest α value occurs in the slow cooling rate casting and is less than 0.1. The lowest α value occurs in the highest cooling rate weld and is less than 10^{-4} . Therefore, since all the solidification conditions have α values which are significantly less than unity, it was concluded that the effects of back-diffusion on solidification segregation could be neglected in this study.

7.4.3 Dendrite Tip Undercooling and Second Phase Formation

In section 7.2.2, a method was described to calculate the characteristics at the tip of a columnar dendrite growing under steady-state conditions. In this section, the dendrite tip model will be used to calculate the undercooling for each of the alloys

and for each of the solidification conditions studied. From these data, the amount of solute segregation will be predicted and these results will be compared with the Scheil approximation.

A computer program was written to solve equation 7.17 for the dendrite tip radius and undercooling. The input to the program consists of C_o , m_L , k , T_L , D_L , σ and ΔS_f for each alloy and G for each welding condition. The output from the program is P_c , r_t , ΔT_s , ΔT_c and C_L^* as a function of velocity for each value of G . The dendrite tip radius calculations were performed on each of the seven alloys for each of the average temperature gradients listed in Table 7.4. The physical property data for the seven alloys is listed in Table 7.5 and the nominal and eutectic compositions are listed in Table 7.2.

The average interface velocity for each melting condition is also listed in Table 7.4. These data were used to determine, r_t , ΔT_s , ΔT_c , and C_L^* for each of the solidification conditions from the computer generated solutions to equation 7.17. These data are summarized in Appendix D. For each alloy, the total undercooling increases with increasing interface velocity from values of about 10°C in the casting to values of about 30°C in the highest speed electron beam melt.

Sarreal et al [7.1] presented a model for predicting the amount of solute segregation that occurs for undercooled dendritic growth conditions. In this model, it is assumed that the undercooling is dissipated at the dendritic tip by forming a certain fraction of the primary phase solid, f_s^o , corresponding to the lever rule at the undercooled temperature. The remaining liquid $(1-f_s^o)$ is then assumed to solidify via the Scheil approximation. Solute conservation equations applied to the dendrite tip under these conditions yield the following equations:

$$f_s^o = \frac{C_o - C_t}{C_t(k-1)} \quad (7.29)$$

$$f_E = (1 - f_s^o) \left(\frac{C_{S.M}}{kC_t} \right)^{1/(k-1)} \quad (7.30)$$

where f_E refers to the fraction eutectic for the undercooled dendrite.

A modification to these equations is required if the undercooling brings the tip temperature below the 'eutectic' temperature. For this case, f_s , as calculated by equation 7.29, is still accurate, assuming the metastable extensions of the liquidus and solidus are linear. However, the eutectic composition and the maximum solid solubility increase to higher solute levels with increasing undercooling. These parameters in turn, influence the percentage of liquid which solidifies as the primary solid phase and C_{SM} must be corrected to account for this difference. Assuming linear behavior for the metastable extensions, Fig. 7.16 illustrates the adjustments that should be made to C_{SM} by the addition of the quantity ΔC_{SM} to account for the undercooling below the eutectic temperature $\Delta T'_E$:

$$C'_{SM} = C_{SM} + \frac{\Delta T'_E}{m_L} \quad (7.31)$$

Therefore, equation 7.30 and 7.31 can be used to represent the fraction of the liquid that solidifies as eutectic for the following conditions:

$$\text{for } \Delta T_C \leq T_L - T_E \quad C_{SM} = C_{SM} \quad (7.32a)$$

$$\text{for } \Delta T_C > T_L - T_E \quad C_{SM} = C'_{SM} \quad (7.32b)$$

Using the above equations and the dendrite tip undercooling calculations, the amount of primary austenite and primary ferrite that forms during solidification was calculated for each solidification condition. Once the amount of primary phase is known the remaining liquid solidifies at the eutectic composition but the percentage of the eutectic liquid that solidifies as ferrite must still be calculated. Figure 7.14 is a plot of the percentage of the eutectic liquid that solidifies as ferrite as a function of temperature along the line of two-fold saturation. From this figure, the average fraction of the liquid that forms second-phase ferrite was determined to be 0.32 and this value was used for all of the calculations.

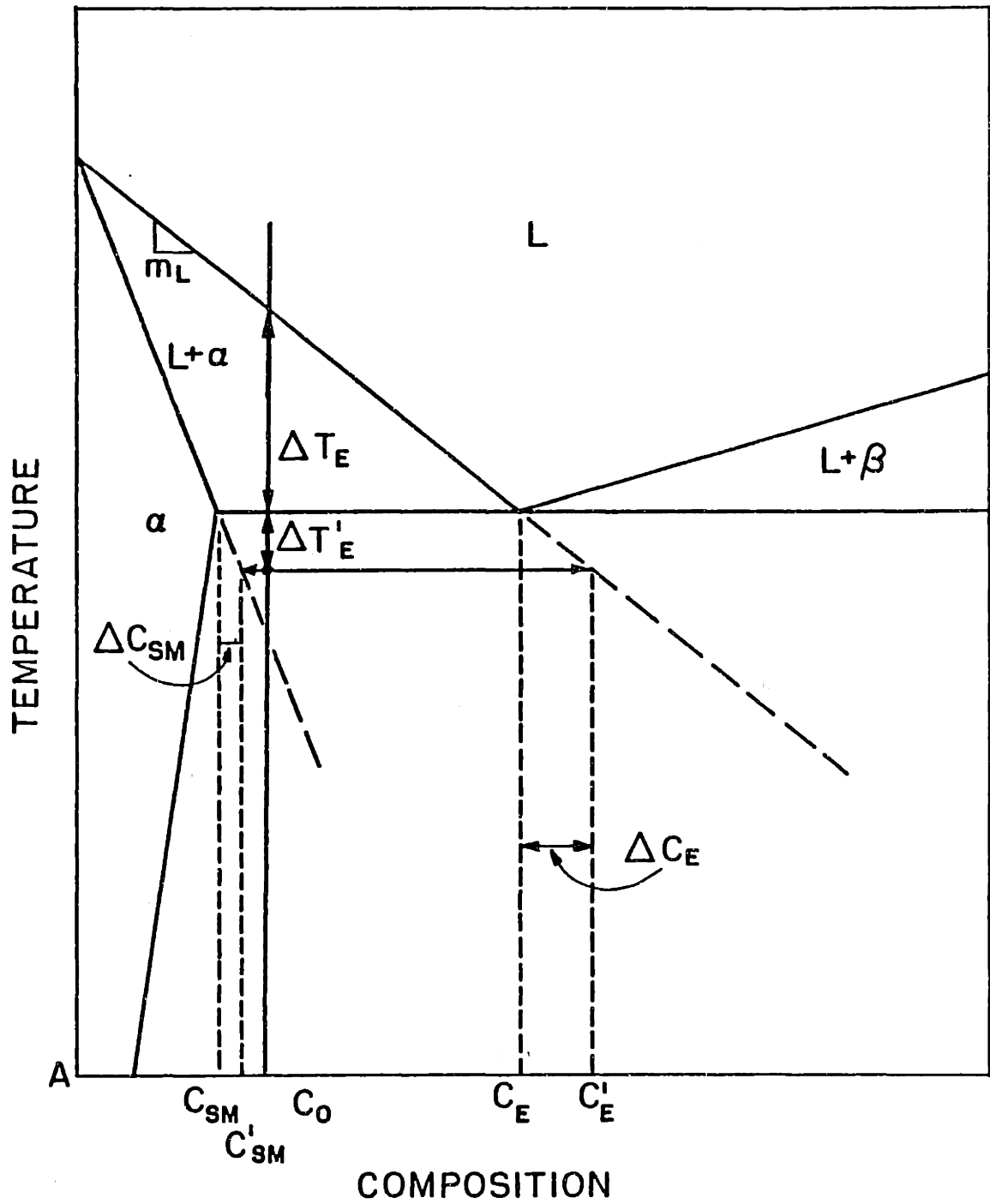


Figure 7.16 Schematic binary alloy phase diagram showing the shift in eutectic composition with undercooling below the eutectic temperature.

The results showing the amount of each phase that solidifies from the melt are tabulated in Appendix D for each of the seven alloys and for each of the solidification conditions. Also included in these tables are the results of the Scheil analysis and the equilibrium solidification predictions for comparison. Since Alloy 4 was observed to solidify in the FA mode at low rates and in the AF mode at high cooling rates, the solidification segregation calculations were performed for both modes of solidification in this alloy.

The solidification segregation calculations, which incorporate dendrite tip undercooling effects, are plotted in the histograms presented in Figures 7.17, 7.18, and 7.19. These figures show the influence of composition, at a given cooling rate, on the amount of ferrite and austenite that solidifies in each alloy. Figure 7.17 represents the slowest cooling rate (cast) condition, Figure 7.18 represents an intermediate cooling rate condition (EB melt 2) and Figure 7.19 represents the highest cooling rate condition (EB melt 6).

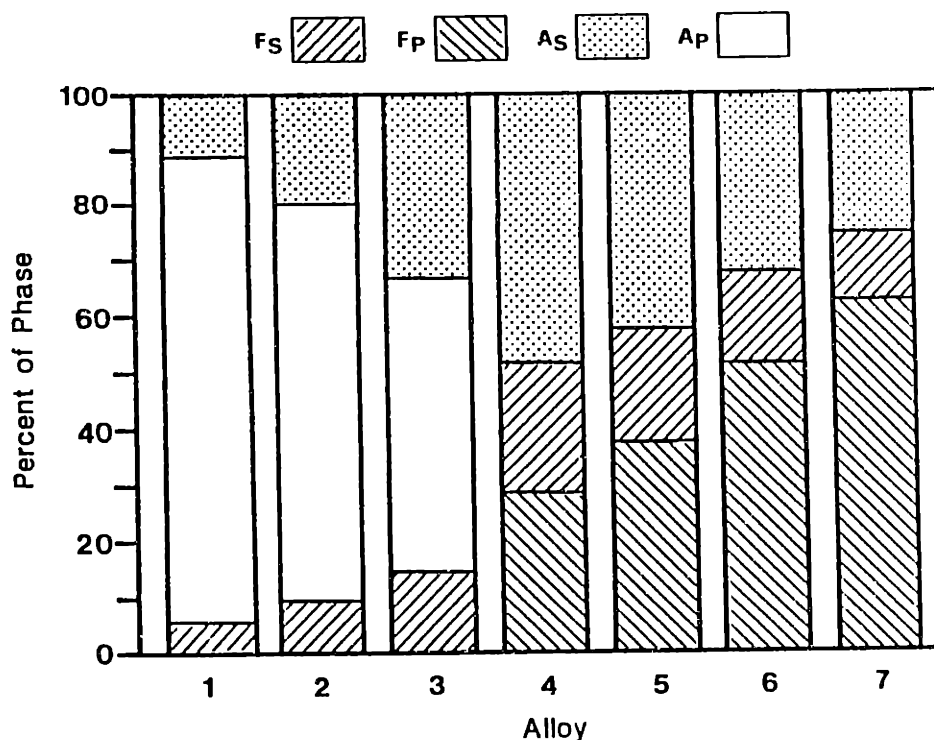


Figure 7.17 Results of the solidification segregation model showing the relative amounts of ferrite and austenite that solidify for the slow cooling rate cast condition. The solidification mode changes from primary austenite to primary ferrite between Alloys 3 and 4.

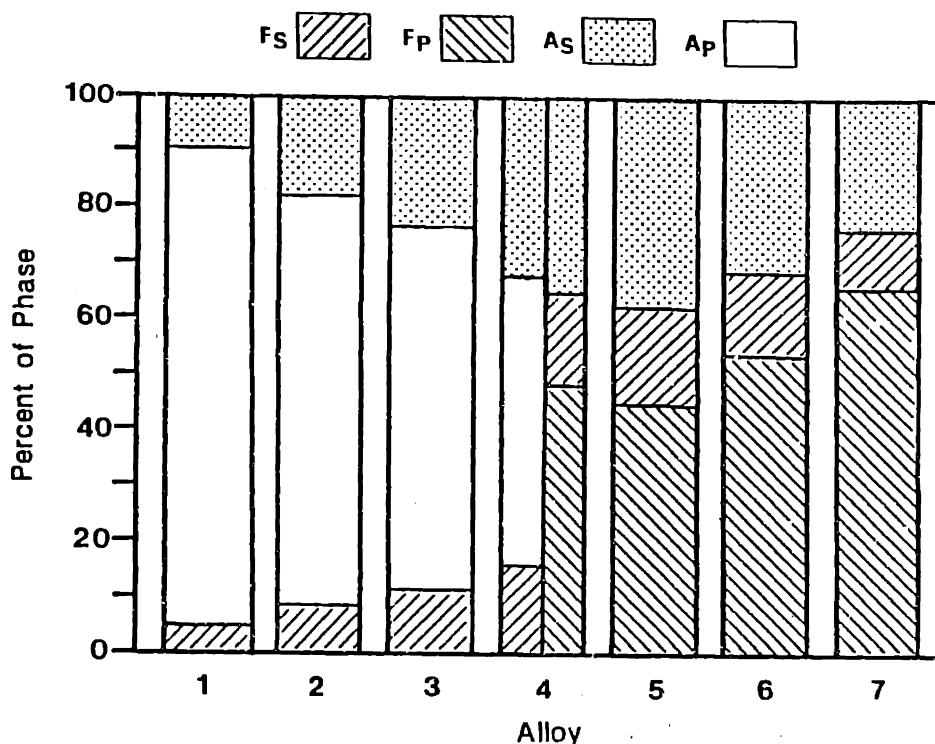


Figure 7.18 Results of the solidification segregation model showing the relative amounts of ferrite and austenite that solidify at intermediate cooling rates in electron beam melt No. 4. The calculations were performed for both primary phases in Alloy 4.

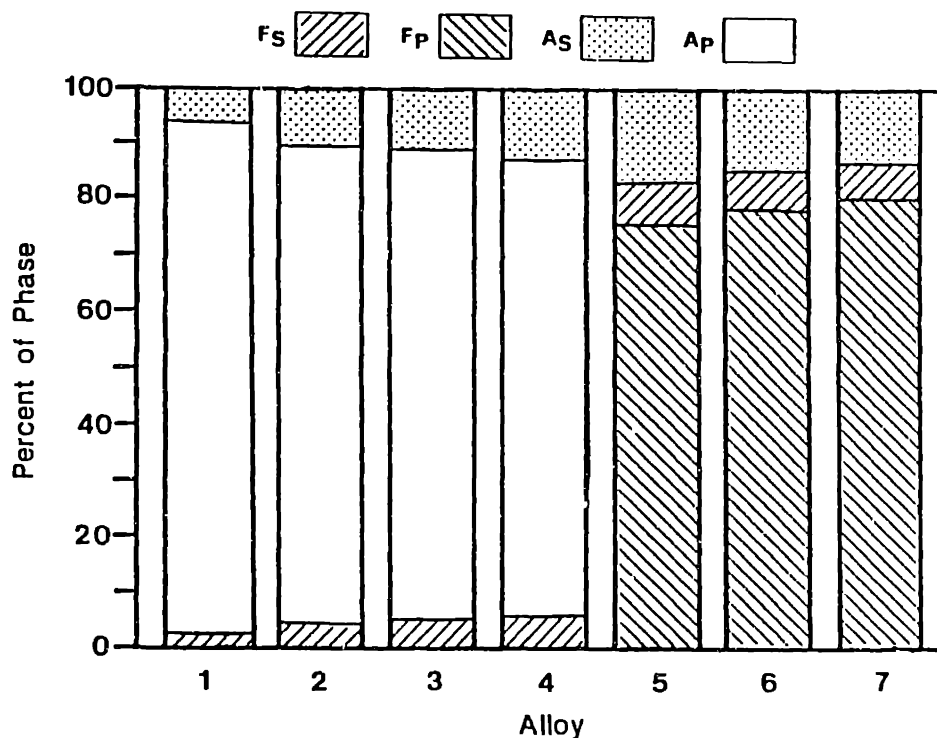


Figure 7.19 Results of the solidification segregation model showing the relative amounts of ferrite and austenite that solidify at high cooling rates in electron beam melt No. 6. The primary mode of solidification changes from primary austenite to primary ferrite between Alloys 4 and 5.

Of the seven solidification conditions, the casting shows the highest amount of second phase formation. As expected, the segregation calculations for the casting are similar to the results predicted by the Scheil equation which were presented in Figure 7.15. In the casting, the calculations indicate that for the primary austenite solidified alloys 1, 2 and 3, the amount of primary phase austenite decreases and the amount of second phase ferrite increase with increasing Cr/Ni ratio. This results in a maximum second phase ferrite content of about 15% in alloy 3 as compared to about 23% predicted by the Scheil equation. For the primary ferrite solidified alloys 4, 5, 6 and 7, the amount of primary phase ferrite increases with Cr/Ni ratio at the expense of second phase austenite. The total ferrite content of these alloys increases from 51% in Alloy 4 to 74% in Alloy 7 as compared with the range of 37% to 73% predicted by the Scheil approach.

The major difference between the Scheil approximation and the castings is in the reduction in the amount of second phases that form. These differences become most apparent when comparing Alloys 3 and 4 which have similar compositions but have different primary modes of solidification. Where the Scheil equation predicts a small increase in the total ferrite content between Alloys 3 and 4 (13%), the segregation calculations for the casting show a larger increase (36%). This discontinuity (the difference in total ferrite content between the primary austenite and primary ferrite solidified alloys) increases as the cooling rate increases and is responsible for the alloys solidifying in either the fully ferritic mode or fully austenitic mode at high cooling rates.

The solidification segregation calculations for EB melt 2 at 25 mm/s and EB melt 6 at 5,000 mm/s are represented by Figures 7.18 and 7.19 respectively. The influence of cooling rate on the phase which forms can be seen by comparing the results for the casting (7°C/s), a 25 mm/s melt ($1.9 \times 10^3^{\circ}\text{C/s}$) and the 5 mm/s melt ($7.5 \times 10^6^{\circ}\text{C/s}$). The amounts of primary phase increase and the amounts of secondary phase decrease which creates the discontinuity in total ferrite content between the primary ferrite and primary austenite solidified alloys. At the highest cooling rate, this discontinuity was calculated to be 77% between Alloys 4 and 5. However, the electron beam resolidification experiments show Alloy 4 to be fully austenitic and Alloy 5 to be fully ferritic at this speed, i.e., the discontinuity in ferrite content is actually 100%.

The difference between the calculations and experimental observations at high

cooling rates is most likely caused by the approximations that were made in deriving the pseudobinary diagrams or in the approximations made in estimating the interface velocity for the high scan speed melts. The fact that no second phase formation is observed in the high speed melts suggests that these alloys are being undercooled to a temperature where single phase solidification can occur, i.e., below the solidus temperature and into the stable (or metastable) single phase region. The necessary undercooling to bring the alloy into the single phase region can be defined as $T_L - T_S$ and is a function of alloy composition. Table 7.9 summarizes $T_L - T_S$ for each of the alloys and compares these values to the undercoolings calculated for the casting, EB melt 2 and EB melt 6. In the highest speed melt, where single phase solidification behavior was observed, the undercoolings that were calculated fall 10 to 15°C above the calculated solidus temperature. Therefore, it is apparent that either the calculated solidus temperatures are too low or the amount of undercooling calculated at the dendrite tip is too low. However, since approximations were made in deriving the pseudobinary diagrams and since approximations were made in the dendrite tip calculations, either one might be in error and additional analysis would need to be performed to specify the solidification conditions more precisely.

Table 7.9: Comparison of the solutal undercooling with the undercooling necessary to reach the solidus temperature.

Alloy	$T_L - T_S$ (°C)	ΔT_c		
		Cast (°C)	E-B 2 (°C)	E-B 6 (°C)
1	31.3	7.3	12.4	22.2
2	34.0	7.6	12.8	23.8
3	35.0	7.8	13.5	24.6
4-A	35.7	8.0	13.9	25.0
4-F	41.0	6.8	12.9	25.5
5	37.1	6.8	12.0	23.0
6	35.6	6.5	11.5	22.8
7	33.0	6.2	11.0	21.9

7.5 Summary and Conclusions

Solidification paths were calculated for primary ferrite and primary austenite solidification conditions. These paths were used to determine pseudobinary diagrams through the Fe-Ni-Cr system to allow the solidification behavior of the ternary alloys to be treated like binary alloys. These diagrams are shown in Figures 7.4 and 7.5 and represent significant improvements over the constant Fe sections that have been used in the past to illustrate the solidification behavior of stainless steel alloys.

Average temperature gradients and average interface velocities were calculated for each of the solidification conditions used in this investigation. These parameters were then used to calculate the dendrite tip radius, and dendrite tip undercooling for each alloy and each solidification condition using a constrained dendrite growth model. The results of these calculations showed that the solutal undercooling varies from about 5°C to about 30°C as the cooling rate is increased from the casting (7°C/s) to the highest speed electron beam melt (7.5×10^6 °C/s).

Based on the minimum in the Peclet number versus interface velocity curves, predictions were made for the cellular to dendritic transition as a function of growth rate and temperature gradient. These calculations were compared with the microstructures from each melt to show that the calculations appeared to be off by a constant multiplying factor. The difference in calculated and experimental behavior was rationalized by the uncertainties in the cellular to dendritic transition theory and in the uncertainties used in developing the assumptions for calculating the dendrite tip characteristics.

Solutal undercooling at the dendrite tip results in an increase in the amount of primary phase and a reduction in the amount of secondary phase that solidifies from the melt. This factor was taken into account to predict the relative amounts of primary and secondary phases which solidify for each of the solidification conditions.

The results of the solute redistribution calculations clearly show the influence that cooling rate has on the microstructure. At low cooling rates, there is a continuous increase in the total ferrite content with Cr/Ni ratio of the alloy. The calculations at slow cooling rates are confirmed by the Scheil predictions and by the general trend in ferrite content measured on the arc cast buttons. As the cooling rate

is increased, the calculations indicate a discontinuity in the total ferrite content which develops between the primary ferrite and primary austenite solidifying alloys. The calculations show that this discontinuity reaches 77% between Alloys 4 and 5 in the highest speed melt, i.e., these results indicate that Alloy 5 should solidify with 77% more ferrite than Alloy 4 in EB melt 6.

The calculated discontinuity in ferrite content helps to explain the single phase nature of the high speed electron beam melts. At high speeds, the reduction in the amount of the second phase that forms is so severe that the alloys solidify in the fully austenitic or fully ferritic mode depending on their PSM. Although the calculations do not predict pure single phase behavior, they do show the trend which explains the experimental observations. The difference between the calculations and the experiments is a result of the approximations made in deriving the pseudobinary diagrams and made in the dendrite tip calculations.

CHAPTER 8

The Influence Of Cooling Rate On The Solid State Transformation Of Ferrite

Metallographic analysis of the electron beam melts was presented in Chapter 5 to illustrate the complex microstructures which develop during the resolidification of stainless steels. These observations indicate that the ferrite which forms during the FA or AF modes of solidification transforms by the diffusion controlled growth (DCG) of preexisting austenite at the ferrite/austenite interface. However, for alloys that solidify in the fully ferritic mode, nucleation of austenite from the ferrite matrix must precede its growth. For these cases, the transformation of ferrite was shown to occur by: 1) the growth of massive austenite, which was limited to alloy 5 and was only observed at high cooling rates, and 2) the growth of Widmanstatten austenite platelets or needles from grain boundary allotriomorphs.

Qualitative analysis of the conditions responsible for the different transformation mechanisms was used to develop the microstructural map of the microstructures shown in Fig. 5.15. This figure shows the cooling-rate and compositions ranges where each transformation mechanism was observed. In this chapter, the empirical observations which were formulated in the previous chapters are studied through the quantitative application of nucleation and growth kinetic analysis applied to the transformation of ferrite in the resolidified melts.

The growth kinetics of ferrite are discussed in two models. The first model is a first order approximation to the diffusion equation, applied to the continuous cooling characteristics of the electron beam surface melts. This model correlates well with the experimental observations and was useful in describing the amount of transformation that occurs as a function of cooling rate for DCG conditions. A more careful analysis of the diffusion problem requires a numerical model to incorporate the complexities of ternary alloy diffusion and the moving boundary nature of the transformation. A mathematical formulation of this problem was developed

specifically for the Fe-Ni-Cr system. When coupled with the thermodynamic equilibrium at the ferrite/austenite interface, this approach can be used to predict the rate and extent of the transformation as a function of cooling rate.

The microstructures which develop during cooling of fully ferritic solidified Fe-Ni-Cr alloys were shown to be analogous to the microstructures which develop during the decomposition of austenite in the Fe-C system. This analogy proved to be useful in understanding the kinetics of the ferrite transformation by providing the wealth of analysis which has been performed on the Fe-C system to be applied to the Fe-Ni-Cr system. Experimental studies of the ferrite to austenite transformation were also conducted on fully ferritic specimens to determine the transformation rate at different temperatures. These results were analyzed by the Johnson-Mehl and Avrami approach to determine the transformation kinetics, and to estimate the influence of cooling rate on the amount of transformation.

8.1 Diffusion Controlled Growth

8.1.1 A First Order Approximation

The solid state transformation of ferrite occurs as the alloy is cooled through the F+A two phase field. Orientation of the tie-lines in the Fe-Ni-Cr system shows that the partitioning of Ni and Cr occurs along constant Fe isopleths at temperatures near the solidus. As the alloy cools, the ferrite which forms during solidification begins to transform by the diffusion of Cr to the ferrite and Ni to the austenite. The rate at which this transformation takes place is governed by the rate at which the slowest moving element can diffuse from the austenite/ferrite interface.

Diffusion coefficients have been measured for Fe, Cr and Ni in ferrite and austenite [8.1-8.8] and the results are summarized in Table 8.1 and 8.2. These results suggest that the diffusion occurs at a slower rate in austenite than in ferrite and that, in general, Ni diffuses at a slower rate than Cr. Therefore, estimations of the transformation rate can be made assuming D_{Ni} controls the reaction.

The reported rates for diffusion of Ni in austenite show that the activation

energy tends to decrease as the alloy content of the stainless steel increases. D_{Ni} has a measured activation energy, Q , of about 65 kcal/mole and a preexponential constant, D_o , of about $5 \times 10^{-5} \text{ m}^2/\text{s}$:

$$D_{Ni}^A = D_o \exp[-Q/RT] \quad (8.1)$$

where R is the gas constant and T is the temperature in Kelvin. This results in a diffusivity of about $9 \times 10^{-14} \text{ m}^2/\text{s}$ at 1350°C .

Table 8.1: Volume diffusion in BCC Ferrite

Element	Alloy	Q (kcal/mole)	D_o ($\text{m}^2 \times \text{s}^{-1}$)	Ref.
Fe	-	-	-	-
Ni	Pure Fe	62.7	9.7×10^{-4}	8.1
	Pure Fe	56.0	1.3×10^{-4}	8.2
	Fe-2.0Cr	63.4	1.2×10^{-5}	8.3
	Fe-10Cr	65.6	3.6×10^{-5}	8.3
	Fe-20Cr	53.6	7.0×10^{-7}	8.3
Cr	Pure Fe	57.3	2.4×10^{-4}	8.4
	Fe-25Cr-5Ni	50.7	6.0×10^{-6}	8.5, 8.8

Table 8.2: Volume diffusion in FCC Austenite

Element	Alloy	Q (kcal/mole)	D_o ($\text{m}^2 \times \text{s}^{-1}$)	Ref.
Fe	Fe-17Cr-12Ni	66.8	3.6×10^{-5}	8.6
Ni	Pure Fe	67.0	7.7×10^{-5}	8.2
	Fe-9Ni	66.4	5.0×10^{-5}	8.3
	Fe-10Ni	65.4	4.1×10^{-5}	8.3
	Fe-17Cr-12Ni	60.1	9.0×10^{-7}	8.7
Cr	Pure Fe	60.3	6.3×10^{-6}	8.4
	Fe-17Cr-12Ni	63.1	1.3×10^{-5}	8.6
	Fe-17Cr-12Ni-3Mo	58.1	6.3×10^{-6}	8.5, 8.8

A first order approximation of the amount of transformation that occurs during cooling in the resolidification melts can be estimated from the above diffusivity of nickel in austenite and the characteristic diffusion distance, L :

$$L \sim 2(D\Delta t)^{1/2} \quad (8.2)$$

Where Δt represents the transformation time and is inversely related to the cooling rate, ϵ , and the temperature range over which transformation is occurring, ΔT :

$$\Delta t = \frac{\Delta T}{\epsilon} \quad (8.3)$$

Since equation 8.2 is nonlinear, a numerical approach is required to calculate the amount of diffusion that occurs as the alloy cools to room temperature. By selecting a small temperature range, ΔT , estimating the diffusivity, D_{Ni} , using equation 8.1 and estimating the transformation time, Δt , over this temperature range using equation 8.3, the product $D_{Ni}\Delta t$ can be determined. The characteristic diffusion distance, L, can then be calculated from the summation of $D_{Ni}\Delta t$ by the following equation:

$$L = 2 \left(\sum_{T=T_s}^{T-25^\circ C} D_{Ni}(T) \left(\frac{\Delta T}{\epsilon} \right) \right)^{1/2} \quad (8.4)$$

The diffusivity of nickel in austenite was assumed to be the rate limiting factor and the continuous cooling characteristics of the E-B process were taken into account in calculating the diffusion distance by using equation 8.4 with a temperature increment of 1°C. The results of these calculations are summarized in Table 8.1 for each of the cooling rates studied in this investigation. The largest degree of transformation was observed in the casting which required 197s to reach room temperature while the least amount of transformation was observed in the highest speed electron beam melt which required only 1.9×10^{-4} s to reach room temperature. This difference in cooling rates reduced the characteristic diffusion distance from 2.9 μm for the casting to 2.8×10^{-3} μm for the highest speed melt.

During cooling, the percentage of ferrite that transforms is related to the characteristic diffusion distance and the thickness of the ferrite particles. Both L and the dendrite arm spacing, λ , decrease with increasing cooling rate. However, since the characteristic diffusion distance is proportional to $\Delta T^{0.5}$ and since the dendrite arm spacing is proportional to about $\Delta t^{0.2}$, L decreases faster than λ with increasing cooling

rate. Therefore, as the cooling rate is increased, less percentage of the ferrite in the microstructure transforms, i.e., the solidification microstructure becomes "quenched in" at high cooling rates. This fact becomes obvious by comparing the ratio of L to λ which is shown in Table 8.3 to decrease from 16.0% in the casting to 0.7% in the highest speed E-B melt.

Table 8.3: Characteristic diffusion distance and dendrite arm spacings.

Melt	Cooling Rate ($^{\circ}\text{C/s}$)	Time to Reach RT (s)	Diffusion Distance, L (μm)	λ_1 (μm)	λ_2 (μm)	L/λ
Cast	7	197	2.9	-	18	1.6×10^{-1}
1	4.7×10^2	2.9	0.35	-	4.7	7.5×10^{-2}
2	1.9×10^3	7.3×10^{-1}	0.17	-	3.0	5.7×10^{-2}
3	1.7×10^4	8.2×10^{-2}	5.8×10^{-2}	3.2	-	1.8×10^{-2}
4	4.4×10^5	3.2×10^{-3}	1.1×10^{-2}	1.1	-	1.0×10^{-2}
5	1.5×10^6	9.2×10^{-4}	6.1×10^{-3}	0.7	-	8.7×10^{-3}
6	7.5×10^6	1.9×10^{-4}	2.8×10^{-3}	0.4	-	7.0×10^{-3}

The percentage of the microstructure that transforms can be calculated for each cooling rate. Figure 8.1 illustrates a simple model that can be used to predict the amount of transformation. The secondary dendrite arms are assumed to be equally spaced right circular cylinders and the distance between the ferrite particles is equal to the secondary arm spacing. To account for second phase austenite between the ferrite dendrites, the diameter of the initial ferrite 'cylinder' before transformation was metallographically measured on several specimens to be about 2/3 of this spacing. Taking this factor into account, the percentage of ferrite that transformed can be approximated by the ratio of areas before and after transformation:

$$\% \text{ Transformed} = \left(\frac{r^2 - (r-L)^2}{r^2} \right) \times 100 \quad (8.5)$$

where r refers to the radius of the ferrite dendrite (2/6 DAS), and L is the characteristic diffusion distance reported in Table 8.3

Table 8.4 summarizes the ferrite transformation calculations and the results show that 73.3% of the ferrite that solidifies in the castings will transform while only 4.0% of the ferrite that solidifies in the highest speed electron beam melt will transform. Therefore, the residual ferrite content of primary ferrite solidified alloys should increase as the cooling rate increases. This behavior was observed in the actual electron-beam melts. For example Alloy 7 which solidifies in the fully ferritic mode has a measured ferrite content of 32 percent in the cast condition which indicates that 68% of the microstructure has transformed. This measured value compares favorably to the predicted value of 73.3%.

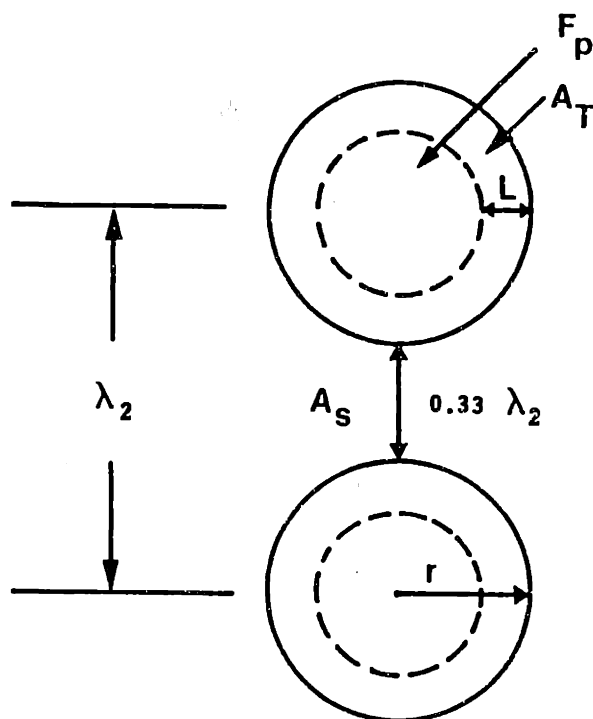


Figure 8.1 Illustration of a model to predict the percentage of ferrite in the microstructure that transforms for a given characteristic diffusion distance, L .

Table 8.4: The amount of ferrite that transforms as a function of cooling rate.

Melt	λ (μm)	r (μm)	L (μm)	% transformed
Cast	18	6.0	2.9	73.3
1	4.7	1.5	0.35	41.2
2	3.0	1.0	0.17	31.1
3	3.2	1.1	5.8×10^{-2}	10.3
4	1.1	0.27	1.1×10^{-2}	8.0
5	0.7	0.24	6.1×10^{-3}	5.0
6	0.4	0.14	2.8×10^{-3}	4.0

The transformation characteristics can also be observed by optical metallography. Figure 8.2 shows the microstructure of Alloy 4 which solidified in the FA mode in melt 1 at a cooling rate of 4.7×10^2 °C/s. Primary ferrite dendrites, Fig. 8.2a, and equiaxed ferrite cells, Fig. 8.2b, were present in the microstructure. This specimen was etched with a color metallographic technique that reveals 1) primary ferrite (white), 2) austenite that transformed from ferrite and envelops the primary ferrite core (dark grey), and 3) second phase austenite that solidified from the melt (light grey). The width of the transformed regions varies from about $0.5 \mu\text{m}$ to $1.0 \mu\text{m}$ which compares favorably to the calculated characteristic diffusion distance of $0.3 \mu\text{m}$.

8.1.2 Finite Difference Approach

Appendix D summarizes a mathematical model which can be used to solve the moving-boundary, ternary-alloy diffusion-controlled phase transformation problem. This formulation is an application of the finite difference form of Fick's second law and, since thermodynamic equilibrium must be maintained at the austenite-ferrite interface, the phase equilibria in the Fe-Ni-Cr ternary system must be coupled with the mass conservation and the kinetic equations governing diffusion. This method is sufficient to develop a computer program to predict the transformation rate and the extent of the ferrite to austenite phase transformation as a function of cooling rate.

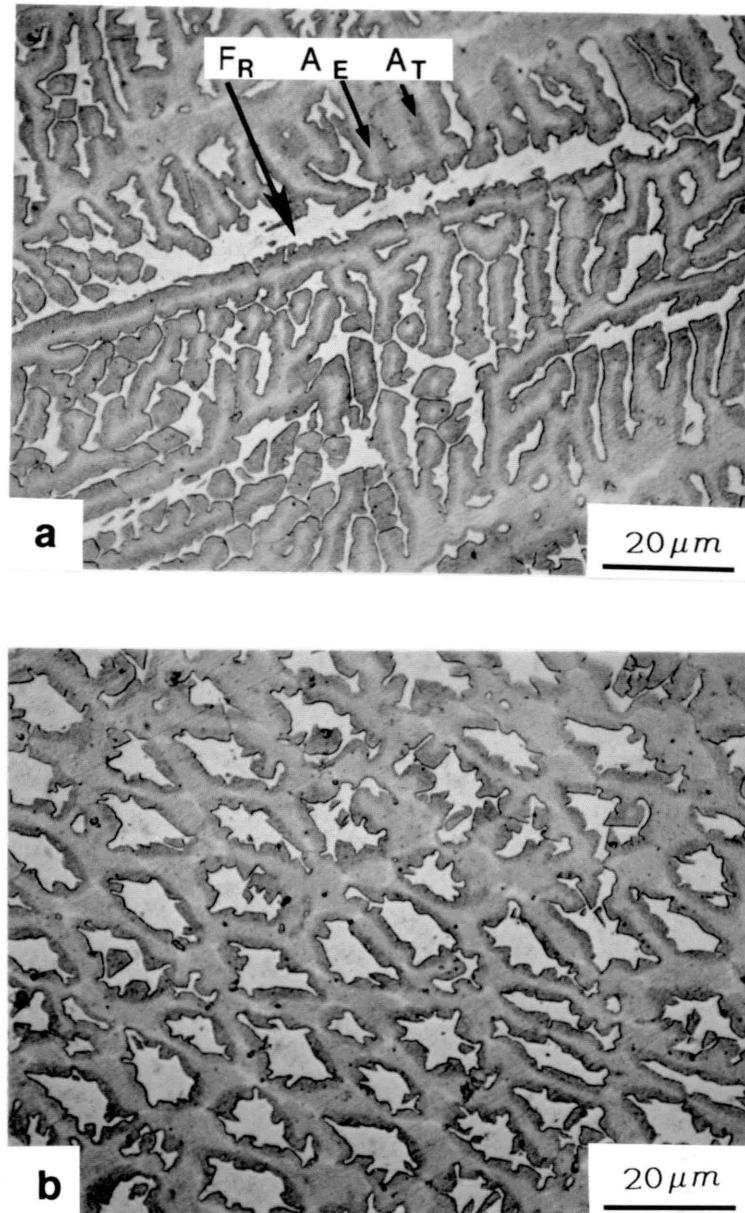


Figure 8.2 Color metallographic technique used to distinguish between the austenite which forms during solidification and the austenite which forms during transformation of ferrite. a) shows ferrite dendrites and b) shows ferrite cells, both from Alloy 4.

8.2 The Massive Transformation

Massive phase transformations change metastable phases to equilibrium phases or other metastable phases by a diffusional process that involves a rapid noncooperative transfer of atoms across a high-energy interface. These transformations are thermally activated and exhibit nucleation and growth characteristics but require only short range diffusion of a few atomic jumps to change one crystal structure to another. The cooling rates necessary for the massive transformation must be sufficiently rapid to suppress the formation of product phases that involve long range diffusion. The resulting massive transformation does not involve any change in the overall composition. This composition invariance is an important characteristic of the massive transformation and can be used to aid in its identification. Characteristic patches of the massively formed phase appear as blocks in the microstructure and exhibit ledge features, planar facets and twinning in some alloy systems. The large driving force for the transformation allows the product phase to cross grain boundaries and other obstacles.

The massive transformation was observed in Alloy 5 at high cooling rates but was not observed in any of the other alloys, even though they had similar compositions. One of the objectives of this chapter is to explain, through thermodynamic and kinetic arguments, the conditions for which the massive transformation occurs in the Fe-Ni-Cr system and use these results to show why the massive transformation was only observed in Alloy 5.

8.2.1 Microstructural Characteristics

At high cooling rates, Alloy 5 solidifies in the fully ferritic mode and upon cooling, transforms to a high volume fraction austenite by the growth of new austenite grains. This transformation has also been observed in a high purity 20Cr 10Ni bal. Fe alloy by Singh et al [8.9]. Although the nominal Fe content of their alloy was 70 wt.% and the nominal Fe content of Alloy 5 is 59 wt.%, both alloys have similar Cr/Ni ratios, 2.0 and 1.85 respectively, which places both alloys close to the line of two-fold saturation.

Figure 8.3 compares the microstructure of massively formed austenite in Alloy 5 with single phase ferrite in Alloy 7. The single phase ferrite microstructure is shown in Fig. 8.3 and indicates that the ferrite grain boundaries etch prominently and a cellular solidification "substructure" can be observed. This specimen is known to be fully ferritic because of its high value of saturation magnetization (107 emu/g).

The microstructure of Alloy 5, prior to the transformation, is single phase ferrite and should be similar in appearance to Fig. 8.3a. However, after the transformation, the microstructure is predominantly single-phase austenite grains and the grain boundaries tend to be aligned perpendicular to the solidification direction with a jagged appearance. Twinning is observed within the austenite grains and the specimen is known to have a high volume fraction austenite due to its low saturation magnetization (18 emu/g). The microstructure also shows that some ferrite is present at the austenite grain boundaries as a result of the incomplete transformation to austenite. This ferrite is responsible for what magnetic moment the specimen has; if the transformation to austenite had been complete, the saturation magnetization of the specimen would be zero.

To prove that the microstructures observed in Alloy 5 are indeed formed by the massive transformation, the composition invariance across the ferrite and austenite patches was determined by electron microprobe analysis. Figure 8.4a shows the microstructure at the root of melt 3. This melt was moving at 100 mm/s, has a solidification cell spacing of $3.2 \mu\text{m}$ and cooled at a rate of about $2000 \text{ }^\circ\text{C/s}$.

Two microhardness indentions were placed on the specimen and between these two indentions is an austenite/ferrite interface. The microprobe was used to measure the Fe, Ni and Cr compositions at $2 \mu\text{m}$ intervals with a $1 \mu\text{m}$ focal spot size. Figure 8.4b shows the results of these measurements and indicates that the average composition of the austenite phase is identical to that of the ferrite phase and that there does not appear to be a change in composition near the austenite/ferrite interface. This evidence indicates the composition invariance of the transformation and, along with the microstructural features, shows that Alloy 5 can transform to austenite by the massive transformation at high cooling rates.

8.2.2 Thermodynamics

It is known that the massive transformation can begin in the F+A two phase region at a temperature, T_0 , where the Gibbs free energy of the ferrite and austenite of the same compositions are equal. However, experimental evidence exists to show that the effective start temperature for the transformation requires additional undercooling so that the nucleation temperature is closer to the austenite solvus [8.10]. Therefore, the alloys which are susceptible to the massive transformation tend to be located close to the line of two-fold saturation to minimize the amount of undercooling required to bring the alloy close to the austenite solvus.

Figure 8.5 plots the composition of the seven alloys on a vertical section through the Fe-Ni-Cr ternary phase diagram. This vertical section was taken along a composition path that represents the partitioning of Ni and Cr at temperatures just below the solidus temperature of these alloys, i.e., the 1400°C tie lines in the F+A two-phase field lies in the plane of Fig. 8.5 and was determined from the isothermal sections presented in Appendix C. As mentioned in Chapter 7, there is a difference in the location of the line of two-fold saturation calculated by Thermocalc and the experimental observations. Since the relative location of the alloys with respect to the line of two-fold saturation is important, this difference was taken into account by shifting the position of the seven alloys by subtracting 2.8% Ni from each composition before plotting them on the diagram. With this adjustment, the thermodynamic calculations can be correlated directly with the experimental observations.

The location of the T_0 line can be determined from the Gibbs free energy versus composition plots in the Fe-Ni-Cr system. These calculations were also performed using Thermocalc and the results for 58wt.% Fe alloys are shown in Fig. 8.6 at 1300°C and 1375°C. The T_0 composition is defined where the free energy of the ferrite and austenite of the same compositions are equal. These two points that were calculated from Fig. 8.6 can be used to estimate the T_0 line in the ferrite + austenite two phase field.

The T_0 line is indicated in Fig. 8.5 and is located approximately midway between the ferrite and austenite solvus lines. This figure indicates that T_0 rapidly decreases in temperature with small changes in composition.

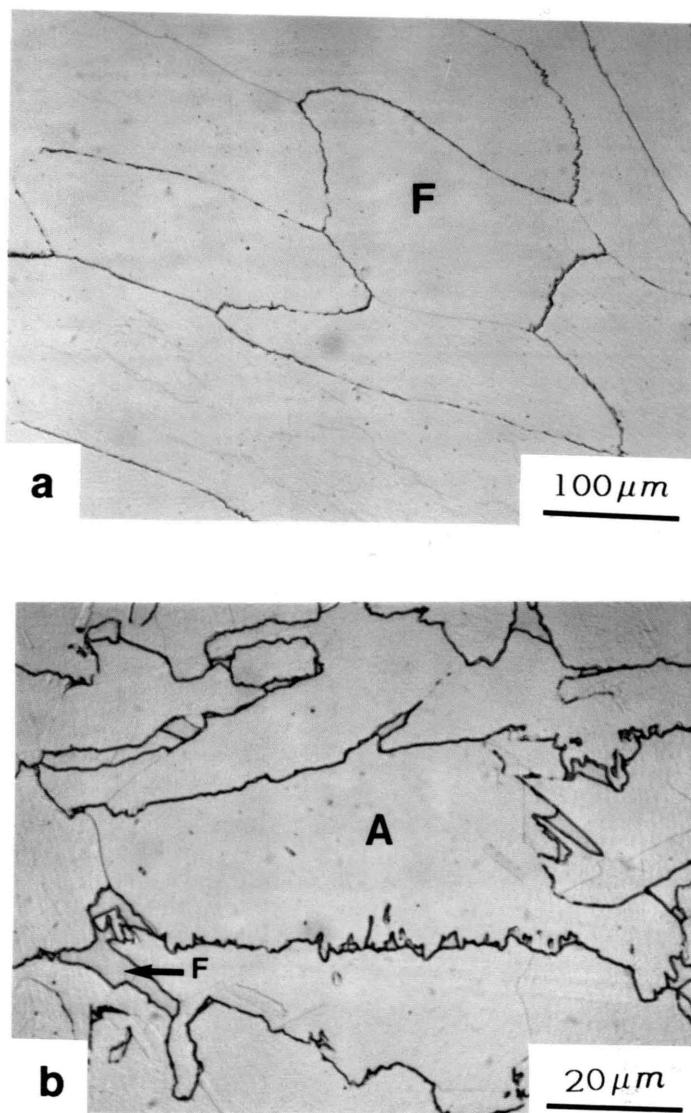


Figure 8.3 Comparison of a) The single phase ferrite microstructure and b) massive austenite which transformed from single phase ferrite in Alloy 5.

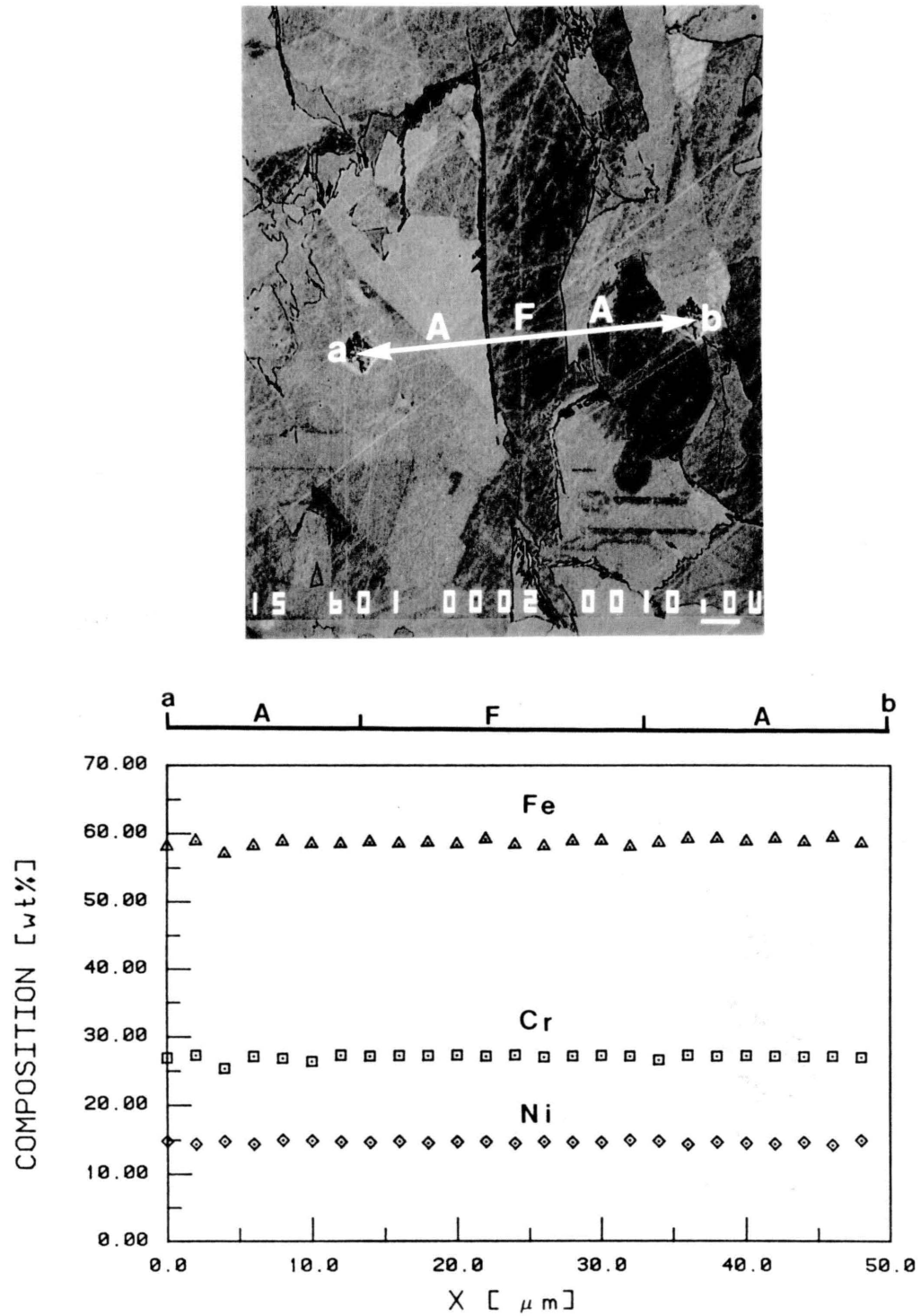


Figure 8.4 Electron microprobe scan across an untransformed ferrite region, surrounded by massive austenite in Alloy 5. The results indicate the composition invariance of the massive transformation. F refers to the ferrite phase and A refers to the austenite phase.

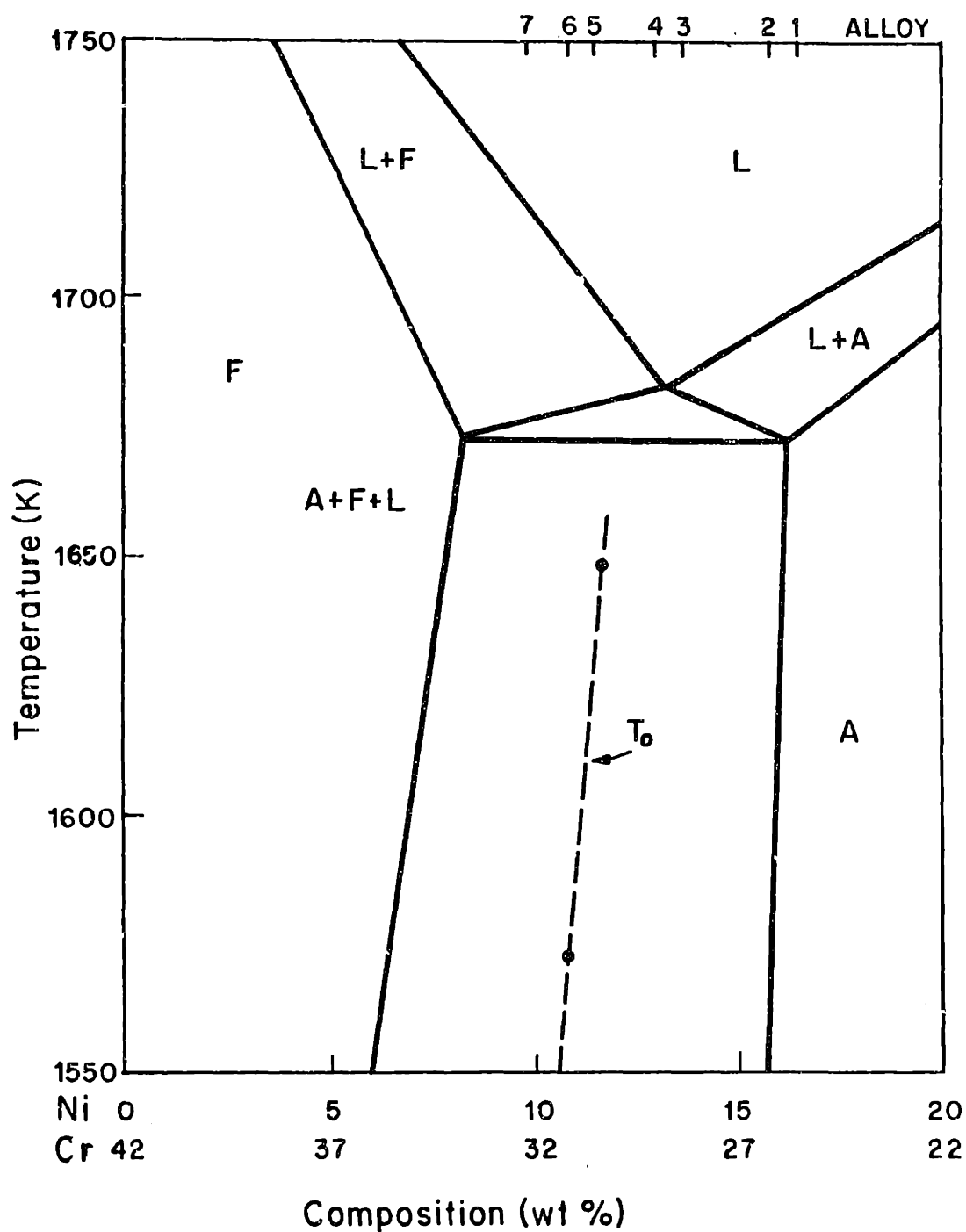


Figure 8.5 Thermodynamically calculated vertical section through the Fe-Ni-Cr diagram along a path that represents partitioning in the F+A two-phase field. Equivalent compositions of the seven alloys are indicated and the T_0 line in the F+A region was calculated at 1575 and 1650 K.

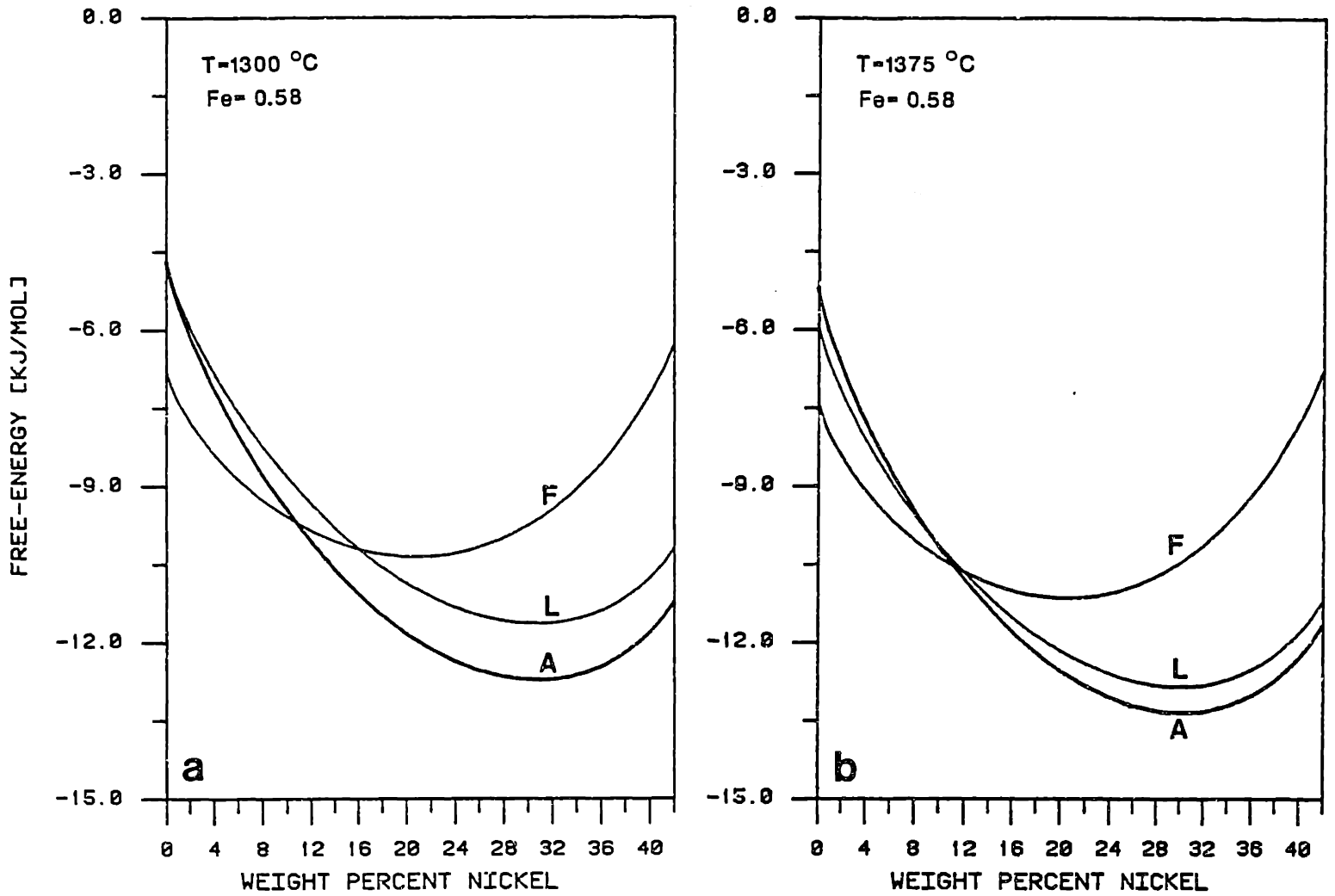


Figure 8.6 Gibbs free energy versus composition plots along the 58 wt% Fe isopleth. a) at 1300°C, b) at 1375°C.

For example, a 1% change in nickel content, drops the T_o temperature 85°C, therefore, Alloys 5, 6 and 7 which solidify in the fully ferritic mode at high cooling rates have significantly different T_o temperatures even though their compositions are similar. Defining ΔT_s to be undercooling required to bring the alloy from its solidus temperature to the T_o temperature, ΔT_s will be an indication of how much undercooling is necessary for the massive transformation to become feasible.

ΔT_s was determined to be 31°C, 101°C and 186°C for Alloys 5, 6 and 7 respectively. Additional undercooling would be required to bring these alloys closer to the austenite solvus temperature where the massive transformation is most likely to occur. However, the trend in undercooling, required to nucleate massive austenite, will be the same: Alloy 5 will require the least undercooling and Alloys 6 and 7 will require significantly more undercooling to bring about the massive transformation.

8.2.3 Nucleation Kinetics

The rate at which the alloy cools through the austenite + ferrite two phase field is largely responsible for the amount of undercooling prior to the nucleation of austenite. At slow cooling rates, nucleation of Widmanstatten platelets occurs before the temperature reaches T_o , i.e., there is insufficient undercooling at slow cooling rates for the massive transformation to occur because it is superseded by the formation of Widmanstatten austenite. At higher cooling rates, nucleation of Widmanstatten austenite can be prevented because of the reduced time available for Widmanstatten austenite nucleation. Under these conditions, the temperature drops to larger undercoolings before the austenite nucleates. The massive transformation of Alloy 5 was observed in the high cooling-rate portion of melt 2 and in all of the higher cooling rate melts. This places the necessary cooling rate for the massive transformation at about 2×10^3 K/s and greater for the 26.4 Cr, 14.3 Ni alloy.

The nucleation kinetics [8.11] and growth kinetics [8.12] of the massive transformation have recently been reviewed. A relationship between the cooling rate and the undercooling for nucleation can be derived from the classical approach. The resulting expression relates the undercooling below ΔT_M ($\Delta T_M = T_o - T_M$) to the cooling rate as follows:

$$\Delta T_M = (T_o - T_M) = \left(\frac{\epsilon}{C} \right)^{1/2} \quad (8.6)$$

where ϵ is the cooling rate C is a material-dependent and embryo-geometry-dependent constant [8.11] and T_M is the nucleation temperature for massive austenite. Therefore, larger undercoolings precede the transformation at higher cooling rates.

In order to explain why Alloy 5 undergoes the massive transformation while Alloys 6 and 7 do not, the effect of composition on the nucleation kinetics of austenite must be examined. From the classical nucleation theory, applied to nucleation at grain boundaries during isothermal transformation [8.13], one can derive the following relationship for the nucleation rate, J^* :

$$J^* = Z\beta^*N\exp\left[\frac{-\Delta G^*}{kT}\right]\exp\left[\frac{-\tau}{t}\right] \quad (8.7)$$

where Z is the Zeldovich nonequilibrium factor relating the percentage of atoms which attach to the number of attempts, β^* is the rate at which individual atoms attempt to attach to the critical nucleus, N is the number of atomic sites per unit volume, ΔG^* is the free energy for the formation of a critical nucleus, τ is the incubation time, t is the isothermal hold time and kT has its usual meaning.

The most important factor in equation 8.7 is the free energy of formation of the critical nucleus which is related to the volume free energy change ΔG_v and the strain energy ΔG_s as follows:

$$\Delta G^* = \frac{16\pi\sigma_{\delta\gamma}^3 k}{3(\Delta G_v + \Delta G_s)^2} \quad (8.8)$$

where k is a factor related to the geometry of the embryo and $\sigma_{\delta\gamma}$ is the interfacial energy between the ferrite and austenite phases. Alloys 5, 6 and 7 differ only slightly in composition, therefore, only $\Delta G_v = C\gamma - C\delta$ changes significantly between these alloys.

The free energy versus composition curve for 59 % Fe alloys at 1250°C is shown in Fig. 8.7. In addition to predicting the T_0 temperature, these curves can be used to estimate the difference in free energy for the ferrite to austenite transformation as a function of composition. At 1250 °C Alloy 5 is 119 °C below its T_0 temperature and $\Delta G_v = -150$ J/mole, Alloy 6 is 49°C below its T_0 temperature and $\Delta G_v = -20$ J/mole. Finally, Alloy 7 is 36 °C above its T_0 temperature and therefore has no driving force for the massive transformation.

The results of the electron beam melting experiments confirm these calculations. At low cooling rates the massive transformation was superseded by the formation of Widmanstatten austenite. At higher cooling rates, nucleation of Widmanstatten austenite platelets was suppressed and the massive transformation was observed in alloy 5 which has the largest ΔG_v for the nucleation at any given amount of

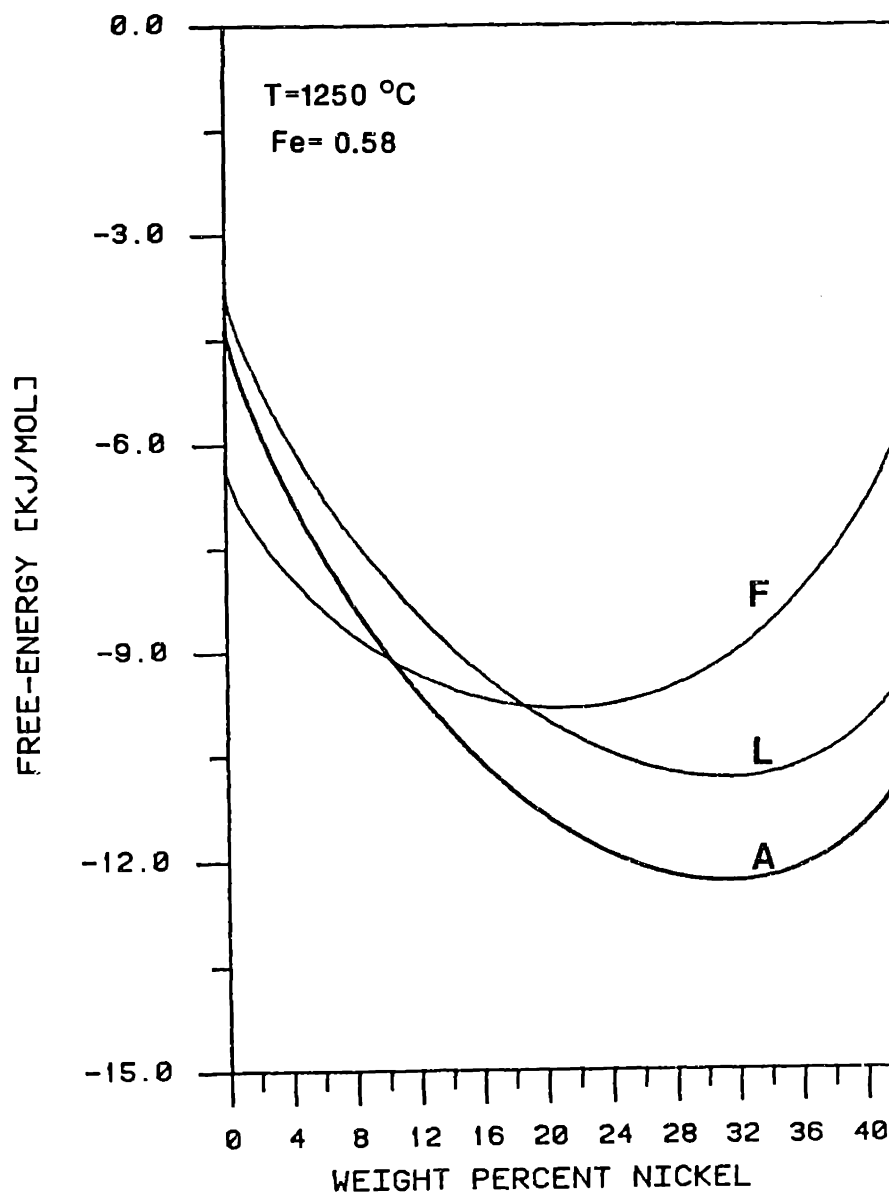


Figure 8.7 Gibbs free energy versus composition plot along the 58 wt.% Fe isopleth showing the volume free energy change for ferrite transforming to austenite in Alloy 5.

undercooling. However, Alloys 6 and 7 apparently did not have sufficient driving force for the nucleation of massive austenite and remained fully ferritic under all of the high cooling rate conditions.

8.2.4 Growth Kinetics

The massive transformation has been observed to grow at very rapid rates in many alloy systems [8.12]. The high growth rates are the result of 1) the high thermodynamic driving force for the transformation which is nearly proportional to the degree of undercooling below T_0 [8.12] and 2) the nature of atomic transfer across the interface which involves a noncooperative rearrangement of atoms involving only a few atomic jumps to change the crystal structure [8.12]. Because of the high growth rates, characterization of the interface velocity, R , is difficult, however, the measurements that have been made show that R is on the order of 1 to 10 mm/s in the Ag-Al system [8.12].

The relationship between undercooling and interface velocity has been studied by Perepezko [8.12] and the results show that the behavior at low undercoolings and high undercoolings are different. At low undercoolings ($\Delta T < 10^\circ\text{C}$ in the Ag-Al system) the results were interpreted by a step growth model. For the case of step formation limiting the reaction rate, the following expression was developed:

$$R = h\nu \exp\left[\frac{(\pi e^2 T_0)}{(3h\Delta H \Delta T kT)}\right] \quad (8.9)$$

where h is the step height and e is the energy per unit edge length of step. This relationship predicts a nearly linear increase in velocity with R and agrees with experiments at low undercoolings. At high undercoolings, the interface velocity increases but at a decreasing rate with undercooling. This behavior is better modeled by a continuous growth expression which can be taken to be:

$$R = M \Delta G_v \quad (8.10)$$

where M is the interface mobility. M and ΔG_v tend to be compensating factors and at high undercoolings where ΔG_v is large, the mobility is low and limits the interface velocity to about 10 mm/s in Ag-24.5% Al alloys.

8.2.5 Massive Austenite Summary

The ferrite content of Alloy 5 can be used as a measure of the degree to which the massive transformation has occurred in each of the electron beam melts. In Chapter 6, ferrite measurements were presented to indicate the total amount of ferrite present in each melt. The results are resummarized in Table 8.5. In this Table, A_w and A_m refer to the percentage of the fully ferritic solidified areas that transformed to Widmanstätten and massive austenite respectively, while F_u refers to the amount of untransformed single-phase ferrite. The microstructures of these melts are shown in Fig. 8.8 to illustrate the regions of massive austenite (light areas) and the regions of Widmanstätten austenite (dark areas)

Table 8.5 Percentage of massive and Widmanstätten austenite that forms in the fully ferritic solidified portions of the electron beam melts in Alloy 5.

melt	ϵ	% Phase		F_u
		A_m	A_w	
1	4.7×10^2	0	100	0
2	1.9×10^3	10	85	5
3	1.7×10^4	30	65	5
4	4.4×10^5	85	0	15
5	1.5×10^6	75	0	25
6	7.5×10^7	70	0	30

8.3 The Decomposition of Single Phase Ferrite

Section 8.1 discussed the transformation of ferrite by the diffusion controlled growth of pre-existing austenite which forms during the AF and FA modes of solidification. Because the austenite was present prior to the solid state transformation, nucleation was not required and the morphology of the resulting microstructure was controlled by the solidification conditions.

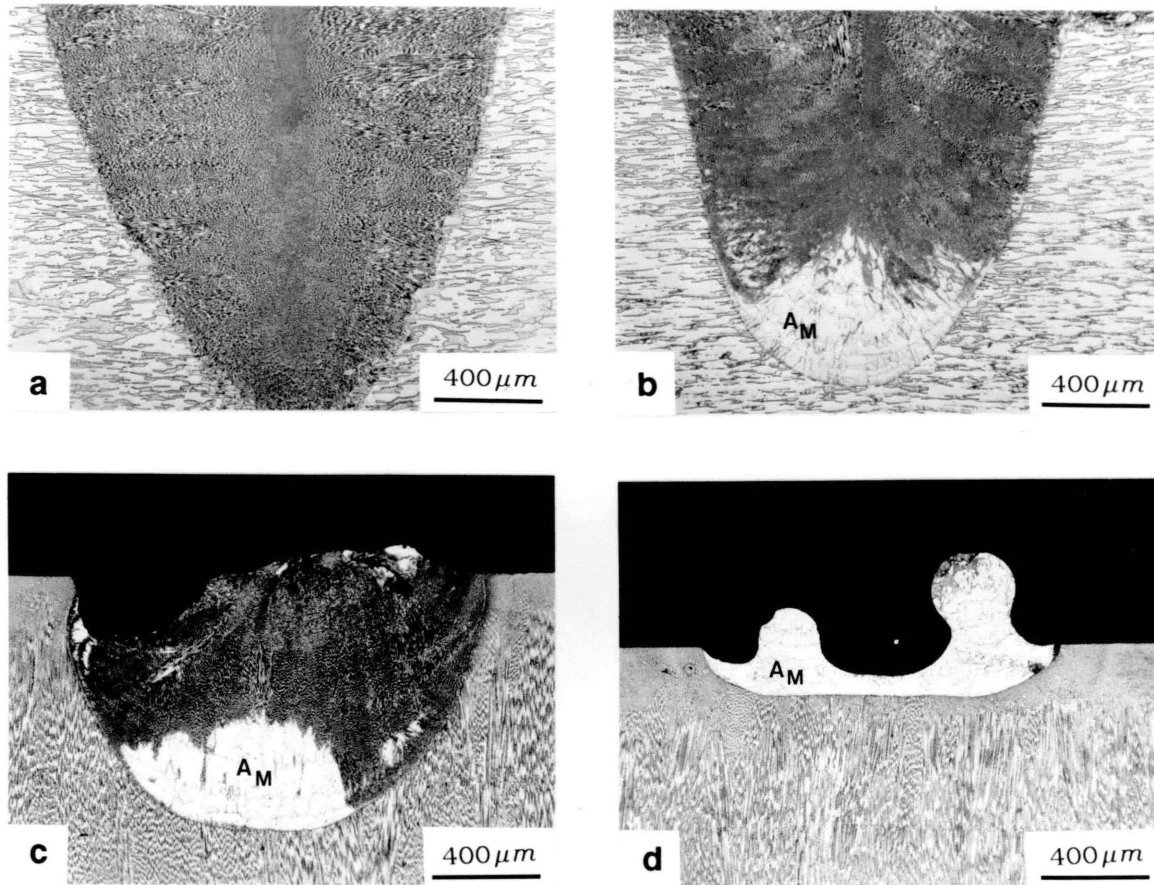


Figure 8.8 The influence of scan speed on the percentage of the melt which undergoes the massive transformation in Alloy 5. Massively transformed areas appear as white regions, while the remainder of the melt transforms by Widmanstatten austenite formation. a) 6.3 mm/s, b) 25 mm/s, c) 100 mm/s and d) 500 mm/s.

Section 8.2 discussed the massive formation of austenite which requires large thermal undercoolings to bring the transformation temperature below the T_0 temperature. Nucleation of austenite embryos occur and they rapidly grow by an interface-controlled reaction mechanism. Under these conditions, the microstructures which develop are equated with the nucleation rate rather than the growth kinetics of massive austenite. In this section, the decomposition of ferrite will be studied with reference to morphologies that require nucleation of austenite from a fully ferritic matrix but where the microstructure is controlled by diffusional growth mechanisms.

The morphologies that were observed in the Fe-Ni-Cr system can be directly equated with morphologies which develop in the Fe-C system. Grain boundary allotriomorphs, Widmanstätten sideplates, sideneedles and degenerate forms of the Widmanstätten morphologies were all observed in the electron beam welds of the high Cr/Ni ratio alloys. The analogy between the Fe-Ni-Cr and Fe-C system appears to be very good and allows the wealth of information about the Fe-C system to be applied to the less-studied Fe-Ni-Cr system.

In this section, the morphological features of the ferrite decomposition will be presented through the examination of the electron beam melts. Because of the large number of morphological features that were observed, detailed modeling of the nucleation and growth kinetics of each variation is not possible. However, general guidelines will be established to show how the diffusion controlled processes can be modeled for a simple sideplate geometry.

Isothermal transformation experiments were also conducted on fully ferritic specimens to monitor the transformation kinetics of the ferrite decomposition. The results of these experiments were analyzed by the Johnson-Mehl-Avrami approach which allows the effects of nucleation and growth to be combined into a single equation.

8.3.1 Morphological Classification

Many of the austenite morphologies that form during the decomposition of ferrite in the Fe-Ni-Cr system have a similar appearance to the ferrite morphologies which develop during the decomposition of austenite in the Fe-C system. In the Fe-Ni-Cr system it is the diffusion of Ni and Cr at the transformation interface which controls

the rate of growth while in the Fe-C system it is the diffusion of carbon which controls the rate of growth. Aside from the difference in mobilities between carbon and nickel or chromium, the solid state transformations that occur in these two systems are analogous. Therefore, the morphological classification system developed by Dube [8.14] and presented by Aaronson [8.15], to describe the Fe-C system morphologies, can be used to represent the Fe-Ni-Cr system as well.

Grain Boundary Allotriomorphs

Grain boundary allotriomorphs are crystals of the product phase which nucleate at grain boundaries and grow preferentially along the boundary. The allotriomorphs tend to have smooth shapes and provide heterogeneous nucleation sites for the other growth morphologies. Figure 8.9 shows typical austenite grain boundary allotriomorphs which form in the Fe-Ni-Cr alloys. The allotriomorphs are very common and are present at nearly all of the grain boundaries in the alloys that have undergone transformation and provide sites for Widmanstätten austenite growth.

Widmanstätten Plates

Widmanstätten sideplates are plate-shaped crystals that grow from the vicinity of grain boundaries into the interior of the grain and can be categorized as having either primary or secondary characteristics. Primary sideplates grow directly from the grain boundary and secondary sideplates develop from crystals of another morphology of the same phase. Secondary sideplates were by far the most commonly observed morphology in the Fe-Ni-Cr alloys and primary sideplates are not abundant. Figure 8.9 shows the sideplate morphology under high and low cooling rate conditions. At high cooling rates (8.9a) the sideplates do not have time to grow across the grain and they appear as finely spaced laths growing along crystallographically defined directions. At low cooling rates (8.9b), Widmanstätten sideplates grow across the entire grain and also coarsen as the melt cools to room temperature.

Widmanstätten plates may also nucleate and grow from the interior of grains. This intragranular morphology tends to be present in the Fe-Ni-Cr alloys which cool at low rates. Figure 8.9c shows the intragranular sideplate morphology. Mixed in with this microstructure are small intragranular blocks of austenite which are referred to as idiomorphs. Individual plates nucleate and grow along crystallographi-

cally defined directions as do the other platelet variants. These plates may provide nucleation sites for other plates and when combined with the sideplates growing from the grain boundaries, they provide an effective means for transforming a large volume fraction of the microstructure.

Widmanstatten Needles

Widmanstatten needles, which are sometimes referred to as acicular needles, are needle-shaped crystals which also can be categorized as having primary and secondary characteristics. Primary sideneedles are again the less dominant variation in the Fe-Ni-Cr alloys studied. Figure 8.10a shows the morphology of the austenite sideneedles which grow "radially" from the grain boundaries and allotriomorphs. The nucleation frequency is easily observed since each needle has a distinct appearance and does not tend to degenerate to other morphologies.

Intragranular needles were also observed and are a common feature of the microstructure. These needles nucleate within the grain and grow along well defined crystallographic directions as well. Figure 8.10b shows this morphology and indicates that intragranular needles provide nucleation sites for other needles.

All of the Widmanstatten needles observed in this investigation were located in the heat affected zone of a previous melt. Therefore, the needle morphology is the product of a high-temperature "heat treatment" rather than the direct product of the resolidification experiments. This behavior can be explained in terms of nucleation behavior and will be discussed in later section of this chapter.

Degenerate Widmanstatten Sideplates

Variations of the austenite sideplate morphology may occur when the plates A) form "facets" on their faces, B) branch to form new plates or C) "sympathetically" nucleate new plates with new habit planes. Each of these variation was observed in the Fe-Ni-Cr alloys studied in this investigation. The 'A' morphology was the most commonly observed degeneration of the sideplates. Figures 8.11a and 8.11b show this microstructure in Alloys 6 and 7 respectively. In this microstructure, the light colored phase is austenite and the dark colored phase is ferrite. Many facets have developed on the austenite plates and give a random appearance to the microstructure.

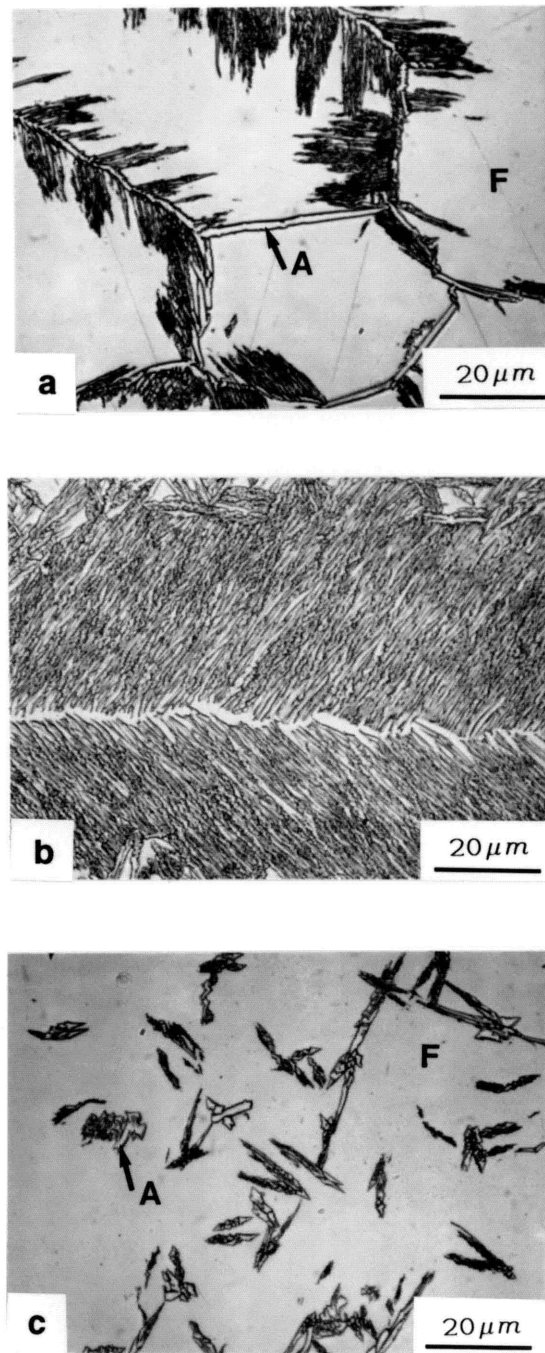


Figure 8.9 a) Widmanstätten austenite sideplates growing from grain boundary allotriomorphs at intermediate cooling rates, b) Widmanstätten sideplates at low cooling rates and c) intragranular Widmanstätten plates in Alloy 7.

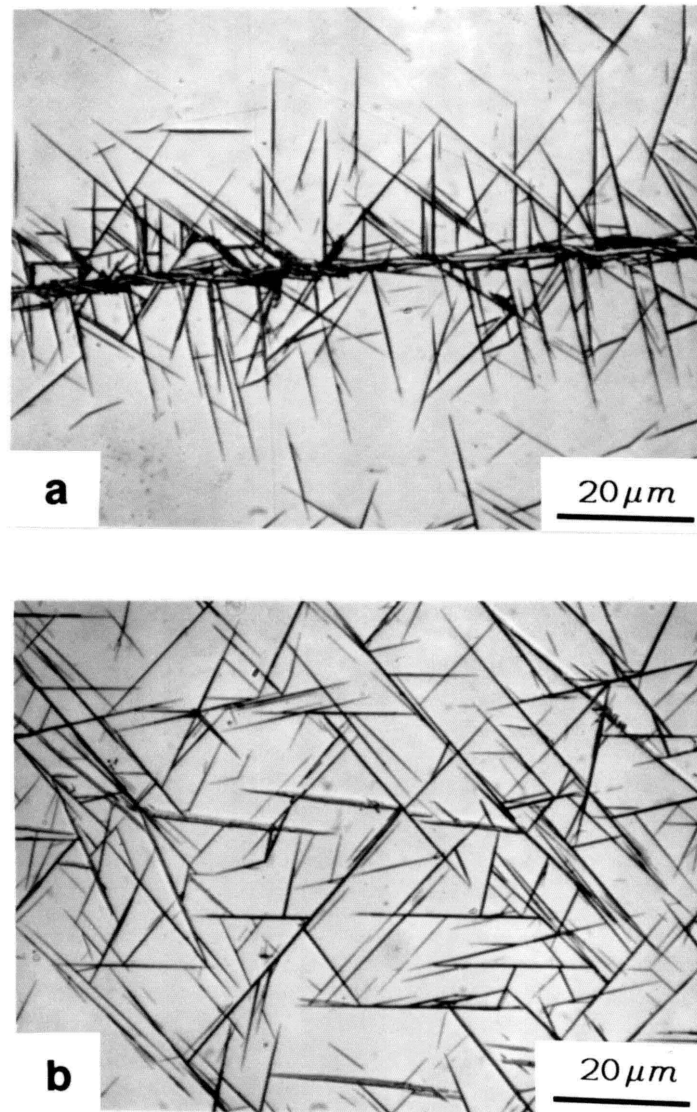


Figure 8.10 a) Primary Widmanstatten side-needles growing from grain boundary allotriomorphs in Alloy 7 and b) intragranular Widmanstatten needles in the heat affected zone of Alloy 7.

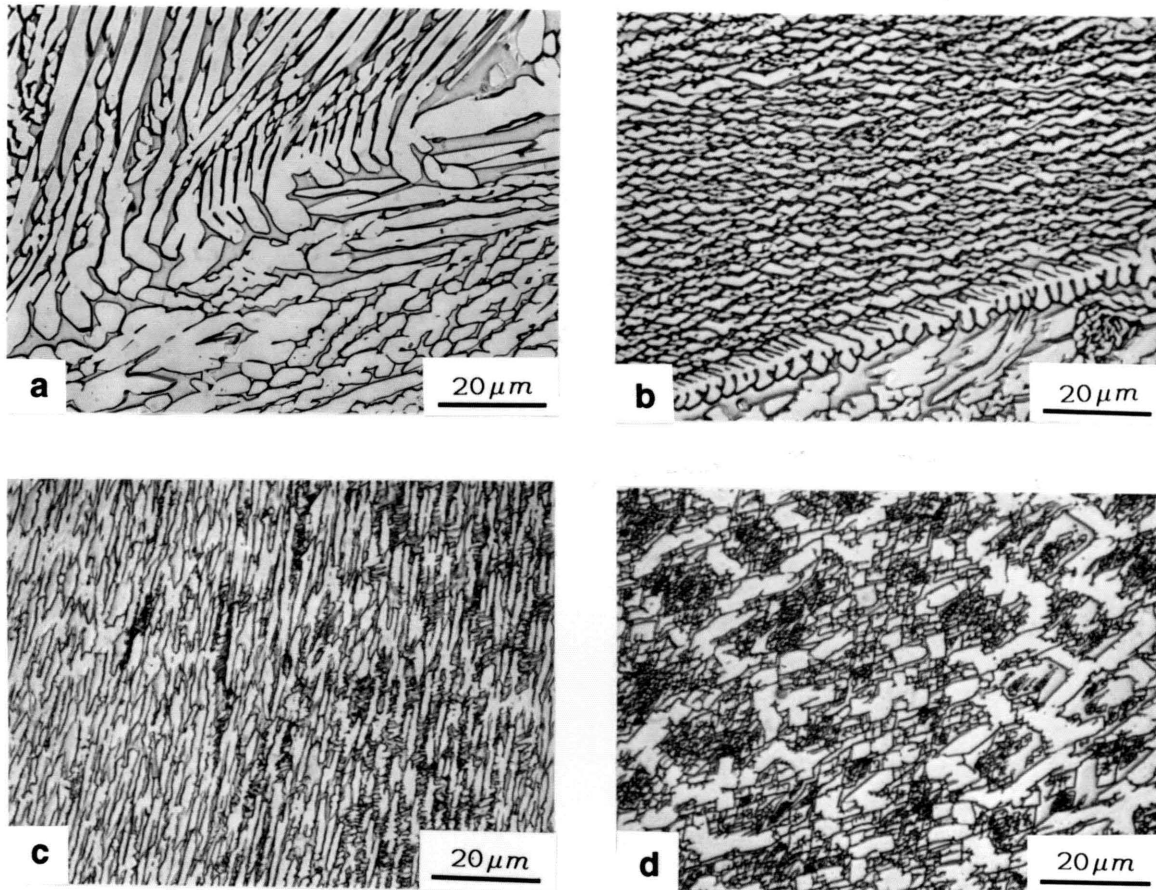


Figure 8.11 Degenerate forms of Widmanstätten sideplates. a) Indicates faceting of the austenite plates, b) and c) show sympathetically nucleated austenite sideplates and d) indicates branching of the austenite plates.

The 'B' morphology was less frequently observed and is shown in Fig. 8.11d. In this microstructure, new austenite plates branch and grow with the same habit plane as the original plate. This gives the microstructure a ladder-like lattice structure.

The 'C' morphology of new austenite plates or needles nucleating as the result of the growth of other plates or needles. Examples of this microstructure are shown in Figure 8.9c and 8.10b for intragranular plates and needles respectively. The 'C' morphology may also combine with 'A' morphology to create the complex microstructures shown in Fig. 8.11c. The micrograph was taken from alloy 5 and occurs in the slower cooling rate portions of melt 3.

8.3.2 The Effect of Cooling Rate on Austenite Morphology

The degree of supersaturation and the primary ferrite grain size are the two most important factors controlling the austenite morphology. Both of these factors are influenced by the cooling rate since the grain size and the transformation temperature both decrease with increasing cooling rate.

The effect that grain size has on the austenite morphology is to provide nucleation sites for grain boundary allotriomorphs and Widmanstätten sideplates or sideneedles. Therefore, as the grain size decreases, the larger grain boundary area results in a microstructure that has a larger percentage of the transformation originating from grain boundaries and a lesser percentage of intragranular morphologies.

The degree of supersaturation (the amount of undercooling) increases with increasing cooling rate and provides the driving force for the transformation. Small supersaturations only provide small driving forces. Therefore, the austenite requires heterogeneous sites such as grain boundaries or allotriomorphs to provide nucleation sites. The resulting microstructures consist of grain boundary allotriomorphs and Widmanstätten sideplates and sideneedles. Large supersaturations provide large driving forces and the austenite may nucleate at matrix or lattice defects within the interior of grains. The resulting microstructures at high supersaturations are typically a combination of grain-boundary nucleated and intragranular morphologies.

8.3.3 Nucleation and Growth Kinetics

Grain Boundary Allotriomorphs

Nucleation of grain boundary allotriomorphs, intragranular plates and intragranular needles leads to the majority of the microstructures observed in this study. Of these three, nucleation of grain boundary allotriomorphs is important since the sideplates that are responsible for the majority of the transformation, grow from the allotriomorphs. Aaronson [8.15] developed an equation to represent the nucleation rate, N_s , for hemispherical shaped embryos heterogeneously nucleated against a planar grain boundary in the Fe-C system. Again, using the analogy between the Fe-Ni-Cr system where diffusion is controlled by the diffusion of Ni in austenite instead of carbon in the Fe-C system, Aaronson's equation becomes:

$$N_s = K \cdot \exp \left[- \left(\frac{\pi (3\sigma_{\delta\gamma} - \sigma_{\delta\delta})^3}{3(\Delta G_v + \Delta G_s)^2} + \Delta G_D \right) / (RT) \right] \quad (8.11)$$

where K is a composition dependent constant, $\sigma_{\delta\gamma}$, and $\sigma_{\delta\delta}$ are interfacial energies for ferrite-austenite and ferrite-ferrite interfaces respectively. ΔG_D is the activation energy for the diffusion of Ni in austenite and the remaining terms have been previously defined.

The most important factor from the standpoint of nucleation kinetics is ΔG_v because it varies considerably with transformation temperature. As transformation temperature decreases, ΔG_v becomes more negative and N_s increases accordingly. Therefore, with larger undercoolings, produced by rapid cooling rate conditions, the nucleation rate increases. However, as the cooling rate increases, less time is available for the nucleation events. Therefore, as experiments will show, the total number of nuclei that form and grow to a perceptible level per unit volume decreases with increasing cooling rate past some critical value. This critical cooling rate was shown to be about 2000 °C/s. Above this value the nucleation of austenite allotriomorphs can be suppressed and the microstructures remain fully ferritic.

Growth of the allotriomorphs is also controlled by diffusion and, once again, the diffusion of nickel in austenite is assumed to be the rate controlling step. The rate at which the allotriomorphs thicken can be shown to be proportional to $(Dt)^{1/2}$:

$$X = \alpha (Dt)^{1/2} \quad (8.12)$$

for planar and spherical geometries [8.15] where the constant X is related to the degree of supersaturation and the diffusion geometry. As previously discussed, the transformation time, diffusivity and diffusion distance decreases with increasing cooling rate which results in less transformation at high cooling rates.

Orientation Relationship

Widmanstätten plates and needles grow with a crystallographic orientation relationship with the parent phase. In plain carbon steels and in Fe-Ni-Cr alloys this relationship is known to follow the Kurdjumov-Sachs specifications:

$$\begin{aligned} (111)_\gamma || (110)_\alpha \\ [\bar{1}\bar{1}0]_\gamma || [1\bar{1}1]_\alpha \end{aligned} \quad (8.13)$$

where the subscript γ refers to the FCC austenite and the subscript α refers to the BCC ferrite.

Widmanstätten Plates

The spacing between adjacent Widmanstätten sideplates is related to the nucleation frequency of the plates along the grain boundary allotriomorph interface. Therefore, a model to describe the sideplate spacing would need to explain how the initially planar austenite allotriomorph interface becomes unstable and forms a series of relatively even spaced platelets growing towards the interior of the grain. Townsend and Kirkaldy [8.18] applied the Mullins and Serkerka [8.19] interface stability analysis to analyze the spacing of Widmanstätten sideplates in Fe-C alloys. Their analysis shows a good correlation between theoretical and experimental results. The details of these calculations will not be presented here, however, one result of their analysis indicates that the perturbation frequency increases parabolically with increasing transformation temperature:

$$\lambda_m \propto T^2 \quad (8.14)$$

Therefore, the spacing of the sideplates should also increase with increasing transformation temperature.

Microstructural examination was performed on the electron beam resolidified alloys to determine how the cooling rate influences the sideplate spacing. In the cast condition, Alloy 6 showed a spacing of 11 mm whereas in the electron beam melts of Alloy 6, the spacing was 1 mm or less. The smaller spacing of the higher cooling rate melts is consistent with the theory proposed by Townsend and Kirkaldy since the higher cooling rates would provide higher undercoolings prior to the nucleation of the sideplates.

The platelet spacing of the castings is significantly smaller for Alloy 7 (2 mm) than for Alloy 6 (11 mm). This difference in spacing cannot be rationalized from simple transformation temperature arguments. Although Alloy 7 should have a lower transformation temperature because of its higher Cr/Ni ratio composition, this difference alone does not explain the order of magnitude difference in spacing for the alloys cooled at the same rate. Therefore, the effect of composition on the thermodynamic driving force for the allotriomorph interface instability must also play a significant role. This factor enters into equation 8.14 through the proportionality constant and is explained in more detail by Townsend and Kirkaldy.

The growth kinetics of the Widmanstätten platelets were also studied by Townsend and Kirkaldy for Fe-C alloys. Following the method developed by Zener [8.20] they derived an expression for the growth rate, R , of a platelet having constant radius of curvature, r :

$$R = \frac{D}{4r} \left(\frac{C_{iF}^0 - C_{iF}}{C_{iF} - C_{iA}} \right) \quad (8.15)$$

Using the analogy between the Fe-Ni-Cr system and the Fe-C system, D is the diffusivity of Ni in austenite, C_{iF}^0 is the equilibrium concentration of element i in ferrite at infinite radius of curvature at the A/F interface, and C_{iF} , C_{iA} are the concentrations of element i in ferrite and austenite respectively at the radius of curvature equal to r .

8.4 Isothermal Transformation Experiments

The transformation kinetics of the decomposition of ferrite were studied under isothermal conditions. Section 2.5 summarized the experimental procedure in which small specimens (~50mg) were heat treated in a salt bath for various times, at 625°C and 720°C. The ferrite content of each specimen was measured before and after each heat treatment using the vibrating sample magnetometer. This technique allowed accurate ferrite measurements to be made so that the percent ferrite that had transformed could be determined as function of time under the isothermal temperature conditions. These experiments were conducted on Alloys 6 and 7 to evaluate the effects of ferrite composition as well as temperature on the transformation kinetics.

The experimental test matrix was formulated so that the amount of time that each specimen was transformed corresponded to a doubling of the previous total transformation time. At 720°C, the transformation rate was rapid and the initial time increment was taken to be 15s, whereas at 625°C, the transformation rate was slower and the initial time increment was taken to be 120s. The experiments were continued to a total transformation time that corresponded to near equilibrium conditions at their respective transformation temperature.

Table 8.5 summarizes the results of these experiments and reports the percent ferrite after each isothermal heat treatment. Figure 8.12 plots the results of Alloys 6 and 7 as fraction transformed (1-fraction ferrite) versus log time at a transformation temperature of 625°C. For all cases, Alloy 6, which has a lower Cr/Ni ratio than Alloy 7, transforms at higher rates than Alloy 7. The transformation curves have the classic sigmoidal shape which is characteristic of nucleation and growth kinetics. At short times, the transformation rate is slow due to the incubation time required to form austenite nuclei. During later stages, the transformation rate again reduces because of impingement effects. The maximum transformation rate occurs at intermediate times where the reaction is approximately half-way to completion. Figure 8.12 also shows similar results for Alloys 6 and 7 at a transformation temperature of 720°C. At the higher temperature, the curves have the same general shape, however, the transformation rates are much higher and there is a larger effect of composition on the transformation rate at 720°C than at 625°C.

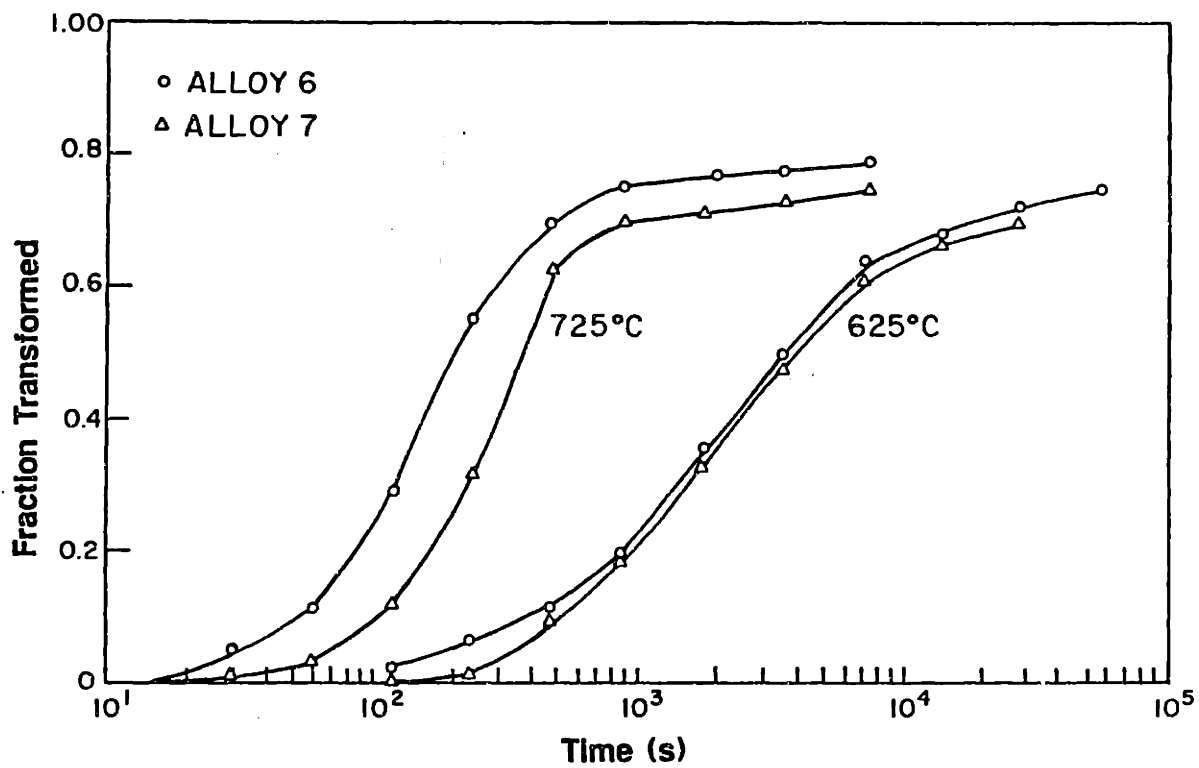


Figure 8.12 Comparison of the isothermal transformation kinetics of Alloys 6 and Alloy 7.

The early studies of the kinetics of nucleation and growth phase transformations were conducted by Johnson and Mehl [8.16]. these studies led to the development of the relationship between the fraction transformed, f , and the isothermal transformation time, t :

$$f = 1 - \exp[-Bt^n] \quad (8.16)$$

For continuous cooling transformation kinetics, Christian [8.13] reports that the time exponent, n , is related to the precipitate morphology and the behavior of the nucleation rate with transformation time B is a material dependent constant. These variables can be determined from a linearization of equation 8.14 by taking repeated logarithms to give the following equation:

$$\text{Log}[\ln(1-f)] = \text{Log} B + n \text{Log} t \quad (8.17)$$

From a plot of $\ln(1-f)$ versus t on a Log-Log scale, n can be determined from the slope of the line and B from the intercept at $t=1s$.

Figure 8.13a and 8.13b shows this relationship for Alloys 6 and 7 respectively. For each alloy, the relationship is approximately linear at short and intermediate transformation times but impingement effects at long transformation times reduce the slope dramatically. The initial slope provides the time exponent. For both alloys, the lower transformation temperature is associated with a lower slope. The measured values for B and n are reported in Table 8.6 and correspond to the coefficients for equation 8.16. At 50% transformation and 625 °C, the values of n are 0.94 and 1.30 for Alloys 6 and 7 respectively, while at 720°C, the values of n are 1.40 and 1.74 for Alloys 6 and 7 respectively.

It was once believed that from the value of n , one could determine the morphology of the precipitate. Although the morphology of the precipitate can influence the rate of transformation, other factors are also incorporated into the rate exponent. Data in the literature seems to indicate that $n= 3/2$ for diffusion controlled growth of plates, spheroids or needles as long as the particles were all present at time zero and had negligibly small initial dimensions [8.13]. Therefore, variations in the observed values of n are the result of non-zero finite initial particle size or non-diffusion controlled growth mechanisms.

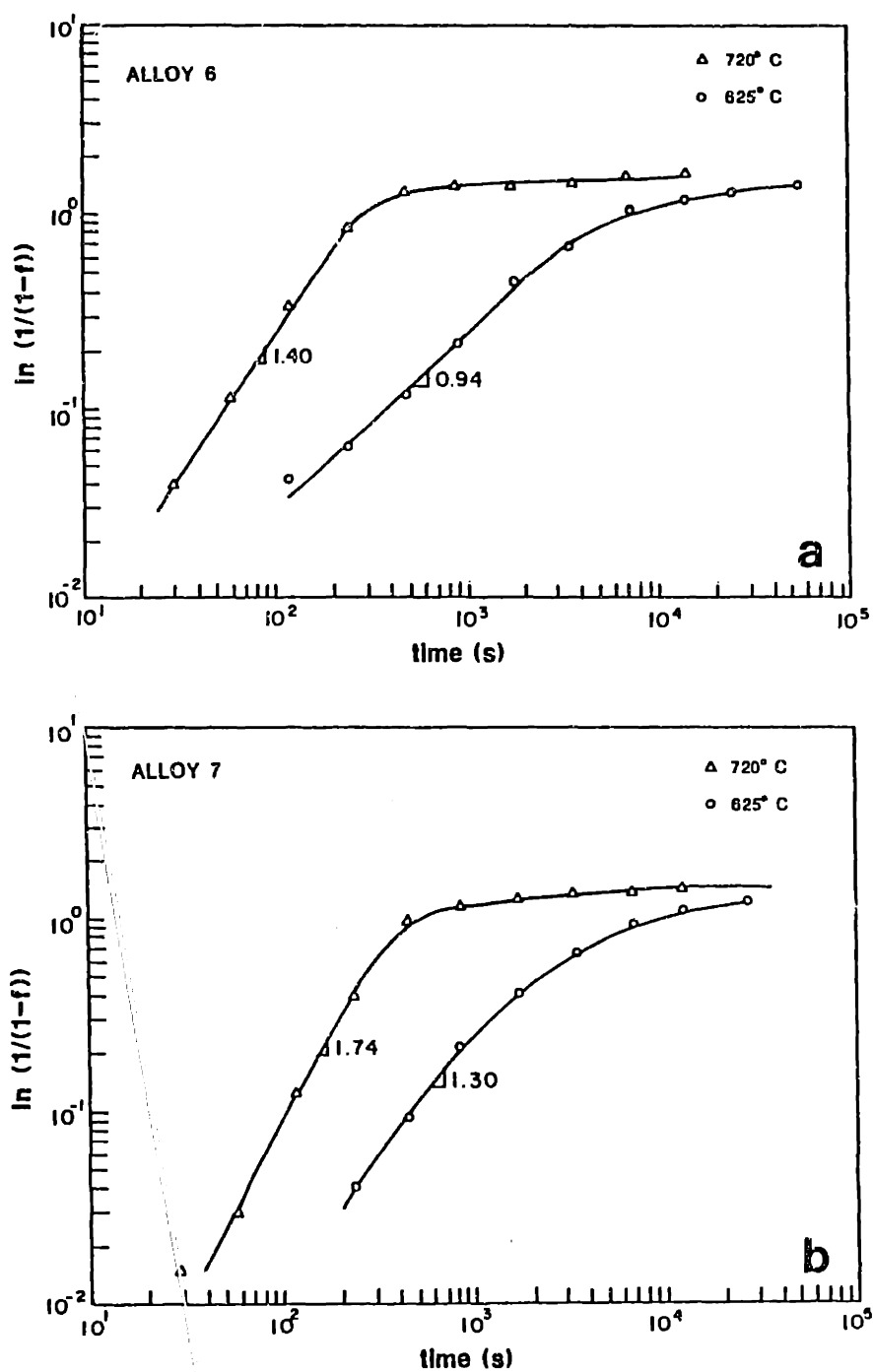


Figure 8.13 Johnson-Mehl-Avrami analysis of the transformation kinetics of a) Alloy 6 and b) Alloy 7.

The significance of differences in the measured values of n , is difficult to evaluate, however, a few observations can be made. Firstly, n was observed to vary from values slightly less than $4/4$ to values of about $7/4$. This range is centered about $n=3/2$ and suggests that diffusion limited growth is controlling the transformation. Secondly, for each alloy, n is approximately 0.4 lower at 625°C than at 720°C . Observations of the microstructure indicates that there is a difference in particle morphology at these two temperatures. Optical metallography clearly indicates that Widmanstatten needles form at 625°C whereas Widmanstatten platelets form at 720°C for both Alloys 6 and 7. If the difference in particle shape is not responsible for these differences in the value of n , then other factors, such as the influence of temperature on nucleation rate must be responsible. Further studies would be required to evaluate the significance of the difference in rate exponents at the two temperatures.

Table 8.6 Results of the isothermal transformation experiments listing wt. fraction ferrite as a function of time.

time (s)	Alloy 6		Alloy 7	
	625°C	720°C	625°C	720°C
0	1.00	1.00	1.00	1.00
1.5×10^1	-	1.00	-	1.00
3.0×10^1	-	0.96	-	0.99
6.0×10^1	-	0.89	-	0.97
1.2×10^2	0.98	.071	1.0	0.88
2.4×10^2	0.94	0.42	0.96	0.68
4.8×10^2	0.89	0.27	0.91	0.38
9.0×10^2	0.80	0.25	0.81	0.30
1.8×10^3	0.64	0.24	0.67	0.29
3.6×10^3	0.50	0.23	0.52	0.27
7.2×10^3	0.38	0.21	0.39	0.25
1.44×10^4	0.32	0.20	0.34	0.24
2.88×10^4	0.28	-	0.30	-
5.76×10^4	0.25	-	-	-

Table 8.7 Coefficients for the Johnson-Mehl-Avrami equation.

Alloy	Temperature (°C)	n	B
6	625	0.94	3.8×10^{-4}
	720	1.40	4.0×10^{-4}
7	625	1.30	3.0×10^{-5}
	720	1.74	3.0×10^{-5}

By comparing the transformation rate at the two temperatures, an estimate of the activation energy for the transformation can be made. Assuming the transformation is thermally activated, given a time, t , required to transform a certain volume fraction ferrite, the temperature dependence of the transformation rate becomes:

$$\frac{1}{t} = A e^{(-Q_T/RT)} \quad (8.18)$$

where Q_T represents the combined activation energies of nucleation, Q_N , and growth Q_G . By taking the ratio of equation 8.18 at the two temperatures and simplifying, the expression, Q_T becomes:

$$Q_T = -R \left(\frac{T_1 * T_2}{T_2 - T_1} \right) \ln \left(\frac{t_2}{t_1} \right) \quad (8.19)$$

where t_1 and t_2 represent the times required for 50% transformation at temperatures T_1 and T_2 respectively.

Applying equation 8.19 to the results presented in Figures 8.12 gives the activation energy for the transformation of Alloy 6 to be 53.6 Kcal/mole and Alloy 7 to be 44.2 Kcal/mole. Comparing these values to the activation energy for diffusion, shown in Tables 8.1 and 8.2, shows that the apparent activation energy for the transformation is 10 to 20 Kcal/mole less than the anticipated activation energy for diffusion of nickel in austenite. This behavior might be caused by a non-zero nucleation rate throughout the transformation experiments, combined with an additional dependence of the nucleation rate on the temperature. This effect would result in a higher volume fraction transformed than that associated with the diffusional growth of a fixed number of nuclei present at time zero. A second

possibility for the lower activation energy might be related to the assumptions made about the mechanism for growth. If the transformation takes place by an interface controlled growth mechanism rather than the assumed diffusion controlled growth mechanism the analysis of the results would have to be altered significantly. Additional experiments would have to be performed in order to separate out the reasons responsible for the activation energy of the transformation.

8.5 Summary and Conclusions

The microstructures which were observed in the Fe-Ni-Cr alloys were shown to depend on the primary mode of solidification, the specific alloy composition and the cooling rate. Many of the microstructural morphologies were related to the solid-state transformations that occur as the resolidified alloy cools to room temperature.

For alloys which solidify in the AF or FA modes, the transformation occurs by the diffusion controlled growth of austenite. The resulting microstructures consist of isolated ferrite particles, vermicular ferrite or lacy ferrite, depending on the initial ferrite content and the cooling rate. The transformation rate for the diffusion controlled growth of austenite was modeled using the diffusion of Ni in austenite as the rate limiting factor. A simple, first-order, model allowed the transformation rate to be calculated for each of the solidification conditions that were studied in this investigation. The results of these calculations showed that a decreasing percentage of the microstructure transforms as the cooling rate increases, despite the fact that the "scale" of the microstructure also decreases with increasing cooling rate. This simple model correlated well with experimental observations and provided a useful approximation to determine the influence of cooling rate on the amount of ferrite that transforms by diffusion controlled growth.

A second, and more accurate, model of the diffusion controlled transformation of ferrite was also developed. This model utilizes the finite difference form of Ficks second law to calculate the rate of interface movement as the ferrite transforms to austenite. However, due to the complexity of applying this approach to a ternary alloy system, the application of this model to the transformation characteristics of ferrite will be postponed to future work.

For the alloys that solidify in the fully ferritic condition, nucleation of austenite is necessary before the transformation can proceed and the temperature at which the austenite phase nucleates dictates the type of transformation that will occur. At the small amount of undercooling which occur at low cooling rates, Widmanstatten austenite platelets grow from grain boundary allotriomorphs. The nucleation characteristics and the instabilities that form from the allotriomorphs are responsible for the spacing of the Widmanstatten platelets. Once the spacing has been determined, the platelets grow by a diffusion controlled mechanism. Therefore, more transformation occurs at low cooling rates.

A second type of Widmanstatten austenite morphology was observed in the heat affected zone of the resolidified melts. This morphology consisted of austenite needles and through isothermal transformation experiments, was shown to occur at larger undercoolings than the platelets.

The transformation kinetics of Widmanstatten austenite were studied by isothermal experiments to measure the fraction of the ferrite that transforms as a function of time at two different temperatures. These experimental measurements were interpreted by a Johnson-Mehl-Avrami analysis to quantify the transformation rate and the effects of temperature were used to estimate the activation energy for the transformation. These calculations showed the activation energy to be about 50 Kcal/mole which correlates with the activation energy for a diffusion controlled transformation with a temperature dependent and non-zero nucleation rate. The Johnson-Mehl-Avrami and activation energy calculations can be used to predict the rate and extent of the phase transformation as a function of time and temperature.

The massive transformation of ferrite to austenite was only observed in Alloy 5. This transformation occurs at high cooling rates and through the use of thermodynamically calculated Gibbs Free energy versus composition curves, the presence of the massive transformation in Alloy 5 can easily be explained. The thermodynamic calculations were also used to show why Alloys 6 and 7, which have higher Cr/Ni ratio than Alloy 5 do not undergo the massive transformation for the cooling rates investigated in this study.

CHAPTER 9

Summary, Conclusions and Future Work

The influence of cooling rate on the microstructure of stainless steel alloys has been investigated through the examination and analysis of electron beam resolidified melts. The Fe-Ni-Cr alloys used in the experiments spanned the line of two-fold saturation along the 59 wt. % isopleth and were cooled at rates between 7°C/s and $7.5 \times 10^6\text{C/s}$. The microstructures which developed from these alloys varied from fully austenitic to fully ferritic and many duplex microstructures were characterized between these two extremes.

The complex microstructures which develop during the resolidification experiments were examined and analyzed to separate the effects of cooling rate on solute redistribution during solidification from the effects of cooling rate on the solid state transformation of ferrite. This required a combination of experimental results, thermodynamic analysis and kinetic analysis of the different alloys and different solidification conditions. The thermodynamic data was acquired by calculations of isothermal sections and Gibbs free energy versus composition plots for the alloys used in this study. The kinetics of the solidification behavior were studied by analyzing the growth characteristics of columnar dendrites. These results were used to model solute redistribution and to calculate the percentage of primary and secondary phases that form in each alloy as a function of cooling rate. Furthermore, the kinetics of the solid state transformation were modeled by a diffusion controlled growth analysis and experimentally verified through isothermal transformation studies.

This chapter summarizes the results of this investigation and is meant to be an overview of the work that was performed. Section 9.1 presents a summary of the important experimental results and a summary of the analysis that was performed. Section 9.2 lists the conclusions from each of the separate studies of this investigation while section 9.3 discusses the areas that were identified for future work.

9.1 Summary

9.1.1 Experimental Results

The experimental results which show the influence of cooling rate on the microstructure of stainless steel alloys are summarized in a number of key figures and tables in Chapters 5, 6 and 8. Figure 5.6 shows the influence of electron beam scan speed (cooling rate) on the primary mode of solidification for each of the seven Fe-Ni-Cr alloys. At low cooling rates, four modes of solidification are present while at high cooling rates only the fully ferritic and fully austenitic modes are present. The regions where each PSM exists are indicated and this figure also shows that the solidification mode of Alloy 4 changes from primary ferrite to primary austenite as the cooling rate increases.

The microstructural morphologies which develop as the resolidified melts cool to room temperature are summarized in Figure 5.15. This figure indicates the cooling rate-composition range where each morphology was observed and shows that the PSM is an important factor in the development of the microstructural morphologies. At low cooling rates, the widest range of microstructures appears. Cellular-dendrite single-phase austenite, interdendritic ferrite, vermicular ferrite, lacy ferrite, blocky austenite and Widmanstätten austenite form at low cooling rates as the Cr/Ni ratio of the alloy increases. At intermediate cooling rates, dendrites are replaced by cells and the most commonly observed microstructures are the cellular and intercellular forms of ferrite and austenite. If a eutectic phase forms, its presence is difficult to characterize and is most likely a divorced eutectic having a microstructure similar to intercellular ferrite or intercellular austenite. At high cooling rates, single phase ferrite or single phase austenite are responsible for the majority of the microstructures observed. One exception is the presence of massive austenite which was only observed in Alloy 5 at high cooling rates.

A comparison of the morphological features observed in this study with those observed by other investigators is presented in Table 5.4. This table allows a comparison to be made between the terminology used by the different investigators to describe the same morphological features. Table 5.6 summarizes the solidification and solid state transformation events which lead up to the development of each of the

morphologies.

One of the methods used to describe the influence of cooling rate on the microstructure was to measure the residual ferrite content for each of the solidification conditions. The results of these measurements are presented in Figure 6.14 and show 1) the ferrite content of Alloys 1, 2 and 3 decrease with increasing cooling rate, 2) the ferrite content of Alloys 4 and 5 go through a maximum with increasing cooling rate and 3) the ferrite content of Alloys 6 and 7 increase with increasing cooling rate. These results were interpreted by the influence of cooling rate on the primary mode of solidification, solute redistribution and the solid state transformation of ferrite. However, in order to decouple these effects, solidification modelling was required to determine the amount of ferrite that solidified from each melt, prior to the solid state transformation.

The transformation of ferrite was studied under isothermal conditions by measuring the amount of ferrite that transformed as a function of time and temperature. The results of these experiments are shown in Figure 8.12 as fraction transformed versus log time and in Figure 8.13 as analyzed by the Johnson-Mehl-Avrami approach.

9.1.2 Analysis and Modelling

Quantitative analysis of the experimental results was performed in Chapters 4, 7 and 8. Chapter 4 investigated the influence of electron beam scan speed on the average interface velocity, temperature gradients and cooling rates at the L/S interface in the resolidified melts. Cooling rates were measured by three techniques: 1) dendrite arm spacing, 2) a modification to Rosenthal's heat flow analysis, and 3) a finite element method. The heat flow models confirm the dendrite arm spacing measurements. The finite element method was also used to calculate the distribution of temperature gradients and cooling rates on the L/S interface of the electron beam melts. These results indicate that the temperature gradient is relatively constant on the melt pool surface but that the cooling rate varies significantly from zero on the melt periphery to a maximum at the top center of the melt.

The experimental observations revealed several areas that required either quantitative analysis or modelling to develop a better understanding of the effects of cooling rate on the microstructure. These areas are 1) the change in PSM of Alloy 4

from primary ferrite to primary austenite with increasing cooling rate, 2) the single phase nature of the high speed melts, 3) the behavior of ferrite content with cooling rate, 4) the presence of the massive transformation in Alloy 5, and 5) the nucleation and growth kinetics of the ferrite to austenite phase transformation.

The change in the primary mode of solidification in Alloy 4 was shown to be related to the dominant growth kinetics of the austenite phase at high cooling rates. Although ferrite is the thermodynamically preferred primary phase in this alloy, the difference in Gibbs free energy between primary phase austenite and primary phase ferrite is small because its composition is close to the line of two-fold saturation. Epitaxial growth of austenite at the melt periphery allows the initial PSM to be dominated by austenite because approximately 90% of the base metal substrate at the melt periphery is austenite. At low cooling rates, the AF solidification mode which initially grows from the periphery quickly reverts to the FA mode because solidification segregation allows the thermodynamically preferred ferrite phase to form as the primary phase. However, at high cooling rates, there is insufficient time for the AF mode to revert to the FA mode and the alloy solidifies entirely in the primary (metastable) austenite condition.

The behavior of the ferrite content with cooling rate and the single phase nature of the high speed electron beam melts can be explained by the influence of cooling rate on solute redistribution. This analysis is presented in Chapter 7 where the effect of dendrite tip undercooling on solute redistribution was calculated. These calculations were performed on each alloy and for each of the solidification conditions to determine the undercooling caused by the radius of curvature effects and the undercooling caused by solutal effects. The solutal undercooling is responsible for changes in the solute redistribution. This effect was shown to produce dendrite tip undercoolings as high as 30°C in the highest speed electron beam melt.

The results of the dendrite tip undercooling calculations were incorporated into a solidification model to predict changes in the amount of primary phase that forms with changes in the solidification conditions. These calculations show that the amount of primary phase increases as the cooling rate increases and in the limit, the alloys would solidify either as 100% ferrite or 100% austenite depending on their primary mode of solidification. However, the calculations fell short of predicting fully austenitic or fully ferritic behavior because of the approximations made in

deriving the pseudobinary diagrams and the approximations made in estimating the solidification front velocity for the high scan speed melts.

The solid state transformation of ferrite was studied by developing a simple, first-order model to predict the amount of transformation that occurs during the continuous cooling of the resolidified melts. This model assumed that the transformation was controlled by the diffusion of nickel in austenite. These results confirmed the experimental observations and showed that the characteristic diffusion distance decreases more rapidly than the dendrite arm spacing with increasing cooling rate. This effect illustrates why the total amount of transformation decreases with increasing cooling rate and indicates the conditions necessary to "quench in" the microstructure.

The massive transformation observed in Alloy 5 was studied from thermodynamic and kinetic standpoints. Thermodynamic calculations were performed using "Thermo-calc" to determine the Gibbs free energy versus temperature plots for Alloys 5, 6, and 7. These diagrams allowed estimations of the driving force for the transformation and showed that Alloy 5 had the most probable composition for the massive transformation from single phase ferrite to austenite.

9.2 Conclusions

Ferrite Content Measurements

1. The amount of ferrite in stainless steel alloys can be determined by measuring the saturation magnetization of a small stainless steel specimen with a vibrating sample magnetometer. This technique is not limited by sample size and can be used to measure the ferrite content of rapidly solidified stainless steel alloys.
2. The saturation magnetization of fully ferritic specimens was experimentally determined on a series of rapidly-solidified Fe-Ni-Cr alloys which had compositions similar to that of residual ferrite in stainless steel alloys. The results of these measurements can be used to predict the saturation magnetization of residual ferrite from its composition.

3. Methods were presented to show how the composition of residual ferrite can be predicted from the nominal alloy composition using thermodynamic calculations. In particular, a range of possible iron contents in the ferrite can be estimated from the nominal alloy composition and the concept of the effective quench temperature. By knowing the iron content of the ferrite, its saturation magnetization can be used to calibrate the VSM to measure the ferrite content of a wide range of stainless steel alloys.
4. The results of the saturation magnetization study can be used as a basis to calibrate the Magne-Gage for non-standard stainless steel alloys. By considering the saturation magnetization of residual ferrite, the ferrite number can be converted directly into % ferrite for a wide range of nominal alloy compositions.

Cooling Rates and Temperature Gradients

5. Dendrite arm spacing estimations of the cooling rate show that the arc cast button solidified at 7°C/s and that the six electron-beam melts solidified at rates which varied between $4.7 \times 10^2^{\circ}\text{C/s}$ and $7.5 \times 10^6^{\circ}\text{C/s}$. These measurements are supported by other cooling rate calculations.
6. An analytic expression was derived, based on Rosenthal's heat flow analysis, to represent the cooling rate in the solid at any location on the surface of the weld. This expression can be simplified to represent the maximum cooling rate in the weld knowing only the length of the weld, the travel speed and the melting temperature of the alloy. Similar expressions were derived to estimate the cooling rate in the liquid at the L/S interface.
7. Dendrite arm spacing measurements and finite element calculations show that there is a variation in cooling rate within a given weld. The majority of the variation occurs close to the melt periphery and the remainder of the weld cools within a factor of about five in cooling rate.
8. Heat flow calculations showed that the highest cooling rate occurs at the top center of the weld pool while the lowest cooling rate occurs at the melt

periphery. On the melt periphery, the cooling rate is zero but rapidly increases within a few dendrite arm spacings of the boundary. Metallographic observations of the microstructure confirm these calculations.

9. The FEM calculations showed that the temperature gradients varied only about 30% around the surface of the melt. These calculations also showed that the temperature gradient increases by a factor of 2 to 3 for a fourfold increase in travel speed.

The Primary Solidification Mode and Ferrite Morphology

10. Five modes of solidification and eleven morphologies were observed during the resolidification of the seven alloys. These microstructural characteristics are believed to be a complete "set" of the possible solidification and solid state transformation events that occur during the resolidification of typical stainless steel alloys. These microstructures were related to the alloy composition, the cooling rate and the extent of the solid state transformation of ferrite.
11. Electron beam scan speed (cooling rate) versus composition diagrams were developed to predict the primary solidification mode and the morphologies of resolidified stainless steel alloys. Figure 5.6 shows the relationship between the primary mode of solidification and the cooling rate for the seven alloys while Figure 5.15 shows the microstructural morphologies which develop from these solidification conditions.
12. Epitaxial growth was observed from all of the two-phase substrates studied in this investigation. Therefore, two phases initially compete to become the primary solid phase. At low cooling rates, the thermodynamic factors take preference and the PSM is dictated by the more thermodynamically stable phase. However, at high cooling rates, the growth kinetics of the metastable phase may supersede the formation of the equilibrium primary phase. This situation was observed in Alloy 4 which solidifies in the FA mode at low rates and in the AF mode at higher rates and in the fully austenitic mode at the highest rates.

13. Nucleation of metastable phases from within the resolidified zone was not observed in this study. Therefore, changes in solidification mode with cooling rate were determined to be the result of the epitaxially grown metastable austenite developing into the primary solid phase due to the favorable growth kinetics of austenite under certain solidification conditions.

The Residual Ferrite Content

14. The composition and the primary mode of solidification determine how the cooling rate will influence the amount of ferrite that solidifies from the melt.
15. At low cooling rates, the residual ferrite content increases for F and FA solidified alloys but decreases for AF solidified alloys. This behavior can be explained by the combined effects of the decreasing amount of solute segregation and the decreasing amount of ferrite transformation with increasing cooling rate.
16. At high cooling rates the alloys solidify in either the fully ferritic or fully austenitic modes with no second phase in the microstructure.
17. Based on conclusions 15 and 16, one would expect the ferrite content of the alloys to either monotonically increase for FA solidified alloys or monotonically decrease for AF solidified alloys as the cooling rate increases. However, the residual ferrite content of Alloys 4 and 5 was shown to go through a maximum at intermediate cooling rates. This behavior was explained by 1) the change in solidification mode of Alloy 4 from FA to AF with increasing cooling rate and 2) the formation of massive austenite in Alloy 5 at high cooling rates.

Solute Redistribution

18. A series of isothermal sections through the Fe-Ni-Cr ternary diagram were created through thermodynamic calculations. These sections show tie-lines in each of the two-phase fields that can be used to predict solidification segregation.

19. Pseudobinary diagrams were created for primary austenite and primary ferrite solidification conditions. These diagrams are shown in Figures 7.4 and 7.5 and represent significant improvements over the constant Fe sections that have been used in the past to illustrate the solidification behavior of stainless steel alloys.
20. Average temperature gradients and average interface velocities were calculated for each of the solidification conditions used in this investigation. These parameters were then used to calculate the dendrite tip radius, and dendrite tip undercooling for each alloy and each solidification condition using a constrained dendrite growth model. The results of these calculations showed that the solutal undercooling varies from about 5°C to about 30°C as the cooling rate is increased from the casting (7°C/s) to the highest speed electron beam melt (7.5×10^6 °C/s).
21. Based on the minimum in the Peclet number versus interface velocity curves, predictions were made for the cellular to dendritic transition as a function of growth rate and temperature gradient. These calculations were compared with the microstructures from each melt to show that the calculations appeared to be off by a constant multiplying factor. The difference in calculated and experimental behavior was rationalized by the uncertainties in the cellular to dendritic transition theory and in the uncertainties used in developing the assumptions for calculating the dendrite tip characteristics.
22. Solutal undercooling at the dendrite tip results in an increase in the amount of primary phase and a reduction in the amount of secondary phase that solidifies from the melt. This factor was taken into account to predict the relative amounts of primary and secondary phases which solidify for each of the solidification conditions. The results clearly show the influence that cooling rate has on the microstructure. At low cooling rates, there is a continuous increase in the total ferrite content with Cr/Ni ratio of the alloy. These calculations are confirmed by the Scheil predictions and by the general trend in ferrite content measured on the arc cast buttons. At high cooling rates, the calculations indicate a discontinuity in the total ferrite content which develops between the primary ferrite and primary austenite solidifying alloys.

23. The calculated discontinuity in ferrite content explains the single phase nature of the high speed electron beam melts. At high speeds, the reduction in the amount of the second phase that forms is so severe that the alloys solidify in the fully austenitic or fully ferritic mode depending on their PSM.

The Solid State Transformation of Ferrite

24. Many of the microstructural morphologies that were observed in the resolidified melts were related to the solid state transformation of ferrite. This transformation occurs by a nucleation and growth mechanism and was shown to be analogous to the transformations that occur during the decomposition of austenite in Fe-C alloys.
25. The microstructures which were observed in the Fe-Ni-Cr alloys were shown to depend on the primary mode of solidification, the specific alloy composition and the cooling rate. For alloys which solidify in the AF or FA modes, the transformation occurs by the diffusion controlled growth of austenite. The resulting microstructures consist of isolated ferrite particles, vermicular ferrite or lacy ferrite, depending on the initial ferrite content and the cooling rate.
26. The transformation rate for the diffusion controlled growth of austenite was modeled using the diffusion of nickel in austenite as the rate limiting factor. A simple, first-order, model allowed the transformation rate to be calculated for each of the solidification conditions that were studied in this investigation. The results of these calculations showed that a decreasing percentage of the microstructure transforms as the cooling rate increases, despite the fact that the "scale" of the microstructure also decreases with increasing cooling rate.
27. A second, and more accurate, model of the diffusion controlled transformation of ferrite was also developed. This model utilizes the finite difference form of Ficks second law to calculate the rate of interface movement as the ferrite transforms to austenite. Application of this model will be postponed for future work.

28. For the alloys that solidify in the fully ferritic condition, nucleation of austenite is necessary before the transformation can proceed and the temperature at which the austenite phase nucleates dictates the type of transformation that will occur. At the small undercoolings, which occur at low cooling rates, Widmanstätten austenite platelets grow from grain boundary allotriomorphs. The nucleation characteristics and the instabilities that form from the allotriomorphs were shown to be responsible for the spacing of the Widmanstätten platelets.
29. A second type of Widmanstätten austenite morphology was observed in the heat affected zone of the resolidified melts. This morphology consisted of austenite needles rather than plates. Through isothermal transformation experiments the needle morphology was shown to occur at larger undercoolings than the platelets.
30. The transformation kinetics of Widmanstätten austenite were studied by isothermal experiments to measure the fraction of the ferrite that transforms as a function of time at two different temperatures. These experimental measurements were interpreted by a Johnson-Mehl-Avrami analysis to quantify the transformation rate. The results of the calculations are consistent with diffusion controlled growth mechanisms and can be used to predict the extent of the transformation as a function of time and temperature.
31. The activation energy for the ferrite to austenite transformation was calculated from the isothermal experiments to be about 50 Kcal/mole. This value is lower than the activation energy for diffusion of nickel in austenite but is consistent with a diffusion controlled growth model and a non-zero nucleation rate.
32. The massive transformation of ferrite to austenite was only observed in Alloy 5. This transformation occurs at high cooling rates and through the use of thermodynamically calculated Gibbs Free energy versus composition curves, the presence of the massive transformation in Alloy 5 can easily be explained. The thermodynamic calculations were also used to show why Alloys 6 and 7, which have higher Cr/Ni ratio than Alloy 5, do not undergo the massive transformation for the cooling rates investigated in this study.

9.3 Future Work

During the course of this investigation, a number of areas were identified that required further analysis or additional computations. This final section discusses these areas of possible future research which would help to develop a better understanding of the influence of cooling rate on the microstructure of stainless steel alloys.

First, solidification of the stainless steel alloys and the solid state transformation of ferrite requires a redistribution of solute. These effects were modeled by assuming local equilibrium at the transformation interface and by calculating the partitioning of elements to their respective phases. In the process of performing these calculations, many assumptions were made that have not yet been fully verified. One method of verification would be to measure the microchemical composition gradients that are present across the ferrite and austenite cells.

At high cooling rates, the solidification microstructure is "quenched in" and the composition gradients would relate information about the solidification behavior of the alloys. At low cooling rates, the solid state transformation of ferrite "erases" the solidification microstructure and establishes composition gradients representative of the ferrite-austenite equilibrium. Therefore, compositional measurements at low cooling rates would relate information about the solid-state transformation of ferrite and could be used to verify the diffusion controlled growth calculations.

Because much of the important composition information is located close to the austenite/ferrite interface, an analytical technique that has high spatial resolution would be required. Low voltage scanning electron microscopy with a focal spot size of 500 to 1000 angstroms is available and might give enough resolution for the low cooling rate melts but scanning transmission electron microscopy would be required to inspect the high cooling rate melts due to the small cell spacings of the microstructure.

Second, in order to perform the solute redistribution calculations, the characteristics at the dendrite tip were modeled. In the past, these calculations have only been performed for binary alloy systems. Therefore, in this study, the Fe-Ni-Cr ternary system was approximated by the appropriate pseudobinary diagrams to represent the solidification behavior. The approximations made in deriving the pseudobinary

diagrams could have been eliminated if the dendrite tip characteristics were modeled directly in the ternary system.

Although these calculations have not been performed in the past, it would be possible by using a numerical approach which incorporates the isothermal sections generated by Thermocalc. From these isothermal sections, the solidification parameters could be determined as a function of liquid composition and temperature and by choosing small enough temperature increments, the dendrite tip characteristics could be modeled in a similar manner as presented in Chapter 7.

Third, a finite difference model was developed to solve for the moving-boundary diffusion-controlled-growth transformation of ferrite. This model was not applied to the alloys investigated in this thesis due to time constraints, however, since the formulation of the problem has been completed, a computer program could be developed that utilizes this approach. Once the program has been developed, the results could be applied to the different alloys and different solidification conditions to determine the extent of the transformation as a function of cooling rate. This model would also be able to calculate the composition gradients that form during the solid state transformation and these results could be compared to the microchemical composition gradient measurements for verification of the model.

REFERENCES

CHAPTER 1

- 1.1 J. C. Borland and R. N. Younger, "Some Aspects of Cracking in Austenitic Steels," *British Welding Journal* 7(1), 22-60 (1960).
- 1.2 F. C. Hull, "Effect of Delta Ferrite on the Hot Cracking of Stainless Steel," *Welding Journal* 46(9), Research Suppl., 399-s to 409-s (1967).
- 1.3 I. Masumoto, K. Tamaki, and M. Kutsuna, "Hot Cracking of Austenitic Stainless Steel Weld Metal," *Trans. JWS* 41(11), 1306-1341 (1972).
- 1.4 W. T. DeLong, "Ferrite in Austenitic Stainless Steel Weld Metal," *Welding Journal* 53(7), Research Suppl., 273-s to 286-s (1974).
- 1.5 Y. Arata, F. Matsuda, and S. Katayama, "Solidification Crack Susceptibility in Weld Metals of Fully Austenitic Stainless Steel (Report I)," *Trans. JWRI* 5(2), 35-51 (1976).
- 1.6 Y. Arata, F. Matsuda, and S. Katayama, "Solidification Crack Susceptibility in Weld Metals of Fully Austenitic Stainless Steel (Report II)," *Trans. JWRI* 6(1), 105-116 (1977).
- 1.7 J. A. Brooks and F. J. Lambert, "The Effects of Phosphorous, Sulfur, and Ferrite Content on Weld Cracking of Type 309 Stainless Steel," *Welding Journal* 57(5), Research., 139-s to 143-s (1978).
- 1.8 V. Kujanpaa, N. Suutala, T. Takalo, and T. Moisio, "Correlation Between Solidification Cracking and Microstructure in Austenitic and Austenitic-Ferrite Stainless Steel Welds," *Weld. Res. Intl.* 9(2), 55-70 (1979).
- 1.9 C. D. Lundin, C-P. D. Chou, and C. J. Sullivan, "Hot Cracking Resistance of Austenitic Stainless Steel Weldments," *Welding Journal* 59(8), Research Suppl., 226-s to 232-s (1980).
- 1.10 J. C. Lippold, and W. F. Savage, "Solidification of Austenitic Stainless Steel Weldments, Part 3 - The Effect of Solidification Behavior on Hot Cracking Susceptibility," *Welding Journal* 61(12), Research Suppl., 338-s to 396-s (1982).
- 1.11 J. C. Lippold, "Weld Cracking Mechanisms in Austenitic Stainless Steels," in *Trends in Welding Research in the United States* (American Society for Metals, Ohio), 209-242 (1982).
- 1.12 J. A. Brooks, A. W. Thompson, and J. C. Williams, "A Fundamental Study of the Beneficial Effect of Delta Ferrite in Reducing Weld Cracking," *Welding Journal* 63(3), Research Suppl., 71-s to 83-s (1984).

- 1.13 M. O. Malone, "Sigma and 885°F Embrittlement of Chromium-Nickel Stainless Steel Weld Metals," *Welding Journal* 46(6), Research Suppl. 241-s to 253-s (1967).
- 1.14 J. Honeycombe and T. G. Gooch, "Effect of Manganese on Cracking and Corrosion Behavior of Fully Austenitic Stainless-Steel Weld-Metals," *Metal Const. & Brit. Weld. J.*, 456-460 (1972).
- 1.15 R. Viswanathan, J. I. Nurminen, and R. G. Aspden, "Stress Corrosion Behavior of Stainless Steel Welds in High Temperature Water Containing Chloride," *Welding Journal* 58(4), Research Suppl., 118-s to 126-s (1979).
- 1.16 T. A. Whipple, H. I. McHenry, and D. T. Read, "Fracture Behavior of Ferrite-Free Stainless Steel Welds in Liquid Helium," *Welding Journal* 60(4), Research Suppl., 72-s to 78-s (1981).
- 1.17 D. T. Read, H. I. McHenry, P. A. Steinmeyer, and R. D. Thomas, Jr., "Metallurgical Factors Affecting the Toughness of 316L SMA Weldments at Cryogenic Temperatures," *Welding Journal* 59(4), Research Suppl., 104-s to 113-s (1980).
- 1.18 C. E. Witherell, "Welding Stainless Steels for Structures Operating at Liquid Helium Temperatures," *Welding Journal* 59(11), Research Suppl., 325-s to 342-s (1980).
- 1.19 D. L. Olson, "Prediction of Austenitic Weld Metal Microstructures and Properties," *Welding Journal* 65(10), Research Suppl., 281-s to 291-s (1985).
- 1.20 A. L. Schaeffler, "Constitution Diagram for Stainless Steel Weld Metal," *Metals Progress* 56, 680 and 680 B (1949).
- 1.21 A. L. Schaeffler, "Selection of Austenitic Electrodes for Welding Dissimilar Metals," *The Welding Journal* 20(10), Research Suppl., 601-s to 620-s (1947).
- 1.22 W. T. DeLong, G. Ostrom, and E. Szumachowski, "Measurement and Calculation of Ferrite in Stainless Steel Weld Metal," *Welding Journal* 35(11), Research Suppl., 526-s to 533-s (1956).
- 1.23 C. J. Long and W. T. DeLong, "The Ferrite Content of Austenitic Stainless Steel Weld Metal," *Welding Journal* 52(7), Research Suppl., 281-s to 297-s (1973).
- 1.24 F. C. Hull, "Delta Ferrite and Martensite Formation in Stainless Steels," *Welding Journal* 52(5), Research Suppl., 193-s to 203-s (1973).
- 1.25 T. Takalo, N. Suutala, and T. Moio, "Influence of Ferrite Content on Its Morphology In Some Austenitic Weld Metals," *Metallurgical Transactions* 7(A), 1591-1592 (1976).
- 1.26 N. Suutala, T. Takalo, and T. Moio, "The Relationship Between Solidification and Microstructure in Austenitic and Austenitic-Ferrite Stainless Steel Welds," *Metallurgical Transactions* 10(A), 512-514 (1979).

- 1.27 N. Suutala and T. Moisiso, "Use of Chromium and Nickel Equivalents in Considering Solidification Phenomena in Austenitic Stainless Steels," in *Solidification Technology in the Foundry and Cast House* (The Metals Society, London, 1980), pp. 310-314.
- 1.28 N. Suutala, "Effect of Solidification Conditions on the Solidification Mode in Austenitic Stainless Steels," *Metallurgical Transactions* 14(A), 191-197 (1983).
- 1.29 G. M. Goodwin, N. C. Cole, and G. M. Slaughter, "A Study of Ferrite Morphology in Austenitic Stainless Steel Weldments," *Weld. Journal* 51(9), Research Suppl., 425-s to 439-s (1972).
- 1.30 S. A. David, "Ferrite Morphology and Variations in Ferrite Content in Austenitic Stainless Steel Welds," *Welding Journal* 60(4), Research Suppl., 63-s to 71-s (1981).
- 1.31 J. A. Brooks, "Solidification and Solid State Transformations of Austenitic Stainless Steel Welds," in *Trends in Welding Research in The United States*, S. A. David, Ed. (ASM, Metals Park, Ohio, 1982), pp. 331-335.
- 1.32 V. G. Rivlin and G. V. Raynor, "Critical Evaluation of Constitution of Chromium-Iron-Nickel System," *International Metals Review*, Review No. 248, No. 1, 21-38 (1980).
- 1.33 E. Schurmann and J. Brauckmann, "Investigation of the Melting Equilibria in the Iron Corner of the Ternary System Iron-Chromium-Nickel," *Arch. Eisenhüttenwesen* 48(1), 3-7 (1977).
- 1.34 E. R. Szumachowski and D. J. Kotecki, "Effect of Manganese on Stainless Steel Weld Metal Ferrite," *Welding Journal* 63(5), Research Suppl., 156-s to 161-s (1984).
- 1.35 O. Hammar and U. Svensson, "Influence of Steel Composition on Segregation and Microstructure During Solidification of Austenitic Stainless Steel," in *Solidification and Casting of Metals* (The Metals Society, London, 1979), pp. 401-410.
- 1.36 C. N. McCowan, T. A. Siewart, R. P. Reed and F. B. Lake, "Manganese and Nitrogen in Stainless Steel SMA Welds for Cryogenic Service," *Welding Journal*, 66(3), 84-s to 92-s, (1987).
- 1.37 O. J. Pereira and J. Beech, "Factors Influencing The Delta Ferrite Content of Cast Austenitic Stainless Steels," in *Solidification Technology in The Foundry and Cast House* (The Metals Society, London, 1980), pp. 315-321.
- 1.38 H. Fredriksson, "Solidification Sequence in 18-8 Stainless Steel, Investigated by Directional Solidification," *Metallurgical Transactions* 3(11), 35-51 (1976).
- 1.39 N. Suutala, "Solidification Studies on Austenitic Stainless Steel, ACTA Universitatis Ouluensis, Series C, Technia No. 23, Metallurgica No. 3, OULU (1982).

- 1.40 J. M. Vitek, A. Dasgupta, and S. A. David, "Microstructural Modification of Austenitic Stainless Steel by Rapid Solidification," *Metallurgical Transactions* 14(A), 1833-1841 (1983).
- 1.41 J. M. Vitek and S. A. David, "Microstructural Analysis of Austenitic Stainless Steel Laser Welds," in *Trends in Welding Research in the United States* (American Society for Metals, Ohio, 1982), pp. 243-258.
- 1.42 S. A. David, J. M. Vitek and R. W. Reed, "Effect of Rapid Cooling On Stainless Steel Weld Microstructure and Its Implications on The Schaeffler Diagram," *Welding Journal*, 66(10), 289-s to 300-s, (1987).
- 1.43 S. Katayama and A. Matsunawa, "Solidification Microstructure of Laser Welded Stainless Steels," *Proc. ICALEO*, P. 60, (1984).
- 1.44 J. C. Lippold, "Centerline Cracking in Deep Penetration Electron Beam Welds in Type 304L Stainless Steel," *Welding Journal* 64(5), Research Suppl. 127-s to 136-s (1985)
- 1.45 F. T. Kelly, M. Cohen, and J. B. Vander Sande, "Rapid Solidification of A Droplet-Processed Stainless Steel," *Metallurgical Transactions* 15(A), 819-833 (1984).

Chapter 2

- 2.1 E. M. Gutierrez and J. Szekely, "A Mathematical Model of the Planar Flow Melt Spinning Process," *Metallurgical Transactions* 17(B), 695-703 (1986).
- 2.2 W. J. Boettinger, D. Shechtman, R. J. Schaefer, and F. S. Biancaniello, "The Effect of Rapid Solidification on the Microstructure of Ag-Cu Alloys," *Metallurgical Transactions* 15(A), 55-66 (1984).
- 2.3 E. Berah and B. Shpigler, *Color Metallography*, ASM, Metals Park, Ohio, p.32, (1977).
- 2.4 S. Ohara, S. Komura and T. Takeda, "Magnetic Properties of Pseudo-Iron $Fe_{1-x}(Cr_{0.5}Ni_{0.5})_x$ Ternary Alloys," *J. Phys. Society Japan*, 34(6), (1973).
- 2.5 "Standard Test Method for Density of Glass by Buoyancy", ASTM STP C693-74, ASTM, Philadelphia, (1974).

Chapter 3

- 3.1 see reference 1.20
- 3.2 see reference 1.21
- 3.3 see reference 1.22

- 3.4 C. N. McCowen, et al., 'Updating the DeLong Diagram, paper presented at the 68th AWS Convention, Chicago, (1987).
- 3.5 C. N. McCowan et al., "FN Predictive Diagram for Stainless Steel Welds," paper presented at the 69th AWS convention, New Orleans (1988).
- 3.6 see reference 1.32
- 3.7 see reference 1.42
- 3.8 American Welding Society, "Recommended Procedures for Calibrating Magnetic Instruments...", AWS, A 4.2, (1974).
- 3.9 E. Stalmasek, "Measurement of Ferrite Content in Austenitic Stainless Steel...", WRC Bulletin 318, September (1986).
- 3.10 P. E. Merinov et al., "A Method for the Quantative Determination of the Ferrite Content of Welded Joints in CrNi Steels," Welding Production, 24(3), p. 49, (1977).
- 3.11 P. Merinov, S. Entin, B. Beketov and A. Runov, "The Magnetic Testing of the Ferrite Content of Austenitic Stainless Steel Weld Metal," NDI Int, 11(1), p. 9, (1978).
- 3.12 S. Chikazumi, Physics of Magnetism, New York, J. Wiley, 1967.
- 3.13 G. C. Curtis and J. Sherwin, "Magnetic Method for the Estimation of Ferrite in Stainless Steel Welds," Britttish JAP, 12(7), p. 344, (1961).
- 3.14 J. A. Brooks, J. C. Williams, and A. W. Thompson, "Microstructural Origin of Skeletal Ferrite Morphology of Austenitic Stainless Steel Welds," Metallurgical Transactions 14(A), 1271-1281 (1983).
- 3.15 F. T. Kelly, M. Cohen, and J. B. Vander Sande, "Rapid Solidification of a Droplet-Processed Stainless Steel," Metallurgical Transactions 15(A), 819-833 (1984).
- 3.16 S. A. David, G. M. Goodwin and D. N. Braski, "Solidification Behavior of Austenitic Stainless Steel Fiber Metals," Welding Journal 58(11), (1979).
- 3.17 J. C. Lippold and W. F. Savage, "Solidification of Austenitic Stainless Steel Weldments: Part 1 - A Proposed Mechanism," Welding Journal 58(12), 1979.
- 3.18 M. J. Cieslak, A. M. Ritter and W. F. Savage, "Solidification Cracking and Analytical Electron Microscopy of Austenitic Stainless Steels," Welding Journal 61(1), (1982).
- 3.19 see reference 2.1
- 3.21 B. D. Cullity, Introduction To Magnetic Materials, Addison-Wesley, Reading, Massachusetts, 1972.
- 3.21 B. Sundman, B. Jansson and J.O. Andersson, "The THERMO-CALC Databank System," CALPHAD, 9(2), pp 153-190, (1985).

- 3.22 J. W. Elmer, "Thermodynamically Calculated Isothermal Sections of the Fe-Ni-Cr Ternary System for Temperatures Above 1023 K," LLNL, UCID-20838, (1987).
- 3.23 J. M. Vitek and S. A. David, "The Concept of an Effective Quench Temperature and its use in Studying Elevated-Temperature Microstructures," Met Trans., 16A, pp1521-1523, August (1985).
- 3.24 see reference 2.4
- 3.25 D. J. Kokecki, "Extension of the WRC Ferrite Number System," Welding Journal, 61(11), (1982).

Chapter 4

- 4.1 M. C. Flemings, Solidification Processing (McGraw-Hill Book Company, New York, NY, (1974).
- 4.2 T. Z. Kattamis., J. C. Coughlin, and M. C. Flemings, "Influence of Coarsening on Dendrite Arm Spacing of Aluminum-Copper Alloys," Transactions AIME 239, 1504-1511 (1967).
- 4.3 M. C. Flemings, D. R. Poirier, R. V. Barone, and H. D. Brody, "Microsegregation in Iron-Base Alloys," J. Iron Steel Inst. 208, 371-381 (1970).
- 4.4 T. F. Bower, H. D. Brody, and M. C. Flemings, "Measurements of Solute Redistribution in Dendritic Solidification," Transactions AIME 236. 624-654 (1966).
- 4.5 See Reference 1.32.
- 4.6 D. Rosenthal, "The Theory of Moving Sources of Heat and Its Application to Metal Treatments," Transactions AIME 43(11), 849-866 (1966).
- 4.7 N. Christensen, V. Davies, and K. Gjermundsen, "The Distribution of Temperatures in Arc Welding," British Welding Journal 12(2), 54-75 (1965).
- 4.8 T. W. Eagar and N. S. Tsai, "Temperature Fields Produced by Traveling Distributed Heat Sources," Welding Journal 62(12), 346s-355s, (1983).
- 4.9 see reference 4.1, Chapter 2
- 4.10 J. Szekeley, private communications, November, 1987.
- 4.11 Mr. M. Kong, Lawrence Livermore National Laboratory, 1986.
- 4.12 Dr. M. Lin, Massachusetts Institute of Technology, 1986.

Chapter 5

- 5.1 A. Munitz, "Epitaxy and Surface Melting of Aluminum Alloys by High Powered Directed Energy," Metallurgical Transactions B 11(B), 563-573 (1980).

- 5.2 R. J. Wallace and E. N. Kaufmann, "Nucleation and Growth in Surface-Melted Crystalline and Amorphous Fe₄₀Ni₄₀P₁₄B₆ Alloys," *J. Mater. Res.* 1(1), (1986).
- 5.3 H. W. Bergmann and B. L. Mordike, "Production and Properties of Amorphous Layers on Metal Substrates by Laser and Electron Beam Melting," *Rapidly Solidified Amorphous and Crystalline Alloys*, Proc. Symp. of Materials Research Society, B. H. Kear, B. C. Giessen and M. Cohen (eds.), North-Holland Amsterdam, 497-503, (1982).
- 5.4 see reference 1.27
- 5.5 see reference 1.28
- 5.6 see reference 1.42
- 5.7 see reference 1.43
- 5.8 see reference 1.40
- 5.9 see reference 1.44
- 5.10 see reference 1.45
- 5.11 see reference 1.31
- 5.12 see reference 3.22
- 5.13 J. C. Lippold and W. F. Savage, "Solidification of Austenitic Stainless Steel Weldments: Part 2 - The Effect of Alloy Composition on Ferrite Morphology," *Welding Journal* 59(2), 48-s to 58-s, (1980).
- 5.14 N. Suutala, T. Takalo and T. Moisio, "Single Phase Ferritic Solidification Mode in Austenitic-Ferritic Stainless Steel Welds," *Metallurgical Transactions* 10(8), 1183-1190, (1979).
- 5.15 S. Katayama and A. Matsunawa, "Solidification Behavior and Microstructural Characteristics of Pulsed and Continuous Laser Welded Stainless Steel," to be published, (1988).
- 5.16 see reference 1.25
- 5.17 see reference 1.26
- 5.18 see reference 1.30
- 5.19 E. L. Brown, T. A. Whipple and G. Krauss, "Metallography of Duplex Stainless Steel Castings," *Duplex Stainless Steels* edited by R. A. Lula, ASM, Metals Park, OH, p. 665 (1983).
- 5.20 J. Singh, G. R. Purdy and G. C. Weatherly, "Microstructural and Micromechanical Aspects of the Solid-State Decomposition of Delta Ferrite in Austenitic Stainless Steels," *Metallurgical Transactions* 16A(8), 1363-1369 (1985).

Chapter 6

- 6.1 see reference 1.32
- 6.2 D. Kundrat, private communications, November, 1987.
- 6.3 Y. Chuang and Y. A. Chang, "A Thermodynamic Analysis and Calculation of the Fe-Ni-Cr Phase Diagram," *Metallurgical Transactions A*, 18A(5), 733-745, (1987).
- 6.4 see reference 3.22
- 6.5 see reference 1.23
- 6.6 J. W. Elmer, D. L. Olson and D. K. Matlock, "The Thermal Expansion Characteristics of Stainless Steel Weld Metal," *Welding Journal* 61(9), 293-301-s, (1982).
- 6.7 D. J. Kotecki, "Welding Parameter Effects on Open-Arc Stainless Steel Weld Metal Ferrite," *Welding Journal* 57(4), 109-s to 117-s, (1978).
- 6.8 see reference 3.28
- 6.9 J. A. Sarreal and G. J. Abbascian, "The Effect of Solidification Rate on Microsegregation," *Metallurgical Transactions A*, 17A(11), 2063-2073, (1986).

Chapter 7

- 7.1 see reference 6.9
- 7.2 D.M. Kundrat, "Thermodynamic Model of the Solidification Process of Alloys, Part I," *CALPHAD*, 11(4), 349-354, (1987).
- 7.3 D.M. Kundrat, "Thermodynamic Model of the Solidification Process of Alloys, Part II," *CALPHAD*, 11(4), 355-360, (1987).
- 7.4 D.M. Kundrat, Private communication and collaboration, September, (1987).
- 7.5 see reference 4.1
- 7.6 W.W. Mullins and R. F. Sekerka, "Morphological Stability of a Particle Growing by Diffusion or Heat Flow," *J. Applied Physics*, 34(2), pp. 323-329, (1963).
- 7.7 J. Lipton, M.E. Glicksman and W. Kurz, "Dendrite Growth into Undercooled Alloy Melts," *Material Science and Eng.*, 65, pp. 57-63, (1984).
- 7.8 W. Kurz and D.J. Fisher, Fundamentals of Solidification, Trans Tec. Publications, Switzerland, (1986).
- 7.9 G.P. Ivanstov: Dohl. Akad. Nauk SSSR, vol.58, p. 567, (1947).
- 7.10 W. Kurz and D.J. Fisher, "Dendrite Growth at the Limit of Stability: Tip Radius and Spacing," Acta Met., (69), pp. 362-366, (1984).

- 7.12 K. Soomboonsuk, J.T. Mason and R.Trivedi,"Interdendritic Spacing: Part I Experimental Studies," Met. Trans. **15A(6)**, pp 967-975, (1984)
- 7.13 Y. Miyata and T. Suzuki, "Cellular and Dendrite Growth" Met. Trans., **(16A)**, pp 1799-1814, (1985).
- 7.14 T.W. Clyne and W. Kurz, "Solute Redistribution During Solidification with Rapid Solid State Diffusion," Met. Trans A, **12A(6)**, pp. 965-71, (1981).
- 7.15 H.D. Brody and M.C. Flemings, "Solute Redistribution in Dendritic Solidification," Trans. AIME, **236(5)**, pp. 615-24, (1966).
- 7.16 M.H. Burden and J.D. Hunt, "Cellular and Dendritic Growth I," J. Crystal Growth, **22**, pp. 99-108, (1974).
- 7.17 M.H. Burden and J.D. Hunt, "Cellular and Dendritic Growth II," J. Crystal Growth, **22**, pp. 109-16, (1974).
- 7.18 K.A. Jackson and J.D. Hunt, "Lamellar and Rod Eutectic Growth," Trans. AIME, **236(8)**, pp. 1129-42, (1966).
- 7.19 Y. Wu, T.J. Piccone, Y. Shiohara and M.C. Flemings, "Dendritic Growth of Undercooled Nickel-Tin Part I," Met. Trans. A, **18A(5)**, pp. 915-24, (1987).
- 7.20 J.C. Baker and J.W. Cahn, "Thermodynamics of Solidification," Am. Soc. for Metals, Metals Park Oh., pp. 23-58, (1970).
- 7.21 W.J. Boettinger, S.R. Coriell and R.F. Sekerka, "Mechanisms of Microsegregation-free Solidification, " Materials Sci. and Eng., **(65)**, pp. 27-36, (1984).
- 7.22 M.J. Aziz, "Model for Solute Redistribution During Rapid Solidification," J Appl. Physics, **53(2)**, pp. 1158-68, (1982).

Chapter 8

- 8.1 D.B. Moharial, I. Jin, and G.R. Purdy, "The Effect of Delta Ferrite on the Post-solidification Homogenization of Alloy Steels," Metallurgical Transactions **5**, 59-63 (1964).
- 8.2 K. Hirano, M. Cohen, and B.L. Averbach, "Diffusion of Nickel into Iron," Acta Metallurgica **9**, 440-445 (1961).
- 8.3 G.F. Hancock and G.M. Leak, "Diffusion of Nickel in Binary Alloys of Iron with Nickel Manganese, and Chromium," Metal Science Journal **1**, 33-36 (1967).
- 8.4 P.J. Alberry and C.W. Haworth, "Interdiffusion of Cr, Mo, and W in Iron," Metal Science **8**, 407-412 (1974).
- 8.5 A.F. Smith, "The Diffusion of Chromium in Type 316 Stainless Steel," Metal Science **9**, 375-378 (1975).

- 8.6 R.A. Perkins, J.R. Padgett, and N.K. Tunali, "Tracer Diffusion in Fe and Cr in Fe, 7 Wt Pct Cr, 12 Wt Pct Ni Austenitic Alloy," Metallurgical Transactions 4, 2535-2540 (1973).
- 8.7 R.A. Perkins, "Tracer Diffusion in Ni in Fe-17 Wt Pct Cr-12 Wt Pct Ni," Metallurgical Transactions 4(A), 1665-1669 (1973).
- 8.8 A.F. Smith and R. Hales, "The Diffusion of Chromium in a Duplex Alloy Steel," Metal Science, 418-423 (1976).
- 8.9 J. Singh, G.R. Pardy, and G.C. Wetherly, "Microstructural and Micromechanical Aspects of the Solid-state Decomposition of Delta Ferrite in Austenitic Stainless Steels," Metallurgical Transactions 16(A), 1363-1369 (1985).
- 8.10 M. Hillert, "Thermodynamics of the Massive Transformation," Metallurgical Transactions 15(A), 411-419 (1984).
- 8.11 M.R. Pichta, W.A.T. Clark, and Aaronson, "The Nucleation Kinetics, Crystallography and Mechanisms of the Massive Transformation," Metallurgical Transactions 15(A), 427-435, (1984).
- 8.12 J.H. Perepezko, "Growth Kinetics and Mechanism of the Massive Transformation," Metallurgical Transactions 15(A), 427-447, (1984).
- 8.13 J.W. Christian, The Theory of Transformation in Metals and Alloys, Part I, Pergamman Press, (1975).
- 8.14 C.A. Dube, H.I. Aaronson, and R.F. Mehl, Rev. Met. 55, 201 (1958).
- 8.15 Decomposition of Austenite by Diffusional Processes, edited by V.W. Zackay, and H.I. Aaronson, AIME, 387-548, (1962).
- 8.16 W. Johnson and R.F. Mehl, "Reaction Kinetics in Processes of Nucleation and Growth," Trans AIME, 135, 416, (1939).
- 8.17 M. Avrami, J. Chem. Phys. 7, 103, (1939)
- 8.18 R. D. Townsend and J. S. Kirkaldy, "Widmanstätten Ferrite Formation In Fe-C Alloys," Transactions ASM, (61), pp. 605-619 (1968).
- 8.19 see reference 7.6
- 8.20 C. Zener, Transactions AIME, (167), p 550, (1946).

Appendices

- B.1 SURFER, Golden Software, Golden, Co.
- C.1 B. Sundman, B. Jansen, and J. Anderson, "The Thermo-Calc Databank System," Calphad 9(2), 153-190 (1985).

- C.2 B. Sundman and J. Agren, "A Regular Solution Model for Phases with Several Components and Sublattices Suitable for Computer Applications," *J. Phys. Chem. Solids* 42, 297-301 (1981).
- D.1 Y. Chuang and Y. A. Chang, "A Thermodynamic Analysis and Calculation of the Fe-Ni-Cr Phase Diagram," *Met. Trans. A*, 18A(6), p. 733, (1987).
- G.1 Christensen, N., Davies, V., and Gjermendsen, K., "The Distribution of temperature in arc welding," *British Welding Journal* 12 (2):54-75, (1965).
- G.2 Rosenthal, D., "The theory of moving source of heat and its application to metal treatment," *Transactions ASME* 43 (11):849-866, (1946).

APPENDIX A

Derivation Of The Cooling Rate Equation

This section presents a mathematical derivation of an analytic expression to represent the cooling rate. The formulation of the problem is discussed in section 4.2.2 for quasi-stationary heat flow conditions and the nomenclature is summarized in Table 4.2.

$$T - T_o = \left(\frac{Q}{2\pi kr} \right) e^{\left(\frac{-v}{2\alpha}(r+x) \right)} \quad (4.3)$$

Let $\theta = T - T_o$

First Derivative of eq. 4.3 wrt x

$$\frac{\partial \theta}{\partial x} = \frac{Q}{2\pi k} \left[\left(\frac{1}{r} \right) e^{\left(\frac{-v}{2\alpha}(r+x) \right)} \left(\frac{\partial r}{\partial x} + 1 \right) \left(\frac{-v}{2\alpha} \right) + e^{\left(\frac{-v}{2\alpha}(r+x) \right)} \left(\frac{-1}{r^2} \right) \frac{\partial r}{\partial x} \right]$$

where,

$$\frac{\partial r}{\partial x} = \frac{\partial (x^2 + y^2 + z^2)^{1/2}}{\partial x} = \frac{2x}{2(x^2 + y^2 + z^2)^{1/2}} = \left(\frac{x}{r} \right)$$

therefore,

$$\begin{aligned} \frac{\partial \theta}{\partial x} &= \frac{-Q}{2\pi k} \left[\left(\frac{1}{r} \right) \left(e^{\left(\frac{-v}{2\alpha}(r+x) \right)} \right) \left[\frac{vx}{2\alpha r} + \frac{v}{2\alpha} - \frac{x}{r^2} \right] \right] \\ \frac{\partial \theta}{\partial x} &= \frac{-Q}{2\pi k} \left(\frac{v}{2\alpha} \right) \left(\frac{1}{r} \right) \left(e^{\left(\frac{-v}{2\alpha}(r+x) \right)} \right) \left[1 + \frac{x}{r} + \frac{2\alpha x}{vr^2} \right] \end{aligned} \quad (A.1)$$

Cooling Rate Equation

$$\epsilon = (-v) \frac{\partial \theta}{\partial x} = \frac{\partial \theta}{\partial t} \quad [^{\circ}\text{C/s}]$$

substitution of equation A.1,

$$\frac{\partial \theta}{\partial x} = \frac{Q}{2\pi k} \left(\frac{v^2}{2\alpha} \right) \left(\frac{1}{r} \right) \left(e^{\left(\frac{-v}{2\alpha}(r+x) \right)} \right) \left[1 + \frac{x}{r} + \frac{2\alpha x}{vr^2} \right] \quad (A.1)$$

since,

$$\theta = \left(\frac{Q}{2\pi kr} \right) e^{\left(\frac{-v}{2\alpha}(r+x) \right)}$$

$$\frac{\partial \theta}{\partial t} = \theta \left(\frac{v^2}{2\alpha} \right) \left[1 + \frac{x}{r} + \frac{2\alpha x}{vr^2} \right] \quad (\text{A.2})$$

Derivation Of The Location Of The Maximun Weld Pool Width

This section derives an expression for the distance behind the source, x_w , on the top surface of the plate ($z = 0$), where the weld pool achieves its maximum width.

x_w depends on the radius at this point, r_w , which must be determined by a trial and error method using equation A.5.

$$T - T_o = \left(\frac{Q}{2\pi kr} \right) e^{\left(\frac{-v}{2\alpha}(r+x) \right)} \quad (4.3)$$

$$T - T_o = \left(\frac{-Q}{2\pi k} \right) \left(\frac{1}{r\alpha} \right) \left(e^{\left(\frac{-v}{2\alpha}(r+x) \right)} \right) \left[\frac{v}{2\alpha}(x+r) + \frac{x}{r} \right] \quad (\text{A.3})$$

set $\frac{\partial \theta}{\partial x} = 0$ and solve for x_w

$$\frac{v}{2\alpha} (r+x) + \frac{x}{r} = 0$$

$$x \left(\frac{v}{2\alpha} + \frac{1}{r} \right) = \frac{-vr}{2\alpha}$$

$$x \left(\frac{vr + 2\alpha}{2\alpha r} \right) = \frac{-vr}{2\alpha}$$

$$x_w = \left(\frac{-vr_w^2}{vr_w + 2\alpha} \right) \quad (\text{A.4})$$

substitution into equation 4.3 gives,

$$r_w = \left(\frac{Q}{2\pi k\theta_m} \right) e^{\left(\frac{-vr_w}{vr_w + 2\alpha} \right)} \quad (\text{A.5})$$

APPENDIX B

Temperature Gradient and Cooling Rate Calculations

This appendix summarizes the programs which must be run in order to calculate the cooling rate in welds. The output of two computer runs are also shown in Tables B.1 and B.2. These results show: (1) the temperature gradient in the solid, T_s , (2) the cosine between the unit normal to the weld pool and the travel speed direction, $\cos n$, and (3) the cooling rate in the solid, ϵ_s , for each of the boundary nodal points on the solidifying half of the weld pool.

Five programs must be run to calculate the cooling rate. The software is written on DEC RT11 and requires a 3-D mesh of the base plate. The program will then calculate the temperature at each nodal point in the plate for quazi steady-state heat flow conditions using the boundary conditions discussed in Chapter 4. From the temperature distribution, a temperature gradient is calculated at each point on the liquid-solid interface and the cooling rate is calculated at each nodal point by the vector product of the temperature gradient and the interface velocity.

The physical property data is assumed to be independent of temperature and should be input in the following units: $T(K)$, $k(W/m-k)$, $C(J/kg-K)$, $\rho(kg/m^3)$, $\alpha(m^2/s)$. The dimensions on the 3-D grid should be in inches and the travel speed should be input in the units of (inch/s). The output from the program gives the temperature gradient ($^{\circ}C/inch$) and the cooling rate ($^{\circ}C/s$).

The data presented in Tables B.1 and B.2 were used to create 'topographical' and orthographic plots. The topographical maps show lines of constant cooling rate and temperature gradient on the $x=0$ cross sectional plane of the melt. These plots are shown in figures 4.6 and 4.7 and represent the behavior on the melt isotherm. The orthographic projections represent this same data in three dimensional form and are shown in figures B.1 through B.4. The topographical maps and the orthographic projections were both calculated with the 'Surfer' software package [B.1] using a 100x100 grid created by the Kriging method.

Table B-1: Results of TMESH3 for a travel speed of 15 ipm

Coord. (inch)			ϵ_s	T_s	cos n
-X	Y	Z	(°C/s)	(°C/inch)	
0.0000	0.0000	0.0470	0.000E+00	-0.215E+05	0.000E+00
0.0000	0.0148	0.0445	0.000E+00	-0.215E+05	0.000E+00
0.0213	0.0000	0.0427	-0.221E+00	-0.227E+05	0.390E+00
0.0204	0.0136	0.0408	-0.221E+04	-0.236E+05	0.374E+00
0.0000	0.0260	0.0391	0.000E+00	-0.236E+05	0.000E+00
0.0184	0.0243	0.0364	-0.211E+04	-0.251E+05	0.337E+00
0.0000	0.0332	0.0332	0.000E+00	-0.255E+05	0.000E+00
0.0161	0.0315	0.0315	-0.192E+04	-0.262E+00	0.294E+00
0.0000	0.0470	0.0000	0.000E+00	-0.219E+05	0.000E+00
0.0000	0.0445	0.0148	0.000E+00	-0.207E+05	0.000E+00
0.0213	0.0427	0.0000	-0.222E+04	-0.228E+05	0.390E+00
0.0204	0.0408	0.0136	-0.221E+04	-0.236E+05	0.374E+00
0.0000	0.0391	0.0260	0.000E+00	-0.230E+05	0.000E+00
0.0184	0.0364	0.0243	-0.215E+04	-0.256E+05	0.337E+00
0.0348	0.0000	0.0343	-0.430E+04	-0.263E+05	0.653E+00
0.0339	0.0110	0.0332	-0.420E+04	-0.265E+05	0.634E+00
0.0315	0.0205	0.0307	-0.388E+04	-0.264E+05	0.586E+00
0.0284	0.0275	0.0275	-0.349E+04	-0.265E+05	0.527E+00
0.0348	0.0343	0.0000	-0.424E+04	-0.259E+05	0.653E+00
0.0339	0.0332	0.0110	-0.413E+04	-0.260E+05	0.634E+00
0.0315	0.0307	0.0205	-0.393E+04	-0.268E+05	0.586E+00
0.0410	0.0000	0.0278	-0.532E+04	-0.272E+05	0.781E+00
0.0402	0.0091	0.0273	-0.518E+04	-0.270E+05	0.765E+00
0.0382	0.0172	0.0258	-0.483E+04	-0.267E+05	0.723E+00
0.0354	0.0238	0.0238	-0.437E+04	-0.262E+05	0.666E+00
0.0410	0.0278	0.0000	-0.516E+04	-0.264E+05	0.781E+00
0.0402	0.0273	0.0091	-0.502E+04	-0.262E+05	0.765E+00
0.0382	0.0258	0.0172	-0.481E+04	-0.266E+05	0.723E+00
0.0510	0.0000	0.0000	-0.699E+04	-0.280E+05	0.100E+01
0.0494	0.0000	0.0113	-0.654E+04	-0.271E+05	0.965E+00
0.0494	0.0113	0.0000	-0.654E+04	-0.267E+05	0.965E+00
0.0481	0.0110	0.0110	-0.624E+04	-0.267E+05	0.934E+00
0.0457	0.0000	0.0208	-0.588E+04	-0.267E+05	0.881E+00
0.0446	0.0101	0.0203	-0.583E+04	-0.272E+05	0.858E+00
0.0457	0.0208	0.0000	-0.573E+04	-0.260E+05	0.881E+00
0.0446	0.0203	0.0101	-0.570E+04	-0.266E+05	0.858E+00

Table B-2: Results of TMESH4 for a travel speed of 60 ipm

Coord. (inch)			$\epsilon_L = \epsilon_s / 2$	T_s	cos n
-X	Y	Z	(°C/s)	(°C/inch)	
0.0000	0.0000	0.0230	0.000E+00	-0.620E+05	0.000E+00
0.0000	0.0072	0.0218	0.000E+00	-0.567E+05	0.000E+00
0.0272	0.0000	0.0204	-0.104E+05	-0.543E+05	0.192E+00
0.0268	0.0065	0.0195	-0.100E+05	-0.528E+05	0.188E+00
0.0000	0.0127	0.0191	0.000E+00	-0.535E+05	0.000E+00
0.0256	0.0115	0.0172	-0.090E+05	-0.504E+05	0.179E+00
0.0000	0.0162	0.0162	0.000E+00	-0.508E+05	0.000E+00
0.0242	0.0148	0.0148	-0.080E+00	-0.485E+05	0.167E+00
0.0000	0.0230	0.0000	0.000E+00	-0.622E+05	0.000E+00
0.0000	0.0218	0.0072	0.000E+00	-0.568E+05	0.000E+00
0.0272	0.0204	0.0000	-0.104E+05	-0.545E+05	0.192E+00
0.0268	0.0195	0.0065	-0.100E+05	-0.531E+05	0.188E+00
0.0000	0.0191	0.0127	0.000E+00	-0.523E+05	0.000E+00
0.0256	0.0172	0.0115	-0.091E+05	-0.513E+05	0.179E+00
0.0473	0.0000	0.0141	-0.241E+05	-0.546E+05	0.442E+00
0.0467	0.0045	0.0136	-0.230E+05	-0.536E+05	0.430E+00
0.0451	0.0084	0.0126	-0.201E+05	-0.502E+05	0.401E+00
0.0429	0.0113	0.0113	-0.174E+05	-0.475E+05	0.366E+00
0.0473	0.0141	0.0000	-0.243E+05	-0.536E+05	0.442E+00
0.0467	0.0136	0.0045	-0.230E+05	-0.525E+05	0.430E+00
0.0451	0.0126	0.0084	-0.202E+05	-0.506E+05	0.401E+00
0.0550	0.0000	0.0091	-0.342E+05	-0.516E+05	0.662E+00
0.0546	0.0030	0.0090	-0.327E+05	-0.505E+05	0.645E+00
0.0534	0.0057	0.0086	-0.289E+05	-0.480E+05	0.602E+00
0.0518	0.0081	0.0081	-0.292E+05	-0.449E+05	0.549E+00
0.0550	0.0091	0.0000	-0.324E+05	-0.481E+05	0.662E+00
0.0546	0.0090	0.0030	-0.322E+05	-0.476E+05	0.645E+00
0.0534	0.0086	0.0057	-0.280E+05	-0.468E+05	0.602E+00
0.0600	0.0000	0.0000	-0.060E+06	-0.609E+05	0.100E+01
0.0592	0.0000	0.0035	-0.060E+06	-0.595E+05	0.927E+00
0.0592	0.0035	0.0000	-0.053E+05	-0.572E+05	0.927E+00
0.0586	0.0034	0.0034	-0.491E+05	-0.565E+05	0.870E+00
0.0574	0.0000	0.0066	-0.434E+05	-0.558E+05	0.787E+00
0.0569	0.0032	0.0065	-0.412E+05	-0.546E+05	0.755E+00
0.0574	0.0066	0.0000	-0.412E+05	-0.524E+05	0.787E+00
0.0569	0.0065	0.0032	-0.390E+05	-0.524E+05	0.755E+00

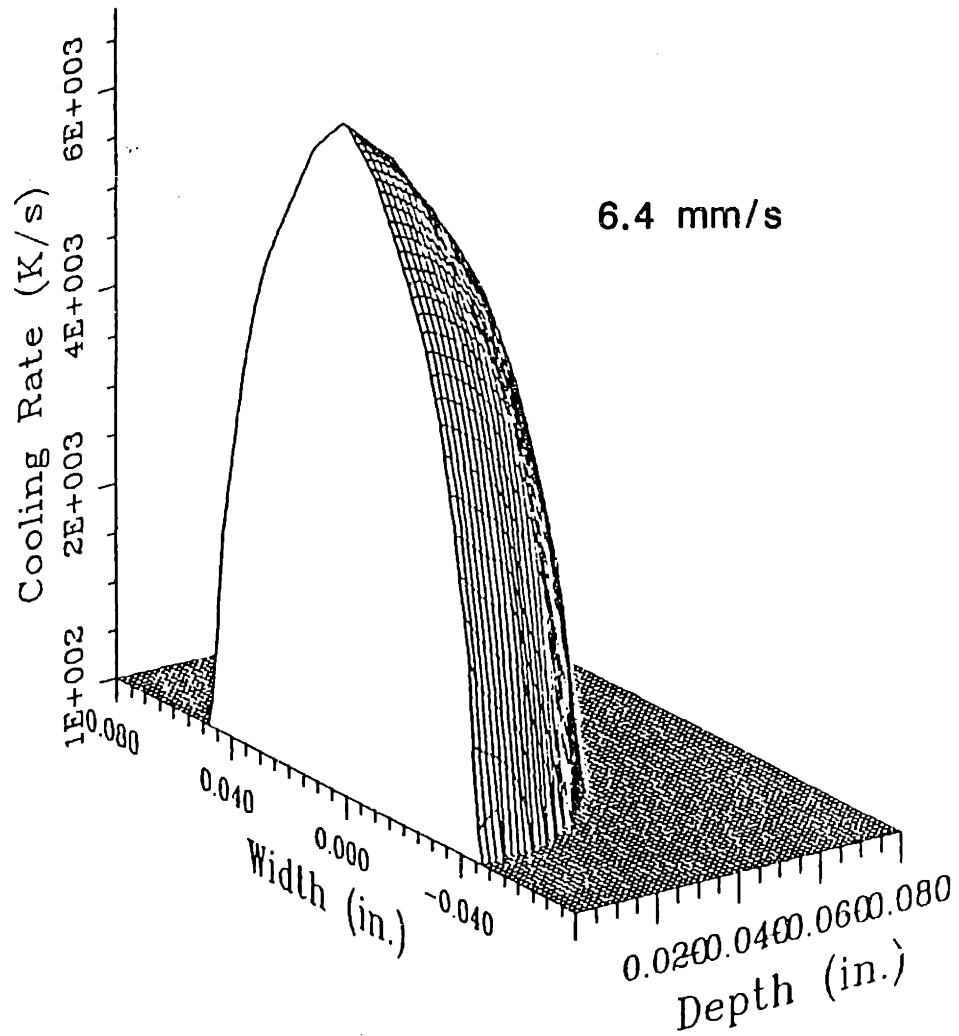


Figure B.1 Results of the FEM program showing the distribution of cooling rates at the L/S interface of a surface melt moving at 6.4 mm/s in 304 stainless steel.

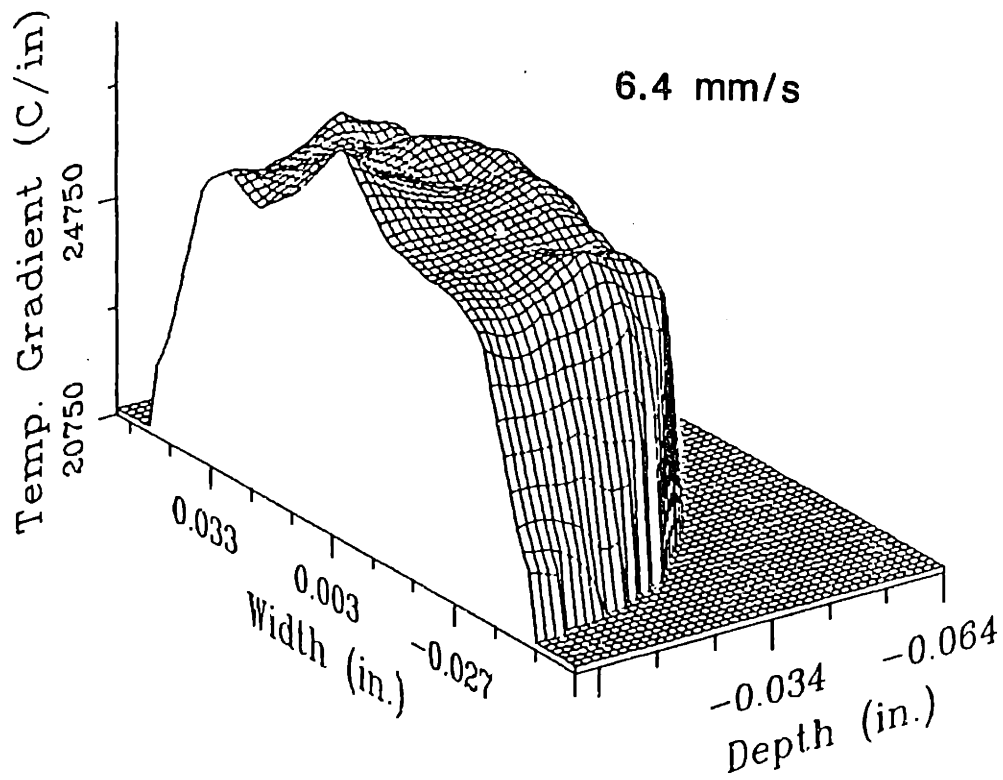


Figure B.2 Results of the FEM program showing the distribution of temperature gradients at the L/S interface of a surface melt moving at 6.4 mm/s in 304 stainless steel.

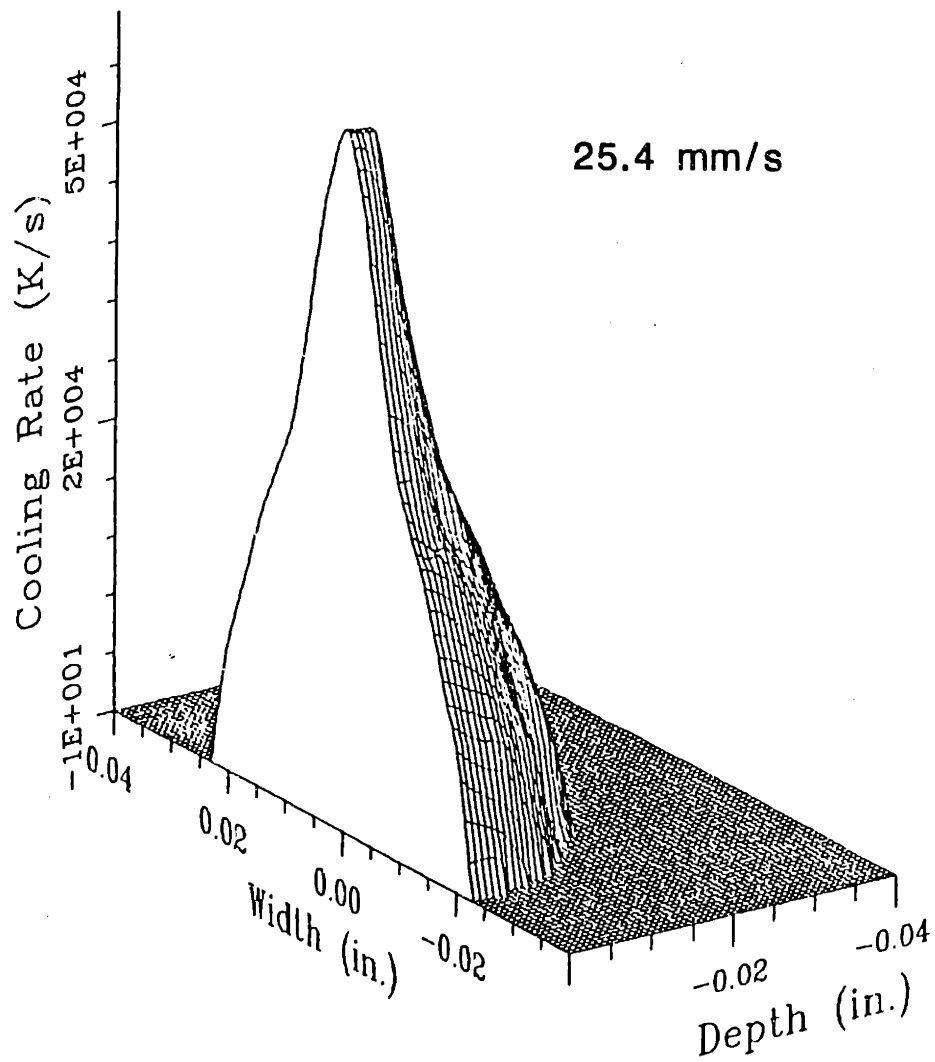


Figure B.4 Results of the FEM program showing the distribution of temperature gradients at the L/S interface of a surface melt moving at 25.4 mm/s in 304 stainless steel.

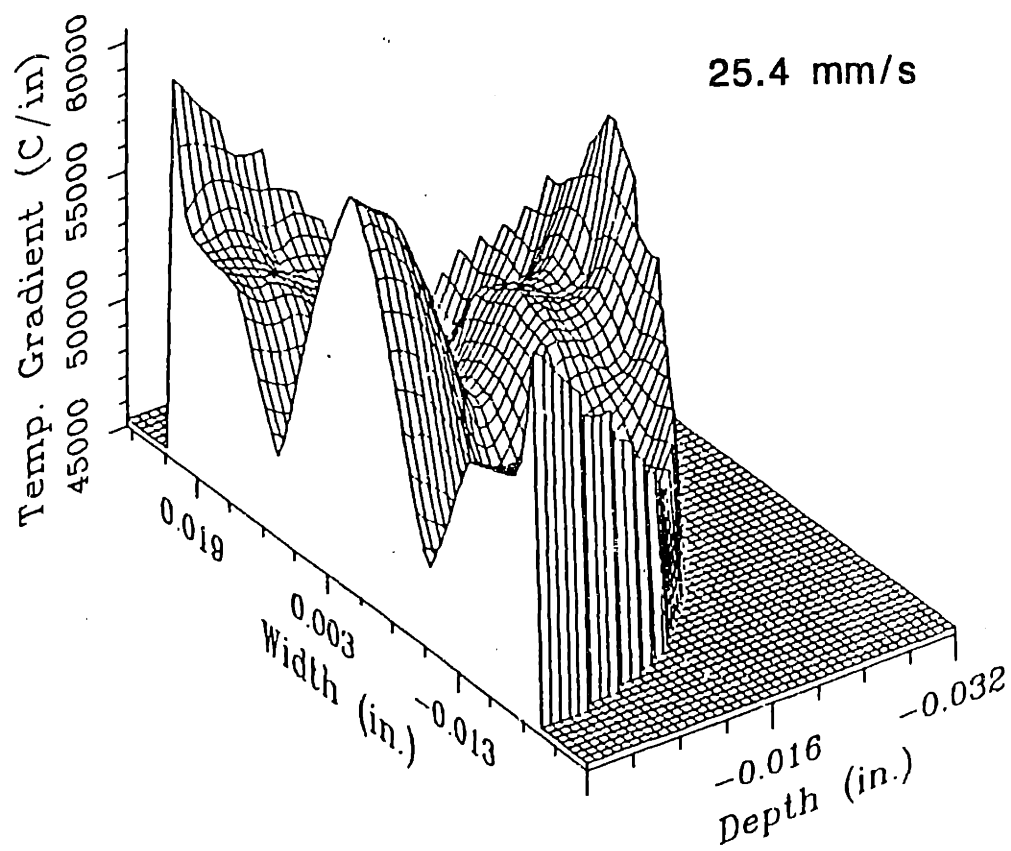


Figure B.3 Results of the FEM program showing the distribution of cooling rates at the L/S interface of a surface melt moving at 25.4 mm/s in 304 stainless steel.

PROGRAMS

(1) REARR

This program rearranges the 9-track tape data which contains the 3-D mesh of the base plate. However, before running this program, take out the weld pool data and leave only the data for the base plate. The input data format for n nodal points is:

line 1	total nodal points				
line 2 to n	node #	x	y	z	
line n+1	total elements				
line n+2 to end	element #	node #	node #	node #	node #

The arranged output data are stored in FEM3D.DAT

(2) OPTNUM

This program reduces the bandwidth to save computational time. The input data file must be FEM3D.DAT output data file is BWRED.DAT (invisible)

(3) BOUND

This program locates the interfacial nodal numbers. Since the weld pool is the combination of two ellipsoids, the complex weld pool shape (option #2) is recommended to locate the interfacial boundary point numbers. Input data files are BWRED.DAT (invisible) and FEM3D.DAT. The output data files are NODE.DAT, ELEINT.DATA, UNKNOWN.DAT, INPUT.DAT, (all are invisible) and BNODE.DAT

Note: In the floppy disk, there is another file called BOUNDO.FOR. This program

locates the boundary interfacial node # when the weld pool is at the 'corner' of the base plate.

(4) FEM3D

This program calculates the temperature profile in the base plate. MAKE SURE THAT YOU CHANGE THE DIMENSIONS IN THE COMMON BLOCKS EVERY TIME YOU CHANGE TO A MESH and then recompile this program. The command to compile is: FORT FEM3D, LINK FEM3D, RUN FEM3D.

In order to find the number to be changed, search for the word COMMON. NCL is always 1 NP is the total node number and NBW is the bandwidth (If you forget NBW, open the file BWRED.DAT and NBW is at the bottom of the file). Input data files are INPUT.DATA (invisible) and FEM3D.DAT and the output data file is TEMP.DAT (invisible).

(5) TEMGRD

This program calculates the temperature gradient in the base plate and from the temperature gradient it calculates the cooling rate. Open BNODE.DAT because it includes all the data points at the interface, and the final result of cooling rate can be found in the COOLRT.DAT file. Input data files are TEMP.DAT (invisible), FEM3D.DAT and/or BNODE.DAT. The output data file is COOLRT.DAT

REARR

```

C   This program is to rearrange the input data from the format of
C   9-track tape to the input format used in FEM3D.FOR program
C
REAL X(2500),Y(2500),Z(2500)
BYTE FILE(15),STRING(80)
INTEGER NS(4),ELENUM,DUMMY
C
TYPE 10
10  FORMAT(1X,'If the number of node is over 2500, you must
    1 change',/)
TYPE 11
11  FORMAT(1X,'the dimension of X,Y,Z in REARR.FOR program',/)
TYPE *,*****
TYPE 20
20  FORMAT('$INPUT THE NAME OF THE ORIGINAL MESH FILE : ')
ACCEPT 25,FILE
25  FORMAT(15A1)
FILE(15) = 0
C
OPEN(UNIT=11,FILE=FILE,TYPE='UNKNOWN')
OPEN(UNIT=22,FILE='FEM3D.DAT',TYPE='UNKNOWN')
C
C   *****
C   NNODE: # OF NODES
C   NEL : # OF ELEMENTS
C   NS() : NODE # IN THE TETRAHEDRON
C   *****
C
READ(11,*) NNODE
WRITE(22,*) NNODE
TYPE *,NNODE
DO 30 J=1,NNODE
READ(11,1001) NCHR,STRING
1001  FORMAT(Q,80A1)
DO 50 I=1,NCHR
50   IF(STRING(I).EQ.'e') STRING(I)=69
    DECODE(NCHR,1002,STRING) DUMMY,X(DUMMY),Y(DUMMY),Z(DUMMY)
1002  FORMAT(15,3(2X,E20.10))
C   TYPE *,DUMMY,X(DUMMY),Y(DUMMY),Z(DUMMY)
WRITE(22,*) DUMMY,X(DUMMY),Y(DUMMY),Z(DUMMY)
30   CONTINUE
C
READ(11,*) NEL
DO 40 J=1,NEL
READ(11,*) ELENUM,NS
C   TYPE *,ELENUM,NS
WRITE(22,*) ELENUM,NS
40   CONTINUE
CALL EXIT
END

```

OPTNUM

```

VIRTUAL NEWJT(2000),JOINT(2000)
VIRTUAL JNT(2000)
VIRTUAL JMEM(2000)
BYTE FILE(15)
VIRTUAL MEMJT(96000)
INTEGER JT(38000)
C *****
C DATA MAXCON/48/,NNODE/4/
C
C For more detail, see International Journal for Numerical Methods
C in Engineering, Vol. 6, 345-356 (1973) by R. J. Collins
C For example:
C If I have 18 triangles with the node # configurated like
C 1 15 2 4
C 14 16 3 5
C 6 7 8 9
C 10 11 12 13
C
C NJTS: TOTAL NODE # (= 16)
C LMENTS: TOTAL ELEMENT # (= 18) (SINCE I HAVE 18 TRIANGLES)
C NBW: ORIGINAL BANDWIDTH
C NNODE: # OF NODE IN ONE ELEMENT ( 3 FOR LINEAR TRIANGLE )
C MAXCON: MAXIMUM CONNECTING POINT # FOR THE INTERIOR POINT
C e.g. in triangular element, MAXCON = 6
C JT: SIZE = LMENTS*NNODE The first row is the list
C of the node # which is included in the element 1, the
C last row is the list of the node # which is included in
C the last element (say 18 in this example)
C e.g. 1 16 15
C 1 14 16
C 15 3 2
C 15 16 3
C and so on
C 8 12 13
C
C MEMJT: SIZE = MAXCON*NJTS
C The first column is the list of the node # which is
C related to node #1, the last column is the list of the
C node # which is related to the last node #.
C e.g. 14 ***** 15
C 16 14
C 15 7
C 0 3
C 0 1
C 0 8
C JMEM: SIZE = 1*NJTS
C The 1st entry is 3 since node 1 has 3 nodes related to it.
C The last entry is 6 since node 16 has 6 nodes related to it.
C e.g (3,4,6,2,*,*,*,*,*,*,*,*,*,6)
C JNTI: NODE # -----
C JJT: NODE # -----
C IDIFF: MODIFIED BW
C MAX: MODIFIED BW
C NEWJT: SIZE = 1*NJTS e.g. [3 9 8 4 1 7 2 5 6-----] old
C 1 2 3 4 5 6 7 8 9 new
C old node # 3 = new node # 1
C old node # 9 = new node # 2
C JOINT: SIZE = 1*NJTS e.g. [5 7 1 4 8 9 6 3 2-----] new
C 1 2 3 4 5 6 7 8 9 old
C new node # 1 = old node # 3
C new node # 2 = old node # 9
C JNT: SIZE = 1*NJTS

```

```

C          Basically, JNT() is the same as JOINT()
C          THIS IS THE FINAL OUTPUT IN BWRED.DAT FILE
          TYPE 1500
1500  FORMAT ('$ENTER NAME OF MESH FILE :')
          ACCEPT 1501,FILE
1501  FORMAT (15A1)
          OPEN (UNIT=48,FILE='BWRED.DAT',TYPE='UNKNOWN')
          OPEN (UNIT=1,FILE=FILE,TYPE='UNKNOWN')
          READ (1,*) NJTS
          DO 5 I=1,NJTS
5      READ (1,*) IDUM
          READ (1,*) LMENTS
          TYPE *,NJTS,LMENTS
C
          DO 10 J=1,LMENTS
          READ(1,*) NDUMMY,(JT(LMENTS*(I-1)+J),I=1,NNODE)
10     CONTINUE
          CLOSE(UNIT=1)
C
C          *****
C          First, I have to use the information in the JT() to generate
C          JMEM() AND MEMJT()
C          *****
C
          IDIFF=NJTS
          DO 20 I=1,NJTS
          JMEM(I)=0
          DO 30 J=1,MAXCON
30     MEMJT((I-1)*MAXCON+J)=0
20     CONTINUE
C
          DO 90 J=1,LMENTS
          DO 80 I=1,NNODE
          JNTI=JT(LMENTS*(I-1)+J)
          JSUB=(JNTI-1)*MAXCON
C
          DO 70 II=1,NNODE
          IF(II.EQ.1) GOTO 70
          JJT=JT(LMENTS*(II-1)+J)
          MEM1=JMEM(JNTI)
C          TYPE *,J,MEM1
          IF(MEM1.EQ.0) GOTO 60
C
          DO 50 III=1,MEM1
          IF(MEMJT(JSUB+III).EQ.JJT) GOTO 70
50     CONTINUE
C
          JMEM(JNTI)=JMEM(JNTI)+1
          MEMJT(JSUB+JMEM(JNTI))=JJT
C
          IF(IABS(JNTI-JJT).GT.IDIFF) IDIFF=IABS(JNTI-JJT)
C
70     CONTINUE
80     CONTINUE
90     CONTINUE
C
C          *****
C          NOW, I HAVE JT(), JMEM(), AND MEMJT(), so I can calculate
C          the minimal BW
C          *****
          TYPE *,'BE PATIENT! I AM STILL WORKING VERY HARD'
C
          MINMAX=IDIFF
          DO 160 IK=1,NJTS
          DO 120 J=1,NJTS
          JOINT(J)=0

```



```

120  NEWJT(J)=0
      MAX=0
      I=1
      NEWJT(1)=IK
      JOINT(IK)=1
      K=1
130  K4=JMEM(NEWJT(I))
      JSUB=(NEWJT(I)-1)*MAXCON
      DO 140 JJ=1,K4
      K5=MEMJT(JSUB+JJ)
      IF(JOINT(K5).GT.0) GO TO 140
      K=K+1
      NEWJT(K)=K5
      JOINT(K5)=K
      NDIFF=IABS(I-K)
      IF(NDIFF.GE.MINMAX) GO TO 160
      IF(NDIFF.GT.MAX) MAX=NDIFF
140  CONTINUE
      IF(K.EQ.NJTS) GO TO 150
145  I=I+1
      GO TO 130
150  MINMAX=MAX
      DO 155 J=1,NJTS
155  JNT(J)=JOINT(J)
160  CONTINUE
      TYPE *, 'BANDWIDTH IS ',MINMAX+1
C
      DO 300 I=1,NJTS
300  NEWJT(I) = 0
C
      DO 400 I=1,NJTS
400  NEWJT(JNT(I)) = I
C
      WRITE(48,2002) NJTS,MINMAX+1
2002  FORMAT(2X,I5,3X,I4)
      WRITE(48,2001) (JNT(J),J=1,NJTS)
2001  FORMAT(10(I5,1X))
      WRITE(48,2001) (NEWJT(J),J=1,NJTS)
5001  FORMAT(16(I4,1X))
      WRITE(48,6002) MINMAX+1
6002  FORMAT(/,1X,'BANDWIDTH IS ',I4)
      CALL EXIT
      END

```

BOUND

```

C   This program is to find the boundary nodal number.
C   However, the output node numbers for the boundary interface nodes
C   are the NEW node number from BWRED.DAT file.
C
INTEGER NS(4),NS1(4),NS2(4),NUM(60),TEST,IBF(6)
INTEGER N(2000),NEWNOD(2000),LTETRA(400)
REAL BF(6),MP(400)
COMMON NBOUN(1500),NBOUN1(1500)
BYTE FILE(16)
C
TYPE 100
100  FORMAT('$ENTER NAME OF THE MESH FILE : ')
ACCEPT 110,FILE
110  FORMAT(15A1)
TYPE 90
90  FORMAT('$MELTING POINT OF THIS MATERIAL ? (deg. K) ')

```

```

ACCEPT *,AMP
104 TYPE 105
105 FORMAT('OYOU CAN CHOOSE THE FOLLOWING WELD POOL SHAPE :',//
1 ' 1= ELLIPSOID',/
2 ' 2= COMPLEX WELD POOL',/)
TYPE 106
106 FORMAT('$WHICH ONE DO YOU LIKE ? ')
ACCEPT *,TEST
IF(TEST.EQ.1.OR.TEST.EQ.2) GOTO 107
TYPE ', 'OOPS ! YOU MAKE A MISTAKE'
GOTO 104

C
107 OPEN(UNIT=77,FILE='BWRED.DAT',TYPE='UNKNOWN')
READ(77,*) NODTOT,IDUM2
READ(77,2001) (NEWNOD(I), I=1,NODTOT)
2001 FORMAT(10(I5,1X))
CLOSE(UNIT=77)

C
XMAX=0
YMAX=0
ZMAX=0
XNEGMX=0
OPEN(UNIT=11,FILE=FILE,TYPE='UNKNOWN')
READ(*,*) NODENU
DO 120 I=1,NODENU
READ(11,*) IDUM,X,Y,Z
IF(Y.GT.YMAX) YMAX=Y
IF(Z.GT.ZMAX) ZMAX=Z
IF(X.LT.0.) GOTO 220
IF(X.GT.XMAX) XMAX=X
GOTO 120
220 IF(X.LT.XNEGMX) XNEGMX = X
120 N(I)=0
REWIND 11
XPOOL=XMAX
YPOOL=YMAX
ZPOOL=ZMAX
XNEGPL=XNEGMX

C
READ(11,*) NODENU
DO 210 I=1,NODENU
READ(11,*) IDUM,X,Y,Z
IF(X.EQ.0..AND.Y.EQ.0..AND.Z.LT.ZPOOL) ZPOOL = Z
IF(Z.EQ.0..AND.X.EQ.0..AND.Y.LT.YPOOL) YPOOL = Y
IF(X.LT.0.) GOTO 230
IF(Y.EQ.0..AND.Z.EQ.0..AND.X.LT.XPOOL) XPOOL = X
GOTO 210
230 IF(Y.EQ.0..AND.Z.EQ.0..AND.X.GT.XNEGPL) XNEGPL = X
210 CONTINUE

C
TYPE ', 'BE PATIENT ! I AM STILL WORKING VERY HARD !'

C
READ(11,*) IELEM
DO 130 I=1,IELEM
READ(11,*) IDUM,NS
DO 140 J=1,4
140 N(NS(J))=N(NS(J))+1
130 CONTINUE

C
DO 240 I=1,NODENU
IF(N(I).NE.24) GOTO 240
TYPE ', 'JOHN, YOU HAVE CHECK NODE POINT ',N(I)
TYPE ', 'THIS POINT HAS 24 CONNECTING TETRAHEDRONS'
240 CONTINUE

C
OPEN(UNIT=22,FILE='NODE.DAT',TYPE='UNKNOWN')

```

```

WRITE(22,160) ((I,N(I)),I=1,NODENU)
160  FORMAT(7(I5,1X,13,2X))
C
DO 150 I=1,60
150  NUM(I)=0
C
DO 170 I=1,NODENU
170  NUM(N(I))=NUM(N(I)) + 1
WRITE(22,180) ((I,NUM(I)),I=1,60)
180  FORMAT(//6(I2,1X,14,5X))
WRITE(22,190) XMAX,XNEGMX,YMAX,ZMAX
190  FORMAT(//1X,'XMAX=',G12.5,'XNEGMX=',G12.5,
1 'YMAX=',G12.5,'ZMAX=',G12.5)
WRITE(22,290) XPOOL,XNEGPL,YPOOL,ZPOOL
290  FORMAT(/1X,'XPOOL=',G12.5,2X,'XNEGPL=',G12.5/
1 1X,'YPOOL=',G12.5,2X,'ZPOOL=',G12.5//)
C
C *****
C NOW, TO FIND THE BOUNDARY NODAL POINT.
C I BOLDLY ASSUME THAT IT IS IMPOSSIBLE EITHER TO HAVE AN
C INTERIOR POINT WHICH HAS 24 CONNECTING TETRAHEDRONS. OR
C TO HAVE AN EXTERNAL POINT WHICH HAS 24 CONNECTING TETRAHEDRONS.
C *****
C
C *****
C I ASSUME ANY POINT WHICH HAS MORE THAN 24 CONNECTING
C TETRAHEDRONS IS THE INTERIOR POINT.
C ALSO, IF THERE ARE N TOTAL TETRAHEDRONS AND n TOTAL NODAL POINTS,
C I SHOULD HAVE N/12 POINTS WHICH HAVE 12 CONNECTING TETRAHEDRONS.
C THESE N/6 POINTS ARE ALL INTERIOR POINTS AND ARE LOCATED FROM
C NODAL NUMBER n - N/12 + 1 to n.
C *****
C
C *****
C TO TAKE INTERIOR POINTS OUT
C *****
C
INTNAL = IELEM/12
LAST = NODENU - INTNAL
J=1
DO 250 I=1,LAST
IF(N(I).GE.24) GOTO 250
NBOUN(J) = I
J=J+1
250  CONTINUE
C
C
OPEN(UNIT=44,FILE='UNKNOW.DAT',TYPE='UNKNOWN')
OPEN(UNIT=55,FILE='ELEINT.DAT',TYPE='UNKNOWN')
OPEN(UNIT=99,FILE='BNODE.DAT',TYPE='UNKNOWN')
C
C ELEINT = ELEMENTS AT INTERFACE
C
REWIND 11
J = 1
J1= 1
READ(11,*) IDUM
DO 300 I=1,LAST
READ(11,*) NUMBER,X,Y,Z
C
IF(TEST.NE.1) GOTO 400
ONE = X**2/XPOOL**2 + Y**2/YPOOL**2 + Z**2/ZPOOL**2
ZERO = ABS(ONE - 1.)
IF(ZERO.GT.0.002) GOTO 400
WRITE(22,*) NUMBER,X,Y,Z
400  IF(NUMBER.NE.NBOUN(J1)) GOTO 300

```

```

J1 = J1 + 1
IF(ABS(Y).GT.1.0E-10) GOTO 310
IF(X.GT.XPOOL.OR.X.LT.XNEGPL.OR.
1 Z.GT.ZPOOL) GOTO 300
C
405 IF(N(NUMBER).GT.12) GOTO 300
IF(N(NUMBER).LT.12) GOTO 315
TYPE *,'John, you have to check file unknow.dat.'
TYPE *,'This file contains nodal points that I cannot'
TYPE *,'determine if they are at the interface or not.'
WRITE (44,*) N(NUMBER),X,Y,Z
GOTO 300
315 NBOUND1(J) = I
IF(TEST.NE.2) GOTO 316
WRITE(22,*) NBOUND1(J),X,Y,Z
WRITE(55,*) NBOUND1(J),X,Y,Z
316 J = J + 1
GOTO 300
310 IF(ABS(Z).GT.1.0E-10) GOTO 330
IF(X.GT.XPOOL.OR.X.LT.XNEGPL.OR.
1 Y.GT.YPOOL) GOTO 300
GOTO 405
330 IF(X.EQ.XMAX.OR.X.EQ.XNEGMX.OR.Y.EQ.YMAX.
1 OR.Z.EQ.ZMAX) GOTO 300
NBOUND1(J) = I
IF(TEST.NE.2) GOTO 335
WRITE(22,*) NBOUND1(J),X,Y,Z
WRITE(55,*) NBOUND1(J),X,Y,Z
335 J = J + 1
300 CONTINUE
IBTOT = J - 1
WRITE(22,340) IBTOT
340 FORMAT(//1X,'There are ',I3,' interface boundary points')
TYPE 340, IBTOT
CLOSE(UNIT=22)
CLOSE(UNIT=44)
WRITE(55,*) 0,0,0,0
C
C .....
C TO create an output file which contains the element #
C that has one side as part of the solid-liquid interface.
C .....
C
DO 560 I=1,INTNAL
560 READ(11,*) IDUM,X,Y,Z
C
K1 = 1
READ(11,*) IELEM
TYPE *,'THIS # SHOULD BE THE TOTAL ELEMENT # ',IELEM
DO 500 I1=1,IELEM
READ(11,*) NELEM,NS
ITOT = 0
DO 550 I2=1,4
NS1(I2) = 0
550 NS2(I2) = 0
L = 1
L2 = 1
C
DO 510 I=1,4
DO 520 J=1,IBTOT
IF(NS(I).NE.NBOUND1(J)) GOTO 520
ITOT = ITOT + 1
NS1(L) = NS(I)
L = L + 1
GOTO 510
520 CONTINUE

```

```

510  CONTINUE
      IF(ITOT.EQ.3) GOTO 535
      IF(ITOT.EQ.2) GOTO 525
      GOTO 500

C
535  DO 530 K=1,4
      IF(NS(K).EQ.NS1(1).OR.NS(K).EQ.NS1(2).OR.NS(K).EQ.NS1(3))
1    GOTO 530
      WRITE(55,*) NELEM,(NS1(M),M=1,3),NS(K)
      LTETRA(K1) = NS(K)
      K1 = K1 + 1
      GOTO 500

C
525  DO 530 K=1,4
      IF(NS(K).EQ.NS1(1).OR.NS(K).EQ.NS1(2)) GOTO 530
      NS2(L2)=NS(K)
      L2 = L2 + 1
      LTETRA(K1) = NS(K)
      K1 = K1 + 1
      IF(L2.NE.3) GOTO 530
      WRITE(55,*) NELEM,(NS1(M),M=1,2),(NS2(M2),M2=1,2)
      GOTO 500

530  CONTINUE
500  CONTINUE
      WRITE(55,*) 0,0,0,0

C
C *****
C   TO WRITE THE (X,Y,Z) FOR THE POINT THAT IS PART OF
C   INTEFACIAL TETRAHEDRON BUT NOT ON THE INTERFACE
C *****
C
      TYPE *, 'YES! I KNOW, I AM STILL YOUR LOYAL SLAVE !'
      JTOT = K1-1

C
      REWIND 11
      READ(11,*) NODENU
      DO 600 I=1,NODENU
      READ(11,*) INODE,X,Y,Z
      DO 650 J=1,JTOT
      IF(LTETRA(J).NE.INODE) GOTO 650
      WRITE(55,*) INODE,X,Y,Z
      GOTO 600

650  CONTINUE
600  CONTINUE
      WRITE(55,*) 0,0,0,0
      CLOSE(UNIT=55)
      CLOSE(UNIT=11);

C
C *****
C   TO WRITE 'AE (X,Y,Z) OF THE BOUNDARY NODAL POINTS
C *****
      OPEN(UNIT=55,FILE='ELEINT.DAT',TYPE='UNKNOWN')
      OPEN(UNIT=99,FILE='BNODE.DAT',TYPE='UNKNOWN')
      WRITE(99,*) IBTOT
      DO 1550 LB=1,IBTOT
      READ(55,*) IDUM,DX,DY,DZ
      WRITE(99,*) DX,DY,DZ

1550 CONTINUE
      CLOSE(UNIT=55)
      CLOSE(UNIT=99)

C
C *****
C   TO create an output file which is the input file
C   in FEM3D.FOR program.
C *****
C

```

```

OPEN(UNIT=33,FILE='INPUT.DAT',TYPE='UNKNOWN')
IBTOT=IBTOT + 1
DO 1330 I=1,6
  IBF(I)=-1
1330  BF(I)=-2.
      WRITE(33,1320) (IBF(I),I=1,6),(BF(J),J=1,6)
1320  FORMAT(1X,6(I4,1X),3X,6(F6.1,1X))
      IQ=INT(IBTOT/6)
      IQ6=IQ*6
      IQ7=IQ6+6
      DO 1340 I=1,IBTOT-1
1340  MP(I)=AMP
      DO 1370 I=IBTOT,IQ7
      NBOUND1(I) = -1
1370  MP(I) = -2.
C
      DO 1350 I=1,IQ7
      IF(NBOUND1(I).LE.0) GOTO 1350
      NBOUND1(I) = NEWNOD(NBOUND1(I))
1350  CONTINUE
C
      DO 1360 I=1,IQ+1
      INIT=6*(I-1)
1360  WRITE(33,1320) (NBOUND1(J),J=INIT+1,INIT+6),
      1 (MP(J),J=INIT+1,INIT+6)
C
      CALL EXIT
      END

```

FEM3D

```

C   THIS PROGRAM IS TO CALCULATE THE TEMPERATURE PROFILE OF THE
C   ELECTRON BEAM WELD.
C
C   Boundary conditions are
C   (1) constant temperature at the liquid-solid interface
C   (2) radiation heat loss at the free surface except at the
C       surface of liquid metal
C
C   This is a Cartesian coordinate.
C
C   The element used in the FEM is tetrahedral element.
C   In the final calculation, this program uses K.G.S. unit.
C   The symbols used in this program are almost identical to the
C   the symbols used in Segerlind's book.
C
REAL  A(*C0000)
REAL  X1(2000),Y1(2000),Z1(2000)
INTEGER MESH(9000,4),N(4),NEWNOD(2000),IOLD(2000)
REAL  B(3,4),BDB1(4,4),BDB2(4,4),BDB3(4,4)
REAL  ESM(4,4),EF(4),X(4),Y(4),Z(4)
INTEGER NS(4)
COMMON NP,NBW,NCL,AMP,A
BYTE  FILE(15)
INTEGER*4 JEND,J5
C   *****
C   DIMENSION OF A MUST BE GE. NP*(NBW+2)
C   *****
DATA NCL/1/
C   #####
C   This program is based on W, kg, inch, and sec.
C   #####

```

```

TYPE 1700
1700 FORMAT('*****./
1 'OJOHN, MAKE SURE THE DIMENSIONS IN THE MAIN PROGRAM',/
2 'OAND THE THREE SUBROUTINES FIT EXACTLY THE SIZE OF',/
3 'ONODE # AND BANDWIDTH #',/
4 '*****./')
C
TYPE 1500
1500 FORMAT ('$ENTER NAME OF MESH FILE :')
ACCEPT 1501,FILE
1501 FORMAT (15A1)
TYPE 1600
1600 FORMAT ('$ENTER ARC TRAVELLING SPEED (inch/sec) :')
ACCEPT *, VEL
TYPE 1800
1800 FORMAT ('$ENTER THE MELTING POINT (deg. K) :')
ACCEPT *, AMP
TYPE 1810
1810 FORMAT ('$ENTER THERMAL CONDUCTIVITY (W/m-K) :')
ACCEPT *,COND
COND = COND*0.01*2.54 ! W/m-K to W/inch-K
TYPE 1820
1820 FORMAT ('$ENTER DENSITY (kg/m**3) :')
ACCEPT *,DENS
DENS = DENS / 39.37**3 ! kg/m**3 to kg/inch**3
TYPE 1830
1830 FORMAT ('$ENTER SPECIFIC HEAT (J/kg-K) :')
ACCEPT *,SPHT
SPHT = SPHT*1. ! J/kg-K
C
OPEN(UNIT=55,FILE='BWRED.DAT',TYPE='UNKNOWN')
READ(55,*) NODEP,NBW
READ(55,2001) (NEWNOD(I), I=1,NODEP)
2001 FORMAT(10(I5,1X))
READ(55,2001) (IOLD(I), I=1,NODEP)
CLOSE(UNIT=55)
C
OPEN (UNIT=1,FILE=FILE,TYPE='UNKNOWN')
READ (1,*) NODEP
DO 10 I=1,NODEP
10 READ (1,*) INODE,X1(NEWNOD(INODE)),Y1(NEWNOD(INODE))
1 ,Z1(NEWNOD(INODE))
READ (1,*) NE
C
DO 20 I=1,NE
READ(1,*) IELEM,N
DO 25 J=1,4
25 MESH(IELEM,J) = NEWNOD(N(J))
20 CONTINUE
CLOSE(UNIT=1)
NP=NCL*NODEP
TYPE *,'DATA READING IS DONE'
TYPE *,'TOAL NODE # AND ELEMENT # ARE ', NP,NE
C
C A THE COLUMN VECTOR CONTAINING TEMPERATURE, F AND K
C NS ELEMENT NODE NUMBERS
C ESM(I,J) ELEMENT STIFFNESS(CONDUCTANCE) MATRIX
C I=1,4 J=1,4 FOR TETRAHEDRAL ELEMENT
C GSM(I,J) CONSTRUCTED GLOBAL STIFFNESS MATRIX as in eq. 7.17 (i.e., it is
C not the true global stiffness matrix, see pp. 120 of LJS)
C I=1,NP J=1,NBW BUT THE "TRUE" GLOBAL STIFFNESS MATRIX HAS
C NP*NP DIMENSION
C EF ELEMENT FORCE VECTOR
C COE(I,J) COEFFICIENT (2/DELTA)*C-K as shown on pp. 217 LJS
C TEMP NODAL VALUES FOR A SINGLE ELEMENT
C NP NUMBFR OF GLOBAL DEGREES OF FREEDOM IN THE ENTIRE PROBLEM.

```

```

C NE  TOTAL NUMBER OF ELEMENTS
C NBW  BANDWIDTH OF THE SYSTEM OF EQUATIONS
C NEL  NUMBER OF AN INDIVIDUAL ELEMENT
C NCL  NUMBER OF LOADING CASES USUALLY=1
C X(1),Y(1)----- COORDINATES OF THE ELEMENT NODES(COUNTER CLOCKWISE)
C B&C  COEFFICIENTS THAT OCCUR DURING THE EVALUATION OF THE ELEMENT MATRIX
C VOL6 SIX TIMES THE TETRAHEDRAL VOLUME
C AR2  TWO TIMES THE ELEMENT AREA
C JGF  A POINTER INDICATING THE LAST STORAGE LOCATION FOR TEMPERATURE IN A
C JGSM A POINTER INDICATING THE LAST STORAGE LOCATION FOR F IN A
C JEND A POINTER INDICATING THE LAST STORAGE LOCATION FOR K IN A
C COND THERMAL UCTIVITY (cal/cm-sec-deg.C)
C SPHT SPECIFIC HEAT (cal/gm-deg.C)
C DENS DENSITY (gm/cm**3.)
C ISIDE WHEN ISIDE(=)1, IT MEANS THIS IS THE "FREE" SURFACE
C      WHEN ISIDE(=)0, IT MEANS THIS IS NOT THE "FREE" SURFACE

C H   HEAT TRANSFER COEFFICIENT (W/m**2*deg C)
C NEWNOD() NEW NODE NUMBER ARRAY
C *****
C      TO CALCULATE POINTERS
C *****
      JGF=NP*NCL
      JGSM=JGF**2
      JEND=JGSM+NP*NBW
C *****
C      INITIALIZATION TO 0 DEGREE K
C *****
      DO 331 I=1,JGF
331  A(I) = 0.
C *****
C      INPUT (X,Y,Z) DATA OF EACH NODAL POINT
C *****
      DO 7 KK=1,NE
      DO 30 I=1,4
30   NS(I)=MESH(KK,I)
      DO 40 I=1,4
      X(I)=X1(NS(I))
      Y(I)=Y1(NS(I))
      Z(I)=Z1(NS(I))
40   CONTINUE
C *****
C      TO CALCULATE 6*VOLUME
C *****
VOL6 = (X(2)-X(1))*(Y(3)-Y(1))*(Z(4)-Z(1))-
1  (Y(2)-Y(1))*(Z(3)-Z(1))*(X(4)-X(1))+
2  (Z(2)-Z(1))*(X(3)-X(1))*(Y(4)-Y(1))-
3  (Z(2)-Z(1))*(Y(3)-Y(1))*(X(4)-X(1))-
4  (Y(2)-Y(1))*(X(3)-X(1))*(Z(4)-Z(1))-
5  (X(2)-X(1))*(Z(3)-Z(1))*(Y(4)-Y(1))
VOL6 = ABS(VOL6)
C *****
C      TO CALCULATE THE COMPONENTS IN SHAPE FUNCTION
C      Ni,Nj,Nk,Nl
C      Note: [1/(6*Volume)]*B(I,J) is the component
C      of the shape function
C *****
45  B(1,1) = -((Y(3)-Y(2))*(Z(4)-Z(2))-
1  (Y(4)-Y(2))*(Z(3)-Z(2)))
      B(1,2) = ((Y(3)-Y(1))*(Z(4)-Z(1))-
1  (Y(4)-Y(1))*(Z(3)-Z(1)))
      B(1,3) = -((Y(2)-Y(1))*(Z(4)-Z(1))-
1  (Y(4)-Y(1))*(Z(2)-Z(1)))
      B(1,4) = ((Y(2)-Y(1))*(Z(3)-Z(1))-
1  (Y(3)-Y(1))*(Z(2)-Z(1)))
      B(2,1) = ((X(3)-X(2))*(Z(4)-Z(2))-

```



```

1      (X(4)-X(2))*(Z(3)-Z(2))
B(2,2) = -((X(3)-X(1))*(Z(4)-Z(1))-
1      (X(4)-X(1))*(Z(3)-Z(1)))
B(2,3) = ((X(2)-X(1))*(Z(4)-Z(1))-
1      (X(4)-X(1))*(Z(2)-Z(1)))
B(2,4) = -((X(2)-X(1))*(Z(3)-Z(1))-
1      (X(3)-X(1))*(Z(2)-Z(1)))
B(3,1) = -((X(3)-X(2))*(Y(4)-Y(2))-
1      (X(4)-X(2))*(Y(3)-Y(2)))
B(3,2) = ((X(3)-X(1))*(Y(4)-Y(1))-
1      (X(4)-X(1))*(Y(3)-Y(1)))
B(3,3) = -((X(2)-X(1))*(Y(4)-Y(1))-
1      (X(4)-X(1))*(Y(2)-Y(1)))
B(3,4) = ((X(2)-X(1))*(Y(3)-Y(1))-
1      (X(3)-X(1))*(Y(2)-Y(1)))
C      *****
C      TO CALCULATE THE VOLUME INTEGRAL OF {B}*{D}*{B}
C      This integral (actually, summation) is expressed by
C      the summation of ESM(I,J)
C      ASSUME it is an isotropic material, i.e., the thermal
C      conductivity is independent of x,y,z direction.
C      *****
DO 920 I=1,4
DO 920 J=1,4
BDB1(I,J) = B(1,I)*B(1,J)
BDB2(I,J) = B(2,I)*B(2,J)
BDB3(I,J) = B(3,I)*B(3,J)
920  CONTINUE
C      *****
C      The volume integral of {B}*{D}*{B} is the summation
C      of BDB1(I,J), BDB2(I,J), and BDB3(I,J) and then
C      multiplied by a constant ( = COND/VOL6 )
C      *****
CONST1 = COND/VOL6
DO 930 I=1,4
DO 930 J=1,4
ESM(I,J) = CONST1*(BDB1(I,J) + BDB2(I,J) +
1      BDB3(I,J))
930  CONTINUE
C      *****
C      TO Consider the additional term vel*Cp*density*temp gradient
C      The arc is travelling in the -ve X direction.
C      *****
C
CONST2 = VEL * DENS * SPHT/24.
DO 35 I=1,4
DO 35 J=1,4
ESM(I,J) = ESM(I,J) + CONST2 * B(1,J) | -ve X direction
35  CONTINUE
C      *****
C      INITIALZATION OF THE FORCE MATRIX
C      *****
C
DO 940 I=1,4
940  EF(I)=0.
C      *****
C      ASSUME that convective and radiative heat loss can be neglected

```

```

C *****
C PUT ELEMENT PROPERTIES INTO THE GLOBAL STIFFNESS MATRIX
C *****
DO 7 I=1,4
II=NS(I)
DO 15 J=1,NCL
J5=JGF+(J-1)*NP+II
15 A(J5)=A(J5)+EF(I)
DO 17 J=1,4
C ***** JJOLD: ORIGINAL MATRIX "COLUMN" # *****
C ***** JJ: BAND MATRIX "COLUMN" # *****
C ***** II: ORIGINAL AND BAND MATRIX ROW # *****
C
JJOLD=NS(J)
JJ=JJOLD-II+1
IF(JJ) 17,17,16
16 J5=JGSM+(JJ-1)*NP+II
A(J5)=A(J5)+ESM(I,J)
17 CONTINUE
7 CONTINUE
CLOSE(UNIT=22)
C
C *****
C MODIFICATION AND SOLUTION OF THE SYSTEM OF EQUATIONS
C *****
C
TYPE *, 'ASSEMBLY OF THE ELEMENTS IS DONE'
C
TYPE *, 'I STILL HAVE 3 SUBROUTINES TO SOLVE'
CALL BDYVAL
TYPE *, 'I STILL HAVE 2 SUBROUTINES TO SOLVE'
CALL DCOMPBD
TYPE *, 'I STILL HAVE 1 SUBROUTINE TO SOLVE'
CALL SLVBD
C
C *****
C NOW, TO ADD THE INITIAL TEMPERATURE 300 K
C SINCE THE ORIGINAL TEMPERATURE IS ASSUMED TO BE 0 K.
C *****
C
DO 700 I=1,NP
CHECK = ABS( A(I) - AMP )
IF(CHECK.LT.0.01) GOTO 700
A(I) = ABS(A(I)) + 300.
IF(A(I).LE.AMP) GOTO 700
A(I) = AMP
700 CONTINUE
C
OPEN(UNIT=44,FILE='TEMP.DAT',TYPE='UNKNOWN')
WRITE(44,*) NP,VEL
DO 50 I=1,NP
WRITE(44,55) IOLD(I),A(I)
50 CONTINUE
55 FORMAT(5(I5,1X,F7.2,3X))
CLOSE(UNIT=44)
C
CALL EXI1'
END
C
SUBROUTINE BDYVAL
COMMON NP,NBW,NCL,AMP,X,GF,GSM
C DIMENSION X(NP,NCL),GF(NP,NCL),GSM(NP,NBW)
DIMENSION X(1397,1),GF(1397,1),GSM(1397,155)
C
C *****
C ***** John! Be Careful !!! *****

```

```

C *****
C THE DIMENSION OF X,GF AND GSM MUST BE "EXACTLY" THE NUMBER
C OF X(NP,NCL),GF(NP,NCL) AND GSM(NP,NBW)
C *****
C
C THIS SUBROUTINE IS TO READ KNOWN VALUES IN F AND PHI AND MODIFY K AS
C ON PP.110 OF L.J.SEGERLIND TO MAKE IT READY TO BE SOLVED
C
C DIMENSION IB(6),BV(6)
C
C *****
C INPUT OF THE NODAL FORCE VALUCES
C *****
C
C OPEN(UNIT=33,FILE='INPUT.DAT',TYPE='UNKNOWN')
C DO 216 JM=1,NCL
C INK=0
202 READ(33,*) IB,BV
C
C *****
C BECAUSE THE DIMENSION OF IB AND BV ARE 6, THE DATA IN TORSI2.DAT
C SHOULD BE LIKE THIS SIX INTEGERS SIX REAL VALUES
C UNTIL SAY 11,23,-1,-1,-1,-1,-2,-1. -1. -1. -1.
C **** -1 MEANS NO MORE DATA,-2 MEANS THE STARTING OF NO DATA FOR BV
C **** NOTE: EVEN NO DATA FOR IB OR BV, YOU HAVE TO PUT -VE # TO SHOW NO DATA
C IB NODE# ON BOUNDARY BV BOUNDARY VALUES, IT MAY BE KNOWN NODAL FORCE
C VALUES(UPPER PART) OR KNOWN NODAL VALUES(SAY, TEMP,POTENTIAL,STRESS)
C BUT BE CAREFUL,THE FIRST SET DATA IN TORSI2.DAT REFERS TO KNOWN NODAL
C FORCES, THE SECOND SET REFERS TO KNOWN NODAL VALUES AND IF THE # OF
C KNG'WN NODAL FORCE SET IS INTEGRAL TIMES OF 6,THEN BETWEEN KNOWN
C NODAL FORCE AND KNOWN NODAL VALUES DATA SET, THERE MUST BE ANOTHER
C DATA -1 IN BETWEEN TO INDICATE THE END OF KNOWN NODAL FORCE DATA SET
C *****
C
C ID=0
C DO 204 L=1,6
C IF(IB(L).LE.0) GO TO 205
C ID=ID+1
C I=IB(L)
204 GF(I,JM)=BV(L)+GF(I,JM)
C GO TO 206
205 INK=1
C IF(ID.EQ.0) GO TO 216
206 IF(INK.EQ.1) GO TO 216
C GO TO 202
C
C *****
C INPUT OF THE PRESCRIBED NODAL VALUES
C *****
C
216 CONTINUE
C INK=0
209 READ(33,*) IB,BV
C
C DO 310 IC=1,6
C IF(BV(IC).EQ.AMP) GOTO 310
C BV(IC) = AMP
310 CONTINUE
C
C ID=0
C DO 221 L=1,6
C IF(IB(L).LE.0) GO TO 215
C ID=ID+1
C I=IB(L)
C BC=BV(L)
C

```

```

C *****
C MODIFICATION OF THE GLOBAL STIFFNESS MATRIX AND THE
C GLOBAL FORCE MATRIX USING THE METHOD OF DELETION OF ROWS AND COLUMNS
C *****
C
C K=I-1
C DO 211 J=2,NBW
C M=I+J-1
C IF(M.GT.NP) GO TO 210
C DO 218 JM=1,NCL
218 GF(M,JM)=GF(M,JM)-GSM(I,J)*BC
C GSM(I,J)=0.
210 IF(K.LE.0) GO TO 211
C DO 219 JM=1,NCL
219 GF(K,JM)=GF(K,JM)-GSM(K,J)*BC
C GSM(K,J)=0.
C K=K-1
211 CONTINUE
212 IF(GSM(I,1).GT.0.) GOTO 300
C TYPE *,'THIS TERM SHOULD BE > 0'
C TYPE *,'GSM(I,1) = ', I, GSM(I,1)
300 IF(GSM(I,1).LT.0.01) GSM(I,1)=500000.
C
C *****
C 500000. WO'NT INFLUENCE ANYTHING, BECAUSE FOR THE NODE #(SAY,75) WHOSE
C NODAL VALUE IS KNOWN, THE FINAL 75TH REARRANGED EQUATION SHOULD LOOK
C LIKE 0+0+--(ALL 0)+--+0+K(75,75)*PHI(75)+0+0+---+0=K(75,75)*PHI(75)
C BUT SINCE THE POSITIVE DEFINITE MATRIX REQUIRES THAT THE VALUE AT
C THE DIAGONAL BE POSITIVE AND LARGE COMPARE TO THE OFF-DIAGONAL
C TERM, THUS IF K(75,75) IS ONLY, SAY, 0.02, WHY NOT MULTIPLYING
C K(75,75) A LARGE VALUE BECAUSE EQUAL SIGN '=' STILL HOLDS.
C FOR DETAIL, SEE L.J.SEGERLIND PP.110 TO PP.112
C *****
C
C DO 220 JM=1,NCL
220 GF(I,JM)=GSM(I,1)*BC
221 CONTINUE
C GOTO 209
C
215 CLOSE(UNIT=33)
C RETURN
C END
C
C SUBROUTINE DCMPCD
C COMMON NP,NBW,NCL,AMP,X,GF,GSM
C DIMENSION X(NP,NCL),GF(NP,NCL),GSM(NP,NBW)
C DIMENSION X(1397,1),GF(1397,1),GSM(1397,155)
C
C *****
C ***** John! Be Careful !!! *****
C *****
C THE DIMENSION OF X,GF AND GSM MUST BE "EXACTLY" THE NUMBER
C OF X(NP,NCL),GF(NP,NCL) AND GSM(NP,NBW)
C *****
C
C THIS SUBROUTINE IS TO DECOMPOSE REGULAR BAND MATRIX K INTO UPPER
C TRIANGULAR MATRIX USING GAUSSIAN ELIMINATION PROCEDURE
C
C NP1=NP-1
C DO 226 I=1,NP1
C MJ=I+NBW-1
C IF(MJ.GT.NP) MJ=NP
C NJ=I+1
C MK=NBW
C IF((NP-I+1).LT.NBW) MK=NP-I+1
C ND=0

```

```

DO 225 J=NJ,MJ
MK=MK-1
ND=ND+1
NL=ND+1
DO 225 K=1,MK
NK=ND+K
225  GSM(J,K)=GSM(J,K)-GSM(I,NL)*GSM(I,NK)/GSM(I,1)
226  CONTINUE
RETURN
END

C
SUBROUTINE SLVBD
COMMON NP,NBW,NCL,AMP,X,GF,GSM
C  DIMENSION X(NP,NCL),GF(NP,NCL),GSM(NP,NBW)
DIMENSION X(1397,1),GF(1397,1),GSM(1397,155)
*****
C  ***** John! Be Careful !!! *****
C  *****
C  THE DIMENSION OF X,GF AND GSM MUST BE "EXACTLY" THE NUMBER
C  OF X(NP,NCL),GF(NP,NCL) AND GSM(NP,NBW)
C  *****
C
C  THIS SUBROUTINE IS TO DECOMPOSE F THEN SOLVES FOR TEMPERATURE
C  USING THE METHOD OF BACKWARD SUBSTITUTION
NP1=NP-1
DO 265 KK=1,NCL
JM=KK

C
C  *****
C  DECOMPOSITION OF THE COLUMN VECTOR GF()
C  *****
C
DO 250 I=1,NP1
MJ=I+NBW-1
IF(MJ.GT.NP) MJ=NP
NJ=I+1
L=1
DO 250 J=NJ,MJ
L=L+1
250  GF(J,KK)=GF(J,KK)-GSM(I,L)*GF(I,KK)/GSM(I,1)
C
C  *****
C  BACKWARD SUBSTITUTION FOR DETERMINATION OF X()
C  *****
C
X(NP,KK)=GF(NP,KK)/GSM(NP,1)
DO 252 K=1,NP1
I=NP-K
MJ=NBW
IF((I+NBW-1).GT.NP) MJ=NP-I+1
SUM=0.
DO 251 J=2,MJ
N=I+J-1
251  SUM=SUM+GSM(I,J)*X(N,KK)
252  X(I,KK)=(GF(I,KK)-SUM)/GSM(I,1)
265  CONTINUE
RETURN
END

```

TEMGRD

```

C   This program is to calculate the temperature gradient.
C
REAL   X(300),Y(300),Z(300),XF(150),YF(150),ZF(150)
REAL   T(300),SUML(400)
REAL   NORM(3),X3(3),Y3(3),Z3(3)
REAL   XNODE(4), YNODE(4), ZNODE(4), TV(4)
REAL   XINT(2),YINT(2),ZINT(2),TINT(2)
BYTE   FILE(15)
INTEGER NS(400,4),NEL(400),NODE(300),OUTNUM(40)
INTEGER NTET(4),TEST
C   COMMON/SLOPE/X0,Z0,Y0,Y2,DEPTMX,A0,B0,A2,B2,NORM
C   COMMON/PLAN/X3,Y3,Z3,A,B,C,D
C   COMMON/INTCP/A1,B,C,D,X0,Y0,Z0,NORM,XI,YI,ZI
C   COMMON/ELLIP/X0,Y0,Z0,AX,CZ,BY,NORM,ITEST
COMMON/SUMORD/X0,Y0,Z0,NODE,X,Y,Z,NS,JTOT,IETOT,SUML,OUTNUM
C   COMMON/ORD/SUML,IETOT1,OUTNUM
COMMON/LIMI/X3,Y3,Z3,XI,YI,ZI,TEST
COMMON/INTPL/XNODE,YNODE,ZNODE,XINT,YINT,ZINT,TV,
1       TINT,TEMG
C
C   EQUIVALENCE (SUML1,SUML)
C
DATA IBCUND/300/
DATA IELTOT/400/
C
C X0,Y0,Z0 : THE SPECIFIED POINT THAT WE WANT TO CALCULATE THE TEMP GRADIENT
C DEPTMX : MAXIMUM DEPTH OF THE WELD POOL ( inch )
C Y2 : Y2 IS A LITTLE BIT LARGER THAN Y0 (in the depth direction)
C A0 : HALF SHORT AXIS LENGTH OF THE ELLIPS AT Y = Y0
C B0 : HALF LONG AXIS LENGTH OF THE ELLIPS AT Y = Y0
C X3,Y3,Z3,A,B,C,D : {X3,Y3,Z3} THESE THREE POINTS CAN MAKE A PLANE
C                   WHICH CAN BE EXPRESSED AS  $AX + BY + CZ + D = 0$ 
C XI,YI,ZI : (XI,YI,ZI) IS THE INTERCEPT POINT BY THE LINE DETERMINED BY
C           (X0,Y0,Z0) WITH NORM() AND PLANE  $AX + BY + CZ + D = 0$ 
C AX,BY,CZ : HALF AXIS LENGTH IN X,Y,Z DIRECTION RESPECTIVELY
C ITEST : IF ITEST = 1, THEN INPUT DATA HAS SOMETHING WRONG
C OUTNUM() : The first 40 tetrahedron NUMBER, which have the smallest
C            summation of the line segment lengths from (x0,y0,z0)
C            I ONLY TAKE THE FIRST 8 DATA.
C IETOT : TOTAL BOUNDARY INTERFACIAL ELEMENTS WHICH HAVE TWO OR
C        THREE NODES AT THE INTERFACE
C JTOT : # of the nodes that are inside the tetrahedron which has 2
C        or 3 nodes at the solid-liquid interface
C X(),Y(),Z() : (X,Y,Z) ARE THE VERTEX OF THE TETRAHEDRON WHICH HAS 2 OR
C              3 NODES AT THE SOLID-LIQUID INTERFACE.
TYPE 10
10  FORMAT(' X : arc travelling direction, trailing sense is + ve',/
1    ' Y : depth direction, downward is + ve',/
2    ' Z : width direction',/)
C
TYPE 12
12  FORMAT(' John, remember that all the interested points',/
1    ' should be VERY CLOSE TO the interface',/)
C
TYPE 20
20  FORMAT('YOU CAN HAVE THE FOLLOWING CHOICES',/
1    ' 1 = TEMP GRADIENT AT SINGLE POINT',/
2    ' 2 = TEMP GRADIENT AT MANY POINTS',/)
TYPE 30
30  FORMAT('$ WHICH ONE DO YOU LIKE ? ')
ACCEPT *,IPOINT
IF(IPOINT.EQ.1.OR.IPOINT.EQ.2) GOTO 40
TYPE *,'OOPS ! YOU MAKE A MISTAKE !'

```

```

GOTO 15
40  IF(IPOINT.EQ.1) GOTO 50
    TYPE 60
60  FORMAT('$ENTER NAME OF THE (X,Y,Z) FILE : ')
    ACCEPT 70,FILE
70  FORMAT(15A1)
    OPEN(UNIT=11,FILE=FILE,TYPE='UNKNOWN')
    READ(11,*) NP
    DO 90 I=1,NP
90  READ(11,*) XF(I),YF(I),ZF(I)
    CLOSE(UNIT=11)
    FILE(15) = 0
    GOTO 80
50  TYPE *,'(X,Y,Z) POINT AT THE INTERFACE ?'
    ACCEPT *,X1,Y1,Z1
C
80  TYPE 700
700  FORMAT('YOU CAN HAVE THE FOLLOWING CHOICES',/
1    ' 1 = ELLIPSOID WELD POOL',/
2    ' 2 = COMPLEX WELD POOL',/)
    TYPE 710
710  FORMAT('$ WHICH ONE DO YOU LIKE ? ')
    ACCEPT *,ISHAPE
    IF(ISHAPE.EQ.1.OR.ISHAPE.EQ.2) GOTO 720
    TYPE *,'OOPS ! YOU MAKE A MISTAKE !'
    GOTO 80
720  IF(ISHAPE.EQ.2) GOTO 730
    TYPE *,'HALF AXIS LENGTHS IN X,Y,Z DIRECTION ? (inch)
1    ' 3 data are required'
    ACCEPT *, AX, BY, CZ
    GOTO 740
730  TYPE 750
750  FORMAT('$ENTER THE NAME OF THE GEOMETRY DATA FILE : ')
    ACCEPT *,FILE
    TYPE *,'John, if you choose this complex weld pool, then'
    TYPE *,'the Y0 of the point interested, (X0,Y0,Z0), will'
    TYPE *,'have to be EXACTLY the same as the Y coordinate'
    TYPE *,'of one of the points contained in this data file.'
    OPEN(UNIT=44,FILE=FILE,TYPE='UNKNOWN')
C
740  OPEN(UNIT=22,FILE='ELEINT.DAT',TYPE='UNKNOWN')
    DO 100 I=1,IBOUND
    READ(22,*) NODE(I),X(I),Y(I),Z(I)
    IF(NODE(I).EQ.0) GOTO 130
100  CONTINUE
130  IBTOT = I - 1 ! Total interface boundary points
    DO 110 I=1,IBTTOT
    READ(22,*) NEL(I),(NS(I,J),J=1,4)
    IF(NEL(I).EQ.0) GOTO 120
110  CONTINUE
120  IETOT = I - 1 ! Total interfacial elements
    DO 140 I = IBTOT+1,IBOUND
    READ(22,*) NODE(I),X(I),Y(I),Z(I)
    IF(NODE(I).EQ.0) GOTO 150
140  CONTINUE
150  JTOT = I - 1 ! Total points related to the interfacial elements
    CLOSE(UNIT=22)
C
    OPEN(UNIT=33,FILE='TEMP.DAT',TYPE='UNKNOWN')
    READ(33,*) NODENU,VEL
    DO 160 I = 1,NODENU
    READ(33,*) INODE,DEGREE
    DO 170 J = 1,JTOT
    IF(NODE(J).NE.INODE) GOTO 170
    T(J) = DEGREE
    GOTO 160

```

```

170 CONTINUE
160 CONTINUE
CLOSE(UNIT=33)
C
OPEN(UNIT=66,FILE='COOLRT.DAT',TYPE='UNKNOWN')
*****
C NOW, I HAVE READ ALL THE NECESSARY DATA
C THE FOLLOWING IS TO CALCULATE THE TEMPERATURE GRADIENTS.
C *****
C
WRITE(66,3030)
3030 FORMAT('-----'
8 '-----')
WRITE(66,1210)
1210 FORMAT(5X,'X0',9X,'Y0',9X,'Z0',12X,'COOLRT',
1 6X,'TEMP GRAD',7X,'NORM(1)')
TYPE 3030
TYPE 1210
WRITE(66,3030)
TYPE 3030
IF(IPOINT.EQ.1) GOTO 180
DO 2000 I1=1,NP
X0 = XF(I1)
Y0 = YF(I1)
Z0 = ZF(I1)
GOTO 200
180 X0 = X1
Y0 = Y1
Z0 = Z1
C
C *****
C TO GET THE NORMAL VECTOR AT (X0,Y0,Z0)
C *****
C
200 IF(ISHAPE.EQ.1) GOTO 210
JONE = 0
REWIND 44
READ(44,*) IP, DEPTMX
C
DO 220 I2=1,IP
IF(JONE.NE.1) GOTO 230
READ(44,*) Y2,A2,B2
GOTO 240
230 READ(44,*) YDUM,A0,B0
IF(YDUM.NE.Y0) GOTO 220
JONE = 1
Y0 = YDUM
IF(Y0.NE.DEPTMX) GOTO 220
Y2 = DEPTMX + 1. ! 1. IS JUST AN ARBITRARY NUMBER
GOTO 240
220 CONTINUE
C
240 CLOSE(UNIT=44)
CALL NORMAL (X0,Z0,Y0,Y2,DEPTMX,A0,B0,A2,B2,NORM)
GOTO 300
C
210 CALL ELLIPS (X0,Z0,Y0,AX,CZ,BY,NORM,ITEST)
C
IF(ITEST.NE.1) GOTO 300
TYPE *, 'SORRY, YOU HAVE TO INPUT ANOTHER (X,Y,Z)'
GOTO 9999
C
300 CALL SUMLEN
CALL ORDER
C
C *****

```



```

C   NOW, START THIS LONG PROGRAM TO CHECK WHICH TETRAHEDRON
C   HAS TWO INTERCEPTS.
C   *****
C
C   DO 320 I=1,40
C
C   KTEST = 0
C   INTCK = 0
C   INTNUM = 1
C
C   DO 370 IZ=1,2
C   XINT(IZ)=0
C   YINT(IZ)=0
370  ZINT(IZ)=0
C
C   DO 310 J=1,IETOT
C   IF(J.NE.OUTNUM(I)) GOTO 310
C   DO 330 K=1,4
C   NTET(K) = NS(J,K)
C   DO 340 K1=1,JTOT
C   IF(NODE(K1).NE.NTET(K)) GOTO 340
C   XNODE(K) = X(K1)
C   YNODE(K) = Y(K1)
C   ZNODE(K) = Z(K1)
C   GOTO 330
340  CONTINUE
330  CONTINUE
C
C   *****
C   NOW, I HAVE (X,Y,Z) OF THE 4 VERTICES OF THIS
C   'POSSIBLE' TETRAHEDRON STORED IN XNODE(),YNODE(), AND ZNODE()
C   *****
C
C   DO 350 L=1,4 ! TETRAHEDRON HAS 4 SIDES
C   IF(KTEST.EQ.1) GOTO 350
395  L1 = L + 1
C   IF(L1.EQ.5) L1 = 1
C   L2 = L1 + 1
C   IF(L2.EQ.5) L2 = 1
C
C   X3(1) = XNODE(L)
C   X3(2) = XNODE(L1)
C   X3(3) = XNODE(L2)
C   Y3(1) = YNODE(L)
C   Y3(2) = YNODE(L1)
C   Y3(3) = YNODE(L2)
C   Z3(1) = ZNODE(L)
C   Z3(2) = ZNODE(L1)
C   Z3(3) = ZNODE(L2)
C
C   *****
C   TO CHECK IF (X0,Y0,Z0) IS ONE OF THE VERTICES
C   OF THIS TRIANGLE. SINCE I ASSUME (X0,Y0,Z0) IS AT EITHER
C   THE INTERFACE OR THE LIQUID REGION, IT IS IMPOSSIBLE TO
C   HAVE X0 = XNODE(4), Y0 = YNODE(4), AND Z0 = ZNODE(4)
C   *****
C
C   IF(L.NE.1) GOTO 400
C   DO 360 IC=1,3
C   ZERO1 = ABS( X3(IC)-X0 )
C   ZERO2 = ABS( Y3(IC)-Y0 )
C   ZERO3 = ABS( Z3(IC)-Z0 )
C   ZTOT = ZERO1 + ZERO2 + ZERO3
C   IF(ZTOT.GT. 0.00001) GOTO 360
C   XINT( 1 ) = X0
C   YINT( 1 ) = Y0

```

```

ZINT( 1 ) = Z0
INTCK = 1
C
IF(IC.EQ.1) GOTO 381
IF(IC.EQ.2) GOTO 382
IF(IC.EQ.3) GOTO 383
381 L = L + 1
GOTO 390
382 L = L1 + 1
GOTO 390
383 L = L2 + 1
390 KTEST = 1
GOTO 395
360 CONTINUE
C
400 CALL PLANE(X3,Y3,Z3,A,B,C,D)
CALL INTCEP (A,B,C,D,X0,Y0,Z0,NORM,XI,YI,ZI)
C
C *****
C NOW, I'VE GOT THE INTERCEPT (XI,YI,ZI). I HAVE TO
C CHECK IF THIS INTERCEPT IS ONE OF THE VERTICES OF THIS
C TRIANGLE.
C *****
C
DO 410 IC=1,3
DIFF1 = ABS(XI - X3(IC))
DIFF2 = ABS(YI - Y3(IC))
DIFF3 = ABS(ZI - Z3(IC))
TOTAL = DIFF1 + DIFF2 + DIFF3
IF(TOTAL.GT.0.00001) GOTO 410
1000 IF(INTCK.EQ.1) INTNUM = 2
XINT( INTNUM ) = XI
YINT( INTNUM ) = YI
ZINT( INTNUM ) = ZI
INTCK = INTCK + 1
IF(INTNUM.NE.2) GOTO 350
C
C *****
C FINALLY, I FOUND THE TETRAHEDRON WHICH HAS TWO INTERCEPTS
C THE (X,Y,Z) OF THE 4 VERTICES OF THIS TETRAHEDRON ARE STORED
C IN XNODE(), YNODE(), AND ZNODE()
C *****
C
DO 1200 JV=1,4
DO 1100 JNODE = 1,JTOT
IF(NODE(JNODE).NE.NTET(JV)) GOTO 1100
TV(JV) = T(JNODE)
GOTO 1200
1100 CONTINUE
1200 CONTINUE
C
CALL INTPOL
COOLRT = TEMG * VEL * NORM(1)
WRITE(66,2420) X0,Y0,Z0,COOLRT,TEMG,NORM(1)
TYPE 2420,X0,Y0,Z0,COOLRT,TEMG,NORM(1)
2420 FORMAT(1X,3(F9.6,2X),3X,2(E12.4,2X),2X,E10.3)
IF(IPOINT.EQ.1) GOTO 9999
GOTO 2000
C
410 CONTINUE
C
C *****
C NOW, I CAN MAKE SURE THE INTERCEPT IS NOT ONE
C OF THE VERTICES OF THIS TETRAHEDRON. ( ACTUALLY, TRIANGLE)
C *****
C

```

```

CALL LIMIT
IF(TEST.EQ.1) GOTO 350
C
C *****
C OK! NOW, I FIND ONE INTERCEPT WHICH IS INSIDE THE TETRAHEDRON
C *****
C
C GOTO 1000
C
350 CONTINUE
IF(INTCK.EQ.2) TYPE *,'IMPOSSIBLE TO BE 2'
GOTO 320
310 CONTINUE
TYPE *,'IMPOSSIBLE NOT TO FIND TETRAHEDRON !'
GOTO 9999
320 CONTINUE
TYPE *,'*****
TYPE *,'MY GOD! I CANNOT FIND THE TETRAHEDRON WHICH HAS'
TYPE *,'TWO INTERCEPTS, HELP! HELP! HELP!'
TYPE *,'John, no data for this (x,y,z) ',X0,Y0,Z0
TYPE *,'*****
IF(IPOINT.EQ.1) GOTO 9999
C
2000 CONTINUE
C
9999 CALL EXIT
END
C
C *****
C SUBROUTINE NORMAL (X0,Y0,Z0,Z2,CMAX,A0,B0,A2,B2,NORM)
C
C This program is to calculate the normal at any point on a
C body whose cross-sectional curve on the xy plane is ellipse
C with half length of the long axis, a, and of the short axis, b.
C
C The x,y,z coordinate used in this program is a little bit
C confusing. Originally, this program is based on the coordinate
C with downward z (+ve z) as the axis to represent the depth of
C the weld pool. Later on, I realize that John wants downward y
C (+ve y) as the axis to represent the depth of the weld pool.
C Therefore, I put the "equivalence"  $X(\text{new}) = X(\text{old})$ ,
C  $Y(\text{new}) = Z(\text{old})$ ,  $Z(\text{new}) = Y(\text{old})$ .
C
C This program is designed to use for the following geometry:
C Long axis of ellips is in the X direction
C Short axis of ellips is in the (new) Z direction
C Cross section paralle to the (new) Y axis (depth axis) can be
C any kind of shape.
C
C The unit used in the program can be arbitrary as long as all
C the data unit are consistent.
C
C The data input are
C (1) ***** Specified (X0,Z0,Y0) point *****
C (2) the 2nd point (X2,Z2,Y2) with Y2 "a little bit" larger than
C Y0. X2 and Z2 have to calculated in this program, thus,
C no need (actually, impossible) to input X2 and Z2.
C (3) the half short axis of the ellips on the y=Y0 cross section, A0
C
C (4) the half long axis of the ellips on the y=Y0 cross section, B0
C (5) the half short axis of the ellips on the y=Y2 cross section, A2
C Y2 = Y0 + small y Note: This program assumes Y2 is a little
C bit larger than Y0. (This program does not use Y1)
C (6) the half long axis of the ellips on the y=Y2 cross section, B2
C

```

```

C   COMMON/SLOPE/X0,Y0,Z0,Z2,CMAX,A0,B0,A2,B2,NORM
C
C***** The COMMON BLOCK in the main program will be X0,Z0,Y0,Y2,DEPTMX,
C   A0,B0,A2,B2,NORM
C***** X <----> A, Z <----> B, Y <----> C
C   CMAX is the half axis length in the depth direction (Y direction)
C
C   REAL LENGTH,NORM(3),COR(3)
C
C   NORM() ARE THE COMPONENTS OF THE UNIT NORMAL VECTOR
C   PASSING THRU (X0,Z0,Y0)
C
C   ****
C   When (x2,y2,z2) is the bottom point, then slope is known.
C   ****
C
C   IF(Z2.GE.CMAX) GOTO 998
C
C   ****
C   To obtain the unit vectorial form to represent the tangential
C   line passing thru point (x0,y0,z0). This line is lying on the
C   plane z=z0
C   ****
C
C   IF(Y0.EQ.0.) GOTO 11
C   TANA=(-B0**2*X0)/(A0**2*Y0)
C   COSA=1./SQRT(1.+TANA**2)
C   IF(TANA.LT.0.) COSA=-1.*COSA
C   SINA=COSA*TANA
C   GOTO 12
11  COSA=0.
C   SINA=1.
C
C   the vectorial form of this tangential line is (cosa,sina,0)
C
C   ****
C   To obtain the unit vectorial form to represent the other tangential
C   line passing thru point (x0,y0,z0).
C   ****
C
C.....TO SOLVE 2nd ORDER EQUATION TO GET THE INTERCEPT (x2,y2).....
C
12  IF(X0.EQ.0.) GOTO 31
C   COEA=(A0/B0)**4*(Y0/X0)**2+(B2/A2)**2 ! 2nd order term
C   COEB=2.*(A0/B0)**2*Y0**2/X0-2.*(A0/B0)**4*Y0**2/X0
C   COEC=Y0**2+(A0/B0)**4*Y0**2-2.*(A0/B0)**2*Y0**2-B2**2
C   B4AC=COEB**2-4.*COEA*COEC
C   IF(B4AC.GE.0.) GOTO 30
C   TYPE *,'IMAGINARY PART IS NOT GT. ZERO ???!'
C   TYPE *,'THE FINAL DATA ARE JUNK, input another (x,y,z)'
C   GOTO 999
30  ROOT1=(-COEB+SQRT(B4AC))/(2.*COEA)
C   ROOT2=(-COEB-SQRT(B4AC))/(2.*COEA)
C   X2=ROOT2 !Arbitrarily assigned
C   DIS1=ABS(X0-ROOT1)
C   DIS2=ABS(X0-ROOT2)
C   IF(DIS1.LT.DIS2) X2=ROOT1
C   Y2=SQRT(B2**2-(B2*X2/A2)**2)
C   GOTO 32
31  X2=0.
C   Y2=B2
32  IF(Y0.LT.0.) Y2=-1.*Y2 ! y0 and y2 should have the same sign
C
C.....TO CALCULATE THE LENGTH BETWEEN (x0,y0,z0) and (x2,y2,z2).....
C
C   LENGTH=SQRT((X2-X0)**2+(Y2-Y0)**2+(Z2-Z0)**2)

```

```

COR(1)=(X2-X0)/LENGTH
COR(2)=(Y2-Y0)/LENGTH
COR(3)=(Z2-Z0)/LENGTH ! COR(1)'S ARE THE 3 COMPONENTS OF THE
C          TANGENTIAL LINE PASSING THRU (x0,y0,z0)
C
C *****
C TO CALCULATE THE UNIT NORMAL VECTOR
C *****
C
NORM(1)=-SINA*COR(3)
NORM(3)=COSA*COR(3)
NORM(2)=SINA*COR(1)-COSA*COR(2)
GOTO 999
998  NORM(1)=0.
     NORM(3)=0.
     NORM(2)=-1.
999  RETURN
     END
C
C *****
C SUBROUTINE ELLIPS (X,Y,Z,A,B,C,N,TEST)
C
C This program is not the same as the NORMAL.FOR. NORMAL.FOR
C is for the "semi-ellipsoid". This program is for the regular
C ellipsoid. This program is to calculate the normal vector passing
C thru a specified point (x,y,z)
C
C Same as NONRMAL.FOR, the x,y,z coordinate system is confusing.
C X(new) = X(old)  Y(new) = Z(old)  Z(new) = Y(old)
C Therefore, the common block in the main program should be
C X,Z,Y instead of X,Y,Z. For more detail, see NORMAL.FOR
C
C Input data are
C (1) Specified (X,Z,Y)
C (2) Half axis length in X direction A
C (3) Half axis length in Y direction B
C (4) Half axis length in Z direction C
C
C COMMON/ELLIP/X,Y,Z,A,B,C,N,TEST
C
C***** The COMMON BLOCK in the main program will be X,Z,Y,A,C,B,N,TEST
C***** X <---> A, Z <---> B, Y <---> C
REAL LENGTH,N(3)
INTEGER TEST
TEST=0
C
C *****
C This will give more accurate X
C *****
C
TEMP=(1.-(Z/C)**2-(Y/B)**2)*A**2
IF(ABS(TEMP).LE.0.00001) TEMP = 0.
IF(TEMP.LT.0.) GOTO 10
X=SQRT(TEMP)
GOTO 20
10  TYPE *,'IMPOSSIBLE !!! Check the input (x,y,z) point'
    TYPE *,'It is impossible to have this point
    1 on the surface of ellipsoid'
    TYPE *,'(x,y,z) is ',X,Z,Y
    TEST=1
C
C IF TEST=1 THEN INPUT DATA (X,Z,Y) HAS SOMETHING WRONG
C
20  TEMP=4.*B**4*C**4*X**2+4*A**4*C**4*Y**2+4.*A**4*B**4*Z**2
    LENGTH=SQRT(TEMP)
    N(1)=2.*B**2*C**2*X/LENGTH

```

```

N(3)=2.*A**2*C**2*Y/LENGTH
N(2)=2.*A**2*B**2*Z/LENGTH
99  RETURN
END
C
C *****
C  SUBROUTINE SUMLEN
C
C  This program is to calculate the summation of the four line
C  segments from (x0,y0,z0) point to the three four of the
C  tetrahedron which has 2 or 3 nodes at the solid-liquid interface
C
C  INPUT DATA ARE
C  (1) (x0,y0,z0) : specified point
C  (2) (x,y,z) of the vertex of the tetrahedron which has 2 or 3
C  nodes at the interface
C  (3) node number of each vertex, NODE(), of the tetrahedron which
C  has 2 or 3 nodes at the interface
C  (4) NS(,) : every node number of the tetrahedron which has 2 or 3
C  nodes at the interface
C  (5) JTOT : total # of the nodes in the tetrahedrons which have
C  2 or 3 nodes at the interface
C  (6) IETOT : total # of the tetrahedrons which have 2 or 3 nodes
C  at the interface
C
C  OUTPUT DATA ARE
C  (1) the summation of the four line segments for each tetrahedron
C
C  COMMON/SUMORD/X0,Y0,Z0,NODE,X,Y,Z,NS,JTOT,IETOT,SUML,OUTNUM
C
C  COMMON/SUM/X0,Y0,Z0,NODE,X,Y,Z,NS,JTOT,IETOT,SUML
C
C  REAL  X(300),Y(300),Z(300),SUML(400)
C  INTEGER NODE(300),NEL(400),NS(400,4),N(4),OUTNUM(40)
C
C  DO 10 I1=1,IETOT
C  SUML(I1) = 0.
C  DO 20 J=1,4
C  N(J) = NS(I1,J)
C  DO 30 I=1,JTOT
C  IF(NODE(I).NE.N(J)) GOTO 30
C  XV = X(I)
C  YV = Y(I)
C  ZV = Z(I)
C  DISTSQ = (X0 - XV)**2 + (Y0 - YV)**2 + (Z0 - ZV)**2
C  DIST = SQRT(DISTSQ)
C  SUML(I1) = SUML(I1) + DIST
C  GOTO 20
30  CONTINUE
C  TYPE *, 'IMPOSSIBLE'
20  CONTINUE
10  CONTINUE
C  RETURN
C  END
C
C *****
C  SUBROUTINE ORDER
C
C  This program is to rearrange the input data, SUML()
C  The sequence of the input data is random. The output data
C  refer to the first 40 tetrahedron NUMBER, that have the smallest
C  summation of line segments length from the specified point,
C  (x0,y0,z0). For more detail, see SUMLEN.FOR
C
C  This program assumes that the data is within the range between
C  -500000. and +500000.

```

```

C   INPNUM: NUMBER OF INPUT DATA
COMMON/SUMORD/X0,Y0,Z0,NODE,X,Y,Z,NS,JTOT,INPNUM,INPUT,OUTNUM
C
C   COMMON/ORD/INPNUM,INPUT,OUTNUM
C
REAL   X(300),Y(300),Z(300),INPUT(400)
INTEGER NODE(300),NS(400,4),OUTNUM(40)
INTEGER N(400)
C
YMIN=500000. ! 500000. IS JUST A LARGE VALUE
EXCLUD=-500000. ! -500000. IS JUST A VERY SMALL VALUE
DO 610 J=1,INPNUM
DO 600 I=1,INPNUM
IF(INPUT(I).LE.EXCLUD) GOTO 600
IF(INPUT(I).GT.YMIN) GOTO 600
YMIN=INPUT(I)
MINI=I
600  CONTINUE
N(J)=MINI
EXCLUD=YMIN
YMIN=500000.
610  CONTINUE
NUM = 1
DO 620 I=1,INPNUM
IF(I.GT.40) GOTO 999
NN = N(I)
OUTNUM(NUM) = NN
NUM = NUM + 1
620  CONTINUE
999  RETURN
END
C
C   *****
SUBROUTINE PLANE (X,Y,Z,A,B,C,D)
C
C   This program is to input 3 points which are not on the
C   same line, then to calculate the coefficients of the
C   general equation for the plane in the space.
C
C   The final equation for the plane is  $ax + by + cz + d = 0$ .
C
COMMON/PLAN/X,Y,Z,A,B,C,D
REAL X(3),Y(3),Z(3)
C
A1 = (Y(2) - Y(1)) * (Z(3) - Z(1))
B1 = (Z(2) - Z(1)) * (X(3) - X(1))
C1 = (X(2) - X(1)) * (Y(3) - Y(1))
A2 = (Y(3) - Y(1)) * (Z(2) - Z(1))
B2 = (Z(3) - Z(1)) * (X(2) - X(1))
C2 = (X(3) - X(1)) * (Y(2) - Y(1))
A = A1 - A2
B = B1 - B2
C = C1 - C2
D = -X(1) * A1 - Y(1) * B1 - Z(1) * C1 +
1  X(1) * A2 + Y(1) * B2 + Z(1) * C2
RETURN
END
C
C   *****
SUBROUTINE INTCEP (A,B,C,D,X0,Y0,Z0,S,X,Y,Z)
C
C   This program is to calculate the intercept (x1,y1,z1).
C   (x1,y1,z1) is the intercept of a plane,  $ax + by + cz + d = 0$ ,
C   and a line which passes thru point (x0,y0,z0) and with a slope
C   s1,s2,s3. s1,s2,s3 are the 3 components of the unit gradient
C   vector.

```

```

C
C   COMMON/INTCP/A,B,C,D,X0,Y0,Z0,S,X,Y,Z
C   REAL S(3),LENGTH
C
C   *****
C   LENGTH: THE DISTANCE BETWEEN (x0,y0,z0) and (x1,y1,z1)
C   *****
C
C   DENOM = A*S(1) + B*S(2) + C*S(3)
C   IF(ABS(DENOM).GE.0.0000001) GOTO 100
C
C   THIS IS TO FORCE TO HAVE NO INTERCEPT
C   X = 0.
C   Y = 0.
C   Z = 0.
C   GOTO 999
100  LENGTH = -(A*X0 + B*Y0 + C*Z0 + D) / DENOM
C
C   X = X0 + S(1) * LENGTH
C   Y = Y0 + S(2) * LENGTH
C   Z = Z0 + S(3) * LENGTH
C
C   999  RETURN
C   END
C
C   *****
C   SUBROUTINE LIMIT
C
C   This program is to find the intercept is within the
C   triangle or not.
C
C   Input data are
C   (1) (x,y,z) of the three nodal points of this triangle
C   (2) (xi,yi,zi) of the intercept
C   Output data is TEST
C   When TEST = 2, then intercept is inside the triangle
C   When TEST = 1, then intercept is outside the triangle
C
C   COMMON/LIMI/X,Y,Z,XI,YI,ZI,TEST
C   REAL X(3),Y(3),Z(3),DIST(3),INNPRO(3),COS(3),THETA(3)
C   REAL SUM(3)
C   INTEGER TEST
C
C   TEST = 1
C
C   DO 10 J=1,3
10   DIST(J) = SQRT( (X(J) - XI)**2 + (Y(J) - YI)**2 +
1     (Z(J) - ZI)**2 )
C
C   DO 20 J=1,3
C   L = J + 1
C   IF(L.EQ.4) L = 1
C   INNPRO(J) = (X(J) - XI) * (X(L) - XI) +
1     (Y(J) - YI) * (Y(L) - YI) +
2     (Z(J) - ZI) * (Z(L) - ZI)
C   COS(J) = INNPRO(J)/(DIST(J) * DIST(L))
20  CONTINUE
C
C   *****
C   COS(1) IS COSINE(THETA), THIS THETA IS THE ANGLE BETWEEN
C   LINE 1 AND LINE 2.
C   COS(2) ----- BETWEEN LINE 2 AND LINE 3
C   COS(3) ----- BETWEEN LINE 3 AND LINE 1
C   LINE 1 : (XI,YI,ZI) TO (X1,Y1,Z1)
C   LINE 2 : (XI,YI,ZI) TO (X2,Y2,Z2)
C   LINE 3 : (XI,YI,ZI) TO (X3,Y3,Z3)

```



```

C *****
C
DO 100 I=1,3
IF(COS(I).EQ.0) GOTO 110
IF(ABS(COS(I) + 1).LE.0.00002) GOTO 120
IF(ABS(COS(I) - 1).LE.0.00002) GOTO 120
GOTO 160
110 THETA(I) = 90.
GOTO 100
120 TAN = 0.
GOTO 165
160 TAN = SQRT(1./COS(I)**2 - 1.)
165 THETA(I) = ATAN(TAN) * 180. /3.1415927
IF(COS(I).GT.0) GOTO 100
THETA(I) = 180. - THETA(I)
100 CONTINUE
C
ANGMAX = AMAX1( THETA(1),THETA(2),THETA(3) )
ANGMIN = AMIN1( THETA(1),THETA(2),THETA(3) )
C
DO 40 I = 1,3
IF(THETA(I).EQ.ANGMAX.OR.THETA(I).EQ.ANGMIN) GOTO 40
ANGBET = THETA(I)
40 CONTINUE
C
C *****
C CHECK IF THE INTERCEPT IS AT THE BOUNDARY OF THIS
C TRIANGLE OR NOT
C *****
C
CHECK = ABS (180. - ANGMAX)
IF(CHECK.GE.0.2) GOTO 50
*****
C NOW, I WILL FORCE THE INTERCEPT TO LOCATE ON THE BOUNDARY
C *****
C
TEST = 2
C
DO 80 I=1,3
IF(THETA(I).NE.ANGMAX) GOTO 80
ID = I
80 CONTINUE
C
ID1 = ID + 1
IF(ID1.EQ.4) ID1 = 1
TEMP = -1.*(Y(ID) - YI) * ( Y(ID1) - YI) - 1.*
1 ( Z(ID) - ZI) * ( Z(ID1) - ZI)
TEMP = TEMP - 1. * DIST(ID) * DIST(ID1)
A = 1
B = -( X(ID) + X(ID1) )
C = X(ID) * X(ID1) - TEMP
B24AC = B**2 - 4*A*C
IF(B24AC.GT.0) GOTO 85
IF( ABS(B24AC).GT.0.000002) GOTO 81
B24AC = 0.
GOTO 85
81 TYPE *, 'SQRT(-VE) ??????'
85 SOLN1 = ( -B + SQRT(B24AC) )/2*A
SOLN2 = ( -B - SQRT(B24AC) )/2*A
DIFF1 = ABS(SOLN1 - XI)
DIFF2 = ABS(SOLN2 - XI)
IF( DIFF1.LT.DIFF2) GOTO 90
XI = SOLN2
GOTO 999
90 XI = SOLN1
GOTO 999

```

```

C
50 DO 60 I=1,3
   J = I + 1
   IF(J.EQ.4) J=1
60 SUM(I) = THETA(I) + THETA(J)
C
   ITOT = 0
   DO 70 I=1,3
   IF(SUM(I).GT.180.) ITOT = ITOT + 1
70 CONTINUE
C
   IF(ITOT.EQ.3) TEST = 2
999 RETURN
END
C
C *****
SUBROUTINE INTPOL
C
C THIS PROGRAM IS TO INTERPOLATE THE TEMPERATURE
C IN THE TETRAHEDRON AND RETURN THE TEMPERATURE
C GRADIENT BETWEEN THESE TWO INTERCEPTS
C
COMMON/INTPL/X,Y,Z,XI,YI,ZI,T,TI,TEMG
C
REAL X(4),Y(4),Z(4),XI(2),YI(2),ZI(2),T(4),TI(2)
REAL B(3,4),C(4),N(4,2)
C
C *****
C TO CALCULATE 6*VOLUME
C *****
VOL6 = (X(2)-X(1))*(Y(3)-Y(1))*(Z(4)-Z(1))+
1 (Y(2)-Y(1))*(Z(3)-Z(1))*(X(4)-X(1))+
2 (Z(2)-Z(1))*(X(3)-X(1))*(Y(4)-Y(1))-
3 (Z(2)-Z(1))*(Y(3)-Y(1))*(X(4)-X(1))-
4 (Y(2)-Y(1))*(X(3)-X(1))*(Z(4)-Z(1))-
5 (X(2)-X(1))*(Z(3)-Z(1))*(Y(4)-Y(1))
C
C *****
C TO CALCULATE THE COMPONENTS IN SHAPE FUNCTION
C Ni,Nj,Nk,Nl
C Note: [1/(6*Volume)]*B(I,J) is the component
C of the shape function
C *****
B(1,1) = -((Y(3)-Y(2))*(Z(4)-Z(2))-
1 (Y(4)-Y(2))*(Z(3)-Z(2)))
B(1,2) = ((Y(3)-Y(1))*(Z(4)-Z(1))-
1 (Y(4)-Y(1))*(Z(3)-Z(1)))
B(1,3) = -((Y(2)-Y(1))*(Z(4)-Z(1))-
1 (Y(4)-Y(1))*(Z(2)-Z(1)))
B(1,4) = ((Y(2)-Y(1))*(Z(3)-Z(1))-
1 (Y(3)-Y(1))*(Z(2)-Z(1)))
B(2,1) = ((X(3)-X(2))*(Z(4)-Z(2))-
1 (X(4)-X(2))*(Z(3)-Z(2)))
B(2,2) = -((X(3)-X(1))*(Z(4)-Z(1))-
1 (X(4)-X(1))*(Z(3)-Z(1)))
B(2,3) = ((X(2)-X(1))*(Z(4)-Z(1))-
1 (X(4)-X(1))*(Z(2)-Z(1)))
B(2,4) = -((X(2)-X(1))*(Z(3)-Z(1))-
1 (X(3)-X(1))*(Z(2)-Z(1)))
B(3,1) = -((X(3)-X(2))*(Y(4)-Y(2))-
1 (X(4)-X(2))*(Y(3)-Y(2)))
B(3,2) = ((X(3)-X(1))*(Y(4)-Y(1))-
1 (X(4)-X(1))*(Y(3)-Y(1)))
B(3,3) = -((X(2)-X(1))*(Y(4)-Y(1))-
1 (X(4)-X(1))*(Y(2)-Y(1)))

```

```

B(3,4) = ((X(2)-X(1))*(Y(3)-Y(1))-
1      (X(3)-X(1))*(Y(2)-Y(1)))
C
C *****
C THE FIRST TERM OF INTERPOLATING FUNCTION
C *****
C
C(1) = X(2)*Y(3)*Z(4) - X(2)*Y(4)*Z(3)
1      + Y(2)*Z(3)*X(4) - Y(2)*Z(4)*X(3)
2      + Z(2)*X(3)*Y(4) - Z(2)*X(4)*Y(3)
C(2) = -X(1)*Y(3)*Z(4) + X(1)*Y(4)*Z(3)
1      - Y(1)*Z(3)*X(4) + Y(1)*Z(4)*X(3)
2      - Z(1)*X(3)*Y(4) + Z(2)*X(4)*Y(3)
C(3) = X(1)*Y(2)*Z(4) - X(1)*Y(4)*Z(2)
1      + Y(1)*Z(2)*X(4) - Y(1)*Z(4)*X(2)
2      + Z(1)*X(2)*Y(4) - Z(1)*X(4)*Y(2)
C(4) = -X(1)*Y(2)*Z(3) + X(1)*Y(3)*Z(2)
1      - Y(1)*Z(2)*X(3) + Y(1)*Z(3)*X(2)
2      - Z(1)*X(2)*Y(3) + Z(1)*X(3)*Y(2)
C
C *****
C TO CALCULATE THE INTERPOLATING FUNCTIONS
C *****
C
DO 10 J=1,2
N(1,J) = (1./VOL6) * ( C(1)
1          + B(1,1)*XI(J) + B(2,1)*YI(J)
2          + B(3,1)*ZI(J) )
N(2,J) = (1./VOL6) * ( C(2)
1          + B(1,2)*XI(J) + B(2,2)* YI(J)
2          + B(3,2)*ZI(J) )
N(3,J) = (1./VOL6) * ( C(3)
1          + B(1,3)*XI(J) + B(2,3)* YI(J)
2          + B(3,3)*ZI(J) )
N(4,J) = (1./VOL6) * ( C(4)
1          + B(1,4)*XI(J) + B(2,4)* YI(J)
2          + B(3,4)*ZI(J) )
10 CONTINUE
C
TI(1) = T(1) * N(1,1) + T(2) * N(2,1)
1      + T(3) * N(3,1) + T(4) * N(4,1)
TI(2) = T(1) * N(1,2) + T(2) * N(2,2)
1      + T(3) * N(3,2) + T(4) * N(4,2)
C
DISTSQ = ( XI(2) - XI(1) )**2 + ( YI(2) - YI(1) )**2
1      + ( ZI(2) - ZI(1) )**2
DIST = SQRT(DISTSQ)
IF(DIST.GT.0.0000001) GOTO 20
TYPE *, 'THE DISTANCE BETWEEN TWO INTERCEPTS IS 0'
TYPE *, '(X,Y,Z) OF INTERCEPT 1 ', XI(1), YI(1), ZI(1)
TYPE *, '(X,Y,Z) OF INTERCEPT 2 ', XI(2), YI(2), ZI(2)
20 TEMG = ( TI(2) - TI(1) )/DIST
RETURN
END

```

APPENDIX C

Thermodynamically Calculated Isothermal Sections

Isothermal sections through the Fe-Ni-Cr ternary system were thermodynamically calculated between 1873 K and 1023 K. The results of these calculations can be used to represent the liquidus surface, solidus surface, and the austenite + ferrite two-phase solvus surfaces for predicting interfacial equilibrium during solidification and solid state transformation of stainless steel alloys. Sigma phase, which occurs at temperatures below 1223 K, was not included as part of this investigation.

Tie-lines were generated in all of the two-phase regions to predict segregation during solidification and partitioning during the ferrite-to-austenite transformation. The thermodynamic calculations correlate well with the existing experimental data for binary and ternary invariant points, phase-field locations, and tie-lines in the two-phase fields. In addition, the metastable phase equilibrium between ferrite and liquid and between austenite and liquid was calculated to low temperatures by suspending the alternate solid phase. The metastable phase equilibrium calculations are useful when conjecturing the possibilities of phase selection during rapid cooling rate conditions.

The calculations were performed by the "Thermo-Calc" software package produced by the Royal Institute of Technology in Stockholm [C.1]. These calculations are based on a subregular lattice solution model [C.2] and the Kauffman database, which are integral portions of the software. The program calculates x-y data pairs that correspond to the compositional end points of the ternary tie-lines. The phase boundaries were constructed by connecting the end points and then every third tie line was plotted in each of the two-phase fields.

The location of the line of two-fold saturation, ferrite solvus and austenite solvus are important to the solidification behavior of Fe-Ni-Cr alloys. These lines can be constructed by connecting the end points of the tie-triangles in the ternary system. Table C.1 summarizes the locations of the tie-triangles and Fig. C.1 plots these data in the Fe-Ni-Cr diagram.

Table C.1: Tie-Triangle locations from the calculated isothermal diagrams

Temperature	Ferrite		Austenite		Liquid	
(°C)	% Ni	% Cr	% Ni	% Cr	% Ni	% Cr
1500	3.1	2.9	4.2	2.7	5.0	3.2
1480	3.6	8.7	5.6	7.7	6.4	9.0
1475	3.8	10.1	6.1	8.8	6.8	10.4
1450	4.7	17.4	8.7	14.3	9.1	17.1
1440	5.1	20.5	10.0	16.4	10.2	19.6
1437	5.3	21.5	10.3	17.1	10.5	20.4
1431	5.5	23.5	11.2	18.3	11.2	21.9
1425	5.8	25.5	12.0	19.6	11.9	23.5
1419	6.1	27.5	12.9	20.8	12.6	25.0
1413	6.4	29.7	13.9	22.1	13.4	26.5
1407	6.7	31.9	14.8	23.4	14.2	28.0
1401	7.1	34.5	16.0	24.8	15.1	29.8
1375	8.8	44.7	21.0	30.1	19.0	36.1
1350	11.2	55.9	27.3	35.5	23.9	42.5
1325	16.0 41.2	66.5 58.7	35.5 44.0	41.6 55.0	30.5 48.6	49.3 51.3

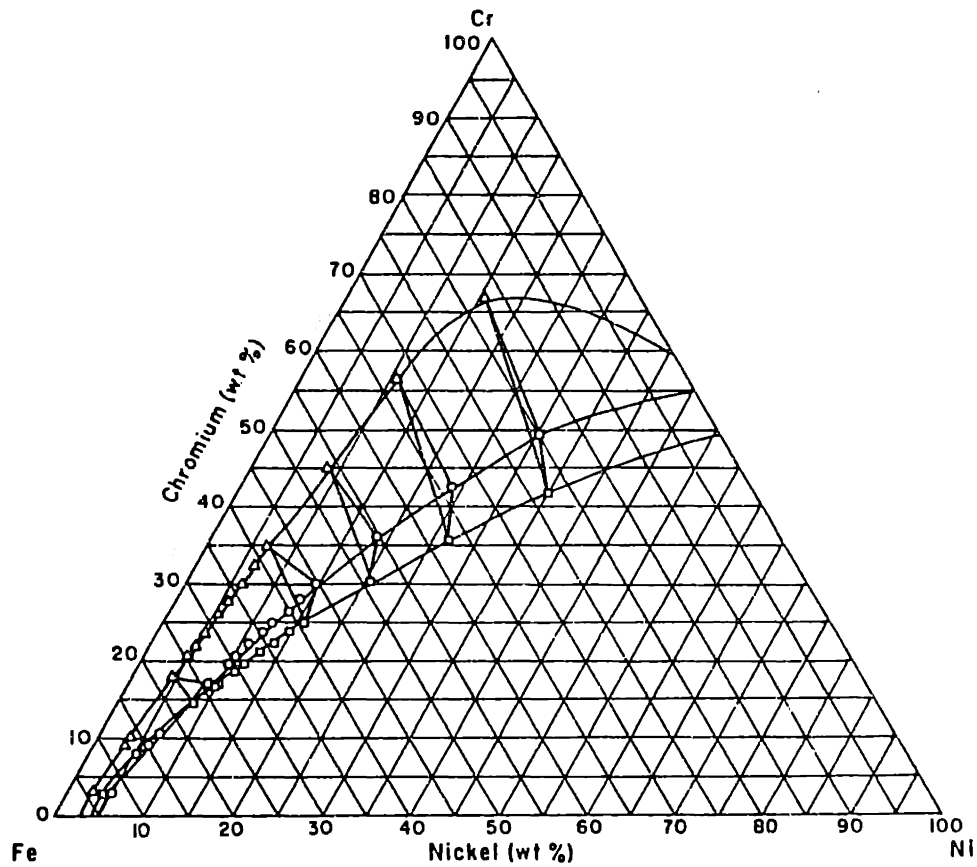
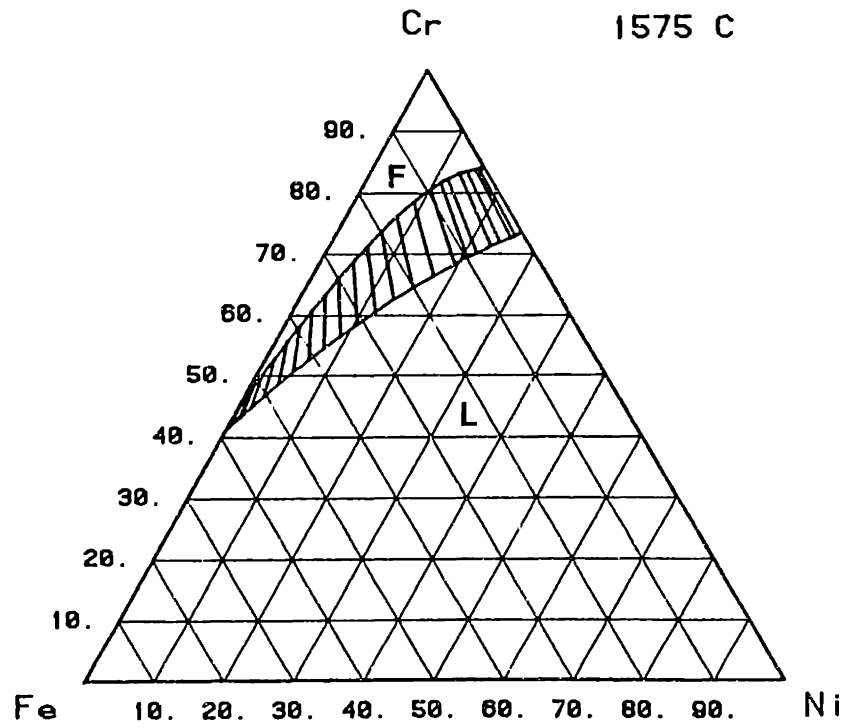
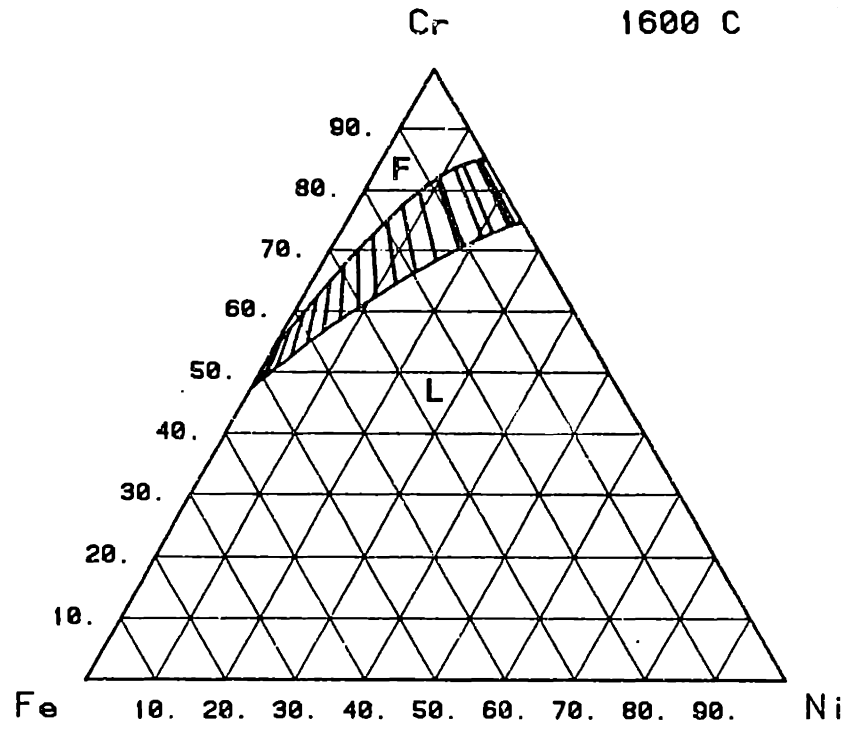
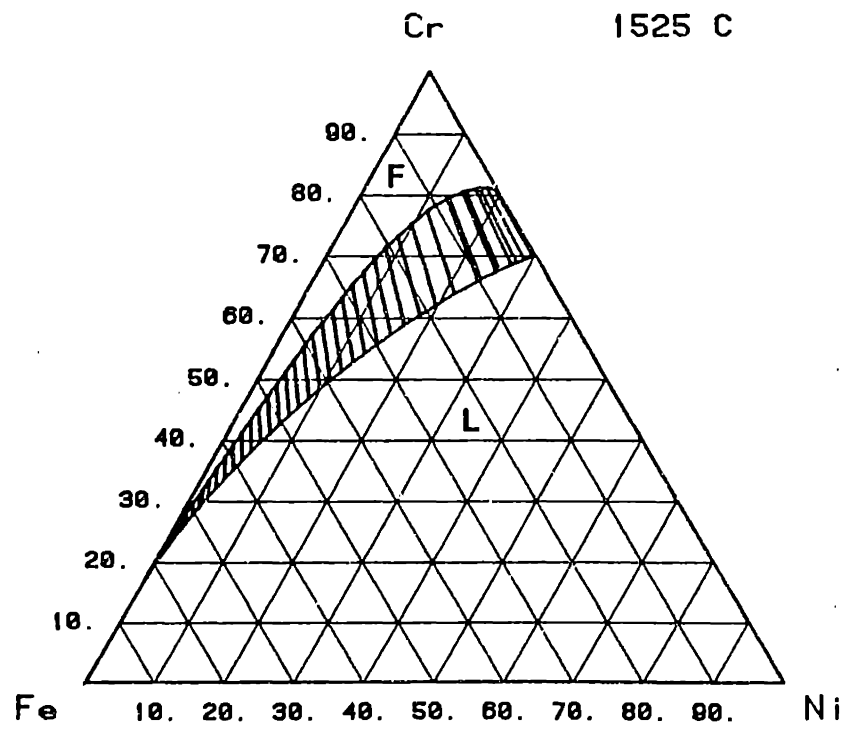
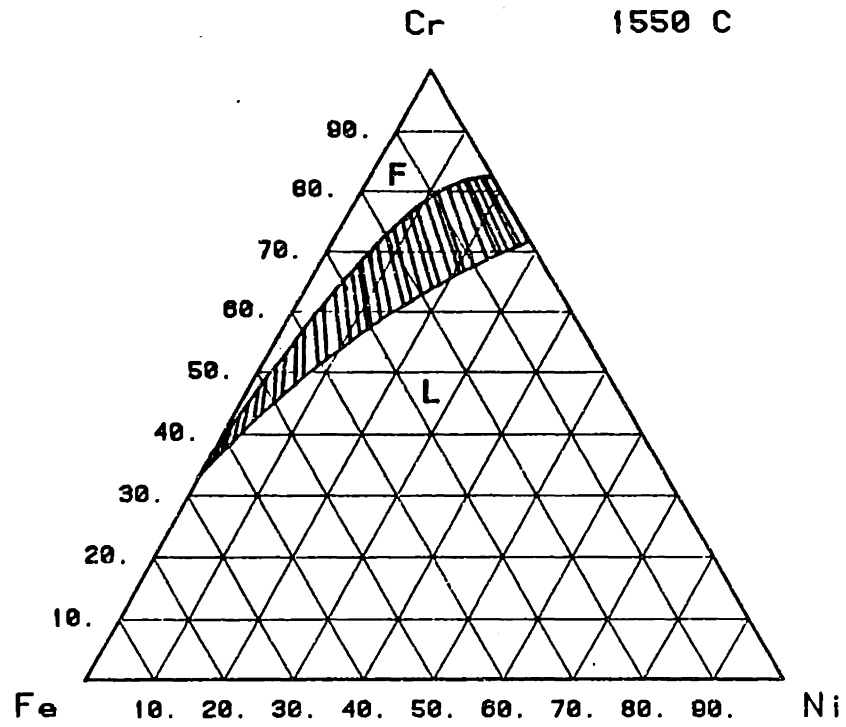
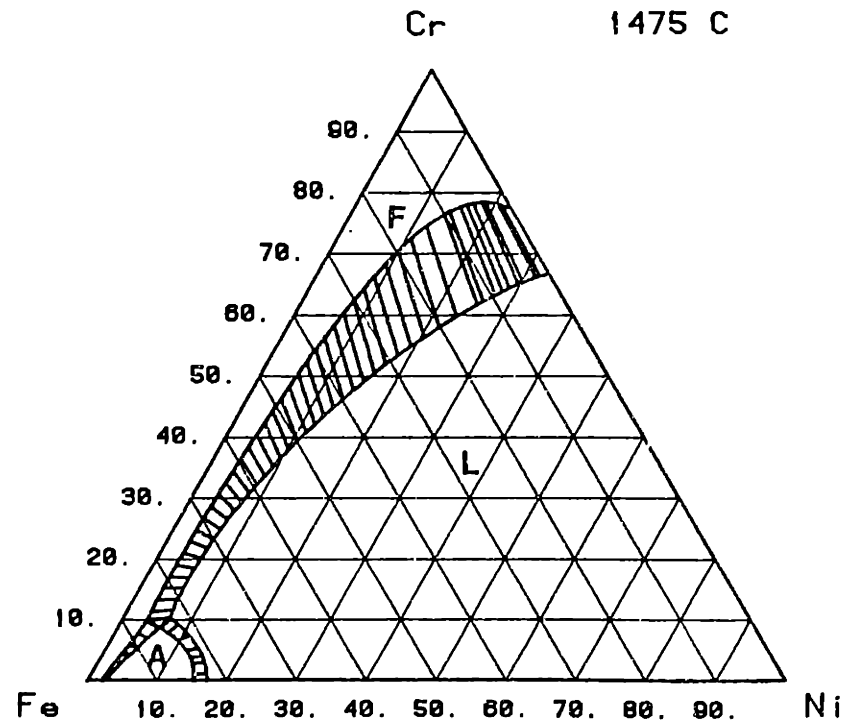
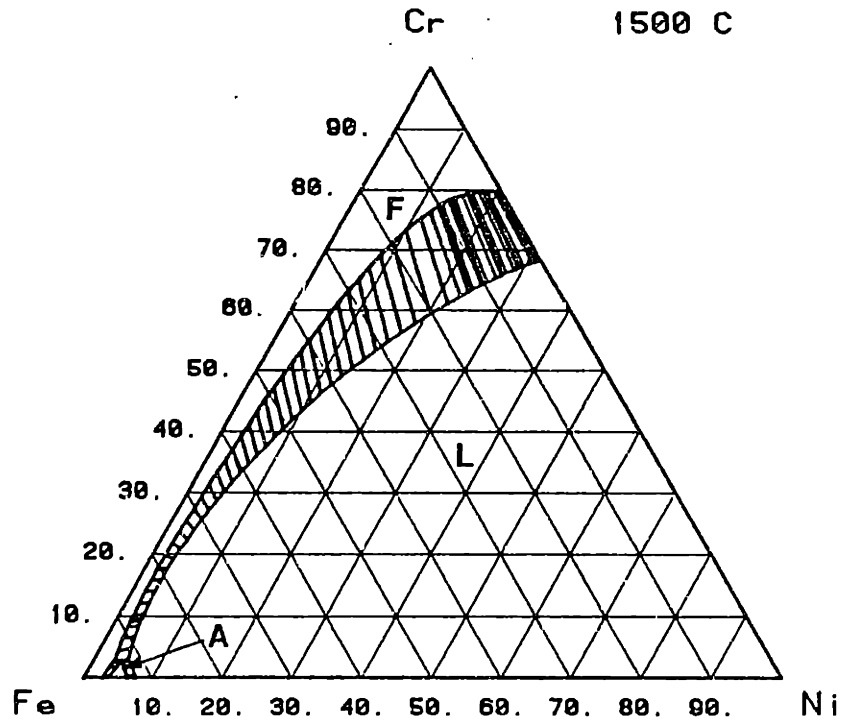


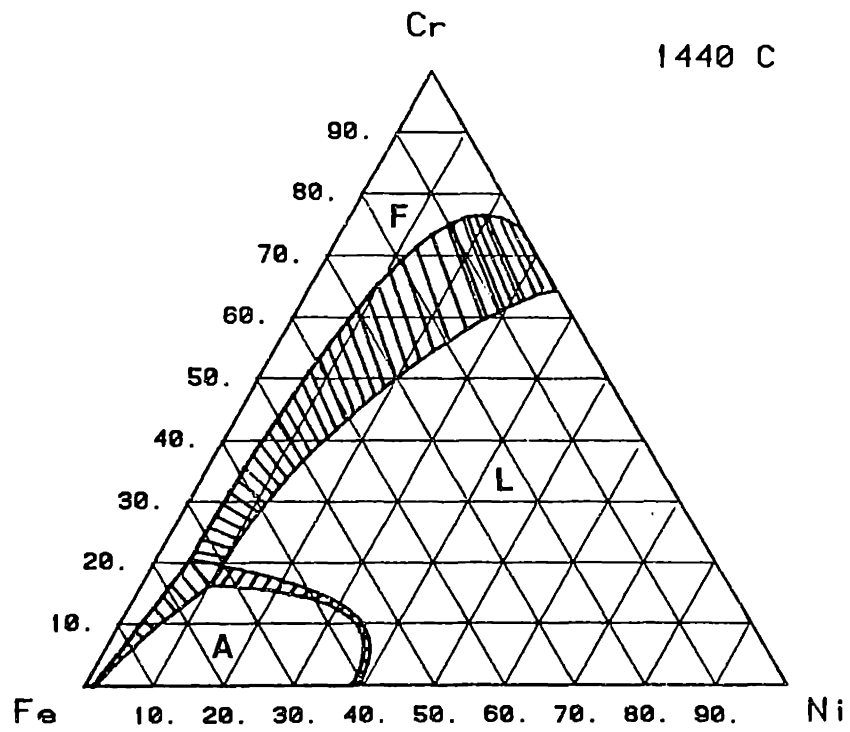
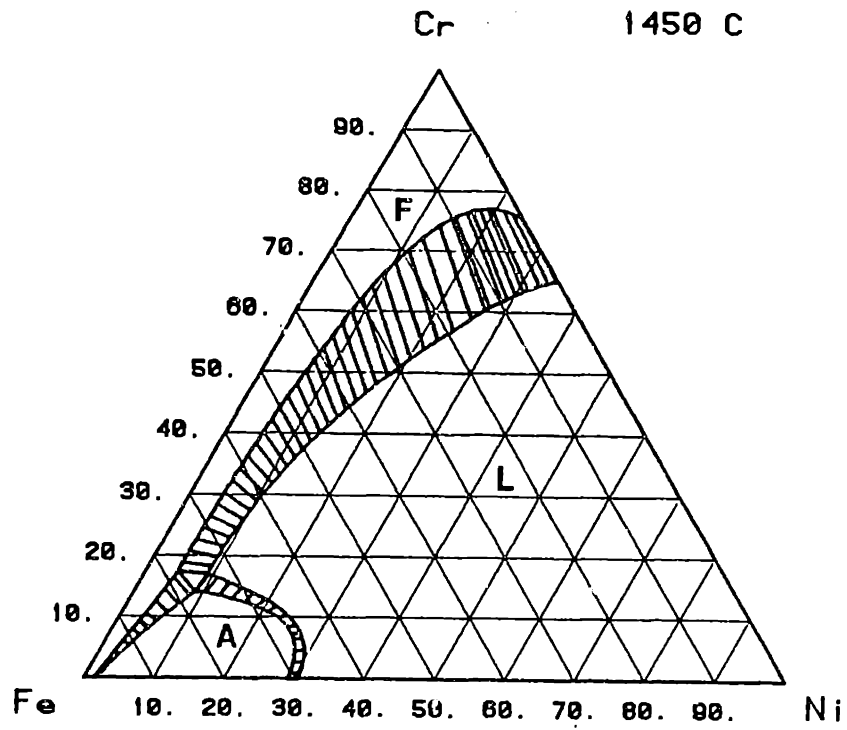
Figure C.1 Location of the ferrite solvus, austenite solvus and line of two-fold saturation (liquid) in the Fe-Ni-Cr system. Tie triangles are indicated and were determined from thermodynamic calculations.

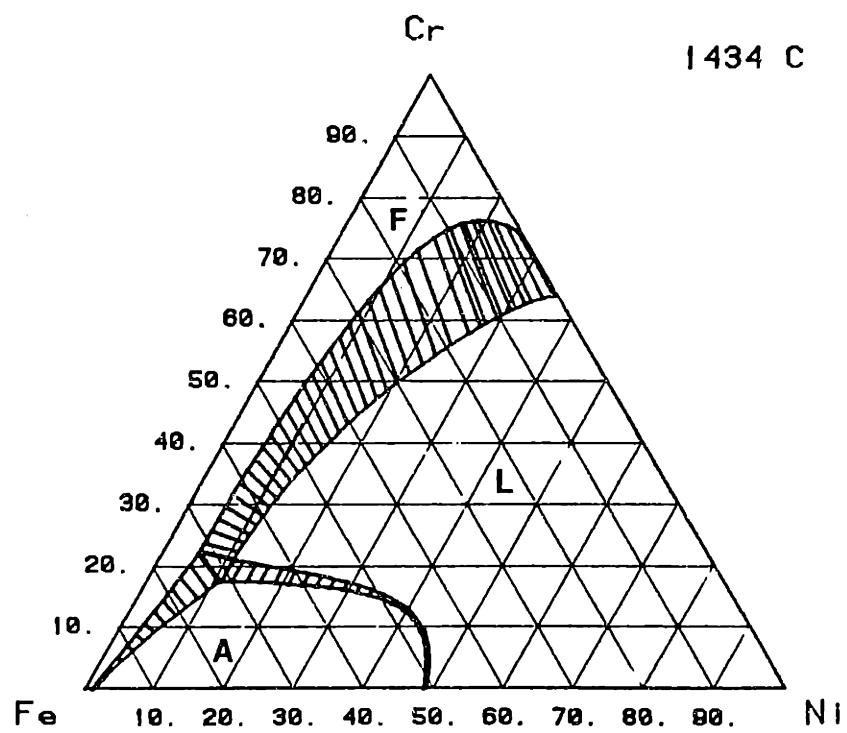
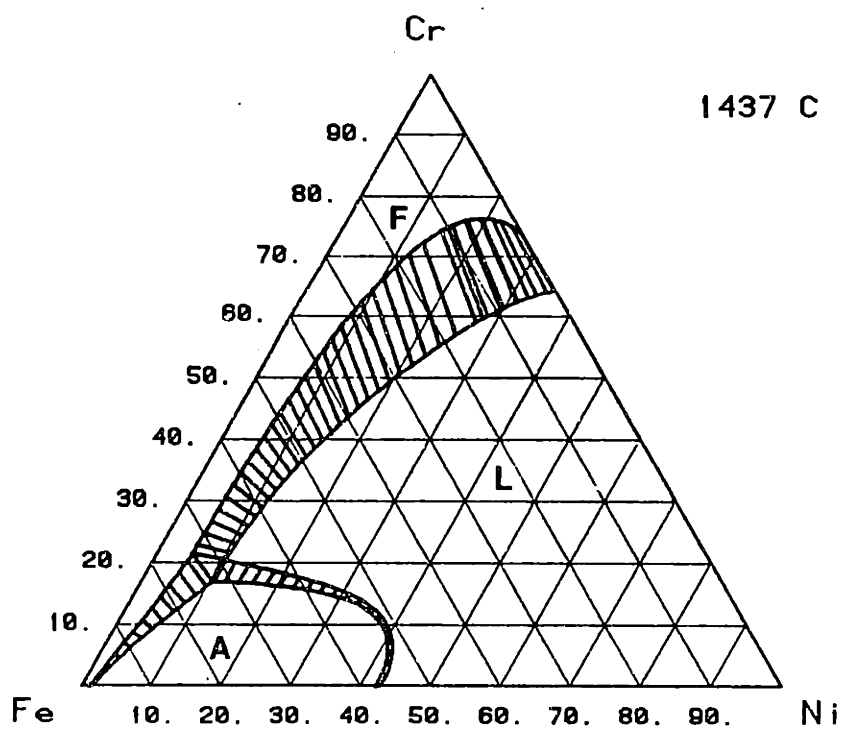
FERRITE-AUSTENITE-LIQUID EQUILIBRIUM

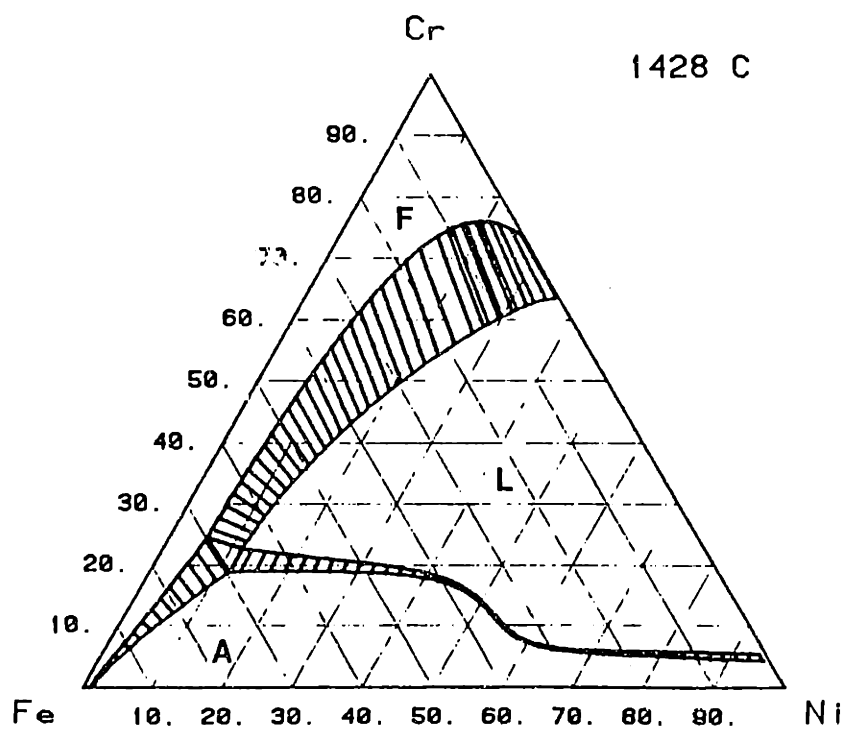
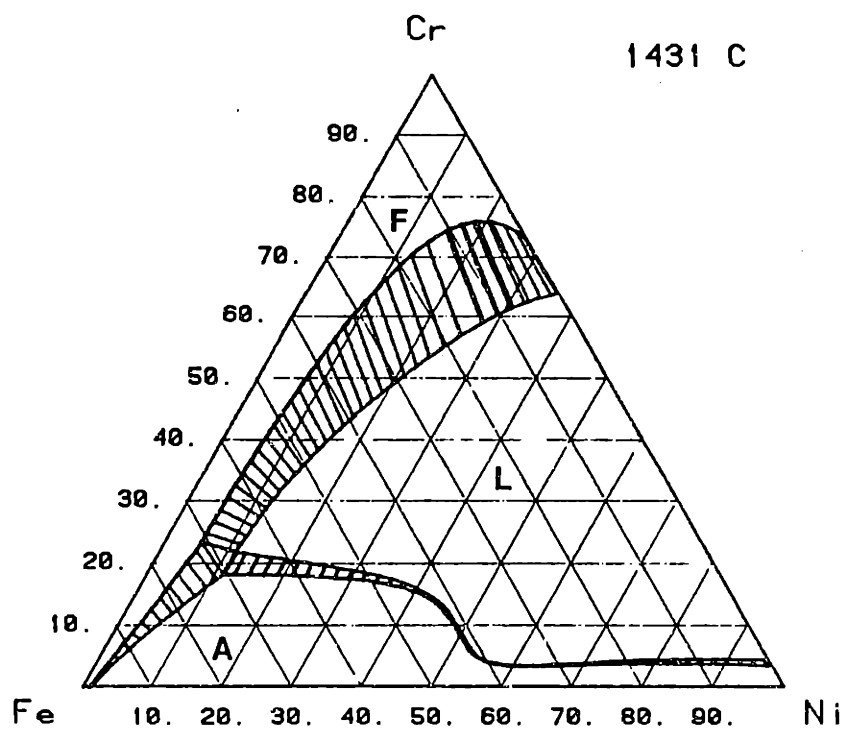


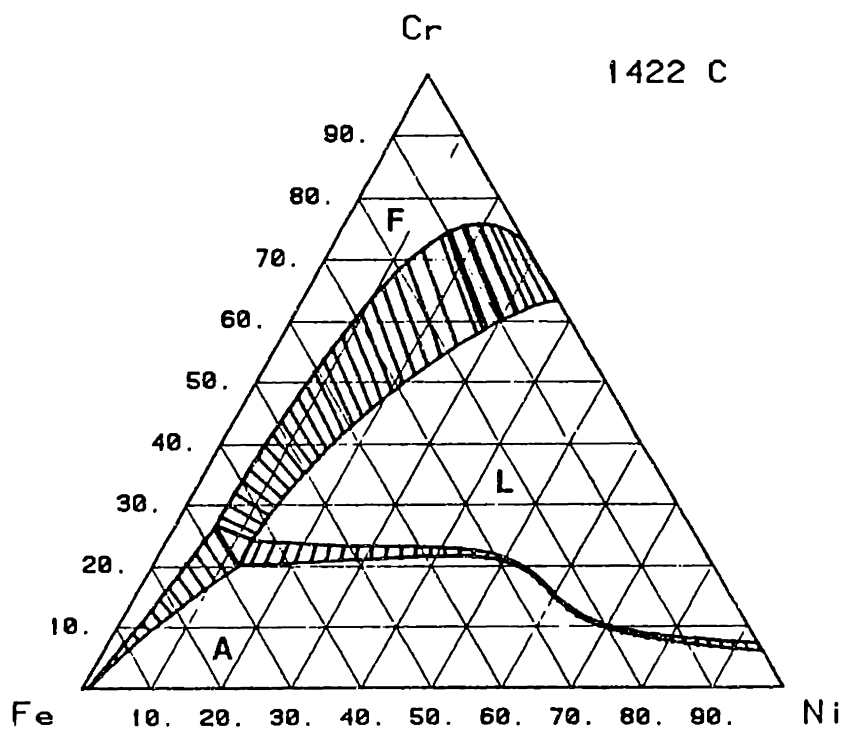
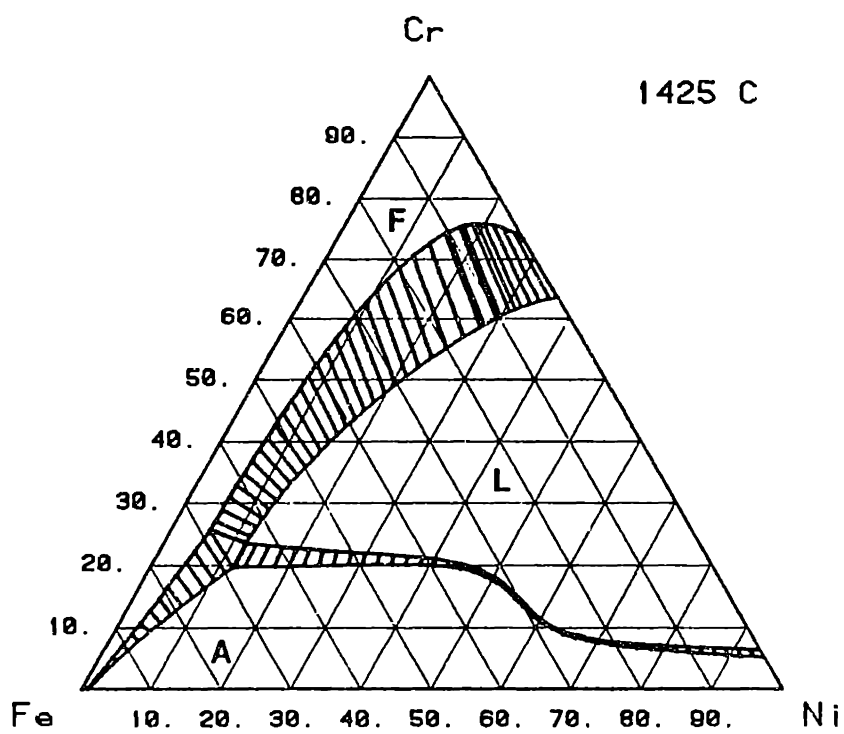


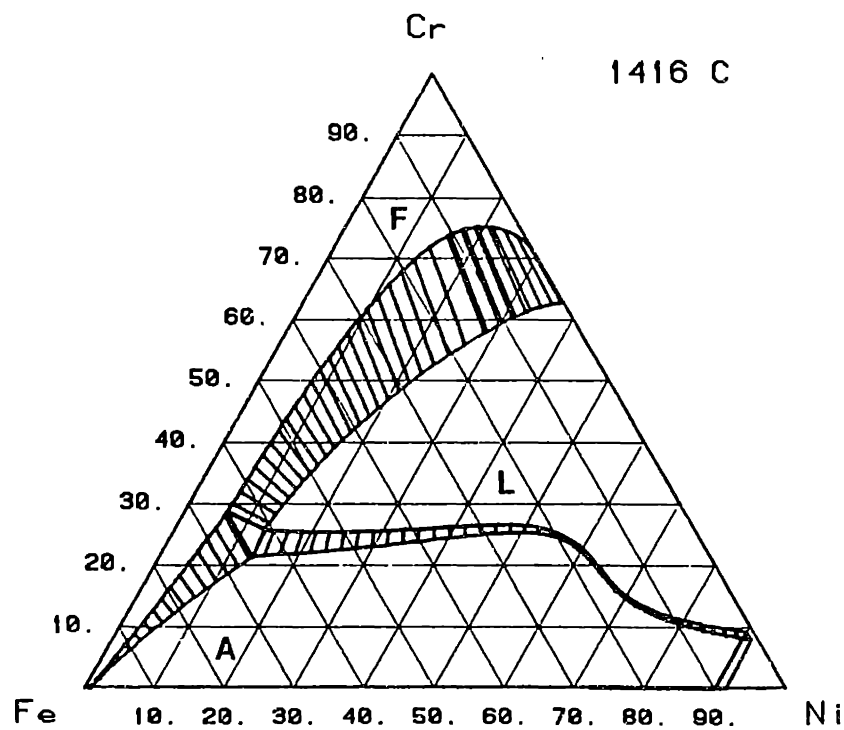
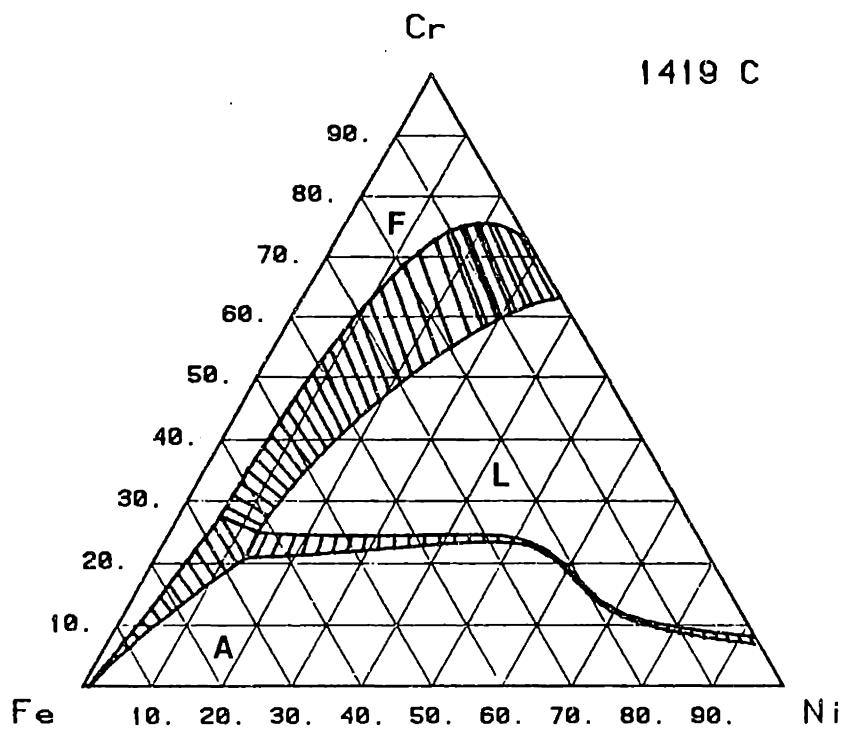


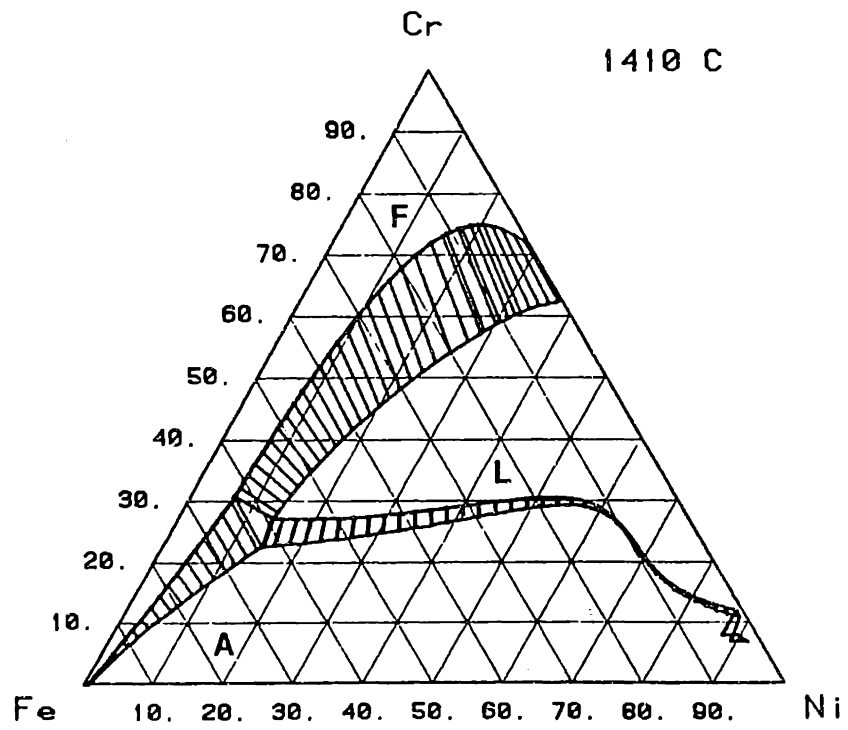
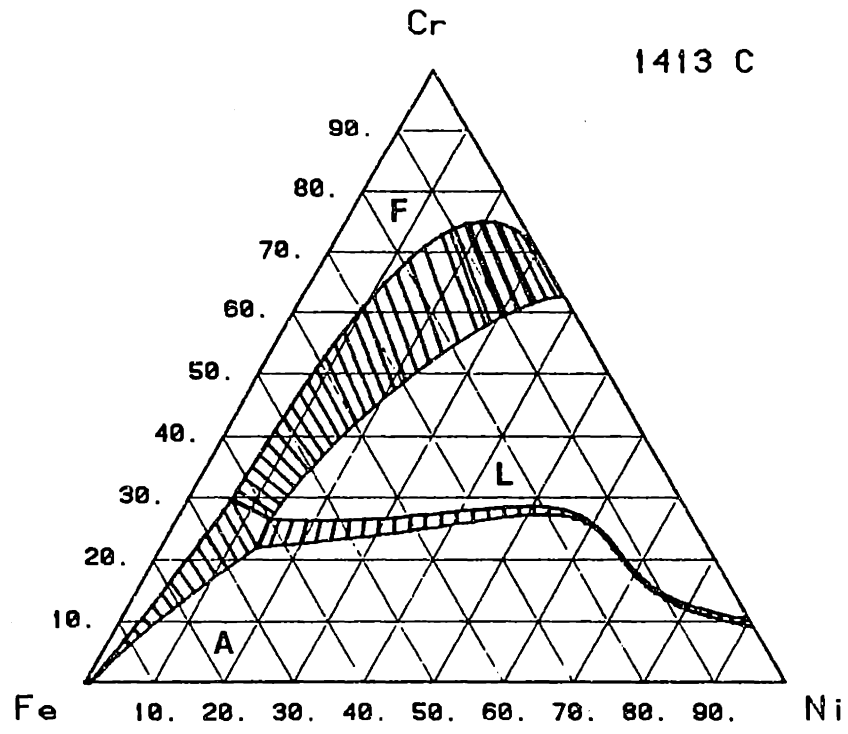


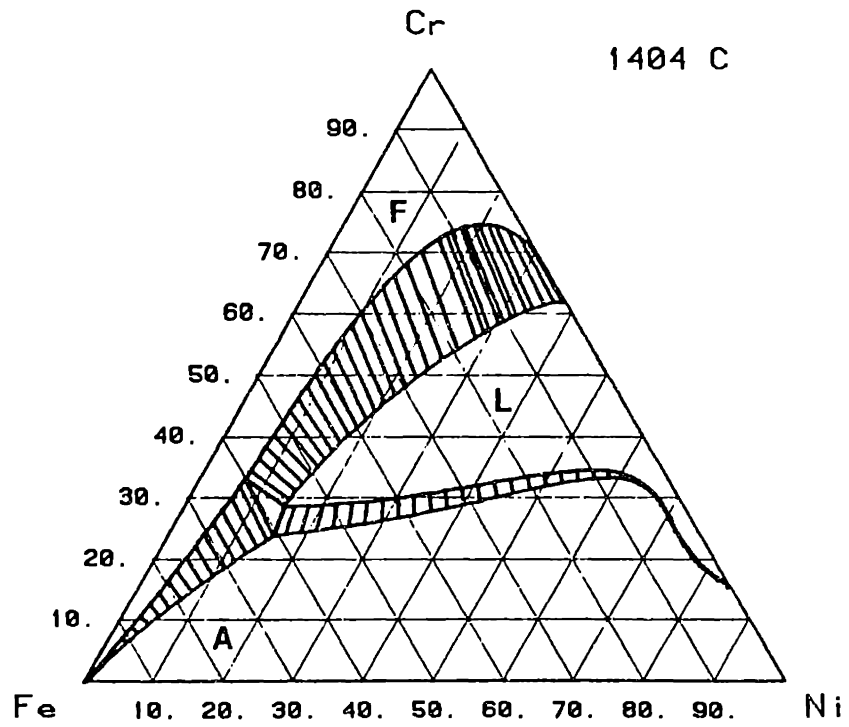
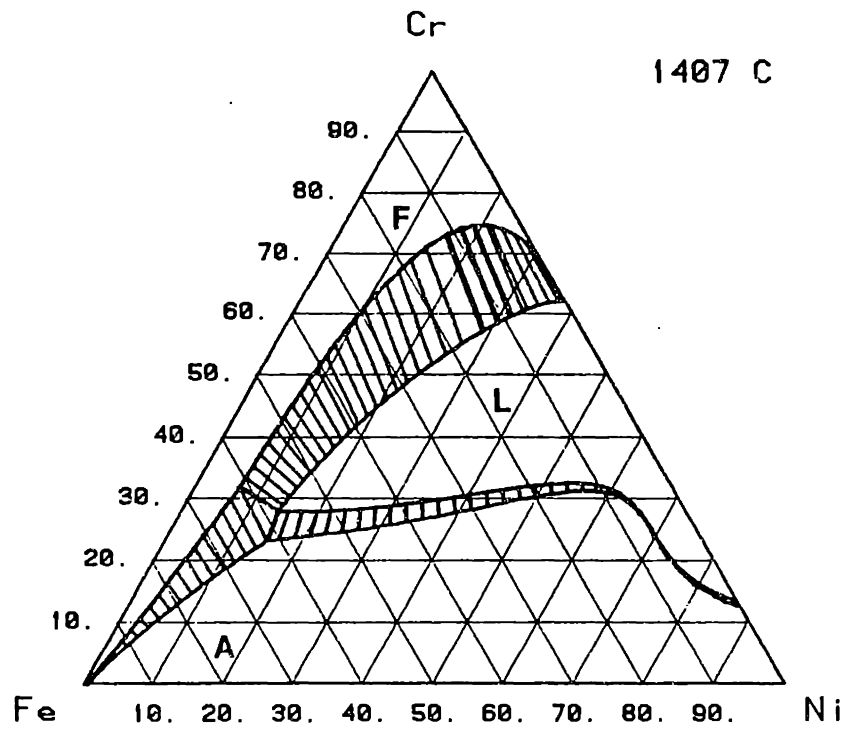


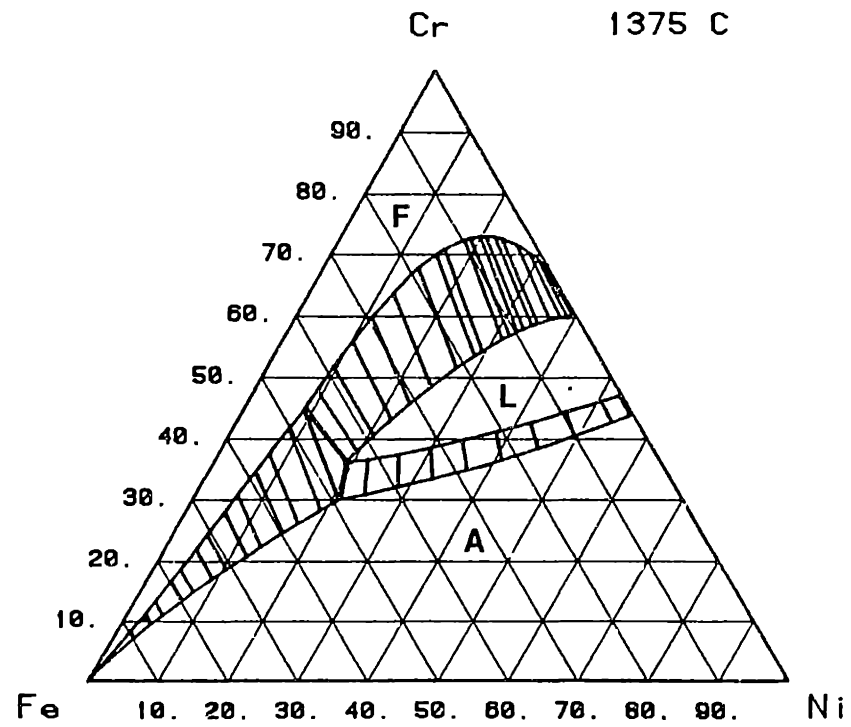
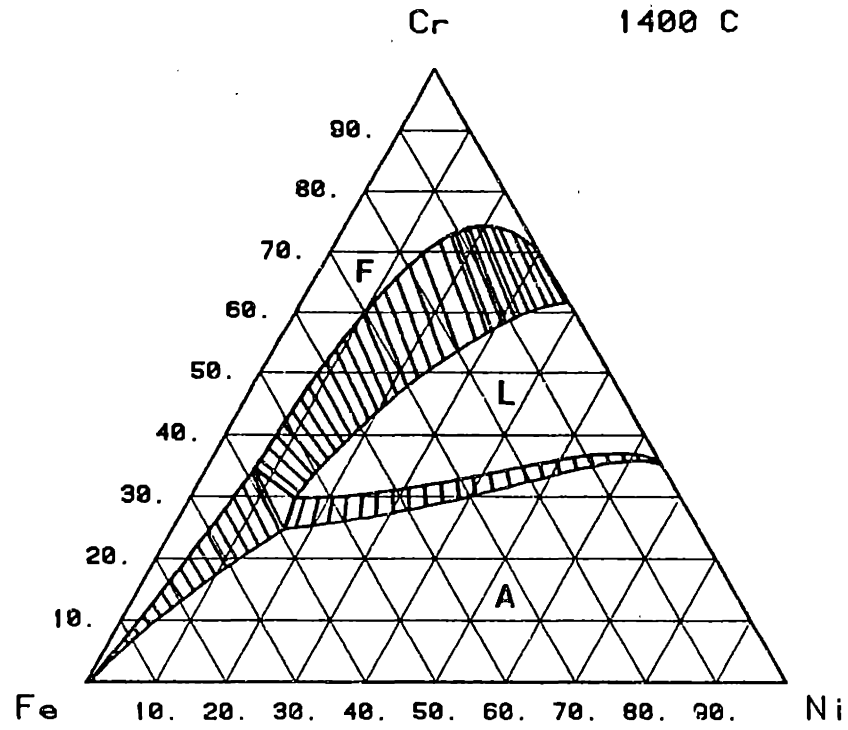


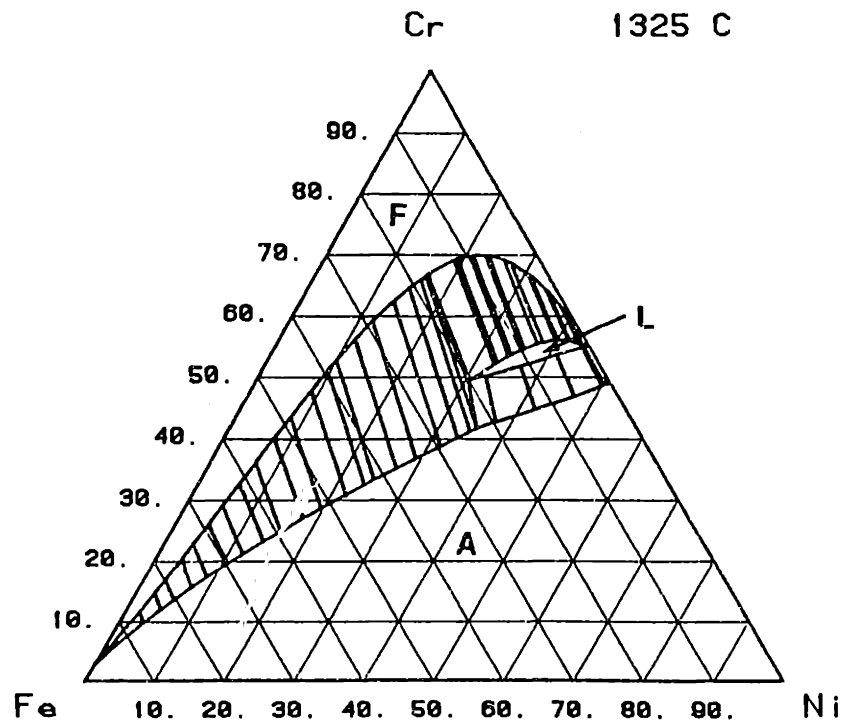
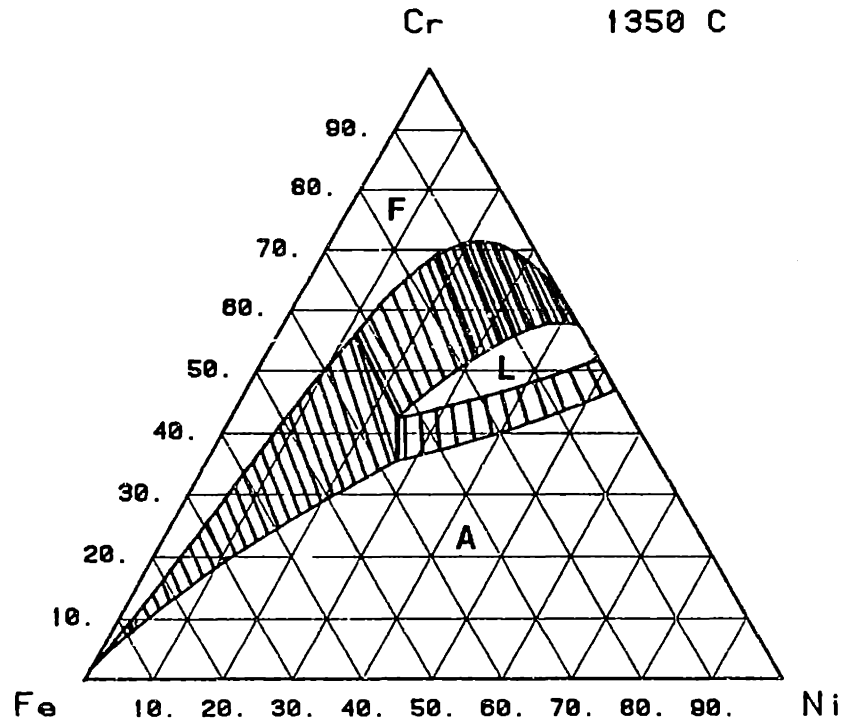


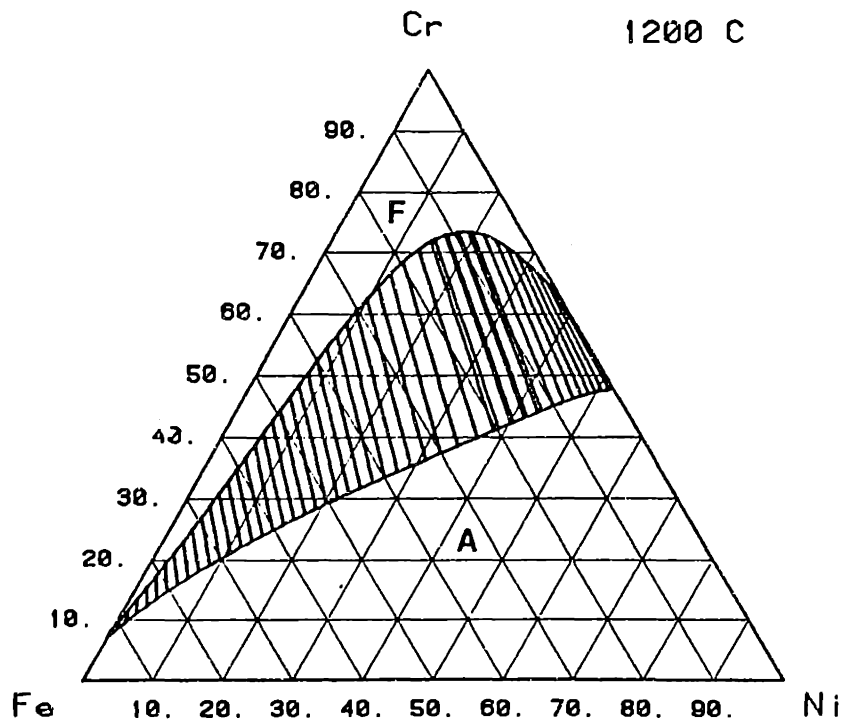
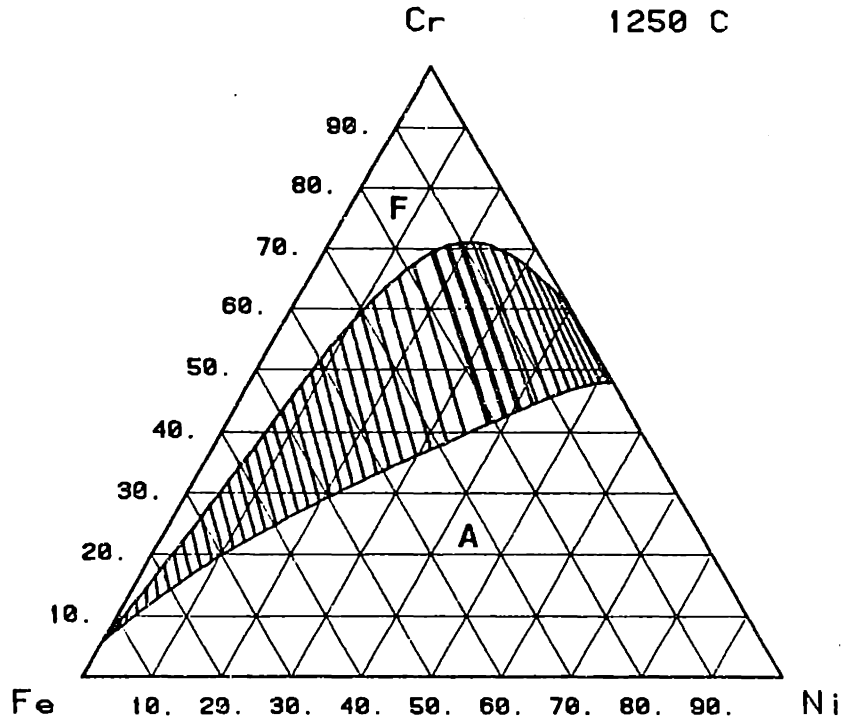


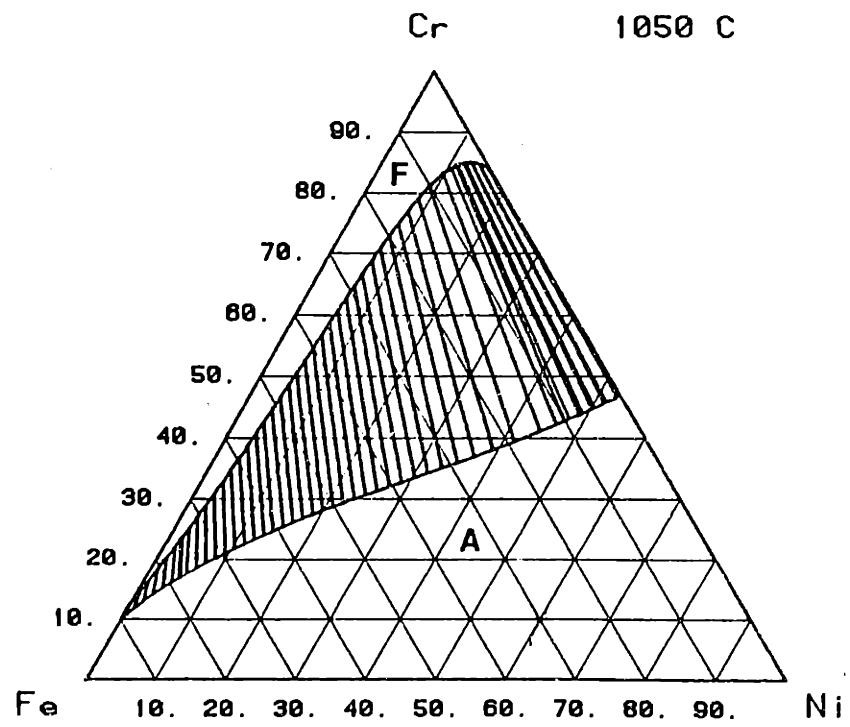
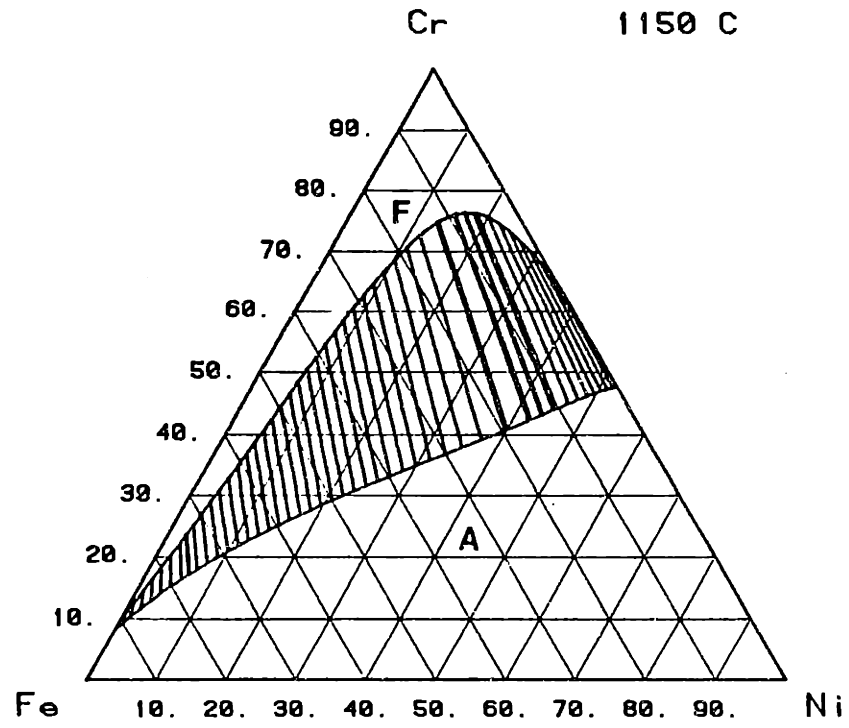


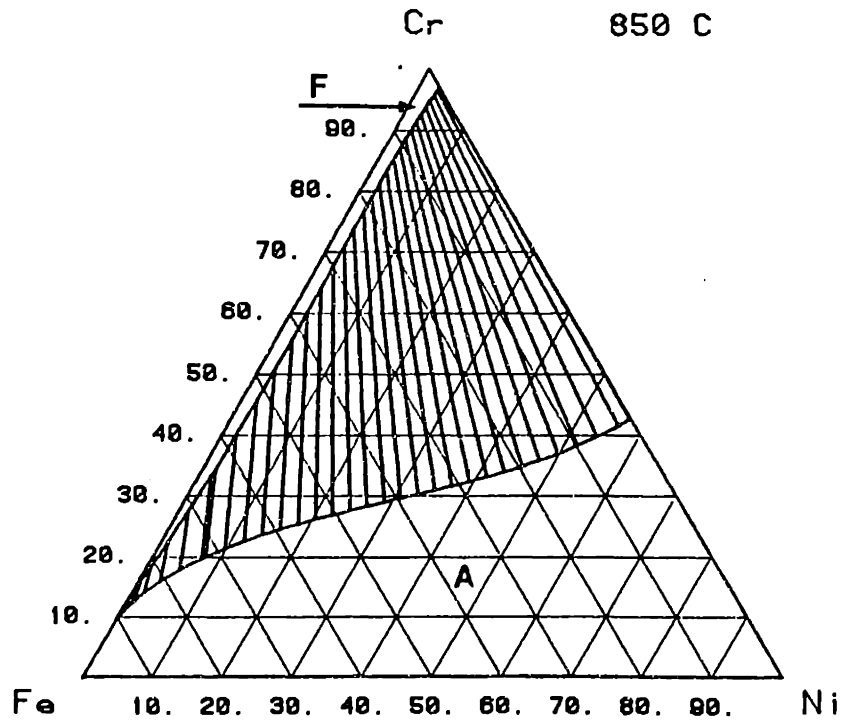
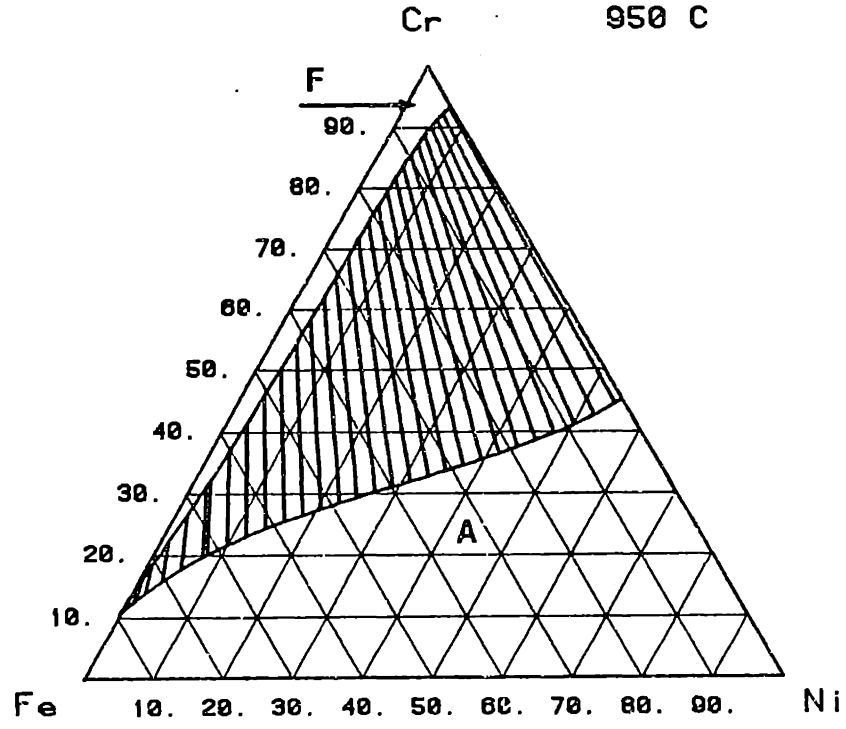




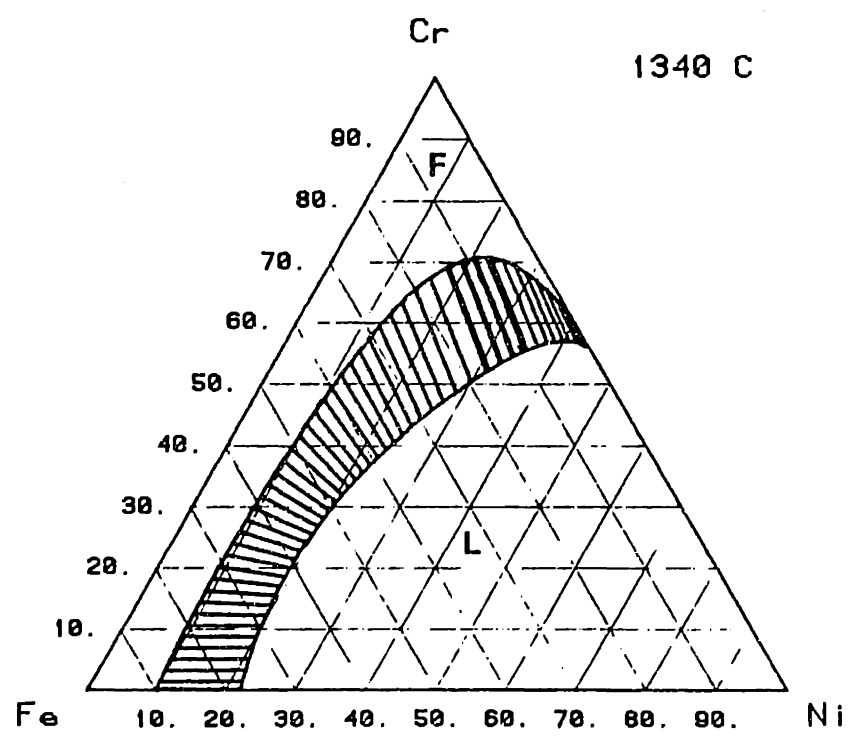
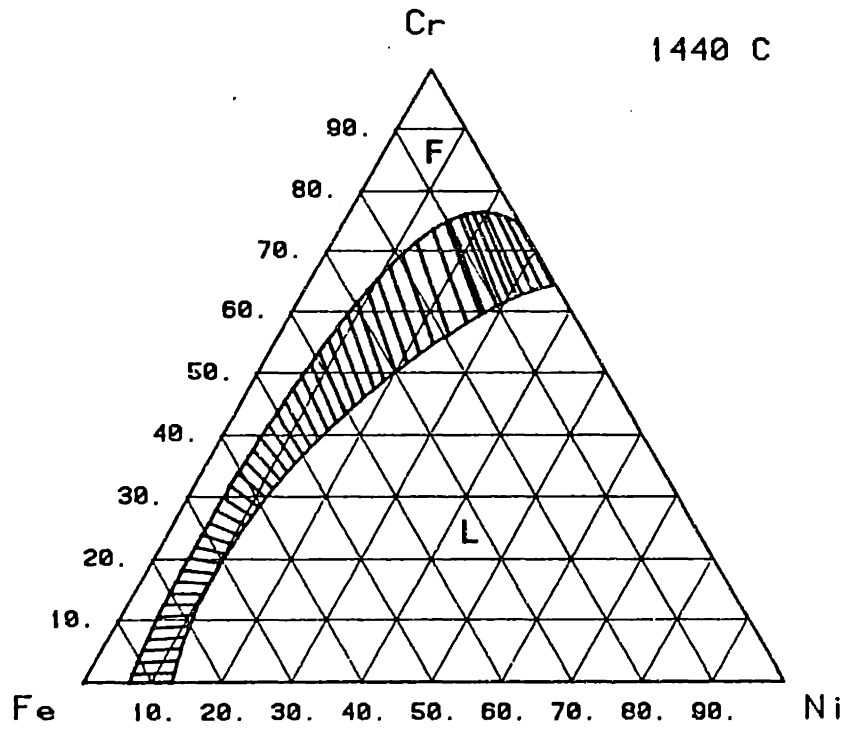


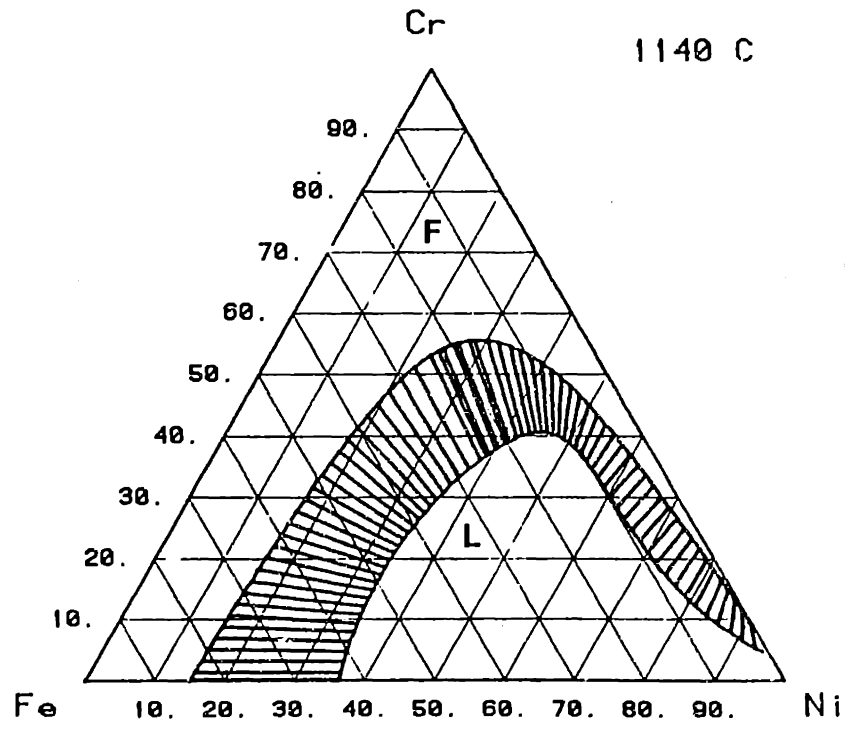
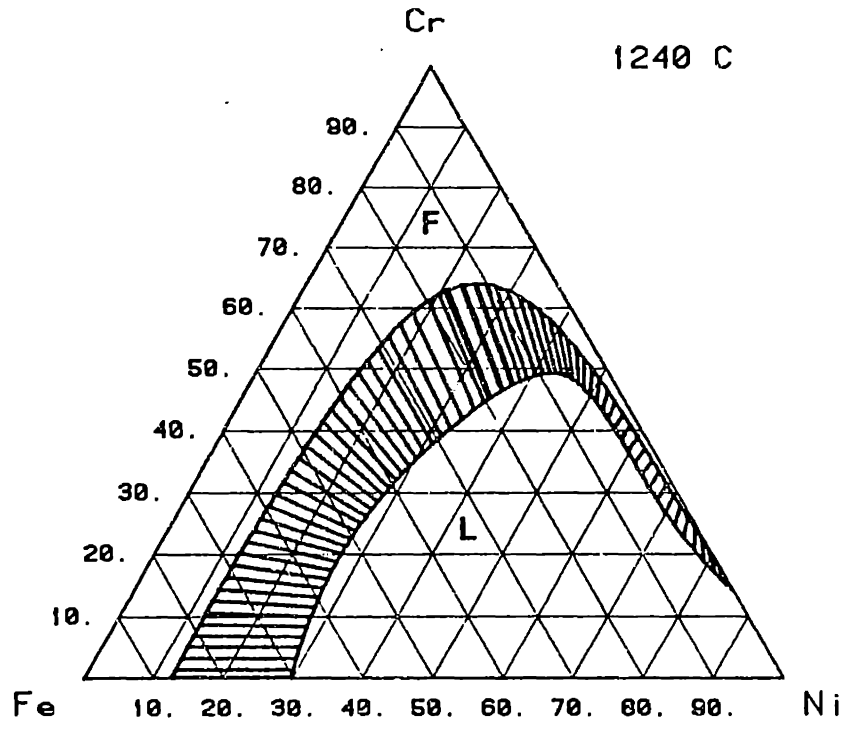


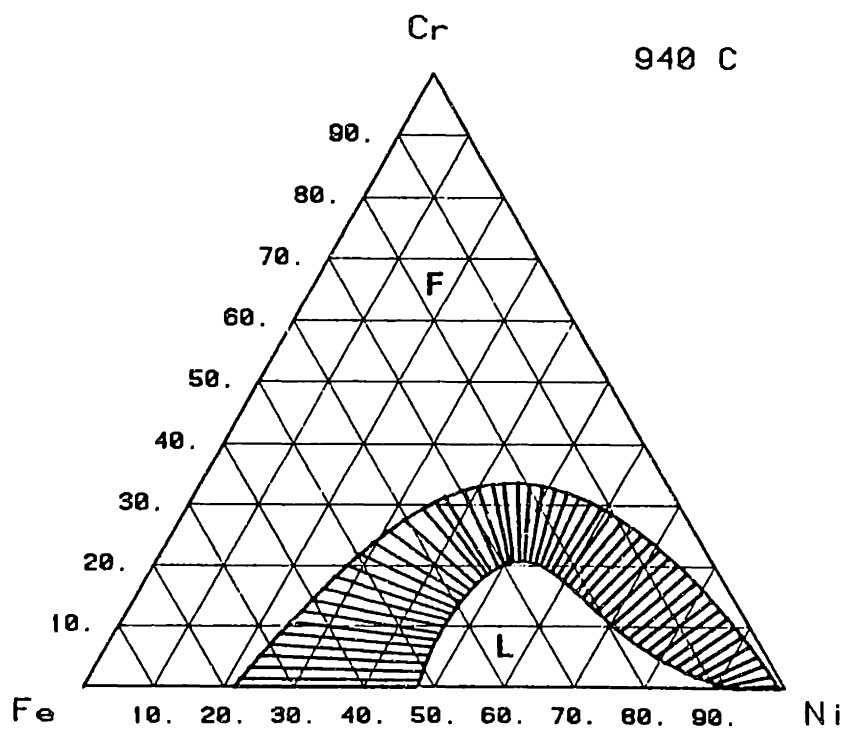
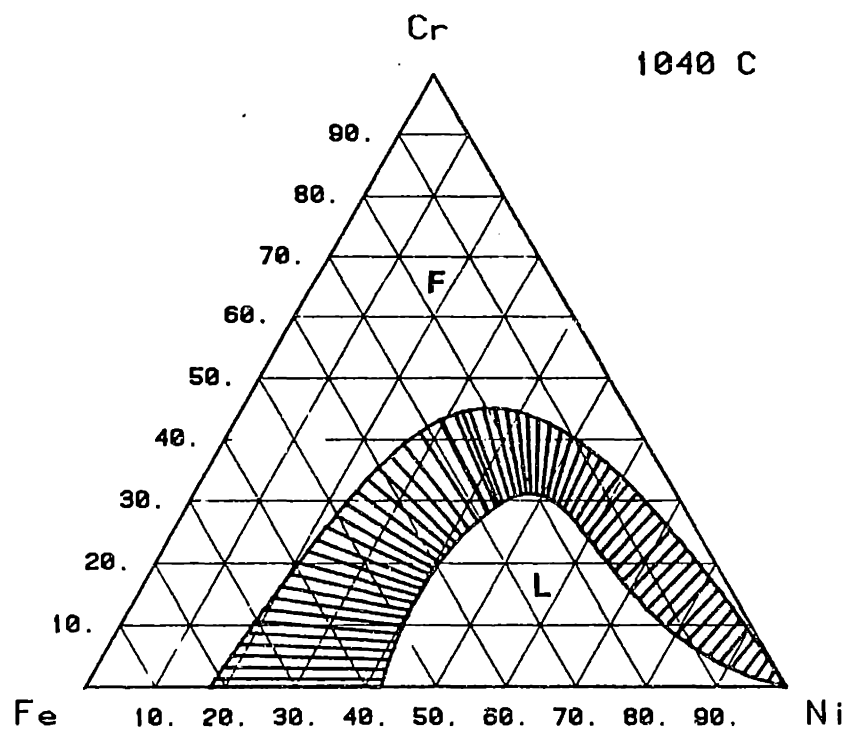


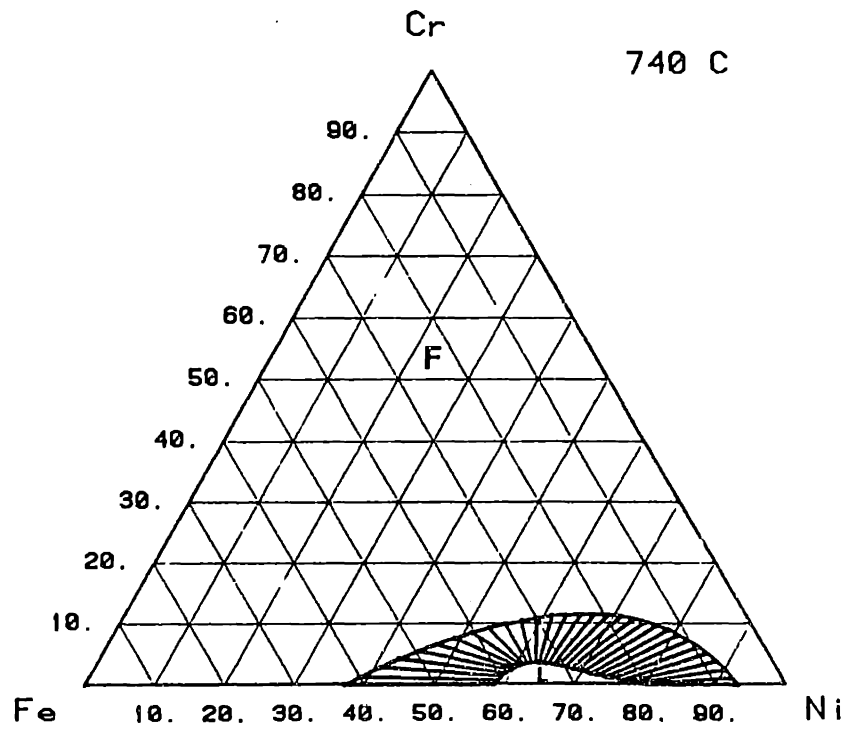
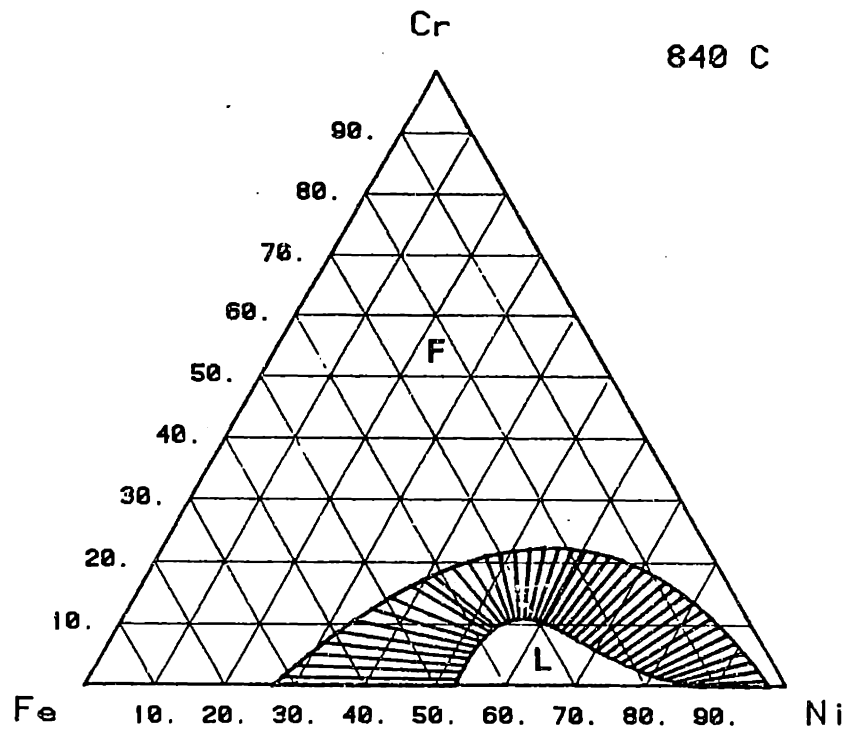


FERRITE-LIQUID METASTABLE EQUILIBRIUM

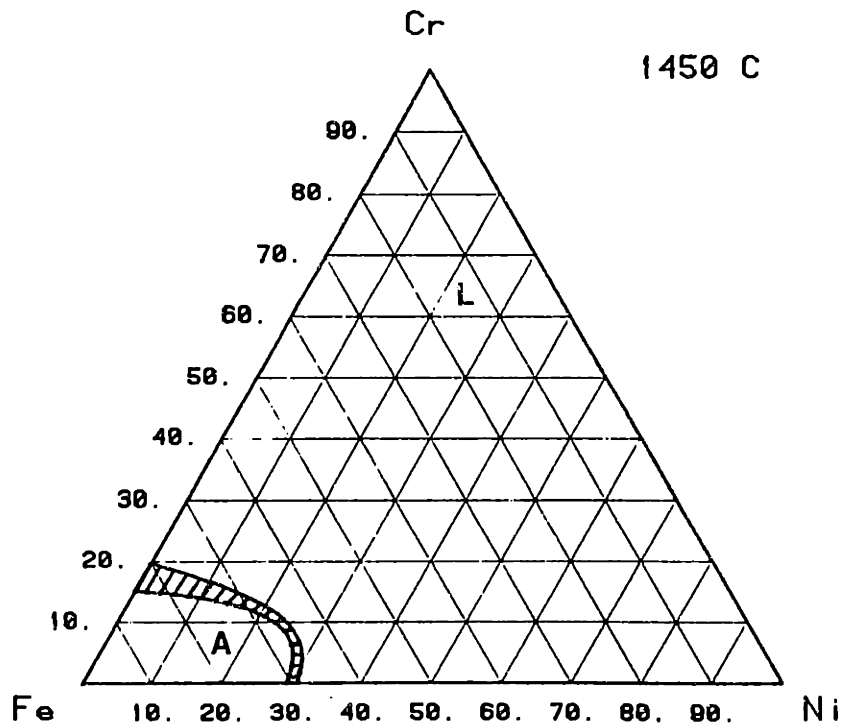
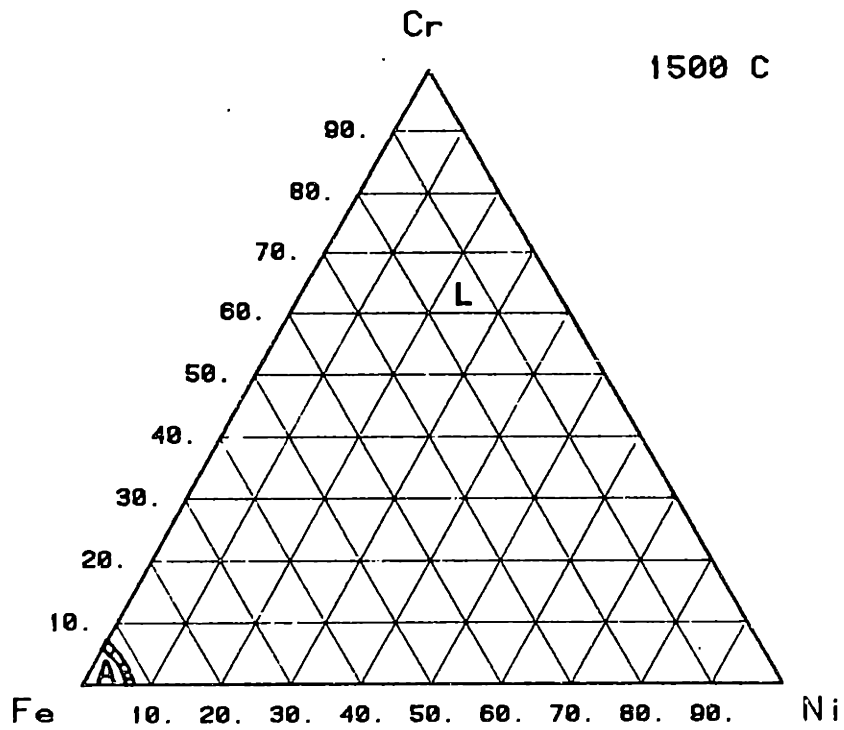


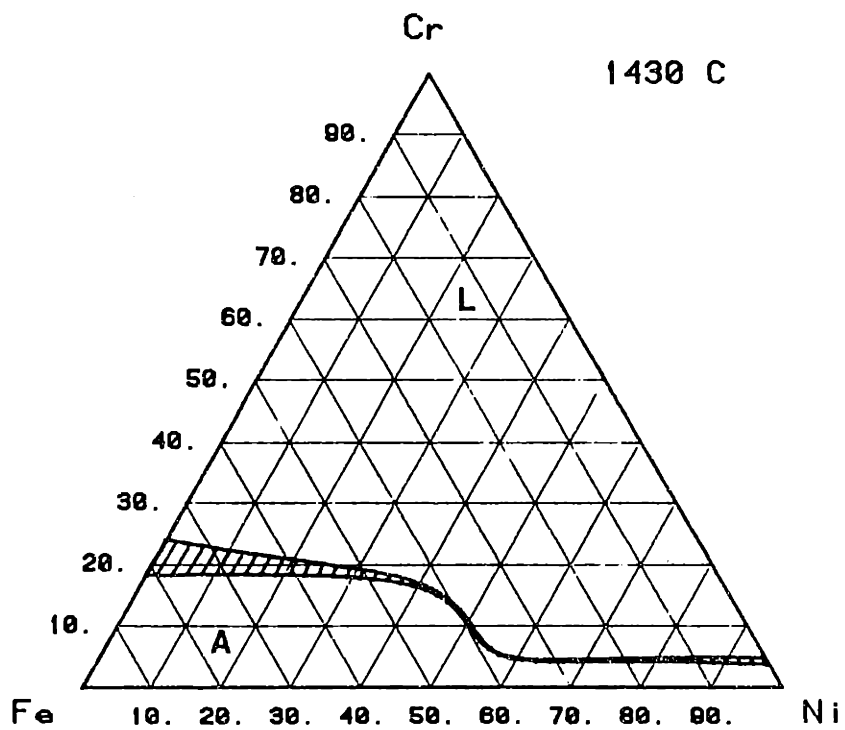
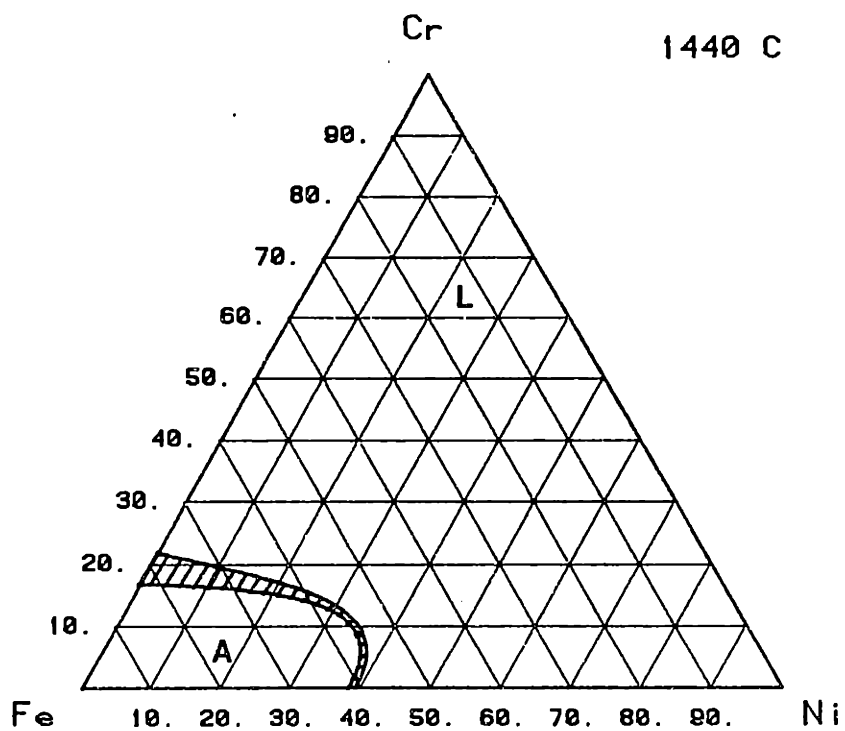


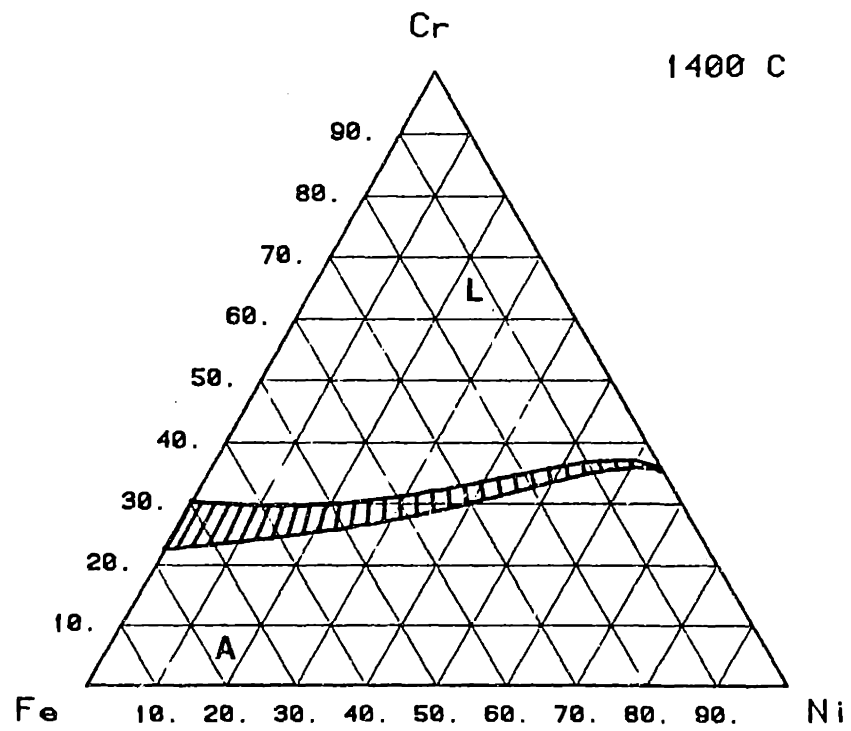
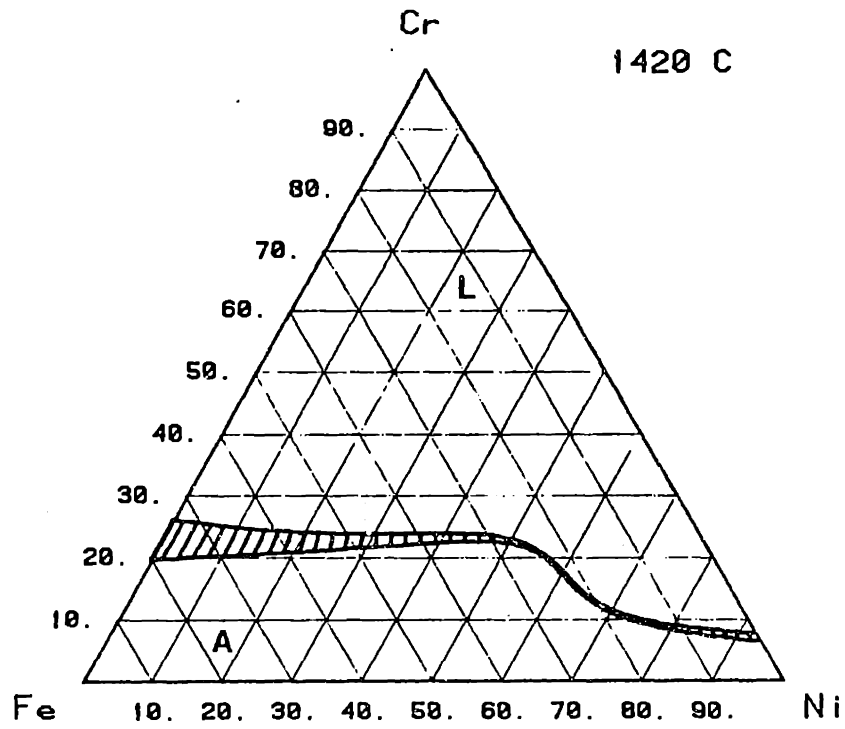


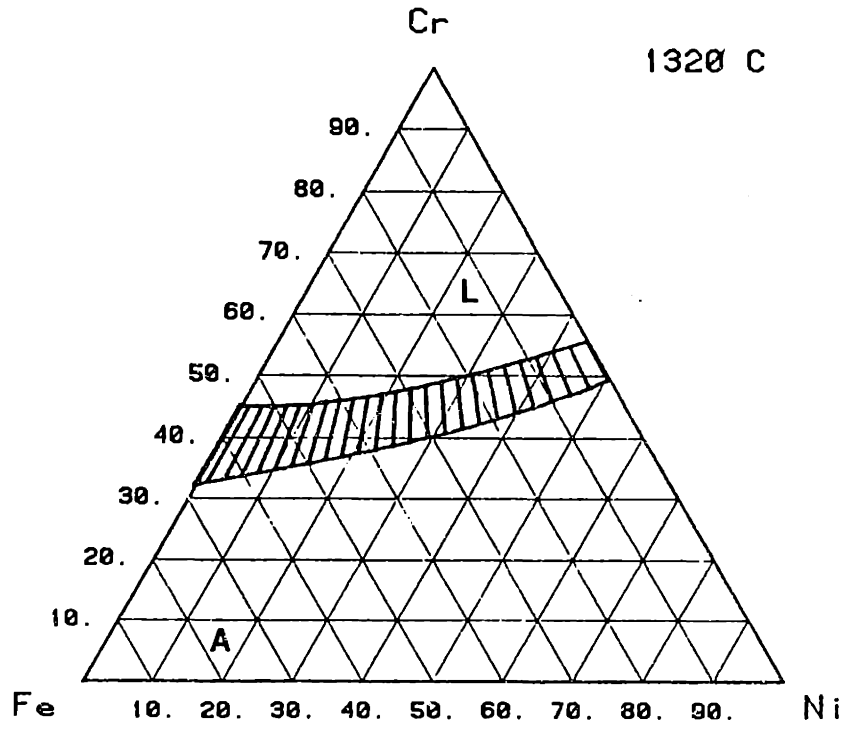
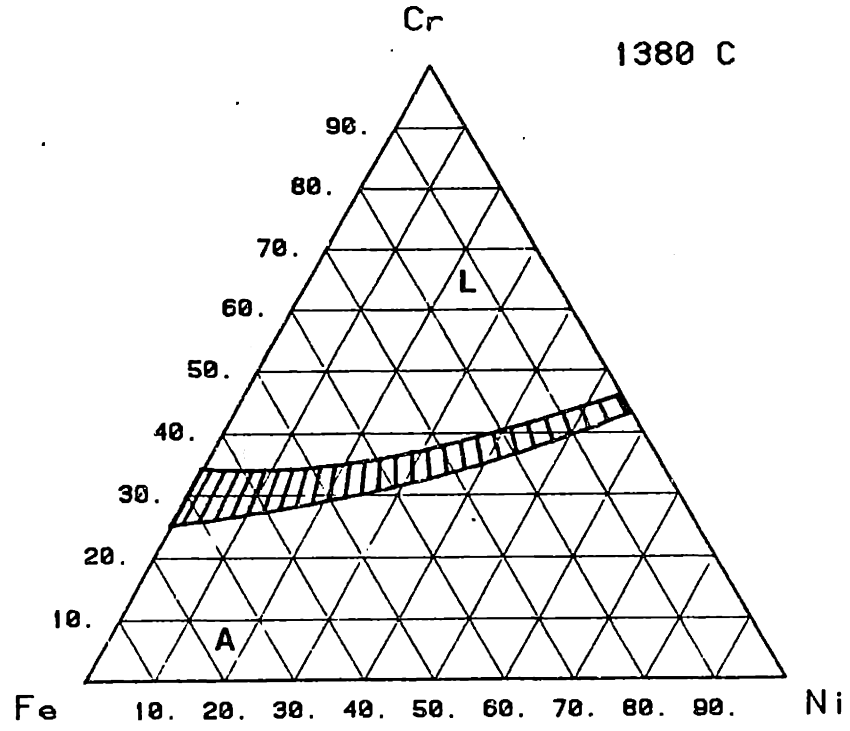


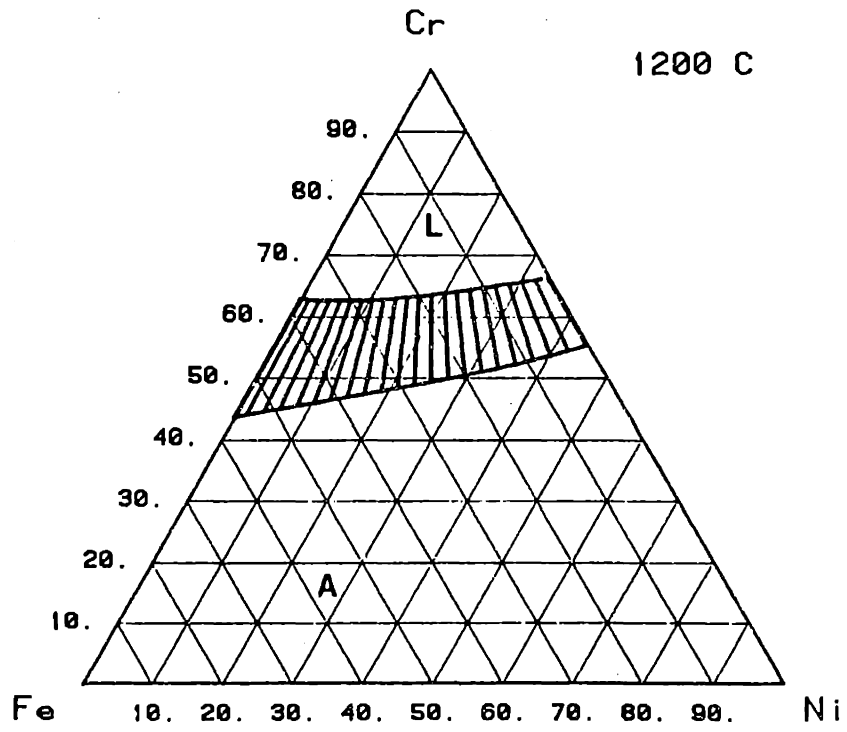
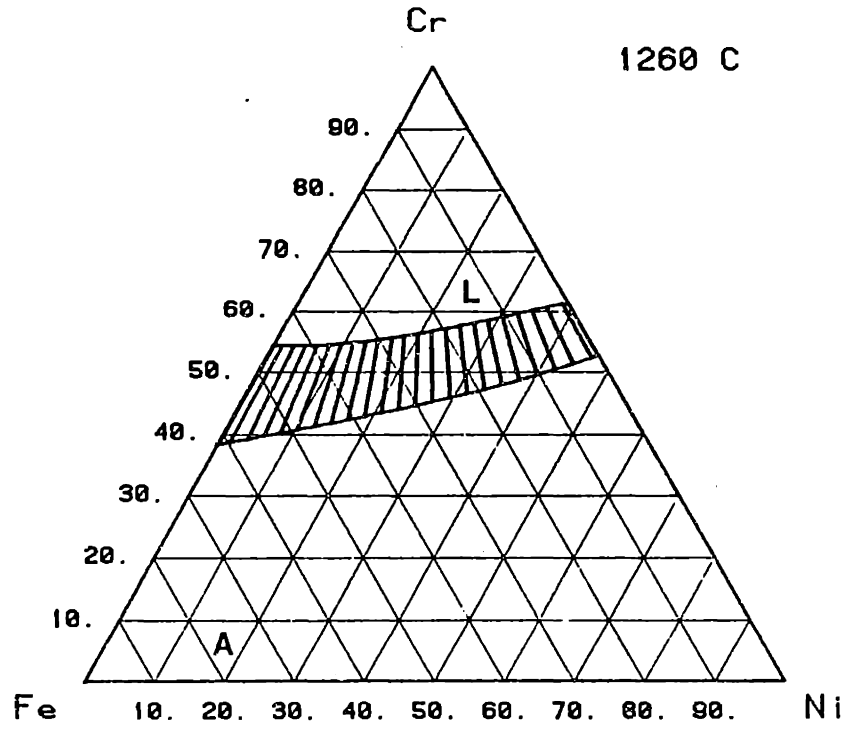
AUSTENITE-LIQUID METASTABLE EQUILIBRIUM

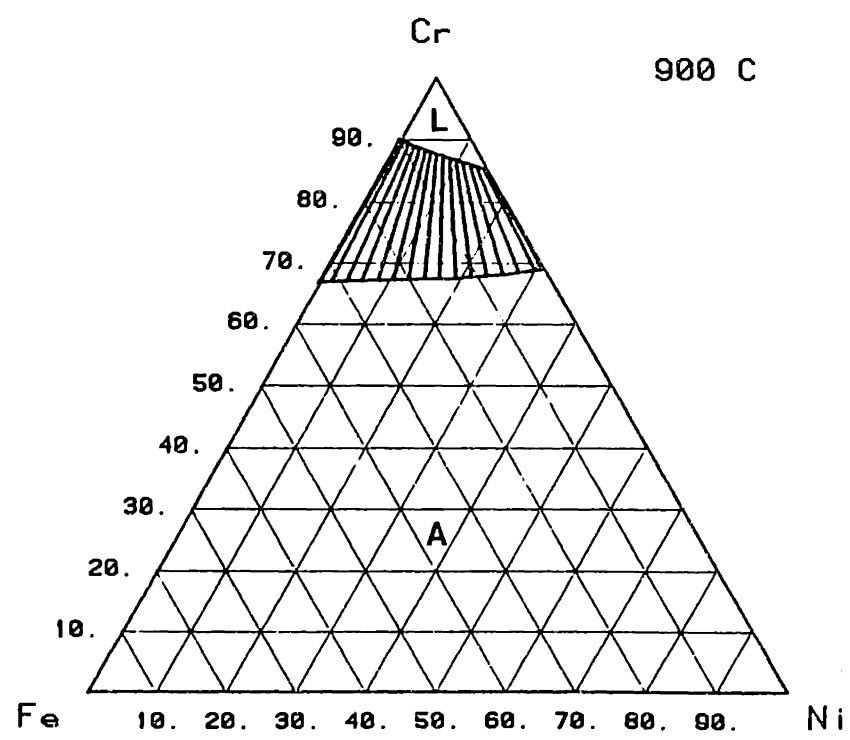
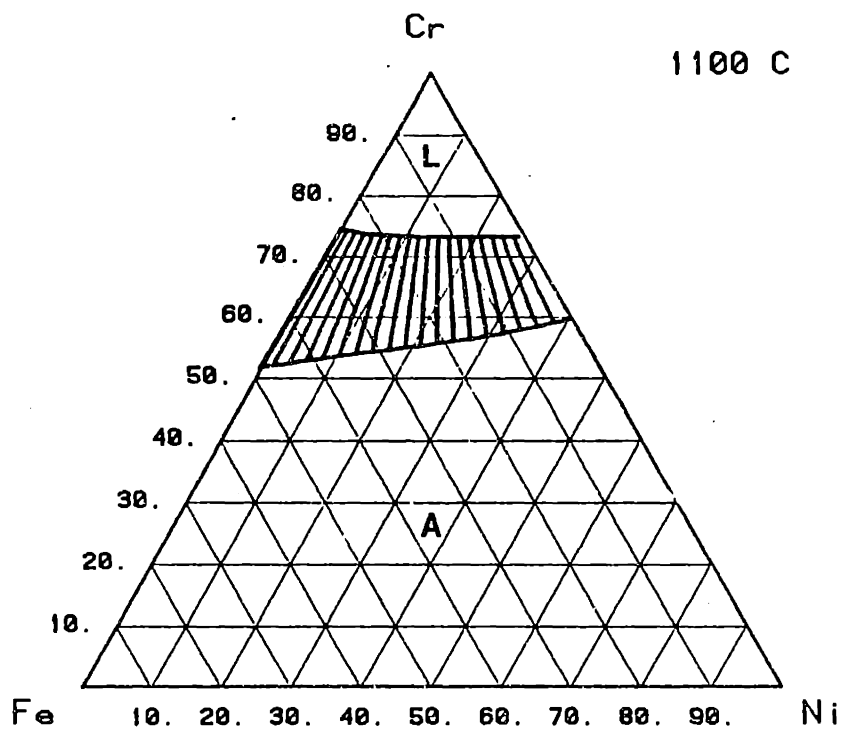












APPENDIX D

Finite Difference Model for Diffusional Growth

The ferrite to austenite transformation occurs by a diffusion controlled mechanism for the majority of conditions observed in this investigation. This appendix sets up the mathematical approach necessary to solve the governing diffusion equations in the Fe-Ni-Cr ternary system. The information provided in this appendix is sufficient to develop a finite difference model of the transformation which can be used to predict the rate and the extent of the ferrite to austenite transformation as a function of cooling rate.

This phase transformation model applies to a two-phase, ternary component system. The problem is complex because of the presence of three diffusing species, therefore, some assumptions are made in order to simplify the problem. Firstly, the sum of the fluxes of the three species will be assumed to be zero. This assumption is represented by equation D.2 and implies that Kirkendall-type vacancies are not created. Secondly, the composition gradients in the transformed austenite will be assumed to be negligibly small. The driving force for the transformation under these conditions is strictly the composition difference between ferrite and austenite at the interface and no back diffusion from the transformed austenite occurs. Third, diffusion will be assumed to occur for simple geometries. Planar diffusion along the x-orthogonal axis is assumed for Widmanstätten austenite platelets while radial diffusion in cylindrical coordinates is assumed for the transformation of ferrite dendrites.

The finite difference method is separated into four sections:

- I Input the arbitrary initial composition profile.
- II Adjust the compositions at each non-interface grid point using the boundary conditions at the interface and the diffusion equation.
- III Adjust the compositions at the interface using thermodynamic information.

- IV Account for the moving boundary, proceed to the next time increment and repeat steps II, III, IV as many times as necessary.

I. Input Initial Composition Profile

In a three-component system, the composition of two components must be specified at each grid point. The two components to be specified will be Cr and Ni since these have the largest compositional differences between the austenite and ferrite phases. Figure D.1 illustrates a possible grid in which a fully ferritic specimen is transforming to austenite. A uniform ferrite composition is assumed and the composition of austenite at the interface can be determined by the equilibrium tie-line at the transformation temperature.

Although a uniform ferrite composition is depicted in Fig. D.1 any arbitrary composition profile in the ferrite could be used without adding complexity to the computational method.

II. Adjusting the Composition of the Non-Interfacial Grid Points

Grid point zero is located at the center of the specimen and at the first time step its composition corresponds to that of the austenite boundary condition. Grid point 1 is in the ferrite phase at the first time step and thus has a different composition than grid point zero. This difference in composition provides a driving force for diffusion and the flux between these points can be calculated using Fick's first law of diffusion:

$$j_k^i = \sum_l D_{kl} \left(\frac{d(c_l)}{dx} \right) \quad (D.1)$$

where k refers to Cr or Ni, l refers to Cr, Ni, and Fe. The subscript i refers to the ferrite or austenite phase, however, since the flux in the austenite phase is assumed to be small, only diffusion in the ferrite is considered. Other nomenclature used in this chapter is summarized in Table D.1. The flux of the third component (Fe) can be determined from the flux balance:

$$j_{Cr}^i + j_{Ni}^i + j_{Fe}^i = 0 \quad (D.2)$$

The change in composition of grid point 1 due to this flux acting over an increment of time, Δt , can be calculated using the finite difference form of Fick's second law:

$$\left(\frac{c_{m+1}^k - c_m^k}{\Delta t} \right)_j = D_k \left(\frac{c_{j+1}^k - 2c_j^k + c_{j-1}^k}{(\Delta x_k)^2} \right)_m \quad (D.3)$$

where m refers to the time increment step and j is the grid point index. In this equation, c_{j+1}^k is the unknown and can be solved for since all other variables are known. Equation 3 should be repeated once to calculate the change in Cr and once to calculate the change in Ni concentrations at grid point 1. The Fe concentration can be calculated by the mass balance

$$c_{Cr}^i + c_{Ni}^i + c_{Fe}^i = 0 \quad (D.4)$$

In order to use equation D.3, the boundary conditions at the zero flux planes must be accounted for. This problem can be treated by artificially creating a grid point outside the sample and setting its composition equal to the surface concentration.

By repeating the above procedure for all grid points, the compositions can be calculated throughout the specimen. However, the composition at the interface, grid point zero, has not yet been adjusted and requires thermodynamic equilibria to be satisfied in addition to the kinetic considerations.

III. Adjusting the Compositions at the Ferrite/Austenite Interface

As diffusion occurs, the austenite phase grows and the austenite/ferrite interface advances into the ferrite. The velocity of the interface motion is related to the flux of the diffusing elements

$$j_k^i = -v(c_k^{\gamma\delta} - c_k^{\delta\gamma}) \quad (D.5)$$

Thus, four sets of kinetic equations need to be solved simultaneously in order to calculate the interface velocity: 1) the mass balance, eq. D.4, 2) the flux balance, eq. D.2, 3) the diffusion equation D.1 and 4) the velocity flux relationship, eq. D.5.

Starting with the diffusion equations in the ferrite phase

$$j_{Cr}^{\delta} = -D_{CrCr}^{\delta} \left(\frac{dc_{Cr}}{dx} \right) - D_{CrNi}^{\delta} \left(\frac{dc_{Ni}}{dx} \right) - D_{CrFe}^{\delta} \left(\frac{dc_{Fe}}{dx} \right)$$

$$j_{Ni}^{\delta} = -D_{NiCr}^{\delta} \left(\frac{dc_{Cr}}{dx} \right) - D_{NiNi}^{\delta} \left(\frac{dc_{Ni}}{dx} \right) - D_{NiF_0}^{\delta} \left(\frac{dc_{F_0}}{dx} \right)$$

$$j_{F_0}^{\delta} = -j_{Ni}^{\delta} - j_{Cr}^{\delta} \quad (\text{flux balance})$$

and substituting the differential form of the mass balance,

$$\frac{dc_{Cr}}{dx} + \frac{dc_{Ni}}{dx} + \frac{dc_{F_0}}{dx} = 0$$

the flux of Cr and Ni can be equated to their concentration gradients

$$j_{Cr}^{\delta} = -\left(D_{CrCr}^{\delta} - D_{CrF_0}^{\delta}\right) \frac{dc_{Cr}}{dx} - \left(D_{CrNi}^{\delta} - D_{CrF_0}^{\delta}\right) \frac{dc_{Ni}}{dx} \quad (D.6a)$$

$$j_{Ni}^{\delta} = -\left(D_{NiCr}^{\delta} - D_{NiF_0}^{\delta}\right) \frac{dc_{Cr}}{dx} - \left(D_{NiNi}^{\delta} - D_{NiF_0}^{\delta}\right) \frac{dc_{Ni}}{dx} \quad (D.6b)$$

Equation's D.6 and the following velocity-flux relationships :

$$j_{Cr}^{\delta} = -v(c_{Cr}^{\gamma\delta} - c_{Cr}^{\delta\gamma})$$

$$j_{Ni}^{\delta} = -v(c_{Ni}^{\gamma\delta} - c_{Ni}^{\delta\gamma})$$

can be solved simultaneously for the interface velocity:

$$v = \left(\frac{1}{(c_{Cr}^{\gamma\delta} - c_{Cr}^{\delta\gamma})} \right) \left((D_{CrCr}^{\delta} - D_{CrF_0}^{\delta}) \frac{dc_{Cr}}{dx} + (D_{CrNi}^{\delta} - D_{CrF_0}^{\delta}) \frac{dc_{Ni}}{dx} \right) \quad (D.7a)$$

$$v = \left(\frac{1}{(c_{Ni}^{\gamma\delta} - c_{Ni}^{\delta\gamma})} \right) \left((D_{NiCr}^{\delta} - D_{NiF_0}^{\delta}) \frac{dc_{Cr}}{dx} + (D_{NiNi}^{\delta} - D_{NiF_0}^{\delta}) \frac{dc_{Ni}}{dx} \right) \quad (D.7b)$$

Equations D.7a and D.7b each represent the interface velocity and the phase transformation problem appears to be overspecified. That is, a given tie line fixes $c_{Cr}^{\delta} - c_{Cr}^{\gamma}$ and $c_{Ni}^{\delta} - c_{Ni}^{\gamma}$ which specifies all variables on the right hand side of both equations. Therefore, there appears to be two independent means of calculating the velocity.

However, in the ternary system, tie-line movement involves one degree of freedom and can be used to "adjust" $c_{Cr}^{\delta} - c_{Cr}^{\gamma}$ and $c_{Ni}^{\delta} - c_{Ni}^{\gamma}$ so that both equation D.7a and D.7b can be satisfied with a common velocity. Movement of the tie-line must satisfy thermodynamic equilibrium at the interface:

$$\bar{G}_k^{\delta} = \bar{G}_k^{\gamma} \quad (D.8)$$

where the partial molar Gibbs energy for component k , \bar{g}_k , is a function of temperature and composition. Expanding equation D.8 into its standard Gibbs energy and activity components gives:

$$G_k^{ob} + RT \ln a_k^b = G_k^{oy} + RT \ln a_k^y \quad (D.9)$$

where k refers to Ni, Cr and Fe.

Equations D.7a, D.7b and D.9 must be solved simultaneously to obtain the interface composition and velocity. Therefore, a means of determining \bar{g}_k^o , \bar{g}_k^y , a_k^b and a_k^y as a function of temperature and c_k^b and c_k^y , must be established. Thermodynamic data for Fe, Ni, and Cr are reported as a function of temperature by Chuang and Chang [D.1]. From these data, the standard free energy and activity coefficients can be calculated.

An alternative scheme for determining the tie-line location could be used to incorporate the previously determined tie-lines in the Fe-Ni-Cr system. These tie-lines are summarized in Appendix C and could be used as a substitute for equation D-9. This approach is less flexible in the sense that only those temperatures where the isothermal sections were calculated are available and the tie-lines at other temperatures would have to be interpolated from the existing data.

IV. Accounting for the Moving Boundary

The composition at all the grid points and at the interface has been adjusted to satisfy kinetic and thermodynamic requirements. However, the phase transformation involves a moving boundary, additional adjustments must be made to the grid in order to keep the same number of grid points in the ferrite phase. Therefore, a grid transformation must be accomplished in which the spacing between points is transformed. Since each grid point moves, the composition at each point must also be readjusted. These manipulations are common to moving-boundary problems and details are not necessary here.

The time increment should be increased one step, $t' = t + \Delta t$, and the program should be repeated from step II using the new interface composition as a boundary condition and the new composition profile.

Table D.1: Nomenclature used in Appendix D

Symbol	Description
j_k^i	flux of component k in phase i
D_{ki}	diffusivity matrix terms
c_k^i	concentration of component k in phase i
v	interface velocity
\bar{G}_k^i	partial molar Gibbs free energy of component k in i
\bar{G}_k^{oi}	standard Gibbs energy of component k in phase i
a_k^i	activity of component k in phase i
j, m	grid spacing index, time index
Δx , Δt	grid spacing, time increment
$c_{Cr}^{\delta\gamma}$	concentration of Cr in the δ phase which is in equilibrium with the γ phase

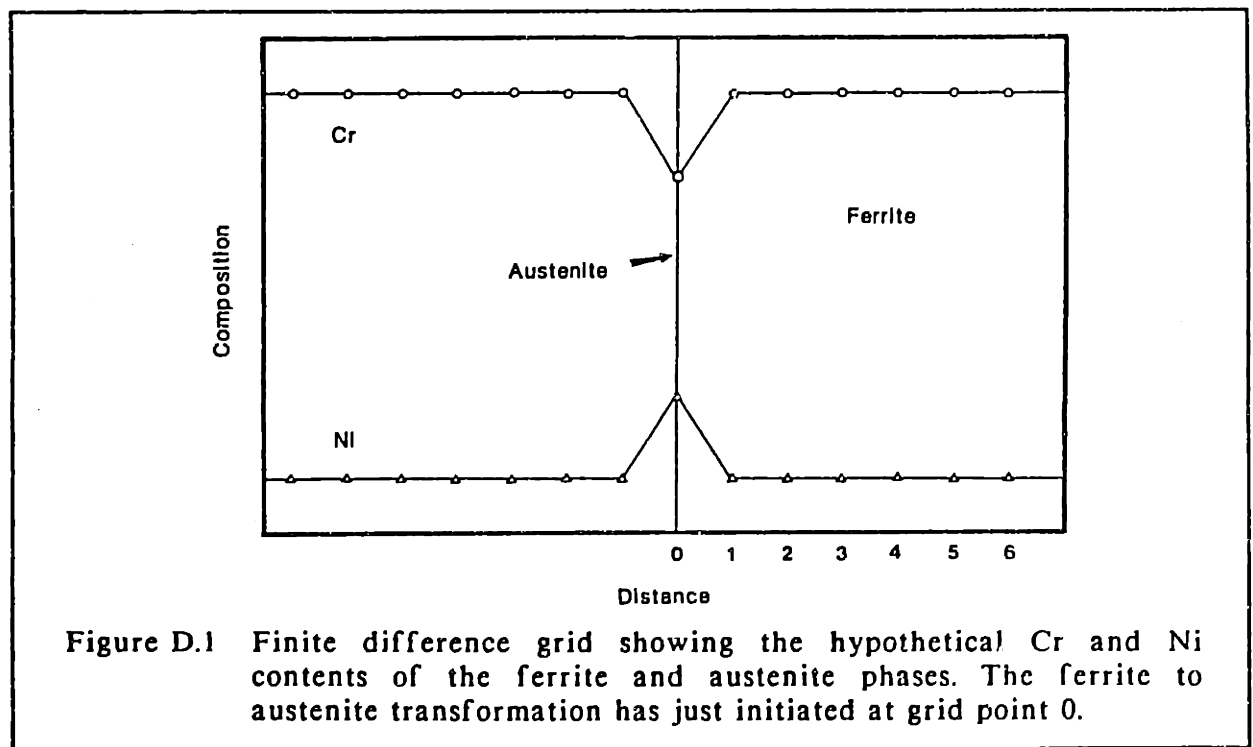


Figure D.1 Finite difference grid showing the hypothetical Cr and Ni contents of the ferrite and austenite phases. The ferrite to austenite transformation has just initiated at grid point 0.

APPENDIX E

Dendrite Tip Calculations

In Chapter 7, methods were presented to calculate the characteristics at the tip of a dendrite growing under steady state conditions. This appendix summarizes these calculations which were performed for each of the solidification conditions investigated in this study. The results are listed in three tables for each alloy. The first table (A) indicates the undercooling calculations, the second table (B) indicates the segregation calculations and the third table (C) indicates the amounts of primary and secondary phases that solidify for each alloy. Since Alloy 4 solidifies in the FA mode at low rates and in the AF mode at high rates, calculations were performed for both conditions. The nomenclature used to describe the solidification calculations is summarized below.

Description of the variables

ΔT_r	undercooling caused by tip radius
ΔT_c	undercooling caused by solutal effects
ΔT_{tot}	total undercooling
ΔT_E	liquidus temp. - eutectic temp.
$\Delta T'_E$	actual undercooling below the eutectic temperature
C_L^*	composition of liquid at the dendrite tip
f_{S^o}	fraction primary phase caused by tip undercooling
f_E	fraction eutectic liquid
A,F	austenite, ferrite
P,S,T	subscripts: primary, secondary, total

D.1A: Alloy 1 Undercooling calculations

Melt	ΔT_r (K)	ΔT_c (K)	ΔT_{tot} (K)	ΔT_E (K)	$\Delta T'_E$ (K)
Cast	0.46	7.25	7.71	46	-
E-B 1	1.30	12.1	13.4	46	-
E-B 2	1.35	12.4	13.7	46	-
E-B 3	2.24	15.3	17.5	46	-
E-B 4	3.96	18.7	22.6	46	-
E-B 5	5.65	20.7	26.4	46	-
E-B 6	7.11	22.2	29.3	46	-

Table D.1B: Alloy 1 Segregation calculations

Melt	C^*_L	f^*_s	f_E	A_P	A_S	F_s
Cast	23.30	0.279	0.17	0.83	0.12	0.05
E-B 1	24.17	0.448	0.15	0.85	0.12	0.05
E-B 2	24.23	0.460	0.15	0.85	0.12	0.05
E-B 3	24.74	0.553	0.14	0.86	0.13	0.04
E-B 4	25.34	0.659	0.12	0.88	0.13	0.04
E-B 5	25.71	0.721	0.10	0.90	0.14	0.03
E-B 6	25.93	0.761	0.09	0.91	0.14	0.03

Table D.1C: Alloy 1 % Primary and secondary phases

Solidification Condition	F_P	F_S	F_T	A_P	A_S	A_T
Equilibrium	0	0	0	100	0	0
Scheil	0	5.80	5.80	82.0	12.2	94.2
Cast	0	5.27	5.27	83	11.7	94.7
E-B 1	0	4.65	4.65	85	12.3	95.3
E-B 2	0	4.60	4.60	85	12.5	95.4
E-B 3	0	4.30	4.30	86	12.8	95.7
E-B 4	0	3.70	3.70	88	13.2	96.3
E-B 5	0	3.10	3.10	90	13.9	96.9
E-B 6	0	2.79	2.79	91	14.2	97.2

Table D.2A: Alloy 2 Undercooling calculations

Melt	ΔT_r (K)	ΔT_c (K)	ΔT_{tot} (K)	ΔT_E (K)	$\Delta T'_E$ (K)
Cast	0.47	7.63	8.10	19.7	-
E-B 1	1.32	12.8	14.1	19.7	-
E-B 2	1.39	13.1	14.5	19.7	-
E-B 3	2.30	16.2	18.5	19.7	-
E-B 4	4.11	19.9	24.0	19.7	0.2
E-B 5	5.84	22.1	27.9	19.7	2.4
E-B 6	7.60	23.8	31.4	19.7	4.1

Table D.2B: Alloy 2 Segregation calculations

Melt	C^*_L	f^*_s	f_E	A_P	A_S	F_s
Cast	25.06	0.27	0.30	0.70	0.21	.093
E-B 1	25.99	0.44	0.27	0.73	0.19	.084
E-B 2	26.05	0.45	0.27	0.73	0.19	.083
E-B 3	26.60	0.54	0.25	0.75	0.17	.078
E-B 4	27.26	0.65	0.23	0.77	0.16	.071
E-B 5	27.65	0.71	0.18	0.82	0.12	.056
E-B 6	27.95	0.76	0.15	0.85	0.10	.047

Table D.2C: Alloy 2 % Primary and secondary phases

Solidification Condition	F_P	F_S	F_T	A_P	A_S	A_T
Equilibrium	0	18	18	-	-	82
Scheil	0	14.4	14.4	55.0	30.6	85.6
Cast	0	9.30	9.30	70.0	20.7	90.7
E-B 1	0	8.37	8.37	73.0	18.6	91.6
E-B 2	0	8.30	8.30	73.1	18.7	91.7
E-B 3	0	7.75	7.75	75.0	17.3	92.3
E-B 4	0	7.13	7.13	77.0	15.9	92.9
E-B 5	0	5.58	5.58	82.0	12.4	94.4
E-B 6	0	4.65	4.65	85.0	10.4	95.3

Table D.3A: Alloy 3 Undercooling calculations

Melt	ΔT_r (K)	ΔT_c (K)	ΔT_{tot} (K)	ΔT_E (K)	$\Delta T'_E$ (K)
Cast	0.47	7.82	8.29	4.5	3.3
E-B 1	1.35	13.2	14.5	4.5	8.7
E-B 2	1.42	13.5	15.0	4.5	9.0
E-B 3	2.34	16.7	19.0	4.5	12.2
E-B 4	4.18	20.5	24.7	4.5	16.0
E-B 5	5.93	22.8	28.7	4.5	18.3
E-B 6	7.80	24.6	32.4	4.5	20.1

Table D.3B: Alloy 3 Segregation calculations

Melt	C^*_L	f_{o_s}	f_E	A_P	A_S	F_s
Cast	26.00	0.27	0.48	0.52	0.33	0.85
E-B 1	26.96	0.43	0.36	0.64	0.25	0.89
E-B 2	27.03	0.44	0.36	0.64	0.25	0.89
E-B 3	27.59	0.54	0.29	0.71	0.20	0.91
E-B 4	28.27	0.64	0.22	0.78	0.15	0.93
E-B 5	28.67	0.70	0.18	0.82	0.12	0.94
E-B 6	29.99	0.76	0.17	0.83	0.12	0.94

Table D3.C: Alloy 3 % Primary and secondary phases

Solidification Condition	F_P	F_S	F_T	A_P	A_S	A_T
Equilibrium	0	32	32	-	-	68
Scheil	0	23.6	23.6	26.0	50.3	76.3
Cast	0	14.9	14.9	52.0	33.1	85.1
E-B 1	0	11.6	11.6	64.0	24.8	88.8
E-B 2	0	11.6	11.6	64.0	24.8	88.8
E-B 3	0	9.00	9.00	71.0	20.0	91.0
E-B 4	0	6.82	6.82	78.0	15.1	93.2
E-B 5	0	5.58	5.58	82.0	12.4	94.4
E-B 6	0	5.30	5.30	83.0	11.7	94.7

Table D.4A: Alloy 4-A (metastable austenite) undercooling calculations

Melt	ΔT_r (K)	ΔT_c (K)	ΔT_{tot} (K)	ΔT_E (K)	$\Delta T'_E$ (K)
Cast	0.487	8.04	8.52	-3.8	11.8
E-B 1	1.37	13.5	14.9	-3.8	17.3
E-B 2	1.44	13.9	15.3	-3.8	17.7
E-B 3	2.38	17.6	19.5	-3.8	21.4
E-B 4	4.25	21.1	25.3	-3.8	24.9
E-B 5	6.03	23.4	29.4	-3.8	27.2
E-B 6	8.0	25.0	33.0	-3.8	28.8

Table D.4B: Alloy 4-A (metastable austenite) segregation calculations

Melt	C^*_L	f_{o_s}	f_E	A_P	A_S	F_s
Cast	26.84	-	-	-	-	-
E-B 1	27.82	-	-	-	-	-
E-B 2	27.88	0.51	0.49	0.51	0.33	0.16
E-B 3	28.46	0.61	0.49	0.51	0.33	0.12
E-B 4	29.17	0.72	0.28	0.72	0.19	0.09
E-B 5	29.59	0.78	0.22	0.78	0.15	0.07
E-B 6	29.8	0.81	0.19	0.81	0.13	0.06

Table D4.C: Alloy 4-A (metastable austenite) % Primary and secondary phases

Solidification Condition	F_P	F_S	F_T	A_P	A_S	A_T
Equilibrium	-	-	-	-	-	-
Scheil	-	-	-	-	-	-
Cast	-	-	-	-	-	-
E-B 1	-	-	-	-	-	-
E-B 2	0	16.0	16.0	51.0	33.0	84.0
E-B 3	0	12.0	12.0	61.0	27.0	88.0
E-B 4	0	9.0	9.0	72.0	19.0	91.0
E-B 5	0	7.0	7.0	78.0	15.0	93.0
E-B 6	0	6.0	6.0	81.0	13.0	94.0

Table D.4D: Alloy 4-F Undercooling calculations

Melt	ΔT_r (K)	ΔT_c (K)	ΔT_{tot} (K)	ΔT_E (K)	$\Delta T'_E$ (K)
Cast	0.35	6.80	7.15	0.7	6.1
E-B 1	1.05	12.3	13.4	0.7	11.6
E-B 2	1.10	12.9	14.0	0.7	12.2
E-B 3	1.75	15.9	17.7	0.7	15.2
E-B 4	3.20	20.5	23.7	0.7	19.8
E-B 5	5.00	23.2	28.3	0.7	22.5
E-B 6	6.1	25.5	31.6	0.7	24.8

Table D.4E: Alloy 4-F Segregation calculations

Melt	C_L^*	f_{α}	f_E	F_P	F_S	A_{α}
Cast	16.6	0.22	0.71	0.29	0.51	0.49
E-B 1	17.3	0.37	0.52	0.48	0.64	0.36
E-B 2	17.3	0.38	0.52	0.48	0.64	0.36
E-B 3	17.8	0.47	0.44	0.56	0.70	0.30
E-B 4	18.4	0.58	0.33	0.67	0.77	0.23
E-B 5	18.8	0.65	0.28	0.72	0.81	0.19
E-B 6	19.0	0.70	0.23	0.77	0.84	0.16

Table D4.F: Alloy 4-F % Primary and secondary phases

Solidification Condition	F_P	F_S	F_T	A_P	A_S	A_T
Equilibrium	-	-	48	0	52	52
Scheil	8	29.4	37.4	0	62.6	62.6
Cast	29.0	22.0	51.0	0	49.0	49.0
E-B 1	48.0	16.1	64.1	0	35.9	35.9
E-B 2	48.0	16.1	64.1	0	35.9	35.9
E-B 3	56.0	13.6	69.6	0	30.3	30.3
E-B 4	67.0	10.2	77.2	0	22.7	22.7
E-B 5	72.0	8.7	80.7	0	19.3	19.3
E-B 6	77.0	7.1	84.1	0	15.9	15.9

Table D.5A: Alloy 5 Undercooling calculations

Melt	ΔT_r (K)	ΔT_c (K)	ΔT_{tot} (K)	ΔT_E (K)	$\Delta T'_E$ (K)
Cast	0.36	6.84	7.21	10.4	-
E-B 1	1.00	11.7	12.7	10.4	1.3
E-B 2	1.06	12.0	13.1	10.4	1.6
E-B 3	1.75	15.2	16.9	10.4	4.8
E-B 4	3.14	19.3	22.4	10.4	8.9
E-B 5	4.47	21.8	26.3	10.4	11.4
E-B 6	6.00	23.0	29.0	10.4	12.6

Table D.5B: Alloy 5 Segregation calculations

Melt	C^*_L	f_o	f_E	F_P	A_S	F_s
Cast	15.32	0.23	0.62	0.38	42.7	42.7
E-B 1	15.98	0.38	0.55	0.45	38.0	38.0
E-B 2	16.03	0.39	0.55	0.45	38.0	38.0
E-B 3	16.46	0.48	0.46	0.54	31.7	31.7
E-B 4	17.00	0.59	0.34	0.66	23.4	23.4
E-B 5	17.35	0.65	0.29	0.71	20.0	20.0
E-B 6	17.50	0.68	0.25	0.75	17.3	17.3

Table D5.C: Alloy 5 % Primary and secondary phases

Solidification Condition	F_P	F_S	F_T	A_P	A_S	A_T
Equilibrium	-	-	72	0	28	28
Scheil	33.0	21.4	54.4	0	45.6	45.6
Cast	38.0	19.2	57.2	0	42.7	42.7
E-B 1	45.0	17.0	62.0	0	38.0	38.0
E-B 2	45.0	17.0	62.0	0	38.0	38.0
E-B 3	54.0	14.2	68.2	0	31.7	31.7
E-B 4	66.0	10.5	76.5	0	23.4	23.4
E-B 5	71.0	9.00	80.0	0	20.0	20.0
E-B 6	75.0	7.80	82.3	0	17.3	17.3

Table D.6A: Alloy 6 Undercooling calculations

Melt	ΔT_r (K)	ΔT_c (K)	ΔT_{tot} (K)	ΔT_E (K)	$\Delta T'_E$ (K)
Cast	0.35	6.47	6.82	17.0	-
E-B 1	0.98	11.2	12.2	17.0	-
E-B 2	1.03	11.5	12.5	17.0	-
E-B 3	1.70	14.58	16.2	17.0	-
E-B 4	3.05	18.4	21.5	17.0	1.4
E-B 5	4.34	20.8	25.2	17.0	3.8
E-B 6	5.90	22.8	28.7	17.0	5.8

Table D.6B: Alloy 6 Segregation calculations

Melt	C^*_L	f^*_s	f_E	F_P	A_S	F_s
Cast	14.46	0.228	0.48	0.52	0.33	0.15
E-B 1	15.12	0.38	0.46	0.55	0.32	0.14
E-B 2	15.17	0.39	0.46	0.55	0.32	0.14
E-B 3	15.57	0.48	0.46	0.57	0.30	0.13
E-B 4	16.10	0.60	0.36	0.64	0.25	0.11
E-B 5	16.42	0.66	0.29	0.71	0.20	0.09
E-B 6	16.70	0.71	0.23	0.77	0.16	0.07

Table D6.C: Alloy 6 % Primary and secondary phases

Solidification Condition	F_P	F_S	F_T	A_P	A_S	A_T
Equilibrium	-	-	88	0	12	12
Scheil	47.0	17.0	64.0	0	36	36
Cast	52.0	14.8	66.8	0	33.1	33.1
E-B 1	54.0	14.3	68.3	0	31.7	31.7
E-B 2	54.0	14.3	68.3	0	31.7	31.7
E-B 3	57.0	13.3	70.3	0	29.6	29.6
E-B 4	64.0	11.2	75.1	0	24.8	24.8
E-B 5	71.0	9.00	80.0	0	20.0	20.0
E-B 6	77.0	7.13	84.1	0	15.9	15.9

Table D.7A: Alloy 7 Undercooling calculations

Melt	ΔT_r (K)	ΔT_c (K)	ΔT_{tot} (K)	ΔT_E (K)	$\Delta T'_E$ (K)
Cast	0.33	6.21	6.55	24.4	-
E-B 1	0.95	10.7	11.7	24.4	-
E-B 2	1.00	11.0	12.0	24.4	-
E-B 3	1.66	13.9	15.5	24.4	-
E-B 4	2.98	17.5	20.5	24.4	-
E-B 5	4.22	19.8	24.0	24.4	-
E-B 6	5.71	21.9	27.6	24.4	3.2

Table D.7B: Alloy 7 Segregation calculations

Melt	C^*_L	f'_b	f_E	F_b	A_S	F_b
Cast	13.64	0.23	0.37	0.63	0.26	0.12
E-B 1	14.25	0.39	0.36	0.64	0.25	0.11
E-B 2	14.30	0.40	0.56	0.65	0.24	0.11
E-B 3	14.68	0.49	0.33	0.67	0.23	0.10
E-B 4	15.17	0.60	0.29	0.71	0.20	0.09
E-B 5	15.48	0.67	0.25	0.75	0.17	0.08
E-B 6	15.70	0.71	0.21	0.79	0.15	0.07

Table D7.C: Alloy 7 % Primary and secondary phases

Solidification Condition	F_P	F_S	F_T	A_P	A_S	A_T
Equilibrium	100	0	100	0	0	0
Scheil	60.0	13	73.0	0	27	27
Cast	63.0	11.5	74.4	0	25.5	25.5
E-B 1	64.0	11.2	75.1	0	24.8	24.8
E-B 2	65.0	10.9	75.9	0	24.1	24.1
E-B 3	67.0	10.2	77.2	0	22.7	22.7
E-B 4	71.0	9.00	80.0	0	20.0	20.0
E-B 5	75.0	7.8	82.7	0	17.2	17.2
E-B 6	79.0	6.5	85.5	0	14.5	14.5

APPENDIX F

The Composition Of Delta Ferrite

The composition of delta ferrite is an important parameter which can be used to calculate the saturation magnetization of ferrite. In Chapter 3, methods were presented that allowed the iron content of ferrite to be determined as a function of temperature, based on the thermodynamically calculated isothermal sections. This method required the composition of ferrite and austenite to be determined as a function of temperature and these results are presented below.

From the thermodynamically calculated isothermal sections, the compositional end points of the tie lines in the ferrite + austenite field were determined at iron contents in the ferrite phase between 80 and 50 wt.%. These calculations were made at five temperatures from just below the solidus (1400°C) to 950°C. These results are summarized in Table F.1, along with the calculations of the Cr/Ni ratio in the austenite and ferrite phases and the ratio of Fe in the ferrite to Fe in the austenite.

Figure F.1 and F.2 present the % Cr and % Ni in the ferrite. As the temperature decreases the amount of chromium in the ferrite increases while the amount of nickel in the ferrite decreases. Although the average composition changes only a few percent over this temperature range, the Cr/Ni ratio varies considerably because of the countervariant segregation characteristics of Cr and Ni. Figure F.3 shows the increase in Cr/Ni ratio of the ferrite with decreasing temperature. At high temperatures, the Cr/Ni ratio is about four to one and does not vary considerably with Fe content in the ferrite. At 950°C, the Cr/Ni ratio is about 14 for the 70, 60 and 50% Fe alloys and is about 21 for the 80% Fe alloys.

Figure F.4 and F.5 present the % Cr and % Ni in the austenite phase. These data were taken from the austenite tie-line end points which are in equilibrium with ferrite of 80, 70, 60 and 50% iron contents. The trend of Cr and Ni contents in the austenite with temperature is the reverse of that in ferrite. With decreasing temperature, the % Cr in austenite tends to increase or remain constant while the % Ni in austenite decreases. The Cr/Ni ratio of austenite is presented in Fig. F.6 and shows much less of variation with temperature than the Cr/Ni ratio of ferrite. In

austenite, the Cr/Ni ratio varies from a minimum of 1.0 to 4.3 as the temperature decreases from 1400 to 950°C.

The Fe content of the ferrite is the most important parameter For predicting the saturization magnetization of ferrite. Figure F.7 shows the influende of temperature on the ratio of the Fe content of ferrite to the Fe content of austenite. At 1400°C this ratio is close to 1.0 which means that only a small amount of Fe partitions between austenite and ferrite. At 950°C, this ratio varies between 0.82 and 0.96 depending on the amount of Fe in the ferrite. Chapter 3 utilizes this relationship to place limits on the maximum amount of Fe that can be present in ferrite, based on the nominal alloy composition.

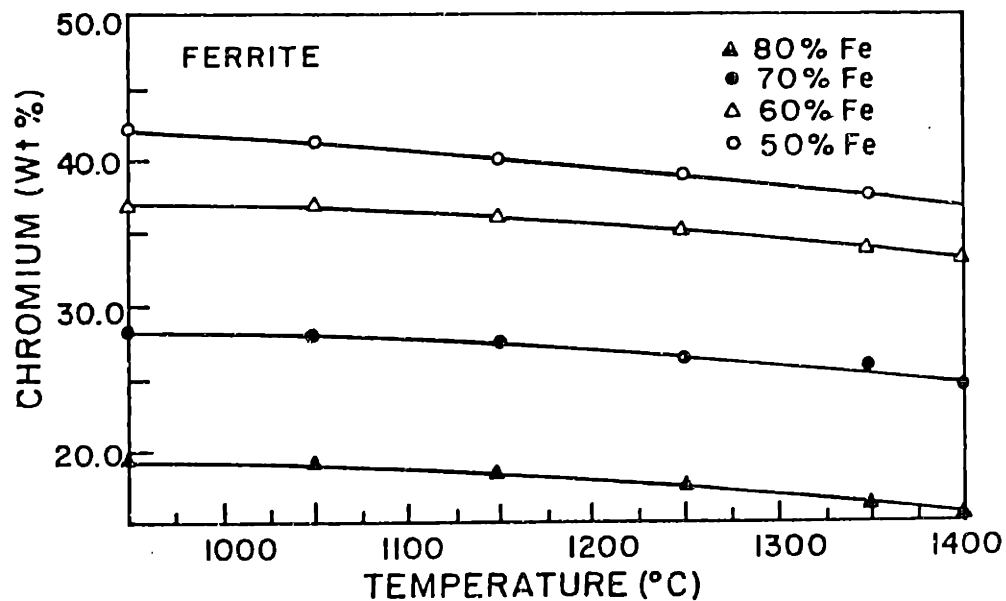


Figure F.1 Thermodynamic calculations of the chromium content in ferrite as a function of temperature and iron content of the ferrite.

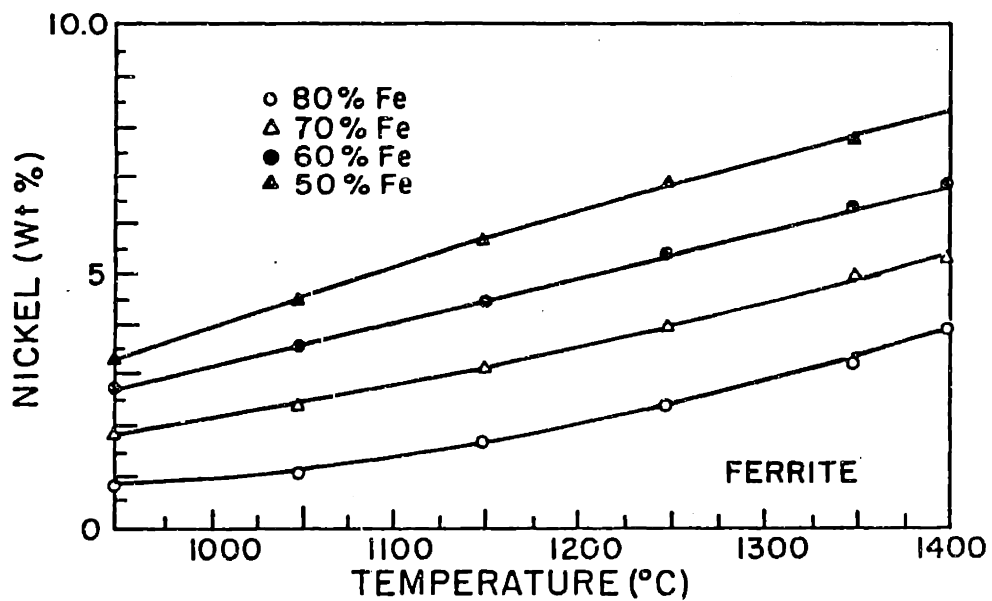


Figure F.2 Thermodynamic calculations of the nickel content in ferrite as a function of temperature and iron content of the ferrite.

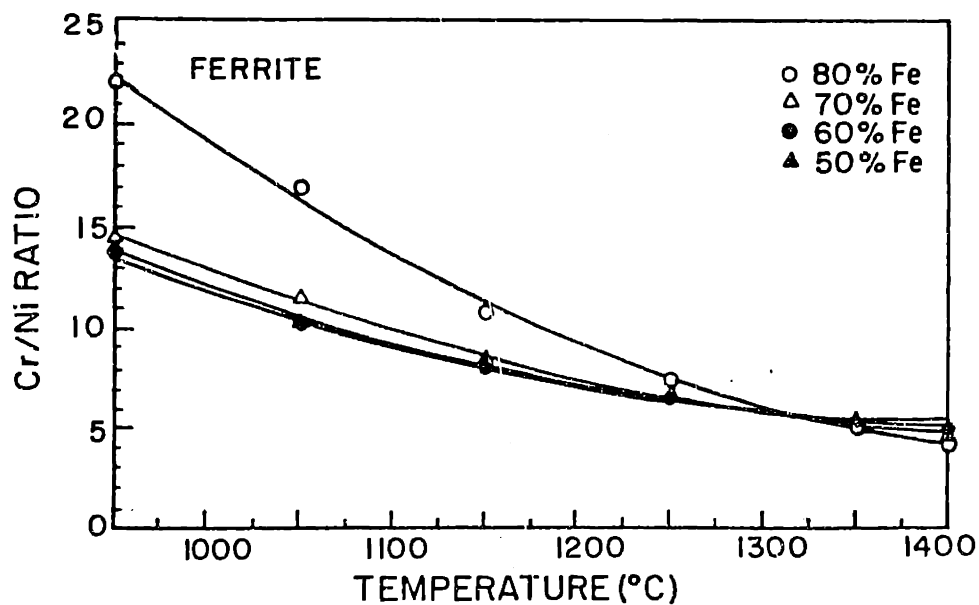


Figure F.3 Thermodynamic calculations of the Cr/Ni ratio of ferrite as a function of temperature and iron content of the ferrite.

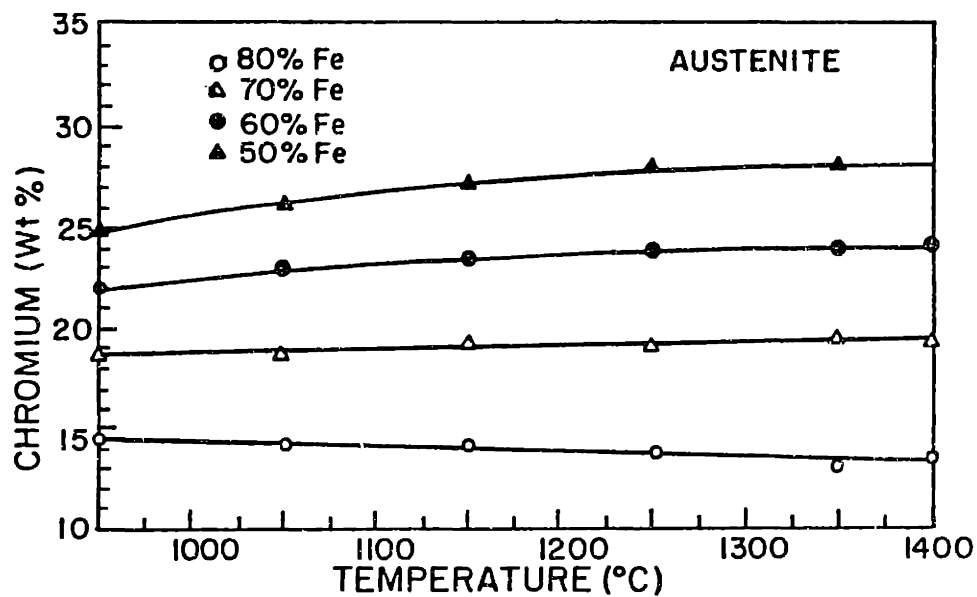


Figure F.4 Thermodynamic calculations of the chromium content in austenite as a function of temperature and iron content of the ferrite.

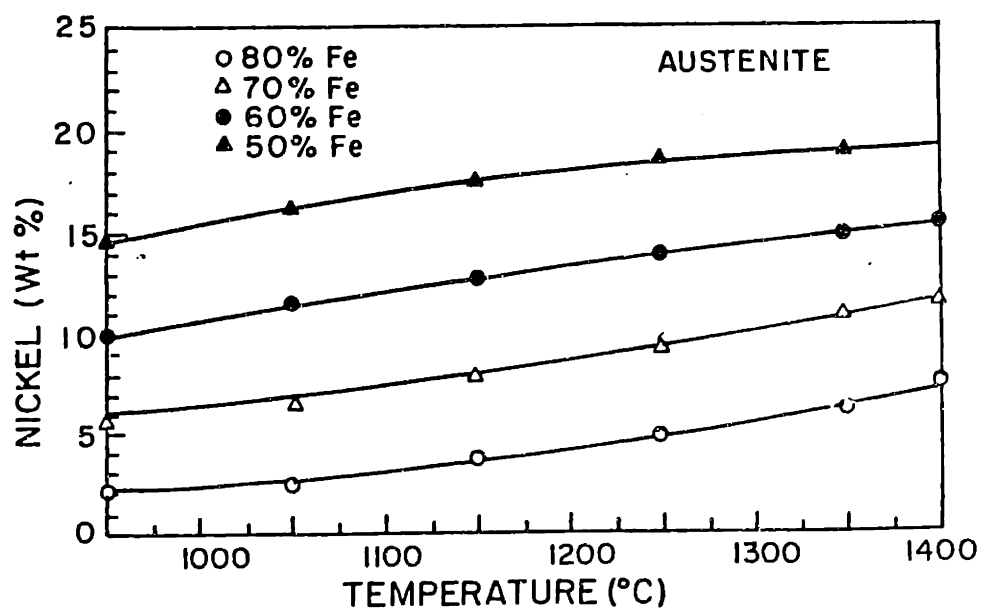


Figure F.5 Thermodynamic calculations of the nickel content in austenite as a function of temperature and iron content of the ferrite.

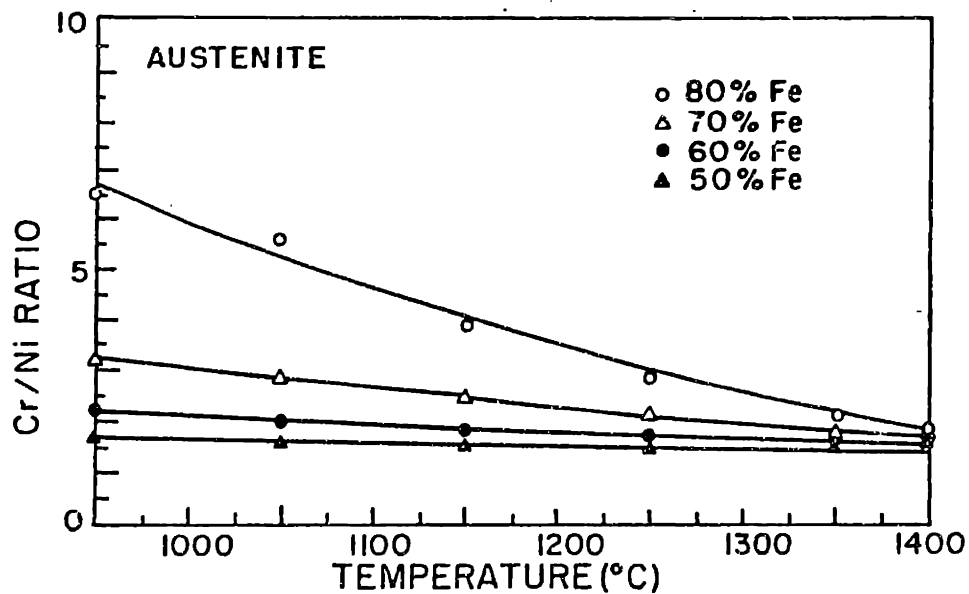


Figure F.6 Thermodynamic calculations of the Cr/Ni ratio in austenite as a function of temperature and iron content of the ferrite.

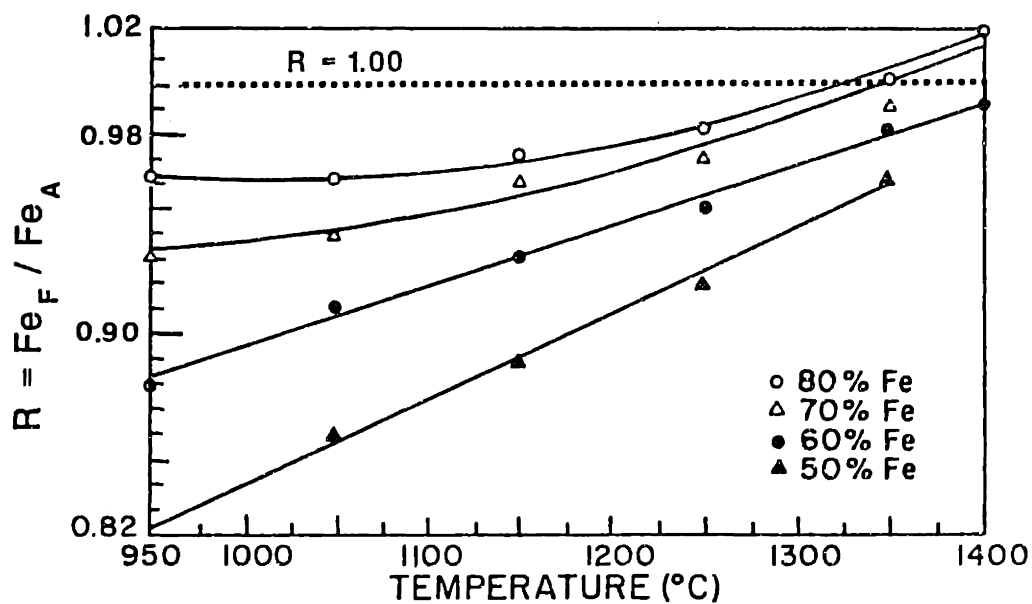


Figure F.7 Thermodynamic calculations of the ratio between the Fe content of ferrite and the Fe content of austenite as a function of temperature and iron content of the ferrite.

APPENDIX G

The Geometry of Electron Beam Surface Melts

Table G.1 summarizes the matrix of electron beam parameters which were used on 304 stainless steel and 6061 aluminum to determine the influence of welding parameters on weld pool shape. This test matrix consisted of three electron beam weld current levels, I , (3,6 and 12 mA), and four travel speeds, S , (6.4, 12.7, 25.4, 50.8 mm/s) at a constant voltage, V , of 100 kV. Through the metallographic examination of the resulting resolidified regions, the influence of travel speed and current on the shape of the molten zone were determined. In addition, by estimating the power density for each of the electron beam parameters, the influence of power density on the depth of penetration was evaluated to show the conditions necessary to form the keyhole penetration mode in high (aluminum) and low (stainless steel) diffusivity alloys.

Melt depth, D , melt width, W , and melt length, L , were measured on each specimen by post-weld metallographic techniques and the results are presented in Table G.2. Since the thermal properties of stainless steel and aluminum are significantly different, each material responds to the electron beam in different ways. To account for the difference in physical properties, the depth, width, and length of each melt was plotted versus the operating parameter, n , in their dimensionless form: DL , DW and DD respectively. This allows the influence of a large range of electron beam parameters to be directly compared by taking into account the travel speed, s , and the thermal diffusivity, α , as defined by Christensen [G.1]:

$$DL = \frac{SL}{2\alpha} \quad (G.1a)$$

$$DW = \frac{SW}{2\alpha} \quad (G.1b)$$

$$DD = \frac{SD}{2\alpha} \quad (G.1c)$$

$$n = \left[\frac{qS}{4\pi\alpha^2 C\theta_m\rho} \right] \quad (G.2)$$

where q = Watts, ρ = density (g/m^3), C = heat capacity ($\text{J/g } ^\circ\text{C}$) and θ_m =melting temperature, ($^\circ\text{C}$). These calculations are summarized in Table G.3 for each of the solidification conditions.

Figure G.1 shows the influence of E-B parameters on melt pool length. Log DL is plotted versus Log n and indicates that Log DL increases linearly with Log n but is independent of travel speed or current at a given operating parameter. Penetration in aluminum and stainless steel both show the same trend with the operating parameter and compare favorably with Christensen's data for GTAW welds.

Figure G.2 shows the influence of E-B parameters on the melt pool depth. Log DD is plotted versus Log n and the results are compared with Christensen's prediction for arc welds. At low current levels, the data are close to Christensen's prediction but the data deviates as the current level is increased. This deviation is caused by an increase in penetration as the electron beam current is increased. At low current levels the electron beam behaves more like a GTA weld which is similar to a point heat source from which Rosenthal [G.2] and Christensen derived their results. At high current levels, the electron beam 'keyholes' into the metal and behaves like a line heat source thus giving more penetration than Christensen would predict.

Figure G.3 shows the influence of E-B parameters on the melt pool width. Log DW is plotted versus Log n and the results are compared to Christensen's reduced width for GTA welds. This plot indicates that the melt width deviates to lower values than the Christensen prediction as the current level is increased. This result follows directly from the previous results. Since DL is independent of beam current and DD increases with increasing current, DW will decrease with increasing current for a constant operating parameter.

The deviation of the EB welds from Christensen's GTA welds is a result of the higher power densities that can be achieved by electron beam welding. These power densities were calculated by estimating the radius of the minimum EBW spot, r^* , for each melt condition, based on the width of the highest speed melt. The results were plotted against the weld aspect ratio (weld depth/weld width) shown in Figure G.4. The 3 mA welds agree with Rosenthal's predicted values. However, as the power density is increased, the aspect ratio increases as the electron beam begins to 'keyhole' into the base metal and the electron beam welds deviate from Christensen's

predictions. The amount of keyholing is also related to the travel speed, and at a constant power density level the weld aspect ratio decreases as the travel speed increases.

Table G1: Heat input

Weld	SST			Al		
	Speed (mm/s)	Current (mA)	Heat (J/mm)	Speed (mm/s)	Current (mA)	Heat (J/mm)
1	6.4	3.5	47	6.4	3.0	55
2		7.0	94		6.0	110
3		14.0	189		12.0	220
4	12.7	3.5	24	12.7	3.0	28
5		7.0	47		6.0	55
6		14.0	94		12.0	110
7	25.4	3.5	12	25.4	3.0	14
8		7.0	24		6.0	28
9		14.0	47		12.0	55
10	50.8	3.5	6	50.8	3.0	6.9
11		7.0	12		6.0	14
12		14.0	24		12.0	28

Table G.2: Weld pool dimensions

Weld	SST			Al		
	Depth (mm)	Width (mm)	Length (mm)	Depth (mm)	Width (mm)	Length (mm)
1	1.16	2.60	1.30	0.80	1.76	0.91
2	3.68	4.00	2.80	2.90	3.00	1.40
3	8.10	3.40	6.00	10.9	3.60	2.10
4	0.51	1.00	1.30	0.62	1.66	1.18
5	1.50	1.20	3.20	2.78	2.80	1.91
6	5.20	2.28	4.60	8.64	3.56	3.50
7	0.61	1.08	1.50	0.61	1.58	0.81
8	1.68	1.46	3.10	2.25	2.34	2.22
9	3.60	1.80	5.30	6.45	2.54	3.74
10	0.46	0.96	1.60	0.49	1.46	0.76
11	0.95	1.16	3.40	1.80	1.76	1.93
12	2.05	1.46	5.50	4.60	2.20	2.80

Table G.3: Physical properties

Property	units	SST	Al
α	(m ² /s)	4.5x10 ⁻⁶	8.1x10 ⁻⁶
ρ	(g/m ³)	7.9x10 ⁶	2.7
C	(J/g°C)	0.5	1.05
T _m -T _o	(°C)	1425	635

Table G.4: Dimensionless weld pool shape

Weld	SST				Al			
	n	$\frac{SD}{2\alpha}$	$\frac{SW}{2\alpha}$	$\frac{SL}{2\alpha}$	n	$\frac{SD}{2\alpha}$	$\frac{SW}{2\alpha}$	$\frac{SL}{2\alpha}$
1	1.56	0.84	1.84	0.92	0.015	0.032	0.068	0.036
2	3.12	2.60	2.81	1.97	0.029	0.115	0.120	0.075
3	6.25	5.70	2.40	4.23	0.060	0.433	0.142	0.083
4	3.12	0.71	1.40	1.83	0.029	0.049	0.130	0.087
5	6.25	2.10	1.68	4.10	0.060	0.219	0.220	0.150
6	12.5	2.30	3.18	6.48	0.120	0.680	0.280	0.276
7	6.25	1.70	3.02	4.23	0.060	0.096	0.248	0.127
8	12.5	4.69	4.08	8.74	0.120	0.354	0.368	0.350
9	25	10.1	5.02	14.2	0.240	1.02	0.400	0.580
10	12.5	2.57	5.36	9.00	0.120	0.154	0.460	0.239
11	25	5.31	6.48	19.2	0.240	0.567	0.554	0.610
12	50	11.7	8.20	31.0	0.480	1.45	0.692	1.10

Table G.5: Power density

weld	SST			Al		
	VI (kW)	r^* (mm)	$\frac{VI}{\pi r^{*2}}$ (kW/mm ²)	VI (kW)	r^* (mm)	$\frac{VI}{\pi r^{*2}}$ (kW/mm ²)
1	0.35	0.24	1.70	0.30	0.37	0.81
2	0.70	0.29	2.30	0.60	0.48	0.97
3	1.40	0.36	2.95	1.20	0.56	1.42
4	0.35	0.24	1.70	0.30	0.37	0.81
5	0.70	0.29	2.30	0.60	0.48	0.97
6	1.40	0.36	2.95	1.20	0.56	1.42
7	0.35	0.24	1.70	0.30	0.37	0.81
8	0.70	0.29	2.30	0.60	0.48	0.97
9	1.40	0.36	2.95	1.20	0.56	1.42
10	0.35	0.24	1.70	0.30	0.37	0.81
11	0.70	0.29	2.30	0.60	0.48	0.97
12	1.40	0.36	2.95	1.20	0.56	1.42

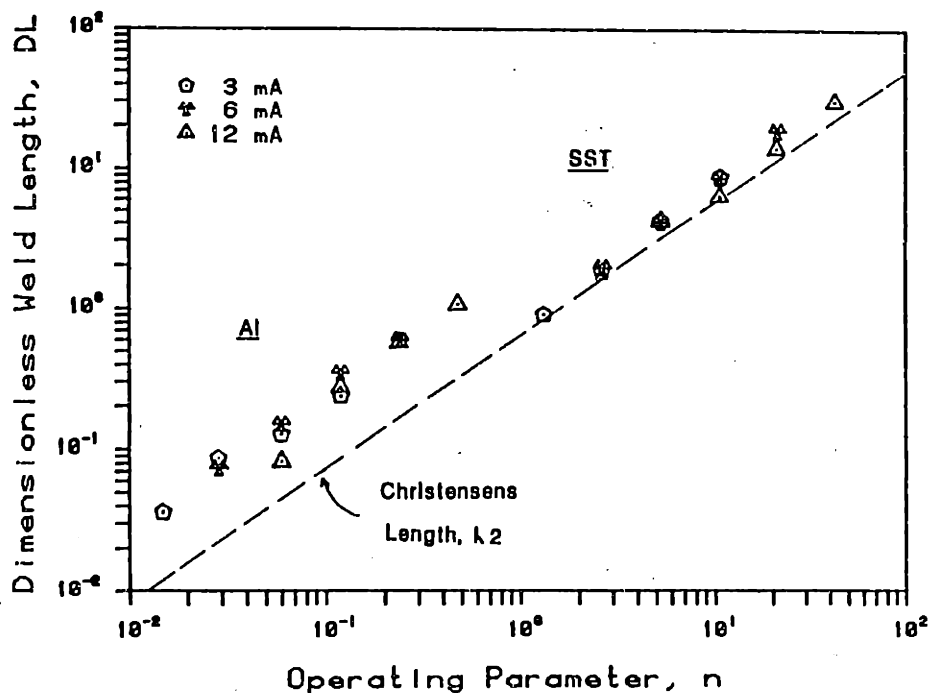


Figure G.1 Dimensionless melt pool length for electron beam surface melts in stainless steel and aluminum, plotted versus the operating parameter. Results for 3, 6, and 12 mA beam currents at 100 kV and various travel speeds are presented.

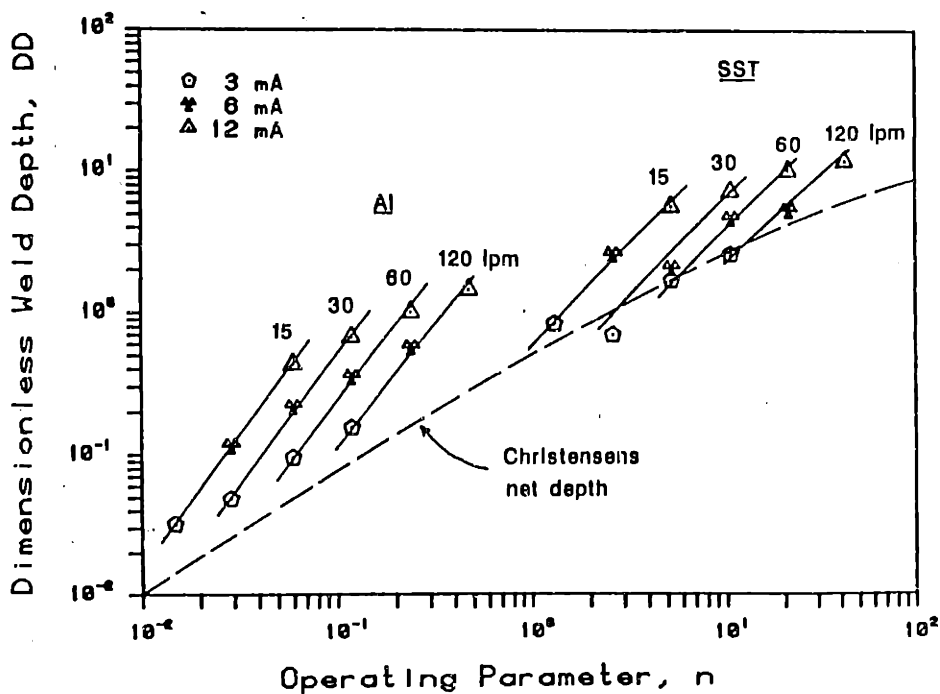


Figure G.2 Dimensionless melt pool depth for electron beam surface melts in stainless steel and aluminum, plotted versus the operating parameter. Results for 3, 6, and 12 mA beam currents at 100 kV and various travel speeds are presented.

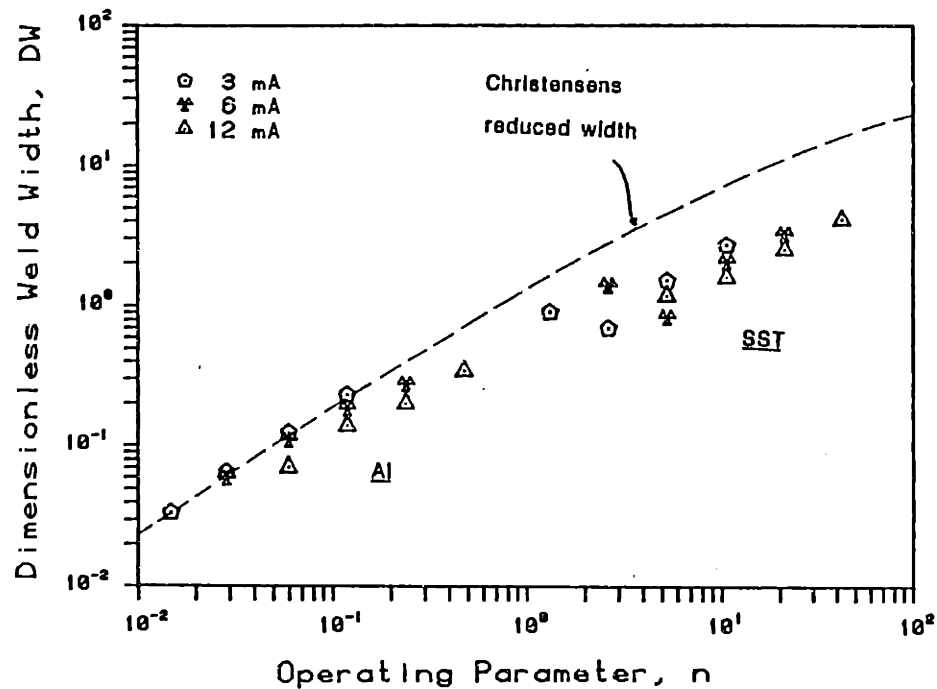


Figure G.3 Dimensionless melt pool width for electron beam surface melts in stainless steel and aluminum, plotted versus the operating parameter. Results for 3, 6, and 12 mA beam currents at 100 kV and various travel speeds are presented.

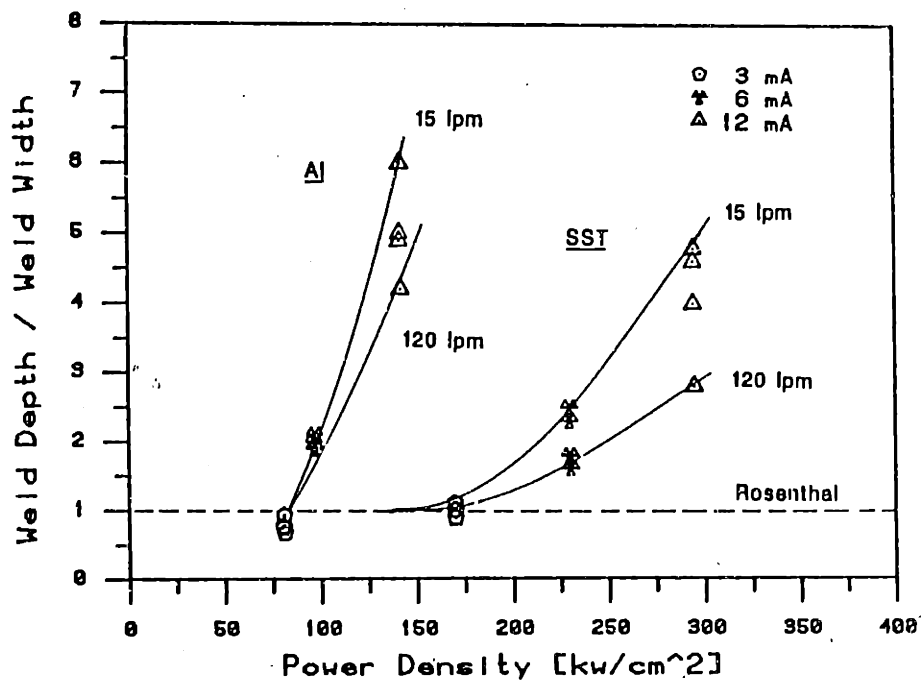


Figure G.4 Melt depth to half-width ratio plotted versus the approximate power density in electron beam melts. Data are plotted for stainless steel and aluminum at 15, 30, 60, and 120 ipm travel speeds. The increased aspect ratio of the melts at high power densities is associated with the formation of a keyhole.

APPENDIX H

Computer Programs

This appendix lists the computer programs that were used to calculate the dendrite tip characteristics (Chapter 7) and the characteristic diffusion distance in the electron beam melts (Chapter 8). These programs were written in Fortran IV on a DEC PDP11.

Dendrite Tip Radius

c This program calculates the characteristics at the tip of a columnar
c dendrite growing under steady-state conditions.

c

c

c

c

J. W. Elmer April, 1988

c

10 a1=8.5733287401

20 a2=18.059016973

30 a3=8.6347608925

40 a4=0.2677737343

c

50 b1=9.5733223454

60 b2=25.632956149

70 b3=21.099653083

80 b4=3.9584969228

c

90 c0=-0.57721566

100 c1=0.99999193

110 c2=-0.24991055

120 c3=.05519968

130 c4=-0.00976004

140 c5=0.00107857

c

150 pi=3.14159265

151 sign=1

c

160 type *, 'Alloy No. '

170 accept *,ial

175 type *, 'Composition (wt.%) '

176 accept *,co

180 type *, 'Liquidus slope (K/%)'

185 accept *,pml

190 type *, 'Partition coeff.'

192 accept *,pk

194 type *, 'Liquidus temp. (K)'

196 accept *,Tl

200 type *, 'Solute diffusivity (m²/s)'

210 accept *,Dl

215 type *, 'Interfacial energy (J/m²)'

```

220 accept *,ss
225 type *,' Entropy of fusion (J/m^3K)'
230 accept *,dS
250 type *,' G (K/m) '
260 accept *,G
c
c
270 print 1003
280 print *,' Alloy Number ',ial
281 print 1001
290 print *,' Co, initial comp. (wt % x)      = ',co
300 print *,' ml, liquidus slope            = ',pml
310 print *,' k, partition coeff.           = ',pk
320 print *,' Tl, liquidus temp. (K)        = ',tl
330 print *,' Dl, solute diffusivity (m^2/s) = ',Dl
340 print *,' s, surface energy (J/m^2)     = ',ss
350 print *,' dS, entropy of fusion (J/m^3K) = ',dS
360 print *,' G, temp. gradient (K/m)       = ',g
365 print 1002
370 print *,'
371 print *,'
372 print 1001
380 print *,' Pc      V      rt      dTr      dTc
      Dt      Tt      Cl**
390 print *,'
      (K)      (K)      (wt%x)'      (m/s)      (m)      (K)      (K)
391 print 1001
c
c
394 ix=1
395 iul=100
396 ill=10
397 istep=-5
398 z=1
399 gt=ss/ds
c
c
High Peclet number (Pc>1) approx
c
400 do 500 ipc= iul,ill,istep
405 pc=float(ipc)/float(ix)
410 piv=(pc**4+a1*pc**3+a2*pc**2+a3*pc+a4)/
      (pc**4+b1*pc**3+b2*pc**2+b3*pc+b4)
420 a=pi**2*gt/(pc**2*d1**2)
430 b=pml*(1-pk)*Co/(d1*(1-(1-pk)*piv))
433 if(sign.eq.-1.) go to 443
435 temp=b**2-4*a*g
436 if (temp.le.0) go to 500
440 v=(-b+ sqrt(temp))/(2*a)
442 go to 450
443 temp =b**2-4*a*g
444 if (temp.le.0) go to 500
445 v=(-b- sqrt(temp))/(2*a)
446 if (v.le.le-07) go to 500
450 r=2*pc*d1/v
460 tr=2*gt/r
470 tc=pml*co*(1-1/(1-(1-pk)*piv))
480 cl=co/(1-(1-pk)*piv)
483 tt=tl-tr-tc
484 Dt=tr+tc
490 print 1000,pc,v,r,tr,tc,Dt,tt,cl
500 continue
c
c
520 if(z.eq.2.) go to 610
530 z=z+1
570 iul=95
580 ill=10
590 istep=-5

```

```

595   ix=10
600   go to 400
c
610   iul=95
620   ill=10
630   istep=-5
635   ix=100
c
c   Low Peclet number (pc<1) approx
c
640   do 790 ipc=iul,ill,istep
643   pc=float(ipc)/float(ix)
650   el=c0+c1*pc+c2*pc**2+c3*pc**3+c4*pc**4+c5*pc**5-alog(pc)
660   piv=pc*exp(pc)*el
670   a=pi**2*gt/(pc**2*d1**2)
680   b=pml*(1-pk)*co/(d1*(1-(1-pk)*piv))
690   if(sign.eq.-1.) go to 715
695   temp= b**2-4*a*g
696   if (temp.le.0) go to 790
700   v=(-b+ sqrt(temp))/(2*a)
710   go to 730
715   temp= b**2-4*a*g
716   if (temp.le.0) go to 790
720   v=(-b-sqrt(temp))/(2*a)
725   if (v.le.le-07) go to 790
730   r=2*pc*d1/v
740   tr=2*gt/r
750   tc=pml*co*(1-1/(1-(1-pk)*piv))
760   cl=co/(1-(1-pk)*piv)
770   tt=t1-tr-tc
772   dt=tr+tc
780   print 1000, pc,v,r,tr,tc,Dt,tt,cl
790   continue
c
820   if (z.eq.3.) go to 900
840   if (z.eq.4.) go to 939
c
850   z=z+1
860   iul=95
870   ill=10
880   istep=-5
885   ix=1000
890   go to 640
c
900   z=z+1
910   iul=95
920   ill=10
930   istep=-5
931   ix=10000
932   if (sign.eq.-1.) go to 990
c
939   print 1003
940   print *,
941   print *,
943   print 1001
950   print *,      Pc      v      rt      dTr      dTc
      DT      Tt      Cl**      (m/s)      (m)      (K)      (K)
      (K)      (K)      (wt%*x)
960   print *,
961   print 1001
970   sign=-1*sign
980   go to 394
990   type *,'Type 99 to quit'
991   accept *,quit
992   sign=-1*sign
993   if (quit.eq.99.) go to 1010

```

LOW VELOCITY BEHAVIOR '
G =',G,'(K/m)'


```
c
275 type *, 'The Diffusion Distance (um) = ',uX
280 print *, 'The Diffusion Distance (um) = ',uX
285 print 1000
290 Type *, 'Try a new Cooling Rate (1=yes, 0=No)'
300 accept *,ans
c
305 sign=-1
310 SmLsq=0
305 X=0
310 uX=0
315 To=Tl
c
320 if (ans.eq.0) go to 1010
330 go to 70
c
c
1000 format (/)
1010 end
```

Biographical Sketch

The author was born in Homestead, Florida on December 9, 1957. He attended elementary school in the South-West United States, living in Arizona and Nevada, before moving to Colorado in 1968. After graduating from Golden High School in 1975, he entered the Colorado School of Mines, in Golden Colorado, where he graduated as a Metallurgical Engineer in 1979. During that time he worked in a cast iron foundry in the Denver area which impressed upon him a desire for higher education.

In September of 1979, the author began graduate school at the Colorado School of Mines and completed a Masters degree in Metallurgical Engineering in 1981. During this time he worked as a Metallurgist in the Fracture and Deformation Division at the National Bureau of Standards in Boulder Colorado, where he performed research on the low-temperature mechanical properties of alloys.

In January of 1982 he joined the staff at Lawrence Livermore National Laboratory, in Livermore California. In the Materials Science Division, he performed short-term research and development projects concerning the metallurgical quality of precision manufactured components. This work dealt with advanced Joining techniques and lead to his interest in the microstructures which develop during the electron beam welding of stainless steel alloys.

In September 1984, the author was admitted to the Doctoral program in the Materials Science and Engineering department at MIT under the guidance of Professor T. W. Eagar. His future plans are to continue research at Lawrence Livermore National Laboratory, with emphasis on the effects that rapid solidification has on the microstructure of metals and alloys.

The author is a member of the American Society for Metals, the American Welding Society, Tau Beta Pi, Sigma Xi, and Alpha Sigma Mu. He is a registered Professional Engineer in Colorado and a registered Metallurgical Engineer in California.